

**NASA
Reference
Publication
1082(04)**

February 1989

Propagation Effects Handbook for Satellite Systems Design

*A Summary of Propagation
Impairments on 10 to 100 GHz
Satellite Links With Techniques
for System Design*

Louis J. Ippolito

Fourth Edition

(NASA-BE-1082(04)) PROPAGATION EFFECTS N89-17060
HANDBOOK FOR SATELLITE SYSTEMS DESIGN. A
SUMMARY OF PROPAGATION IMPAIRMENTS ON 10 TO
100 GHz SATELLITE LINKS WITH TECHNIQUES FOR
SYSTEM DESIGN (Westinghouse Electric Corp.) H1/32 Unclas 0177314

NASA

**NASA
Reference
Publication
1082(04)**

1989

Propagation Effects Handbook for Satellite Systems Design

*A Summary of Propagation
Impairments on 10 to 100 GHz
Satellite Links With Techniques
for System Design*

Louis J. Ippolito
*Westinghouse Electric Corporation
Baltimore, Maryland*

Fourth Edition

NASA

National Aeronautics
and Space Administration

Scientific and Technical
Information Division

Foreword

This fourth edition of the NASA Propagation Effects Handbook for Satellite Systems Design - A Summary of Propagation Impairments on 10 to 100 GHz Satellite Links With Techniques for System Design was prepared by Dr. Louis J. Ippolito of the Westinghouse Electric Corporation, under contract to The NASA Jet Propulsion Laboratory. Dr. Ippolito also coauthored earlier editions of the Handbook published in 1980, 1981, and 1983.

This Handbook was developed under NASA's Radio Science and Support Studies Program, which, with its predecessor programs, has been involved for two decades in the study of radiowave propagation over earth-space paths.

A companion NASA Handbook treats propagation effects at frequencies below 10 GHz (Propagation Effects on Satellite Systems at Frequencies Below 10 GHz - A Handbook for Satellite Systems Design, NASA Reference Publication 1108(02), 1987). Together, these two documents provide a comprehensive description of propagation factors affecting telecommunications systems involving earth-space links.

Earlier editions of the Handbook have enjoyed wide distribution and have served as a useful resource to the systems designer and planner in the evaluation of propagation impairments on satellite links. A NASA review panel, meeting in September, 1986, praised these handbooks and suggested that they be updated every four years, in synchronization with the CCIR cycle. It is our intention to adhere to that recommendation.

The NASA handbooks are evolving documents which strive to provide relevant information for both the propagation specialist and the satellite system designer/planner. Comments or recommendations for additional areas to be covered, or for improving the presentation of material, are always welcome.

John Kiebler, Manager
Radio Science and Support Studies Program
NASA Headquarters

PRECEDING PAGE BLANK NOT FILMED

ABSTRACT

The NASA Propagation Effects Handbook for Satellite Systems Design provides a systematic compilation of the major propagation effects experienced on space-Earth paths in the 10 to 100 GHz frequency band region. The Handbook provides both a detailed description of the propagation phenomena and a summary of the impact of the effect on communications system design and performance.

The dominant effect - path attenuation due to rain - is dealt with in detail, in terms of both experimental data and the mathematical and analytical models devised to explain and predict the data. Other propagation problems covered include; rain and ice depolarization, gaseous attenuation, cloud and fog attenuation, scintillations, angle of arrival, bandwidth coherence, and sky noise.

The Handbook is arranged in two parts to facilitate efficient reference and application of the information. Chapters II through V comprise the descriptive part, which describes the propagation effects, prediction models, and available experimental data bases. Chapters VI and VII make up the system design portion of the Handbook. In Chapter VI design techniques and prediction methods available for evaluating propagation effects on space-Earth communications systems are presented. Chapter VII addresses the system design process and how the effects of propagation on system design and performance should be considered. Chapter VII also covers several mitigation techniques, such as site diversity and adaptive forward error correction (FEC), for overcoming adverse propagation impairments, and describes representative operational and planned K_u , K_a , and EHF satellite communications systems.

PREFACE

In the five years since the previous (third) edition of the NASA Propagation Effects Handbook for Satellite Systems Design was published, there have been many new developments in the analysis and evaluation of propagation effects on space communications links, as well as continuing growth of developmental and operational systems in the K_u , K_a , and EHF frequency bands, for civil, government, and international applications.

Major additions to this edition include:

- o updated versions of prediction models for gaseous attenuation, rain attenuation, and depolarization, including the latest CCIR models,
- o new measured data and propagation statistics,
- o a new fog attenuation prediction procedure,
- o new information on fade duration, low elevation angle effects, and ice depolarization,
- o up-to-date discussions on new technology topics relevant to above 10 GHz satellite communications, including SS/TDMA, beam switching/beam scanning systems, VSAT's, and adaptive mitigation techniques, and
- o descriptions of representative K_u , K_a , and EHF systems, including ACTS, INTELSAT VI, ITALSAT, and Olympus.

Extensive sample calculations and examples are included to highlight key analysis and prediction procedures. A new expanded index has been included to allow rapid access to topics of interest.

The contributions of Les Riddle and Katherine S. Han to Chapter VII of this edition, and the contributions of Roger Kaul, Ron Wallace, and George Kinal to earlier editions, are gratefully acknowledged. The contributions of Dr. Ernest K. Smith, University of Colorado, to Sections 6.8 and 6.9, and to the extensive draft reviews of this document, are also gratefully acknowledged.

Louis J. Ippolito
Senior Advisory Engineer
Westinghouse Electric Corporation
Baltimore, Maryland

TABLE OF CONTENTS

	<u>Page</u>
ABSTRACT	iii
FOREWORD	v
LIST OF COMMON SYMBOLS	xiii
 CHAPTER I. INTRODUCTION	 1-1
1.1 OVERVIEW OF THIS BOOK	1-2
1.2 OVERVIEW OF PROPAGATION EFFECTS	1-3
 CHAPTER II. CHARACTERISTICS OF RAIN AND RAIN SYSTEMS	 2-1
2.1 INTRODUCTION	2-1
2.2 TYPES AND SPATIAL DISTRIBUTIONS OF RAIN	2-2
2.2.1 Stratiform Rain	2-2
2.2.2 Convective Rain	2-2
2.2.3 Cyclonic Storm	2-2
2.2.4 Long-Term Distributions	2-3
2.2.5 Short-Term Horizontal Distributions	2-4
2.2.6 Short-Term Vertical Distributions	2-4
2.3 SPECIFIC RAIN ATTENUATION	2-7
2.3.1 Scattering	2-7
2.3.2 Drop Size Distributions	2-7
2.3.3 Measurement Techniques for Drop Size Distributions	2-10
2.3.4 Estimates of the Specific Attenuation	2-11
2.4 RAINFALL DATA	2-13
2.4.1 U.S. Sources	2-16
2.4.2 Canadian Sources	2-26
2.4.3 Worldwide Sources	2-28
2.5 ESTIMATION OF RAIN RATE	2-28
2.6 REFERENCES	2-33

CHAPTER III.	AN OVERVIEW OF SEVERAL RAIN AND RAIN ATTENUATION MODELS	3-1
3.1	INTRODUCTION	3-1
	3.1.1 Summary of Models	3-1
	3.1.2 Concepts of Rainfall Statistics	3-3
3.2	RICE-HOLMBERG MODEL	3-5
	3.2.1 Types of Storms	3-5
	3.2.2 Sources of Data	3-5
	3.2.3 RH Model Parameters	3-6
	3.2.4 Time Intervals	3-7
	3.2.5 Model Results for One-Minute Intervals	3-8
3.3	DUTTON-DOUGHERTY MODEL	3-12
	3.3.1 DD Rain Characterization	3-12
	3.3.2 Attenuation Prediction in the DD Model	3-15
	3.3.3 Dutton-Dougherty Computer Model	3-17
3.4	THE GLOBAL MODEL	3-17
	3.4.1 Rain Model	3-18
	3.4.2 Description of the Rain Attenuation Region	3-19
	3.4.3 Attenuation Model	3-28
	3.4.4 Application of the Global Model	3-39
3.5	THE TWO-COMPONENT MODEL	3-39
	3.5.1 Volume Cell Rain Rate	3-41
	3.5.2 Debris Rain Rate	3-42
	3.5.3 Probability of Exceeding an Attenuation Threshold	3-43
3.6	THE CCIR MODEL	3-44
	3.6.1 CCIR Rain Characterization	3-44
	3.6.2 CCIR Attenuation Model	3-53
3.7	THE LIN MODEL	3-54
	3.7.1 Empirical Formulas	3-54
	3.7.2 Rain Path Averaging	3-55
	3.7.3 Earth-Satellite Path Length	3-58
3.8	THE SIMPLE ATTENUATION MODEL (SAM)	3-58
3.9	THE EFFECTIVE PATH LENGTH CONCEPT	3-63
	3.9.1 Definition of Effective Path Length	3-63
	3.9.2 Frequency Dependence of Effective Path Length	3-64
	3.9.3 Effective Path Length Versus Measurement Period	3-65
	3.9.4 Comparison of Effective Length Factors	3-67
3.10	REFERENCES	3-72
CHAPTER IV.	DEPOLARIZATION ON EARTH-SPACE PATHS	4-1
4.1	INTRODUCTION	4-1
	4.1.1 Definition of Terms	4-1
	4.1.2 Hydrometeor Sources of Depolarization	4-4
4.2	MATHEMATICAL FORMULATIONS FOR DEPOLARIZATION	4-7
	4.2.1 Specifying the Polarization State of a Wave	4-7

4.2.2	Wave-Antenna Interaction	4-8
4.2.3	Crosspolarization Discrimination (XPD)	4-13
4.2.4	Effect of Non-Ideal Antenna Performance	4-15
4.3	RAIN DEPOLARIZATION	4-23
4.3.1	Theory of Rain Depolarization	4-23
4.3.2	Relationship between Depolarization and Attenuation due to Rain	4-33
4.3.3	Statistical Characteristics of Rain Depolarization	4-39
4.3.4	Experimental Depolarization Data	4-39
4.3.5	Phase of Crosspolarized Signal	4-43
4.3.6	Rate of Change of Depolarization	4-44
4.3.7	Rain Depolarization Dependence on Elevation Angle and Frequency	4-45
4.4	ICE DEPOLARIZATION	4-47
4.4.1	Meteorological Presence of Ice	4-47
4.4.2	Model for Ice Depolarization	4-49
4.5	REFERENCES	4-52
CHAPTER V. PROPAGATION DATA BASES		5-1
5.1	SUMMARIES OF EXPERIMENTAL DATA	5-1
5.2	SATELLITES USED IN PROPAGATION RESEARCH	5-3
5.3	FORMAT OF DATA PRESENTED	5-5
5.4	EXPERIMENTAL CUMULATIVE ATTENUATION STATISTICS	5-8
5.4.1	11.5 - 11.7 GHz Data	5-8
5.4.2	15-16 GHz Data	5-18
5.4.3	19-20 GHz Data	5-22
5.4.4	28-35 GHz Data	5-22
5.4.5	Frequency Scaling of Attenuation Data	5-25
5.5	TEMPORAL DISTRIBUTION OF FADES	5-28
5.5.1	Monthly Distribution of Attenuation	5-28
5.5.2	Diurnal Distribution of Attenuation	5-29
5.6	FADE DURATION	5-32
5.7	EXPERIMENTAL DEPOLARIZATION DATA	5-33
5.7.1	19 GHz Data	5-36
5.7.2	28 GHz Data	5-36
5.7.3	Joint Attenuation - Depolarization Data	5-36
5.8	PHASE AND AMPLITUDE DISPERSION	5-39
5.9	REFERENCES	5-40
CHAPTER VI. PREDICTION TECHNIQUES		6-1
6.1	INTRODUCTION	6-1
6.1.1	Purpose	6-1
6.1.2	Organization of this Chapter	6-2
6.1.3	Frequency Bands for Earth-Space Communication	6-2
6.1.4	Other Propagation Effects Not Addressed in this Chapter	6-5
6.2	PREDICTION OF GASEOUS ATTENUATION ON EARTH-SPACE PATHS	6-6
6.2.1	Sources of Attenuation	6-6

6.2.2	Gaseous Attenuation	6-7
6.2.3	Estimation Procedure for Gaseous Attenuation	6-12
6.2.4	Conversion of Relative Humidity to Water Vapor Density	6-16
6.2.5	A Sample Calculation for Gaseous Attenuation	6-16
6.3	PREDICTION OF CUMULATIVE STATISTICS FOR RAIN ATTENUATION	6-19
6.3.1	General Approaches	6-19
6.3.2	Analytic Estimates of Rain Attenuation from Location and Link Parameters	6-22
6.3.3	Estimates of Attenuation Given Rain Rate Statistics	6-41
6.3.4	Attenuation Estimates Given Limited Rain Rate and Attenuation Statistics	6-43
6.3.5	Fading Duration	6-50
6.3.6	Rate of Change of Attenuation	6-56
6.3.7	Worst-Month Statistics	6-59
6.4	CLOUD, FOG, SAND AND DUST ATTENUATION	6-62
6.4.1	Specific Attenuation of Water Droplets	6-62
6.4.2	Clouds	6-64
6.4.3	Fog	6-71
6.4.4	Sand and Dust Attenuation	6-73
6.5	PREDICTION OF SIGNAL FLUCTUATIONS AND LOW-ANGLE FADING ON EARTH-SPACE PATHS	6-74
6.5.1	Antenna Aperture Effects	6-75
6.5.2	Amplitude Fluctuations	6-76
6.5.3	Phase Variations	6-90
6.5.4	Angle-Of-Arrival Variation	6-94
6.5.5	Fading and Gain Degradation Design Information	6-95
6.5.6	A Sample Computation of Signal Fluctuations and Gain Degradation	6-101
6.6	PREDICTION OF DEPOLARIZATION ON EARTH-SPACE PATHS	6-104
6.6.1	Introduction	6-104
6.6.2	Rain Depolarization	6-106
6.6.3	Ice-Crystal Depolarization	6-115
6.6.4	Other Sources of Depolarization	6-120
6.6.5	Prediction of Depolarization Statistics	6-122
6.7	DISPERSION AND BANDWIDTH COHERENCE EFFECTS	6-126
6.7.1	Tropospheric Effects on Bandwidth Coherence	6-126
6.7.2	Ionospheric Effects on Bandwidth Coherence	6-129
6.8	DOWNLINK NOISE AT EARTH STATIONS	6-130
6.8.1	Introduction	6-130
6.8.2	Clear Air Sky Noise	6-131
6.8.3	Sky Noise Due to Rain	6-136
6.8.4	Sample Calculations	6-136
6.8.5	Sky Noise Due to Clouds, Fog, Sand and Dust	6-139
6.8.6	Total Sky Noise Temperature Arising from Several Contributors	6-140
6.8.7	Extraterrestrial Sources of Sky Noise	6-140
6.9	UPLINK NOISE IN SATELLITE ANTENNAS	6-143
6.9.1	Components of Uplink Noise	6-143
6.9.2	Sample Calculations	6-143
6.10	REFERENCES	6-147

CHAPTER VII.	APPLICATION OF PROPAGATION PREDICTIONS TO EARTH/ SPACE TELECOMMUNICATIONS SYSTEMS DESIGN . . .	7-1
7.1	INTRODUCTION	7-1
7.2	COMMUNICATION SYSTEM PERFORMANCE CRITERIA AND SPECIFIC SATELLITE SYSTEMS	7-7
	7.2.1 Performance Criteria	7-7
	7.2.2 Recent Satellite Technology	7-16
	7.2.3 Representative Systems	7-23
7.3	DESIGN PROCEDURE	7-36
	7.3.1 Introduction	7-36
	7.3.2 Path Performance Versus Overall Channel Performance: Availability Allocation . .	7-37
	7.3.3 Summary of Procedures for Application of Propagation Data	7-40
	7.3.4 Specifics of Application, Initial Phase . .	7-43
	7.3.5 Design Synthesis and Tradeoff Phase	7-46
	7.3.6 Propagation Analysis and Iterations Phase .	7-55
	7.3.7 Supplementary Design Tools	7-70
7.4	RAIN FADE MITIGATION	7-78
	7.4.1 Measures of Diversity Performance	7-80
	7.4.2 Space Diversity	7-83
	7.4.3 Signal Diversity	7-111
	7.4.4 Simultaneous Fade Probabilities	7-121
7.5	REFERENCES	7-123
	SUBJECT INDEX	I-1

LIST OF COMMON SYMBOLS

Note: Throughout the Handbook the following symbols have been employed wherever practicable.

English

a	coefficient in specific attenuation (aRb - dB/km) relation
a	multiplicative coefficient in diversity gain relation (dB)
a	coefficient in XPD relation
a _{1t} , a _{2t} , a _{3t} , a _{4t}	coefficients in DD equations
A	total attenuation (dB)
A _{div}	total attenuation with diversity (dB)
b	coefficient in specific attenuation (aRb - dB/km) relation
b	coefficient in diversity gain relation
b	coefficient in XPD relation
b _{1t} , b _{2t} , b _{3t} , b _{4t} , b _{5t} , b _{6t}	coefficients in DD equations
B	beamwidth (degrees)
B _n	noise bandwidth (Hz)
c	speed of light in free space
C ² _n	Tatarski model coefficient
cm	centimeter
CNR	carrier to noise ratio
CP	circularly polarized

d'	separation between earth terminals
d _a	antenna diameter (m)
D	horizontal projection (basal) length of the path, raindrop diameter, number of hours of rain per year in RH model.
D'	parameter in DD model
DØ(p)	mean square phase variation
DD	Dutton-Dougherty
e	partial pressure of water vapor (mb)
f	frequency (GHz)
f _f	fluctuation frequency (Hz)
F	probability modification factor of Dutton
g	gram
G _D	diversity gain (dB)
G _R	gain reduction (dB)
G/T	performance parameter of a ground station
h	hour
h _p	Planck's constant = 6.626×10^{-34} Watt sec ²
h _t	height of turbulence
H	height of OoC isotherm (km)
I	antenna isolation
I(A)	diversity advantage
I _c	coherent field component in Ishimaru model
I _i	incoherent field component in Ishimaru model
J-D	Joss-drizzle
J-T	Joss-thunderstorm
k	Boltzmann's constant = 1.38×10^{-23} joule/degree
km	kilometer

K_c	specific attenuation per unit water vapor density
K_ϕ	constant in phase variation model
l	effective path length (km)
l_c	effective path length of clouds
l_n	scale length of turbulent eddy (m)
l_o	parameter in Gaussian rain distribution scaling
ℓ	scale length of turbulent eddy (m)
L	path length (km)
L_e	effective path length (km)
L_e'	normalized effective path length (km)
L_o	parameter in turbulence model
L_t	path length through turbulence (km)
LP	Laws and Parsons, linearly polarized
m	meter
m_p	polarization mismatch factor
mm	millimeter
M	average annual rainfall (not including snow)
M'	link margin (dB)
M_d	mass of dry air (kg)
M'_o	no rain link margin (dB)
M_w	mass of water vapor (kg)
MP	Marshall-Palmer
N	refractivity
$\overline{\Delta N^2}$	mean square fluctuations in the refractivity N
N_d	raindrop size distribution function ($m^{-3}mm^{-1}$) or (cm^{-4})
N_o	constant in raindrop size distribution function ($m^{-3}mm^{-1}$) or (cm^{-4})

N_R	number of raindrops at rainrate R
p	pressure (N/m^2)
$P()$	conditional probability
P_{NOISE}	noise power (watts)
$P_t(R)$	percentage of year that t -minute rainfall rates R occur
Q_{1t}, Q_{2t}	parameters in RH rainfall model
r	path averaged rainrate (mm/h), axial ratio
r_e	mean earth radius = 6371 km
R	instantaneous rainrate in mm/h at one location
R_{1t}	parameter in Dutton-Dougherty Model
R_{ave}	path averaged rainrate (mm/h)
R_c	amount of water in a column (kg/m^2)
R_d	dry gas constant (joule/kgK)
R_w	wet gas constant (joules/kgK)
R_{st}	parameter in DD Model
R'_{t}	parameter in DD Model
RH	relative humidity, Rice-Holmberg
s	path length along the path
S^2	signal variance
t	time
T	temperature (K or °C)
T	time period
$T_1, etc.$	instant in time period T
T_{2t}	parameter in DD Model
T_m	mean absorption temperature (K)
T_s	apparent sky temperature (K)

T_{st}	parameter in Dutton-Dougherty Model
$T_t(R)$	number of minutes the rainrate exceeds R for t-minute intervals
v	specific volume (m^3/kg)
v_d	detector voltage
v_c	visibility in fog (km)
XPD	crosspolarization discrimination
XPI	crosspolarization isolation
XPR	crosspolarization ratio

Greek

α	specific attenuation (dB/km), raindrop orientation angle
α_c	specific attenuation for clouds (dB/km)
β	ratio of rainfall during thunderstorms to total rainfall
β'	orientation of earth-terminal baseline
γ	multiplier in path averaged rain rate
δ	exponent in path averaged rain rate
θ	elevation angle, raindrop canting angle
λ	wavelength (m)
Λ	constant in raindrop size distribution function (cm^{-1})
ρ	distance along path (km)
ρ_ϕ	distance between phase variation points (m)
ρ_w	water vapor density (g/m^3)
σ^2_1	amplitude variance
σ^2_2	angle-of-arrival variance (deg^2)
σ^2_x	log-amplitude variance of signal amplitude
σ_ϕ	r.m.s. phase fluctuation

σ_e	r.m.s. phase scintillations
τ	polarization tilt angle
$\Delta\tau$	group delay (m)
\varnothing	azimuthal angle
$\Delta\varnothing$	group delay in radians

CHAPTER I INTRODUCTION

The satellite communications industry is currently in the process of a "frequency evolution", moving from the frequency bands that have been in use for decades, C-Band, X-band, SHF, etc., to the higher allocated bands above 10 GHz. These new bands, designated as K_U band (12-18 GHz), K_a band (27-40 GHz), and EHF (30-300 GHz), offer wider bandwidths, higher data rates, and smaller component sizes, as well as vastly improved anti-jam performance for secure communications applications.

The advantages of these bands can be offset very quickly however, by the realities of increased propagation problems as the frequency of operation is increased. Attenuation caused by rain in the path can be a serious problem, and careful design and adequate "rain margins" are essential for successful system performance.

There are other propagation mechanisms affecting Earth-space communications performance that are also of concern to the systems designer and planner. These include gaseous attenuation; cloud and fog attenuation; rain and ice depolarization; amplitude, phase, and angle-of-arrival scintillation; and sky noise.

The purpose of this Handbook is to provide, in one complete reference source, the latest information on critical propagation effects and how they impact communications system design and performance. NASA, who has supported a large part of the experimental work in radiowave propagation on space communications links, recognized the need for a reference handbook of this type,

and initiated a program in the late 1970's to develop and update a document which will meet this need. This present publication is the fourth edition of the NASA Handbook which focuses on propagation effects from 10 to 100 GHz. A companion handbook (Flock-1987) covers propagation effects on satellite systems at frequencies below 10 GHz.

1.1 OVERVIEW OF THIS BOOK

The NASA Propagation Effects Handbook for Satellite Systems Design provides a concise summary of the major propagation effects experienced on earth-space paths in the 10 to 100 GHz frequency range. The dominant effect--attenuation due to rain--is dealt with in some detail, in terms of both experimental data from measurements and the mathematical and conceptual models devised to explain and predict the data.

Other effects such as clear air attenuation and depolarization are also presented. The estimation of depolarization due to rain and ice has not been developed to the degree required for preparing good design estimates for satellite systems. Therefore, a comprehensive chapter on depolarization has been included that attempts to consolidate the work of several investigators in this area.

The Handbook has been arranged in two parts. Chapters II through V comprise the descriptive part. They deal in some detail with rain systems, rain and attenuation models, depolarization, and experimental data. This descriptive part of the Handbook is intended to provide background for system engineers and planners who want more detail than that presented in the later design chapters.

Chapters VI and VII make up the design part of the Handbook and may be used almost independently of the earlier chapters. In Chapter VI, the design techniques recommended for predicting propagation effects in earth-space communications systems are presented. Some selection has been made from alternative models in

order that only one design technique be utilized. This selection was made based on the ability of the technique to model the experimental results. The chapter includes step-by-step procedures for using the prediction models and numerous examples.

Chapter VII addresses the questions of where in the system design process the effects of propagation should be considered, and what precautions should be taken when applying the propagation results. The unadvised use of propagation results in the link margin can result in overdesign. This chapter bridges the gap between the propagation research data and the classical link budget analysis of earth-space communications system. This chapter presents generalized design procedures, and illustrates their use through extensive examples.

1.2 OVERVIEW OF PROPAGATION EFFECTS

The troposphere, and the hydrometeors (rain, snow, cloud droplets, etc.) it contains, can impair satellite communication links using the bands above 10 GHz in four ways:

Amplitude Reduction

The amplitude of the received signal is reduced from the "free-space" value through absorption and/or scattering by oxygen, water vapor, rain drops, and cloud and fog droplets. Of these, oxygen absorption in the 55-65 GHz band has the largest effect. Attenuation in this band is so great as to make Earth-space communication (at least from the surface) virtually impossible. At frequencies below the oxygen absorption band, water vapor becomes the most prominent attenuating gas. It causes a weak absorption peak (generally less than 1 dB on a vertical path, depending on humidity) in a band around 22 GHz. Both gases also cause appreciable attenuation above the oxygen band. Aside from oxygen absorption around 60 GHz, the greatest attenuation effect comes from rainfall. Because of its severity and unpredictability, rain attenuation rightly receives the most attention in the satellite system design

process for frequencies above 10 GHz. (Accordingly, it also receives the most attention in this Handbook.) Attenuation due to clouds is relatively minor compared to that of rain, but it is normally present for a much larger percentage of the time. It should be considered in systems operating above about 30 GHz, in locations where heavy rain is rare but cloudiness is common. Fog attenuation is not normally of concern in satellite systems because fog layers are relatively thin and do not usually occupy very much of the propagation path.

Thermal Noise Increase

Elementary physics tells us that anything that absorbs electromagnetic energy radiates it as well. The energy radiated by the tropospheric absorbing media (oxygen, water vapor, rain drops, etc.) is incoherent and broadband. It is received by the Earth station antenna along with the downlink signal, and appears at the receiver output as thermal noise - indistinguishable from the thermal noise generated in the receiver front end. The effect of the received noise energy is accounted for by adding a "sky noise" temperature to the Earth station receiver noise temperature. This sky noise temperature turns out to be related to the attenuation that the absorbing medium produces. Disregarding extraterrestrial sources such as the sun, sky noise temperature is zero when the attenuation is zero, and it asymptotically approaches the physical temperature of the medium as the attenuation becomes large. The effect of the thermal noise increase on system performance is to reduce the downlink carrier-to-noise ratio, which has exactly the same effect as an amplitude reduction on the downlink. However, because the thermal noise increase is additive, the magnitude of the effect depends greatly on the Earth station noise temperature in the absence of sky noise. For example, a 100°K sky noise contribution (corresponding to about 2 dB of rain attenuation) would produce a signal-to-noise ratio degradation of 3 dB if the system noise temperature was 100°K without rain, but the same sky noise

contribution would be negligible if the Earth station noise temperature started out at 1000°K.

Interference Increase

Systems that employ orthogonal polarizations to reuse the spectrum are subject to self-interference through crosstalk between the oppositely-polarized channels. The degree of self-interference is established by satellite and Earth station antenna performance, and by the depolarizing effects of rain drops and ice crystals in the path. Rain depolarization increases with rain rate and frequency and is well-correlated with rain attenuation. Depolarization from high-altitude ice clouds is normally associated with thunderstorms but can occur in the absence of rain attenuation. The effect of depolarization on the communication channel depends on the type of modulation used. For example, a given degree of depolarization will produce a greater increase in bit error rate on a digital link using QPSK than it would with BPSK. The effect of depolarization interference is fundamentally different from the amplitude reduction or noise increase propagation effects in that increasing the link power does not reduce the interference. This is because a power increase raises the level of the desired and the interfering signals simultaneously. Crosspolarization can be reduced, however, by employing a special adaptive rotation network on the antenna feed. Another type of interference that can be made worse by propagation effects is intersystem interference. Rain can cause scattering of electromagnetic energy out of the line-of-sight, resulting in increased leakage of uplink power into the receive beam of an adjacent satellite, or between terrestrial line-of-site systems and low-angle Earth station antennas.

Signal Modulation

Earth stations operating at low elevation angles are subject to scintillation caused by tropospheric turbulence. This consists of fast random fluctuations in the amplitude and phase of the signal. The effects of scintillations on the channel depend on the type of

modulation used and the receiver AGC performance. The power spectrum of the fluctuation falls off quickly with increasing frequency, so the effects should be expected to be primarily brief signal drop-outs or losses of synchronization, rather than any actual modulation of the information-carrying waveforms.

Propagation impairments are dependent on the following:

Operating Frequency. With the exception of signal attenuation by gaseous absorption lines, the severity of tropospheric impairments increases with frequency.

Antenna Elevation Angle and Polarization. The length of the part of the propagation path passing through the troposphere varies inversely with elevation angle. Accordingly, propagation losses, noise, and depolarization also increase with decreasing elevation angle. Rain attenuation is slightly polarization-sensitive. Depolarization is also polarization-sensitive, with circular polarization being the most susceptible.

Earth Station Altitude. Because less of the troposphere is included in paths from higher altitude sites, impairments are less.

Earth Station Noise Temperature. This determines the relative contribution of sky noise temperature to system noise temperature, and thus the effect of sky noise on the downlink signal-to-noise ratio.

Local Meteorology. The amount and nature of the rainfall in the vicinity of the Earth station are the primary factors in determining the frequency and extent of most propagation impairments. Rain-caused impairments depend on the rate of rain fall, so how the rain tends to fall (thunderstorms versus steady showers) is as important as the cumulative amount of rainfall. The type and extent of cloud cover, and local humidity characteristics, are other meteorological factors that determine the magnitude of propagation impairments.

Figure 1-1 shows the magnitude and variation of three significant tropospheric propagation effects: rain attenuation, sky noise due to rain, and rain depolarization. These are presented in

terms of their estimated exceedance statistics. The curves give the approximate percentage of an average year in which the magnitude of the effect exceeds the value given on the horizontal axis. The first plot gives rain attenuation for three frequencies: 14, 20 and 30 GHz. The second plot shows the signal-to-noise ratio degradation caused by rain attenuation and the accompanying sky noise increase. This is shown for 30 GHz, with three values of Earth station receiver noise temperature. The third plot is the cross-polarization isolation (XPI), assuming that the antenna's axial ratio is 0.4 dB. XPI is the ratio of the power received in one of the polarization channels to the "cross talk" power from the oppositely-polarized channel. The plot also gives, for two digital modulation schemes, the reduction in signal to noise density ratio that would have an effect on bit error rate equivalent to that of the cross-polarized interference.

The predictions shown in Figure 1-1 were derived using the procedures presented in this Handbook. The rain attenuation statistics were computed using the Global Model, following the steps outlined in Section 6.3.2. The thermal noise increase due to rain was computed using the formula given in Section 6.7.4. The depolarization curve was based on what is known in this Handbook as the "CCIR Approximation," which is presented in Sections 4.3.2 and 6.6.2. The correspondence between depolarization and equivalent degradation for BPSK and QPSK uses the results of Prabhu (1969).

This brief overview has been intended to introduce the system designer to the range of tropospheric effects to be expected on earth-space links operating at frequencies above 10 GHz so that he or she may more effectively use this Handbook. Other references relating to the general area of radiowave propagation effects include (Ippolito, 1981) (Ippolito, 1986), the IEEE Proceedings on Antennas and Propagation, and Radio Science. An excellent bibliography is also available (Dutton and Steele - 1982) for those seeking further general (or specific) literature.

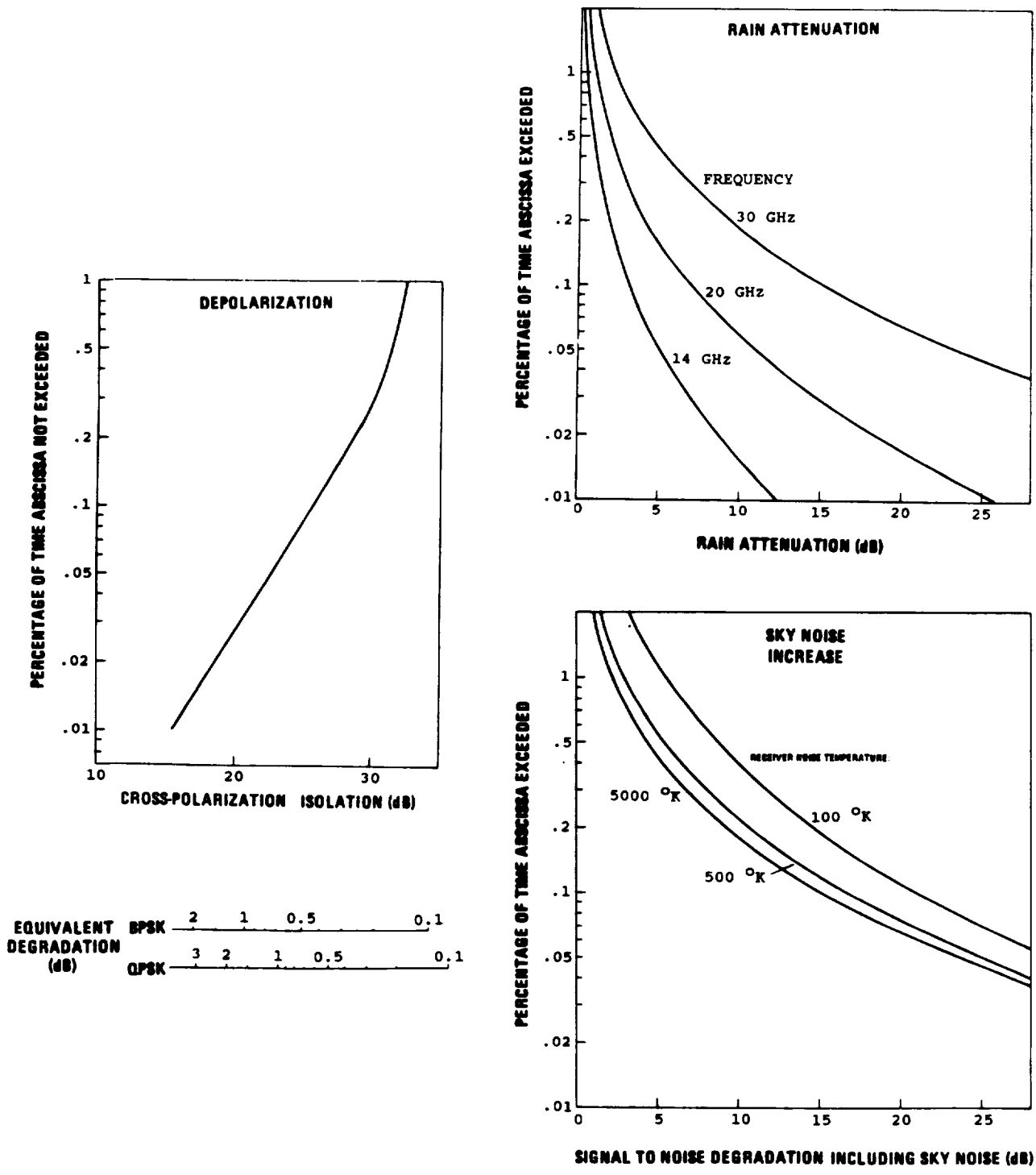


Figure 1-1. Predicted Propagation Impairments for Washington, D.C., at sea level, Elevation Angle = 45.4°

1.3 References

- Dutton, E.J. and F.K. Steele (1982), Bibliography and Synopsis of Literature Concerned with Microwave and Millimeter Wave Propagation Effects, NTIA Report 82-107, U. S. Department of Commerce, September.
- Flock, W.L. (1987), "Propagation Effects on Satellite Systems at Frequencies Below 10 GHz, A Handbook for Satellite Systems Design", NASA Reference Publication 1108(02), Washington, D.C.
- Ippolito, L.J. (1981b), "Radio Propagation for Space Communications Systems," Proceedings of the IEEE, Vol. 69, No. 6 (June), pp. 697-727.
- Ippolito, L.J. (1986), "Radiowave Propagation in Satellite Communications," Van Nostrand Reinhold, New York.
- Prabhu, V.K. (1969), "Error Rate Considerations for Coherent Phase-Shift Keyed Systems with Co-Channel Interferences," BSTJ, Vol. 48, No. 2, pp. 743-767.

CHAPTER II CHARACTERISTICS OF RAIN AND RAIN SYSTEMS

2.1 INTRODUCTION

The attenuating and depolarizing effects of the troposphere, and the statistical nature of these effects, are chiefly determined by both the macroscopic and microscopic characteristics of rain systems. The macroscopic characteristics include items such as the size, distribution and movements of rain cells, the height of melting layers and the presence of ice crystals. The microscopic characteristics include the size distribution, density and oblateness of both rain drops and ice crystals. The combined effect of the characteristics on both scales leads to the cumulative distribution of attenuation and depolarization versus time, the duration of fades and depolarization periods, and the specific attenuation/depolarization versus frequency. In this chapter, we discuss how the characteristics are described and measured, and how the microscopic and macroscopic aspects are statistically related to each other. We also describe how one major propagation effect, specific attenuation, can be estimated. This information will serve as background for the rain and attenuation models of the next chapter.

2.2 TYPES AND SPATIAL DISTRIBUTIONS OF RAIN

2.2.1 Stratiform Rain

In the midlatitude regions, stratiform rainfall is the type of rain which typically shows stratified horizontal extents of hundreds of kilometers, durations exceeding one hour and rain rates less than about 25 mm/h (1 inch/h). This rain type usually occurs during the spring and fall months and results, because of the cooler temperatures, in vertical heights of 4 to 6 km. For communications applications, these stratiform rains represent a rain rate which occurs for a sufficiently long period that the link margin may be required to exceed the attenuation associated with a one-inch per hour (25 mm/h) rain rate. As shown below, this is much easier to do at frequencies below the 22 GHz water absorption line, than for frequencies above the H₂O line.

2.2.2 Convective Rain

Convective rains arise because of vertical atmospheric motions resulting in vertical transport and mixing. The convective flow occurs in a cell whose horizontal extent is usually several kilometers. The cell usually extends to heights greater than the average freezing layer at a given location because of the convective upwelling. The cell may be isolated or embedded in a thunderstorm region associated with a passing weather front. Because of the motion of the front and the sliding motion of the cell along the front, the high rain rate duration is usually only several minutes. These rains are the most common source of high rain rates in the U.S. and Canada.

2.2.3 Cyclonic Storm

Tropical cyclonic storms (hurricanes) often pass over the eastern seaboard during the August-October time period. These circular storms are typically 50 to 200 km in diameter, move at 10-

20 kilometers per hour, extend to melting layer heights up to 8 km and have high (greater than 25 mm/h) rain rates.

2.2.4 Long-Term Distributions

The stratiform and cyclonic rain types cover large geographic locations and so the spatial distribution of total rainfall from one of these storms is expected to be uniform. Likewise the rain rate averaged over several hours is expected to be rather similar for ground sites located up to tens of kilometers apart.

Convective storms, however, are localized and tend to give rise to spatially nonuniform distributions of rainfall and rain rate for a given storm. S.C. Bloch, et al (1978) at EASCON 78, demonstrated an image-enhanced weather radar display which clearly showed the decay and redevelopment of a convective cell while passing over Tampa Bay. Clearly the total rainfall and rain rate varies significantly over the scale of 10 km for this region. The effect is attributed to the presence of the large water mass and the heat-island associated with Tampa.

Over more uniform terrain, Huff and Shipp (1969) have observed precipitation correlation coefficients of 0.95 over 5 mile extents for thunderstorms and rainshowers in Illinois. The correlation was also higher along the path of storm motion compared to perpendicular to the path, as would be expected. This correlation is computed for the period of the storm and is not the instantaneous spatial correlation coefficient required to estimate the effectiveness of ground station site diversity.

Goldhirsh (1983) evaluated five years of rain gauge measurements at Wallops Island, VA, and developed cumulative rain-rate distributions for yearly and combined average time periods. Year to year deviations in the measured rain rates, relative to the five year average, varied between 12 and 20 percent in the percentage interval between .01 and 1.0. The results also showed that the four year and five year averages fit a log normal distribution almost

exactly down to 0.01 percent of the time, corresponding to rain rates up to about 50 mm/h. For larger rain rates, the distribution deviates from the log normal functional representation.

2.2.5 Short-Term Horizontal Distributions

Radars operating at nonattenuating frequencies have been utilized to study both the horizontal and vertical spatial components of convective rain systems. A typical horizontal distribution (actually observed at 1.4 degrees elevation angle) is shown in Figure 2.2-1 for a thunder shower in New England (Crane and Blood - 1979). Here rain rate variations of 100:1 are observed over ranges of 10 km for a shower containing four intense cells. Similar measurements have been made by Goldhirsh (1976), at Wallops Island, VA. Goldhirsh (1976) has also observed that the rain cells are elongated along the northeast-southwest direction (the direction of motion). This direction also correlated well with the average or median wind directions. The impact of this result is that the fading was maximum and the space diversity gain a minimum in the northeast-southwest direction. (Space diversity is described in detail in Chapter VII).

2.2.6 Short-Term Vertical Distributions

The calibrated radars are also ideal for measurement of the vertical profile of rain events. The median reflectivity profiles for a group of rain cells measured from the ground as a function of rain rate is presented in Figure 2.2-2 (Goldhirsh and Katz - 1979). The numbers in parentheses are the number of cells measured and the abscissa is the reflectivity factor based on the relation $Z=200R^{1.6} \text{ mm}^6/\text{m}^3$. These experimental results clearly demonstrate that the rain rate is uniform up to 4 km altitude and then decreases dramatically at altitudes in the 6 to 8 km range. This decrease is also associated with the 0°C isotherm height. Note how the median isotherm height increases with the updraft, convective, high rain rate cells. This effect will be used later in a Global Rain Prediction Model along with the seasonal dependence of the median isotherm height.

Contours 5 dB Apart

Code	log Z	Attenuation (7.78 GHz)	Rate (Z = 200R ^{1.6})
█	5.5	2.1 dB/km	4 in./hr (100 mm/hr)
▣	4.5	0.3 dB/km	1 in./hr (24 mm/hr)
▤	3.5	0.04 dB/km	0.2 in./hr (6 mm/hr)
▥	2.5	0.006 dB/km	0.05 in./hr (1 mm/hr)

WEATHER RADAR DATA
 24 JUL 1967 2052 GMT
 MILLSTONE HILL RADAR
 1.4° EL, 275° - 290° AZ

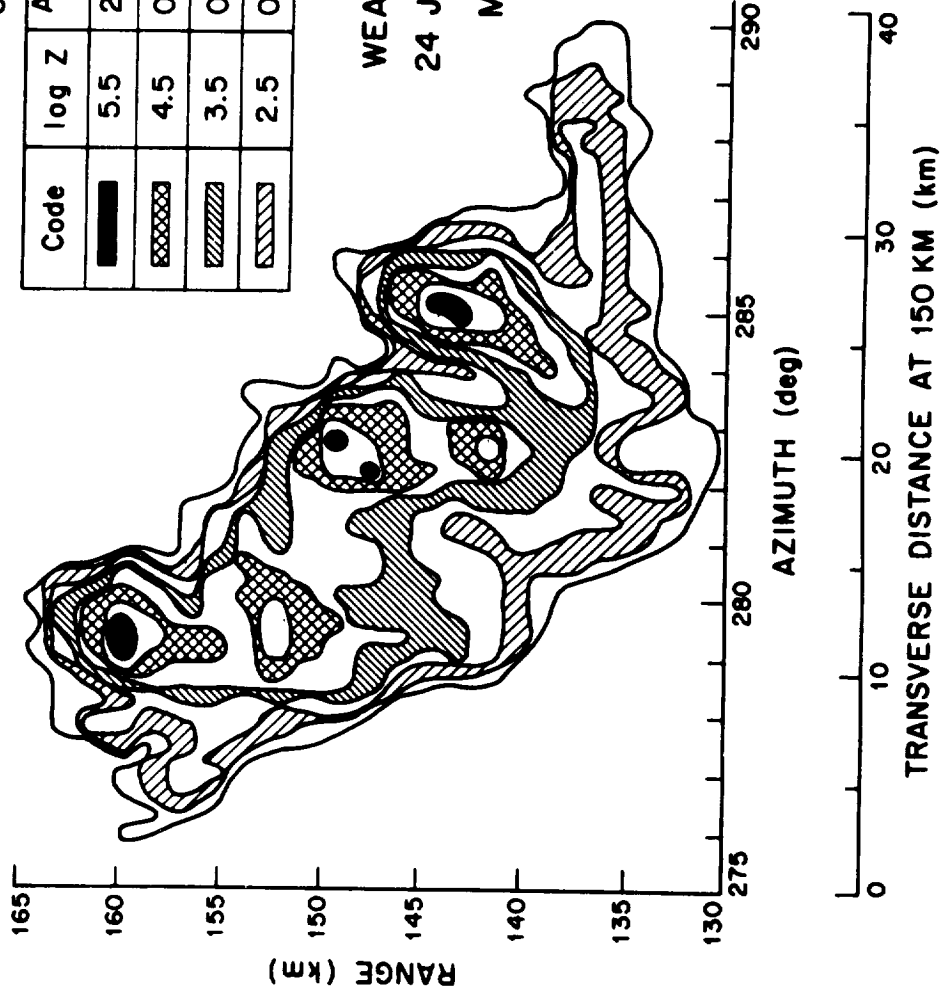


Figure 2.2-1. Weather Radar Map for New England Showers

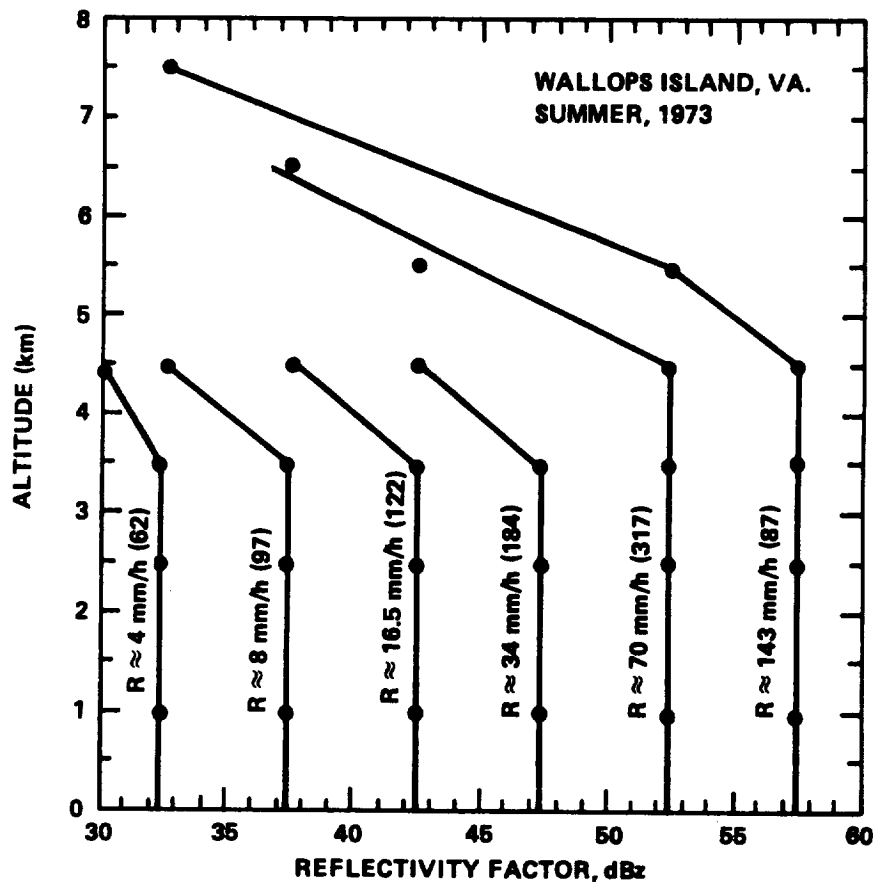


Figure 2.2-2. Median Reflectivity Factor Profiles for Given Rain Rates as Measured at Wallops Island, VA, During Summer of 1973

Above this isotherm, the hydrometeors exist in the form of ice crystals and snow. These forms of hydrometeors do not contribute significantly to the attenuation, but they can give rise to depolarization effects.

2.3 SPECIFIC RAIN ATTENUATION

2.3.1 Scattering

Rain drops both absorb and scatter microwave energy along an earth-space path. From the basic Rayleigh scattering criteria (the dimensions of the scatterer are much smaller than the wavelength) and the fact that the median rain drop diameter is approximately 1.5 mm, one would expect that Rayleigh scattering theory should be applied in the frequency (wavelength) range from 10 GHz (3cm) to 100 GHz (3mm). However, Rayleigh scattering also requires that the imaginary component of the refractive index be small, which is not the case for water drops (Kerker - 1969). Because of this effect and the wide distribution of rain drop diameters, the Rayleigh scattering theory appears to apply only up to 3 GHz (Rogers - 1978). Above 3 GHz Mie scattering applies and is the primary technique utilized for specific rain attenuation (attenuation per unit length, dB/km) calculations. Mie scattering accounts for the deficiencies of Rayleigh scattering and has proven to be the most accurate technique.

2.3.2 Drop Size Distributions

Several investigators have studied the distribution of rain drop sizes as a function of rain rate and type of storm activity. The three most commonly used distributions are

Laws and Parsons (LP)

Marshall-Palmer (MP)

Joss-thunderstorm (J-T) and drizzle (J-D)

In general the Laws and Parsons distribution (Laws and Parsons 1943) is favored for design purposes because it has been widely tested by comparison to measurements for both widespread (lower rain rates) and convective rain (higher rain rates). In the higher rain rate regime (>25 mm/hr) and at frequencies above 10 GHz, the LP values give higher specific rain attenuations (Olsen, et al - 1978) than the J-T values (Joss, et al - 1968). It has been observed that the raindrop temperature is most accurately modeled by the 0°C data rather than 20°C, since for most high elevation angle earth-space links the raindrops are cooler at high altitudes and warm as they fall to earth.

An example of the measured number distribution of raindrops with drop diameter as a function of rain rate R (mm/h) is given in Figure 2.3-1. Here the measurements of Laws and Parsons (1943) and Marshall and Palmer (1948) are fitted by an exponential relation of the form

$$N_D = N_0 e^{-\Lambda D} \text{ cm}^{-4} \quad (2.3-1)$$

where

$$N_0 = 0.08 \text{ cm}^{-4}$$

and

$$\Lambda = 41 R^{-0.21} \text{ cm}^{-1}$$

Note that the units in the equations and Figure 2.3-1 are different. Multiply the N_D obtained from the above formula by 10^5 to convert to the units of Figure 2.3-1. The number of raindrops with diameters between D and D + δD in a volume V (cm^3) at rain rate R is

$$N_R = N_D (\delta D) V \quad (2.3-2)$$

As shown in Figure 2.3-1, the measured data deviates from the exponential relation for diameters below 1.5 mm. However, the larger drops tend to dominate the specific attenuation at the higher rain rates of most concern for the system engineer, and so this deviation tends not to be reflected in the integral over drop diameters utilized in specific attenuation calculations.

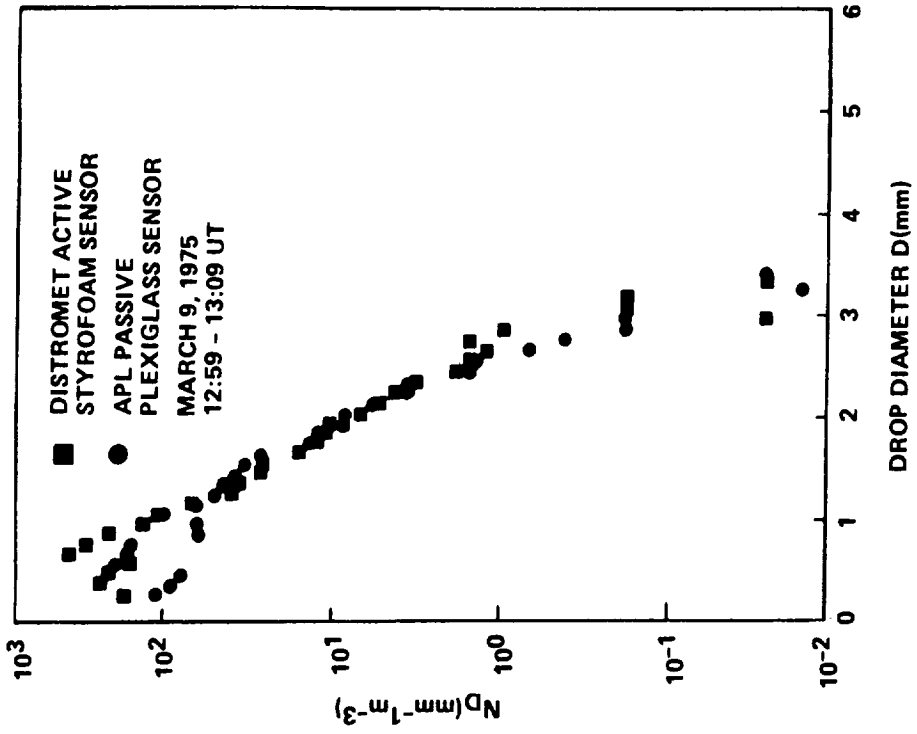


Figure 2.3-2. Raindrop Size Distribution Measured With Two Disdrometers

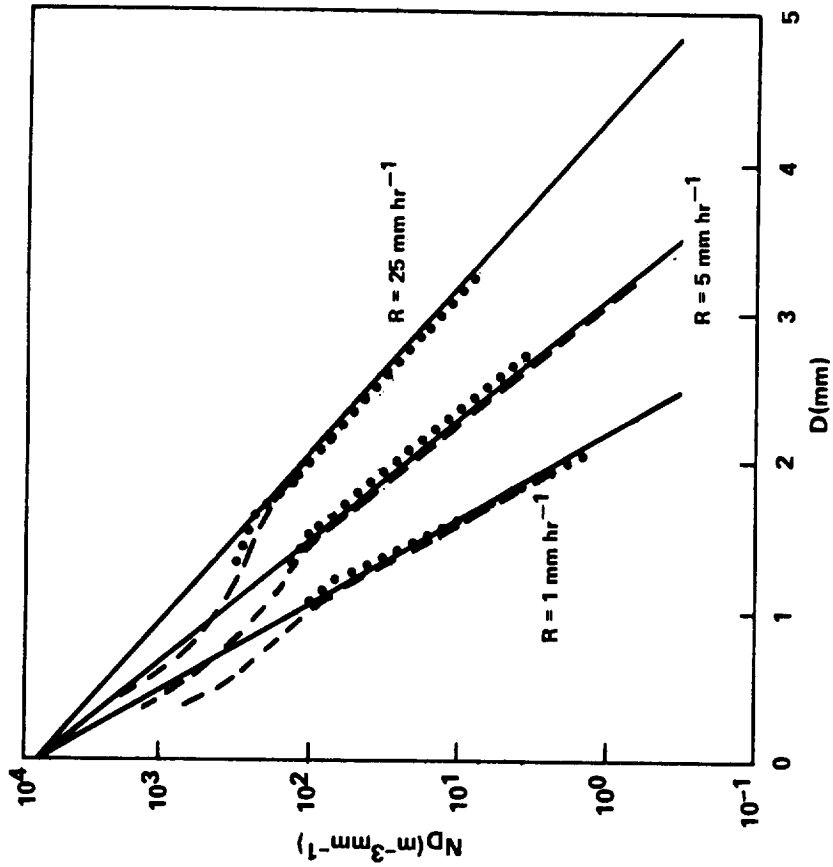


Figure 2.3-1. Rain Drop Size Distribution Function Compared with Experimental Results

Joss, et al (1968) have found significant variations of N_D and Λ for different types of rainfall based on one year's measurements at Locarno, Switzerland. These results are presented in Table 2.3-1; however, the climatic regions where the Joss statistics apply have not been determined. Therefore, it appears best to utilize the Laws and Parsons results, realizing that in certain areas of the U.S. and Canada they have not been verified.

Table 2.3-1. Values of N_0 , Λ Versus Rain Event as Determined by Joss, et al (1968)

Rainfall Type	N_0 (cm^{-4})	Λ (cm^{-1})
drizzle	0.3	57R-0.21
widespread	0.07	41R-0.21
thunderstorm	0.014	30R-0.21

2.3.3 Measurement Techniques for Drop Size Distributions

Experimenters have employed a wide variety of techniques to measure raindrop size distributions in situ. These include: (1) optical systems requiring imaging or scattering light from raindrops, (2) replicating techniques where a permanent record of each drop size is made such as the flour method (Laws and Parsons - 1943), dyed filter paper (Marshall and Palmer - 1948), sugar coated nylon or foil impactors, (3) capacitive techniques due to changing dielectric constant, and (4) impact types of sensors (Rowland - 1976).

Today the impact-type of sensor (called a disdrometer after drop distribution meter), is the favored technique. The Applied Physics Laboratory has developed two styles of disdrometer with decided advantages over the commercially available Distromet Ltd unit. These three types have been described by Rowland (1976) and their calibration has been compared. A typical experimental result for two disdrometers measuring the same rain event on 9 March 1975, is shown in Figure 2.3-2. Note that the data for the APL passive plexiglas sensor which utilizes a piezoelectric crystal to "hear"

the impact of raindrops may be invalid below a 1 mm/h rain rate because of noise in the preamplifier. Normally, this data would more clearly follow the Distromet active styrofoam sensor data.

2.3.4 Estimates of the Specific Attenuation

The scattering properties of raindrops and the dropsize distributions are inputs for the calculation of the attenuation per kilometer (specific attenuation) of a uniform rain at rain rate R.

It has been empirically observed (Ryde and Ryde - 1945, Kerr - 1951) that the specific attenuation α (dB/km) is related to the rain rate R (mm/h) by a relation

$$\alpha = a(f)R^{b(f)} \quad (2.3-3)$$

where the coefficients a and b are functions of frequency.

Olsen, et al (1978) have made extensive calculations of the a and b coefficients. These calculations extend from 1 to 1000 GHz and have been presented in both tabular and graphical format for several raindrop distributions and temperatures. For the U.S. and Canada the 0°C numbers are most applicable (Rogers - 1978). Table 2.3-2 (Olsen, et al 1978) is given below for selected frequencies of interest. The LP_L and LP_H refer to Laws and Parsons drop size distributions associated with rain rates R from 1.27 to 50.8 mm/h and 25.4 to 152.4 mm/h, respectively. Olsen, et al (1978) have also provided analytic approximations for a(f) and b(f) which are quite adequate for systems engineering applications. These are

$$a(f) = 4.21 \times 10^{-5}(f)^{2.42} \quad 2.9 \leq f \leq 54 \text{ GHz} \quad (2.3-4)$$

$$= 4.09 \times 10^{-2}(f)^{0.699} \quad 54 \leq f \leq 180 \text{ GHz}$$

and

$$b(f) = 1.41 (f)^{-0.0779} \quad 8.5 \leq f \leq 25 \text{ GHz} \quad (2.3-5)$$

$$= 2.63 (f)^{-0.272} \quad 25 \leq f \leq 164 \text{ GHz}$$

Table 2.3-2. Regression Calculations for a and b in $\alpha = aR^b$ (dB/km) as Functions of Frequency and Dropsiz Distribution, Rain Temperature = 0°C

FREQ. (GHz)	a					b				
	LP _L	LP _H	MP	J-T	J-D	LP _L	LP _H	MP	J-T	J-D
10	1.17x10 ⁻²	1.14x10 ⁻²	1.36x10 ⁻²	1.69x10 ⁻²	1.14x10 ⁻²	1.178	1.189	1.150	1.076	0.968
11	1.50x10 ⁻²	1.52x10 ⁻²	1.73x10 ⁻²	2.12x10 ⁻²	1.41x10 ⁻²	1.171	1.167	1.143	1.065	0.977
12	1.86x10 ⁻²	1.96x10 ⁻²	2.15x10 ⁻²	2.62x10 ⁻²	1.72x10 ⁻²	1.162	1.150	1.136	1.052	0.985
15	3.21x10 ⁻²	3.47x10 ⁻²	3.68x10 ⁻²	4.66x10 ⁻²	2.82x10 ⁻²	1.142	1.119	1.118	1.010	1.003
19.04	5.59x10 ⁻²	6.24x10 ⁻²	6.42x10 ⁻²	8.68x10 ⁻²	4.76x10 ⁻²	1.123	1.091	1.001	0.957	1.017
19.3	5.77x10 ⁻²	6.46x10 ⁻²	6.62x10 ⁻²	8.99x10 ⁻²	4.90x10 ⁻²	1.122	1.089	1.100	0.954	1.018
20	6.26x10 ⁻²	7.09x10 ⁻²	7.19x10 ⁻²	9.83x10 ⁻²	5.30x10 ⁻²	1.119	1.083	1.097	0.946	1.020
25	0.105	0.132	0.121	0.173	8.61x10 ⁻²	1.094	1.029	1.074	0.884	1.033
28.56	0.144	0.196	0.166	0.243	0.115	1.071	0.983	1.052	0.839	1.041
30	0.162	0.226	0.186	0.274	0.128	1.061	0.964	1.043	0.823	1.044
34.8	0.229	0.340	0.264	0.368	0.177	1.023	0.909	1.008	0.784	1.053
35	0.232	0.345	0.268	0.372	0.180	1.022	0.907	1.007	0.783	1.053
40	0.313	0.467	0.362	0.451	0.241	0.981	0.864	0.972	0.760	1.058
50	0.489	0.669	0.579	0.629	0.387	0.907	0.815	0.905	0.709	1.053
60	0.658	0.796	0.801	0.804	0.558	0.850	0.794	0.851	0.682	1.035
70	0.801	0.869	1.00	0.833	0.740	0.809	0.784	0.812	0.661	1.009
80	0.924	0.913	1.19	0.809	0.922	0.778	0.780	0.781	0.674	0.980
90	1.02	0.945	1.35	0.857	1.10	0.756	0.776	0.753	0.663	0.953
100	1.08	0.966	1.48	0.961	1.26	0.742	0.774	0.730	0.637	0.928

Note: Values for 19.04, 19.3, 28.56 and 34.8 GHz obtained from D. V. Rogers, Comsat Lab., Clarksburg, MD

where f is in GHz. Thus for 20 GHz

$$\alpha = a(f)R^{b(f)} \text{ dB/km} \quad (2.3-6)$$

$$= 4.21 \times 10^{-5} (20)^{2.42} R^{1.41} (20)^{-0.0779} \text{ dB/km}$$

$$= 0.059 R^{1.117} = 2.19 \text{ dB/km @ } R = 25.4 \text{ mm/hr.}$$

The value in Table 2.3-2 for this frequency is $0.0626 R^{1.119} = 2.34$ dB/km @ $R = 25.4$ mm/hr, an error of 6%.

The specific attenuations for several of the common earth-space bands are shown in Figure 2.3-3 for rain rates from 0.1 to 10 inches/h (2.54 to 254 mm/h), calculated using the approximate equations given. The 85 and 94 GHz curves overlap the 50 GHz data because of inaccuracies in the approximations. More accurate results are obtained from interpolation of Table 2.3-2. The CCIR (1986) has recently published tables of coefficients for specific attenuation that show the dependence of specific attenuation on wave polarization. These coefficients are given in Table 2.3-3. The H and V subscripts refer to horizontal and vertical polarization, respectively.

An earlier calculation of the specific attenuation coefficients by Crane (1966) may be compared to the results listed above. Crane employed the Laws and Parsons (1943) number density model to obtain the aR^b power law relation coefficients. The results of these earlier calculations are given in Chapter 3.

2.4 RAINFALL DATA

The largest long-term sources of rainfall data in the U.S. and Canada are their respective weather services. The data collected by these agencies is an excellent starting data base for rain rate estimation. However, in situ measurements are still the most accurate, but quite expensive technique for acquiring rain rate statistics.

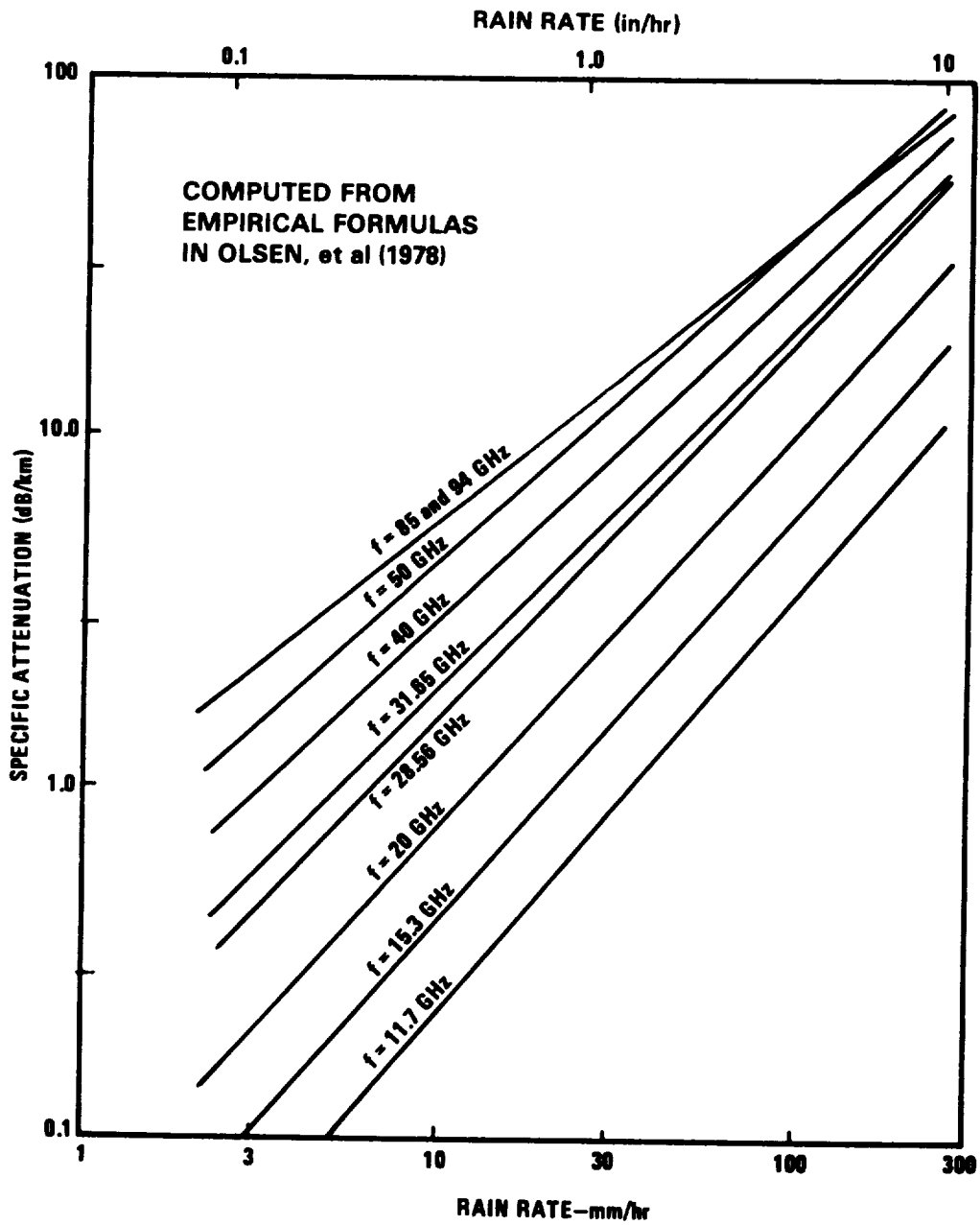


Figure 2.3-3. Specific Attenuation Versus Rain Rate for Common Earth-Space Frequencies

Table 2.3-3. Specific Attenuation Coefficients* (CCIR-1986)

Frequency (GHz)	a_H	a_V	b_H	b_V
1	0.0000387	0.0000352	0.912	0.880
2	0.000154	0.000138	0.963	0.923
3	0.000650	0.000591	1.121	1.075
6	0.00175	0.00155	1.308	1.265
7	0.00301	0.00265	1.332	1.312
8	0.00454	0.00395	1.327	1.310
10	0.0101	0.00887	1.276	1.264
12	0.0188	0.0168	1.217	1.200
15	0.0367	0.0347	1.154	1.128
20	0.0751	0.0691	1.099	1.065
25	0.124	0.113	1.061	1.030
30	0.187	0.167	1.021	1.000
35	0.263	0.233	0.979	0.963
40	0.350	0.310	0.939	0.929
45	0.442	0.393	0.903	0.897
50	0.536	0.479	0.873	0.868
60	0.707	0.642	0.826	0.824
70	0.851	0.784	0.793	0.793
80	0.975	0.906	0.769	0.769
90	1.06	0.999	0.753	0.754
100	1.12	1.06	0.743	0.744
120	1.18	1.13	0.731	0.732
150	1.31	1.27	0.710	0.711
200	1.45	1.42	0.689	0.690
300	1.36	1.35	0.688	0.689
400	1.32	1.31	0.683	0.684

* Values for a and b at other frequencies can be obtained by interpolation using a logarithmic scale for a and frequency and a linear scale for b.

2.4.1 U.S. Sources

2.4.1.1 Published Data. In the U.S., the National Weather Service's National Climatic Center* prepares and maintains extensive precipitation records obtained from Weather Service Offices and over 12,000 observers and agencies. This rain data is available in several documents available from the National Climatic Center. Several of the key publications of interest to the earth-space path engineer are:

- Hourly Precipitation Data (HPD)
 - 15 minute rain rate resolution
 - published monthly by state
 - District of Columbia included in the Virginia HPD
 - available about 6 months following date of recording
 - \$1.95 per copy
 - \$25.40 per year

- Climatological Data (CD)
 - 1 hour rain rate resolution
 - published monthly by state(s)
 - District of Columbia included in the Maryland and Delaware CD
 - Washington National Airport WSO included in the Virginia CD
 - available about 3 months following date of recording
 - \$1.50 per copy
 - \$19.50 per year

- Climatological Data - National Summary, Annual Summary
 - one 5 minute rain rate resolution event per month
 - available about 18 months following last date of recording
 - \$1.50 per copy

*National Climatic Data Center, Federal Building, Asheville, North Carolina 28801, phone (704) 259-0682

- Local Climatological Data (LCD)
 - hourly rain rate resolution
 - published monthly by location
 - available about 4 months following date of recording
 - \$0.65 per copy, \$8.45 per year
 - annual issue also published for each location, \$0.65

- Storm Data
 - published monthly for the U.S.
 - describes type of storm and extent of damage.
 - \$1.05 per copy, \$12.60 per year

The local Climatological Data is available for the 287 stations shown in Table 2.4-1; however, the Hourly Precipitation Data is available for many more stations.

Examples of the precipitation-related data available in each of these publications are given in Figures 2.4-1 to 2.4-4. Comparing the results for either the Baltimore Weather Station Office (WSO) at the Airport (AP) or the Beltsville results, one observes that precipitation data up to 15-minute resolution is available in the HPD's, while the monthly CD lists only the total precipitation per day (see Figure 2.4-2). In the Annual Summary of the National CD (see Figure 2.4-3) the total precipitation, snowfall (all frozen precipitation except hailstones) and the amount and date(s) of the highest precipitation accumulation during the year for periods of 5 to 180 minutes are given. Unfortunately it only includes one 5 minute event per month, only the highest will be indicated in the data. Additional techniques to retrieve more data will be described below.

The Local Climatological Data (LCD) provides the rainfall by hour at each of the 287 stations shown in Table 2.4-1. An example for Asheville, NC, is shown in Figure 2.4-4. In this publication the type of weather is provided so that one can ascertain if the rainfall is from a thunderstorm or a general wide-coverage weather system. The water equivalent of the snow is shown in the hourly

Table 2.4-1. Logical Climatological Data Stations

U.S. DEPARTMENT OF COMMERCE
 NATIONAL OCEANIC AND ATMOSPHERIC ADMINISTRATION
 NATIONAL ENVIRONMENTAL SATELLITE, DATA AND INFORMATION SERVICE

(Stations for which Local Climatological Data are issued, as of January 1, 1982)

ALABAMA	FLORIDA	MASSACHUSETTS	NEW YORK	SOUTH CAROLINA
abc BIRMINGHAM AIRPORT	abc APALACHICOLA	abc BOSTON	abc ALBANY	abc ABE ROSEN III
abc BIRMINGHAM CITY OFFICE	abc DAYTONA BEACH	abc BLUE HILL OBS.	abc BINGHAMTON	abc HURON
abc HUNTSVILLE	abc FORT MYERS	abc WORCESTER	abc BUFFALO	abc RAPID CITY
abc MOBILE	abc JACKSONVILLE		abc NEW YORK CENTRAL PARK	abc SIOUX FALLS
abc MONTGOMERY	abc KEY WEST	MICHIGAN	abc N.Y. J.F. KENNEDY INT'L AIRPORT	MISSOURI
ALASKA	abc MIAMI	abc ALPENA	abc N.Y. LAGUARDIA FIELD	abc SYRACUSE
abc ANCHORAGE	abc ORLANDO	abc DETROIT CITY AIRPORT	abc ROCHESTER	abc SYRACUSE
abc ANNETTE	abc PENSACOLA	abc DETROIT METRO AP		NORTH CAROLINA
abc BARROW	abc TALLAHASSEE	abc FLINT	abc ASHEVILLE	abc BRISTOL
abc BARTER ISLAND	abc TAMPA	abc GRAND RAPIDS	abc CAPE HATTERAS	abc CHATTANOOGA
abc BETHEL	abc WEST PALM BEACH	abc HOUGHTON LAKE	abc CHARLOTTE	abc KNOXVILLE
abc BETTLES		abc LANSING	abc GREENSBORO	abc MEMPHIS
abc BIG DELTA	GEORGIA	abc MARQUETTE	abc RALEIGH	abc NASHVILLE
abc COLD BAY	abc ATHENS	abc MUSKOGON	abc WILMINGTON	abc OAK RIDGE
abc FAIRBANKS	abc ATLANTA	abc SAULT STE. MARIE		TEXAS
abc GULKANA	abc AUGUSTA			abc ABILENE
abc HOMER	abc COLUMBUS	MINNESOTA		abc AMARILLO
abc JUNEAU	abc MACON	abc DULUTH	NORTH DAKOTA	abc AUSTIN
abc KING SALMON	abc SAVANNAH	abc INTERNATIONAL FALLS	abc BISMARK	abc BROWNSVILLE
abc KODIAK		abc MINNEAPOLIS - ST PAUL	abc FARGO	abc CORPUS CHRISTI
abc KOTZEBUE	HAWAII	abc ROCHESTER	abc WILLISTON	abc DALLAS-FORT WORTH
abc McGRATH	abc HILO	abc ST. CLOUD	OHIO	abc DEL RIO
abc NOME	abc HONOLULU		abc AKRON-CANTON	abc EL PASO
abc ST. PAUL ISLAND	abc KAHULUI	MISSISSIPPI	abc CINCINNATI ABBE OBS	abc GALVESTON
abc TALKEEENA	abc LIHUE	abc JACKSON	abc CINCINNATI AIRPORT	abc HOUSTON
abc UNALAKLEET		abc MERIDIAN	abc CLEVELAND	abc LUBBOCK
abc VALDEZ	IDAHO		abc COLUMBUS	abc MIDLAND
abc YAKUTAT	abc BOISE	MISSOURI	abc DAYTON	abc PORT ARTHUR
ARIZONA	abc LEWISTON	abc COLUMBIA	abc MANSFIELD	abc SAN ANGELO
abc FLAGSTAFF	abc POCATELLO	abc KANSAS CITY INT'L AP	abc TOLEDO	abc SAN ANTONIO
abc PHOENIX		abc KANSAS CITY DOWNTOWN AP	abc YOUNGSTOWN	abc VICTORIA
abc TUCSON	ILLINOIS	abc ST. JOSEPH (B)		abc WACO
abc WINSLOW	abc CAIRO	abc ST. LOUIS	OKLAHOMA	abc WICHITA FALLS
abc YUMA	abc CHICAGO O'HARE AIRPORT	abc SPRINGFIELD	abc OKLAHOMA CITY	UTAH
ARKANSAS	abc MOLINE		abc TULSA	abc MILFORD
abc FORT SMITH	abc PEORIA	MONTANA		abc SALT LAKE CITY
abc LITTLE ROCK	abc ROCKFORD	abc BILLINGS	OREGON	VERMONT
abc NO LITTLE ROCK	abc SPRINGFIELD	abc GLASGOW	abc ASTORIA	abc BURLINGTON
CALIFORNIA	INDIANA	abc GREAT FALLS	abc BURNS	VIRGINIA
abc BAKERSFIELD	abc EVANSVILLE	abc HAVRE	abc EUGENE	abc LYNCHBURG
abc BISHOP	abc FORT WAYNE	abc HELENA	abc MEDFORD	abc NORFOLK
abc BLUE CANYON	abc INDIANAPOLIS	abc KALISPELL	abc PENDELTON	abc RICHMOND
abc EUREKA	abc SOUTH BEND	abc MILES CITY	abc PORTLAND	abc RICHMOND
abc FRESNO		abc MISSOULA	abc SALEM	abc ROANOKE
abc LONG BEACH	IOWA		abc SEXTON SUMMIT	abc WALLS ISLAND
abc LOS ANGELES AIRPORT	abc DES MOINES	abc GRAND ISLAND	PACIFIC ISLANDS	WASHINGTON
abc LOS ANGELES CIVIC CENTER	abc DUBUQUE (2)	abc LINCOLN	abc GUAM	abc OLYMPIA
abc MT. SHASTA	abc SIoux CITY	abc NORFOLK	abc JOHNSTON	abc QUILLAYUTE AIRPORT
abc RED BLUFF	abc WATERLOO	abc NORTH PLATTE	abc KODOR	abc SEATTLE-TACOMA AP
abc SACRAMENTO		abc OMAHA	abc KWAJALEIN	abc SEATTLE URBAN SITE
abc SAN DIEGO	KANSAS	abc OMAHA (NORTH)	abc MAJURO	abc SPOKANE
abc SAN FRANCISCO AIRPORT	abc CONCORDIA	abc SCOTT'S BLUFF	abc PAGO PAGO	abc STAMPA DE PASS
abc SAN FRANCISCO CITY	abc DODGE CITY	abc VALENTINE	abc RONAPPE	abc WALLA WALLA
abc SANTA MARIA	abc GOODLAND		abc TRUK (HDEM)	abc YAKIMA
abc STOCKTON	abc TOPEKA	NEVADA	abc WAKE	WEST INDIES
COLORADO	abc WICHITA	abc ELKO	abc YAP	abc SAN JUAN, P. R.
abc ALAMOSA	KENTUCKY	abc ELY		WEST VIRGINIA
abc COLORADO SPRINGS	abc JACKSON	abc LAS VEGAS	PENNSYLVANIA	abc BECKLEY
abc DENVER	abc LEXINGTON	abc RENO	abc ALLENTOWN	abc CHARLESTON
abc GRAND JUNCTION	abc LOUISVILLE	abc WINNEMUCCA	abc AVOCA, WILKES-BARRE SCRANTON AP	abc ELKINS
abc PUEBLO (A)		NEW HAMPSHIRE	abc ERIE	abc HUNTINGTON
CONNECTICUT	LOUISIANA	abc CONCORD	abc HARRISBURG	abc PARKERSBURG
abc BRIDGEPORT	abc BATON ROUGE	abc MT. WASHINGTON	abc PHILADELPHIA	
abc HARTFORD	abc LAKE CHARLES	NEW JERSEY	abc PITTSBURGH AIRPORT	WISCONSIN
DELAWARE	abc NEW ORLEANS	abc ATLANTIC CITY AIRPORT	abc WILLIAMSPORT	abc GREEN BAY
abc WILMINGTON	abc SHREVEPORT	abc ATLANTIC CITY STATE MARINA		abc LA CROSSE
DISTRICT OF COLUMBIA		abc NEWARK	RHODE ISLAND	abc MADISON
abc WASHINGTON - NATIONAL AP	MAINE	abc TRENTON (B)	abc BLOCK ISLAND	abc MILWAUKEE
abc WASHINGTON - DULLES INT'L AP	abc CARIBOU	NEW MEXICO	abc PROVIDENCE	WYOMING
	abc PORTLAND	abc ALBUQUERQUE	SOUTH CAROLINA	abc CASPER
	MARYLAND	abc CLAYTON	abc CHARLESTON AIRPORT	abc CHEYENNE
	abc BALTIMORE	abc ROSWELL	abc CHARLESTON CITY	abc LANDER
			abc GREENVILLE SPARTANBURG	abc SHERIDAN

a. Monthly summary issued.

b. Monthly summary includes available 3-hourly observations.

c. Annual Summary issued.

SUBSCRIPTION: Price and ordering information available through: National Climatic Center, Federal Building Asheville, North Carolina 28801, ATTN: Publications.

- (1) NWS Operations Terminated September 1, 1981. Publications Discontinued.
- (2) NWS Operations Terminated September 4, 1981. Publications Discontinued.
- (3) NWS Operations Terminated November 1, 1981. Publications Discontinued.
- (4) NWS Operations Terminated January 1, 1982. Publications Discontinued.
- (5) NWS Operations Terminated December 1, 1981. Publications Discontinued.

precipitation data. Note that the same information is available on the Hourly Precipitation Data records but that the type of rainfall event is not noted in the latter.

Finally the National Climatic Center prepares a Storm Summary on a monthly basis. This information is of little value to system engineers since it emphasizes the damage done by the storm rather than the meteorological parameters of the storm. For example, the most severe rain event in Asheville, NC, in 1975 occurred on August 24; however, this event is not indicated in the Storm Summary because it apparently caused no significant damage.

2.4.1.2 Rain Gauges. If more information is desired regarding higher rain rates associated with thunderstorms it can be obtained for most first-order Weather Service Office (defined as those offices manned by Weather Service personnel) sites. These sites generally have both tipping bucket and universal weighing gauge precipitation monitors. The tipping bucket gauges generally accumulate the number of 0.01 inch precipitation events in a day which is utilized to collaborate with the accumulation in the other gauges. However, some tipping bucket gauges employ a readout strip chart (triple register chart of operations recorder register) similar to that shown in Figure 2.4-5. By estimating the time between tips the rain rate may be estimated. The location of those stations having triple register charts was not available from the National Climatic Center.

The universal weighing gauge is also capable of providing rain rate information and is the main instrument utilized to provide the 5-minute to 1 hour precipitation data. This measurement is accomplished by reading directly from the 24-hour strip chart on the gauge. An example of one of these strip charts is shown in Figure 2.4-6. These charts are available dating back about 10 years from the National Climatic Center for 25 cents per chart. By measuring the slope of the line, the rain rate to at least 5 minute resolution may be obtained and even 1-minute rain rates may be inferred from

ORIGINAL PAGE IS
OF POOR QUALITY

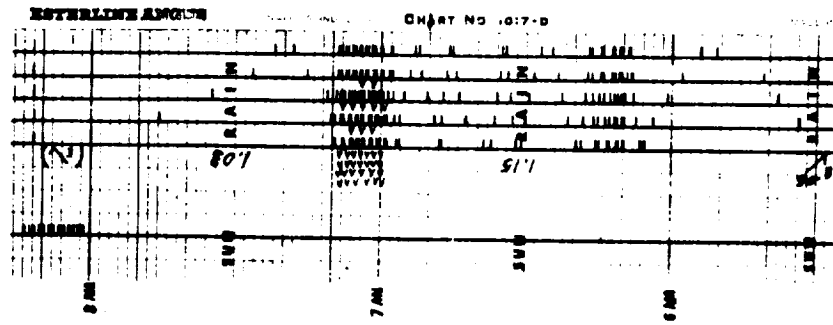


Figure 2.4-5. Example of Operations Recorder Record (from N.W.S. Field Measurements Handbook, No. 1, PG B7-9)

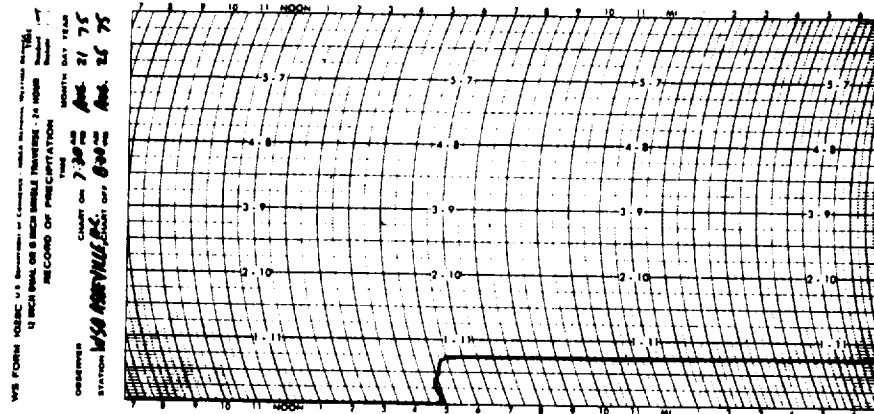


Figure 2.4-6. An Example of a Universal Weighing Gauge Strip Chart

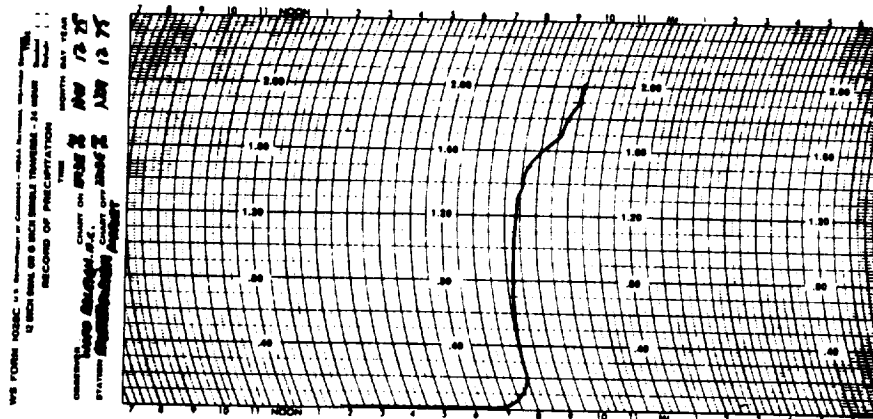


Figure 2.4-7. An Example of an Intense Rain Event

some charts. It appears that these charts are the best source of information for a short duration rate data.

The last automated rain gauge utilized by the U.S. Weather Service is the Fischer-Porter gauge. This unit is a weighing gauge which punches a paper strip chart in a binary coded decimal (BCD) format every 15 minutes. The gauge may be set to record every 5 minutes, but that resolution is generally not utilized by the Weather Service. The gauge records to only the nearest 0.1 inch.

2.4.1.3 Estimating Rain Rate From Gauge Records. An example of how intense rain rates may be estimated is now given. The dates of the highest rain rate events are found in the CD, Annual Summary. Note that from Figure 2.4-3 the most intense rain rates (0.38 inches in 5 minutes) at the Asheville, NC, WSO occurred on August 24, ending at 1658 Eastern Standard Time. This occurred during a thunderstorm (see Figure 2.4-4) but it was not the most rain in a 24-hour period, which occurred on August 17. The amount of precipitation between 1500 and 1700 EST on August 17 is noted in the LCD in Figure 2.4-4. This process is utilized to determine the list of dates for the high rain rate events. Copies of the rain gauge charts for these dates are then obtained from National Climatic Center. For the August 24 event, the most accurate data appears directly on the gauge readout shown in Figure 2.4-6. By estimating the slope of the cumulative data, the rain rate just before 4 PM was more than 4.56 inch/hr (116 mm/hr) for the first several minutes. Interpolation yields a rate approaching 150 mm/hr for 2 minutes. Another example of a cloud burst is shown in Figure 2.4-7. Herein rain rates approaching 300 mm/hr (12 inches/hr) occurred at 8 PM and contributed to the airline crash at this airport at that time. Clearly the attenuation at a ground station would be significant for this severe 2 minute event (0.00038% of a year).

Bodtmann and Ruthroff (1974) have demonstrated a technique of estimating rain rate distributions directly from these rain gauge charts with 1-minute resolution. Since computing derivatives from these charts is notoriously inaccurate, considerable processing is

necessary to get accurate results, especially at high rain rates. Figure 2.4-8 is an example of a Dallas, TX rain event cumulative and rain rate (1-minute integration) distribution. Clearly the method is powerful and readily adaptable to field measurements made using a commercial weighing gauge.

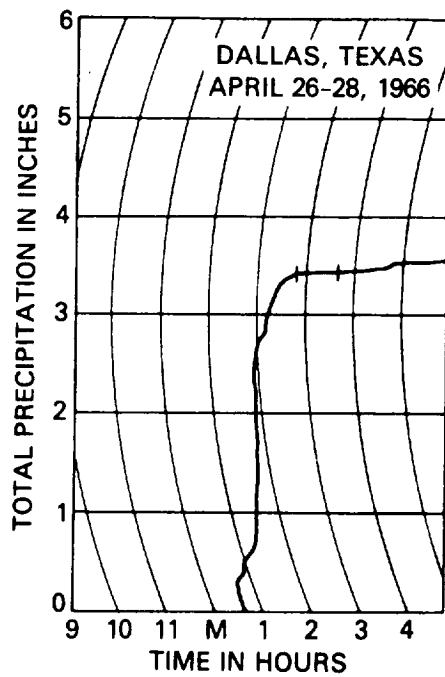
2.4.2 Canadian Sources

The Atmospheric Environment Office* prepares several documents containing rain and snow precipitation data. These documents** are:

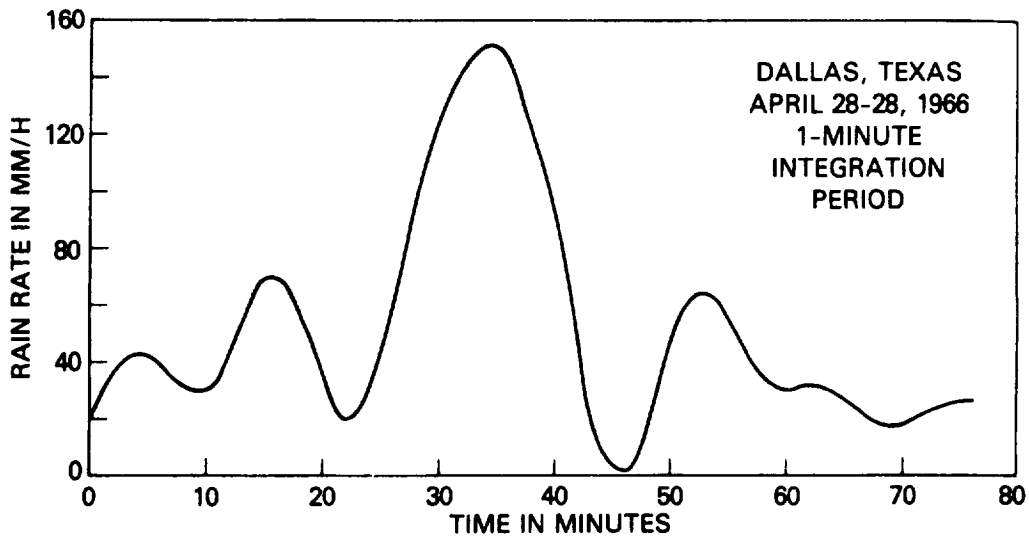
- Monthly Record - Western Canada - Part 1
 - Provinces of British Columbia, Alberta, Saskatchewan and Manitoba
 - \$23.40 foreign per year
 - \$ 2.40 foreign per issue
- Monthly Record - Northern Canada - Part 2
 - Territories of Yukon and Northwest
 - \$14.90 foreign per year
 - S 1.50 foreign per issue
- Monthly Record - Eastern Canada - Part 3
 - Provinces of Ontario, Quebec, Nova Scotia and New Brunswick
 - \$23.40 foreign per year
 - \$ 2.40 foreign per issue
- Canadian Weather Review
 - published monthly
 - covers about 250 surface stations throughout Canada
 - \$8.40 foreign per year
 - \$.85 foreign per issue
 - available about one month following the date of recording

* Head Office, 4905 Dufferin Street, Downsview, Ontario M3H 5T4, Canada

** Available from: Supply and Services Canada, Publishing Centre, Hull, Quebec, KDA 0S9, Canada. Make checks payable to Receiver General for Canada. Canadians should request domestic price schedule.



a) National Weather Service Weighing Gauge Chart



b) Rain Rates vs. Time Computed From Weighing Gauge Data

Figure 2.4-8. An Example of Generation of Rain Rate Data From a Weighing Gauge Chart

The data in the Monthly Records (available about four months following recording) is of most importance to the earth space path engineer. As shown in Figure 2.4-9, the rainfall, snowfall and total precipitation are given for each day of the month. The Monthly Summary table indicates the number of thunderstorms, etc., and the recording rain gauge data for selected cities is given. These are the maximum amounts for the duration periods indicated on the date of occurrence. In addition, the number of hourly periods with rainfall accumulations between 0.01-0.09, 0.1-0.19, etc., inches is noted. These data are obtained from tipping bucket rain gauges measuring in increments of 0.01 inches.

The tipping bucket rain gauge data is available for many more Canadian locations. The charts from these gauges are available upon request from the Climatological Recording Services Branch of the Head Office in Downsview, Ontario, at a nominal charge.

2.4.3 Worldwide Sources

Many countries prepare meteorological data similar to the U.S. and Canada. Many of these are on file at the National Weather Service Library, Room 816, Gramax Bldg., 13th Street, Silver Spring, MD. One document, the Monthly Climatic Data for the World, does list the number of days per month a station receives more than 1 mm of rain and the total rainfall per month. The data is coarse and can only provide a general indication of the precipitation climate. An example is shown in Figure 2.4-10. This document was discontinued with the December 1980 issue, but back issues are available for \$4.20 per monthly copy from the National Climatic Center.

2.5 ESTIMATION OF RAIN RATE

The rain rate measurement is an inexact process because of the discrete nature of rainfall. Obviously, because rain falls as raindrops, the rain rate is computed by measuring the rain accumulation per given area for a known period of time at a point. The shortest period of time reported by the U.S. and Canadian

ORIGINAL PAGE IS
OF POOR QUALITY

SURFACE DATA															OCTOBER 1977	
STATION	LATITUDE	LONGITUDE	ELEVATION	NUMBER OF DAYS OF OBSVS.	PRESSURE		TEMPERATURE		VAPOR PRESSURE		PRECIPITATION		SUN-SHINE			
					MEAN STATION	MEAN SEA LEVEL	MEAN	DEPARTURE	MEAN	DEPARTURE	NO. OF DAYS ≥ 1 MM.	TOTAL	DEPARTURE	QUINTILE	PERCENTAGE OF LONG-TERM AVERAGE	
					MB	MB	°C	°C	MB	MB	MM	MM	X			
CANADA-EASTERN																
ALERT	82 30 N	62 20 W	63	31	1003.7	1012.2	-18.9	+ 0.9	1.1	-0.1	4	9	- 7			
EUREKA	80 00 N	85 56 W	10	31	1008.5	1009.9	-21.0	+ 0.5	1.2	+0.1	1	4	- 3			
RESOLUTE	74 43 N	94 59 W	67	31	998.0	1006.9	-14.3	+ 0.3	2.1	+0.2	6	22	+ 8	106		
CLYDE	70 27 N	86 33 W	8	31	1002.1	1005.4	- 7.6	- 1.2	3.2	-0.3	11	55	+ 21			
HALL BEACH	68 47 N	81 15 W	13	31	1004.9	1005.8	- 9.4	+ 1.6	3.0	+0.2	9	27	+ 4			
BAKER LAKE	84 18 N	96 00 W	19	31	1007.0	1008.6	- 5.1	+ 2.4	4.0	+0.5	10	57	+ 17			
CORAL HARBOUR	64 12 N	83 22 W	64	31	999.0	1007.3	- 3.8	+ 2.2	3.9	+0.4	16	46	+ 37			
FROBISHER BAY	63 45 N	68 33 W	34	31	1002.3	1006.7	- 5.8	+ 0.9	4.0	+0.2	13	52	+ 18	97		
CHURCHILL	58 45 N	94 04 W	29	31	1005.5	1009.1	2.5	+ 3.6	5.7	+0.6	6	23	- 15	142		
INDUCCOJUAUC	58 27 N	78 07 W	5	31	1008.1	1008.7	1.7	+ 2.1	6.3	+0.7	14	48	+ 9	131		
FORT CHIMO	58 06 N	88 25 W	37	31	1004.4	1009.1	0.1	+ 0.4	5.4	+0.2	12	71	+ 22	5		
TROUT LAKE	53 50 N	89 52 W	220	31	987.0	1014.2	4.9	+ 3.1	8.2	-0.1	5	47	- 16			
NITCHEOUJON	53 12 N	70 54 W	538	31	948.7	1014.0	0.9	+ 0.3	5.7	0.0	13	84	+ 16			
MOOSONEE	51 18 N	80 39 W	10	31	1013.4	1014.7	5.3	+ 1.4	6.8	-0.4	6	58	- 15	173		
ARMSTRONG	49 25 N	88 54 W	323	31			4.1	+ 1.0			5	34	- 25	147		
KAPUSKASING	49 25 N	82 28 W	227	31	998.4	1016.5	4.3	- 0.3	6.5	-0.8	9	69	- 3			
GERALDTON	49 42 N	86 57 W	331													
SEPT-ILES	50 13 N	86 16 W	55	31	1006.6	1013.4	4.8	+ 0.9	6.5	-0.2	14	157	+ 74	107		
GOOSE	53 19 N	80 25 W	49	31	1005.2	1011.3	1005.2	1011.3	5.4	- 1.2	7.2	-1.0	9	62	- 22	102
NORTH BAY	46 22 N	79 25 W	371	31	972.4	1017.4	5.4	- 1.2	7.2	-1.0	9	62	- 22	128		
HANIMAKI	46 23 N	75 58 W	170	31	995.8	1016.7	5.8	- 1.1	7.2	-0.9	9	63	- 5	106		
TORONTO/WALTON INT AP	43 41 N	79 38 W	173	31	996.2	1017.3	8.0	- 1.5	8.5	-0.4	11	113	+ 35			
MONTREAL/DORVAL INT AP	45 28 N	73 45 W	36	31	1011.6	1016.0	7.6	- 1.4	8.5	-0.4	11	113	+ 35			
BROOKVILLE	48 20 N	71 00 W	159	31	995.6	1015.2	5.6	- 0.1	6.7	-0.6	10	81	- 2			
CHATHAM	47 01 N	85 27 W	34	31	1009.6	1013.7	7.2	- 0.2	8.1	-0.2	16	257	+174	5		
STEPHENVILLE	48 32 N	58 33 W	28	31	1009.6	1012.8	7.8	+ 0.6	8.4	0.0	17	183	+ 84			
GANDER INT AP	48 57 N	59 34 W	151	31	993.8	1012.4	6.3	0.0	8.1	+0.1	14	127	+ 28	90		
SHEARWATER	44 38 N	63 30 W	51	31	1008.7	1015.0	9.8	+ 0.2	10.2	0.0	13	142	+ 33	108		
SYDNEY	43 43 N	65 15 W	30	31	1006.8	1014.4	8.7	- 0.4	8.7	-1.1	13	130	+ 15	4		
SHELburne	43 56 N	60 01 W	4	31	1015.4	1015.9	11.7	+ 0.1	11.7	0.0	14	122	+ 12	4		
SABLE ISLAND	47 37 N	52 45 W	141													
ST. JOHN'S (TORBAY)	47 37 N	52 45 W	141													
ST PIERRE AND MIQUELON																
ST PIERRE	46 48 N	56 10 W	5	31	1013.9	1014.5	9.1	+ 0.2	9.8	+0.4	13	87	- 50	1		
UNITED STATES-NORTHEAST																
INTERNATIONAL FALLS	48 34 N	93 23 W	361	31	975.0	1016.7	6.3	- 0.1			20	- 23				
DULUTH	46 50 N	92 11 W	432	31	975.4	1017.3	6.8	- 0.6			81	+ 23		104		
ST. CLOUD	45 35 N	94 11 W	318	31	979.0	1017.6	7.8	- 0.9								
SAULT STE. MARIE	46 28 N	84 22 W	221	31	993.8	1016.8	7.1	- 0.8	8.1	0.0	8	47	- 25	2		
BURLINGTON	44 28 N	73 09 W	104	31	1001.8	1016.6	8.1	- 1.2	8.2	-1.1	11	119	+ 5	81		
CARIBOU	46 52 N	68 01 W	146	31	991.5		6.4	- 0.2			10	128	+ 58	5		
DES MOINES	41 32 N	93 39 W	294	31	986.8	1018.0	11.3	- 1.1	9.4	-0.2	10	135	+ 51			
COLUMBIA	38 49 N	92 13 W	274	31	990.1	1018.5	13.1	- 1.3			11	130	+ 75	3		
CHICAGO	41 47 N	87 45 W	190	31	995.6	1018.3	11.0	- 2.0	8.9	-0.8	9	112	+ 26	85		
ST. LOUIS	38 45 N	90 23 W	172	31	998.3	1018.9	13.1	- 2.0	11.5	+0.7	7	95	- 24	2		
DAYTON	39 54 N	84 13 W	306	31	985.8	1018.6	11.0	- 2.1	8.6		9	98	+ 48	5		
COLUMBUS	42 56 N	78 44 W	254	31	986.5	1018.5	13.1	- 1.3	8.3	-1.9	9	85	+ 17	4		
BUFFALO	40 00 N	82 53 W	215	31	989.3	1017.5	9.8	- 1.1	9.1	0.0	9	66	- 10	3		
NEW YORK LA GUARDIA	42 22 N	71 02 W	9	31	1005.4	1016.9	12.7	- 1.8	11.1	-0.3	2	148	+ 73	6		
BOSTON	42 13 N	71 07 W	195	31	1011.4	1016.0	12.9	- 0.1	11.2	+0.6	2	118	+ 41	5		
BLUE HILL OBS	41 40 N	69 58 W	16		992.1	1015.2	10.7	- 1.1	10.6	+0.6	12	163	+ 71	5		
CHATHAM	38 57 N	77 27 W	98													
WASHINGTON DULLES	38 51 N	77 02 W	20	31	1013.5	1017.8	15.0	- 0.4	11.0	-0.7	7	136	+ 68	5		
WASHINGTON NATIONAL																

Figure 2.4-10. An Example of the Monthly Climatic Data for the World

Weather Services is five minutes. Assuming the rain rate is uniform for that period of time, the computed point rain rate and the "instantaneous" point rain rate are equal. However, the question arises as to how the apparent rain rate varies as the integration (computing) time is varied. This effect has been addressed experimentally by experimenters at the Bell Telephone Laboratories.

At Holmdel, NJ, measurements (Bodtmann and Ruthroff-1974) of the apparent rain rate versus the gauge integration period over a 2-year period have yielded the results in Figure 2.5-1. These results extend from 1.5 seconds to 2 minutes and are normalized to a one-minute integration time. Unfortunately, the measurement do not extend to a 5-minute integration time which would be very convenient for comparison of the Lin model with other rain models which employ a one-minute integration period (see Chapter 3). The variation between a 2-minute and a 5-minute integration time is expected to be significant for high rain rates. However, Figure 2.5-1 clearly shows that for rain rates below 50 mm/h the error due to the integration time is small. This effect arises because the low rain rate events tend to be spatially and temporally uniform, while the rain rates between 50 and 120 mm/h are dominated by spatially and temporally nonuniform convective rains.

Only the most severe cells create rain rates above 120 mm/h and these are highly variable. Therefore, a significant peak rain rate two or three times as high as the one-minute average can occur for one second during the one-minute period. As an example, a typical rain rate versus time profile comparing the one-minute and ten-second integration times is shown in Figure 2.5-2 (Bodtmann and Ruthroff-1974).

The impact of varying integration times can be significant for both the measurement of cumulative rain rate statistics (related to cumulative attenuation statistics) and rain rate duration measurements (related to attenuation fade duration). Lin (1978) has experimentally determined the effect of the integration time on cumulative statistics. The results for Palmetto, GA are shown in

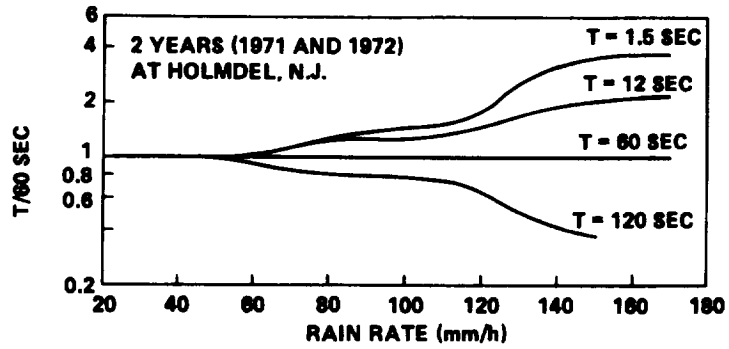


Figure 2.5-1. Rain Rate Distribution Versus Gauge Integration Time

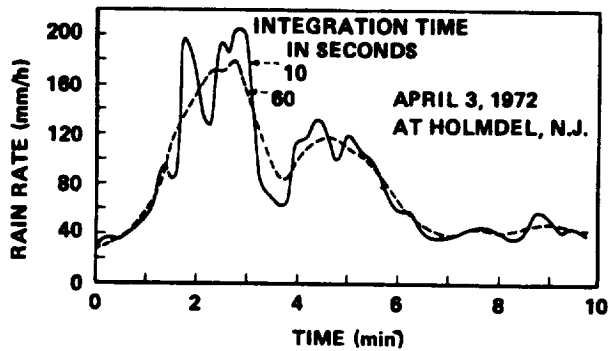


Figure 2.5-2. Integrating Rain Gauge Results for Two Integration Times

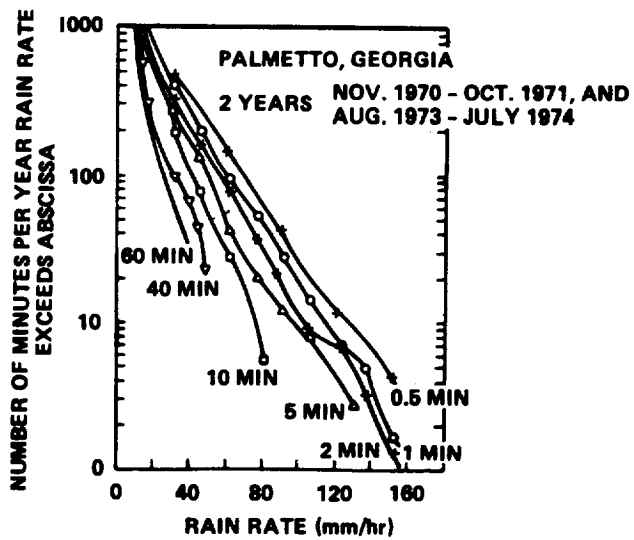


Figure 2.5-3. Cumulative Rain Rate Statistics Versus Integration Period

Figure 2.5-3. Clearly the difference between a 1-minute and 30-second integration time is significant. Similar results for rain rate duration statistics are not available.

2.6 REFERENCES

- Block, S.C., D. Davidson and D.D. Tang (1978), "Rain-Attenuation Experience With the Tampa Triad Using 19-GHz Comstar Satellite Beacon Signals," Record, EASCON '78, September 25-27, Arlington, Va., pp. 379-384.
- Bodtmann, W.F. and C.L. Ruthroff (1974), "Rain Attenuation on Short Radio Paths: Theory, Experiment and Design," Bell Syst. Tech. Jnl., Vol. 53, pp. 1329-1349.
- CCIR (1986), Attenuation by Hydrometeors, in Particular Precipitation, and Other Atmospheric Particles, Report 721-2, Geneva, Switzerland.
- Crane, R.K. (1966), "Microwave Scattering Parameters for New England Rain," MIT Lincoln Lab. Tech. Rpt. 426, ASTIA Doc. AD647798
- Crane, R.K. and D.W. Blood (1979), "Handbook for the Estimation of Microwave Propagation Effects - Link Calculations for Earth-Space Paths," ERT Doc. No. P-7376-TR1, prepared under NASA Contract NAS5-25341.
- Goldhirsh, J. (1976), "Path Attenuation Statistics Influenced by Orientation of Rain Cells," IEEE Trans. Ant. Prop., Vol. AP-24, No. 6, pp. 792-799.
- Goldhirsh, J. and I. Katz (1979), "Useful Experimental Results for Earth Satellite Rain Attenuation Modeling," IEEE Trans. Ant. Prop., Vol. AP-27, No. 3, pp. 413-415.
- Goldhirsh, J. (1983), "Yearly Variations of Rain-Rate Statistics at Wallops Island and their Impact on Modeled Slant Path Attenuation Distributions," IEEE Trans. Ant. Prop., Vol. AP-31, No. 6, pp. 918-921.
- Huff, F.A. and W.L. Shipp (1969), "Spatial Correlations of Storm, Monthly and Seasonal Precipitation," Jrnl. Appl. Meteorology, Vol. 8, August, pp. 542-550.
- Ippolito, L.J. (1979), private communication.
- Joss, J., J.C. Thams and A. Waldvogel (1968), "The Variation of Raindrop Size Distributions at Locarno," Proc. Int. Conf. Cloud Phys., Toronto, Canada, pp. 369-373.
- Kerker, M. (1969), The Scattering of Light and Other Electromagnetic Radiation, Academic Press, New York.

- Kerr, D.E. (1951), Propagation of Short Radio Waves, Vol. 13, Radiation Laboratory Series, McGraw-Hill, pp.674-685.
- Laws, J.O. and D.A. Parsons (1943), "The Relation of Raindrop Size to Intensity," Trans. Am. Geophys. Union, Vol. 24, pp. 452-460.
- Lin, S.H. (1978), "Empirical Calculation of Microwave Path Attenuation Distributions on Earth-Satellite Paths," Record, EASCON '78, Arlington, Va., pp. 372-378.
- Marshall, J.S. and W.M. Palmer (1948), "The Distribution of Raindrops With Size," Jrnl. Meteorology, Vol. 5, pp. 165-166.
- Olsen, R.L., D.V. Rogers and D.B. Hodge (1978), "The aR^b Relation in the Calculation of Rain Attenuation," IEEE Trans. Ant. Prop., Vol. AP-26, pp. 318-329.
- Rogers, D.V. (1978), private communications.
- Rowland, J.R. (1976), "Comparison of Two Different Raindrop Disdrometers," 17th Conf. Radar Meteorology, Seattle, Wa., pp. 398-405.
- Ryde, J.W. and D. Ryde (1945), "Attenuation of Centimetre and Millimetre Waves by Rain, Hail, Fogs, and Clouds," Rpt. No. 8670, Research Laboratory of the General Electric Company, Wembley, England.

CHAPTER III
AN OVERVIEW OF SEVERAL RAIN AND
RAIN ATTENUATION MODELS

3.1 INTRODUCTION

3.1.1 Summary of Models

Several models for estimation of the cumulative attenuation statistics on earth-space millimeter paths have been developed. Each of these models appears to have advantages and disadvantages depending on the specific application. In this chapter an attempt is made to briefly summarize the key features of commonly used models. Chapter VI provides information on the application of these models and includes examples. Many of the models employ the concept of "effective path length," which is explained at the end of this chapter.

Table 3.1-1 summarizes the key inputs, outputs and other important features of seven models in their current format. Nearly all of these models are being updated and modified based on recent experimental results and analyses. In addition, other models prepared by major communications companies, such as Comsat, are utilized (Gray and Brown-1979), but these are generally not published in the open literature and are accordingly omitted here.

The models provide rain rate statistics, attenuation statistics, or both. Generally, these statistics can be related by use of the specific attenuation and effective path length relations. (Specific attenuation is described in Chapter II, while the effective path

Table 3.1-1. Summary of Model Parameters

Model	Inputs	Outputs	Comments
Rice-Holmberg	Climate or Site-Specific Mean Annual Rainfall plus Ratio of Thunderstorm-to-Total Rain.	Cumulative Time Distribution of Rainfall.	Two Rain Modes Considered: Thunderstorm & Uniform Rains. Probability of Rain Rate Exceedance for Either or Both Modes is Available.
Dutton-Dougherty	Same as Rice-Holmberg and Link Parameters (e.g., Frequency, Elevation Angle).	Rain or Gaseous Attenuation Associated with a Given Exceedance Time Percentage.	Utilizes Modified Rice-Holmberg Rain Model. Provides Confidence Limits, Given Two Additional Rain Rate Distributions.
Global	Location and Link Parameters.	Rain Attenuation Associated with a Given Exceedance Time Percentage.	All Rain Attenuation Parameter Values are Selfcontained. Globally Applicable.
Two-Component	Same as Global.	Exceedance Time Percentage Associated with a Given Rain Attenuation.	Same Rain Model (& Comments) as for Global Model. Two Rain Modes Considered: Convective Cell and Debris Rains.
CCIR	Same as Global.	Rain Attenuation Associated with a Given Exceedance Time Percentage.	All Rain Attenuation Parameter Values are Selfcontained. Globally Applicable.
Lin	Five Minute Rain Rate and Link Parameters.	Attenuation Associated with a Given Rain Rate.	Simple Extension of Terrestrial Path Rain Attenuation Model.
Simple Attenuation (SAM)	Rain Statistics and Link Parameters.	Attenuation Associated with a Given Rain Rate.	Assumes Exponential Shaped Rain Profile.

length concept is summarized at the end of this chapter.) For example, the Rice-Holmberg model only computes the exceedance probability statistics for rain rate, but this is relatable to attenuation by use of the specific attenuation and the effective path length. The Dutton-Dougherty, CCIR, Two-Component, and Global models provide the attenuation statistics given the geographic and link parameters. That is, they give the rain rate statistics within the model.

3.1.2 Concepts of Rainfall Statistics

3.1.2.1 Cumulative Statistics. The cumulative statistics for either rain rate or attenuation are usually presented as the probability of exceedance (abscissa) versus the rain rate or attenuation (ordinate). They represent stable statistics averaged over a period sufficiently long that variations in the lowest frequency component of the time distribution are averaged. For rain rate and rain attenuation the period corresponding to the lowest frequency is generally considered to be one year. Higher frequency components are the seasonal and daily variation of the rain rate. For example, in the eastern US, the higher frequency components arise because more rain falls in the summer than in the winter, and more rain falls between noon and 6 PM than between 6 AM and noon local time. Some people have suggested that the 11-year solar cycle is the lowest frequency component, but this has not been observed by the Weather Service.

Based on the above considerations the cumulative statistics for several years are required before "stable" annual statistics are obtained. For this reason, experimentally generated data bases for both rain and attenuation are not generally good until 5 or 10 years of data are included. However, because of the limited lifetime of the beacon satellites, attenuation data at a known frequency and elevation angle is generally not available for this length of period (Kaul et al-1977). Therefore data from several satellites launched over a long period are required. Since they are not at the same frequency and elevation angle, these results must be scaled in order

to be combined. Frequently this process has not been done accurately, resulting in small segments of attenuation data which are not representative of the long term statistics.

Based on the above discussions it appears that the only present recourse is to utilize rain rate data as derivable from Weather Bureau or other long-term measurements. This leads to the exceedance curves or rain rate. The attenuation is then derived from the relations between rain rate and attenuation.

3.1.2.2 Outage Period Statistics. System designers are also interested in the average length of time a given threshold of rain rate or attenuation is exceeded (also termed the outage time). In addition, the distribution of the outage time about the average is desired. Theoretical work of Lin (1973) has shown that the distribution is approximately lognormal.

Besides the outage time, Hyde (1979) has identified the desire to know the average time between outage periods within a given rain event, and the average time between outages between two rain events. The first case recognizes that outages may occur several times during the same general rain event because the rain rate is highly variable during an event. For example, the passage of several rain cells associated with a given rain front may cause several outages as each cell dominates the path attenuation. It is desirable to know the approximate period between these outages and the distribution of these outage periods as a function of attenuation threshold and type of rain event. This type of data is expected to be dependent on the geographic region because the weather fronts are distorted by the presence of mountain ranges, lakes, cities, etc. Therefore, extrapolation to other regions is difficult unless their weather systems are similar.

The second case (average time between outages in two rain events) correlates the period between severe storms in a given region. This period is expected to be seasonally dependent because in most regions the high rain rate storms usually occur during a

short period of the year. Again, some statistical estimate of the average period and the distribution of the periods would be desirable.

Generally, outage period data is not as readily available as the cumulative attenuation statistics data. Therefore, the designer must rely on the limited data bases available from CCIR (1986, Rpt 564-3), Comsat (Rogers and Hyde-1979) or Lin (1973, 1980). Vogel (1982) has calculated time-between fade (intermission) statistics for 19 and 28 GHz at Austin, Texas. An estimate of the upper limit of the outage time is presented in Chapter VI.

3.2 RICE-HOLMBERG MODEL

3.2.1 Types of Storms

The Rice-Holmberg (R-H) Model (Rice and Holmberg-1973) is based upon two rainfall types: convective ("Mode 1", thunderstorm) rains and stratiform ("Mode 2", uniform) rains. The statistical model is based upon the sums of individual exponential modes of rainfall rates, each with a characteristic average rate R. According to this descriptive analysis

$$\text{rainfall} = \text{Mode 1 rain} + \text{Mode 2 rain}$$

The exponential distribution chosen to describe "Mode 1 rain" corresponds to a physical analysis of thunderstorms, while "Mode 2 rain," represented by the sum of two exponential distributions, is all other rain. In temperate climates only convective storms associated with strong updrafts, high radar tops, hail aloft and usually with thunder can produce the high rainfall rates identified by Mode 1. Only the highest rates from excessive precipitation data are used to determine parameters for Mode 1, which is intended to represent a physical mechanism as well as a particular mathematical form.

3.2.2 Sources of Data

The rainfall statistics in the R-H model are based upon the following:

- 1) Average year cumulative distributions of hourly rates for the 10 years 1951 to 1960 and for a total of 63 stations, with 49 in the continental U.S. as summarized in the Weather Service Climatological Data for this period;
- 2) Distributions for 15-year averages with recording intervals of 6, 12, and 24 h for 22 of these stations (Jorgenson, et al-1969);
- 3) Accumulations of short-duration excessive precipitation for 1951 to 1960 for recording intervals of 5, 10, 15, 20, 30, 45, 60, 80, 100, 120, and 180 min for 48 U.S. stations;
- 4) A U.S. map of the highest 5-min rates expected in a two-year period (Skerjanec and Samson-1970);
- 5) Maximum monthly rainfall accumulations and the average annual number of thunderstorm days for the period 1931 to 1960 for 17 U.S. stations and 135 additional stations reported by the World Meteorological Organization.

3.2.3 R-H Model Parameters

The average annual total rainfall depth M is the sum of contributions M_1 and M_2 from the two modes:

$$M = M_1 + M_2 \text{ mm} \quad (3.2-1)$$

and the ratio of "thunderstorm rain" M_1 to total rain M is defined as

$$\beta = M_1/M \quad (3.2-2)$$

The number of hours of rainy t-min periods for which a surface point rainfall rate R is exceeded is the sum of contributions from the two modes:

$$T_t (R) = T_{1t} Q_{1t}(R) + T_{2t} Q_{2t} (R) \text{ hours}$$

There are 8766 hours per year, so $T_t(R)/87.66$ is the percentage of an average year during which t-min average rainfall rates exceed R

mm/h. The data show that the average annual clock t-min rainfall rate for each of the modes is fairly constant. On the other hand, the total number of rainy t-min periods for each mode is relatively much more variable from year-to-year and between stations or climate regions. Rainfall climates defined by Barry and Chorley (1970) for the United States were found to correspond very well with observed regional variations of the parameter β .

The average annual total of t-min periods of Mode 1 and Mode 2 rainfall are T_{1t} and T_{2t} , respectively. The average annual Mode 1 and Mode 2 rainfall rates are therefore

$$\begin{aligned}\bar{R}_{1t} &= M_1/T_{1t} \text{ mm/h} \\ \bar{R}_{2t} &= M_2/T_{2t} \text{ mm/h}\end{aligned}\tag{3.2-3}$$

Note that M_1 and M_2 are not functions of t , since the amount of rainfall collected over a long period of time does not depend on the short-term recording interval t . But the total number of hours T_{1t} or T_{2t} of rainy t-min intervals (collecting at least 0.01 in or 0.254 mm of rain per interval) will depend on t .

The factors $q_{1t}(R)$ and $q_{2t}(R)$ are the complements of cumulative probability distributions. Each factor is the number of hours that a rate R is exceeded by Mode 1 or Mode 2 rain divided by the total number of hours, T_{1t} or T_{2t} , that there is more than 0.254 mm of rain in a t-min period.

3.2.4 Time Intervals

The formulas to be presented are for $t=1$ clock-minute rates. Here clock-minutes are defined as beginning "on the minute" for a continuous t-minute period.

For the more general case where $t>1$ min, one more prediction parameter is required in addition to the two that have been defined as M and B . This additional parameter is the number of hours of

rain per year, D. The formulas proposed here for $q_{1t}(R)$ and $q_{2t}(R)$ assume that the number of rainy days in an average year is

$$D/24 = 1 + M/8 \text{ rainy days} \quad (3.2-4)$$

where D is in hours and M is in millimeters. This relation has been found good, on the average, for continental U.S. stations. A comparison of the cumulative distributions versus the surface rainfall rate R for various values of t from 1 minute to 1 day is shown in Figure 3.2-1. Clearly, for $\beta=0.125$ and $M=1000\text{mm}$, the values for t=1 and 5 minutes are nearly equal, but longer periods give a significantly different value for $T_t(R)$.

3.2.5 Model Results for One-Minute Intervals

For t=1, the more general formulas are almost independent of D, so that

$$\begin{aligned} q_{1t}(R) &= \exp(-\bar{R}/R_{1t}) \\ q_{2t}(R) &= 0.35 \exp(-0.453074 R/R_{2t}) \\ &\quad + 0.65 \exp(-2.857143 R/\bar{R}_{2t}) \end{aligned} \quad (3.2-5)$$

and the annual average Mode 1 and Mode 2 rates \bar{R}_{1t} and \bar{R}_{2t} are very nearly equal to 33.333 and 1.755505 mm/h, respectively. Then $T_1(R)$ may be written as

$$\begin{aligned} T_1(R) = M \{ &0.03 \beta \exp(-0.030R) + 0.21(1-\beta) [\exp(0.258R) \\ &+ 1.86 \exp(-1.63R)] \} h. \end{aligned} \quad (3.2-6)$$

Use of this relation allows normalized cumulative time distributions to be calculated. Figure 3.2-2 is an example of this result for t=1 minute and B values from 0 to 0.75. Typical values for B and M throughout the US and Canada are given in Figures 3.2-3 and 3.2-4, respectively. Note that the values quoted in Figure 3.2-4 are in inches rather than millimeters required for M. Rice

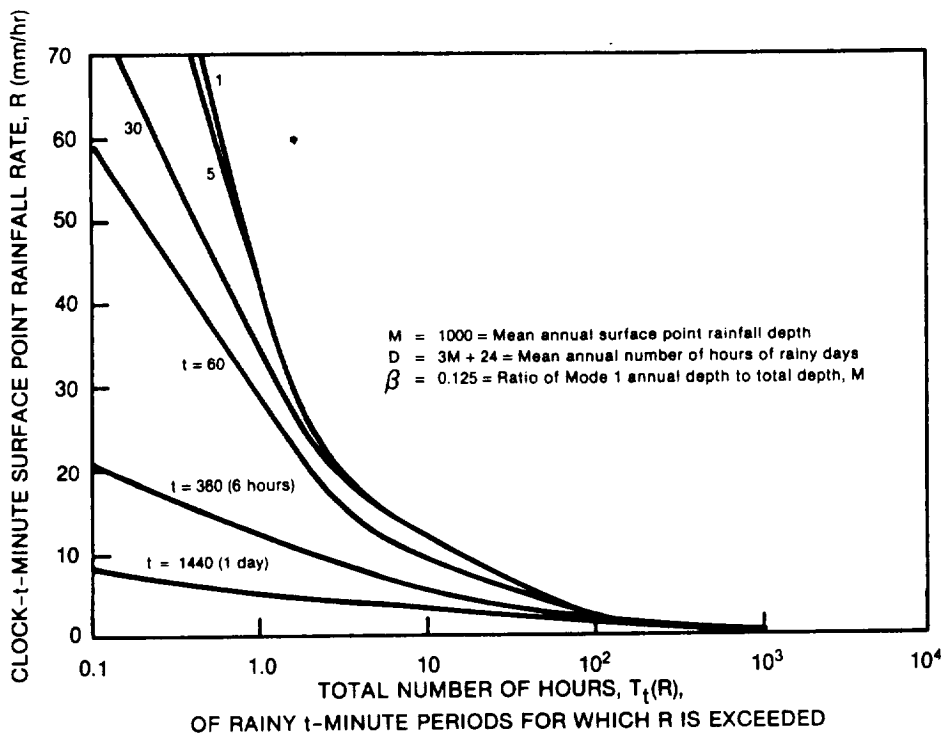


Figure 3.2-1. Average Year Cumulative Time Distributions

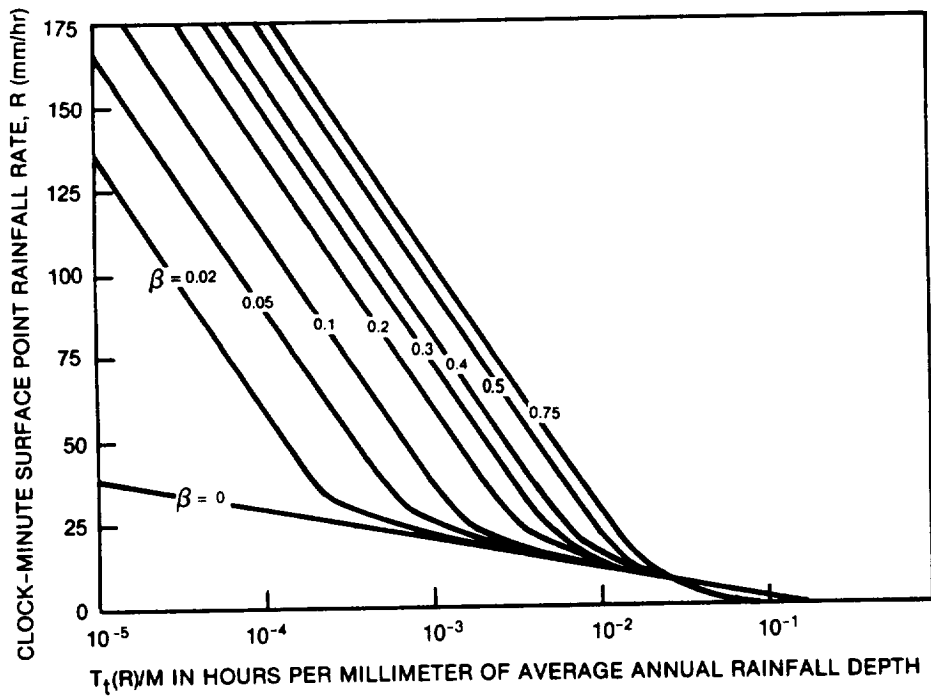


Figure 3.2-2. Normalized Cumulative Time Distributions

ORIGINAL PAGE IS
OF POOR QUALITY

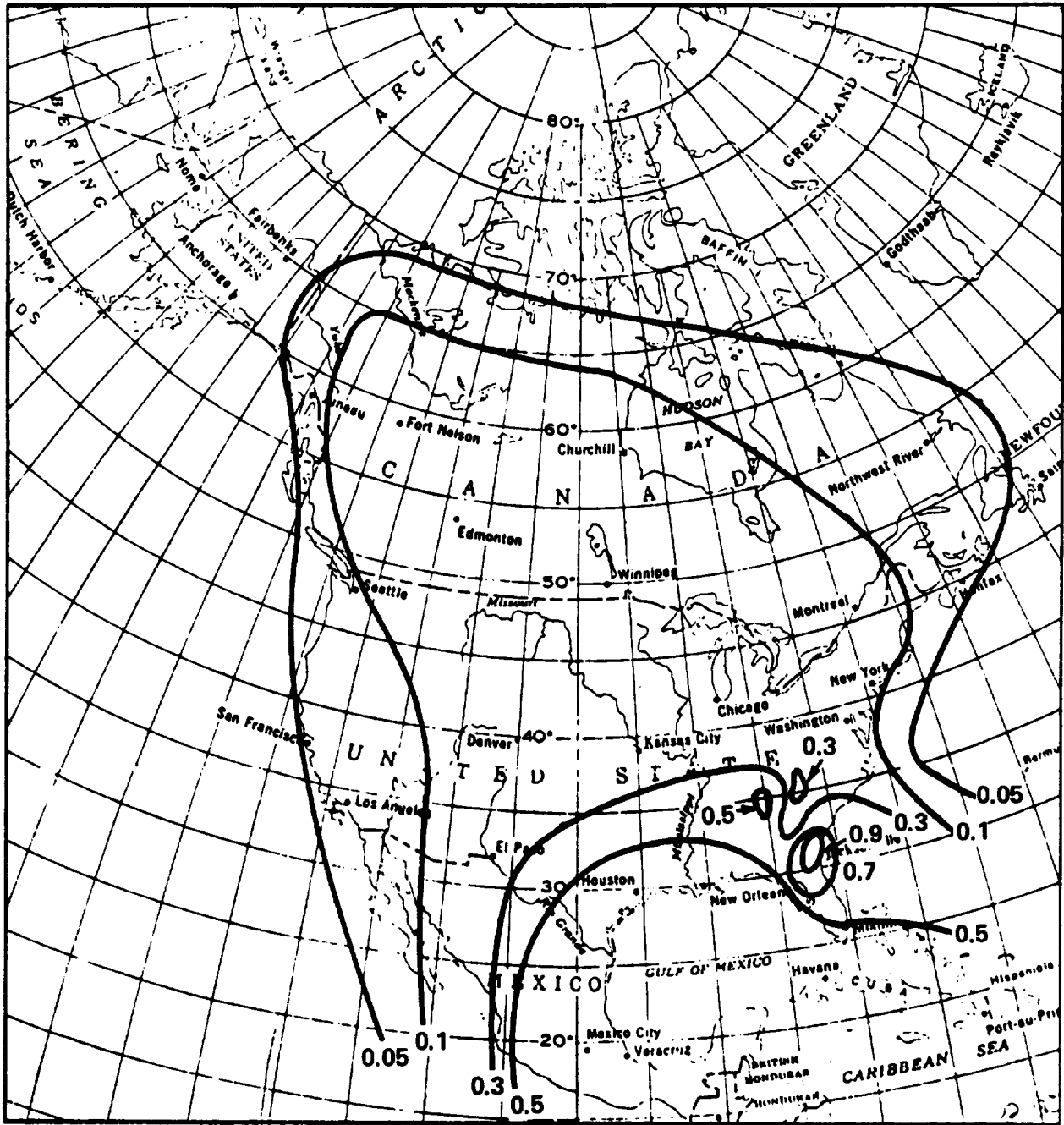


Figure 3.2-3. The Parameter β in the Rice-Holmberg Model Over the U.S. and Canada

ORIGINAL PAGE IS
OF POOR QUALITY

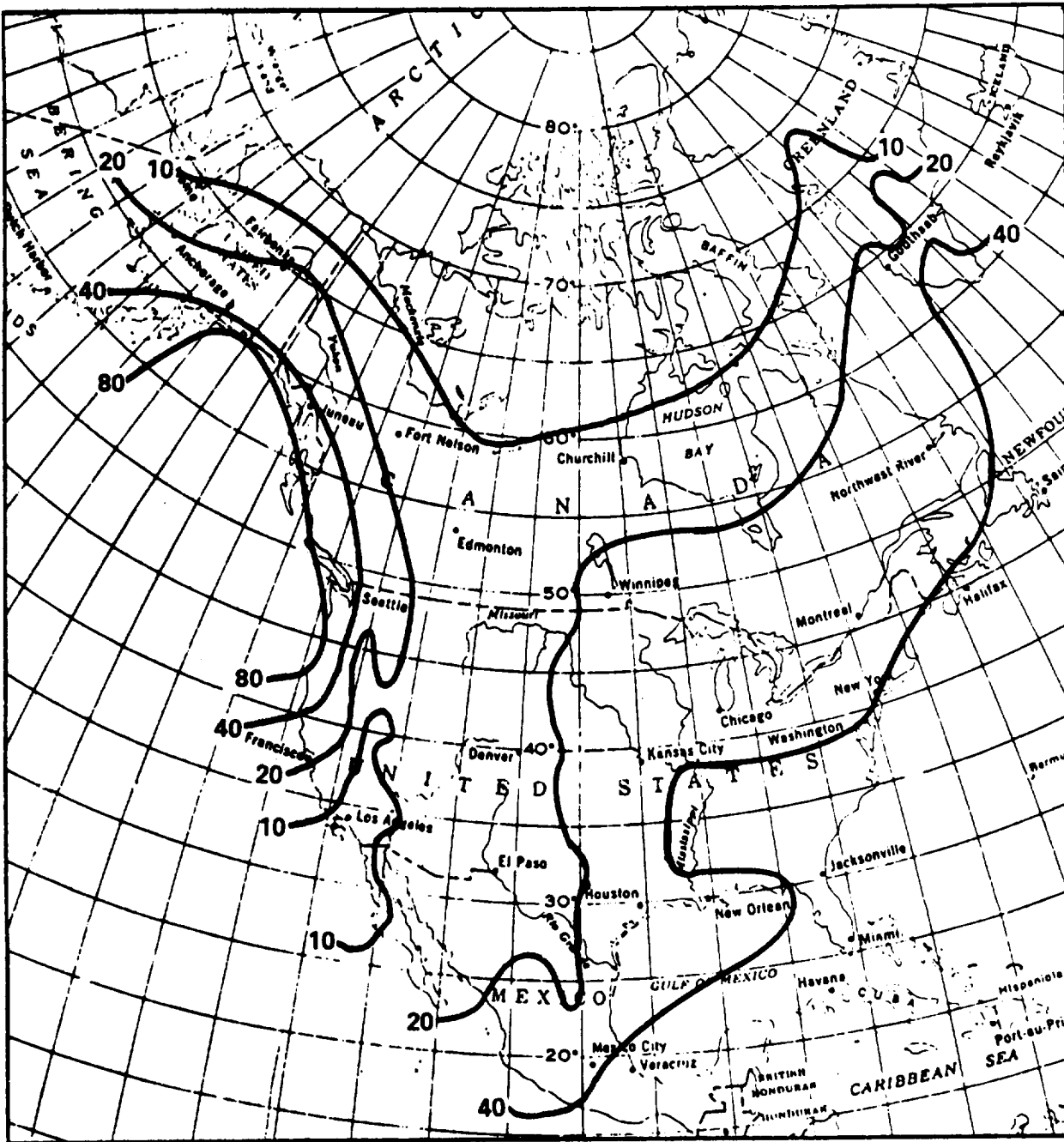


Figure 3.2-4. Mean Annual Precipitation in Inches in U.S. and Canada (1 inch = 25.4 mm)

and Holmberg (1973) have also presented values throughout the world in their original article.

Dutton and Dougherty (1979), (1984), provided a less cumbersome version of the R-H model by fitting relatively simple formulations to various parts of the R-H distribution curve. This "modified Rice-Holmberg model" was applied to a data base of 304 geographically diverse, data intensive locations in the U.S., (including Alaska and Hawaii), and year to year standard deviations of rain rate were developed. The results showed a marked improvement in the bounds of prediction, which appear to encompass the measured data more completely.

These same authors also extended the R-H rain-rate distribution to include a direct prediction of attenuation distributions for specified paths and locations. This attenuation prediction model is the subject of the next section.

3.3 DUTTON-DOUGHERTY MODEL

The Dutton-Dougherty (DD) Model (Dutton and Dougherty-1973, Dutton-1977; Dutton, Kobayashi, and Dougherty-1982) includes attenuation due to both rain and gases. The rainfall rate distributions it uses are based on a series of modifications to the Rice-Holmberg Model (Dutton, et al-1974). The DD Model has been incorporated into a computer program which is available to users from the National Telecommunications and Information Administration. The DD rain and attenuation model components are described separately below.

3.3.1 DD Rain Characterization

The modified Rice-Holmberg (R-H) Model, as used in the DD Model, determines the number of hours of rainy t-minute periods, $T_t(R)$, for which a surface rain rate, R , is expected to be exceeded. The value $T_t(R)$ is given in the modified R-H model as

$$T_t(R) = \begin{cases} T_{1t} \exp(-R/\bar{R}_{1t}) & R \geq R_c \\ (T_{1t} + T_{2t}) \exp(-R/R_t') & R < R_c \end{cases} \quad (3.3-1)$$

with

$$T_{1t} = \beta M / \bar{R}_{1t} \text{ hours} \quad (3.3-2)$$

$$T_{2t} = (1 - \beta) M / \bar{R}_{2t} \text{ hours} \quad (3.3-3)$$

Where R_c is a "crossover" rain rate between a convective mode of rainfall ($R \geq R_c$) and stratiform mode of rainfall ($R < R_c$) and other parameters are defined in the R-H Model description. R_t' is a new parameter not used in the R-H Model. This biexponential representation of $T_t(R)$ is strictly analogous to the rainfall conceptions of Rice and Holmberg (1973). From (3.3-1), R_c can be evaluated by setting

$$T_{1t} \exp(-R_c/\bar{R}_{1t}) = (T_{1t} + T_{2t}) \exp(-R_c/R_t') \quad (3.3-4)$$

because it represents the intersection of the two curves in (3.3-1). Thus, we obtain

$$R_c = \bar{R}_{1t} R_t' / (\bar{R}_{1t} - R_t') \ln[(T_{1t} + T_{2t}) / T_{1t}] \quad (3.3-5)$$

The modified R-H model uses direct estimation of T_{1t} , T_{2t} , \bar{R}_{1t} , and R_t' from M , β , and D . This was achieved by using a multiple linear regression to obtain a best fit of T_{2t} , \bar{R}_{1t} , and R_t' in terms of the parameters M , β , and D . It was not necessary to fit T_{1t} , since it is given very simply in terms of M , β , and \bar{R}_{1t} by (3.3-2). The resulting best fits were of the form

$$\bar{R}_{1t} = a_{1t}M + a_{2t}\beta + a_{3t}D + a_{4t} \pm S_1 \quad (3.3-6)$$

$$T_{2t} = b_{1t}N + b_{2t} \pm S_2 \quad (3.3-7)$$

$$R_t = b_{3t}M + b_{4t}\beta + b_{5t}D + b_{6t} \pm S_3 \quad (3.3-8)$$

where the coefficients are $a_{1t} \dots a_{4t}$ and $b_{1t} \dots b_{6t}$, and the sample standard errors of estimate are $S_1 \dots S_3$.

The third modification is to the portion of the distribution that lies between the rainfall rates of 5 and 30 mm/hour, since two difficulties arise if the equation (3.3-1) is used exclusively for the entire distribution:

- 1) the transition between curves at R_c is decidedly not smooth, and
- 2) predictions via (3.3-1) can be noted to be as much as 50 percent below the R-H model in the same vicinity.

In order to partially alleviate these difficulties, it was arbitrarily determined that

$$T_t(R) = T_{st} \exp(-\sqrt[4]{R/R_{st}}) \quad (3.3-9)$$

could be reasonably fit to the data, with proper curvature and simplicity, for $1 \leq t \leq 60$ min and $5 \leq R \leq 30$ mm/hour.

For $t > 60$ min (i.e., $t=360, 1440$ min), the formulation (3.3-1) fits the R-H model sufficiently well over the entire rain rate distribution for operational purposes, so that no additional modification of (3.3-1) is necessary. In summary, then, the resultant modification of the R-H model is:

$$T_t(R) = \begin{cases} T_{1t} \exp(-R/\bar{R}_{1t}) & R > 30 \text{ mm/h} \\ (T_{st} \exp(-\sqrt[4]{R/R_{st}})) & 5 \text{ mm/h} \leq R \leq 30 \text{ mm/h} \\ (T_{1t} + T_{2t}) \exp(-R/R_t') & R < 5 \text{ mm/h} \end{cases} \quad (3.3-10)$$

for $1 \text{ min} \leq t \leq 60 \text{ min}$. and

$$T_t(R) = \begin{cases} T_{1t} \exp(-R/\bar{R}_{1t}) & R \geq R_c \\ (T_{1t} + T_{2t}) \exp(-R/R_t') & R < R_c \end{cases} \quad (3.3-11)$$

for $t > 60$ min.

3.3.2 Attenuation Prediction in the DD Model

Dutton (1977) has estimated the variance and confidence levels of the rain rate prediction, and Dougherty and Dutton (1978) have estimated the year-to-year variability of rainfall within a given rain zone. The DD Model attenuation prediction range now extends to 0.001 percent of a year.

Extending the rain model to include attenuation on earth-space paths, Dutton (1977) has assumed the Marshall and Palmer (1948) raindrop distribution. He has also included some degree of modeling of rainfall in the horizontal direction. This is achieved by means of what is termed the "probability modification factor" on earth-space links.

The probability modification factor, F , is given by

$$F \cong \frac{(f/15)^2}{A(f,\theta)} (0.274\theta + 0.987) \quad (3.3-12)$$

the factor cannot exceed unity, however. In (3.3-12), f is the frequency in GHz, θ is the elevation angle to the satellite in degrees, and $A(f,\theta)$ is the path attenuation in dB. The form was derived from rain storm cell size data given in a particularly useful form by Rogers (1972). The Rogers data, however, were all taken in the vicinity of Montreal, Canada. It would be desirable to have more globally diverse data in order to provide a basis for a more general probability modification factor.

The probability modification factor, applied strictly to attenuation, multiplies the percent of time, P_0 , during an average year that a point rainfall rate is expected at a given location. The multiplied value represents the percent of time, P , ($P \leq P_0$), that attenuation corresponding to R is expected along the path to a

satellite. In effect, a point-to-path rain rate conversion accounting for horizontal inhomogeneity is accomplished.

The probability modification factor given by (3.3-12) applies for exceedance percentages down to 0.01% of a year. The DD model has been extended (Dutton, et al - 1982) to 0.001% of a year by both empirical and analytical means. The empirical extension is simply to make the probability modification factor at 0.001% equal to the value at 0.01%:

$$F(0.001\%) = F(0.01\%) \quad (3.3-13)$$

The analytical extension gives essentially identical results. The extensions recognize that the nature of the very heavy convective rains occurring on the order of 0.001% of the time is different from that of the more "routine" rains of the 0.1% to 0.01% regime.

In the DD model the surface rainfall rate is translated into liquid water content per unit volume, L_0 , measured at the ground. The liquid water content at some height, h , above the ground, $L(h)$, can be modeled as a function of L_0 (Dutton - 1971). The modeling of $L(h)$ is different for the stratiform and convective rain systems. In the stratiform modeling $L(h)$ is assumed constant to the rain-cloud base, then decreases to zero at the storm top height H . In the convective modeling $L(h)$ increases slightly to the rain-cloud base and then decreases to zero at H , the storm top height.

Attenuation per unit length, $\alpha(f,h)$, due to rain can be calculated from $L(h)$ via expressions of the form

$$\alpha(f,h) = c(f)[L(h)]^{d(f)} \quad (3.3-14)$$

using the data of Crane (1966). Hence, the distinction between the Rayleigh region ($f < 10$ GHz, approximately) and the Mie region ($f > 10$ GHz) is implicit, because the coefficients $c(f)$ and $d(f)$ are frequency dependent. In the Rayleigh region, it can be shown that $d(f)=1$. An interpolation scheme on Crane's data obtains $c(f)$ and $d(f)$ for any frequency in the 10 to 95 GHz region.

Variability of attenuation of earth-space links is, as yet, not directly assessable by theoretical formulation. Thus, it is necessary to input, say, two additional rain rate distributions corresponding to the lower and upper confidence limits of R_0 in order to evaluate corresponding confidence limits on an attenuation distribution. This, of course, assumes no variance in the many parameters surrounding the attenuation formulation. This is clearly not so, and indicates that the procedure for evaluating attenuation confidence limits is still in need of refinement.

3.3.3 Dutton-Dougherty Computer Model

Dutton has developed an updated computer program (Steele-1979 and Janes, et al - 1978) to predict the annual distribution of tropospheric attenuation due to rain, clouds and atmospheric gases. Entitled DEGP80, the program also computes the phase delay and reflectivity. The required inputs to the program are:

Frequency

Earth station antenna elevation angle

Identification of data stations

Height above surface

Ratio of thunderstorm to non-thunderstorm rain

Time availability

Rainfall rate

Values for average annual atmospheric pressure, humidity, and temperature

The program is valid for frequencies from 1 to 30 GHz and for satellite elevation angles greater than 5 degrees. The program is available from the Institute for Telecommunications Sciences. [See U.S. Dept. of Commerce (1981)].

3.4 THE GLOBAL MODEL

The Global Model has been developed in two forms. Both of these forms utilize cumulative rain rate data to develop cumulative attenuation statistics. The first form, called the Global

Prediction Model (CCIR-1978a, Doc. P/105-E, 6 June), employs a path averaging parameter "r" to relate the point rain rate to the average rain rate along the path from the ground station to the point where the hydrometeors exist in the form of ice crystals. The later form of the model (Crane and Blood - 1979, Crane - 1980a, 1980b) includes path averaging implicitly, and adjusts the isotherm heights for various percentages of time to account for the types of rain structures which dominate the cumulative statistics for the respective percentages of time. Both forms will be described here because the latter is the recommended form for use by system designers, but the earlier form is computationally easy to implement and allows rapid computation with a hand-held calculator.

3.4.1 Rain Model

The rain model employed in both forms of the attenuation model is used for the estimation of the annual attenuation distribution to be expected on a specific propagation link. It differs from most other rain models in that it is based entirely on meteorological observations, not attenuation measurements. The rain model, combined with the attenuation estimation, was tested by comparison with attenuation measurements. This procedure was used to circumvent the requirement for attenuation observations over a span of many years. The total attenuation model is based upon the use of independent, meteorologically derived estimates for the cumulative distributions of point rainfall rate, horizontal path averaged rainfall rate, the vertical distribution of rain intensity, and a theoretically derived relationship between specific attenuation and rain rate obtained using median observed drop size distributions at a number of rain rates.

The first step in application of the model is the estimation of the instantaneous point rain rate (R_p) distribution. The Global Prediction Model provides median distribution estimates for broad geographical regions; eight climate regions A through H are designated to classify regions covering the entire globe.

Figures 3.4-1 and 3.4-2 show the geographic rain climate regions for the continental and ocean areas of the earth. The United States and European portions are further expanded in Figures 3.4-3 and 3.4-4 respectively.

The climate regions depicted by the Global Model are very broad. The upper and lower rain rate bounds provided by the nearest adjacent region have a ratio of 3.5 at 0.01 percent of the year for the proposed CCIR climate region D, for example, producing an attendant ratio of upper-to-lower bound attenuation values of 4.3 dB at 12 GHz. This uncertainty in the estimated attenuation value can be reduced by using rain rate distributions tailored to a particular area if long term statistics are available. Using the subdivision of climate regions B and D in the continental United States, Canada, and Europe also helps to reduce the uncertainty in the estimates.

The values of R_p may be obtained from the rain rate distribution curves of Figure 3.4-5. Figure 3.4-5a shows the curves for the eight global climate regions designated A through H for one minute averaged surface rain rate as a function the percent of year that rain rate is exceeded. The distributions for the region B and D subregions are shown in Figure 3.4-5b. Note that the distribution for region D_2 corresponds to that for D. Numerical values of R_p are provided in Table 3.4-1 for all regions and subregions.

3.4.2 Description of the Rain Attenuation Region

A path averaged rainfall rate $R = rR_p$, where r is defined as the effective path average factor, is useful for the estimation of attenuation for a line-of-sight radio relay system but, for the estimation of attenuation on a slant path to a satellite, account must be taken of the variation of specific attenuation with height. The atmospheric temperature decreases with height and, above some height, the precipitation particles must all be ice particles. Ice or snow do not produce significant attenuation; only regions with liquid water precipitation particles are of interest in the

Table 3.4-1. Point Rain Rate Distribution Values (mm/hr)
Versus Percent of Year Rain Rate is Exceeded

Percent of Year	RAIN CLIMATE REGION												Minutes per Year	Hours per Year
	A	B ₁	B	B ₂	C	D ₁	D=D ₂	D ₃	E	F	G	H		
0.001	28.5	45	57.5	70	78	90	108	126	165	66	185	253	5.26	0.09
0.002	21	34	44	54	62	72	89	106	144	51	157	220.5	10.5	0.18
0.005	13.5	22	28.5	35	41	50	64.5	80.5	118	34	120.5	178	26.3	0.44
0.01	10.0	15.5	19.5	23.5	28	35.5	49	63	98	23	94	147	52.6	0.88
0.02	7.0	11.0	13.5	16	18	24	35	48	78	15	72	119	105	1.75
0.05	4.0	6.4	8.0	9.5	11	14.5	22	32	52	8.3	47	86.5	263	4.38
0.1	2.5	4.2	5.2	6.1	7.2	9.8	14.5	22	35	5.2	32	64	526	8.77
0.2	1.5	2.8	3.4	4.0	4.8	6.4	9.5	14.5	21	3.1	21.8	43.5	1052	17.5
0.5	0.7	1.5	1.9	2.3	2.7	3.6	5.2	7.8	10.6	1.4	12.2	22.5	2630	43.8
1.0	0.4	1.0	1.3	1.5	1.8	2.2	3.0	4.7	6.0	0.7	8.0	12.0	5260	87.7
2.0	0.1	0.5	0.7	0.8	1.1	1.2	1.5	1.9	2.9	0.2	5.0	5.2	10520	175
5.0	0.0	0.2	0.3	0.3	0.5	0.0	0.0	0.0	0.5	0.0	1.8	1.2	26298	438

ORIGINAL PAGE IS
OF POOR QUALITY

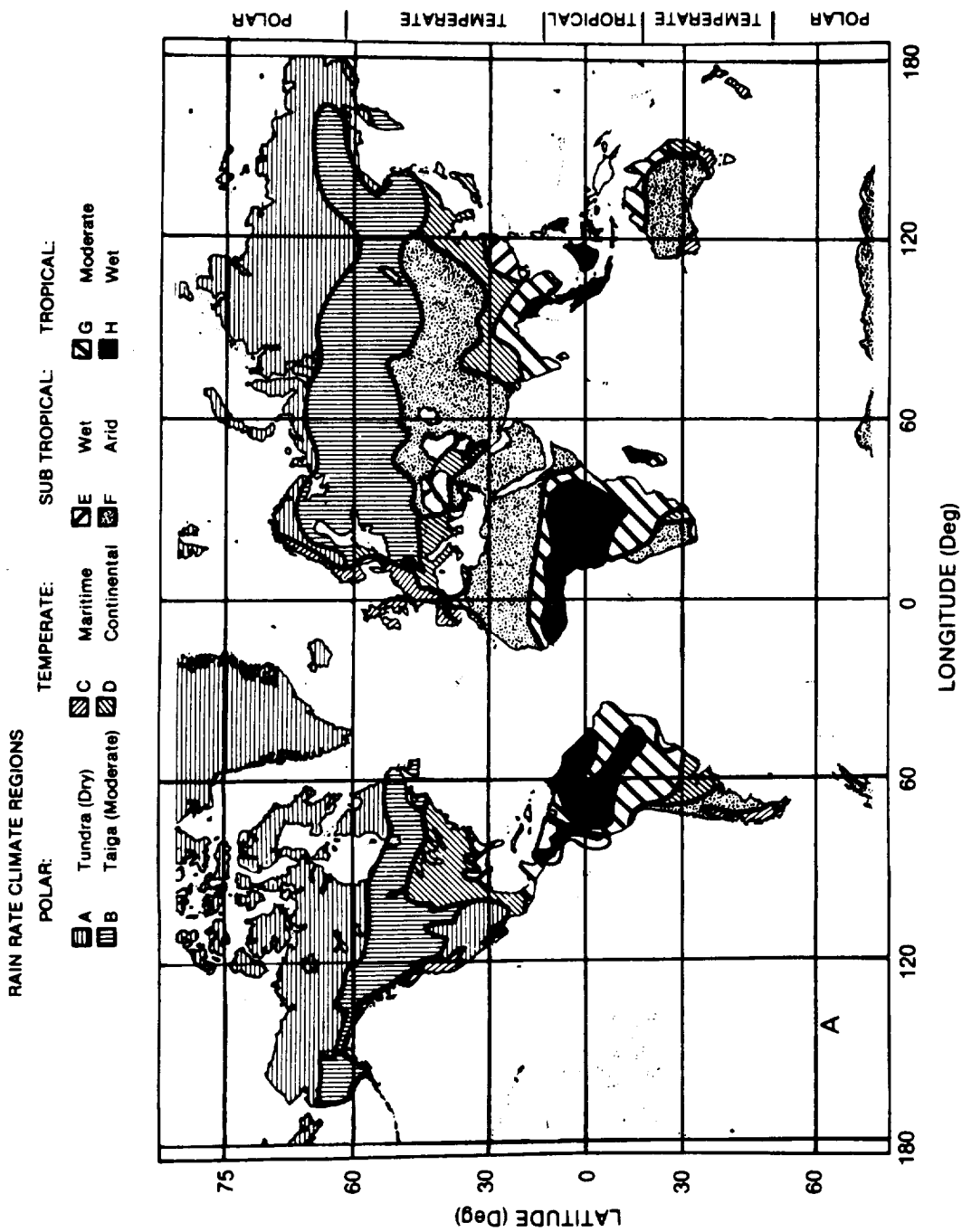


Figure 3.4-1. Global Rain Rate Climate Regions for the Continental Areas

ORIGINAL PAGE IS
OF POOR QUALITY

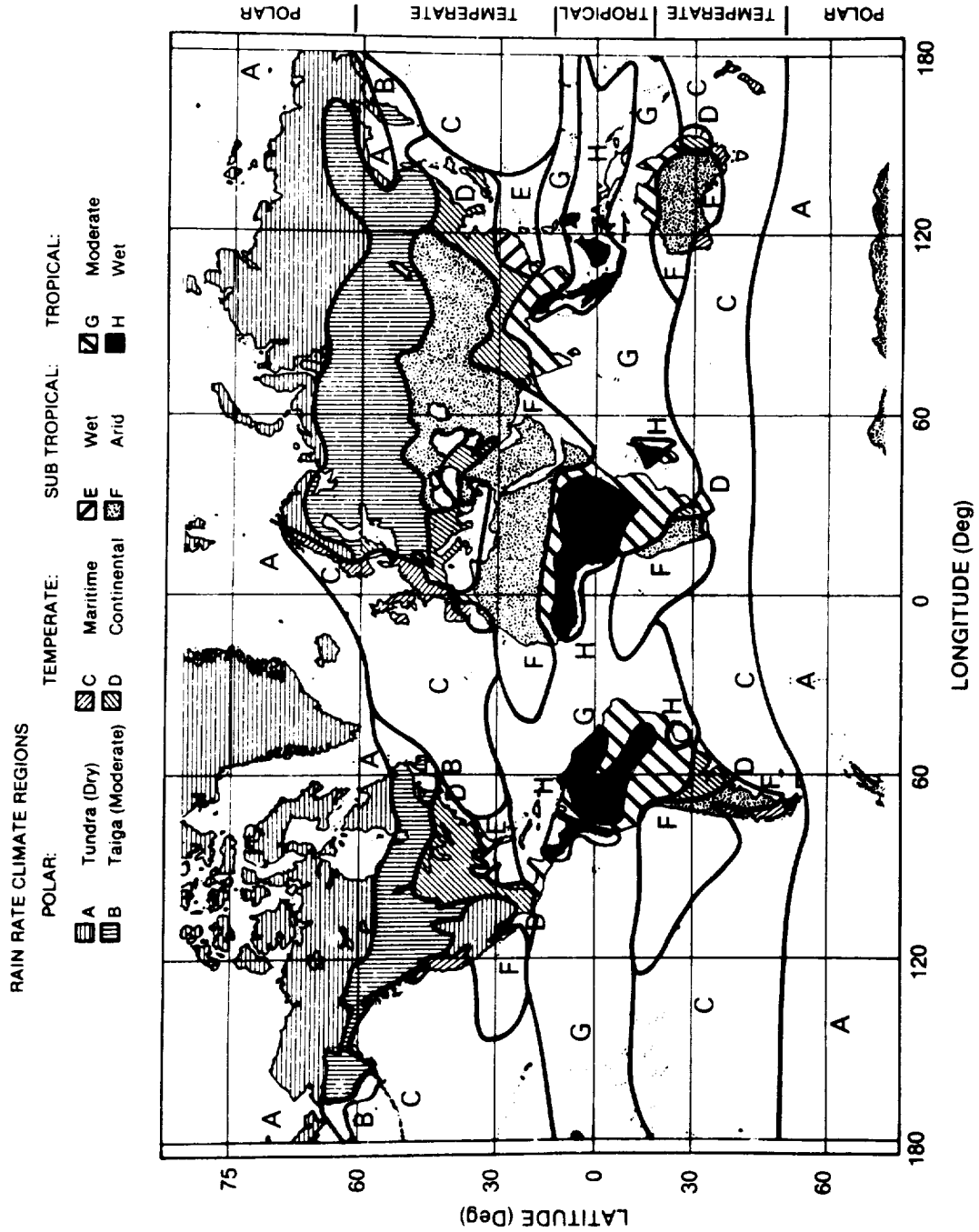


Figure 3.4-2. Global Rain Rate Climate Regions Including the Ocean Areas

ORIGINAL PAGE IS
OF POOR QUALITY

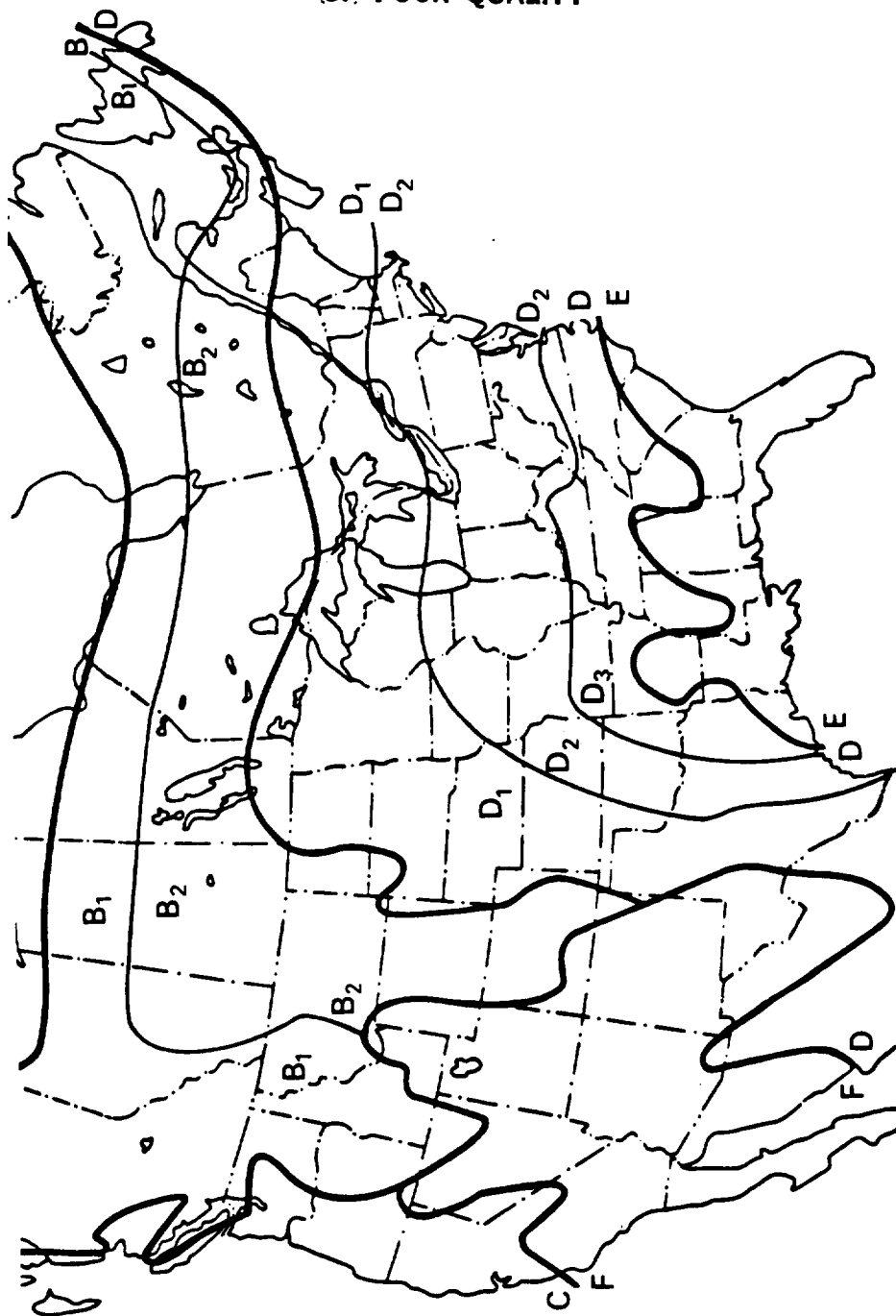


Figure 3.4-3. Rain Rate Climate Regions for the Continental U.S. and Southern Canada

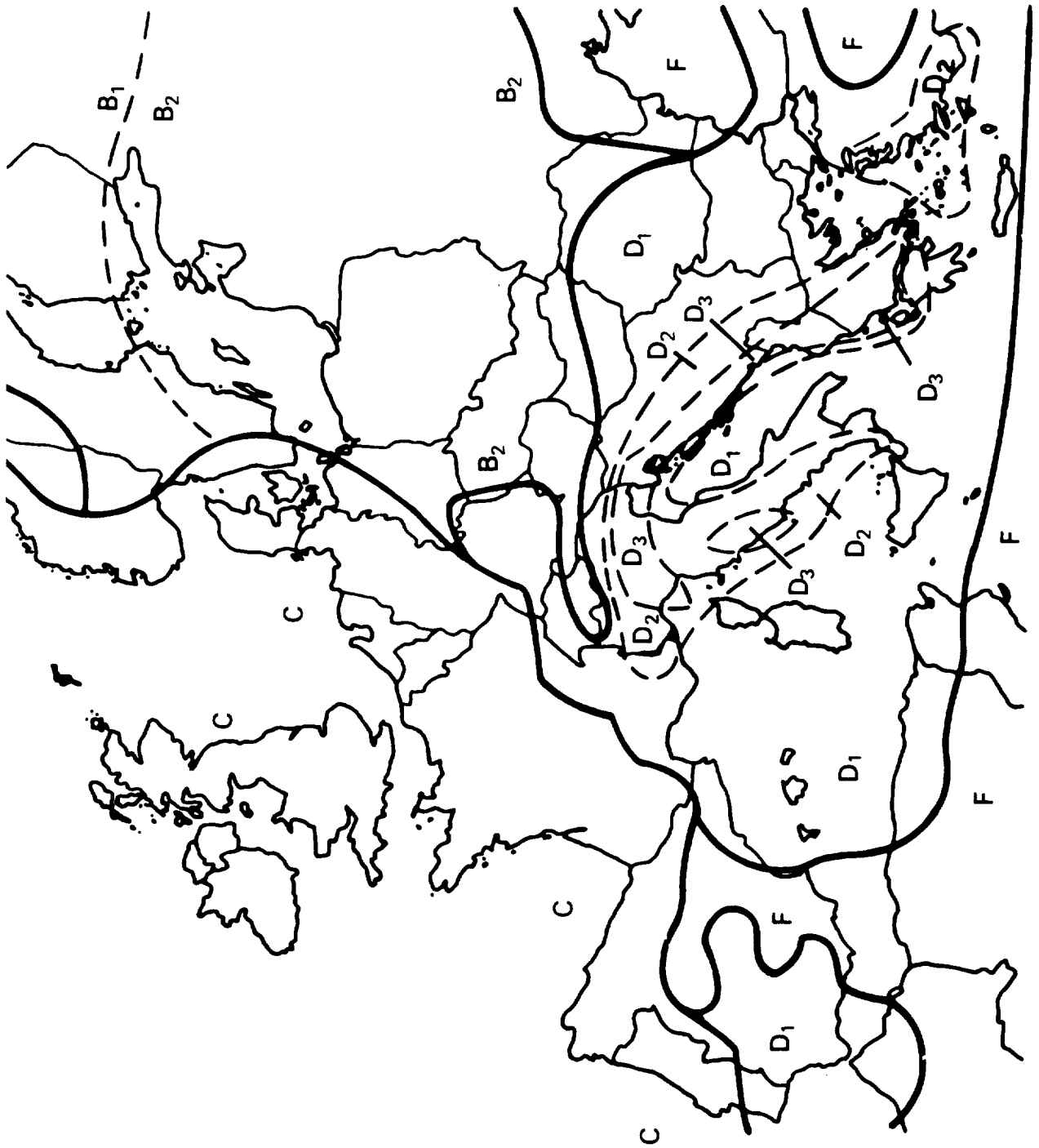


Figure 3.4-4. Rain Rate Climate Regions of Europe

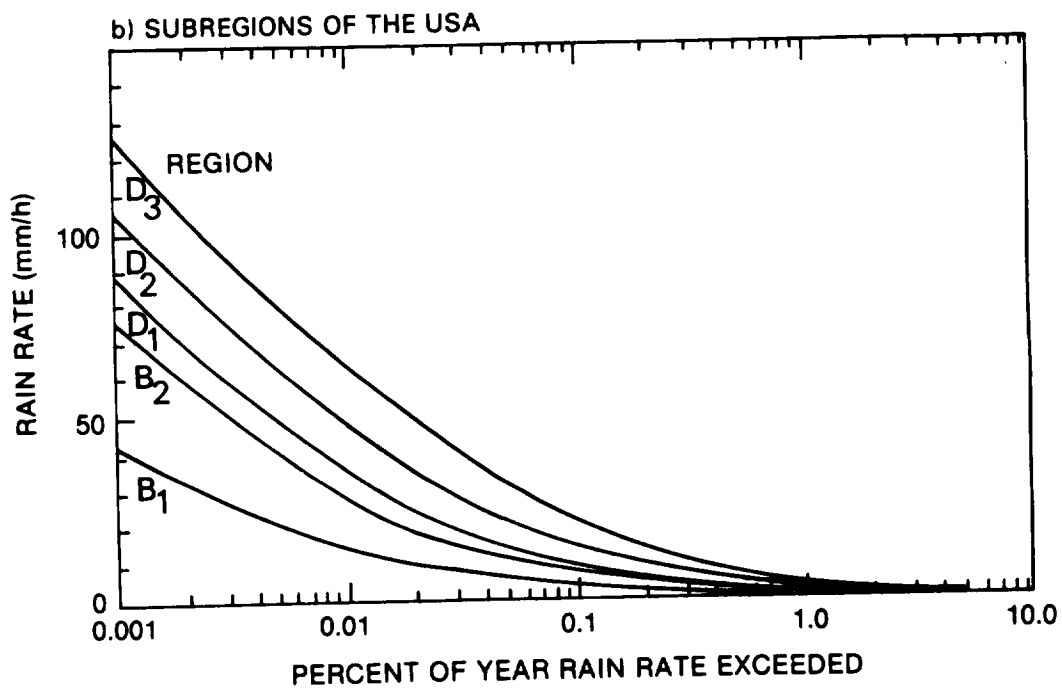
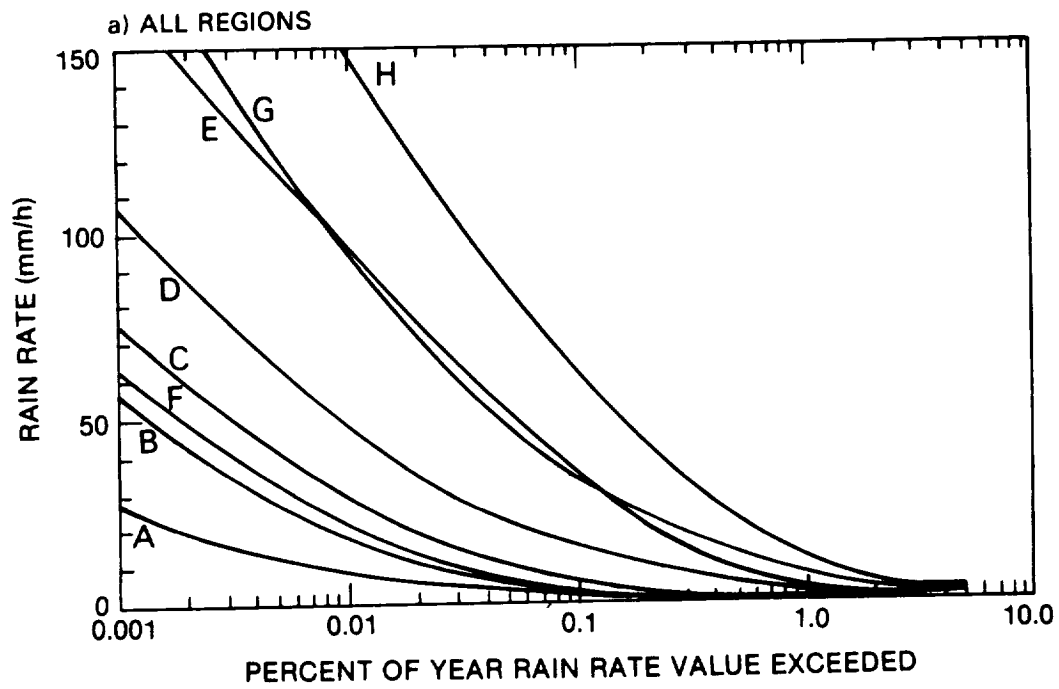
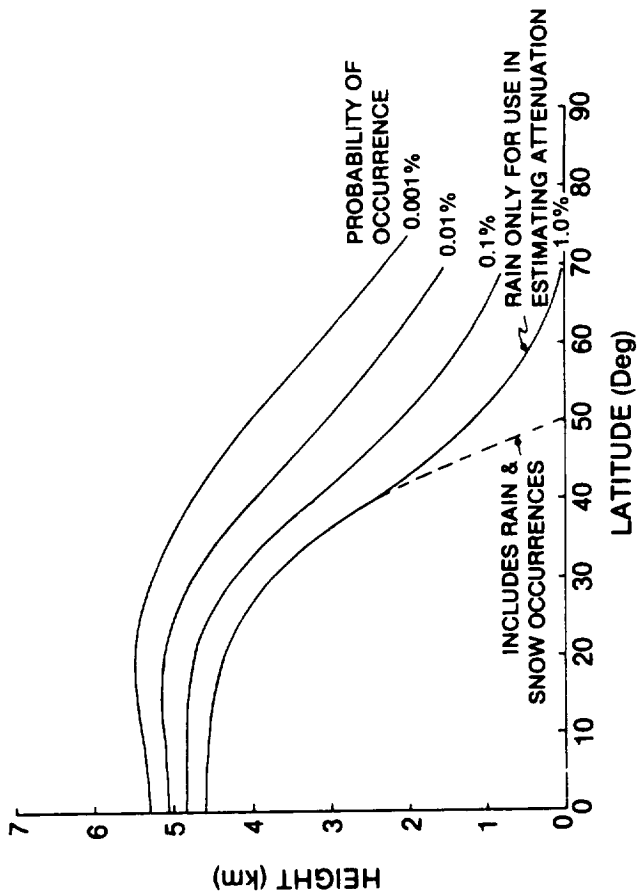


Figure 3.4-5. Point Rain Rate Distributions as a Function of Percent of Year Exceeded

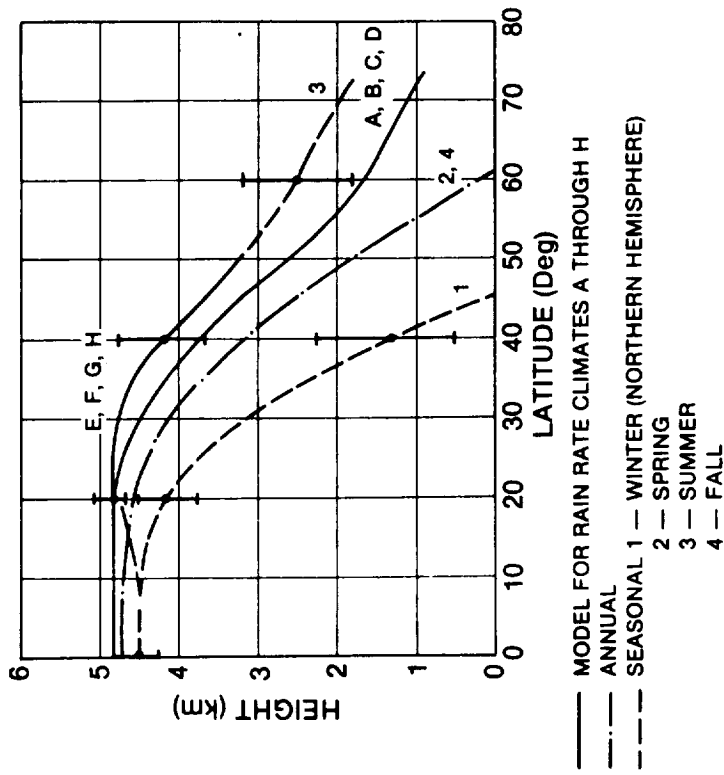
estimation of attenuation. The size and number of rain drops per unit volume may vary with height. Measurements made using weather radars show that the reflectivity of a rain volume may vary with height but, on average, the reflectivity is roughly constant with height to the height of the 0°C isotherm and decreases above that height. The rain rate may be assumed to be constant to the height of the 0°C isotherm at low rates and this height may be used to define the upper boundary of the attenuating region. A high correlation between the 0°C height and the height to which liquid rain drops exist in the atmosphere should not be expected for the higher rain rates because large liquid water droplets are carried aloft above the 0° height in the strong updraft cores of intense rain cells. It is necessary to estimate the rain layer height appropriate to the path in question before proceeding to the total attenuation computation since even the 0°C isotherm height depends on latitude and general rain conditions.

As a model for the prediction of attenuation, the average height of the 0° isotherm for days with rain was taken to correspond to the height to be expected one percent of the year. The highest height observed with rain was taken to correspond to the value to be expected 0.001 percent of the year, the average summer height of the -5°C isotherm. The latitude dependences of the heights to be expected for surface point rain rates exceeded one percent of the year and 0.001 percent of the year were obtained from the latitude dependences provided by Oort and Rasmussen (1971). The resultant curves are presented in Figure 3.4-6. For the estimation of model uncertainty, the seasonal rms uncertainty in the 0°C isotherm height was 500 m or roughly 13 percent of the average estimated height. The value of 13 percent is used to estimate the expected uncertainties to be associated with Figure 3.4-6.

The correspondence between the 0°C isotherm height values and the excessive precipitation events showed a tendency toward a linear relationship between R_p and the 0°C isotherm height H_0 for high values of R_p . Since, at high rain rates, the rain rate distribution



a) Variable Isotherm:



b) 0°C Isotherm Height

Figure 3.4-6. Effective Heights for Computing Path Lengths Through Rain Events

function displays a nearly linear relationship between R_p and $\log P$ (P is probability of occurrence), the interpolation model used for the estimation of H_0 for P between 0.001 and one percent is assumed to have the form, $H_0 = \underline{a} + \underline{b} \log P$. The relationship was used to provide the intermediate values displayed in Figure 3.4-6a. In Figure 3.4-6b are shown the 0°C isotherms for various latitudes and seasons.

3.4.3 Attenuation Model

The complete model for the estimation of attenuation on an earth-space path starts with the determination of the vertical distance between the height of the earth station and the 0°C isotherm height ($H_0 - H_g$ where H_g is the ground station height) for the percentage of the year (or R_p) of interest. The path horizontal projection distance (D) can then be obtained by:

$$D = \begin{cases} (H_0 - H_g)/\tan \theta & \theta \geq 10^\circ \\ E\psi \ (\psi \text{ in radians}) & \theta < 10^\circ \end{cases} \quad (3.4-1)$$

where

H_0 = height of 0°C isotherm

H_g = height of ground terminal

θ = path elevation angle

and

$$\begin{aligned} \psi &= \sin^{-1} \left\{ \frac{\cos \theta}{H_0 + E} \left[(H_g + E)^2 \sin^2 \theta + 2E(H_0 - H_g) \right. \right. \\ &\quad \left. \left. + H_0^2 - H_g^2 \right]^{1/2} - (H_g + E) \sin \theta \right\} \\ &= \cos^{-1} \left[\frac{\cos \theta}{H_0 + E} (E + H_g) \right] - \theta \end{aligned} \quad (3.4-2)$$

where

E = effective earth's radius (8500 km).

The specific attenuation may be calculated for an ensemble of rain drops if their size and shape number densities are known. Experience has shown that adequate results may be obtained if the Laws and Parsons (1943) number density model is used for the attenuation calculations (Crane-1966) and a power law relationship is fit to calculated values to express the dependence of specific attenuation on rain rate (Olsen et al-1978). The parameters a and b of the power law relationship:

$$\alpha = aR_p^b \quad (3.4-3)$$

where α = specific attenuation (dB/km)

R_p = point rain rate (mm/hour)

are both a function of operating frequency. Figures 3.4-7 and 3.4-8 give the multiplier, $a(f)$ and exponent $b(f)$, respectively, at frequencies from 1 to 100 GHz. The appropriate a and b parameters may also be obtained from Table 3.4-2 and used in computing the total attenuation from the model. Alternately, values of a and b from Tables 2.3-2 or 2.3-3 may be used.

3.4.3.1 Path Averaged Rain Rate Technique. The path averaged rain rate exceeded for a specified percentage of the time may differ significantly from the surface point rain rate exceeded for the same percentage of the time. The estimation of the path averaged values from the surface point values requires detailed information about the spatial correlation function for rain rate. Adequate spatial data are not currently available. A sufficient number of observations using rain gauge networks are available to provide a basis for a point to path average model. Observations for 5 and 10 km paths are presented in Figures 3.4-9 and 3.4-10, respectively. The effective path average factor, r , represents the relationship between point and path averaged rain rate as

$$R_{\text{path}} = r \cdot R_p \quad (3.4-4)$$

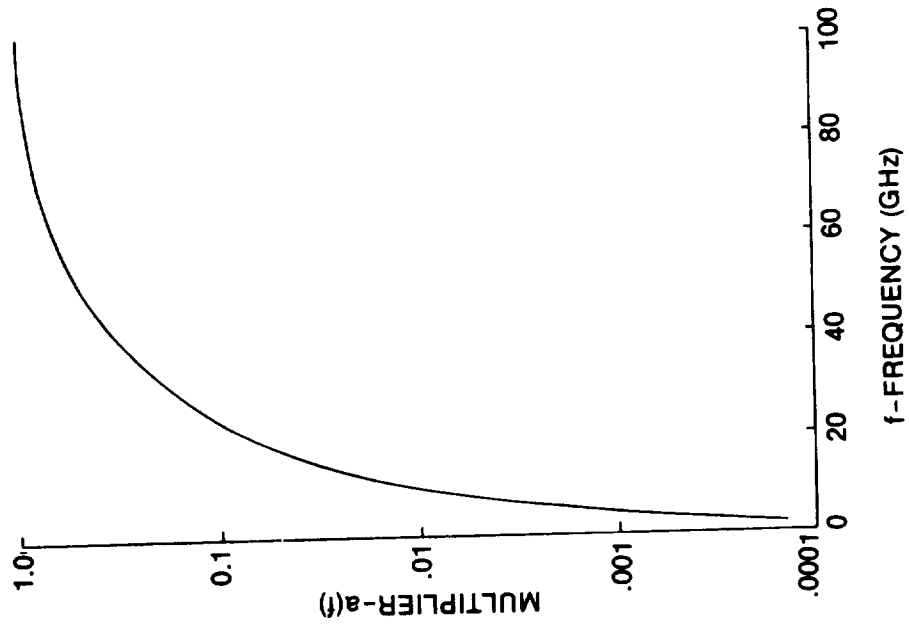


Figure 3.4-7. Multiplier Coefficient in the Specific Attenuation Relation

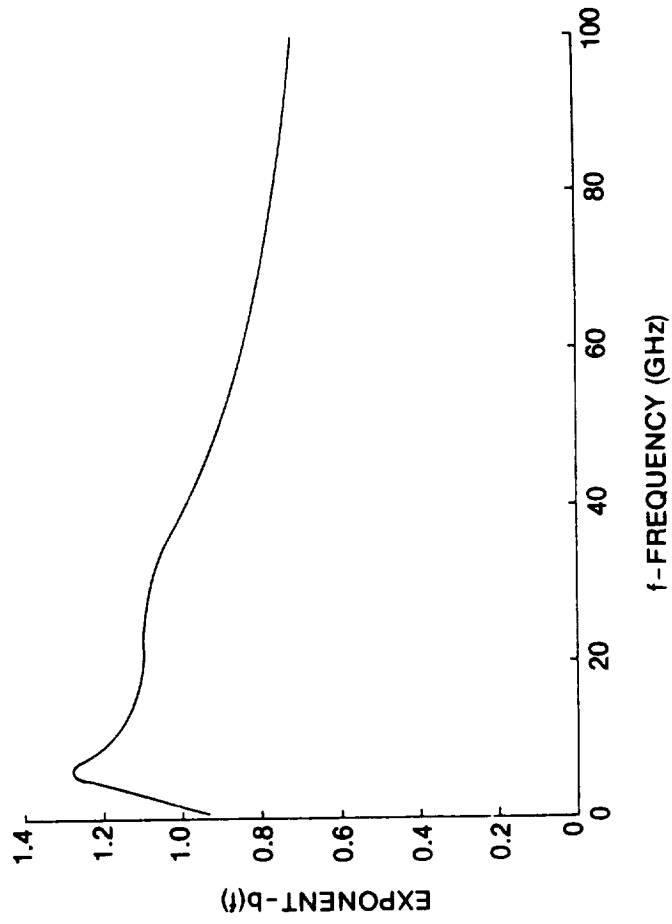


Figure 3.4-8. Exponent Coefficient in the Specific Attenuation Relation

Table 3.4-2. Parameters for Computing Specific Attenuation:
 $= aR^b$, 0°C, Laws and Parson Distribution
 (Crane-1966)

Frequency f - GHz	Multiplier a(f)	Exponent b(f)
1	0.00015	0.95
4	0.00080	1.17
5	0.00138	1.24
6	0.00250	1.28
7.5	0.00482	1.25
10	0.0125	1.18
12.5	0.0228	1.145
15	0.0357	1.12
17.5	0.0524	1.105
20	0.0699	1.10
25	0.113	1.09
30	0.170	1.075
35	0.242	1.04
40	0.325	0.99
50	0.485	0.90
60	0.650	0.84
70	0.780	0.79
80	0.875	0.753
90	0.935	0.730
100	0.965	0.715

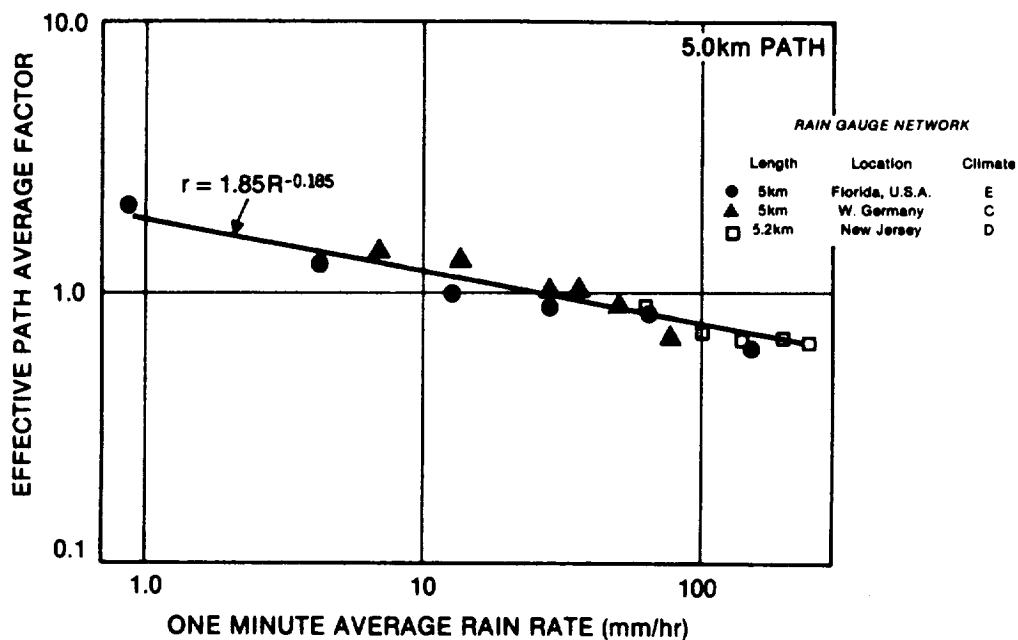


Figure 3.4-9. Effective Path Average Factor Versus Rain Rate, 5 km Path

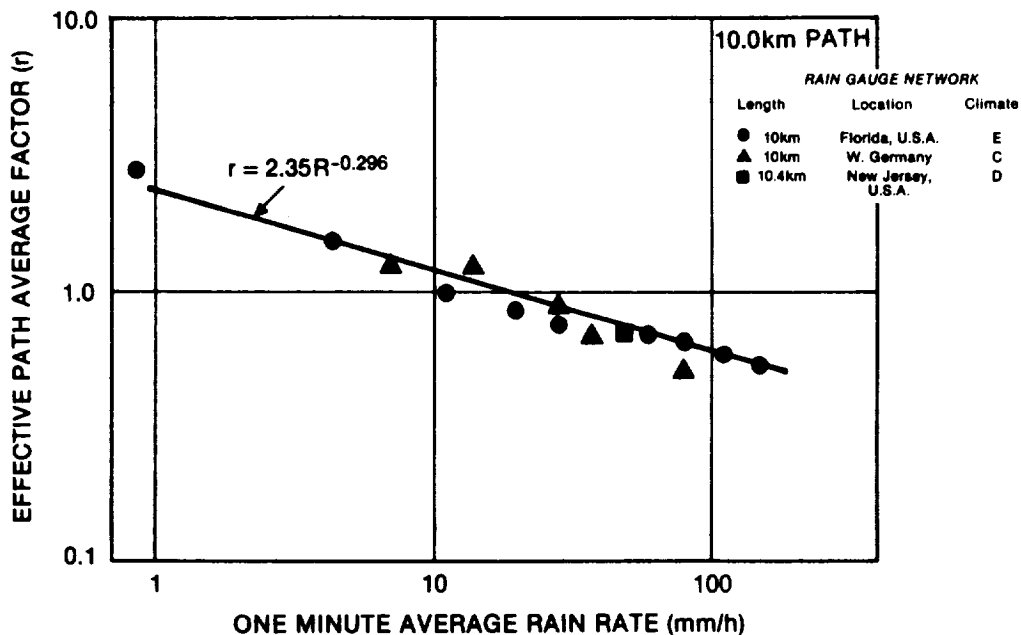


Figure 3.4-10. Effective Path Average Factor Versus Rain Rate, 10 km Path

where R_{path} and R_p are the path and point rainfall rates at the same probability of occurrence.

Figure 3.4-11 represents the construction of an effective path average factor using data from paths between 10 and 22.5 km in length. The values of r were obtained by assuming that the occurrence of rain with rates in excess of 25 mm/hour were independent over distances larger than 10 km. The estimation of path averaged rain rate then depends upon modeling the change in occurrence probability for a fixed path average value, not the change in path average value for a fixed probability. Using D_0 as the reference path length ($D_0 = 22.5$ km for Figure 3.4-11), the exceedance probabilities for the path averaged values were multiplied by D_0/D where D was the observation path length to estimate the path average factor for a path of length D_0 .

The path attenuation caused by rain is approximately determined from the path averaged rain rate by

$$A \approx L r^a R_p^b \quad (3.4-5)$$

where A is path attenuation, L is the length of the propagation path or D_0 , whichever is shorter, r is the effective path average factor, R is the point rainfall rate exceeded P percent of the time, and a and b are coefficients used to estimate specific attenuation for a given rain rate. Using this model and propagation paths longer than 22.5 km, the effective path average factor for 22.5 km path may be calculated from simultaneous point rain rate distribution and attenuation distribution data. Results for a number of paths in rain rate climates C and D are presented in Figure 3.4-12. The line plotted on this figure is the power law relationship fit to all the data displayed in Figure 3.4-11. The observations at 13 and 15 GHz are in excellent agreement with the model based solely on rain gauge network data. At lower frequencies, the discrepancy is larger, being as much as a factor of 2. At 11 GHz, the model appears to underestimate the observed attenuation by a factor of 2. It is

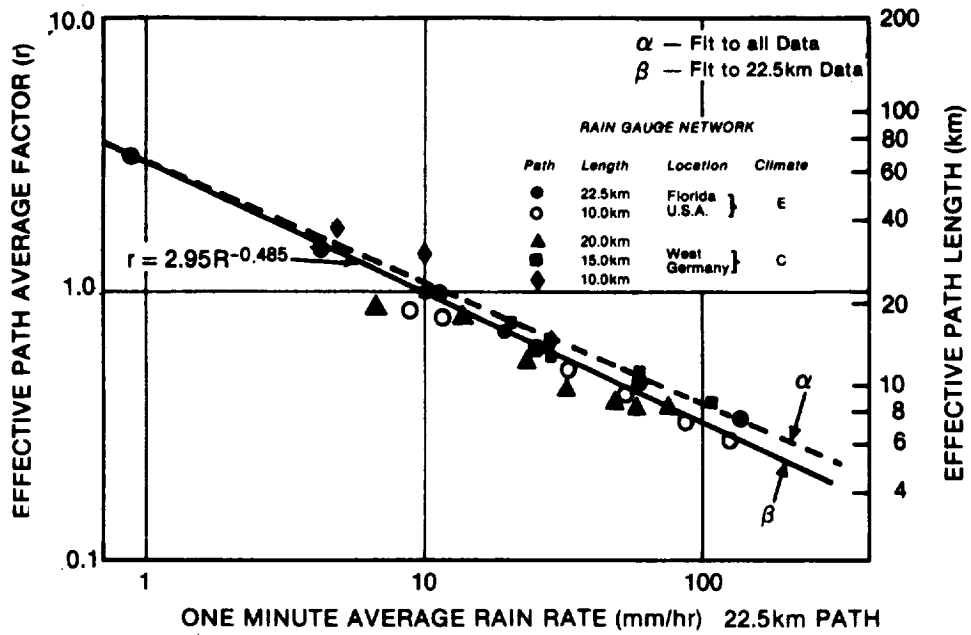


Figure 3.4-11. Effective Path Average Factor Versus Rain Rate

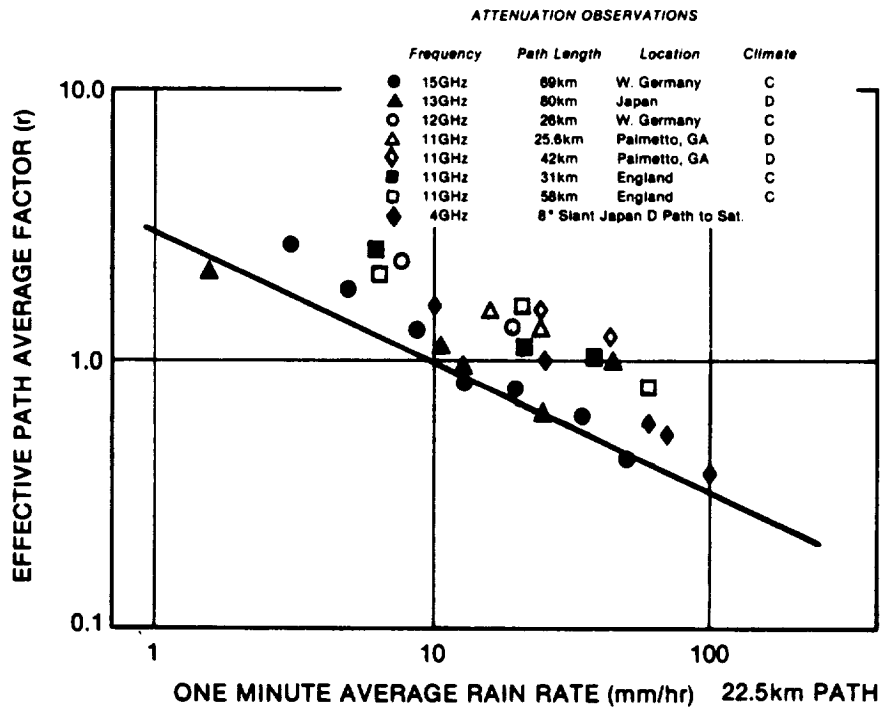


Figure 3.4-12. Effective Path Average Factor Versus Rain Rate Derived from Attenuation Measurements

noted that simultaneous point rain rate observations were used in the construction of Figure 3.4-12, not the rain rate distributions for each climate region. Since fades due to multipath must be removed from the analysis prior to making the comparison in Figure 3.4-12 and multipath effects tend to be relatively more important at frequencies below 13 GHz, the lack of agreement displayed in Figure 3.4-12 may be due to effects other than rain.

A power law approximation to the effective path average factors depicted in Figures 3.4-9 through 3.4-11 may be used to model the behavior of the effective path average factor for paths shorter than 22.5 km. Letting the effective path average factors be expressed by

$$r \approx \gamma(D) R_p^{-\delta(D)} \quad (3.4-6)$$

where D is the surface projection of the propagation path and the model curves for $\gamma(D)$ and $\delta(D)$ are given in Figure 3.4-13 and 3.4-14. Figure 3.4-15 displays the dependence of the modeled effective path average factor on point rain rate.

Attenuation prediction for Earth-space paths requires the estimation of rain rate along a slant path. Statistical models for rain scatter indicate that the reflectivity, hence, specific attenuation or rain rate, is constant from the surface to the height of the 0°C isotherm (Goldhirsh and Katz 1979). By assuming that the specific attenuation is statistically independent of height for altitudes below the 0°C isotherm the path averaged rain rate (or specific attenuation) can be estimated using the model in Figures 3.4-13 and 3.4-14. For application, the surface projection of the slant path below the melting layer is used to define the surface path length, D . The attenuation on an Earth-space path for an elevation angle higher than 10° is given by:

$$A = \frac{H}{\sin \theta} a(f) \gamma(D) R_p^{b(f) - \delta(D)} \quad (3.4-7)$$

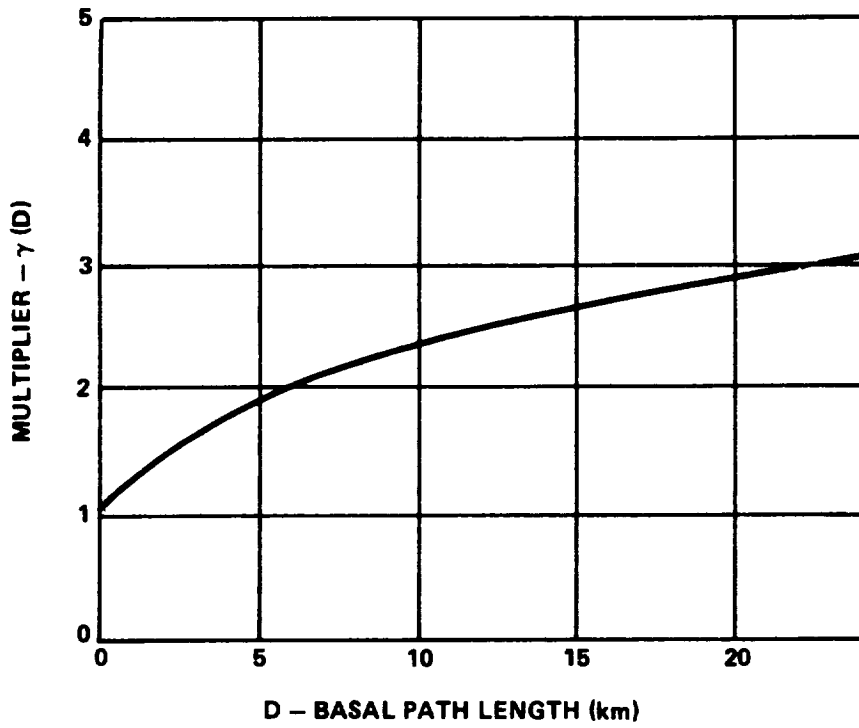


Figure 3.4-13. Multiplier in the Path Averaging Model

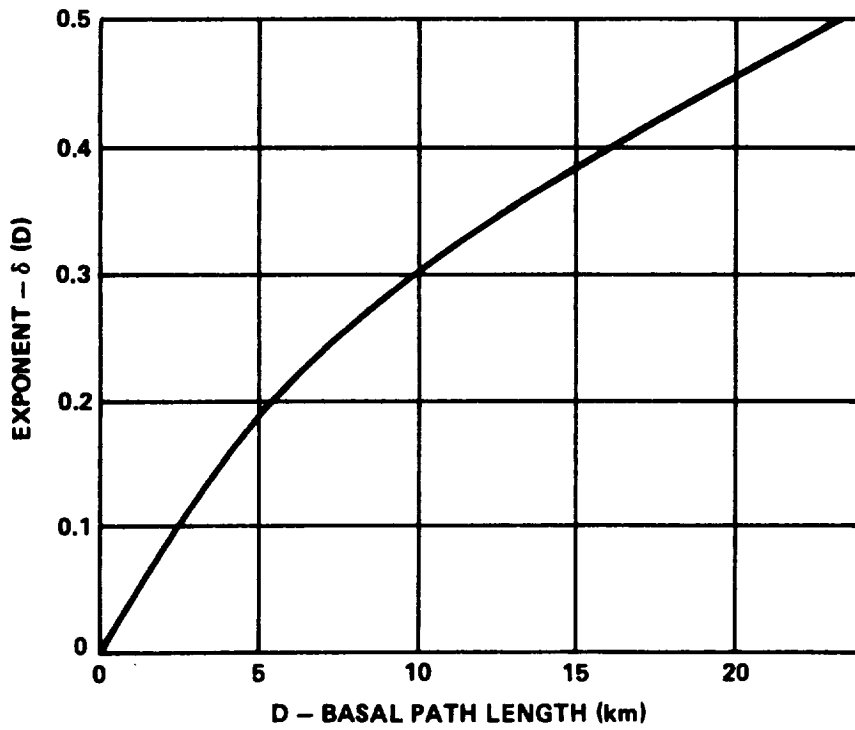


Figure 3.4-14. Exponent in the Path Averaging Model

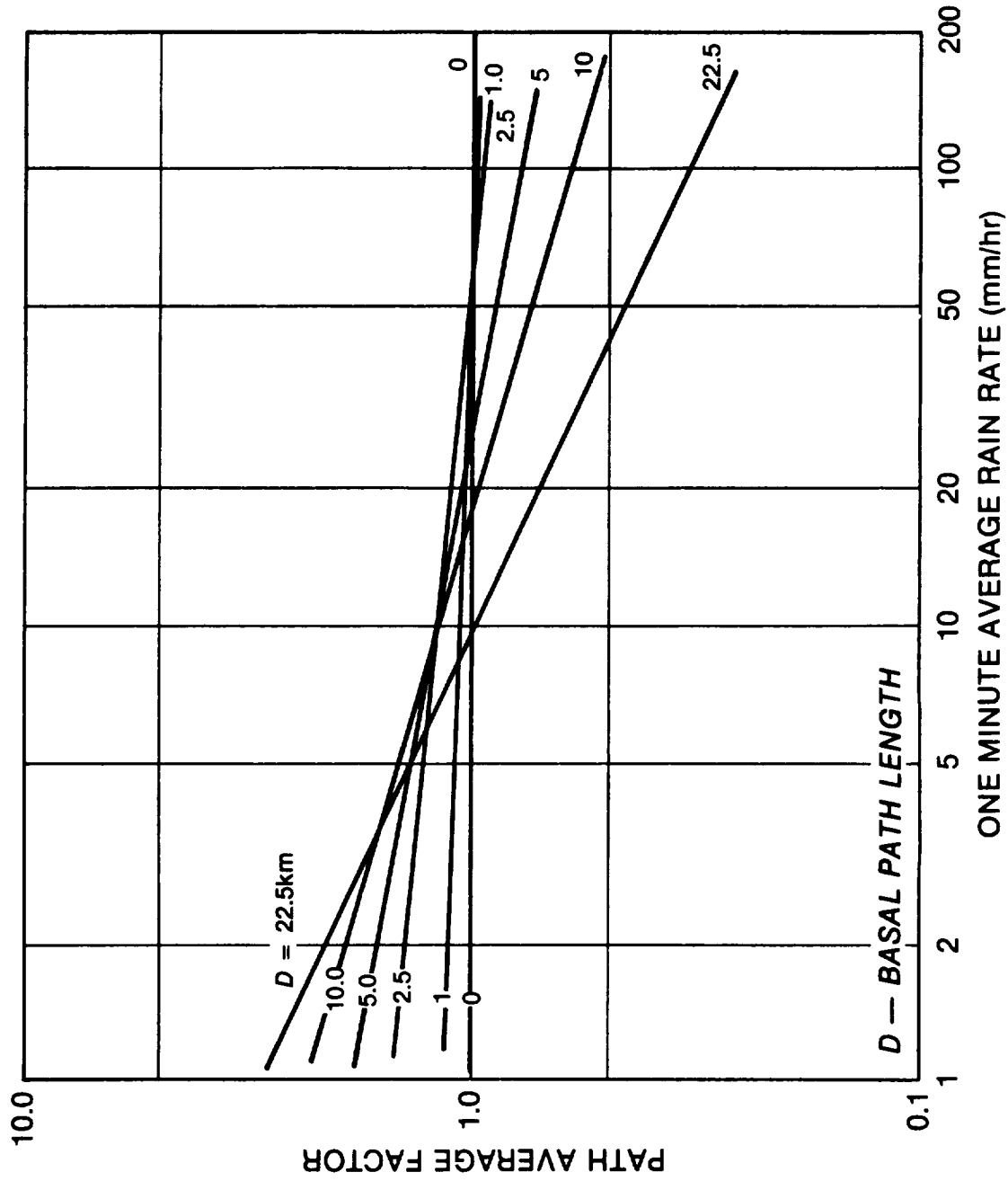


Figure 3.4-15. Effective Path Average Factor Model for Different Basal Path Lengths

where H is the height of the 0°C isotherm (see Figure 3.4-6b), θ is the elevation angle ($\theta > 10^\circ$) and $D = H/\tan \theta$. For application at elevation angles lower than 10° , the effect of refraction by the troposphere and of the earth's curvature should be taken into account in the calculation of D. If D exceeds 22.5 km, a D_0 of 22.5 km is used for the calculation of the effective path average factor and the occurrence probabilities are multiplied by D/D_0 .

3.4.3.2 Variable Isotherm Height Technique. The variable isotherm height technique uses the fact that the effective height of the attenuating medium changes depending on the type of rainfall event. Also, various types of rainfall events selectively influence various percentages of time throughout the annual rainfall cycle. Therefore, a relation exists between the effective isotherm height and the percentage of time that the rain event occurs. This relation has been shown earlier in Figure 3.4-6a. Again the total attenuation is obtained by integrating the specific attenuation along the path. The resulting equation to be used for the estimation of slant path attenuation is:

$$A = \frac{a R_p^b}{\cos \theta} \left[\frac{e^{UZb-1}}{U^b} - \frac{X^b e^{YZb}}{Y^b} + \frac{X^b e^{YDb}}{Y^b} \right]; \theta \geq 10^\circ \quad (3.4-8)$$

where U, X, Y and Z are empirical constants that depend on the point rain rate. These constants are:

$$U = \frac{1}{Z} [\ln(Xe^{YZ})] \quad (3.4-9)$$

$$X = 2.3 R_p^{-0.17} \quad (3.4-10)$$

$$Y = 0.026 - 0.03 \ln R_p \quad (3.4-11)$$

$$Z = 3.8 - 0.6 \ln R_p \quad (3.4-12)$$

for lower elevation angles $\theta < 10^\circ$

$$A = \frac{L}{D} a R_p^b \left[\frac{e^{UZb-1}}{Ub} - \frac{X^b e^{YZb}}{Yb} + \frac{X^b e^{YDb}}{Yb} \right] \quad (3.4-13)$$

where

$$L = [(E + H_g)^2 + (E + H_o)^2 - 2(E + H_g)(E + H_o) \cos \psi]^{\frac{1}{2}} \quad (3.4-14)$$

$$= [(E + H_g)^2 \sin^2 \theta + 2E(H_o - H_g) + H_o^2 - H_g^2]^{\frac{1}{2}} - (E + H_g) \sin \theta$$

ψ = path central angle defined above.

3-4.4 Application of the Global Model

Section 6.3.2.1 gives a step-by-step procedure for applying the Global Model, using the variable isotherm technique. Schwab (1980) applied this model on a worldwide basis to find downlink availability for specified margin and frequency. An example of the results of his work is shown in Figure 3.4-16. It is interesting to compare this figure with the rain climate region map of Figure 3.4-2.

3.5 THE TWO-COMPONENT MODEL

The Two-Component (T-C) rain attenuation model (Crane-1982) determines the probability of exceeding a given attenuation threshold. The Model's name relates to the fact that two distinctive types of rain events are addressed: convective cell and widespread "debris." The characterization of climatic zones is identical to the Global Model in terms of rain rates. The T-C Model was formulated in such a way that it might later be extended to site diversity systems, rain scatter interference, and attenuation duration statistics.

The fundamental approach in the T-C Model is to determine the probabilities for exceeding a given attenuation with convective rain and debris separately. The sum of these probabilities is then taken as the total probability of exceeding the given rain attenuation threshold.

ORIGINAL PAGE IS
OF POOR QUALITY

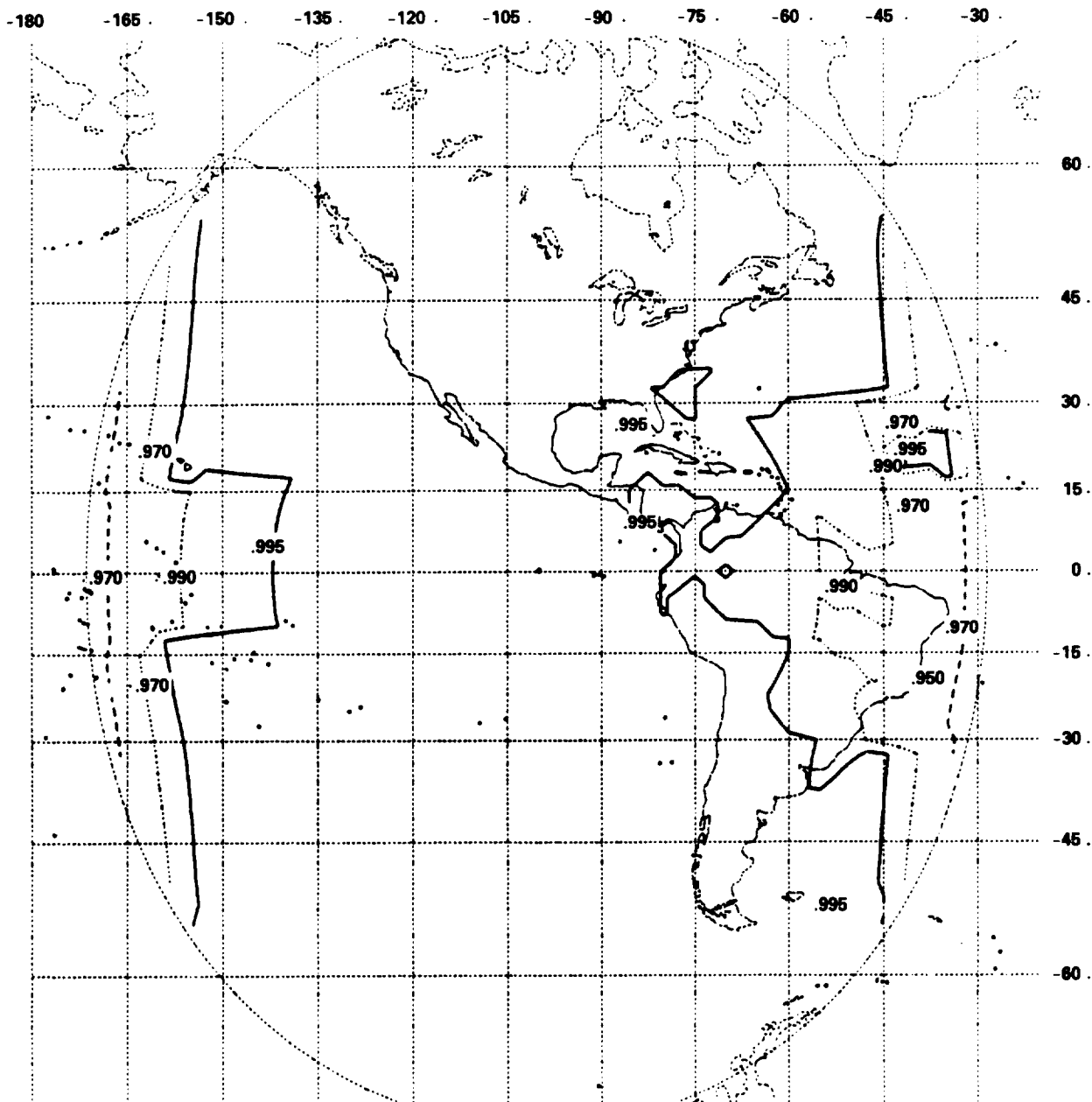


Figure 3.4-16. Availability Contours for Satellite at 100°W With 6 dB Margin Operating at 20 GHz

The projected (horizontal) path lengths for both types of rain are first determined geometrically from 0°C isotherm heights. These heights were modeled from observations during precipitation events using radiosonde data, rain occurrence data and excessive-precipitation data for seven spatially separated sites in the US (Crane-1980a). The data were extrapolated globally using averaged temperature profiles, where only summertime data was used at latitudes higher than 50°. The resulting height versus latitude variations, which do not employ the correlation between rain rate and rain rate height assumed in other models (e.g., Global), are:

$$H_c = 3.1 - 1.7 \sin [2(A-45)] \quad (3.5-1)$$

$$H_d = 2.8 - 1.9 \sin [2(A-45)] \quad (3.5-2)$$

where H_c , H_d are the rain heights in kilometers for volume cell (convective) and debris rain types, respectively, and A is the latitude (deg.). The corresponding projected path lengths are then determined geometrically as:

$$D_c D_d = \frac{(H_{c,d} - H_o) [2 - 2 (H_{c,d} - H_o) / 8500]}{\tan \theta \sqrt{\tan^2 \theta + (H_{c,d} - H_o) / 8500}} \quad (3.5-3)$$

where θ is the slant path elevation angle and H is height of the earth station above sea level (km).

The attenuation along the projected path is determined geometrically from the given slant path attenuation threshold and path elevation angle. This is then used to determine the corresponding rain rates, for volume cell and debris rain types, which would produce that amount of attenuation. The two rain types are addressed separately below.

3.5.1 Volume Cell Rain Rate

The average length of a line through a (circular) volume cell (W_c) is assumed to be about 2.2 km, based on the average volume cell

area data from a three year radar measurement program conducted in Goodland, Kansas. Thus, the effective projected path length through rain (L_c) must be taken to be the lesser of 2.2 km and D_c . If L_c is not determined from D_c ($D_c > W_c$), an adjustment factor (C) is required. In this case, the projected path D_c is longer than the average volume cell width and the integrated path rain rate must embody the effect of debris that is close to the cell. This is modeled as:

$$C = \frac{1 + 0.7 (D_c - W_c)}{1 + (D_c - W_c)}; (D_c - 2.2) > 0 \quad (3.5-4)$$

$$C = 1 \quad ;(D_c - 2.2) \leq 0 \quad (3.5-5)$$

The effective point rain rate (R') for volume cell rain can then be readily determined as:

$$R' = \left(\frac{CA}{KL_c} \right)^{1/\alpha} \quad (3.5-6)$$

where A is the attenuation along the projected path and k and α are the common specific attenuation coefficients for point rainfall rates ($\gamma = KR^\alpha$).

3.5.2 Debris Rain Rate

In debris rain, the rain extent can readily exceed the slant path projection distance. The rain extent (W_d) is, however, dependent on rain rate. The Kansas radar observations indicated a relationship between average rain rate in debris and W_d :

$$W_d = 29.7R^{-0.34}$$

where W_d is the length scale (km) and R is the rain rate (mm/h) for debris. This is more conveniently expressed in terms of attenuation for determining the effective rain rate (R'') in debris.:

$$W_d = 29.7^{a/(a-.34)} K^{.34/(a-.34)} A^{-.34/(a-.34)} \quad (3.5-7)$$

$$W'_d = \text{minimum } (W_d, D_d) \quad (3.5-8)$$

$$R'' = \left(\frac{A}{kW'_d} \right)^{1/a} \quad (3.5-9)$$

where R'' is the effective rain rate for debris.

3.5.3 Probability of Exceeding an Attenuation Threshold

A simple approximation to the observed (Kansas) rain rate distribution produced by volume cells is an exponential distribution. The debris distribution function was nearly log-normal. The sum of these independent distributions was found to closely fit the empirical rain rate distributions for all climate regions. Thus:

$$P(r \geq R) = P_c(r \geq R) + P_d(r \geq R) \quad (3.5-10)$$

$$= p_c(1 + D_c/W_c) \exp(-R'/R_c)$$

$$+ p_d(1 + D_d/W_d) \eta[(1/\sigma_d)[\ln R'' - \ln R_d]] \quad (3.5-11)$$

where $P(r \geq R)$ is the probability of the observed rain rate r exceeding the specified rain rate R ; $P_{c,d}(r \geq R)$ are the distribution functions for volume cells and debris, respectively; $p_{c,d}$ are the probabilities of a cell and debris, respectively; $R_{c,d}$ are the average rain rates in cells and debris, respectively; σ_d is the standard deviation of the logarithm of the rain rate; and η is the normal distribution function. Values for the parameters p_c , p_d , R_c , and σ_d have been tabulated for each of the Global Model rain climate regions (Crane-1982).

3.6 THE CCIR MODEL

The International Radio Consultative Committee, CCIR, adopted a procedure for the prediction of attenuation caused by rain at its XVth Plenary Assembly in Geneva in February 1982 (CCIR-1982a). This result was preceded by several years of intense deliberations by representatives of CCIR Study Group V from several nations. The procedure provided the basis for rain attenuation calculations required for international planning and coordination meetings, and Regional and World Administrative Radio Conferences.

The original CCIR procedure has undergone several modifications, including deliberations for the 1982 Conference Preparatory Meeting for RARC-83 for the Broadcasting Satellite Service (CCIR-1982b, CCIR-1982c), and the Study Group 5 Inputs for the XVIth Plenary Assembly, in Dubrovnik, Yugoslavia (CCIR-1985a, CCIR-1985b). The rain characterization and attenuation prediction procedures described in this handbook are the latest published versions, as provided in Reports 563-3 (CCIR-1986a), and 564-3 (CCIR-1986b), respectively, from the XVIth Plenary Assembly. Readers interested in tracing the evolution of the CCIR prediction procedure development process are referred to the earlier documents referenced above.

3.6.1 CCIR Rain Characterization

The first element of the CCIR Model involves a global map of fourteen rain climatic zones with associated rainfall intensity cumulative distributions for each region specified (CCIR-1986a). Average annual rain rates are given for exceedance times from 0.001 to 1.0 percent. Figure 3.6-1 presents the global map of the CCIR rain climatic zones, ranging from A (light rains) to P (heavy rains). A more detailed map of the CCIR climatic zones for the continental United States and Canada is shown in Figure 3.6-2 (Ippolito, 1986). Table 3.6-1 lists the rain rate distributions for the fourteen rain climatic zones.

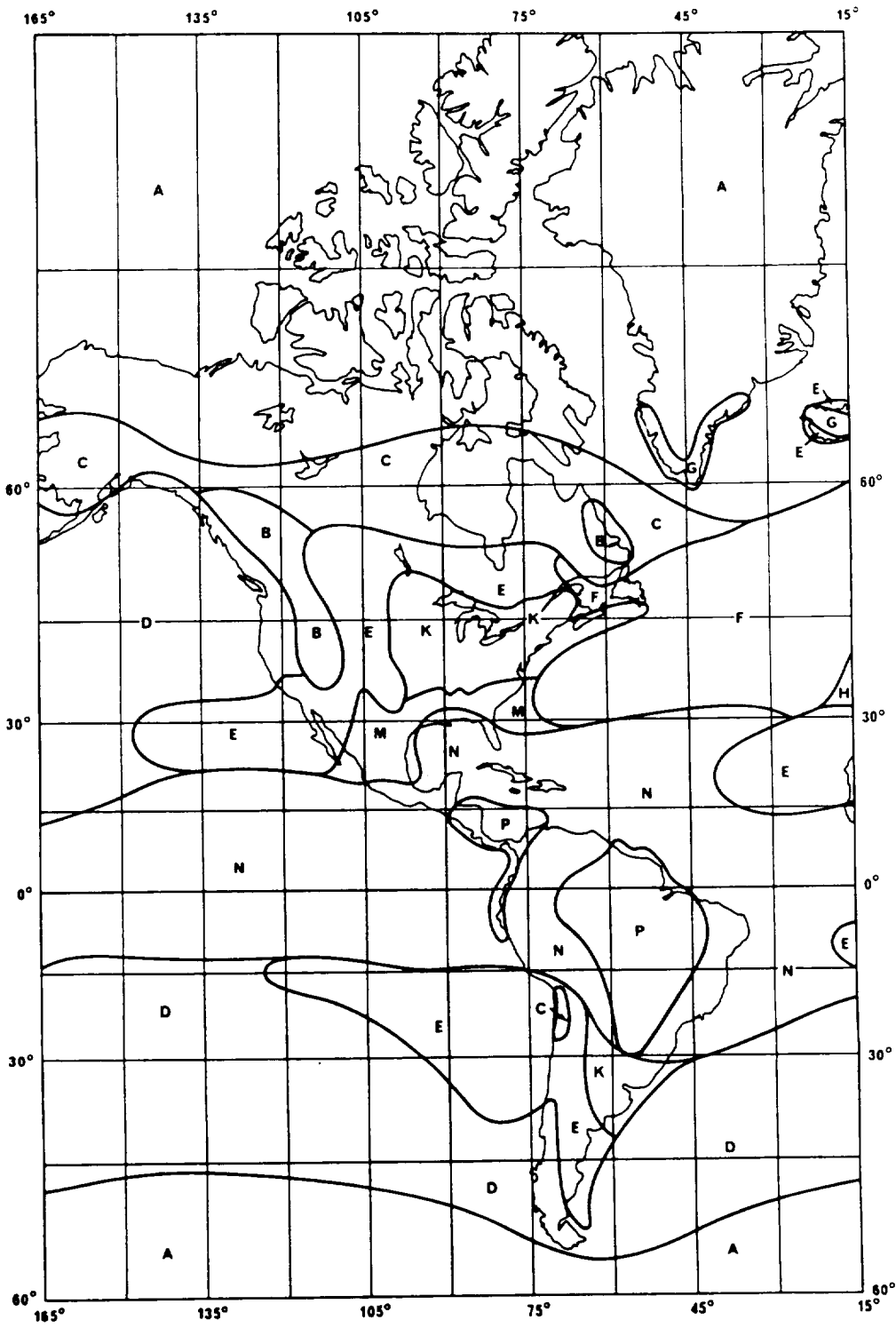


Figure 3.6-1. CCIR Rain Climate Zones (Sheet 1 of 3)

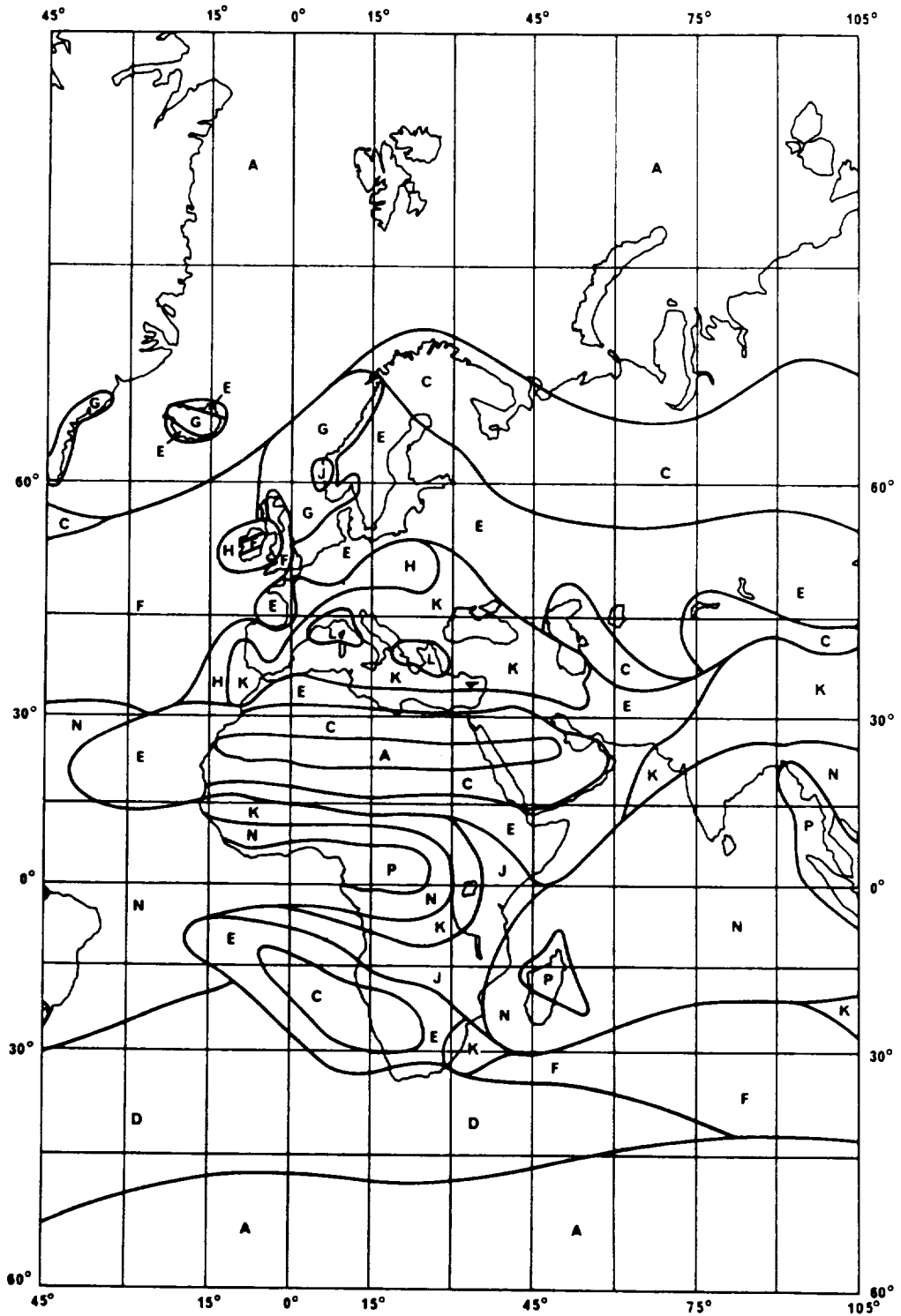


Figure 3.6-1. CCIR Rain Climate Zones (Sheet 2 of 3)

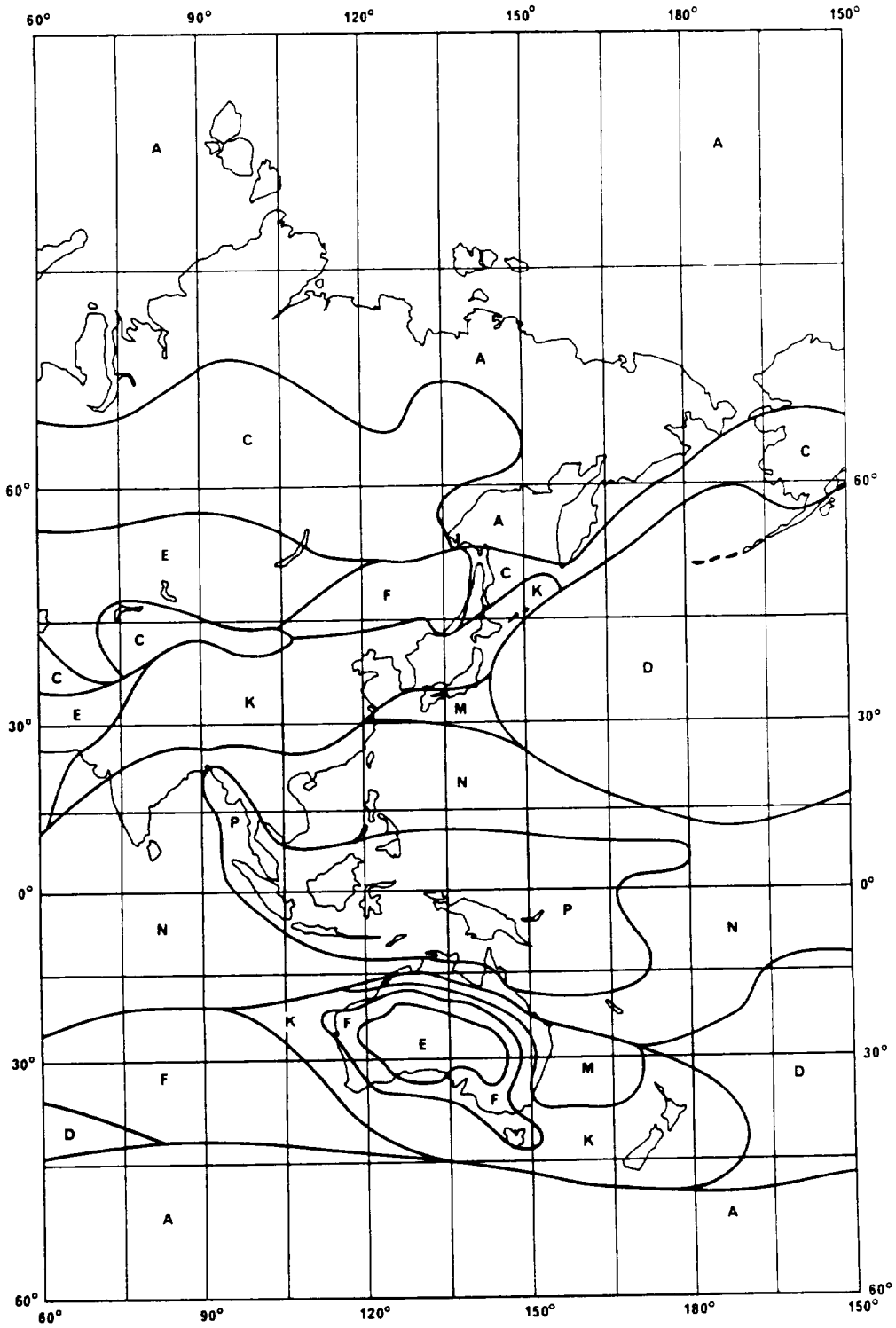


Figure 3.6-1. CCIR Rain Climate Zones (Sheet 3 of 3)

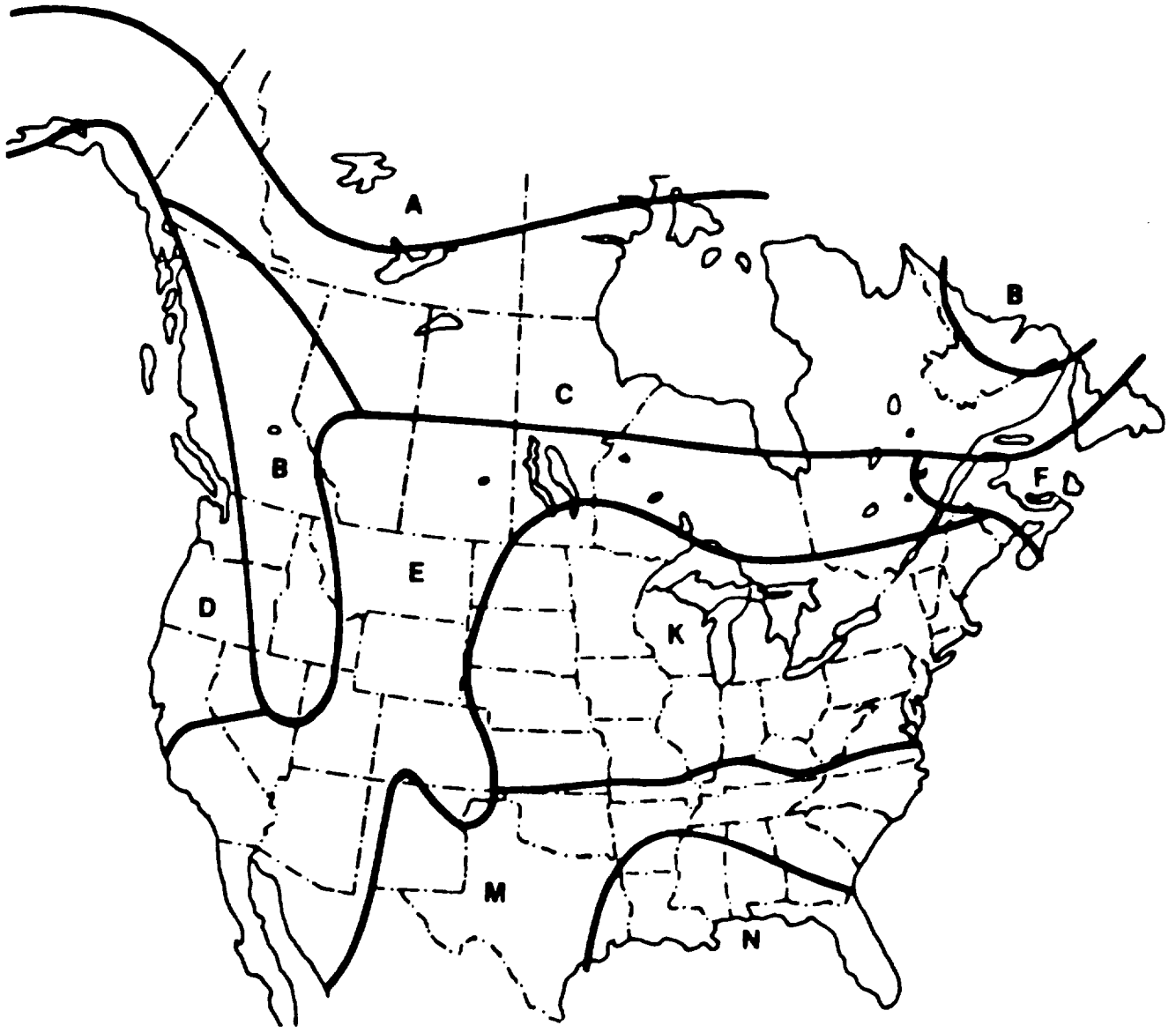


Figure 3.6-2. CCIR Rain Climatic Zones for the Continental United States and Canada

Table 3.6-1. Rainfall Intensity Exceeded (mm/h) for CCIR
Rain Climatic Zones

% Time	A	B	C	D	E	F	G	H	J	K	L	M	N	P
1.0	<0.5	1	2	3	1	2	3	2	8	2	2	4	5	12
0.3	1	2	3	5	3	4	7	4	13	6	7	11	15	34
0.1	2	3	5	8	6	8	12	10	20	12	15	22	35	65
0.03	5	6	9	13	12	15	20	18	28	23	33	40	65	105
0.01	8	12	15	19	22	28	30	32	35	42	60	63	95	145
0.003	14	21	26	29	41	54	45	55	45	70	105	95	1409	200
0.001	22	32	42	42	70	78	65	83	55	100	150	120	180	250

The CCIR also provides maps showing isometric rain rate contours for the 0.01 percent exceedance value, which will be used in the attenuation model procedure. This isometric map is given as Figure 3.6-3.

The CCIR model assumes that the horizontal extent of the rain is coincident with the ambient 0°C isotherm height, which will vary with location, season of the year, time of day, etc. An average value of the 0°C isotherm weight is used in the CCIR model, obtained from,

$$\begin{aligned}
 h_r &= 4.0 && \text{for } 0 < \phi < 36^\circ \\
 &= 4.0 - 0.075 (\phi - 36) && \text{for } \phi \geq 36^\circ
 \end{aligned}
 \tag{3.6-1}$$

where ϕ is the latitude of the location of interest, in degrees N or S.

This estimate is recognized as having high variability, particularly at higher latitudes, and for locations where the significant rain accumulation occurs at other than the summer rainy season.

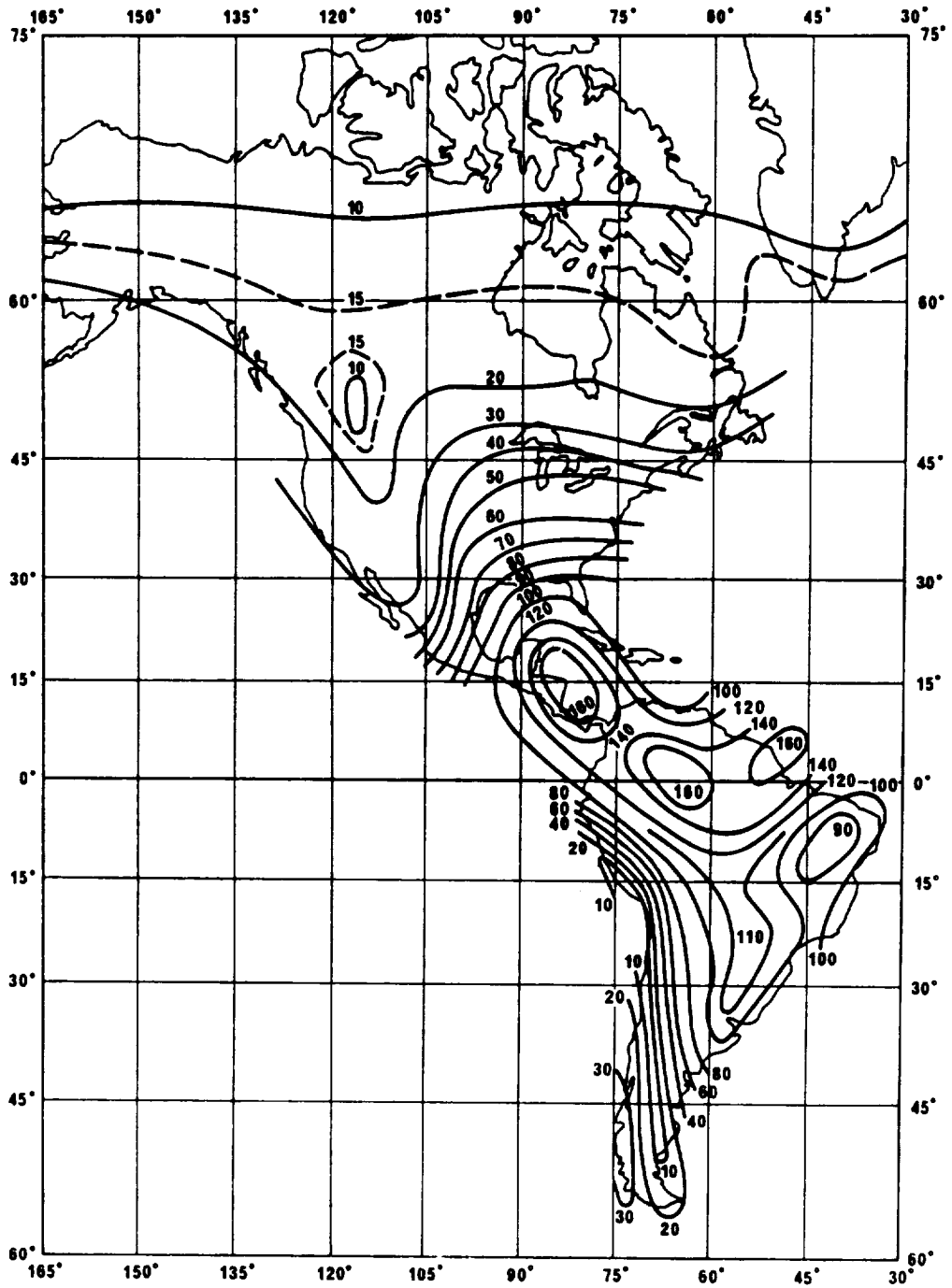


Figure 3.6-3. Contours of Rain Rate Exceeded for 0.01% of the Time (mm/hr) (Sheet 1 of 3)

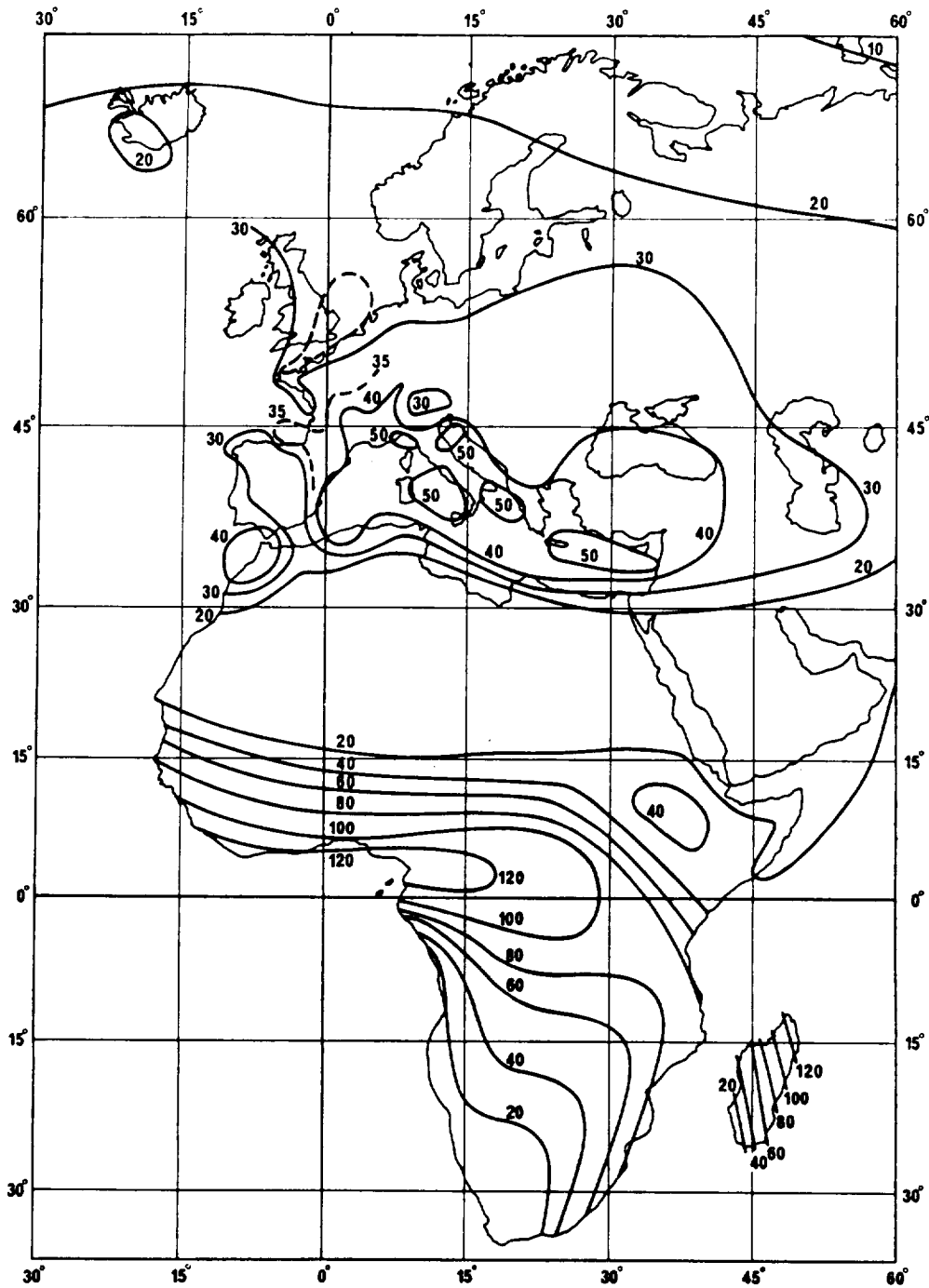


Figure 3.6-3. Contours of Rain Rate Exceeded for 0.01% of the Time (mm/hr) (Sheet 2 of 3)

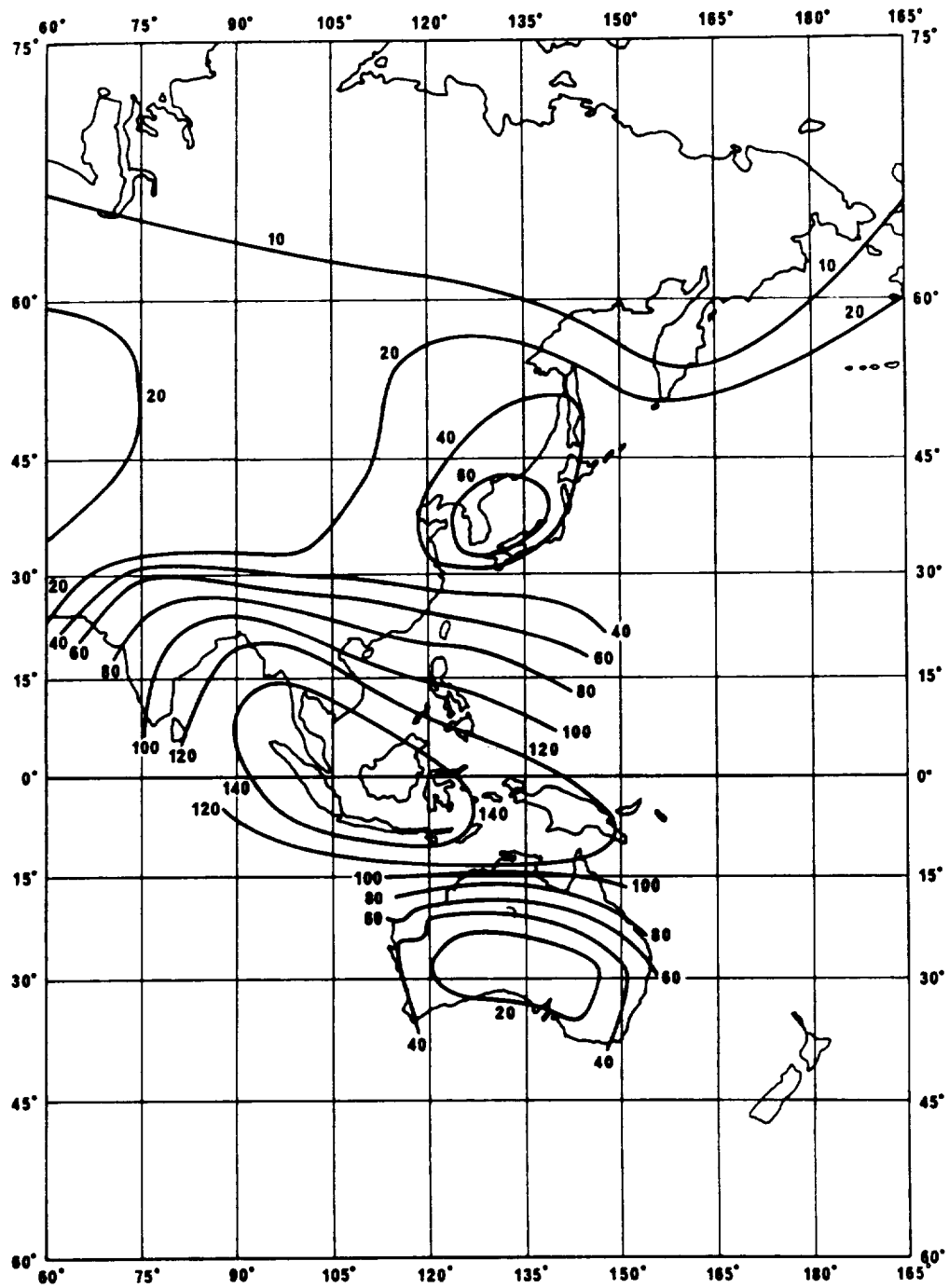


Figure 3.6-3. Contours of Rain Rate Exceeded for 0.01% of the Time (mm/hr) (Sheet 3 of 3)

3.6.2 CCIR Attenuation Model

The CCIR attenuation prediction requires the following input parameters:

- frequency (GHz)
- latitude of earth station (degrees),
- height above mean sea level of earth station (km)
- elevation angle to the satellite (degrees), and
- point rainfall rate for the location for 0.01% of an average year (mm/h).

The rain height, h_r , is determined from the latitude by equation (3.6-1) above. The projected path length on the earth's surface, L_g , and the slant path length through the rain, L_s , are geometrically determined from h_r , the elevation angle, and the height above sea level. A slant path length reduction factor is then applied to account for the horizontal non-uniformity of rain for the 0.01% of the time condition. The reduction factor, r_p , is given by:

$$r_p = \frac{1}{1 + 0.045 L_g} \quad (3.6-2)$$

The product of L_s and r_p is the effective path length through rain for 0.01% of the time.

The specific attenuation for 0.01% of an average year, $\alpha_{0.01}$, in dB/km, is determined from the power-law relationship with rain rate, [see equation (2.3-5)], utilizing the rain rate at 0.01% of the year from locally measured data (preferred), or from Table 3.6-1. The power law coefficients at the frequency and polarization of interest can be obtained from Table 2.3-2, Table 2.3-3, or other

suitable sources. The specific attenuation in the CCIR model is assumed to be constant up to the rain height.

The attenuation exceeded for 0.01% of an average year is then obtained from,

$$A_{0.01} = \alpha_{0.01} L_{srp} \text{ dB} \quad (3.6-3)$$

The attenuation exceeded for other percentages of an average year, p , in the range 0.001% to 1%, are then determined from $A_{0.01}$ by,

$$A_p = 0.12 A_{0.01} p^{-(0.546 + 0.043 \log p)} \text{ dB} \quad (3.6-4)$$

The CCIR reports that when the above prediction method was tested with measured data for latitudes above 30°, the prediction was found to be in agreement at the 0.01% point to within 10%, with a standard deviation of 30%, when used with simultaneous rain rate measurements. Between latitudes of 20° and 30° the prediction method consistently over-estimated the attenuation by a factor of about one-third. When local measured rain rate statistics are used instead of the average year values given in the CCIR climatic zone tables, the errors are found in general to be less, at all latitudes (CCIR-1986a).

The detailed step-by-step procedure for the CCIR attenuation prediction model, including an example application, is presented in Section 6.3 of the handbook.

3.7 THE LIN MODEL

3.7.1 Empirical Formulas

The set of empirical formulas presented here for earth-satellite path attenuation is an extension of those obtained previously for terrestrial microwave radio paths (Lin-1978). In the case of terrestrial paths, the calculation of the expected rain attenuation

distribution from a long term (20 years) distribution of 5-minute point rain rates has been accomplished using empirical formulas deduced from available rain rate and rain attenuation data measured on nine 11 GHz radio paths (5-43 km) at five different U.S. locations (Lin-1977).

These empirical formulas for terrestrial paths, are (Lin's notation (1978) reverses the role of α and β)

$$\alpha(R) = a R^b \text{ dB/km} \quad (3.7-1)$$

$$\beta(R,L) = \alpha(R) L \left[1 + \frac{1}{\bar{L}(R)} \right]^{-1} \text{ dB} \quad (3.7-2)$$

where

$$\bar{L}(R) \approx \frac{2636}{R - 6.2} \text{ km} \quad (3.7-3)$$

R is the 5-minute point rain rate in mm/h, L is the radio path length in km, $\beta(R,L)$ is the path rain attenuation in dB at the same probability level as that of R, and the parameters a and b are functions (Setzer-1970, Chu-1974, Saleh-1978) of the radio frequency, as shown in Figure 3.7-1. (Strictly speaking, the parameters a and b are also functions of wave polarization.)

3.7.2 Rain Path Averaging

If the rain rates were uniform over a radio path of length L, the path rain attenuation $\beta(R,L)$ would be simply $\alpha(R) \cdot L$, representing a linear relationship between β and L. However, actual rainfalls are not uniform over the entire radio path, and therefore the increase of $\beta(R,L)$ with L is nonlinear.

Two factors in the empirical method account for the radio path averaging effect. First, the method is based upon the long term distribution of 5-minute point rain rates in which the 5-minute time averaging partially accounts for the fact that the radio path performs a spatial averaging of non-uniform rain rates (Freeny and Gabbe-1969, Drufuca and Zawadzki-1973, Bussey-1950). A 5-minute average of the rain rate seen at a point corresponds to spatially averaging approximately 2.1 km of vertically variable rain rates, assuming 7 meters/second average descent velocity of rain drops.

Figure 3.7-2 shows how the point rain rate distribution, from two years of measurements at Palmetto, Georgia, depends on the average time intervals (range: 0.5-60 minutes). The probability of a 5-minute rain rate exceeding the 40 mm/h threshold is 1/2 that of a 0.5-minute rain rate exceeding the same threshold. From another viewpoint, increasing the averaging time interval from 0.5 to 5 minutes reduces the 0.01 percentile (i.e., 53 minutes/year) rain rate from 87 to 58 mm/h.

However, since most radio paths of interest are longer than 2.1 km, the fixed 5-minute average interval cannot adequately account for all the path length variations. This deficiency is compensated for by the factor

$$\left[1 + \frac{1}{L(R)} \right]^{-1} \quad (3.7-4)$$

In other words, the auxiliary nonlinear factor represents the empirical ratio between the 5-minute point rain rate R and the radio path average rain rate $R_{av}(L)$ at the same probability level. Since the significant difference between the 5-minute point rain rate and the 0.5-minute point rain rate in Figure 3.7-2 already accounts for the major portion of the difference between the radio path average rain rate $R_{av}(L)$ and the 0.5-minute point rain rate, the auxiliary factor is a weak nonlinear function of L . Obviously, many different analytic functions can be used to approximate this mildly nonlinear

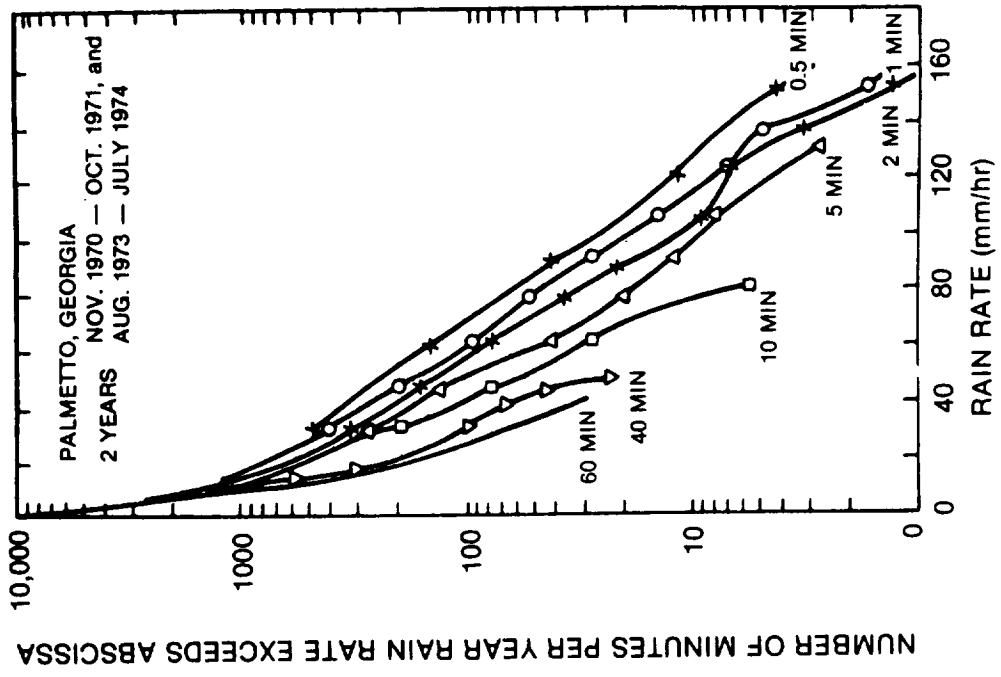


Figure 3.7-2. Dependence of Rain Rate Distribution on Tipping Bucket Rain Gauge Integration Time From Two Years of Measurement at Palmetto, Georgia

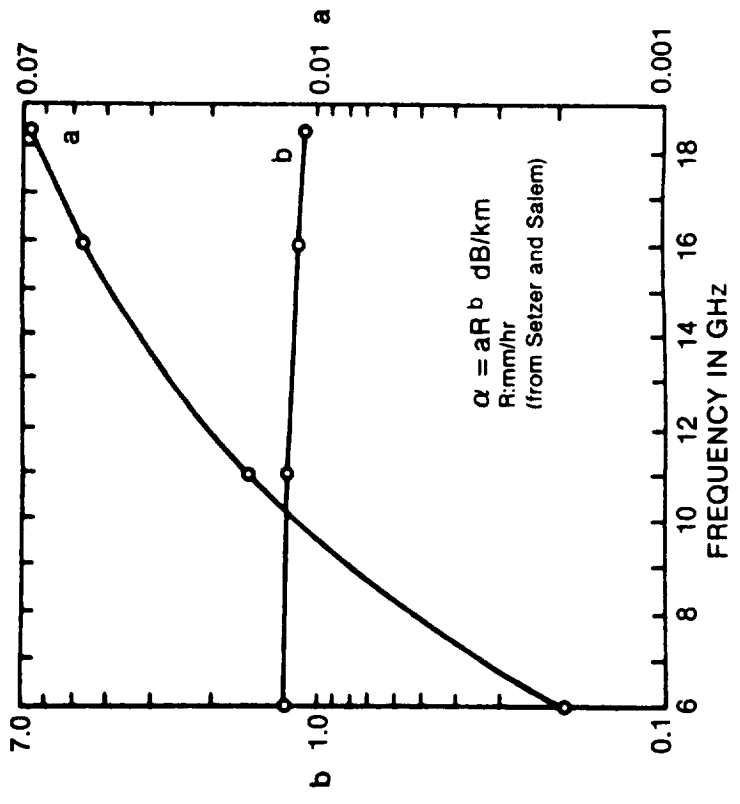


Figure 3.7-1. Dependence of Parameters a and b on the Radio Frequency

behavior. The single parameter function is selected for its simplicity. The adequacy of this simple approximation is supported by the rain rate and rain attenuation data measured on nine, 11-GHz, terrestrial radio paths at five U.S. locations (Lin-1977).

3.7.3 Earth-Satellite Path Legend

To extend the method to earth-satellite paths, let H be the long-term average height of the freezing level in the atmosphere, measured relative to sea level. The effective average length of the earth-satellite path affected by rain is then

$$L = (H - H_g) / \sin \theta \quad (3.7-5)$$

where θ is the satellite elevation angle as viewed from the earth station, and H_g is the ground elevation measured from the sea level. The radar measurements of rainfall reflectivity at Wallops Island, Virginia indicate that on the average rainy day (CCIR-1977)

$$H \approx 4 \text{ km} \quad (3.7-6)$$

Thus given the elevation angle θ , the ground elevation H_g and the distribution of 5-minute point rain rates, we can calculate the rain attenuation distribution on the earth-satellite path through the use of equations 3.7-1, 2 and 5.

Notice that equation 3.7-5 implies that the path rain attenuation (R, L) varies exactly as the cosecant of the elevation angle θ with this simple extension of the terrestrial model. Also note that these simple formulas are valid only on the long term average. The short term relationships between the surface point rain rate and the earth-satellite path rain attenuation, on a storm-by-storm basis, have been observed to be erratic and difficult to predict.

3.8 THE SIMPLE ATTENUATION MODEL (SAM)

The Virginia Polytechnic Institute and State University (VPI&SU), Blacksburg, VA, has been engaged for several years in the

development of rain attenuation models and related measurement programs. Several iterations of a quasi-physical model of rain attenuation on a slant path have been provided. One of the earliest versions of a comprehensive rain attenuation prediction model was the Piecewise Uniform Rain Rate Model, (Persinger, et al-1980) [described in detail in the previous (3rd) edition of this handbook]. The Piecewise Uniform Model accounted for the nonuniform spatial characteristics of rain with two simplifying assumptions: a) the spatial rain rate distribution is uniform for low rain rates, and b) as peak rain rate increases, the rain rate distribution becomes increasingly nonuniform.

The Piecewise Uniform Model was later extended with an expanded global data base to an exponential shaped rain rate profile (Stutzman and Dishman - 1982, 1984), and was called the Simple Attenuation Model (SAM). The model was further modified to include the effects of rain depolarization and an even larger data base (Stutzman and Yon, 1986). This latest version of the SAM will be described here.

The SAM is a semiempirical model that describes the spatial rainfall along a slant path ℓ by:

$$\begin{aligned}
 R(\ell) &= R_0 & R_0 \leq 10 \text{ mm/h} \\
 &= R_0 \exp[-\lambda \ln(R_0/10) \ell \cos \beta] & R_0 > 10 \text{ mm/h}
 \end{aligned}
 \tag{3.8-1}$$

where

$$\ell \leq L, \quad L = (H_e - H_0)/\sin \beta \tag{3.8-2}$$

and

R_0 is the point rainfall rate in mm/h,
 H_0 is the earth station altitude in km,
 H_e is the effective rain height in km,
 β is the slant path elevation angle, and
 λ is an empirically developed parameter
controlling the rate of decay of the horizontal profile.

The effective rain height is approximated by

$$\begin{aligned} H_e &= H_i & R_o &\leq 10 \text{ mm/h} & (3.8-3) \\ &= H_i + \log(R_o/10) & R_o &> 10 \text{ mm/h} \end{aligned}$$

where H_i is the 0°C isotherm height in km. The seasonal average is obtained from (Crane-1978),

$$\begin{aligned} H_i &= 4.8 & \varepsilon &\leq 30^\circ \\ &= 7.8 - 0.1\varepsilon & \varepsilon &> 30^\circ & (3.8-4) \end{aligned}$$

here ε is the station latitude, in degrees N or S.

The total attenuation due to a point rainfall rate R_o is found by integrating Eq (3.8-1) over the path L:

$$A(R_o) = aR_o^b L \quad R_o \leq 10 \text{ mm/h} \quad (3.8-5)$$

$$A(R_o) = aR_o^b \frac{1 - \exp[-b\lambda \ln(R_o/10) L \cos \beta]}{b\lambda \ln(R_o/10) \cos \beta}$$

$$R_o > 10 \text{ mm/h}$$

An evaluation of 36 data sets in the expanded VPI&SU data base for which both attenuation and rain rate data were available found that a value of

$$\lambda = 1/14 \quad (3.8-6)$$

gave the best fit to the data. The functional dependence of λ is such that large changes do not produce changes in attenuation.

The revised SAM model was found by its authors to give equal to or slightly better predictions than the CCIR or the Global prediction models, for the available data base (Stutzman and Yon - 1986). Figure 3.8-1 shows a comparison of the models for 64 global data sets. Predictions are based on rain rates calculated from the CCIR rain rate model except for the Global Model which uses the Global rain rate model. Mean deviation and standard deviation of predicted attenuation as a percent based on measured attenuation are shown. Figure 3.8-2 shows a similar comparison for 31 long term

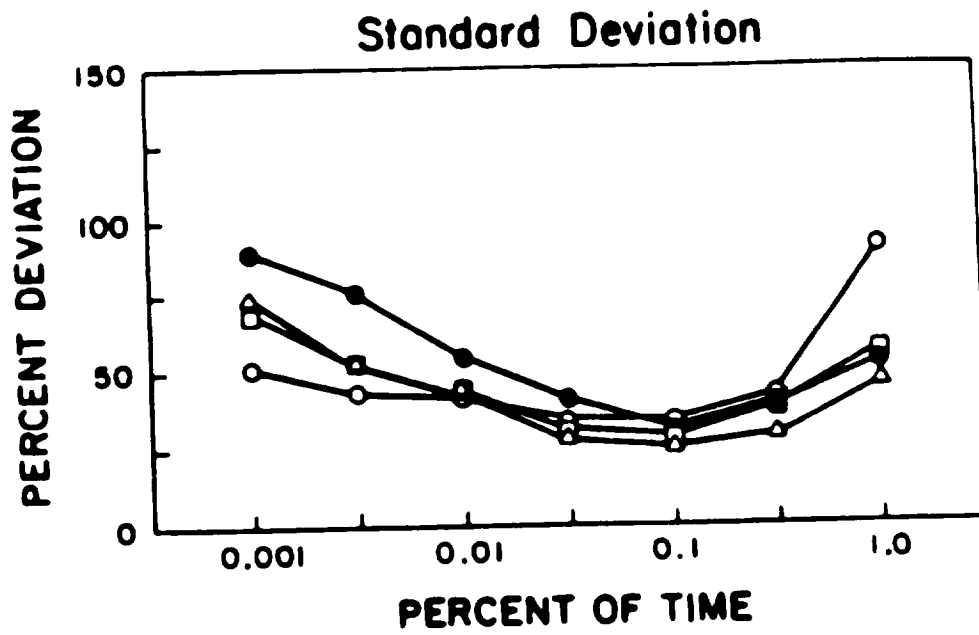
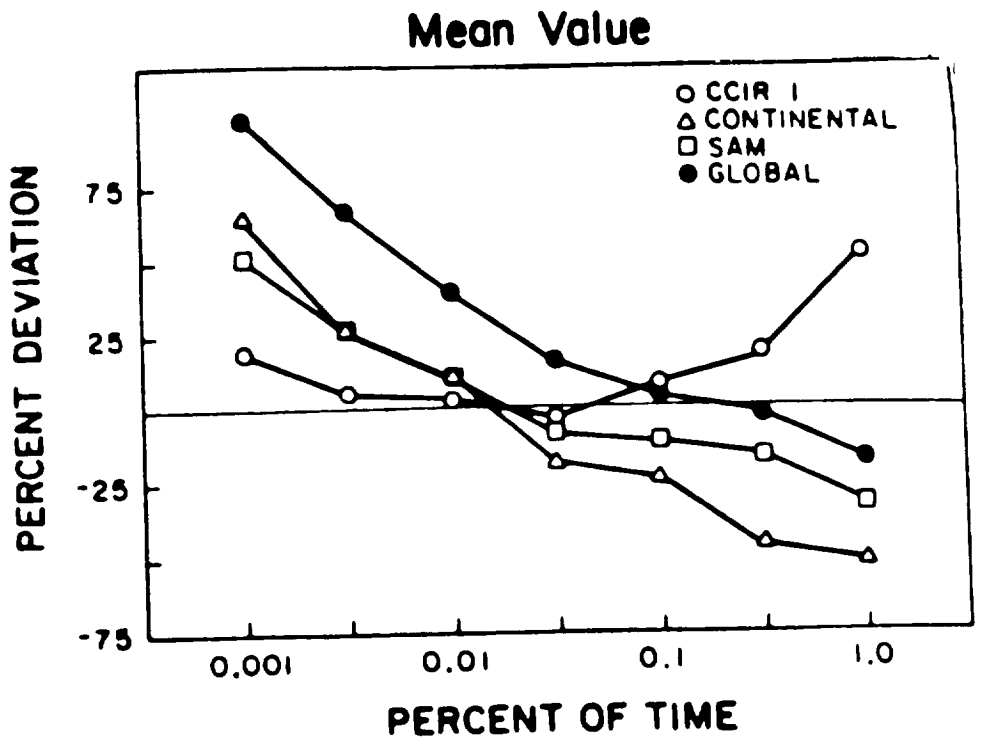


Figure 3.8-1. Comparison of the SAM model with the CCIR and Global models, for 62 measured data sets

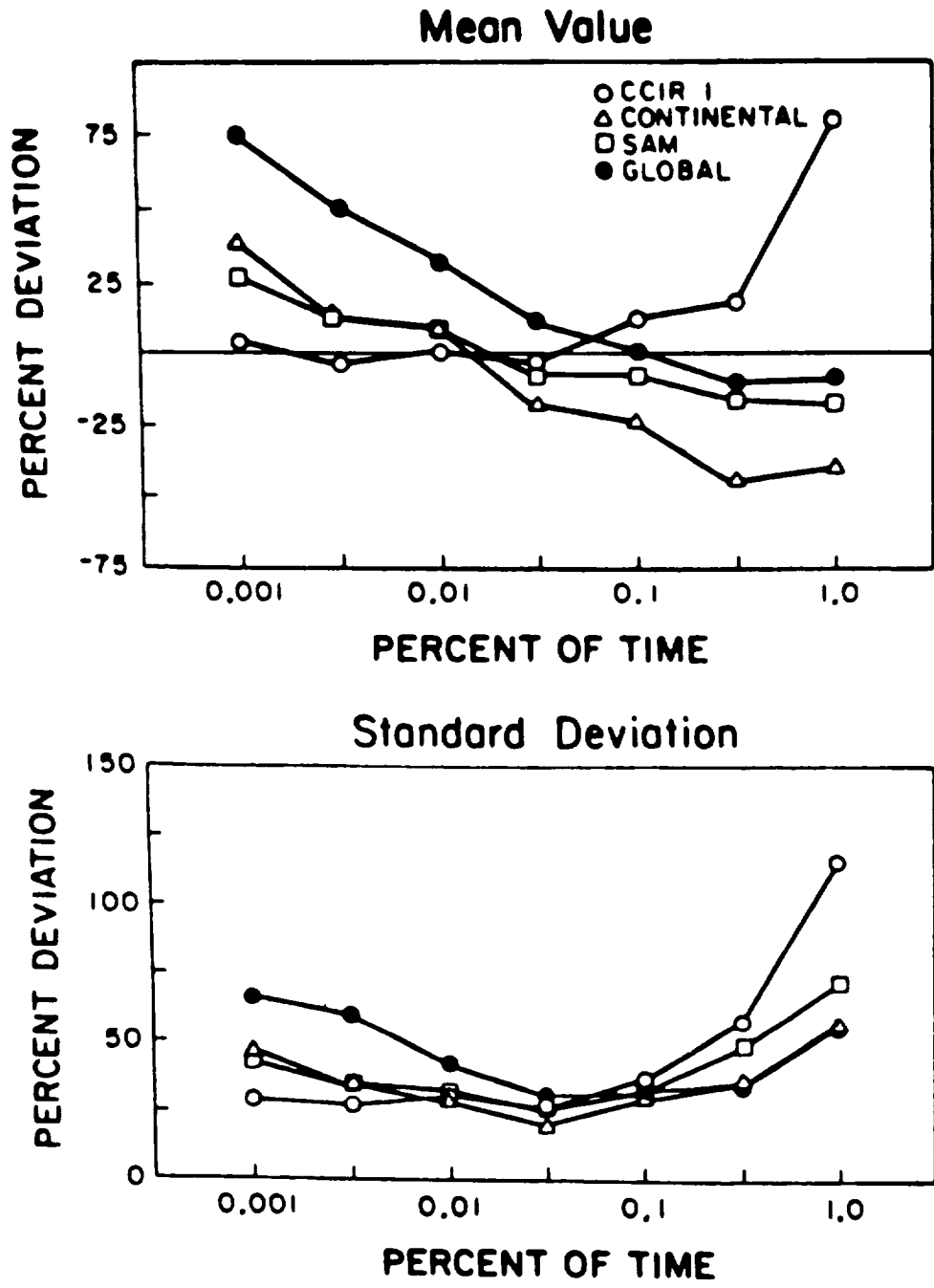


Figure 3.8-2. Comparison of the SAM model with the CCIR and Global models, for 32 long term (two years or more) measured data sets

(two years or more) data sets from the data base. All four models give better predictions for long term data sets, as expected, since they are more representative of average rain behavior, for which the models are based.

3.9 THE EFFECTIVE PATH LENGTH CONCEPT

3.9.1 Definition of Effective Path Length

The effective path length L_e is usually defined as that parameter which relates the specific attenuation to the total attenuation along the earth-space path. Mathematically it is written

$$A = aRbL_e \quad (3.9-1)$$

Alternatively, L_e is the hypothetical path length of uniform rain rate R which will produce the same total path attenuation as the real varying rain rate does along the path. The form of L_e and the technique employed for its derivation has been quite variable. For example, in some cases it is termed effective path length and in others the path averaging factor.

Since rains are not usually uniform over the extent of the storm (rain cells of higher rain rates are small compared to the extent of the storm), the total attenuation is

$$A = \int_0^L a_1 dl \quad (3.9-2)$$

where A is the total attenuation at a given frequency and time through the storm of extent L along the path ℓ . The factor a_1 is a "high resolution" specific attenuation depending on the rain rate at each point along the path. The effective path length in kilometers

$$L_e = \frac{A}{\alpha_{avg}} \quad (3.9-3)$$

is where α_{avg} is an analytically determined attenuation per kilometer assuming a uniform average rain rate. The average rain rate is based on rain rate measurements taken over a long period of time. The measured attenuation is also indirectly a function of average rain rate. Measured attenuation and measured rain rate data are compared on an equal probability of occurrence basis over a long time base. This removes the instantaneous time dependence of the measurements. Note that if rain rate is not a function of length ℓ , then $A = \alpha_{avg}L$ and the effective path length would equal the physical rain extent L . This is one limit which occurs for low rain rates. For example, for stratiform rains the rain rate is nearly spatially uniform.

3.9.2 Frequency Dependence of Effective Path Length

Some frequency dependence to the effective path length has been observed at higher rain rates. To investigate the frequency dependence of L_e consider the ratio of two L_e 's for two frequencies f_1 and f_2 . Namely,

$$\frac{L_e(f_1)}{L_e(f_2)} = \frac{\alpha_{avg}(f_2)}{\alpha_{avg}(f_1)} \frac{\int_0^L \alpha_1(f_1) d\ell}{\int_0^L \alpha_1(f_2) d\ell} = r_p r_m^{-1} \quad (3.9-4)$$

where r_m is the ratio of the measured attenuations, and r_p is the ratio of the predicted attenuations assuming uniform rain conditions, which is also the ratio of predicted specific attenuations. For the effective path length to be independent of frequency r_m must equal r_p and the effective path length versus rain rate must be identical for the two frequencies. Experimental results shown in Figure 3.9-1 demonstrate that for two frequencies

(19 and 28 GHz) and rain rates exceeding one inch per hour the effective path length of the higher frequency is as much as 20% longer than the lower frequency. This is an effect which must be considered when frequency scaling attenuation measurements over a wide frequency range.

The frequency dependence of effective path length shown in Figure 3.9-1 arises from the nonuniformity of rain along the propagation path in combination with the nonlinear dependence of the specific attenuation on rain rate. Using the definition in equation 3.9-1, the relation (Kheirallah, et al-1980)

$$L_e(f_2) = L_e(f_1)^{b(f_2)/b(f_1)} \quad (3.9-5)$$

has been derived. This relation has been compared with some experimental data and appears to apply best to the low frequency (4 to 10 GHz) data for high rain rates (exceeding 25 mm/h). Kheirallah, et al (1980) attributes this to the relatively significant effects of cloud attenuation at higher frequencies and low rain rates.

Rewriting equation 3.9-5 one has

$$[L_e(f_1)]^{1/b(f_1)} = [L_e(f_2)]^{1/b(f_2)} = L_e' \quad (3.9-6)$$

L_e' is defined as the normalized effective path length and is much less dependent on frequency than L_e . Kheirallah, et al (1980) suggests that for small percentages of time for which rain attenuation dominates, data sets should be expressed in terms of L_e' before data at various frequencies and elevation angles are combined.

3.9.3 Effective Path Length Versus Measurement Period

Experimentally determined effective path lengths for varying measurement periods (such as annual and worst month) show a high variability. For example, in Figure 3.9-2 each curve was developed from equal probability attenuation - rain rate measurements for the

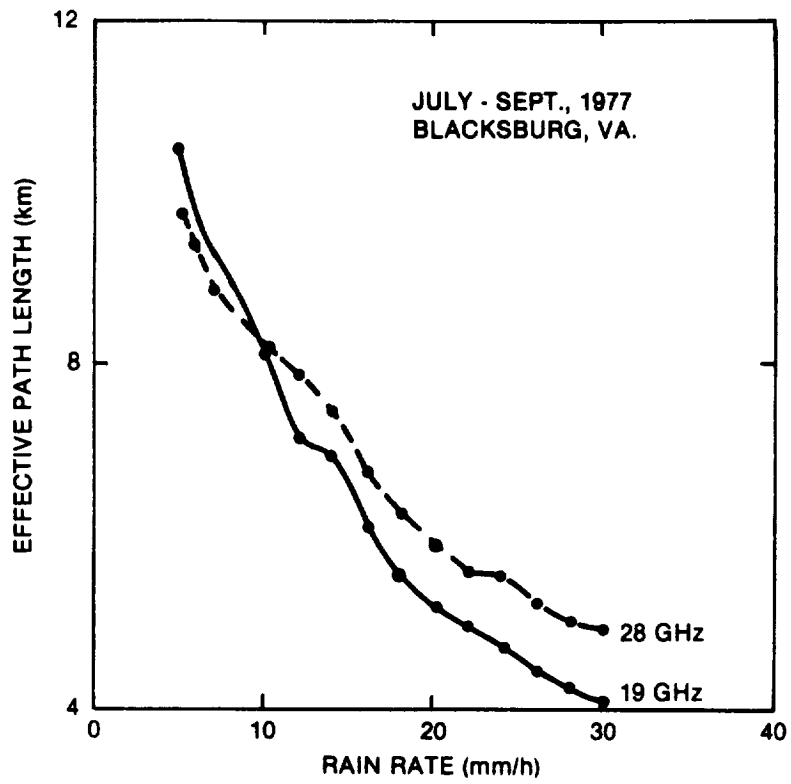


Figure 3.9-1. Effective Path Lengths for the VPI & SU COMSTAR 19 and 28 GHz Systems

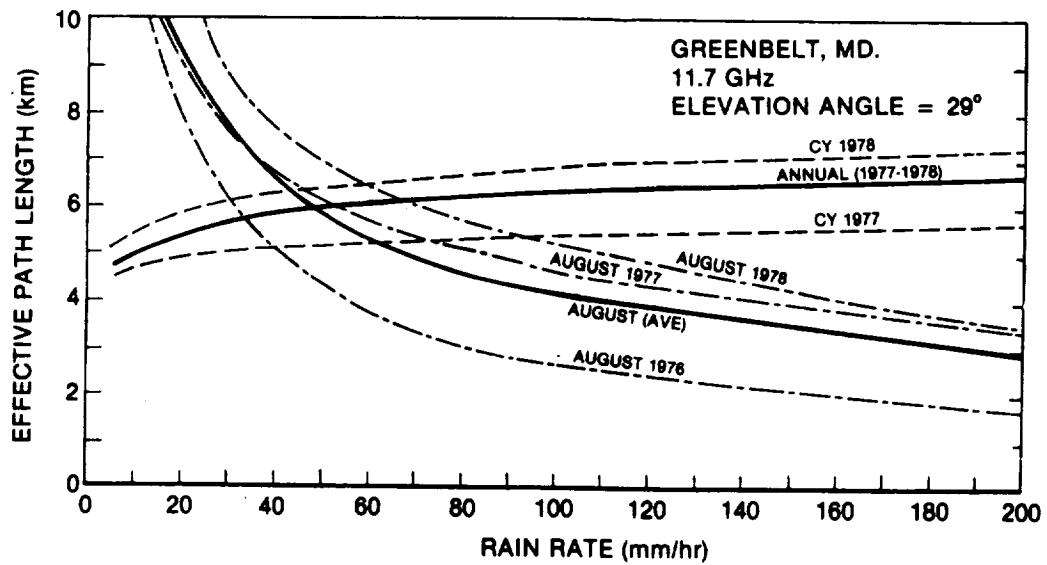


Figure 3.9-2. Effective Path Length for Annual & Worst Month Periods

period indicated. Two trends are apparent. First, the monthly curves show a decreasing path length with increasing rain rate, and second, the annual curves show a path length which increases slightly with rain rate. The first effect arises because the high rain rate events in August are primarily convective storms with intense localized rain rates. The second effect is probably accounted for because the winter rains in Maryland are more uniform in nature and the zero degree isotherm is significantly lower in winter. For this case L_e approaches L for cold weather low rain rate events. However, this effect has not always been observed (see below) and probably indicates that regions with low rainfall during the cold weather months will show a rain rate dependence to L_e similar to that for the worst month.

3.9.4 Comparison of Effective Length Factors

Several of the attenuation models utilize a factor easily related to L_e . It is of interest to compare these factors and determine their relative differences based on a similar set of assumptions. First consider the L_e factor in each model separately.

3.9.4.1 Dutton-Dougherty Model. This model does not explicitly employ an effective path length. An effective path length may be evaluated, however, and it has been by Dutton, et al (1982) for the purpose of comparison with the Global model. The relation between the effective path length given by the DD Model and the rain rate is a complex one, being determined by the liquid water content versus height function, $L(h)$, and the probability modification factor, F . There are two choices for $L(h)$, corresponding to stratiform and convective rain, and the model combines these for some time percentage values. Because a simple expression for L_e is not possible, no attempt is made here to define an effective path length for this model.

3.9.4.2 Global Model. Both forms of the Global model employ a term which can be related to the effective path length. For the path averaging technique (Global Prediction Model)

$$L_e = \frac{H}{\sin \theta} \gamma(D) R_p^{-\delta(D)} \quad (3.9-7)$$

where R_p is the point rain rate, H is the height of the 0°C isotherm, D is the basal distance and γ and δ are the path averaging factors defined in Section 3.4. For a 45° elevation angle at a sea-level ground station near 40°N latitude

$$L_e = 9.14 R_p^{-0.14\text{km}} \quad (3.9-8)$$

For the variable isotherm height form of the Global model,

$$L_e = \frac{1}{\cos \theta} \left[\frac{e^{UZb-1}}{Ub} - \frac{X^{be}YZb}{Yb} + \frac{X^{be}YDb}{Yb} \right] \quad (3.9-9)$$

where the terms are defined in Section 3.4.3.2. The value of L_e is a complex function of R_p since U , X , Y and Z (implicitly) are functions of R_p .

3.9.4.3 Two-Component Model. Two effective path lengths could be identified in the T-C Model: one for convective cellular rain and one for debris. Differing 0°C isotherm heights are computed for the two types of rain which form a basis for the differing effective path lengths. The lateral modeling of rain also differs for the two rain modes: cellular rain effective path length must be modified to include nearby debris contributions, whereas debris rain is assumed to be uniform. Thus, no attempt is made to identify a single parameter L_e in the T-C Model.

3.9.4.4 CCIR Model. The CCIR Model directly employs the concept of effective path length. The (corrected) 0°C isotherm height is used to define the vertical extent of rain. A slant path length reduction factor is used to adjust the physical path length through rain to account for the horizontal non-uniformity of rain. The resulting effective path length applies only for 0.01% of the time. The attenuation predictions for other time percentages are determined directly from the 0.01% value, without reverting to the path length. For this reason, the dependence of effective path length on rain rate is obscure.

3.9.4.5 Lin Model. The Lin model utilizes two techniques for obtaining the average path length. The first is to temporally average the instantaneous rain rate to five minute intervals. The effect of this averaging process in terms of the effective path length comparison is unclear. However, as will be shown, the other parameter agrees well with the results of other models. Specifically Lin (1978) finds that

$$L_e = \frac{4}{\sin \theta} \left[1 + \frac{4(R_p - 6.2)}{2636 \sin \theta} \right]^{-1}$$

$$= \frac{2636}{659 \sin \theta + R_p - 6.2}$$

(3.9-10)

At $\theta = 45$ degrees the result is

$$L_e = 2636(460 + R_p)^{-1}$$

(3.9-11)

3.9.4.6 Simple Attenuation Model (SAM). The simple attenuation model does not readily allow definition of a single L_e parameter. Therefore this parameter is not derived.

3.9.4.7 Experimental Measurements. Ippolito (1978) has employed over sixty months of long term attenuation and rain rate statistics at 11.7, 15, 20 and 30 GHz to derive an effective path length based on experimental measures. The result is

$$L_e = \frac{9.065}{\sin \theta} R_p^{-0.296} \text{ km} \quad (3.9-12)$$

for elevation angles from 20 to 90 degrees. At 45 degrees elevation angle

$$L_e = 12.82 R_p^{-0.296} \quad (3.9-13)$$

3.9.4.8 Comparison of Effective Path Lengths. Assuming a ground station at sea level, 40 degrees North latitude and observing at 45 degrees elevation angle, the L_e factors are plotted in Figure 3.9-3 for the two forms of the Global model, the Lin model and the experimental results of Ippolito (1978) and CTS results (Ippolito-1979). The latter experimental results (labeled $L_e, \text{exp}(11.7\text{GHz})$ in Figure 3.9-3) were scaled from the 29 degree elevation angle measurements made at Greenbelt, MD to CTS, to 45 degrees using the ratio of the cosecants of the two angles. The original data is the annual curve for 1977 and 1978 shown in Figure 3.9-2. This data is the longest set of continuous, single-site effective path length data published to date for CTS and therefore more weight should be given this curve.

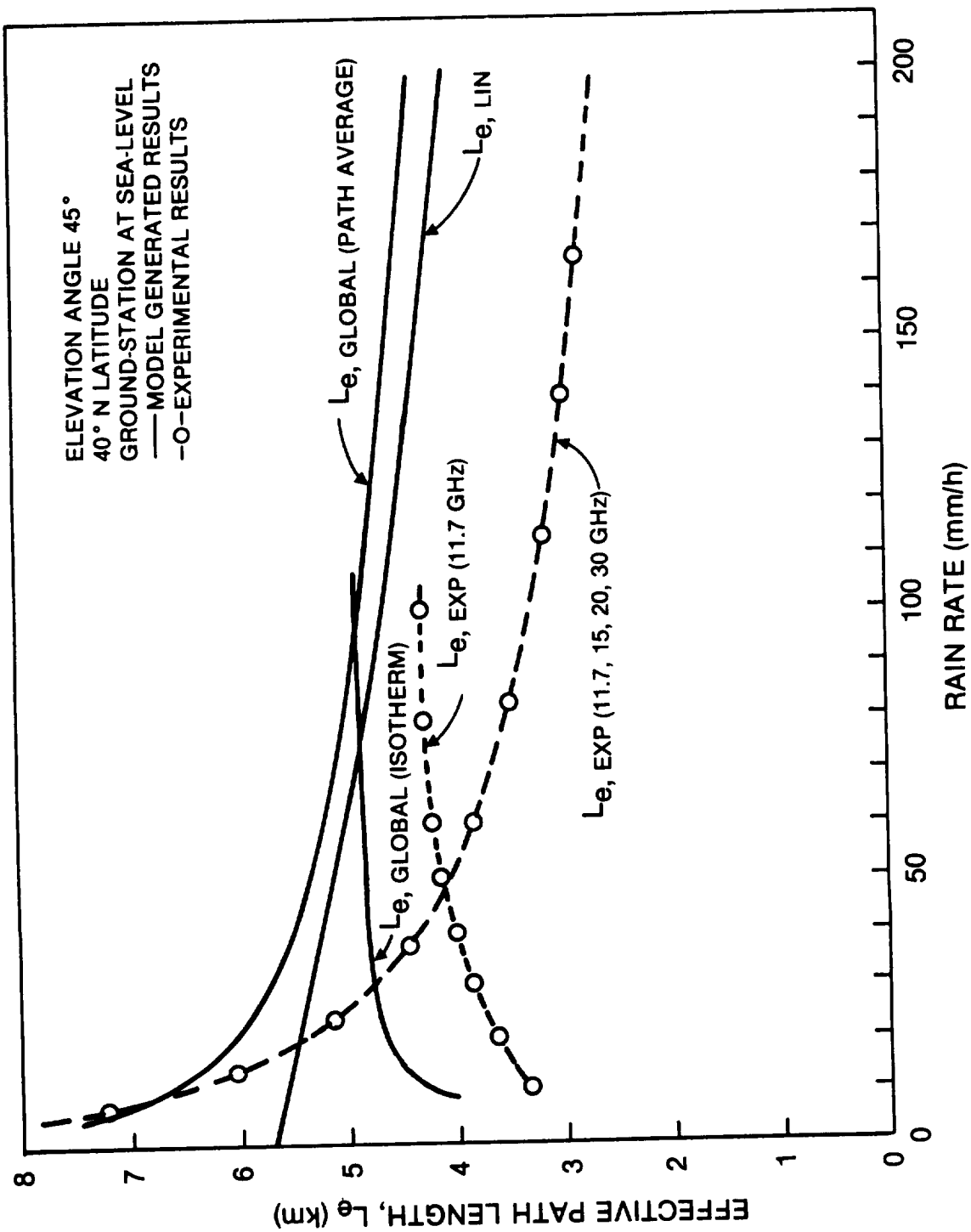


Figure 3.9-3. A Comparison of Effective Path Lengths

The most important result in Figure 3.9-3 is that the use of an effective path length between 4 and 5 kilometers is reasonable. A significant variation occurs below 30 mm/h which may arise due to the presence of winter rains, but this remains unproven. Fortunately for most design problems the most accurate estimates of effective path length are required for annual percentages in the range from 0.01 and 0.001 percent of a year, and in this range both the experimental and model-generated effective path lengths are approximately 4 to 5 km. However, assuming a ± 1 km error bound on L_e the error in estimating L_e is about ± 1 dB. If L_e is directly related to the total attenuation, at least a ± 1 dB error bound must be placed on the estimate of the path attenuation. This error bound will increase as the elevation angle decreases.

3.10 REFERENCES

- Barry, R.C. and R.J. Chorley (1970), Atmosphere, Weather and Climate, Holt, Reinhart and Winston, Inc., New York, p. 205.
- Bussey, H.E. (1950), "Microwave Attenuation Statistics Estimated from Rainfall and Water Vapor Statistics," Proc. IRE, Vol. 38, pp. 781-785.
- CCIR (1977), "Influence of the Non-Ionized Atmosphere on Wave Propagation," CCIR Study Groups Period 1974-1978, DOC. 5/169-E, May 10 United States of America, Modification to Report 233-3 (REV. 76).
- CCIR (1978), "Propagation in Non-Ionized Media", Volume V, XIV Plenary Session, Kyoto, Japan.
- CCIR (1978a), Special Preparatory Meeting (WARC-79) Documents.
- CCIR (1982a), "Propagation Data Required for Space Telecommunications Systems," Report 564-2, in Volume V, Recommendations and Reports of the CCIR - 1982, International Telecommunications Union, Geneva.
- CCIR (1982b), "Prediction of Attenuation Due to Rain on an Earth-Space Path," CCIR Interim Working Party (IWP) 5/2 Meeting, June 1982, Geneva.
- CCIR (1982c), "Technical Bases for the Regional Administrative Radio Conference - 1983 for the Planning of the Broadcasting Satellite Service in Region 2," Report of the CCIR Conference Preparatory Meeting, Geneva, 28 June - 9 July 1982.

- CCIR (1985a), "Radiometeorological Data," Report 563-2 (MOD F), Study Group 5 Inputs to XVth Plenary Assembly, Document 5/1017, 6 Nov. 1985.
- CCIR (1985b), "Propagation Data and Prediction Methods Required for Earth-Space Telecommunication Systems," Report 564-2 (Mod-F), Study Group 5 Inputs to XVth Plenary Assembly, Document 5/1040, 28 Nov. 1985.
- CCIR (1986a), "Radiometeorological Data," Report 563-3, in Volume V, Recommendations and Reports of the CCIR - 1986, International Telecommunications Union, Geneva.
- CCIR (1986b), "Propagation Data and Prediction Methods Required for Earth-Space Telecommunication Systems," Report 564-3, in Volume V, Recommendations and Reports of the CCIR - 1986, International Telecommunications Union, Geneva.
- Chu, T.S. (1974), "Rain Induced Cross-Polarization at Centimeter and Millimeter Wavelengths," B.S.T.J., Vol. 53, pp. 1559-1579.
- Crane, R.K. (1966), "Microwave Scattering Parameters for New England Rain," MIT Lincoln Laboratory Report 426, ASTIA Doc. AD-647798.
- Crane, R.K. and D.W. Blood (1979), "Handbook for the Estimation of Microwave Propagation Effects - Link Calculations for Earth-Space Paths," Environmental Research and Technology Rpt. No. 1, Doc. No. P-7376-TRL.
- Crane, R.K. (1978), "A Global Model for Rain Attenuation Prediction," Eascon Record, pp. 391-395.
- Crane, R.K. (1980a), "Prediction of Attenuation by Rain," IEEE Trans. Comm., Vol. COM-28, No. 9, pp. 1717-1733.
- Crane, R.K. (1980b), "Earth-Space and Terrestrial Microwave Propagation - Estimation of Rain Attenuation with the Global Model," ERT Technical Report P-A414-TR, prepared for NASA Headquarters under Contract NASW-3337 (October 1980).
- Crane, R.K. (1982), "A Two-Component Rain Model for the Prediction of Attenuation Statistics," Radio Science, Vol. 17, No. 6, pp. 1371-1387
- Dougherty, H.T. and E.J. Dutton (1978), "Estimating Year-to-Year Variability of Rainfall for Microwave Applications," IEEE Trans. Comm., Vol. COM-26, No. 8, pp. 1321-1324.

- Drufuca, G. and I.I. Zawadzki (1973), "Statistics of Rain Gauge Records," Inter-Union Commission on Radio Meteorology (IUCRM) Colloquium on "The Fine Scale Structure of Precipitation and Electromagnetic Propagation," Nice, France, Conference Record, Vol. 2.
- Dutton, E.J. (1971), "A Meteorological Model for Use in the Study of Rainfall Effects on Atmospheric Radio Telecommunications " Off. Telecomm. Rpt. OT/TRER-24, NTIS No. COM-75-10826/AS, Springfield, Va.
- Dutton, E.J. (1977), "Earth-Space Attenuation Prediction Procedures at 4 to 16 GHz," Off. Telcom. Rpt. 77-123.
- Dutton, E.J. and H.T. Dougherty (1973), "Modeling the Effects of Clouds and Rain Upon Satellite-to-Ground System Performance," Off. Telecom. Report 73-5, NTIS No. COM-75-10950, Springfield, Va.
- Dutton, E.J. and H.T. Dougherty (1979), "Year-to-Year Variability of Rainfall for Microwave Applications in the U.S.A.," IEEE Trans. Comm., Vol. COM-27, pp. 829-832.
- Dutton, E.J. and H.T. Dougherty (1984), "A Second Modeling Approach to Year-to-Year Rainfall Variability in the U.S.A. for Microwave/Millimeter Wave Applications," IEEE Trans. Comm., Vol. COM-32, No. 10, pp. 1145-1148.
- Dutton, E.J., H.T. Dougherty and R.F. Martin, Jr. (1974), "Prediction of European Rainfall and Link Performance Coefficients at 8 to 30 GHz," Off. Telecom., Dept. of Commerce, NTIS No. AD/A-000804, Springfield, Va.
- Dutton, E.J., H.K. Kobayashi, and H.T. Dougherty (1982), "An Improved Model for Earth-Space Microwave Attenuation Distribution Prediction," Radio Science, Vol. 17, No. 6, pp. 1360-1370.
- Freeny, A.E. and J.D. Gable (1969), "A Statistical Description of Intense Rainfall," B.S.T.J., Vol. 48, No. 6, pp. 1789-1851.
- Goldhirsh, J. and I. Katz (1979), "Useful Experimental Results for Earth-Satellite Rain Attenuation Modeling," IEEE Trans. Ant. Prop., Vol. AP-27, No. 3, pp. 413-415.
- Gray, L.F. and M.P. Brown, Jr. (1979), "Transmission Planning for the First U.S. Standard C (14/11-GHz) INTELSAT Earth Station," Comsat Tech. Rev., Vol. 9, No. 1, pp. 61-89.

- Hyde, G. (1979), private communication.
- Ippolito, L.J. (1978), "Rain Attenuation Prediction at 10 to 100 GHz from Satellite Beacon Measurements," Abstract, Record, EASCON '78, September 25-27, Arlington, Va.
- Ippolito, L.J. (1979), "11.7 GHz Attenuation and Rain Rate Measurements with the Communications Technology Satellite (CTS)," NASA TM 80283.
- Ippolito L.J. (1986), Radiowave Propagation in Satellite Communications, Van Nostrand Reinhold, New York, p. 88.
- Janes, H.B., J.T. Collins and F.K. Steele (1978), "A Preliminary Catalog of Programs and Data for 10-100 GHz Radio System Prediction," Off. Telecomm. Rpt. 78-141.
- Jorgenson, D.L., W.H. Klein and C.F. Roberts (1969), "Conditional Probabilities of Precipitation Amounts in the Conterminous United States," U.S. Dept. Comm., Env. Sci. Serv. Ad., Weather Bur., Silver Spring, Md., ESSA Tech Memo WBTM-T DL-18.
- Kaul, R., D.V. Rogers and J. Bremer (1977), "A Compendium of Millimeter Wave Propagation Studies Performed by NASA," ORI Final Report, prepared under NASA Contract NAS5-24252.
- Kheirallah, H.N., J.P. Knight, R.L. Olsen, K.S. McCormick and B. Segal (1980), "Frequency Dependence of Effective Path Length in Prediction of Rain Attenuation Statistics," Electr. Letters, Vol. 16, No. 12, pp. 448-450.
- Laws, J.O. and D.A. Parsons (1943), "The Relation of Raindrop-Size to Intensity," Am. Geophys. Union Trans., Vol. 24, pp. 274-276.
- Lin, S.H. (1973), "Statistical Behavior of Rain Attenuation," B.S.T.J., Vol. 52, No. 4, pp. 557-581.
- Lin, S.H. (1977), "Nationwide Long Term Rain Rate Statistics and Empirical Calculations of 11 GHz Microwave Rain Attenuation," B.S.T.J., Vol. 56, No. 9, pp. 1581-1604.
- Lin, S.H. (1978), "Empirical Calculation of Microwave Rain Attenuation Distributions on Earth-Satellite Paths," Record, EASCON '78, Arlington, Va., pp. 372-378.
- Lin, S.H., H.J. Bergmann, and M.V. Pursley (1980), "Rain Attenuation on Earth-Satellite Paths - Summary of 10-Year Experiments and Studies," BSTJ, Vol. 59, No. 2, pp. 183-228.

- Marshall, J.S. and W.M. Palmer (1948), "The Distribution of Raindrops With Size," Jrnl. Meteorology, Vol. 51, pp. 165-166.
- Olsen, R.L., D.V. Rogers and D.B. Hodge (1978), "The aR^b Relation in the Calculation of Rain Attenuation," IEEE Trans. Ant. Prop., Vol. AP-26, pp. 318-329.
- Oort, A.H. and E.M. Rasmusson (1971), "Atmospheric Circulation Statistics," NOAA Professional Paper No. 5, U.S. Dept. Commerce.
- Persinger, R.R., W.L. Stutzman, R.E. Castle and C.W. Bostian (1980), "Millimeter Wave Attenuation Prediction Using a Piecewise Uniform Rain Rate Model," IEEE Trans. Ant. Prop., Vol. AP-28, No. 2, pp. 149-153.
- Rice, P.L. and N.R. Holmberg (1973), "Cumulative Time Statistics of Surface Point Rainfall Rates," IEEE Trans. Comm., Vol. COM-21, No. 10, pp. 1131-1136.
- Rogers, D.V. and G. Hyde (1979), "Diversity Measurements of 11.6-GHz Rain Attenuation at Etam and Lenox, West Virginia," Comsat Tech. Rev., Vol. 9, No. 1, pp. 243-254.
- Rogers, R.R. (1972), "Radar-Derived Statistics on Slant-Path Attenuation at 10 GHz," Radio Science, Vol. 7, No. 6, pp. 631-643.
- Saleh, A.A.M. (1978), private communication.
- Setzer, D.E. (1970), "Computed Transmission Through Rain at Microwave and Visible Frequencies," B.S.T.J., Vol. 49, No. 8, pp. 1873-1892.
- Skerjanec, R.E. and C.A. Samson (1970), "Rain Attenuation Study for 15 GHz Relay Design," NTIS, AD-709-348, Springfield, Va.
- Steele, F.K. (1979), private communication.
- Stutzman, W.L., and Dishman (1982), "A simple model for the estimation of rain-induced attenuation along earth-space paths at millimeter wavelengths," Radio Science, Vol. 17, pp. 1465-1476.
- Stutzman, W.L., and Dishman (1984), Correction to "A simple model for the estimation of rain-induced attenuation along earth-space paths at millimeter wavelengths," Radio Science, Vol. 19, p. 946.

Stutzman, W.L., and Yon, K.M. (1986), "A Simple Rain Attenuation Model for Earth-Space Radio Links Operating at 10-35 GHz," Radio Science, Vol. 21, NO. 1, pp. 65-72.

U.S. Dept. of Commerce, "Telecommunications Analysis Services - Reference Guide," National Telecommunications and Information Agency, Institute for Telecommunications Sciences, Spectrum Utilization Division, 325 South Broadway, Boulder, CO, 80303, June 2, 1981.

Vogel, W.J. (1982), "Measurement of Satellite Beacon Attenuation at 11.7, 19.04, and 28.56 GHz and Radiometric Site Diversity at 13.6 GHz," Radio Science, Vol. 17, No.6, pp. 1511-1520.

CHAPTER IV

DEPOLARIZATION ON EARTH-SPACE PATHS

4.1 INTRODUCTION

By using orthogonal polarizations, two independent information channels occupying the same RF frequency band can be transmitted over a single link. This technique is used in satellite communications systems to effectively increase the available spectrum. While the orthogonally-polarized-channels are completely isolated in theory, some degree of interference between them is inevitable, owing to less-than-theoretical performance of spacecraft and Earth station antennas, and depolarizing effects on the propagation path. The main sources of this depolarization at millimeter wave frequencies are hydrometeor absorption and scattering in the troposphere.

4.1.1 Definition of Terms

Frequency reuse satellite communications systems utilize either orthogonal linear or circular polarization states. The orthogonal linear polarization (LP) states are normally referred to as vertical and horizontal, but except for Earth stations at the satellite's longitude, the polarization directions are rotated somewhat from the local vertical and horizontal references. The orthogonal circular states are left-hand and right-hand circular polarization (LHCP, RHCP), differing in the sense of rotation of the electric field vector. The "handedness" is defined as follows: a wave is RHCP if the sense of rotation of the field corresponds to the natural curl

of the fingers of the right hand when the right thumb is pointed along the propagation direction. Likewise for LHCP. Thus a RHCP wave coming out of the paper would have an electric field rotating counterclockwise.

A measure of the degree of interference between the two orthogonally-polarized channels is the crosspolarization discrimination (denoted XPD), defined as follows: Let E_{ij} be the magnitude of the electric field at the receiver that is transmitted in polarization state i and received in the orthogonal polarization state j ($i, j=1, 2$). E_{11} and E_{22} denote the copolarized waves E_{12} and E_{21} refer to the crosspolarized waves. This is illustrated in Figure 4.1-1. XPD is the ratio (in dB) of the power in the copolarized wave to the power in the crosspolarized wave that was transmitted in the same polarization state.

$$\text{XPD} = 20 \log \frac{E_{11}}{E_{12}} \quad (4.1-1)$$

If state "1" is RHCP and "2" is LHCP, for example, then the XPD is the ratio of the RHCP power to the LHCP power, given that only a RHCP wave was transmitted.

A closely related measure is the crosspolarization isolation (XPI), which compares the copolarized received power with the crosspolarized power that is received in the same polarization state:

$$\text{XPI} = 20 \log \frac{E_{11}}{E_{21}} \quad (4.1-2)$$

Again letting the states "1" and "2" refer to RHCP and LHCP, the XPI compares the power in the RHCP received wave that was transmitted as RHCP to the power that was transmitted as LHCP. XPI is the

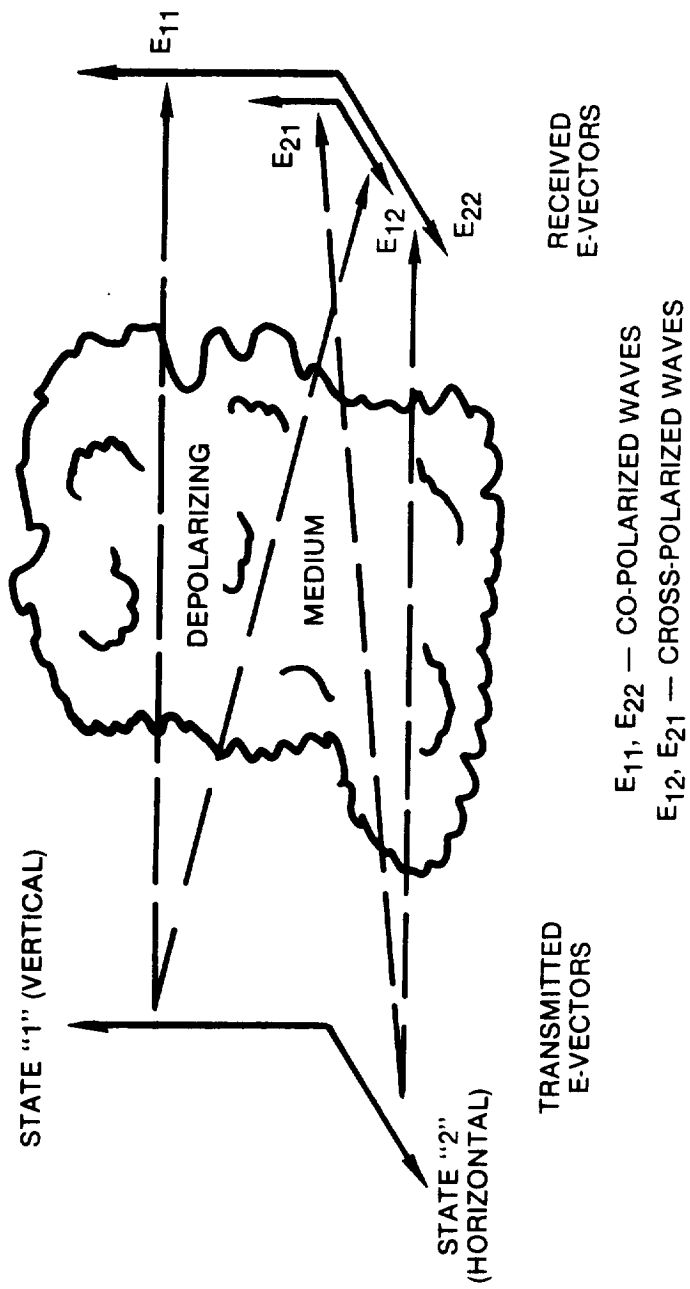


Figure 4.1-1. Definition of Co- and Crosspolarization

parameter that is most meaningful to system engineers, since it directly gives the carrier-to-interference ratio in a received channel. However, XPD is the parameter that is most easily measured. It has been shown (Watson and Arbabi-1973) that XPI and XPD are the same if the hydrometeors responsible for the depolarization have certain symmetry properties. The geometric models that have been used for raindrops and ice crystals have the necessary symmetry, so XPI = XPD in theory. In practice, it has been found that there is not a significant difference between XPI and XPD.

Another term used to describe depolarization, cross polarization ratio (CPR), is the reciprocal of XPD. Other parameters in use, e.g., crosstalk discrimination, crosspolarization distortion, depolarization ratio, crosspolarization level, usually reduce to XPD or XPI.

In the discussion that follows, it is often important to distinguish between polarization properties of a wave in space, and the parameters that we actually measure at the output of the receiver. We shall use XPD to describe the wave properties and a different term, Isolation (I) (after Stutzman-1977) to describe the receiver output. In general,

$$I = \frac{\text{copolarized channel output power}}{\text{crosspolarized channel output power}}$$

Isolation takes into account the performance of the receiver antenna, feed, and other components as well as the propagating medium. When this performance is close to ideal, and/or the XPD of the wave is low (i.e. severe depolarization), then I=XPD. This will be discussed in more detail later.

4.1.2 Hydrometeor Sources of Depolarization

The major sources of depolarization on Earth-space paths are hydrometeors, ionospheric Faraday rotation, and multipath. The

predominant source at millimeter wave frequencies is hydrometeors, and rain is the hydrometeor species that has the greatest effect.

4.1.2.1 Rain. To determine the attenuation due to rain, the raindrops are modelled as spheres of water suspended in space. Real raindrops are falling at their terminal velocity and, due to the complex aerodynamic and hydrostatic forces acting on them, they are in general not spherical. The very small drops (≥ 0.03 cm in diameter) are very nearly spherical, drops in the range of about 0.03 to 0.10 cm in diameter can be considered oblate spheroids, and drops with diameters larger than about 0.10 cm are asymmetric blobs with flat or concave bottoms (Pruppacher and Pitter-1971). Depolarization occurs because of this lack of spherical symmetry, along with the tendency for the drops to have a preferred orientation (i.e., top and bottom flattened). The effects of the rain-filled medium on a wave propagating through it are dependent on the orientation of the electric field vector with respect to the preferred drop orientation.

It is easy to picture the effect of the "flattened" raindrops on linearly polarized (LP) waves propagating horizontally: The fields of horizontal LP waves encounter more water, on the average, than do vertical LP wave fields, and so are subjected to more attenuation and phase shift. An LP wave at some arbitrary orientation, say 45° from the vertical, can be resolved into an equivalent set of component waves having horizontal and vertical polarization. After passing through the rain, the horizontal component has suffered a greater decrease in amplitude, so the polarization direction has been shifted toward the vertical. In addition, the differential phase shift between the components has caused the wave to become slightly elliptically polarized. These depolarizing effects of rain are described more rigorously later.

4.1.2.2 Ice Crystals. Most of the depolarizing effect of rain is produced by differential attenuation. Therefore rain depolarization and attenuation are fairly well correlated. Starting in 1975, when ATS-6 propagation experiments were well underway in Europe,

researchers were surprised to see occasions of severe depolarization that were completely uncorrelated with rain attenuation. The cause of this "anomalous" depolarization has since been identified as oriented ice crystals. Ice can occur at altitudes above the freezing level in cirrus clouds and at the tops of cumulonimbus clouds. When something causes the ice crystal symmetry axes to align themselves, it brings on a polarization-selective phase effect. We are now fairly certain that the electrostatic fields associated with electrically-active storms are at least one aligning force. This is consistent with the observed abrupt changes in XPD coincident with lightning flashes.

Ice depolarization has been theoretically modelled in a manner analogous to rain depolarization. For that purpose, the ice crystals are assumed to be either oblate or prolate ellipsoids, corresponding respectively to "plates" and "needles," which are two distinct types of crystals that are known to exist in clouds. The model is in good agreement with observations and explains the rapid changes in the phase of the crosspolarized waves that accompany lightning flashes.

4.1.2.3 Snow, Graupel and Hail. The anisotropy that is responsible for depolarization by rain and high-altitude ice crystals apparently also exists in snow. From S-band and Ku-band radar measurements, Hendry, et. al. (1976) have observed significant differential phase shifts between the right-and left-hand CP radar returns in moderate to heavy snow. The differential phase shift along the propagation path was found to vary between 0.16° and 1.17° per km at 16.5 GHz, values comparable to that of moderate rainfall. Unlike rain, however, snow produces very little differential attenuation. The differential phase shift in snow should produce measureable depolarization on Earth-space paths, but little or no direct experimental evidence of this has been reported.

Graupel, or snow pellets, may also exhibit some anisotropy, and resulting depolarization. Hail particles, which have a rough

spherical symmetry, probably would not cause depolarization. (McCormick and Hendry-1977).

4.2 MATHEMATICAL FORMULATIONS FOR DEPOLARIZATION

This section presents the mathematical background required to discuss the effects of the propagation medium characteristics and antenna performance on signals in dual polarization Earth-space links. It should enable the system designer to properly interpret experimental data and assess system performance, considering both the medium's depolarizing effects on the wave and the wave's interaction with the antenna system. Most of this development is from Stutzman (1977).

4.2.1 Specifying the Polarization State of a Wave

In the most general case, the tip of the electric field vector of a plane electromagnetic wave traces out an ellipse in the plane perpendicular to the direction of propagation. The polarization state of the wave is given by specifying the shape and orientation of the ellipse, along with the sense of rotation of the field vector. Figure 4.2-1 shows the general polarization ellipse and defines the notation. The electric field vector $\vec{E}(t)$ is the resultant of sinusoidal components $E_x(t)$ and $E_y(t)$ which have different amplitudes E_1 and E_2 and a phase difference δ :

$$\begin{aligned}\vec{E}(t) &= \hat{x} E_x(t) + \hat{y} E_y(t) \\ &= \hat{x} E_1 \cos \omega t + \hat{y} E_2 \cos (\omega t + \delta)\end{aligned}\tag{4.2-1}$$

where \hat{x} and \hat{y} are unit vectors in the x and y directions, respectively, ω is the radian frequency, and t is time. The polarization ellipse is fully described by the angle, τ , between the ellipse major axis and the x-axis, and the ratio of the major and minor axes of the ellipse. This ratio is the magnitude of an important parameter known as the axial ratio, and is the ratio of

the maximum to the minimum magnitude of the electric field vector. The axial ratio's sign is assigned to be positive if the vector rotation has a left-hand sense and negative for rotation with a right-hand sense: (See Figure 4.2-2.) Linearly polarized waves have an infinite axial ratio; circularly polarized waves have an axial ratio $r = \pm 1$, corresponding to LHCP and RHCP respectively.

It is convenient to define another parameter

$$\epsilon = \cot^{-1} r ; -45^\circ \leq \epsilon \leq 45^\circ \quad (4.2-2)$$

The specifying parameters ϵ and τ are related to the quantities used to describe the fields earlier by

$$\epsilon = \frac{1}{2} \sin^{-1}(\sin 2\gamma \sin \delta) \quad (4.2-3)$$

$$\tau = \frac{1}{2} \tan^{-1}(\tan 2\gamma \cos \delta) \quad (4.2-4)$$

where

$$\gamma = \tan^{-1} \frac{\text{max y-component of } \vec{E}}{\text{max x-component of } \vec{E}} \quad (4.2-5)$$

$$= \tan^{-1} (E_2/E_1)$$

There are other methods used to specify polarization state (Stutzman-1977). The Stokes parameter representation is a matrix formulation. The Poincare sphere is a mapping of polarization states into points on a unit sphere. The complex polarization factor is a single number specifying polarization state. All these various representations are directly relatable to the angles ϵ and τ , or δ and γ .

4.2.2 Wave-Antenna Interaction

The power available (P_R) at the output of an antenna illuminated by a uniformly polarized incident plane wave of flux density S is

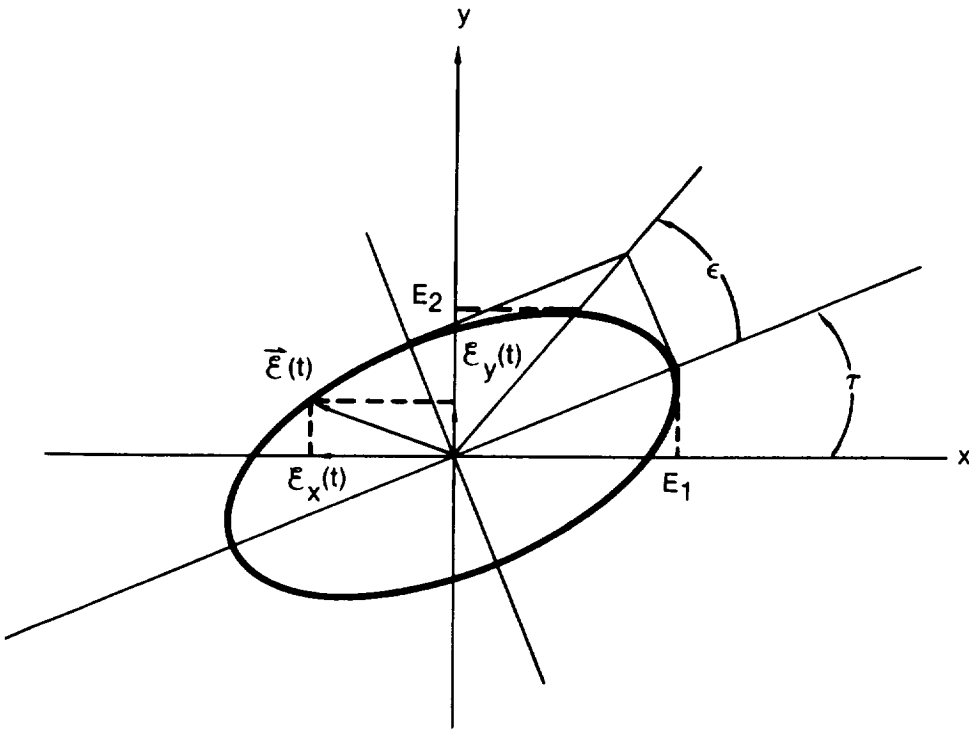


Figure 4.2-1. Polarization Ellipse

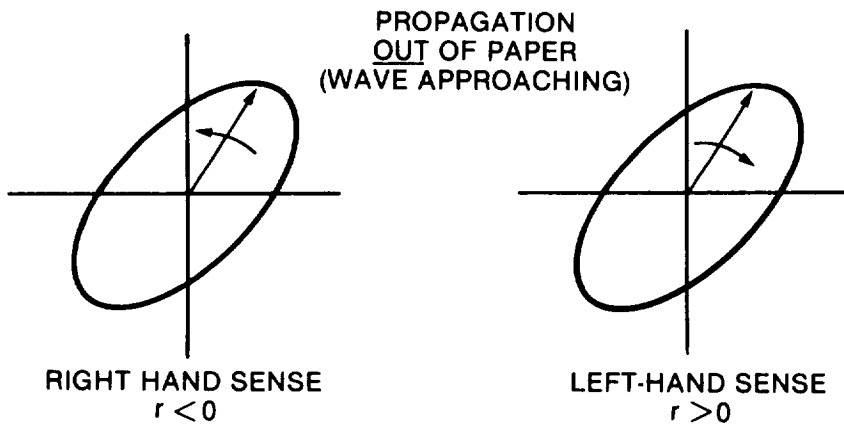


Figure 4.2-2. Definition of Sign of Axial Ratio, r

$$P_R = S A_e m_p$$

(4.2-6)

where A_e is the effective aperture of the antenna in the direction of the incident wave, and m_p is the polarization mismatch factor. This factor is a real number between zero and one that depends on the degree of match of the polarization state of the wave and the antenna. The polarization state of a receiving antenna is defined as the state of the wave that the same antenna would transmit, but with time reversed. (A time-reversal changes the direction of propagation of a wave but retains the sense of rotation and axial ratio.) A RHCP incident wave, for example, is perfectly matched to a RHCP antenna. This means the antenna absorbs the maximum amount of power from the wave, and $m_p = 1$. A RHCP antenna absorbs no power from a LHCP wave, and $m_p = 0$. The general expression m_p , assuming arbitrary elliptical polarization states of both the antenna and the wave, is

$$m_p(w,a) = \frac{1}{2} + \frac{4r_w r_a + (r_w^2 - 1)(r_a^2 - 1) \cos 2(\tau_a - \tau_w)}{2(r_w^2 + 1)(r_a^2 + 1)} \quad (4.2-7)$$

where

r_a = axial ratio of antenna

r_w = axial ratio of wave

τ_a = major axis angle of antenna

τ_w = major axis angle of wave

We consider some examples to confirm that (4.2-7) is plausible:

Antenna RHCP, Wave LHCP

$$r_a = -1, r_w = +1$$

$$m_p = 1/2 + \frac{4(1)(-1) + (1-1)(1-1)}{2(1+1)(1+1)} = 1/2 - 1/2 = 0$$

Antenna LP, Wave CP

$$r_a = \infty, r_w = 1$$

By dividing the numerator and denominator of the second term of (4.2-7) by r_a^2 , then taking the limit as $r \rightarrow \infty$, we find that $m_p = 1/2$, which is intuitively agreeable.

Antenna LP, Wave LP

$$r_a = r_w = \infty$$

Here we divide the numerator and denominator by $r_a^2 r_w^2$ and pass to the limit, giving

$$m_p = 1/2 + 1/2 \cos 2(\tau_a - \tau_w) = \cos^2(\tau_a - \tau_w) \quad (4.2-8)$$

This equals one when the orientation of the linear polarization axes of the antenna and wave are aligned ($\tau_a - \tau_w$), and equals zero when the axes are orthogonal ($\tau_a - \tau_w = \pm 90^\circ$)

Antenna LP, Wave Elliptically Polarized

$$r_a = \infty \quad r_w = r$$

Dividing through by r_a^2 and taking the limit as before, we obtain

$$m_p = 1/2 + \frac{1/2 (r^2 - 1) \cos 2(\tau_a - \tau_w)}{2(r^2 + 1)} \quad (4-2.9)$$

Figure 4.2-3 is a polar plot of m_p versus the angle difference $\tau_a - \tau_w$, for $r=1.5$ and 2 .

Letting

$$(m_p)_{\max} = m_p \text{ for } \tau_a = \tau_w \text{ (aligned)}$$

$$(m_p)_{\min} = m_p \text{ for } \tau_a = \tau_w + 90^\circ \text{ (orthogonal)}$$

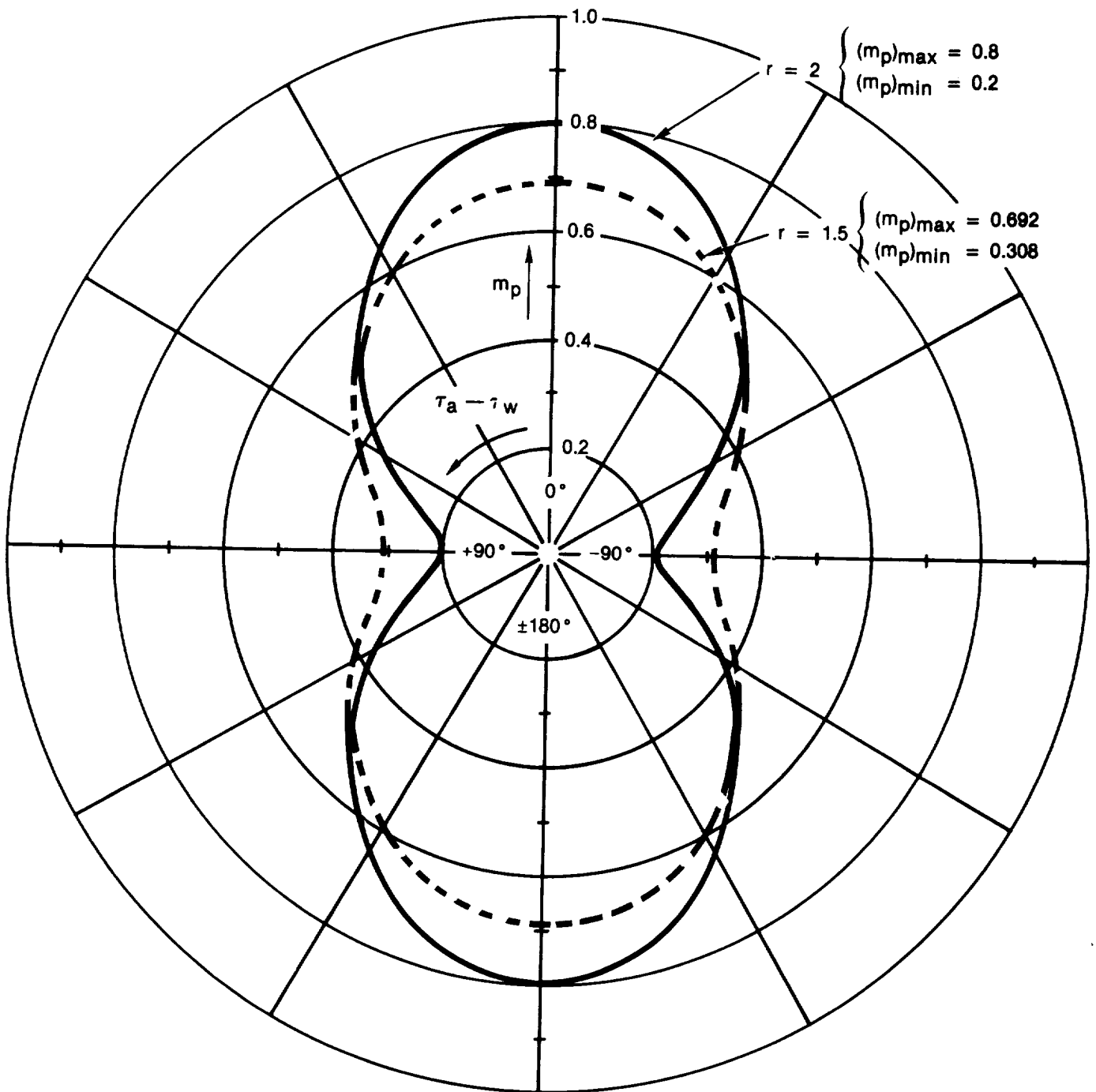


Figure 4.2-3. Polarization Mismatch Factor m_p for LP Antenna and Elliptically Polarized Waves

Some algebra yields

$$r = \left[\frac{(m_p)_{\max}}{(m_p)_{\min}} \right]^{1/2} \quad (4.2-10)$$

This is confirmed in Figure 4.2-3.

This formula suggests a technique for measuring the axial ratio and principal axis orientation of a received wave: The power received by a linearly polarized antenna (e.g., a dipole) is measured as the antenna axis is rotated through 180°. The ratio of the maximum to the minimum received power, assuming a perfect antenna, is then the square of the axial ratio of the wave, and the orientation of the wave's principal axis is just the antenna's orientation when maximum power is measured.

4.2.3 Cross Polarization Discrimination (XPD)

Having defined the polarization mismatch factor, we now present a more useful definition of XPD than that given earlier. Orthogonal polarization states are defined, in general, to have axial ratios that are equal in magnitude and opposite in sign (i.e., opposite in rotation sense), and have polarization ellipses with spatially orthogonal axes. Vertical/horizontal LP, and RHCP/LHCP are common examples of orthogonal states. The polarization mismatch factor for a wave with a given polarization state incident on an antenna that is matched to the orthogonal state is zero.

It is always possible to decompose a wave into two components with orthogonal polarization states. An arbitrary wave can be considered as being composed of a component with a polarization state matching the antenna, and a second component with the orthogonal state. The antenna extracts maximum power from the matched component, but completely rejects the orthogonal component. The polarization mismatch factor is then seen to be the proportion

of the total flux density impinging on the antenna that is being carried by the polarization-matched wave component. Denoting the received wave's polarization state by the index w' , and the antenna's polarization state by w , the antenna output power is

$$P = SA_e m_p(w', w) \quad (4.2-11)$$

A second antenna with equal effective aperture A_e but with a polarization state w_0 , that is exactly orthogonal to w , gives an output power

$$P_o = SA_e m_p(w', w_0) \quad (4.2-12)$$

The XPD is the ratio of the orthogonal components of the wave,

$$XPD = 10 \log [m_p(w', w) / m_p(w', w_0)] \quad (4.2-13)$$

assuming that the " w " polarization state is the one the system is designed to maximize, or the copolarized state. The " w_0 " state is designated as crosspolarized.

Suppose a LP wave is received, and the copolarized state (w) is designated as horizontally polarized. Let $\tau = \tau_w$, = the angle of the received wave with respect to horizontal. For this case,

$$m_p(w', w) = \cos^2 \tau \quad (4.2-14)$$

$$m_p(w', w_0) = \sin^2 \tau \quad (4.2-15)$$

$$XPD = 10 \log (\cot^2 \tau) \quad (4.2-16)$$

Assume an elliptically polarized wave is received with axial ratio $r_w = r$, and copolar is designated as LHCP. For this case,

$$r_w = +1, r_{w_0} = -1 \quad (4.2-17)$$

$$m_p(w', w) = (1/2) \frac{(r+1)^2}{r^2+1} \quad (4.2-18)$$

$$m_p(w', w_0) = (1/2) \frac{(r-1)^2}{r^2+1} \quad (4.2-19)$$

$$XPD = 20 \log [(r + 1)/(r-1)] \quad (4.2-20)$$

XPD is plotted versus r for the elliptically polarized case in Figure 4.2-4. An alternate "axial ratio," AR_{dB} , is shown in the figure. This is commonly used and is related to r by

$$AR_{dB} = 20 \log |r| \quad (4.2-21)$$

In terms of this parameter, XPD is closely approximated by

$$XPD \approx 24.8 - 20 \log (AR_{dB}) , \text{ for } AR_{dB} < 10 \text{ dB} \quad (4.2-22)$$

4.2.4 Effect of Non-Ideal Antenna Performance

The XPD describes the polarization characteristics of a received wave with respect to some "copolarized" reference. The true XPD could be measured with an ideal antenna, capable of being matched exactly to the co- and cross polarized state. Actual antennas are not ideal. They can be built with outputs that closely approximate the copolarized and crosspolarized components of the wave, but some degree of degradation is always present in their performance. Here we present a method of quantifying the polarization performance of the antenna and taking this performance into account in interpreting polarization measurements.

From this point on, the receive antenna polarization states that are close to the true co- and crosspolarized wave states will be distinguished from the true states by putting their names within quotation marks.

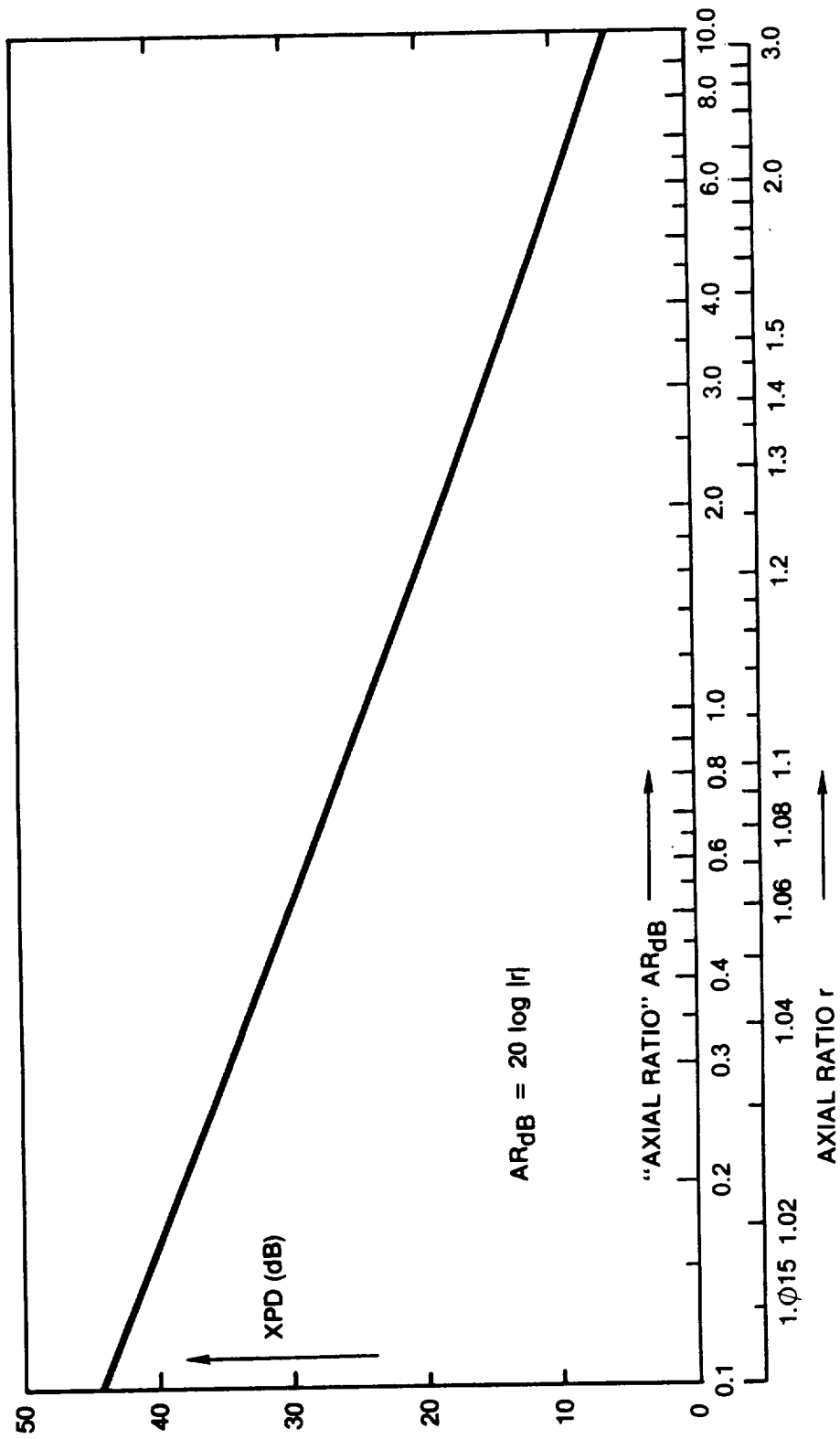


Figure 4.2-4. XPD vs. Axial Ratio of Elliptically Polarized Wave (LHCP is Copolarized)

Isolation, I, is defined as the ratio of the output power available at the antenna's "copolarized" port (P_c) to the output power at the "crosspolarized" port (P_x). The polarization states coupled to the "copolarized" and "crosspolarized" ports are a_c and a_x , respectively. Since the antenna is non-ideal, a_c and a_x are not necessarily orthogonal, and a_c does not necessarily correspond to the pure copolarized state. Denoting the state of the received wave as w' and the wave's power flux density as S_w' , we have from (4.2-11):

$$I = 10 \log \frac{P_c}{P_x} = 10 \log \frac{S_w' A_e m_p(w', a_c)}{S_w' A_e m_p(w', a_x)} \quad (4.2-23)$$

$$= 10 \log \frac{m_p(w', a_c)}{m_p(w', a_x)}$$

It is useful to be capable of finding XPD in terms of I, which is measurable. The power available at the "copolarized" antenna port can be written in terms of the true copolarized and crosspolarized wave components, w and w_o .

$$P_c = A_e [S_w m_p(w, a_c) + S_{w_o} m_p(w_o, a_c)] \quad (4.2-24)$$

Likewise for the "crosspolarized" power

$$P_x = A_e [S_w m_p(w, a_x) + S_{w_o} m_p(w_o, a_x)] \quad (4.2-25)$$

S_w and S_{w_o} are the power flux density in the true copolarized and crosspolarized states, respectively. Now we have

$$I = 10 \log \frac{S_w m_p(w, a_c) + S_{w_o} m_p(w_o, a_c)}{S_w m_p(w, a_x) + S_{w_o} m_p(w_o, a_x)}$$

$$= 10 \log \frac{(xpd)m_p(w,a_c) + m_p(w_o,a_c)}{(xpd)m_p(w,a_x) + m_p(w_o,a_x)} \quad (4.2-26)$$

where $xpd = S_w/S_{w_o} = \log^{-1} (XPD/10)$

Since the "copolarized" state of the antenna is assumed to be well-matched to the true copolarized wave component,

$$m_p(w_o,a_c) \ll m_p(w,a_c)$$

So this term is negligible and

$$I = 10 \log \frac{m_p(w,a_c)}{m_p(w,a_x) + m_p(w_o,a_x)/(xpd)} \quad (4.2-27)$$

Note that when the antenna is nearly ideal,

$$m_p(w,a_c) = 1, m_p(w_o,a_x) = 1, m_p(w,a_x) = 0$$

and so $I = XPD$. On the other hand, when the XPD is very high,

$$I = 10 \log [m_p(w,a_c)/m_p(w,a_x)]$$

which is a function of the antenna only. This implies that a given antenna can be used to measure XPD to a given accuracy up to a certain maximum XPD value which is determined by the antenna performance parameters.

For the CP case, the equation for I becomes

$$I = 10 \log \frac{\frac{1}{2} + \frac{r_c}{r_c^2 + 1}}{\frac{1}{2}(xpd^{-1} + 1) + \frac{r_x}{r_x^2 + 1} (xpd^{-1} - 1)} \quad (4.2-29)$$

where r_c and r_x are the axial ratios of the antenna's "copolarized" and "crosspolarized" states, respectively. Figure 4.2-5 shows I versus XPD for various values of axial ratio AR_{dB} . The "copolarized" and "crosspolarized" axial ratios are made equal in the figures, but I is actually nearly independent of r_x . The figure gives the amount of error to be expected when measuring XPD.

For the LP case, we obtain

$$I = 10 \log \frac{1 + Q_c \cos 2\tau_c}{(1 + xpd^{-1}) - (1 - xpd^{-1}) Q_x \cos 2(\tau_x - 90^\circ)} \quad (4.2-30)$$

where $Q_{c,x} = (r_{c,x}^2 - 1) / (r_{c,x}^2 + 1)$

$\tau_{c,x}$ = antenna "copolarized",
"crosspolarized" axis orientation angle

$r_{c,x}$ = antenna "copolarized",
"crosspolarized" axial ratio

The copolarized wave axis is taken as the reference for the antenna axis orientation angles. Figures 4.2-6 and 4.2-7 show I versus XPD for various antenna axial ratios and axis misalignment angles. The first figure is for perfect axis alignment and varying axial ratio. As with the CP case, equal axial ratios for the "copolarized" and "crosspolarized" states were assumed, but isolation is practically independent of the "copolarized" axial ratio, r_c , when it is large ($>20dB$). Figure 4.2-7 shows the effect of axis misalignment for the $AR_{dB}=30dB$ case. The antenna axes are assumed orthogonal, with $\tau_x = \tau_c - 90^\circ$, but the isolation is not strongly dependent on τ_c for $\tau_c < 10^\circ$.

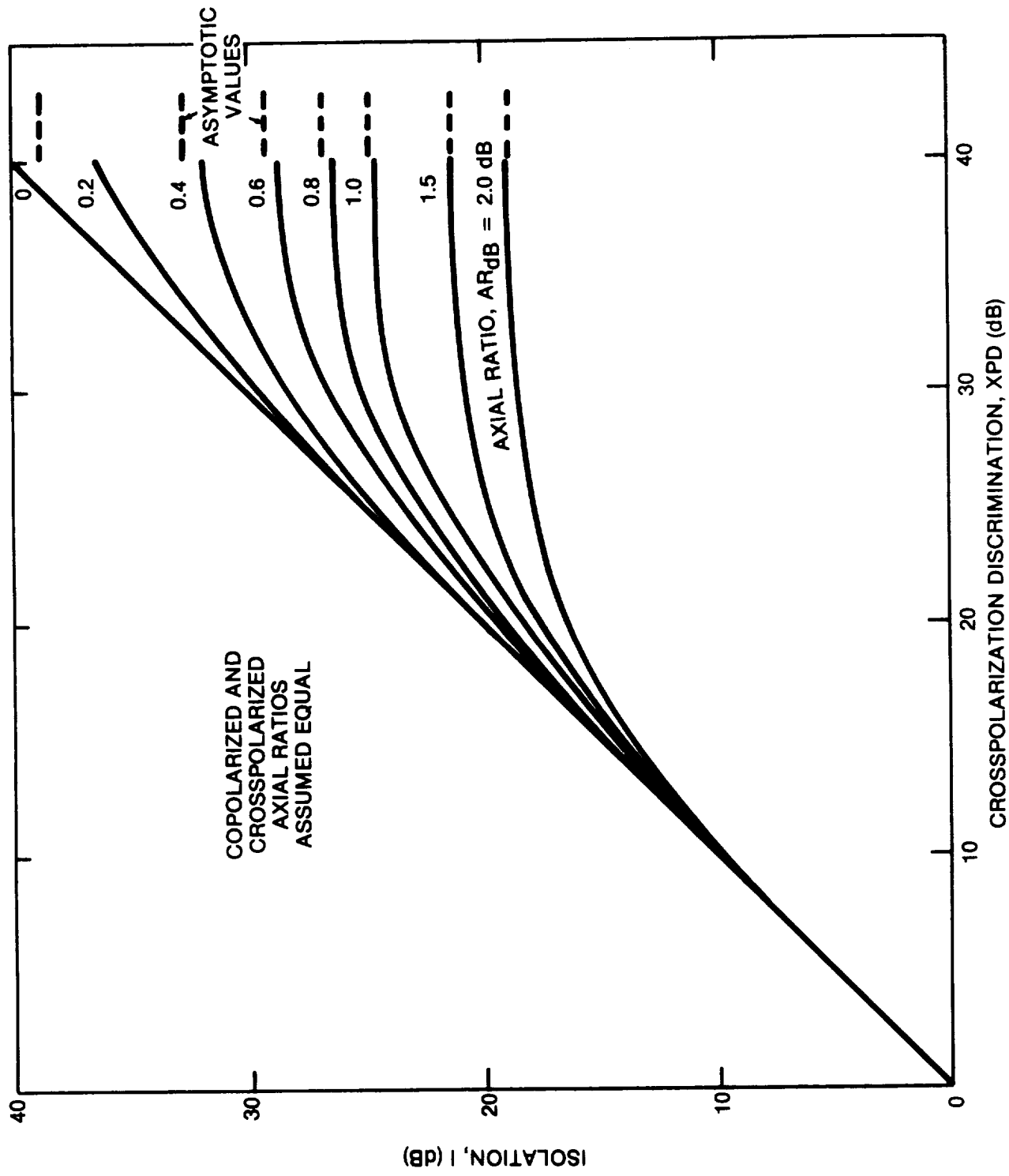
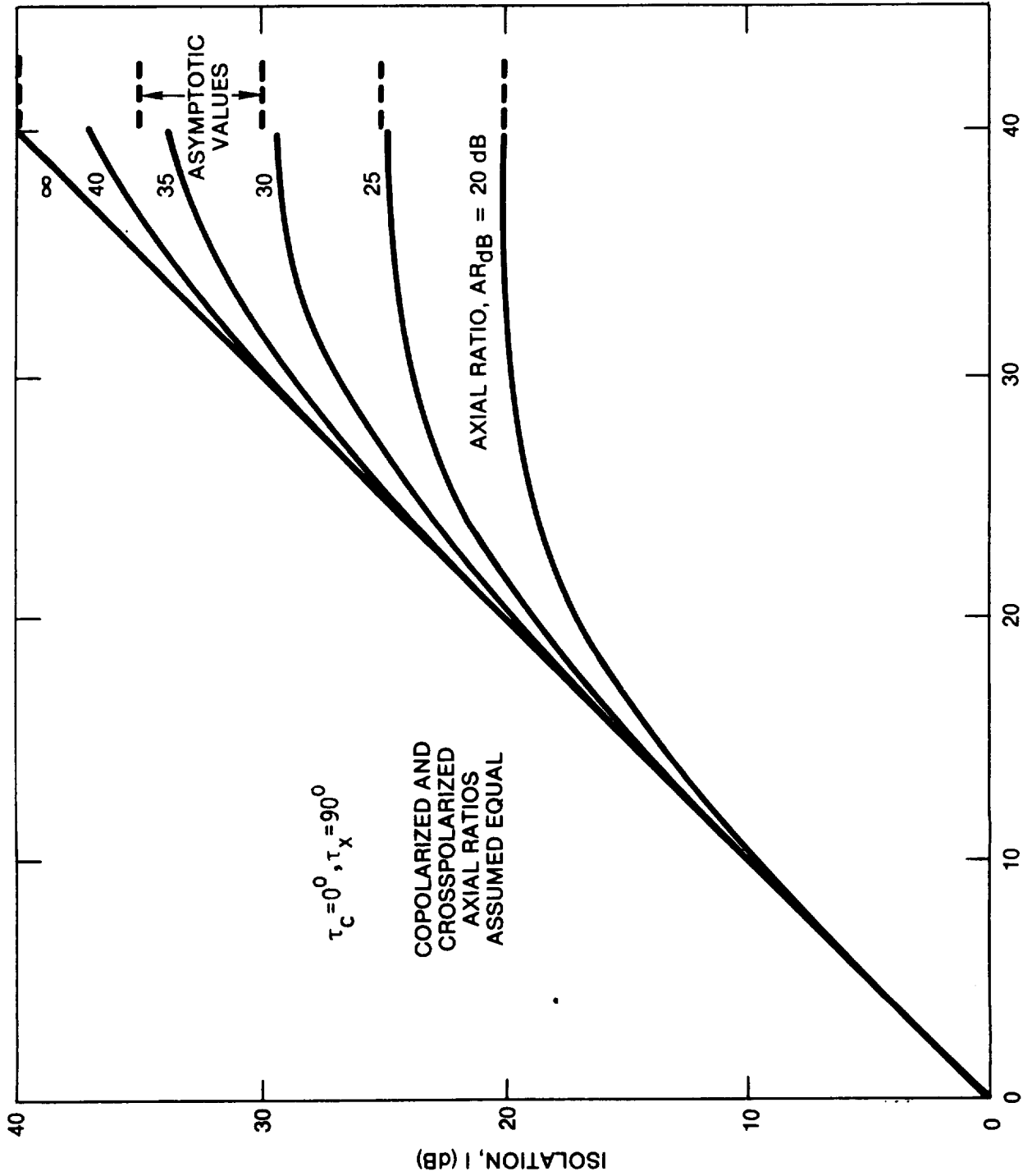


Figure 4.2-5. XPD and Antenna Axial Ratio - Circular Polarized Case



CROSSPOLARIZATION DISCRIMINATION, XPD (dB)

Figure 4.2-6. Isolation vs. XPD and Antenna Axial Ratio - Linear Polarized Case, No Angle Misalignment

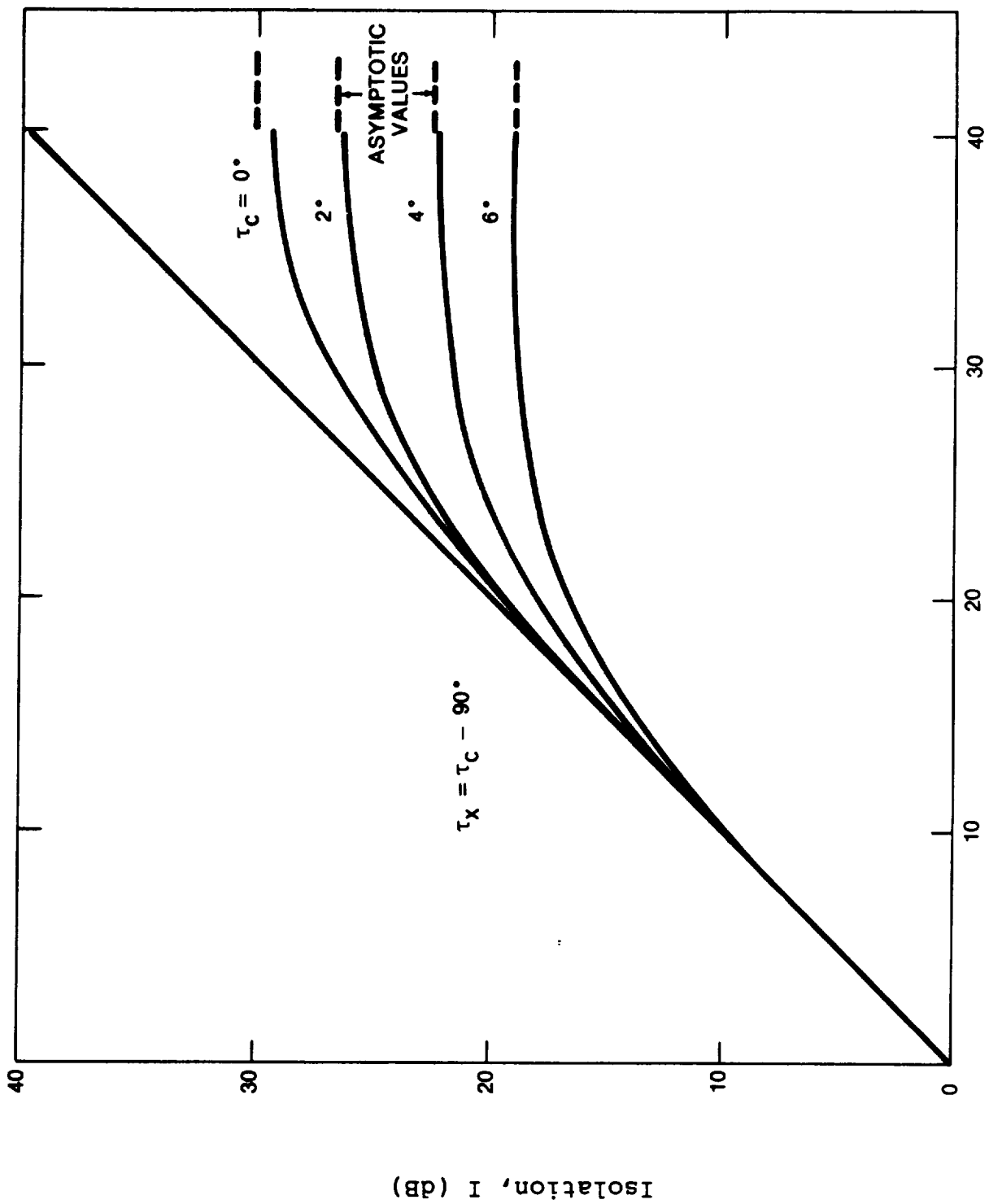


Figure 4.2-7. Isolation vs. XPD and Major Axis Misalignment - Linear Polarized Case, Axial Ratio, $AR_{dB} = 30dB$

4.3 RAIN DEPOLARIZATION

4.3.1 Theory of Rain Depolarization

Rain depolarization can be modelled using the same techniques applied to rain attenuation. The essential difference is that in examining depolarization, the raindrops are assumed to be oblate spheroids. The attenuation analysis assumed that the raindrops were spherical. Figure 4.3-1 shows the geometry for a dual LP wave incident on an oblate spheroidal raindrop. The raindrop is at an arbitrary orientation with respect to the direction of propagation of the wave. The orientation is specified by the angle q , between the propagation vector and the raindrop's symmetry axis. The plane containing q will be referred to as the plane of incidence.

E_x and E_y are electric field vectors of two orthogonal LP waves. They are in a plane normal to the propagation vector, and each one can be resolved into two components: a component in the plane of incidence, and a component normal to it. Parallel to these components, we define two symmetry axes, labeled I and II in the figure. The projection of the raindrop into the plane containing the electric field vectors is an ellipse, and axes I and II are its minor and major axes, respectively. Figure 4.3-2 shows this ellipse and how the electric fields are resolved into their "I" and "II" components.

The total electric field magnitudes in the I and II directions (E_I and E_{II}) are given by

$$\begin{bmatrix} E_I \\ E_{II} \end{bmatrix} = \begin{bmatrix} \cos \theta & -\sin \theta \\ \sin \theta & \cos \theta \end{bmatrix} \begin{bmatrix} E_x \\ E_y \end{bmatrix} = R \begin{bmatrix} E_x \\ E_y \end{bmatrix} \quad (4.3-1)$$

where θ , the canting angle, is the angle between the x and I axes.

Now consider a region of space containing many identical raindrops with the same orientation distributed throughout it. According to scattering theory, the effect of many scatterers along

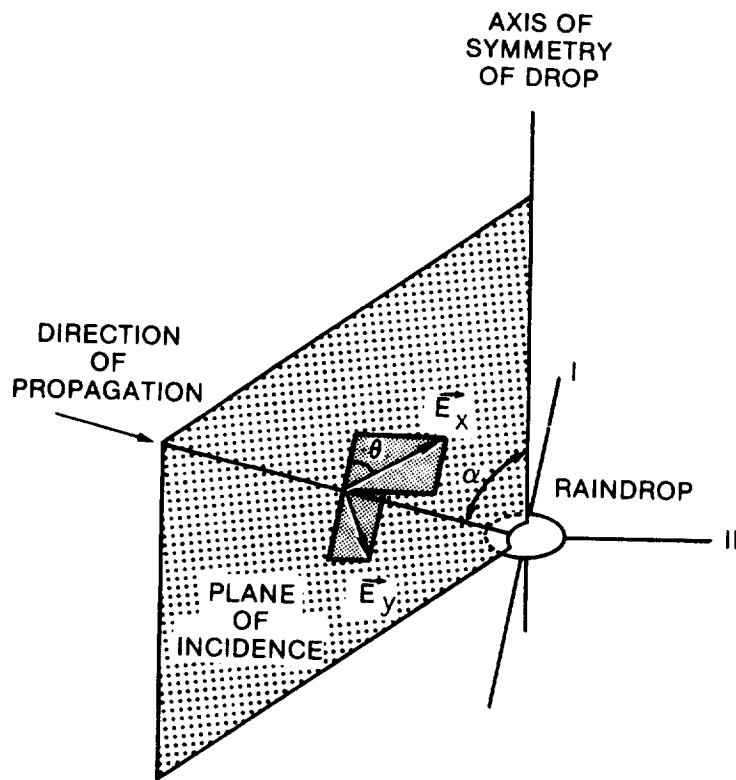


Figure 4.3-1. Geometry for Rain Depolarization Analysis

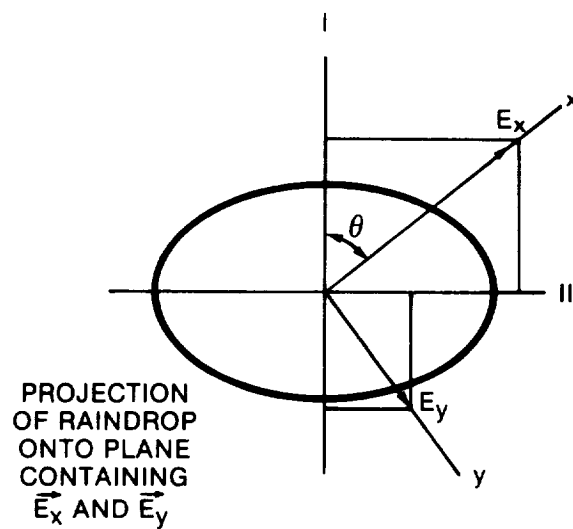


Figure 4.3-2. Resolution of Electric Fields into I and II Components

the propagation path of a wave is to multiply the electric field vector by a transmission coefficient of the form

$$T = \exp[-(a-j\phi)L] \quad (4.3-2)$$

where L is the path length through the scattering region. The a term of the exponent produces attenuation of the wave, and ϕ produces a phase lag. This phase lag is in addition to the normal free-space phase retardation of the fields. Instead of a and ϕ , which have units of nepers per unit length and radians per unit length, respectively, the more useful parameters, A and Φ , are normally used:

A = specific attenuation of power flux density of wave, in dB/km.

$$= 20(\log_{10}e)a = 8.686 a$$

Φ = specific phase lag of wave, in degrees/km.

$$= (180/\pi) \phi$$

A region filled with oblate spheroidal raindrops must be characterized by two transmission coefficients: T_I , applied to the "I" component of the electric field, and T_{II} , applied to the "II" component. Denoting the fields of the wave incident on the scattering region by a subscript i , and the fields of the wave exiting the region by s (for scattered), we can write

$$\begin{bmatrix} E_{Is} \\ E_{IIs} \end{bmatrix} = \begin{bmatrix} T_I & 0 \\ 0 & T_{II} \end{bmatrix} \begin{bmatrix} E_{Ii} \\ E_{IIi} \end{bmatrix} = T \begin{bmatrix} E_{Ii} \\ E_{IIi} \end{bmatrix} \quad (4.3-3)$$

Now the coordinate rotation R , defined above, can be applied to get an equation for the effect of the scattering region on the field vectors in the x and y directions.

$$\begin{bmatrix} E_{xs} \\ E_{ys} \end{bmatrix} = R^{-1} T R \begin{bmatrix} E_{xi} \\ E_{yi} \end{bmatrix} = T' \begin{bmatrix} E_{xi} \\ E_{yi} \end{bmatrix} \quad (4.3-4)$$

Figure 4.3-3 shows how the three component transformations are successively applied to produce T' . The overall transformation matrix T' can be evaluated to yield

$$T' = \begin{bmatrix} t_{xx} & t_{xy} \\ t_{yx} & t_{yy} \end{bmatrix}$$

$$t_{xx} = T_{\perp} \cos^2 \theta + T_{\parallel} \sin^2 \theta$$

$$t_{yy} = T_{\perp} \sin^2 \theta + T_{\parallel} \cos^2 \theta$$

$$t_{xy} = t_{yx} = \frac{1}{2} (T_{\parallel} - T_{\perp}) \sin 2\theta$$

(4.3-5)

Chu (1974) gives expressions for these parameters in terms of the A_s and ϕ_s .

Calling the LP wave polarized in the x direction the copolarized wave, we can now obtain expressions for the XPD:

$$\text{XPD}_x = 10 \log \frac{|E_{xs}|^2}{|E_{ys}|^2} \quad \text{with } E_{yi} = 0$$

$$= 10 \log \frac{|t_{xx}|^2}{|t_{yx}|^2}$$

$$= 20 \log \frac{1 + \gamma \tan^2 \theta}{(\gamma - 1) \tan \theta}$$

(4.3-6)

where

$$\gamma = T_{\parallel} / T_{\perp} = \exp [-(a_{\parallel} - a_{\perp})L + j(\phi_{\parallel} - \phi_{\perp})L]$$

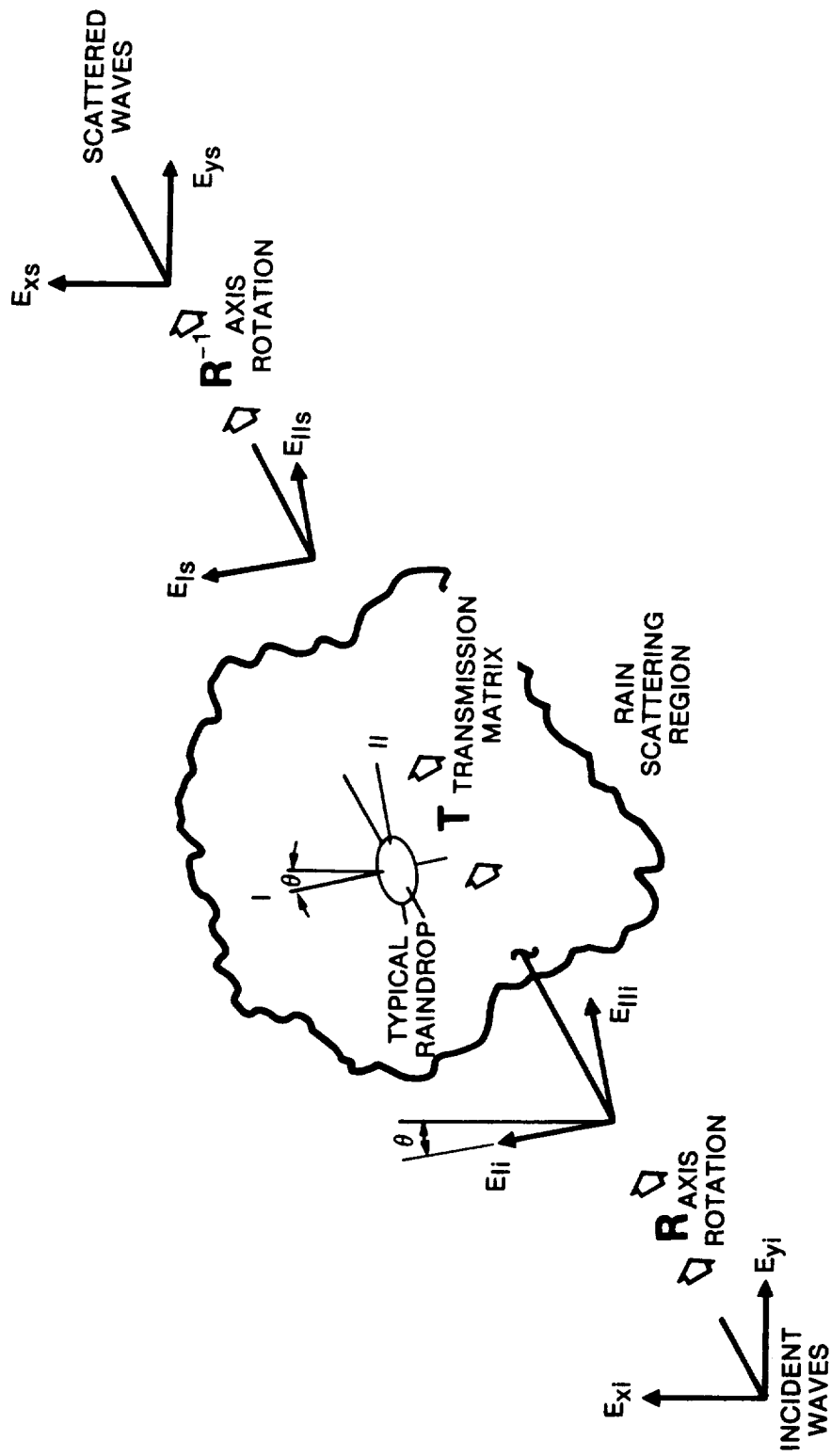


Figure 4.3-3. Components of Overall Transformation matrix T' Describing Rain Depolarization

Or, calling the γ - direction the copolarized state,

$$\begin{aligned}
 \text{XPD}_\gamma &= 10 \log \frac{|E_{\gamma s}|^2}{|E_{\gamma s}|^2} \text{ with } E_{x_i} = 0 \\
 &= 10 \log \frac{|t_{\gamma\gamma}|^2}{|t_{\gamma\gamma}|^2} \\
 &= 20 \log \frac{\gamma + \tan^2\theta}{(\gamma-1) \tan\theta}
 \end{aligned} \tag{4.3-7}$$

For the case of circular polarization, Chu (1974) shows

$$\text{XPD}_c = 10 \log (|t_{xx}/t_{yx}|^2)_{\theta=45^\circ} = 20 \log \frac{\gamma + 1}{\gamma - 1} \tag{4.3-8}$$

which is independent of the sense of rotation of the copolarized wave.

Thus far, we have assumed that all raindrops are of equal size and have the same orientation. The model must account for the distribution of sizes and shapes of raindrops and the distribution of angles θ and α that are present in the rain along the path. Scattering theory allows for this. The scattering effect of a single raindrop is determined as a function of some parameter (like size), then the distribution of that parameter over the population of raindrops is used in calculating the transmission coefficients. The transmission coefficients (more exactly, the specific attenuations and phase lags, A and $\bar{\Phi}$) have been calculated in this manner as a function of rain rate by several authors. The first calculations (Chu-1974, Watson and Arbabi-1973a) used oblate spheroidal raindrops. The drops were assumed to be distributed

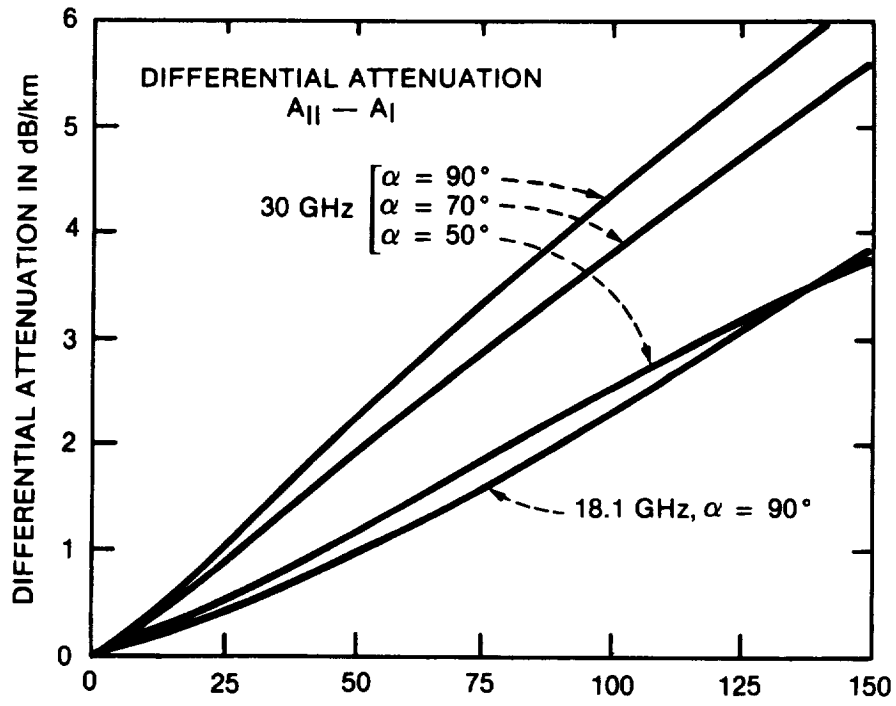
be distributed according to the well-known Laws and Parsons distribution, and to have eccentricities that were directly related to their sizes, with the largest drops being the most deformed. Later work has considered the more realistic Pruppacher-Pitter (1971) drop shapes (Oguchi-1977). Figure 4.3-4 (from Morrison, et al -1973) is an example of the results of these calculations. These curves give the difference in the specific attenuation and phase between the I and II axes. The angle between the direction of propagation and the raindrop symmetry axis, α , is a parameter, and the canting angle, θ , is set to 25° . The differential attenuation and phase are of most interest because they actually determine XPD. As can be seen from the curves, the worst case for differential attenuation and phase corresponds to $\alpha = 90^\circ$. This agrees with intuition, since the projection ellipse of the drop onto the plane containing the field vectors has the greatest eccentricity for that case. For values of α different from 90° , Chu (1974) shows that the following approximation is quite accurate:

$$A_{II} - A_I = \sin^2 \alpha (A_{II} - A_I)_{\alpha=90^\circ} \quad (4.3-9)$$

$$\Phi_{II} - \Phi_I = \sin^2 \alpha (\Phi_{II} - \Phi_I)_{\alpha=90^\circ}$$

Accounting for the distribution of α and θ is more difficult than doing so for drop size and shape. We have little information about the distribution of the orientation of raindrops. It is expected that wind and wind gusts produce an appreciable spatial correlation in the orientation. In the absence of wind, a fairly symmetric distribution about the vertical would be expected.

The α component of drop orientation is usually considered to be equal to a constant 90° for line-of-sight (horizontal) paths and the complement of the elevation angle for satellite (oblique) paths. The effect of α on XPD is apparently so small compared with the canting angle dependence that allowing for a distribution of α is not worthwhile.



$\theta = 25^\circ$
 DROP TEMP = 20°

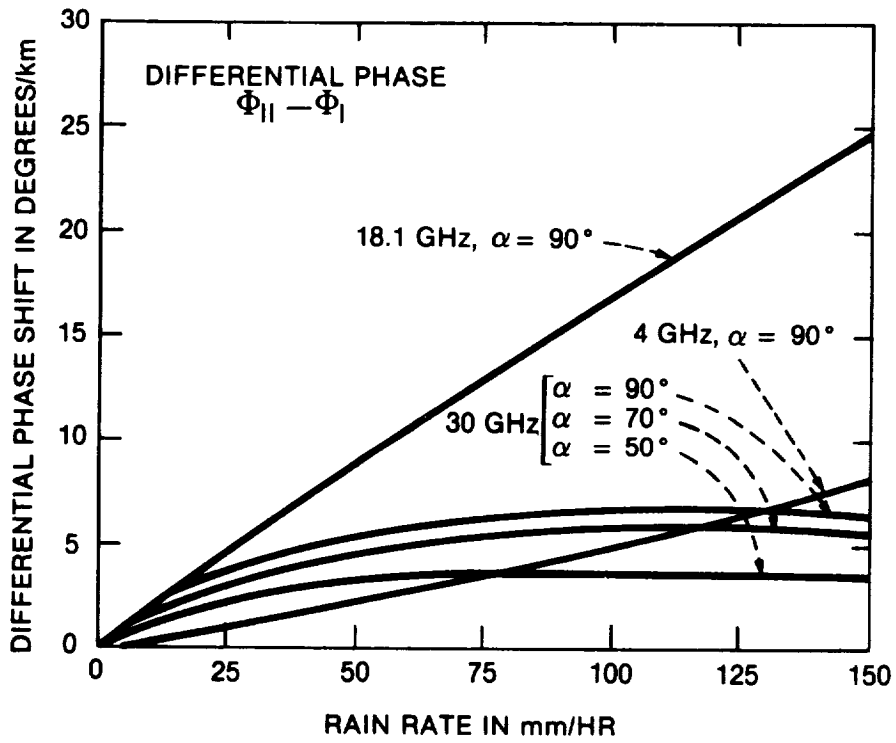


Figure 4.3-4. Differential Attenuation and Phase for Rain, From Morrison, et. al. (1973)

The canting angle distribution, as it affects XPD, has been studied extensively. Thomas (1971) presents an experimentally determined canting angle distribution and derives an "average" angle of 15° . He further notes that the crosspolarizing effects of canting angles of positive and negative sense tend to cancel, so the overall effect is proportional to the excess of one sense over the other. Based on some experimental evidence, he chooses 25% as the worst case imbalance of canting angle sense. The predicted worst case XPD, then, is roughly that produced by 25% of the raindrops at a 15° canting angle. Chu (1974) uses similar reasoning, but gives evidence that the mean canting angle is about 25° , and that the effective angle sense imbalance is about 14%. Watson and Arbabi (1973b) calculate XPD versus rain rate at 11 GHz assuming a Gaussian canting angle distribution with a non-zero mean value, and uncorrelated drop orientations. The results were nearly the same as those assuming a fixed canting angle equal to the mean value.

Distributions of both α and θ can be accounted for by the following transformation (Oguchi-1977).:

$$\begin{bmatrix} a_{\perp} - j\phi_{\perp} \\ a_{\parallel} - j\phi_{\parallel} \end{bmatrix} = \begin{bmatrix} 1 + m_{\theta}m_{\alpha} & 1 - m_{\theta}m_{\alpha} \\ 1 - m_{\theta}m_{\alpha} & 1 + m_{\theta}m_{\alpha} \end{bmatrix} \begin{bmatrix} a_{\perp}' - j\phi_{\perp}' \\ a_{\parallel}' - j\phi_{\parallel}' \end{bmatrix} \quad 4.3-10)$$

where the unprimed a 's and ϕ 's are effective attenuation and phase constants and the primed ones correspond to $\alpha=90^\circ$. The canting angles and incidence angles are assumed to be randomly distributed with means θ and α variances $\delta\theta^2$ and $\delta\alpha^2$. The transformation parameters, assuming Gaussian distributions, are

$$m_{\theta} = \exp(-2\delta\theta^2) \quad (4.3-11)$$

$$m_{\alpha} = \exp(-2\delta\alpha^2)$$

$$m_{\alpha} = \frac{1}{2} [1 + \exp(-2\delta\alpha^2) \sin 2\bar{\alpha}]$$

where σ_θ and σ_α are in radians. The effective canting angle used in the formulas for XPD, etc. is $\bar{\theta}$. Substituting the effective attenuation and phase constants a , ϕ into the formula for XPD (4.3-6), making the small argument approximation

$$\begin{aligned} \gamma &= \exp [-(a_{11}' - a_1')L + j(\phi_{11}' - \phi_1')L] \\ &\approx 1 - (a_{11}' - a_1')L + j(\phi_{11}' - \phi_1')L \end{aligned} \quad (4.3-12)$$

and making further approximations based on the known values of the a 's and ϕ 's, we arrive at

$$\text{XPD} \approx -20 \log \left\{ \frac{1}{2} m_\theta m_\alpha L [(\Delta a')^2 + (\Delta \phi')^2]^{1/2} \sin 2\bar{\theta} \right\} \quad (4.3.13)$$

where'

$$\Delta a' = a_{11}' - a_1'$$

$$\Delta \phi' = \phi_{11}' - \phi_1'$$

This is good approximation for frequencies in the 4-50 GHz range and rain rates less than 150 mm/hr. If, in addition, we neglect the effect of the distribution of a and assume that the drops are oriented horizontally in the plane of incidence, as do Nowland, et.al. (1979), we can write

$$\begin{aligned} \sigma_\alpha^2 &\ll 1 \\ \bar{\alpha} &= 90^\circ - \varepsilon \end{aligned} \quad (4.3-14)$$

where ε is the antenna elevation angle. This implies

$$m_\alpha = \cos^2 \varepsilon \quad (4.3-15)$$

which further simplifies the approximation for XPD. The result is

$$\text{XPD} \approx -20 \log \left[\frac{1}{2} m_{\theta} L |\Delta k'| \cos^2 \epsilon \sin 2\bar{\theta} \right] \quad (4.3-16)$$

with

$$|\Delta k'| = [(\Delta a')^2 + (\Delta \phi')^2]^{1/2}$$

4.3.2 Relationship between Depolarization and Attenuation due to Rain

An empirical relation has been observed between the exceedance statistics for attenuation and those for XPD on the same path. The relation is

$$\text{XPD} \approx \tilde{a} - \tilde{b} \log(\text{CPA}) \quad (4.3-17)$$

where XPD is the value of cross-polarization discrimination not exceeded for a given percentage of the time, and CPA is the copolarized attenuation value in decibels, exceeded for the same percentage of the time. The empirical constant \tilde{a} is typically found to be in the 30-50 dB range and \tilde{b} is usually around 20. We present below the theoretical basis supporting this relation, and examine some of the experimental evidence for it.

Referring back to Section 4.3.1, we can obtain an expression for attenuation of the copolarized wave in a manner similar to finding the XPD. The copolarized attenuation, assuming a LP incident wave oriented in the x-direction, is given by

$$\begin{aligned} \text{CPA} &= -10 \log \frac{|E_{xs}|^2}{|E_{xi}|^2} \text{ with } E_{yi} = 0 \\ &= -10 \log |t_{xx}|^2 \\ &= -20 \log |T_{\perp} \cos^2 \theta + T_{\parallel} \sin^2 \theta| \\ &= -20 \log |T_{\perp} [1 + (e^{-(\Delta a - j\Delta \phi)} - 1) \sin^2 \theta]| \end{aligned} \quad (4.3-18)$$

where Δa and $\Delta \phi$ are defined under equation (4.3-13). Using the small argument approximation (4.3-12) we can obtain

$$\begin{aligned} \text{CPA}_x &\approx -20 \log [\exp(-a_I L \cos^2 \theta - a_{II} L \sin^2 \theta)] \\ &= (A_I \cos^2 \theta + A_{II} \sin^2 \theta) L \end{aligned} \quad (4.3-19)$$

The same expression, with I and II subscripts interchanged, is found for CPA_y . Note that the above expression applies only when all the raindrops have the same orientation. Averaging over distributions of orientation angles α and θ , as was done earlier to find the XPD, we obtain

$$\text{CPA}_x = \frac{1}{2} [(A_I' + A_{II}') + m_\theta m_\alpha (A_I' - A_{II}') \cos 2\bar{\theta}] L \quad (4.3-20)$$

where A_I' and A_{II}' are the attenuation coefficients, in dB/km, for $\alpha = 90^\circ$. Again assuming as before, that the raindrops are not distributed in α , and that $\alpha = 90^\circ - \epsilon$,

$$\text{CPA}_x = \frac{1}{2} [(A_I' + A_{II}') + m_\theta (A_I' - A_{II}') \cos^2 \epsilon \cos 2\bar{\theta}] L \quad (4.3-21)$$

CPA_y is the same except that the sign of the second term is minus.

To relate XPD and CPA, we assume that the CPA, the attenuation coefficients A_I and A_{II} , the magnitude of the differential propagation constant, and the effective path length all bear a power law relation to the effective rain rate, R (Nowland, et al-1977):

$$\text{CPA} = a_0 R^{b_0} L \quad (4.3-22a)$$

$$A_{I'} = a_1 R^{b_1} \quad (4.3-22b)$$

$$A_{II'} = a_2 R^{b_2} \quad (4.3-22c)$$

$$L = u R^v \quad (4.3-22d)$$

$$|\Delta k| = c R^d \quad (4.3-22e)$$

Substituting (4.3-22a-c) into (4.3-21) gives approximate expressions for a_0 and b_0 in terms of a_1 , a_2 , b_1 and b_2 , which can be determined by regression fitting to the calculated propagation constants. The parameters u , v , c and d can also be determined by regression fitting to theoretical or empirical relations.

Substituting (4.3-22d) and (4.3-22e) into the formula for XPD, (4.3-16), gives XPD in terms of R and regression parameters. Likewise, using (4.3-22d) in (4.3-22a) gives CPA in terms of R and regression parameters. Eliminating R then relates XPD and CPA:

$$\text{XPD} \cong \tilde{a} - \tilde{b} \log \text{CPA} \quad (4.3-23)$$

with

$$\tilde{a} = 20 \left(\frac{d+v}{b_0+v} \right) \log(a_0 u) - 20 \log \left(\frac{1}{2} c u m_0 \cos^2 \xi \sin 2\bar{\theta} \right)$$

$$\tilde{b} = 20 \left(\frac{d+v}{b_0+v} \right) \quad (4.3-24)$$

In the 11-14 GHz range, $b_0 = d$, which simplifies the formulas:

$$\tilde{a} \cong -20 \log \left(\frac{1}{2a_0} c m_0 \cos^2 \xi \sin 2\bar{\theta} \right)$$

$$\tilde{b} \cong 20 \quad (4.3-25)$$

Throughout the preceding development, linear polarization in the y -direction was assumed. For LP waves in the y -direction, the l

and 2 subscripts in the formulas for a_0 and b_0 are reversed. For CP waves, θ is set to 45° , which gives the lowest value of XPD.

The CCIR developed a provisional formula based on the above analysis, which provided a simplified form to allow for the prediction of XPD for a given percentage of the time. The CCIR formula was first presented in CCIR Report 564-1, (CCIR-1978), and later updated and modified in Report 564-3, (CCIR-1986). The CCIR formula essentially sets

$$d \cong b_0$$

$$\frac{cm_\theta}{2a_0} \approx [f(\text{GHz})]^{-3/2} \quad (4.3-26)$$

$\theta \approx \tau$ = polarization tilt angle with respect to horizontal

to arrive at the "CCIR Approximation"

$$\begin{aligned} \text{XPD} = & 30 \log[f(\text{GHz})] - 40 \log(\cos \epsilon) - 10 \log[1 - .484(1 + \cos(4\tau))] \\ & - 20 \log(\text{CPA}) + .0052\sigma_\phi^2 \end{aligned} \quad (4.3-27)$$

where σ_ϕ is the effective standard deviation of the raindrop canting angle distribution, expressed in degrees. [The CCIR prediction procedure is described in detail in Chapter VI, Prediction Techniques.]

The "exact" evaluation of the a and b coefficients requires first finding a_1 , b_1 , a_2 , b_2 , c and d by regression fitting to the parameters A_I , A_{II} , and Δk versus rain rate and frequency. These parameters in turn are determined by the propagation constants (a_I , ϕ_I , etc.) corresponding to the raindrop symmetry axes. Nowland, et

al (1977) report the results of regression calculations performed in this manner for oblate spheroidal and Pruppacher-Pitter-form raindrops, for the Laws-and Parsons drop size distribution. More extensive results are included in CCIR Document 5/206 (1977), a Canadian submission to the Study Group 5 Final Meeting. That report also contains the regression coefficients for path length, u and v . These are given as functions of elevation angle for three ranges of rain rate, and were computed based on an empirical formula for path length.

The orientation distribution of the raindrops is the rain characteristic about which we know the least. It enters into the computation in finding a_0 and b_0 from a_1 , a_2 , b_1 and b_2 , and in finding $\bar{\alpha}$. As stated earlier, it is apparently quite safe to ignore the effect of the angular distribution in the plane of incidence (see Figure 4.3-1). This allows us to set $\alpha = 90^\circ - \epsilon$, the complement of the elevation angle of the path. The drop orientation angle θ with respect to the polarization direction, measured in the plane normal to the path, can be expressed as the difference $\theta = \phi - \tau$ where ϕ is the drop canting angle and τ is the polarization direction, both measured with respect to the horizontal. Since τ is known, it is the statistics of ϕ that determines $\bar{\theta}$ and σ_θ (or m_θ), i.e.

$$\bar{\theta} = \bar{\phi} - \tau, \quad \sigma_\theta = \sigma_\phi \quad (4.3-28)$$

It is convenient to describe the distribution of ϕ by an equivalent canting angle ϕ_e , defined by

$$\sin 2|\phi_e - \tau| = m_\phi \sin 2|\phi - \tau| \quad (4.3-29)$$

The equivalent canting angle is the canting angle that identically oriented raindrops would need to have in order to produce the same XPD. Nowland, et al (1977) cite a measured value of 4° for ϕ_e that is consistent with independently-determined values of $\bar{\phi}$ and σ_ϕ , but give other experimental results that show little consistency. More work is clearly needed in characterizing the canting angle.

Chu (1980) employed a "two-tiered" Gaussian model for the canting angle. It assumes first that the instantaneous canting angle has a Gaussian distribution with mean ϕ_m and standard deviation S_ϕ . Second, the mean angle ϕ_m , which varies with time, is itself assumed to be Gaussian. The distribution of ϕ_m has zero mean and standard deviation S_m . The values of these parameters that apparently give the best agreement with experimental data are $S_\phi = 30^\circ$ and $S_m = 3^\circ$.

Based on this two-tiered model, Chu (1982) derived a semi-empirical formula for depolarization versus attenuation that agrees with experimental results over a wide range of frequency, polarization tilt angle and elevation angle. Cross-polarization discrimination for circular polarization XPD_c , in decibels, is given by

$$XPD_c = 11.5 + 20 \log f - 20 \log (CPA) - 40 \log (\cos \epsilon) \quad (4.3-30)$$

where f is frequency in gigahertz, CPA is copolar attenuation in decibels, and ϵ is elevation angle. The formula for cross-polarization discrimination with linear polarization, XPD_L , in decibels, is

$$XPD_L = 11.5 + 20 \log f - 20 \log (CPA) - 40 \log (\cos \epsilon) - 10 \log 1/2 (1 - 0.978 \cos 4\tau) - 0.075 (CPA) \cos^2 \epsilon \cos 2\tau \quad (4.3-31)$$

where τ is the polarization tilt angle measured from the horizontal.

Note that the formulas (4.3-30) and (4.3-31) contain a frequency dependence of $20 \log f$. This disagrees with the provisional formula of the CCIR (Equation 4.3-27), which has a $30 \log f$ frequency dependence. There is little discrepancy between the predictions

given by the two formulas for frequencies in the vicinity of 12 GHz, but the above formulas give better agreement with data at 19 and 28 GHz.

4.3.3 Statistical Characteristics of Rain Depolarization

Two models have been proposed for predicting the statistical characteristics of rain depolarization. Chu (1980) determined functional dependencies of cross polarization on frequency, polarization and elevation angle, and presented techniques for finding depolarization statistics on the basis of rain rate or rain attenuation statistics. Kanellopoulos and Clarke (1981) developed a method of predicting long-term rain depolarization statistics on short terrestrial links. The distribution of cross-polarization isolation, in decibels, turns out to be approximately Gaussian. An assumption of uniform rain rate restricts the model to short paths, but an extension to the more general case of varying rain rate along the path is in progress. The general method should also be applicable to satellite paths.

Experimental depolarization data on satellite paths appears to be approximately normally distributed. Combining this with the observed log-normal distribution of rain attenuation, a probabilistic model of depolarization in combination with attenuation has been proposed (Wallace - 1981). In this model the joint probability density of XPD, in decibels, and the logarithm of rain attenuation, in decibels, is approximated by a bivariate Gaussian density. This description agrees fairly well with experimental results. The proposed model has been used in the analysis of single-site and diversity system availability.

4.3.4 Experimental Depolarization Data

The most extensive experimental investigations of depolarization above 10 GHz to date have been performed at Virginia Polytechnic Institute and State University (VPI & SU) at Blacksburg (Bostian and Dent - 1979) (Stutzman et.al. - 1983), the University of Texas (UT)

at Austin (Vogel - 1978), and the Bell Telephone Laboratories (BTL) in Holmdel, and Crawford Hill, N.J. (Arnold, et al - 1979). The signal sources for depolarization measurements conducted at these facilities have been beacons on the following spacecraft.

ATS-6	20 GHz, 30 GHz, LP
CTS	11.7 GHz, RHCP
COMSTAR	19.04 GHz, Vert. & Horiz. LP
COMSTAR	28.56 GHz, Vert. LP
SIRIO	11.6 GHz, RHCP

Four COMSTAR spacecraft, D-1 through D-4, have been used.

In the experiments, the signal levels in the copolarized and cross polarized channels were measured, either continuously or during periods of rain. The measurement records were typically used to generate XPD and CPA statistics and plots of XPD versus CPA. Some results of these experiments are presented in section 6.7.2.

Both the VPI and SU and the UT data bases have been processed to give XPD vs CPA on an instantaneous basis, and on a statistical basis. In the former case, XPD values that were observed at the same time as the corresponding CPA value are plotted. In the latter case, the XPD value that was not exceeded for a particular percentage of time is plotted against the CPA value that was exceeded for the same time percentage. An instantaneous XPD vs CPA plot was prepared for each month, and a curve of the form $XPD = \tilde{a} - \tilde{b} \log CPA$ was fitted to it. Table 6.7-1 shows the \tilde{a} and \tilde{b} parameters giving the best fit for each monthly plot for the 1978 VPI and SU data. The parameter R, which indicates how well the data fits the analytical curve ($R^2 = 1$ for perfect fit), is given for each case. The best-fit \tilde{a} and \tilde{b} values are quite variable month-to-month, and some months have very low R^2 values. The UT data gave similar results. This indicates that the formula is probably not very reliable for predicting XPD versus CPA on an instantaneous basis. Statistical plots, on the other hand, generally show very

good fit to the formula. The VPI and SU CTS data (11.7 GHz) for the 1978 calendar year yielded $\tilde{a} = 41$ dB and $\tilde{b} = 23.2$ with $R^2 = 0.95$ when all data for CPA < 5dB is ignored. The UT data, covering about 18 months, gave $\tilde{a} = 41$ dB, $\tilde{b} = 20.6$ with $R^2 = 0.99$.

Figure 6.7-3 shows how the experimentally determined values of a and b for various frequencies and polarizations compare with the theoretically determined values from the formulas given previously. The theoretical predictions in general overestimate the depolarizing effects of the rain.

In the BTL experiment, co- and crosspolarized signal phase as well as amplitude was measured. This allowed the investigators to calculate XPD for arbitrary polarization states by vector manipulations. The beacon signal used, from a COMSTAR satellite, was linear polarized and oriented at about 21° from the local horizontal. Through the data conversion process, XPD versus CPA was determined on a statistical basis for linear polarization oriented 0°, 45° and 90° from horizontal, and RHCP. Figure 4.3-5 shows the median 19 GHz curves for the true polarizations (21° from vertical and horizontal) and for vertical, horizontal and 45°. The experiment confirmed the theoretical result that maximum XPD occurs at 45°. Also, the XPD values calculated for RHCP were virtually identical to those at 45°, which is predicted by theory. The figure shows that the 21° curves fall between the 45° and the vertical/horizontal curves, and that XPD for horizontal polarization is greater than for vertical polarization. Both of these results agree with physical reasoning. A general agreement with the $XPD = \tilde{a} - \tilde{b} \log CPA$ relation is evident for the lower three curves, in that they tend to lie near a straight line on the semilogarithmic plot. The CCIR approximation (4.3-27) is shown on the plot for the tilt angles 21° and 45°. In this case, the CCIR approximation appears to underestimate the depolarization.

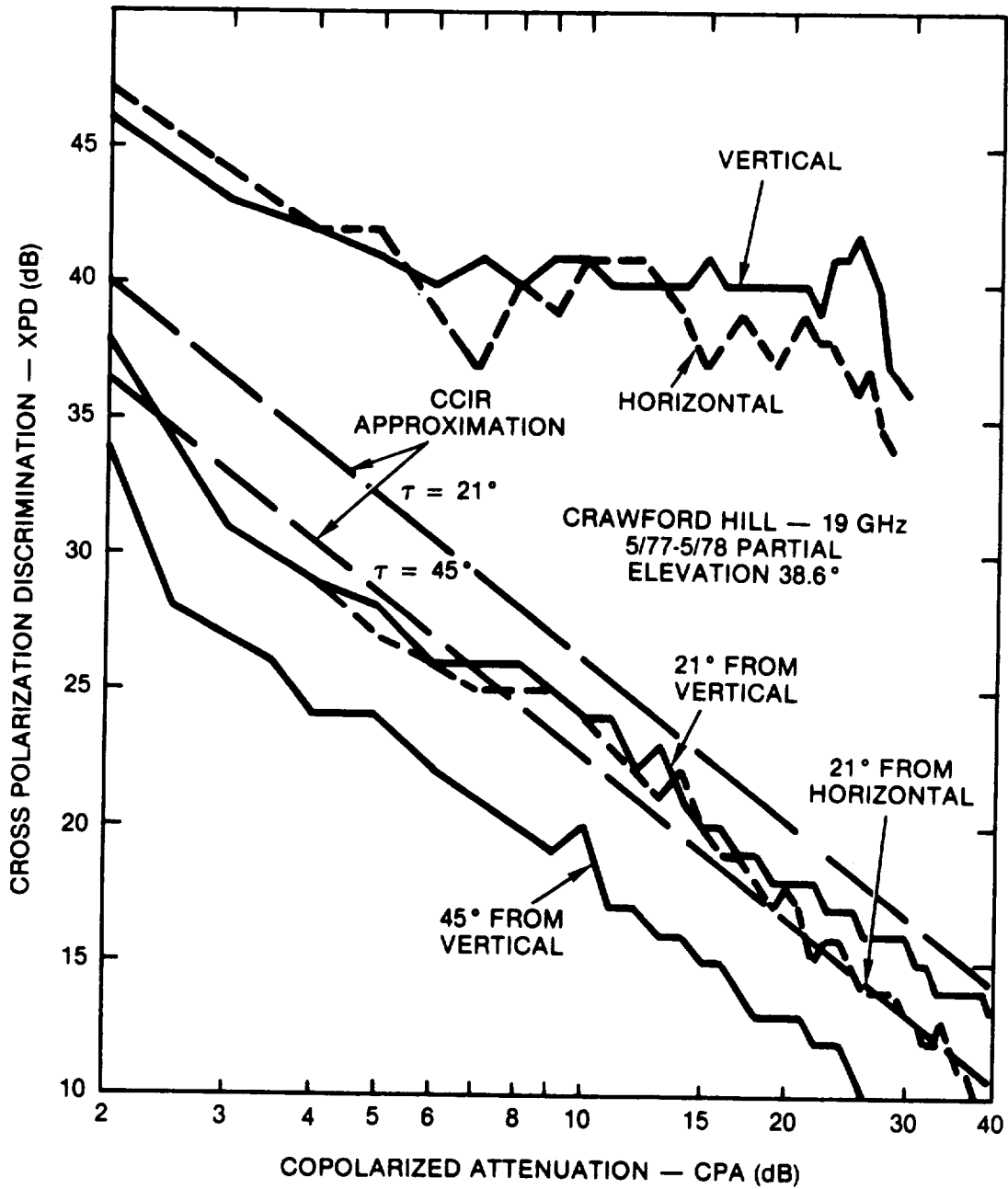


Figure 4.3-5. BTL COMSTAR Depolarization Experiment Results (Arnold, et.al. - 1979)

4.3.5 Phase of Crosspolarized Signal

Techniques have been developed for compensating for depolarization in dual-polarized satellite systems. They involve cancelling the crosstalk in one channel by inserting a properly levelled and phased sample of the opposite channel's signal. The signal sample used for cancelling must be exactly 180° out of phase from the crosspolarized signal for the technique to work. Its effectiveness depends, therefore, on how well the control system can determine and track the phase of the crosspolarized signal. This is a function of variability and rate of change of that phase.

Estimating the performance of crosstalk cancellation systems is one motivation for investigating crosspolarized signal phase. Another reason is that the signal phase is sensitive to certain properties of the rain medium (e.g. canting angle), and its measurement can aid in modelling the propagation properties of rain phenomena.

Overstreet and Bostian (1978) at VPI and SU derived a theoretical description of the phase between the copolarized and crosspolarized signals when rain depolarization is present. They assumed identically oriented raindrops, canted at an angle θ with respect to a copolarized reference direction, having known differential attenuation and phase and a known effective path length. Using Chu's differential attenuation and phase values for the frequencies and elevation angles of the CTS and COMSTAR D-2 beacons, they predicted the phase as a function of θ and rain rate, then found phase versus the XPD value for the same rain rate. The path lengths used were derived from attenuation statistics for those beacons at the VPI and SU station. For linearly polarized signals at 11 and 28 GHz, it was found that the phase was a fairly weak function of XPD and t , typically remaining within a 45° sector for XPD values down to 15 dB over the expected range of θ . For circular polarization, it was found that the phase difference Δ_c is given by

$$\Delta_c = \pm 2\theta + \Delta\ell(\theta = 45^\circ) \quad (4.3-30)$$

where $\Delta\ell$ is the phase difference for LP waves, and the sign of the first term depends on whether RHCP or LHCP is copolarized. The LP phase difference at $\theta = 45^\circ$ is only weakly dependent on XPD so the 2θ term predominates in Δ_c .

Experimental data from the CP CTS beacon at 28.56 GHz generally confirmed the theoretical expectations. The phase difference of the LP signal normally remained in a 20-30° range during a rain depolarization event, whereas the CP signal phase difference varied widely during the course of a rain event. The phase versus XPD changes generally followed a characteristic sequence during convective storms. This indicated the changes in the nature of the depolarizing medium, primarily in predominant canting angle of the raindrops present, through the passage of the storm cell.

The experimental evidence suggests that crosstalk cancellation schemes would be more effective using LP than CP waves. The phase of the crosspolarized signal, which must be estimated by the cancellation system, is much less variable with linear polarization. In fact, setting the phase of the cancellation signal to a constant value would give a degree of effectiveness, while eliminating the need for a complex phase shifter control system.

4.3.6 Rate of Change of Depolarization

To more fully characterize depolarization, some quantitative description of the rate of change of the amplitude and phase of the crosspolarized signal would be desirable. This information would assist us in designing adaptive controls for crosstalk cancellation systems, and may also provide further insight into the nature of the meteorological process responsible for depolarization. However, there has apparently been little research effort expended to this end. Further experimental work, or further analysis of existing data bases, is needed in this area.

4.3.7 Rain Depolarization Dependence on Elevation Angle and Frequency

Knowledge of the dependence of crosspolarization discrimination on elevation angle and frequency is quite valuable because it allows us to extend the usefulness of time-consuming and costly measurements. Unfortunately, the present limited body of experimental evidence does not overwhelmingly support the theoretical scaling relations, so they must be used with caution.

The expression obtained earlier for XPD (eq. 4.3-16),

$$\text{XPD} = -20 \log \left[\frac{1}{2} m_{\theta} L |\Delta k'| \cos^2 \epsilon \sin 2\bar{\theta} \right] \quad (4.3-31)$$

can be rewritten to explicitly show the elevation angle and frequency dependencies. For the CP case, corresponding to the minimum XPD, we have $\bar{\theta} = 45^\circ$ which gives

$$\begin{aligned} \text{XPD} &= -20 \log (L \cos^2 \epsilon) \\ &\quad -20 \log |\Delta k'| \\ &\quad -20 \log (m_{\theta}/2) \end{aligned} \quad (4.3-32)$$

Using the empirical relations (Nowland, et al-1977):

$$\begin{aligned} L &= [7.41 \times 10^{-3} R^{0.766} + (0.232 - 1.8 \times 10^{-4} R) \sin \epsilon]^{-1} \\ |\Delta k'| &\cong c(f) R^{d(f)} \end{aligned} \quad (4.3-33)$$

It is apparent that the first term in the XPD expression is a function of rain rate and elevation angle only, and the second term is a function of rain rate and frequency only. These terms are plotted in Figure 4.3-6. The last term can be considered constant, though it may also be a function of rain rate. For $m_{\theta} = 0.8$, the last term is 8 dB.

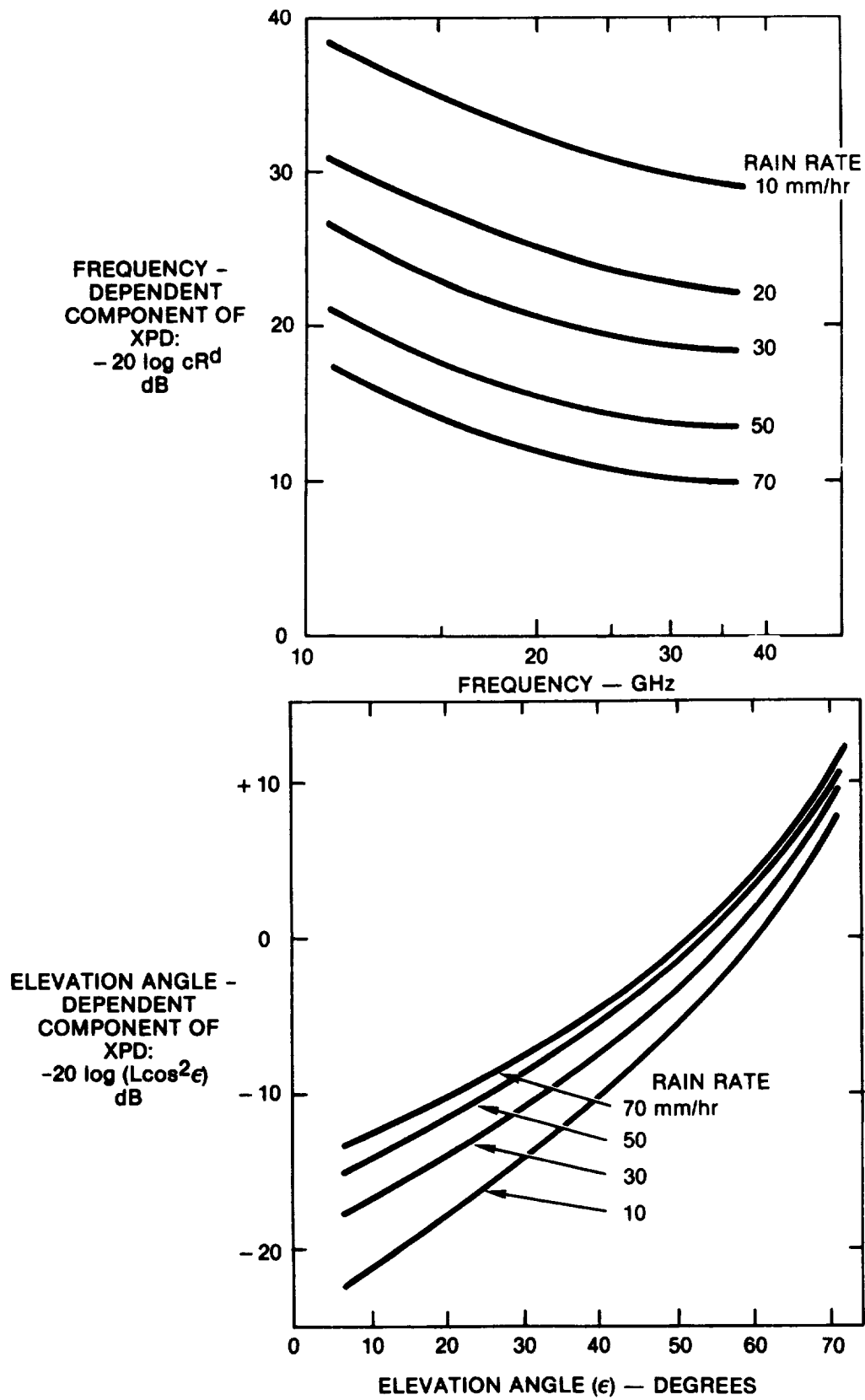


Figure 4.3-6. Frequency and Elevation Angle Dependence of XPD for CP

Another depiction of the frequency dependence of XPD is shown in Figure 4.3-7. It shows the predicted XPD vs CPA relations for fixed frequencies and elevation angle. It is clear that, for any given rain rate, both CPA and XPD get worse as frequency increases. However, for a given value of CPA, XPD improves with frequency.

4.4 ICE DEPOLARIZATION

The second major cause of depolarization on Earth-space paths, besides rain, is the presence of ice crystals in clouds at high altitudes. Ice crystal depolarization is different from rain depolarization in that it is not accompanied by appreciable copolarized attenuation. This is because the depolarization is caused primarily by differential phase shifts, rather than differential attenuation, which is responsible for rain depolarization. Another distinguishing characteristic is that the amplitude and phase of the crosspolarized signal often undergo abrupt, coincident changes with large excursions.

4.4.1 Meteorological Presence of Ice

Clouds present above the freezing level consist, completely or in part, of ice crystals. Cirrus clouds, and the "anvil" that forms at the top of mature thunderstorms are all ice, and the upper parts of cumulonimbus clouds are predominately ice. The crystals that are present have one of two shapes determined by the temperature at the time of formation. Very cold temperatures, below about -25°C , favor the formation of needle-shaped crystals. Flat, plate-like crystals form in a moderately cold environment (-9° to -25°C). The dimensions of the crystals vary between about 0.1 and 1 mm.

Ice crystals form on dust particle nuclei in the atmosphere. The relative abundance of dust particles has been hypothesized as the reason for differences observed in ice depolarization at different locations. In maritime regions, the air contains relatively few dust particles compared with continental areas. As a result of this, maritime air tends to have fewer, but larger ice

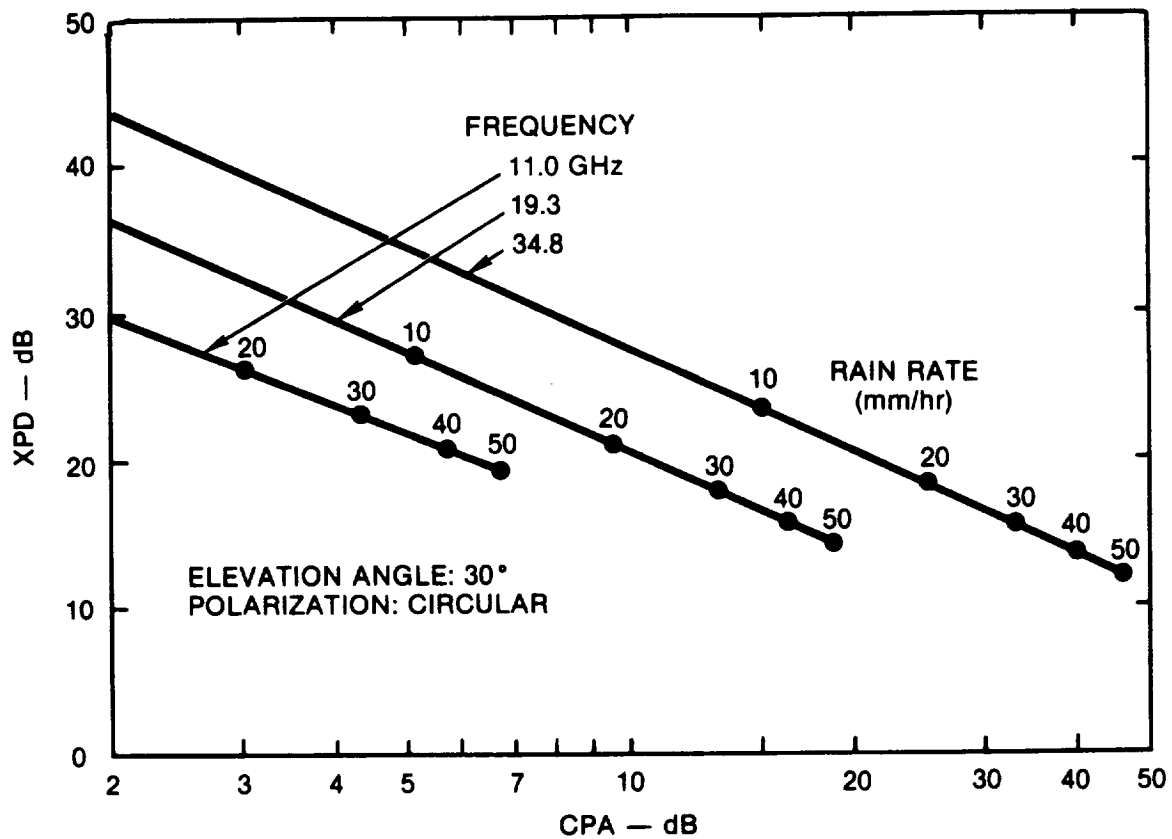


Figure 4.3-7. Frequency and Rain Rate Dependence of XPD and CPA

particles than continental air under similar conditions. It is believed that the presence of larger crystals accounts for the generally higher values of XPD observed in maritime versus inland locations (i.e., BTL versus VPI & SU).

Like raindrops, ice crystals are non-symmetrical and they have a dielectric constant much different from air. These are two of the necessary conditions for depolarization. A third condition, a preferred particle alignment, is also required. Oblate raindrops are aligned by aerodynamic forces, and their preferred alignment direction is affected by the prevailing winds. Aerodynamics also plays a role in aligning ice particles, but it is believed electrostatic forces also play a large part. This belief is supported by many observations during thunderstorms of rapid XPD changes coinciding with lightning flashes. This coincidence may be explained by the following: Electric fields present in regions between oppositely-charged clouds exert torques on the highly non-symmetrical ice crystals. When the field is sufficiently strong, these torques become significant in comparison with the turbulent aerodynamic forces, resulting in an average alignment of the "needle" crystal axes and the "plate" crystal planes along the direction of the field lines. When a lightning discharge takes place between the clouds, charges are equalized and the electric field intensity drops. Aerodynamic forces then predominate, and the crystals quickly lose their preference for a particular direction of orientation (Bostian and Allnut - 1979).

4.4.2 Model for Ice Depolarization

Propagation through a region containing ice crystals can be analyzed in a manner analogous to that applied to rain. In the case of ice, the crystals are modelled as highly eccentric prolate spheroids ("needle" crystals) or oblate spheroids ("plate" crystals). Haworth, Watson and McEwan (1977) have performed this analysis. They assumed that due to aerodynamic forces, the "plate" crystals were oriented horizontally and the axes of the "needle" crystals stayed in the horizontal plane. Under this assumption, an

electrostatic field has no effect on "plates", and aligns the "needles" along the horizontal component of the field. Figure 4.4-1 shows the magnitude of the predicted ice XPD. The "needle"-produced XPD varies with ϕ , the average orientation angle of the crystal axes measured in the horizontal plane. The parameter α is a measure of the degree of alignment of the crystal axes. When the axes are uniformly distributed in all directions, $\alpha = 0$, and when all crystals are oriented in the same direction, $\alpha = 1$.

The phase of the crosspolarized signal, as predicted by the model, undergoes an abrupt change of 180° as ϕ passes through the values corresponding to the XPD peaks, (crosspolarized signal nulls). These are at 80° and 130° in the figure. When α is below some critical value, however, (falling between 0.5 and 1.0 for the example shown) the double null and accompanying phase jump don't occur. This phase reversal phenomenon has been observed at the time of lightning flashes in thunderstorms (see Figure 6.7-8) and is accompanied by a jump in XPD amplitude. Bearing the earlier discussion in mind, we would expect changes in α and ϕ to accompany lightning discharges. The same behavior has also been detected during the passage of non-electrically-active clouds (Shutie, et al-1978). This implies that a particular mechanism, probably wind shear, is responsible for crystal alignment, besides electrostatic fields.

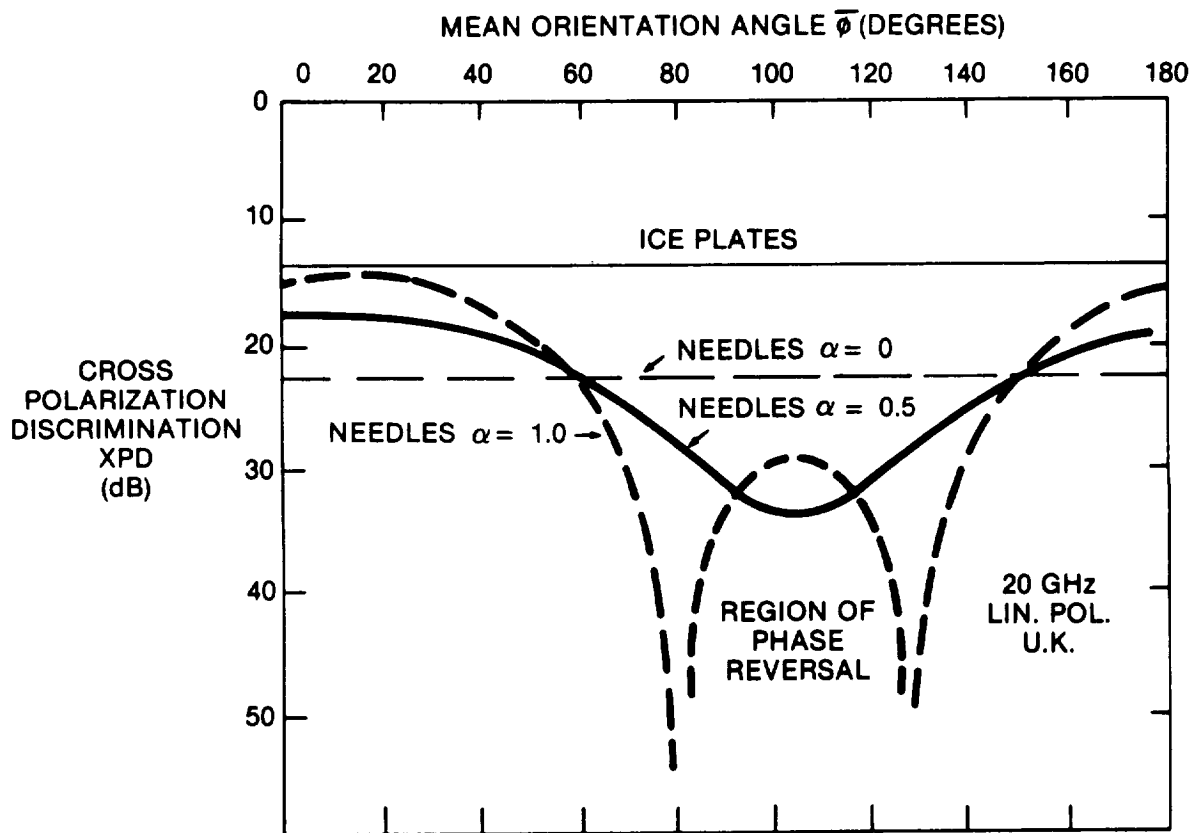
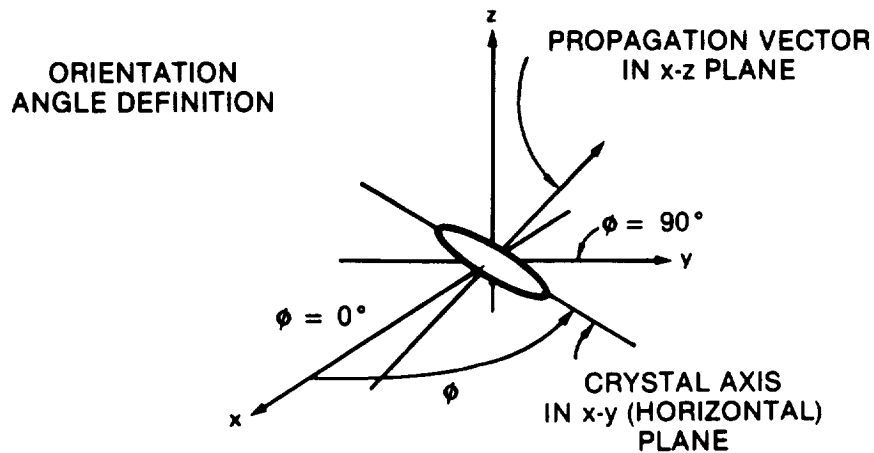


Figure 4.4-1. Definition of Orientation Angle ϕ and Predicted XPD (From Bostian and Allnut, 1979)

4.5 REFERENCES

- Arnold, H.W. et al (1979), "Characteristics of Rain and Ice Depolarization for a 19 and 28 GHz Propagation Path from a Comstar Statellite," Record, Int'l Conf. on Communications.
- Bostian, C.W. and J.E. Allnut (1979), "Ice-Crystal Depolarization on Satellite-Earth Microwave Radio Paths," Proc. IEE, Vol. 126, p. 951.
- Bostian, C.W. and J.R. Dent (1979), "CTS 11.7 GHz Isolation Data for the Calendar Year 1978," VPI & SU Report, prepared for NASA under Contract No. NAS5-22577.
- CCIR (1977), Document 5/206 (Canada), "Techniques for the Prediction of Rain Depolarization Statistics at Microwave and Millimeter Wavelengths."
- CCIR (1978), "Propagation Data Required for Space Telecommunications Systems," Report 564-1, in Volume V, Recommendations and Reports of the CCIR - 1978, International Telecommunications Union, Geneva.
- CCIR (1986), "Propagation Data and Prediction Methods Required for Space Telecommunications Systems," Report 564-3, in Volume V, Recommendations and Reports of the CCIR - 1986, International Telecommunications Union, Geneva.
- Chu, T.S. (1974), "Rain-Induced Cross-Polarization at Centimeter and Millimeter Wavelengths," Bell Syst. Tech. Jrnl, Vol. 58, No. 8, pp. 1557-1579.
- Chu, T.S. (1980), "Microwave Depolarization of an Earth-Space Path," BSTJ, Vol. 59, No. 6 (July-Aug) pp. 987-1107.
- Chu, T.S. (1982), "A Semi-Empirical Formula for Microwave Depolarization Versus Rain Attenuation on Earth-Space Paths," IEEE Trans. on Communications, Vol. COM-30, No. 12, (Dec) pp 2550-2554.
- Haworth, D.P., P.A. Watson, and N.J. McEwan (1977), "Model for the Effects of Electric Fields on Satellite-Earth Microwave Radio Propagation," Elect. Letters, Vol. 13, p. 562.
- Hendry, A., G.C. McCormick and B.L. Barge (1976), "Ku-Band and S-Band Observations of the Differential Propagation Constant in Snow," IEEE Trans. Ant. Prop., Vol. AP-24, No. 4, pp. 521-525.
- Kanellopoulos, J.D. and R.H. Clarke (1981), "A Method of Calculating Rain Depolarization Distributions on Microwave Path," Radio Science, Vol. 16, No. 1 (Jan-Feb), pp. 55-65.

- McCormick, G.C. and A. Hendry (1977), "Depolarization by Solid Hydrometeors," Electronics Letters, Vol. 13, No. 3.
- Morrison, J.A., M.J. Cross, and T.S. Chu (1973), "Rain-Induced Differential Attenuation and Differential Phase Shift at Microwave Frequencies," BSTJ, Vol. 52, No. 4, pp. 599-604.
- Nowland, W.L., R.L. Olsen, and I.P. Shkarofsky (1977), "Theoretical Relationship Between Rain Depolarization and Attenuation," Electronics Letters, Vol. 13, No. 22, pp. 676-677.
- Oguchi, T. (1977), "Scattering Properties of Pruppacher-and-Pitter Form Raindrops and Cross Polarization Due to Rain: Calculations at 11, 13, 19.3 and 34.8 GHz," Radio Science, Vol. 12, pp. 41-51.
- Pruppacher, H.R. and R.L. Pitter (1971), "A Semi-empirical Determination of the Shape of Cloud and Rain Drops," J. Atmos. Science, Vol. 28, pp. 86-94.
- Shutie, P.F., E.C. MacKenzie and J.E. Allnut (1978), "Relative Phase Measurements at 30 GHz Between Copolar and Induced Crosspolar Signals Produced by Ice Particles on a Satellite-to-Ground Link," Elect. Letters, Vol. 14, No. 4, p. 105.
- Stutzman, W.L. (1977), "Mathematical Formulations and Definitions for Dual Polarized Reception of a Wave Passing Through a Depolarizing Medium (A Polarization Primer)," Virginia Polytechnic Institute & State Univ. Report, prepared under NASA Contract NAS5-22577.
- Stutzman, W.L., C.W. Bostian, A. Tsolakis, and T. Pratt, (1983), "The Impact of Ice Along Satellite-to-Earth Paths on 11 GHz Depolarization Statistics," Radio Science, Vol. 18, No. 5, pp. 720-724.
- Thomas, D.T. (1971), "Cross-Polarization Distortion in Microwave Radio Transmission Due to Rain," Radio Science, Vol. 6, No. 10, pp. 833-839.
- Vogel, W.J. (1978), "CTS Attenuation and Cross-Polarization Measurements at 11.7 GHz," Final Report, Elect. Eng. Res. Lab., Univ. Texas at Austin, prepared under NASA Contract NAS5-22576.
- Wallace, R.G. (1981), "Site Diversity Effects on Communication Satellite System Availability," ORI Technical Report 1891, prepared for NASA Headquarters under Contract NASW-3436.

- Watson, P.A., and M. Arbabi (1973a), "Rainfall Crosspolarization at Microwave Frequencies," Proc. IEE, Vol. 120, No. 4, pp. 413-418.
- Watson, P.A., and M. Arbabi (1973b), "Cross-Polarization Isolation and Discrimination," Electronics Letters, Vol. 9, N. 22, pp. 516-519.

CHAPTER V

PROPAGATION DATA BASES

Researchers have been performing experiments to gather propagation data on millimeter-wave Earth-space links since the late 1960's, and in the process, have accumulated sizable data bases. In this chapter, we describe the various satellites used in this work, and present summary results of the significant experiments conducted in the United States. The results presented are primarily cumulative attenuation statistics, though some depolarization measurements are included as well. This is, by necessity, a limited sampling of the existing data bases. We therefore preface the data by citing additional summaries of propagation data for the interested reader.

5.1 SUMMARIES OF EXPERIMENTAL DATA

The International Radio Consultative Committee (CCIR) publishes a summary of worldwide experimental data in the Recommendations and Reports issuing from its periodic plenary assemblies. Volume V of this publication, "Propagation in Non-Ionized Media," deals with all aspects of microwave propagation--both terrestrial and earth-to-space. Within Volume V, the data is presented as a series of reports and recommendations submitted to and adopted by the CCIR. Because of this presentation format, data of interest to designers may be found in several places.

The most complete collection of measured propagation data is found in the two CCIR documents;

1. Report 564-3, "Propagation Data and Prediction Methods Required for Earth-Space Telecommunications Systems," (CCIR-1986a), and
2. Document 5/378, "Data Banks Used for Testing Prediction Methods in Sections E, F and G of Volume V," (CCIR-1986b).

The CCIR separates the data between the two reports based on the availability of an acceptable prediction method for that type of measurement. Data for which an accepted method does not exist is presented in the first document (Report 564-3), while data for which an accepted method does exist is presented in the second document.

The data summaries in Report 564-3 are presented in Annex I, and include sections on the following subjects:

- Seasonal variations - worst month
- Duration of individual fades
- Rates of change of attenuation
- Scintillation and multipath effects
- Noise temperature
- Cross-polarization due to hydrometeors
- Angle-of-arrival

Document 5/378 presents detailed tabulations of earth-space path data for:

- Annual slant-path rain attenuation statistics (Table II-1),
- Worst month slant-path attenuation statistics (Table II-2),

- Fade duration statistics (Table II-3), and
- Annual XPD statistics based on satellite measurements (Table II-4).

The results of extensive NASA sponsored measurements conducted in the 1970's is documented in a report entitled "A Compendium of Millimeter Wave Propagation Studies Performed by NASA," (Kaul, et al - 1977). The report contains a reasonably complete summary and references to the 15.3 and 31.65 GHz measurements with ATS-5, and the 13.2, 17.8, 20 and 30 GHz measurements with ATS-6.

5.2 SATELLITES USED FOR PROPAGATION RESEARCH

Within the United States and Canada, four satellite systems (seven satellites) have been utilized to obtain the bulk of the earth-space propagation data. A brief summary of the satellite characteristics that relate to propagation studies is given in Table 5.2-1.

European researchers used 20 and 30 GHz transmissions from the ATS-6 during the 1975/76 period when the satellite was stationed over Europe. The Italian satellite SIRIO, carrying a circularly polarized three-carrier beacon at 11.331, 11.597 and 11.836 GHz, began operation in October 1977. Finally, the Orbiting Test Satellite (OTS), launched by the European Space Agency, provided beacon transmissions at 11.575 and 11.786 GHz starting in May 1978. The Japanese have launched four satellites supporting propagation research. These are designated ETS-II, CS, BS and ECS, and carry beacons at various frequencies near 12, 20 and 34 GHz (Hayashi, et al-1979).

Satellite propagation beacons are not the only means for collecting experimental data. Radars, radiometers (fixed and sun synchronous) and low-orbiting satellites can also provide valuable data, but usually with some deficiency. A general deficiency is the lack of polarization data available from these measurement

Table 5.2-1. Satellite Parameters Related to Propagation Studies

Satellite	Launch Date	Satellite Position	Uplink Frequencies	Downlink Frequencies	Antenna
ATS-5	8/12/69	Initially over Indian Ocean, drifted to 108° W. longitude; remained spinning at 76 rpm	31.65 GHz with sidebands at ± 1 , ± 10 , and ± 50 MHz from carrier	15.3 GHz with sidebands at ± 0.1 , ± 1 , ± 50 MHz from carrier	Linearly polarized conical horns with 20° coverage and 19.1 dB boresight gain
ATS-6	5/30/74	94° W. longitude for first year then move to 35° E. long. and returned to 140° W.	COMSAT Exp.: 13.19 - 13.2 GHz 17.74 - 17.8 GHz	COMSAT Exp.: 4.14 - 4.15 GHz 4.16 - 4.17 GHz NASA/GSFC Exp.: 20 and 30 GHz 8 sidetones Spaced ± 180 MHz	COMSAT Exp.: Dual-frequency linearly polarized dish NASA/GSFC Exp.: 20 GHz: 6° x 9° horn 2° dish 30 GHz: similar to above
CTS	1/17/76	116° W.	14.0 - 14.5 GHz	11.7 GHz beacon 11.7 - 12.2 GHz	16° horn, RHCP for beacon
COMSTAR (satellites D1, D2, D3 and D4)	D1: 5/13/76 D2: 7/22/76 D3: 6/29/78 D4: 2/21/81	D1: 95° W. long. D2: 95° W. long. D3: 87° W. long. D4: 127° W. long.	5.9 - 6.4 GHz	19.04 and 28.56 GHz beacons 3.9 - 4.2 GHz	Linearly polarized offset parabolic dishes. 19.04 GHz switched between vertical and horizontal polarization. 28.56 GHz vertically polarized. Sidebands of 28.56 GHz ± 528.9 MHz (D3) ± 264.4 MHz (D1 and D2)
ETS-11	2/77	130° E. long.		1.7, 11.5, 34.5 GHz beacons	
SIRIO	8/77	15° W. long.	17.4 GHz	11.3, 11.6, 11.9 GHz beacons	
CS	12/77	135° E. long.	27.6 - 6.3 GHz 6.0 - 6.3 GHz	3.95, 19.45 GHz beacons 17.9 - 20.2 GHz 3.8 - 4.1 GHz	
BS	4/78	110° E. long.	14.0 - 14.4 GHz	11.7 GHz beacon 12.0 - 12.1 GHz	
OTS	5/78	10° E. long.	14.2 - 14.5 GHz	11.6 - 11.8 GHz beacons 11.5 - 11.8 GHz	

techniques. Specifically, the expense of calibrating and operating radar systems and the attenuation saturation effect in radiometer systems limit their use.

5.3 FORMAT OF DATA PRESENTED

Because of the volume and variety of data being presented by experimenters throughout the United States and Canada, it is impossible to claim that the following data is complete. However it is certainly representative of the tropospheric effects on earth-space paths for the location indicated.

To limit the volume of data presented, the cumulative attenuation statistics will be emphasized, since this is the most complete data base available and, from this, the rain rate and depolarization may be inferred (as described in Chapters 3 and 4). The results will be presented by frequency range or satellite beacon frequency, as appropriate.

To assist with the comparison of data from various experimenters, NASA has encouraged the use of standardized cumulative statistics plot formats. The use of these formats, given in Figures 5.3-1 and 5.3-2, will permit experimental results from different sources to be overlaid for direct comparison. The forms cover from 0.0001 to 10 percent of the total period, which should be a sufficiently large range for most applications. The attenuation scales cover from 0-35 and 0-45 dB, which should be sufficient to cover the link margin range of most systems. The 45 dB graph is recommended for use above 15 GHz. These same forms may be utilized for depolarization statistics if the attenuation labels are changed to cross-polarization discrimination. Each chart should be labeled with the period of the measurement, frequency, location and elevation angle. This provides, on the figure, all the information needed for comparison of data.

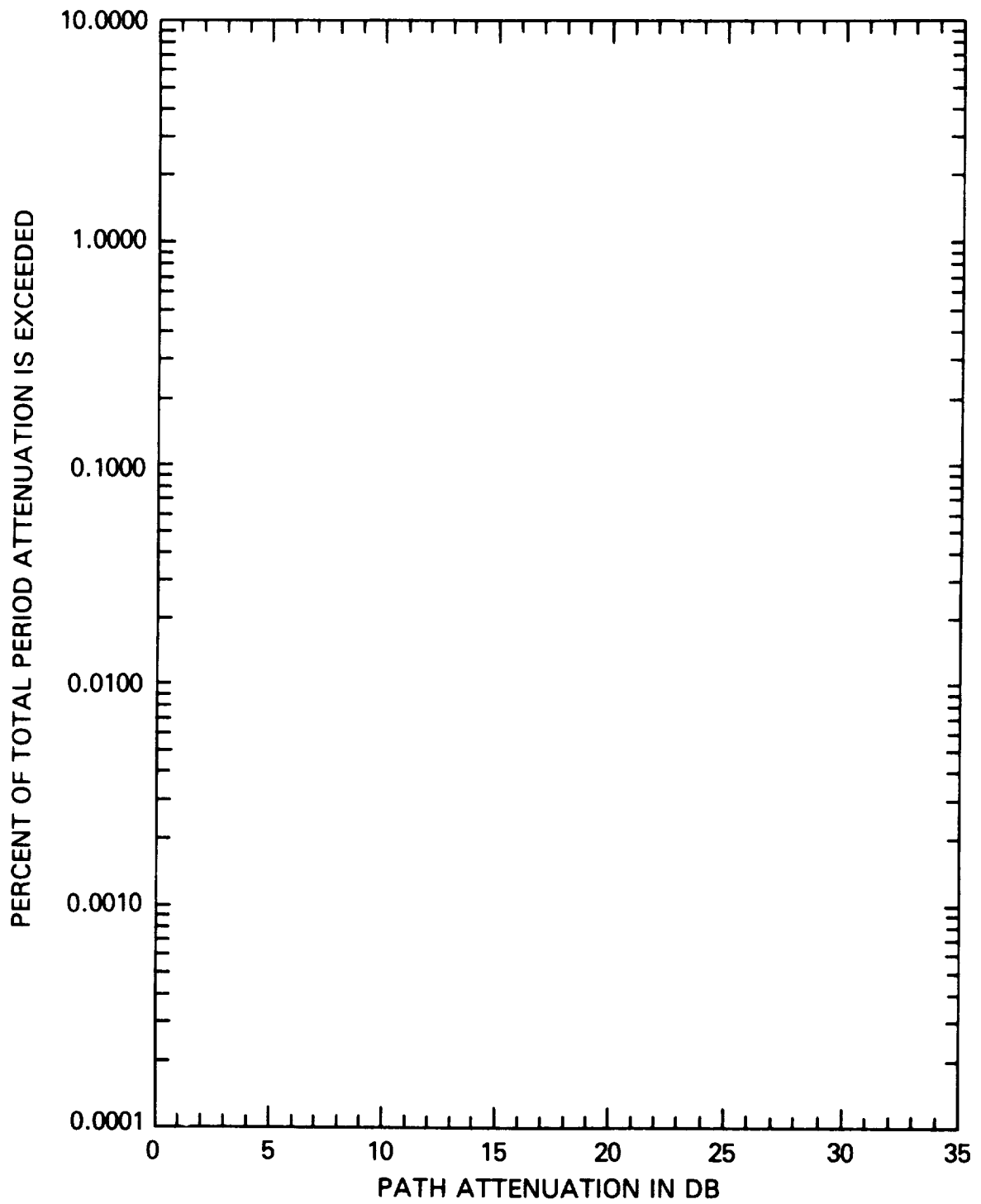


Figure 5.3-1. Cumulative Attenuation Graph for Use in the 11/14 GHz Bands

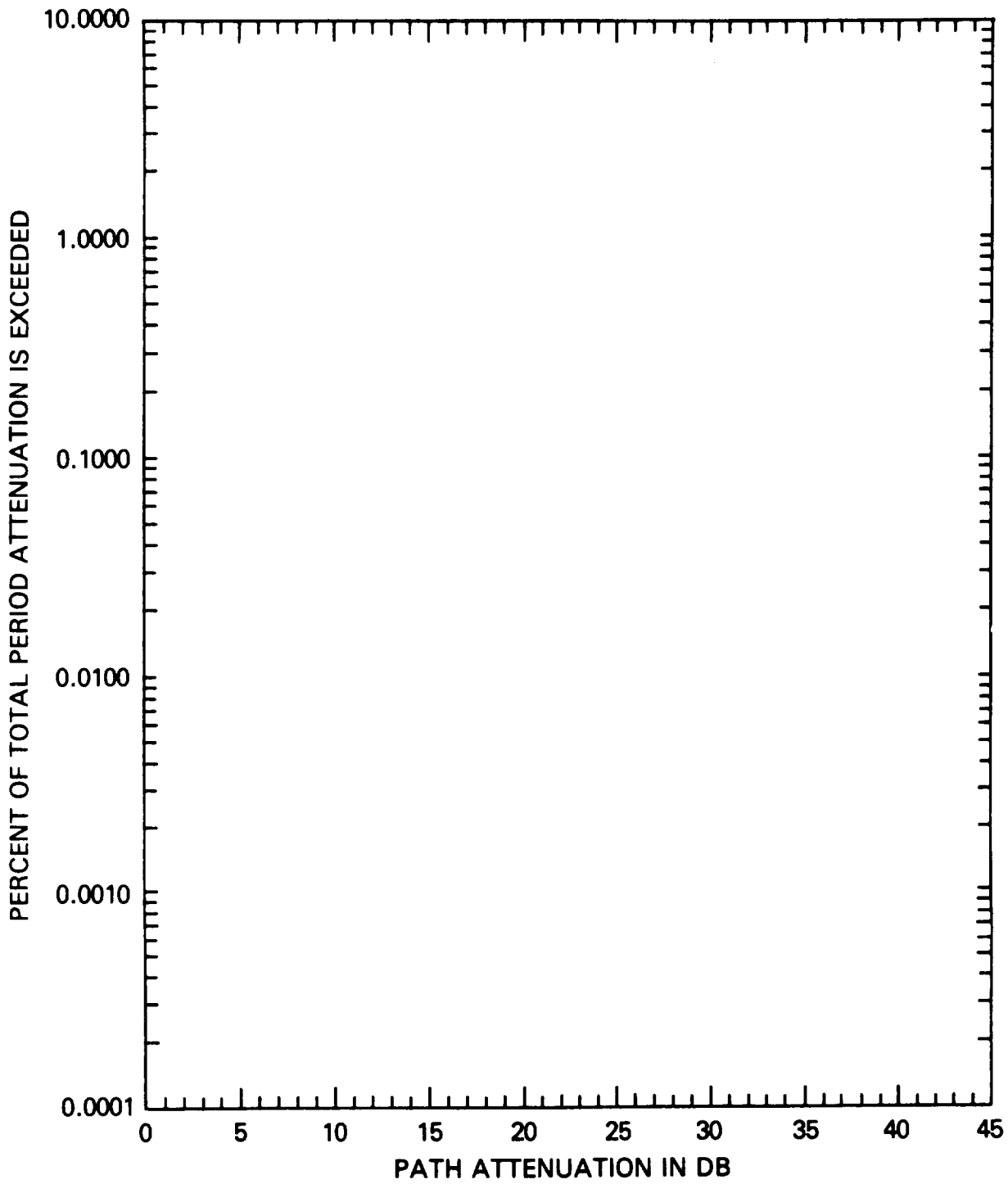


Figure 5.3-2. Cumulative Attenuation Graph for Use above 15 GHz

5.4 EXPERIMENTAL CUMULATIVE ATTENUATION STATISTICS

5.4.1 11.5-11.7 GHz Data

The Communications Technology Satellite (CTS) has provided the opportunity for extensive long-term measurements of rainfall attenuation and other propagation effects in the 11.7 to 12.2 GHz band. A continuous 11.7 GHz circularly polarized beacon operated from launch through late 1979, except for two periods during solar eclipse (March 4 through April 16, 1976 and August 31 through October 17, 1976).

Figures 5.4-1 through 5.4-5 show the cumulative statistics for the five United States locations of (listing in order of ascending elevation angle):

Waltham, MA (GTE Laboratories, Inc.)

Holmdel, NJ (Bell Telephone Labs.)

Greenbelt, MD (NASA Goddard Space Flight Center)

Blacksburg, VA (Virginia Polytechnic Institute and State University)

Austin, TX (University of Texas at Austin)

All of the distributions are based on 12 calendar months of continuous data. Details of the recording methods and processing techniques are given in the references in each figure. Table 5.4-1 summarizes the attenuation statistics at each of the locations for 0.001, 0.005, 0.01, 0.05, 0.1, 0.5 and 1% of the observation period. Note that the data shows a wide range of variations, even for consecutive years at one location.

Elevation angle differences between the five locations prevents a direct comparison of the measured distributions. The distributions can be converted to a common elevation angle by assuming the precipitation to be horizontally stratified in the

Table 5.4-1. Annual 11.7 GHz Attenuation Statistics Summary

LOCATION	ELEVATION ANGLE	TIME PERIOD	ATTENUATION (dB) FOR GIVEN PERCENT OUTAGE							
			1%	0.5%	0.1%	0.05%	0.01%	0.005%	0.001%	
Waltham, MA	24°	Feb '77 - Jan '78	<1	<1	2.5	4	10.5	14.5	(23)	
		Feb '78 - Jan '79	<1	<1	1.5	2.8	8.5	11	15.3	
Holmdel, N.J.	27°	Jun '76 - Jun '77	<1	<1	3	5	13.5	-	-	
		Jun '77 - Jun '78	<1	<1	3	5	13.5	19.5	-	
		Jun '78 - Jun '79	<1	<1	2.5	3.8	9.2	12.2	29	
Greenbelt, MD	29°	Jul '76 - Jun '77	<1	<1	1.8	3.2	8.8	14.5	>30	
		Jul '77 - Jun '78	<1	1	2.1	3.8	12	18	26.4	
		Jul '78 - Jun '79	<1	<1	1.8	3.2	14	21	29.2	
Blacksburg, VA	33°	Jan '77 - Dec '77	2	2.5	4	5	13	16.5	24	
		Jan '78 - Dec '78	2	2.7	3.7	4.3	6.8	8.6	13	
Austin, TX	49°	Feb '78 - Jan '79	<1	1	3	5.5	13	18	23	

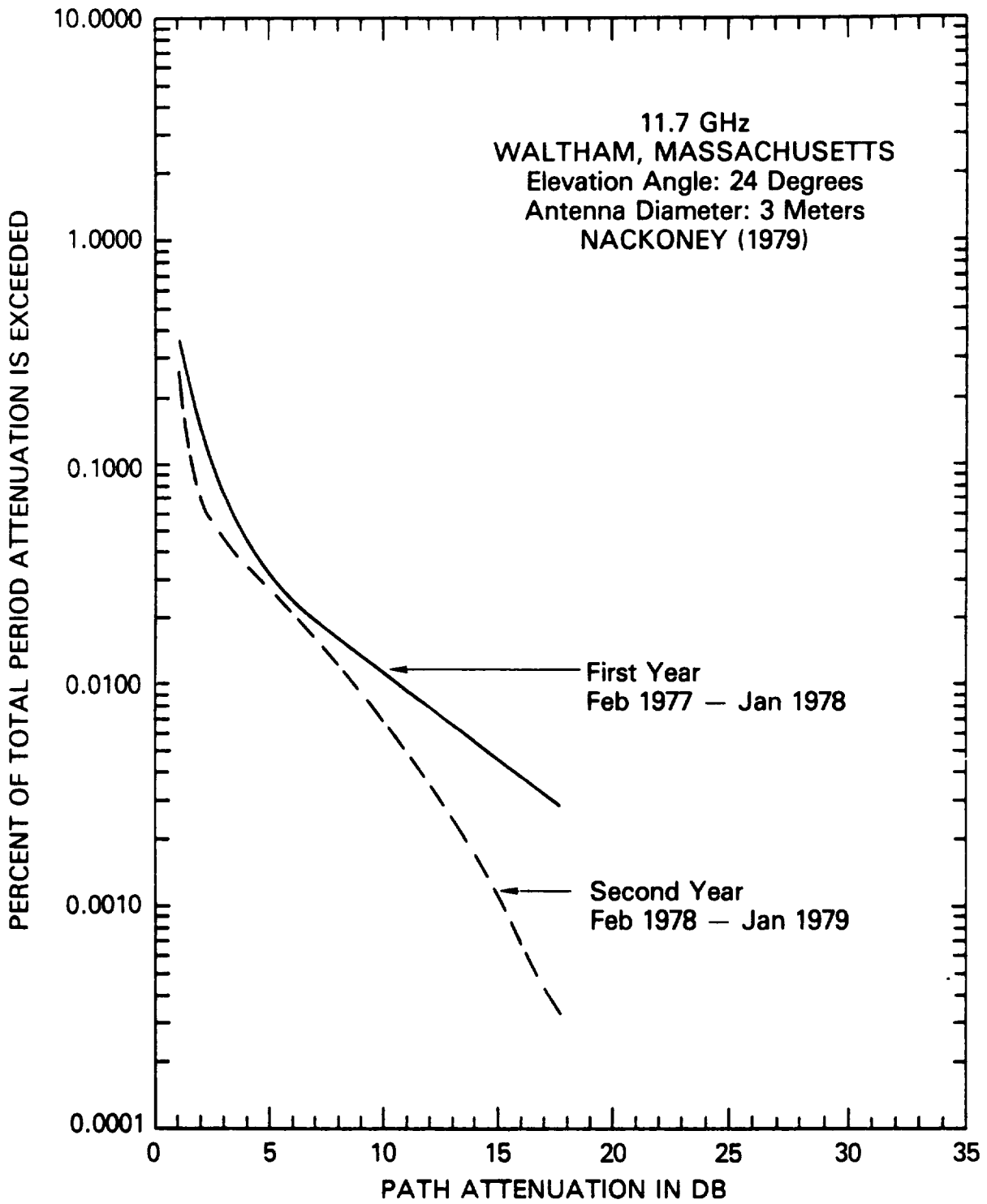


Figure 5.4-1. Annual 11.7 GHz Attenuation Distributions for Waltham, MA

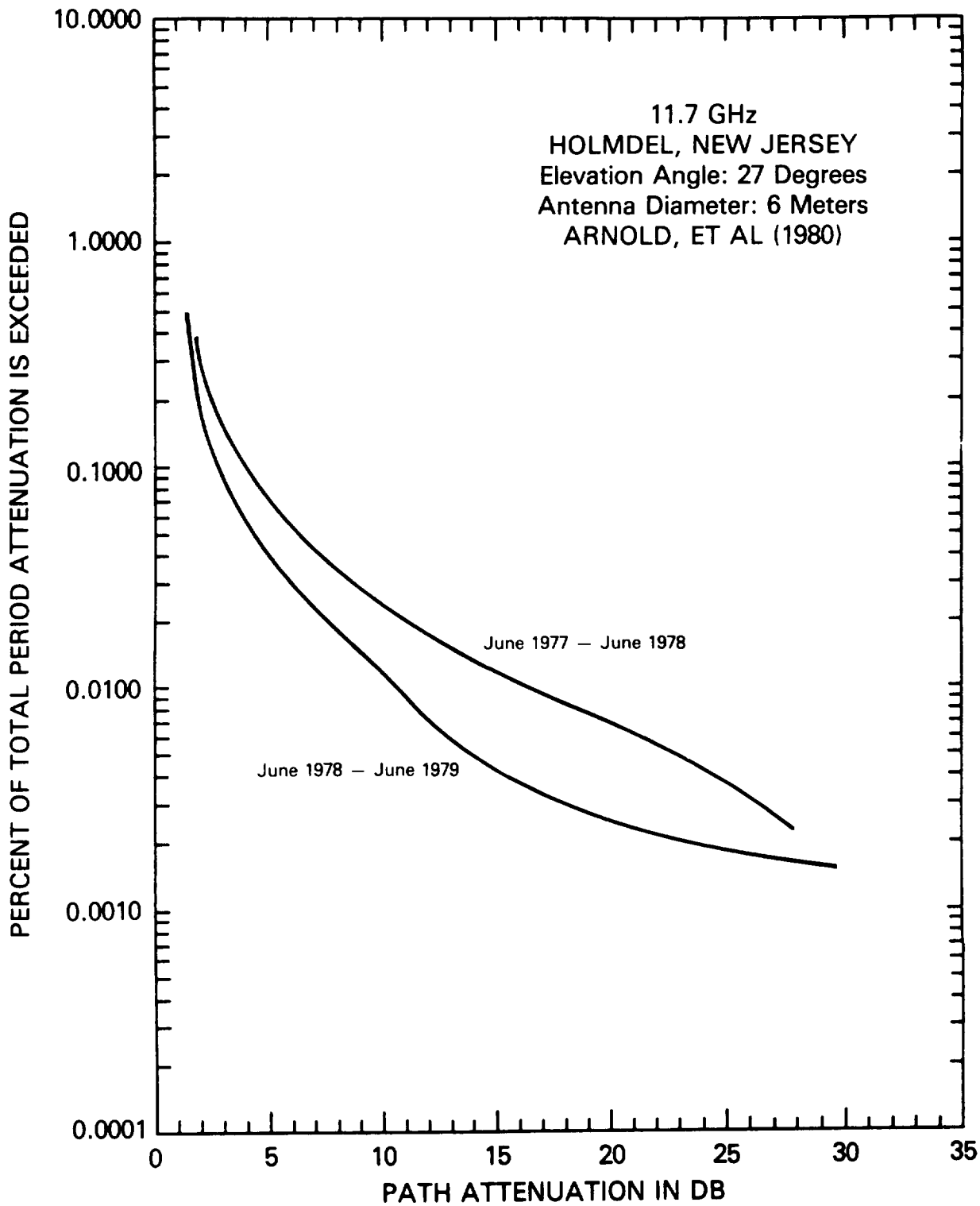


Figure 5.4-2. Annual 11.7 GHz Attenuation Distribution for Holmdel, NJ

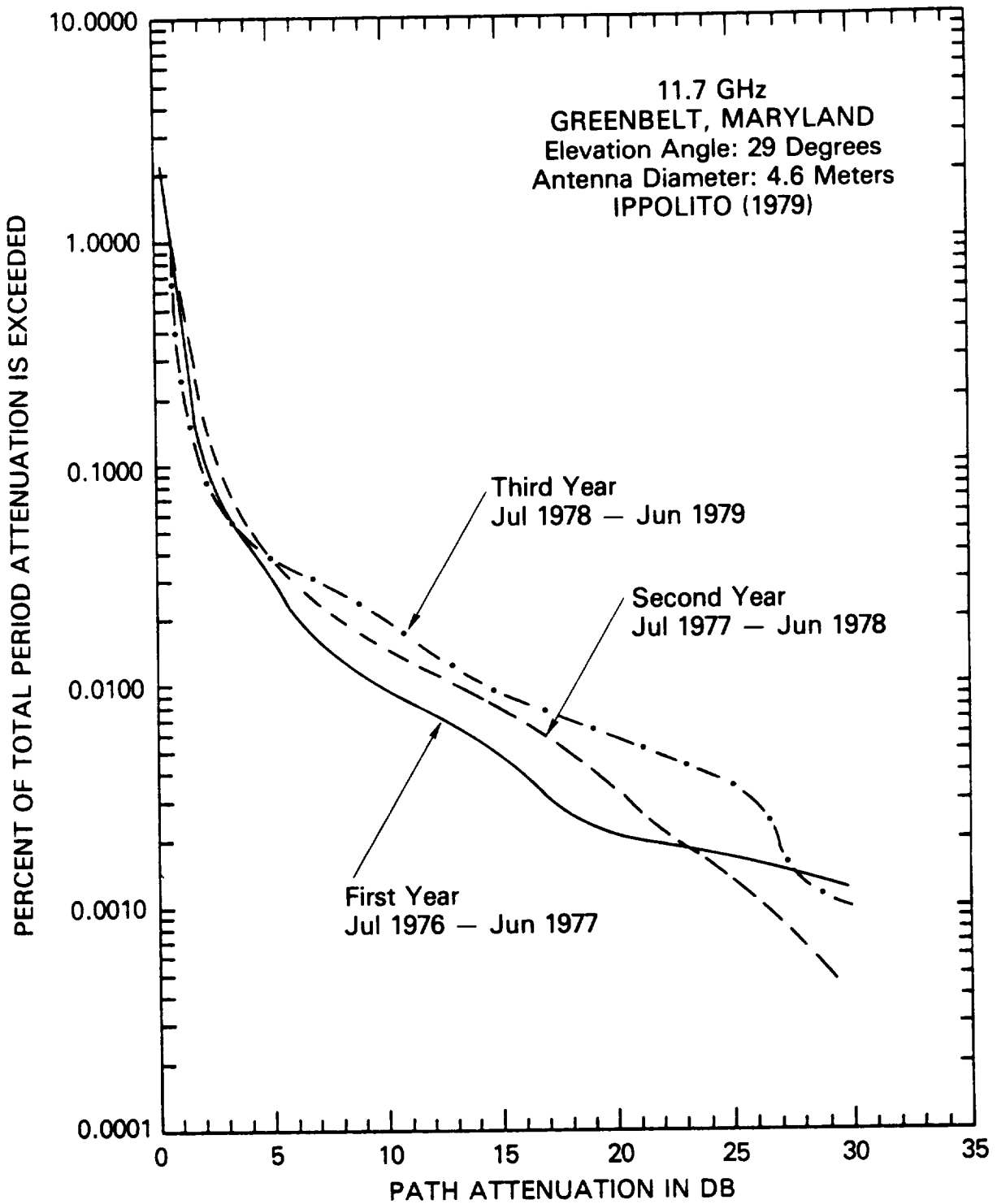


Figure 5.4-3. Annual 11.7 GHz Attenuation Distributions for Greenbelt, MD

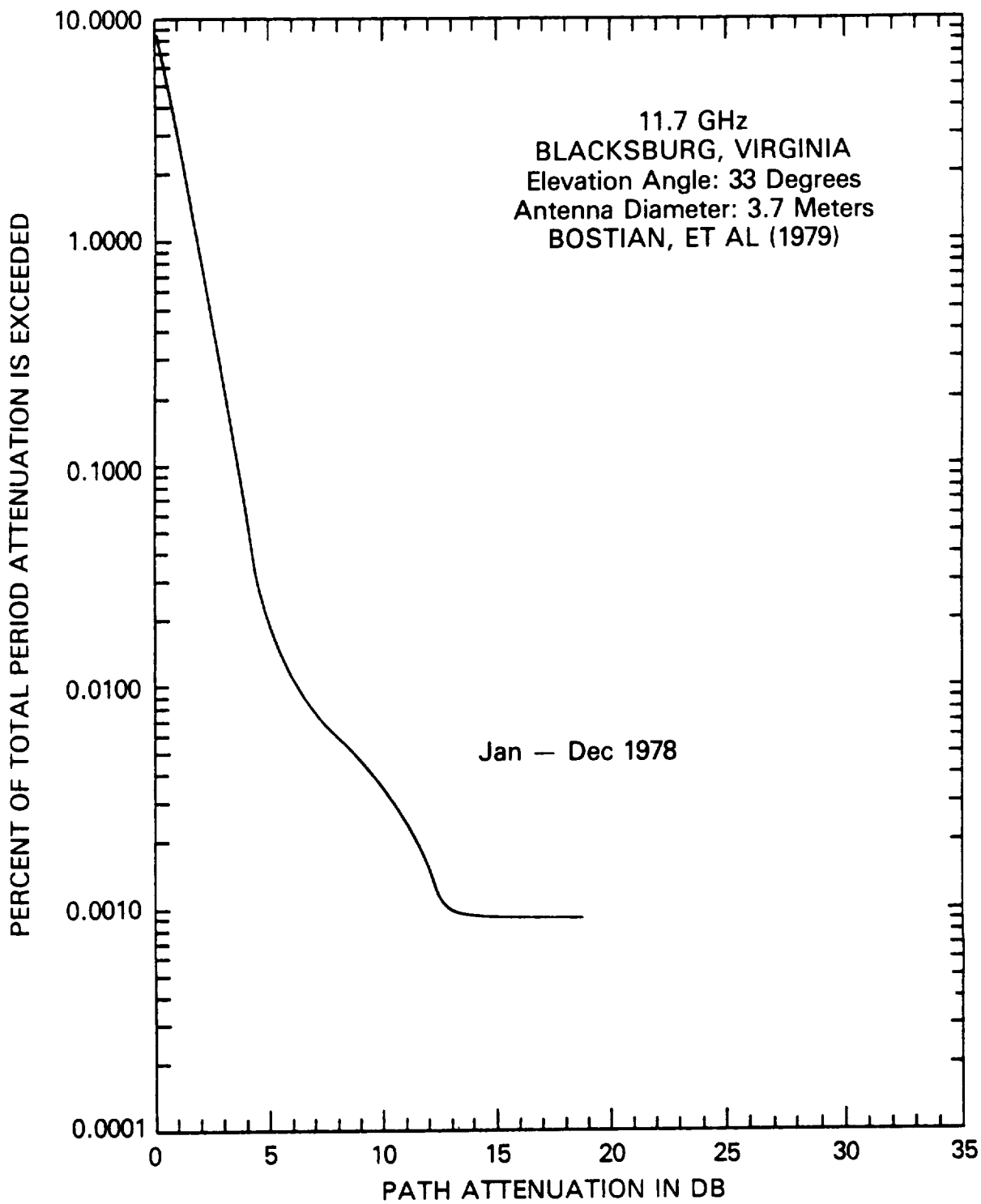


Figure 5.4-4. Annual 11.7 GHz Attenuation Distribution for Blacksburg, VA

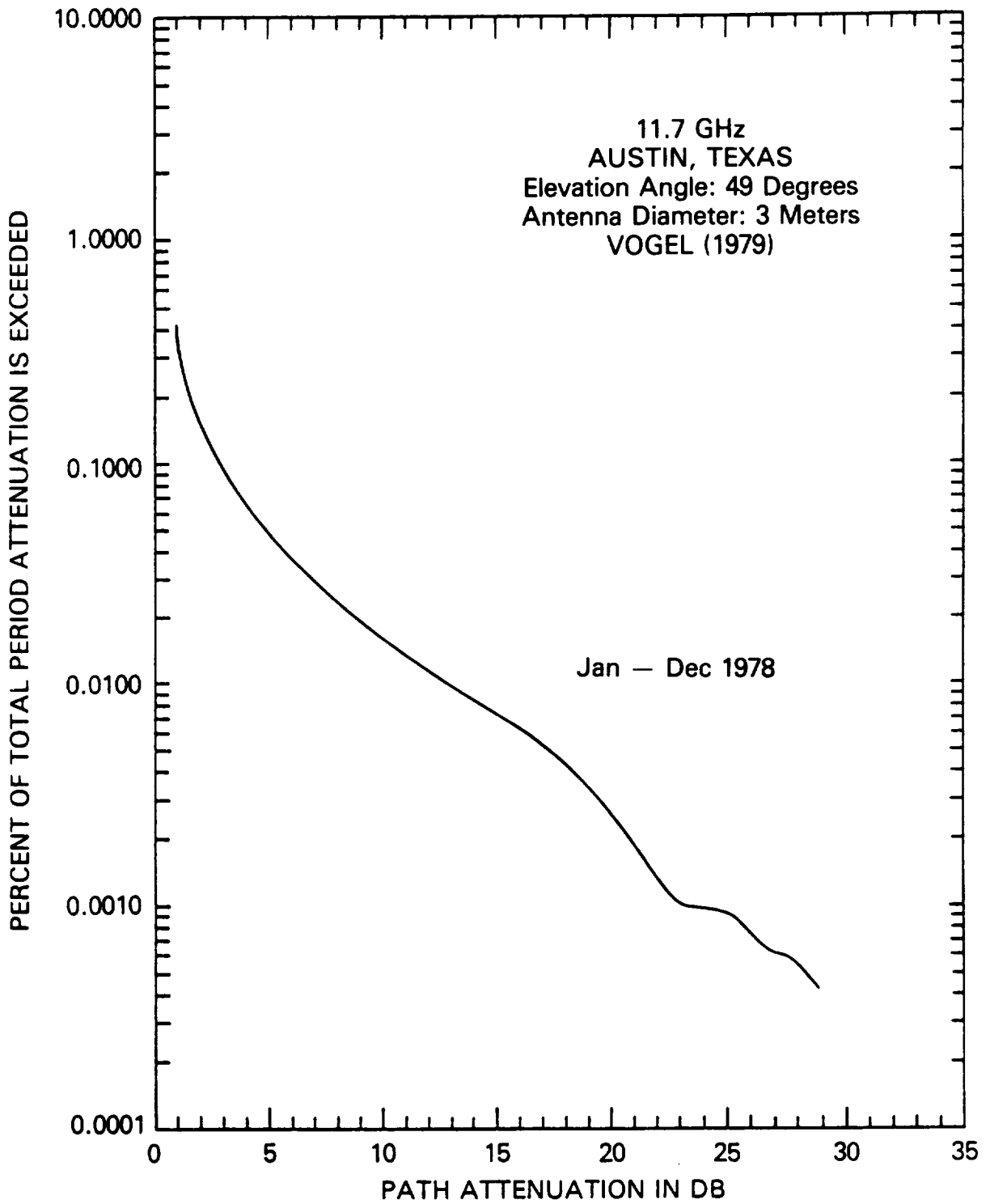


Figure 5.4-5. Annual 11.7 GHz Attenuation Distribution for Austin, TX

region of the elevation angle variations. Four of the sites have elevation angle differences of less than 9°; and, except for the 49° elevation angle at Austin, the sites differ by only a few degrees. Figure 5.4-6 presents annual 1978 distributions for each location converted to a 30 degree elevation angle. The distributions were converted to a 30° elevation angle by the relation

$$A_{30} = (\sin \theta / \sin 30^\circ) A_\theta \quad (5.4-1)$$

where A_θ is the measured attenuation in dB at the elevation angle θ , and A_{30} is the attenuation at an elevation angle of 30°. The distributions for the two nearest locations, Greenbelt and Holmdel, show some similarity, while the distributions for Blacksburg and Waltham are significantly lower. Comparisons of this kind should be observed with some caution, however, since the distributions are based on only 12 months of continuous data, and local precipitation conditions will vary greatly from year to year (see above).

It is interesting to note, however, that all five locations are in similar temperate continental rain climate regions. Both the CCIR and global rain models place the five locations discussed here in the same climate zones. Thus, attenuation prediction models based on the two above referenced procedures would yield similar attenuation distributions for all five locations. Such a similarity is not evident for the measured annual distributions presented here for those five locations.

Figure 5.4-7 presents distributions at three locations where long-term measurements, extending from 29 to 36 months duration, were available. The long-term distributions are much smoother than the individual 12 month distributions, and the curves for Holmdel and Greenbelt are very similar, particularly in the region from .01 to .0025%, which is the area of great interest for system design margin criteria. The results point out the desirability for multi-year continuous measurements in the evaluation of rain attenuation effects on communications system performance.

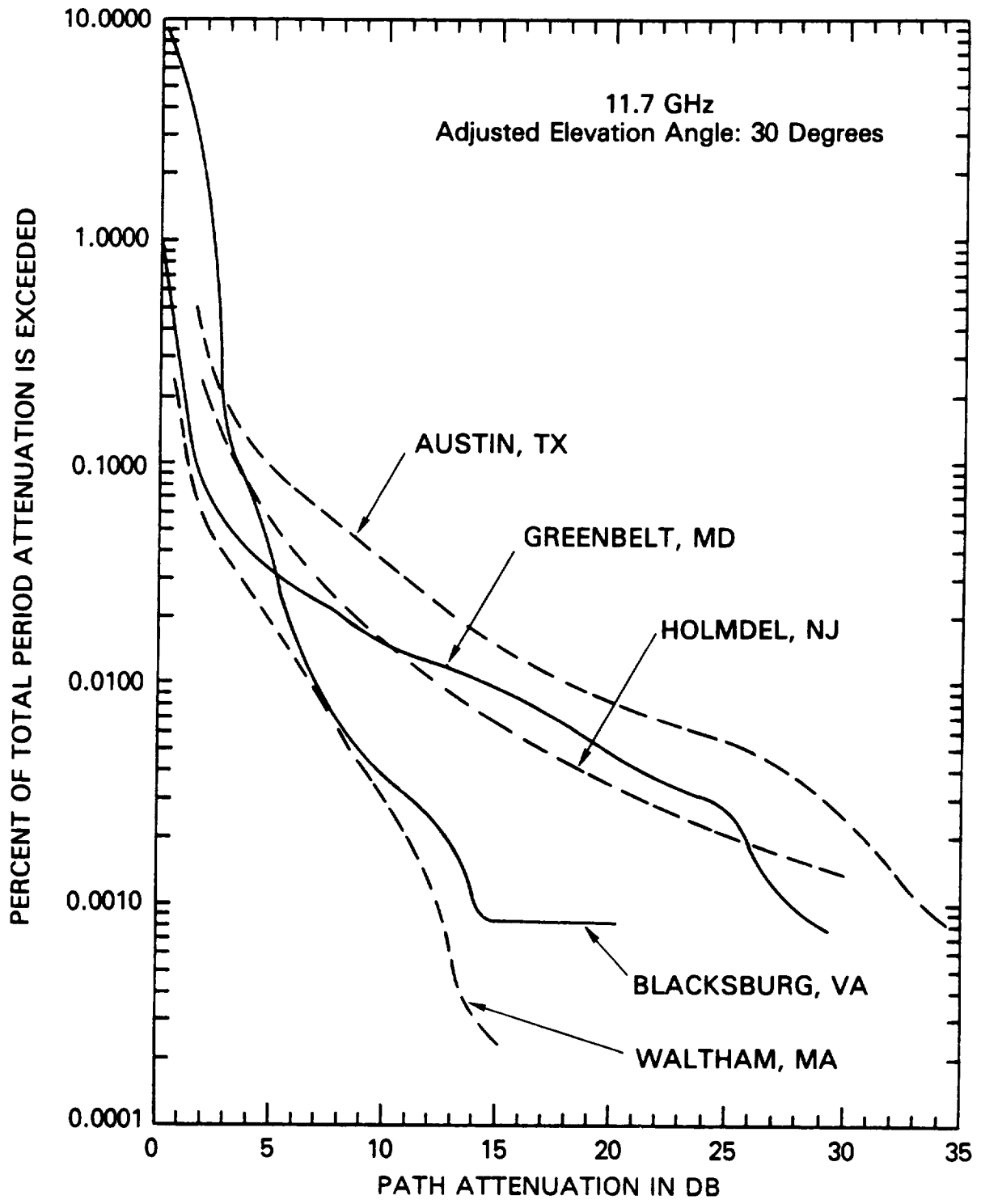


Figure 5.4-6. Comparison of 1978 Annual 11.7 GHz Attenuation Distribution of Measurements at Five Locations Adjusted to 30 Degrees Elevation Angle

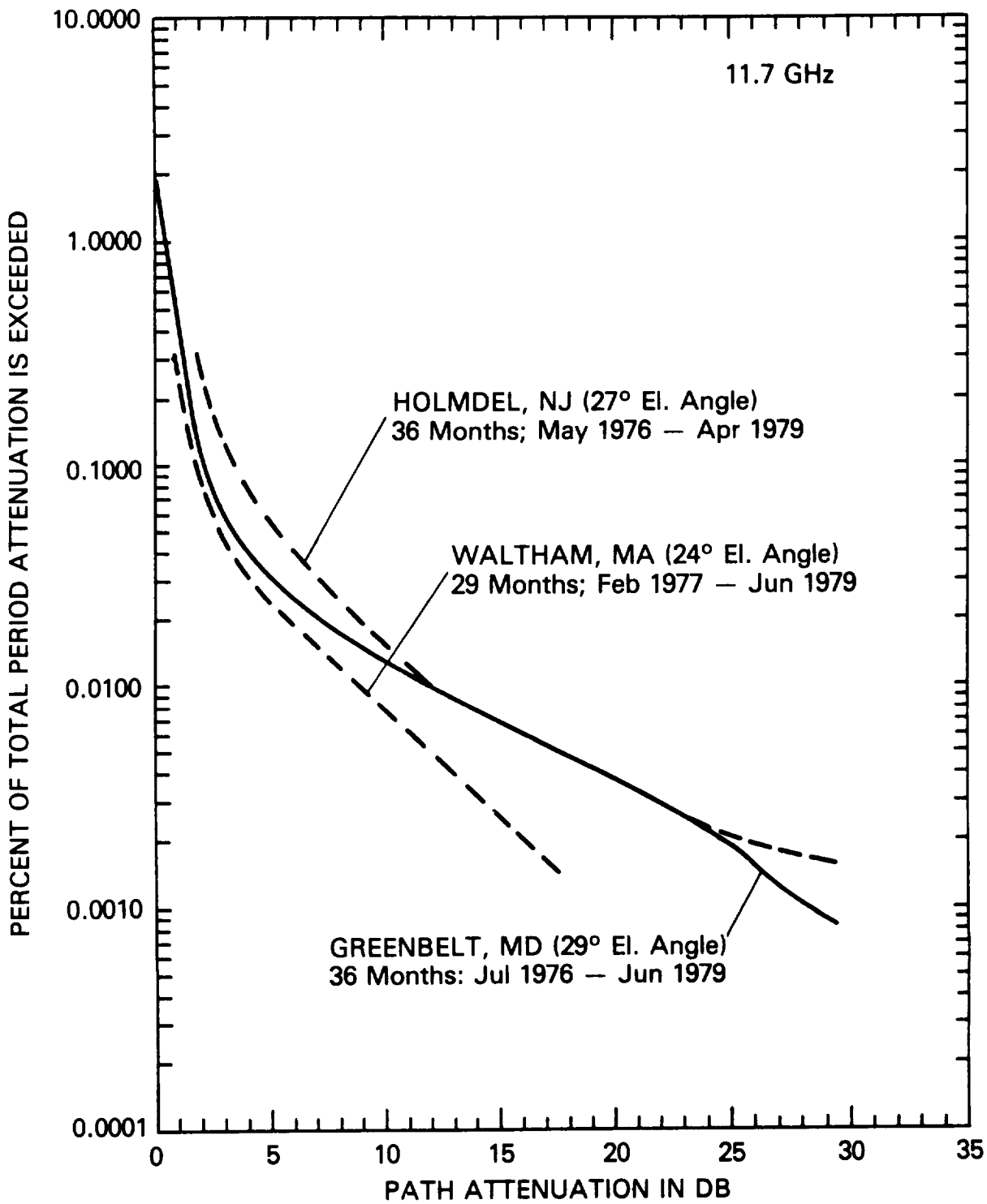


Figure 5-4.7. Long-Term 11.7 GHz Attenuation Distributions for Three Locations with Nearly Identical Elevation Angles

Representative European and Japanese attenuation data for frequencies near 11.7 GHz are shown in Figure 5.4-8 and -9. Figure 5.4-8 shows 11.6 GHz attenuation distribution curves for locations in Italy (Fucino, near Rome and Gera Lario, near Lake Como), France (Gometz-la-Ville, near Paris), and England (Slough, near London). Sources of these data are Macchiarella and Mauri (1980), Ramat (1980), and Davies (1981), respectively. Also shown is 11.5 GHz data for Japan (Kashima, on the coast east of Tokyo), from Hayashi (1979). Satellites used for the experiments represented here are SIRIO and ETS-II. Figure 5.4-9 presents data from an experiment in which separate antennas at the same station (near Darmstadt, Germany) simultaneously monitored 11.6 GHz beacon signals from the OTS and SIRIO spacecraft. The elevation angles of the two paths were within 4° of each other, but they differed by about 30° in azimuth. The large difference that is evident in the distributions has been attributed to orographic effects on local weather patterns: The SIRIO link passes over a hilly area for several kilometers while the OTS link lies over the Rhine river valley. These results (from Rucker - 1980) demonstrate the degree to which local climatic variations can affect rain attenuation statistics.

5.4.2 15-16 GHz Data

The 15 to 16 GHz experimental data base shown in Figure 5.4-10 is limited. The satellite beacon measurements were taken by NASA and COMSAT at North Carolina and Maryland. The earlier radiometer measurements by Bell Telephone Laboratories are included to supplement this satellite data. These radiometer measurements appear to agree with the satellite data up to 14 dB where the radiometer measurements stop because of sky temperature saturation. No other long-term 15 GHz data bases are known to exist in the U.S. or Canada. However, the Tracking and Data Relay Satellite System will eventually provide extensive data for 7 to 22 degree elevation angles from White Sands, NM.

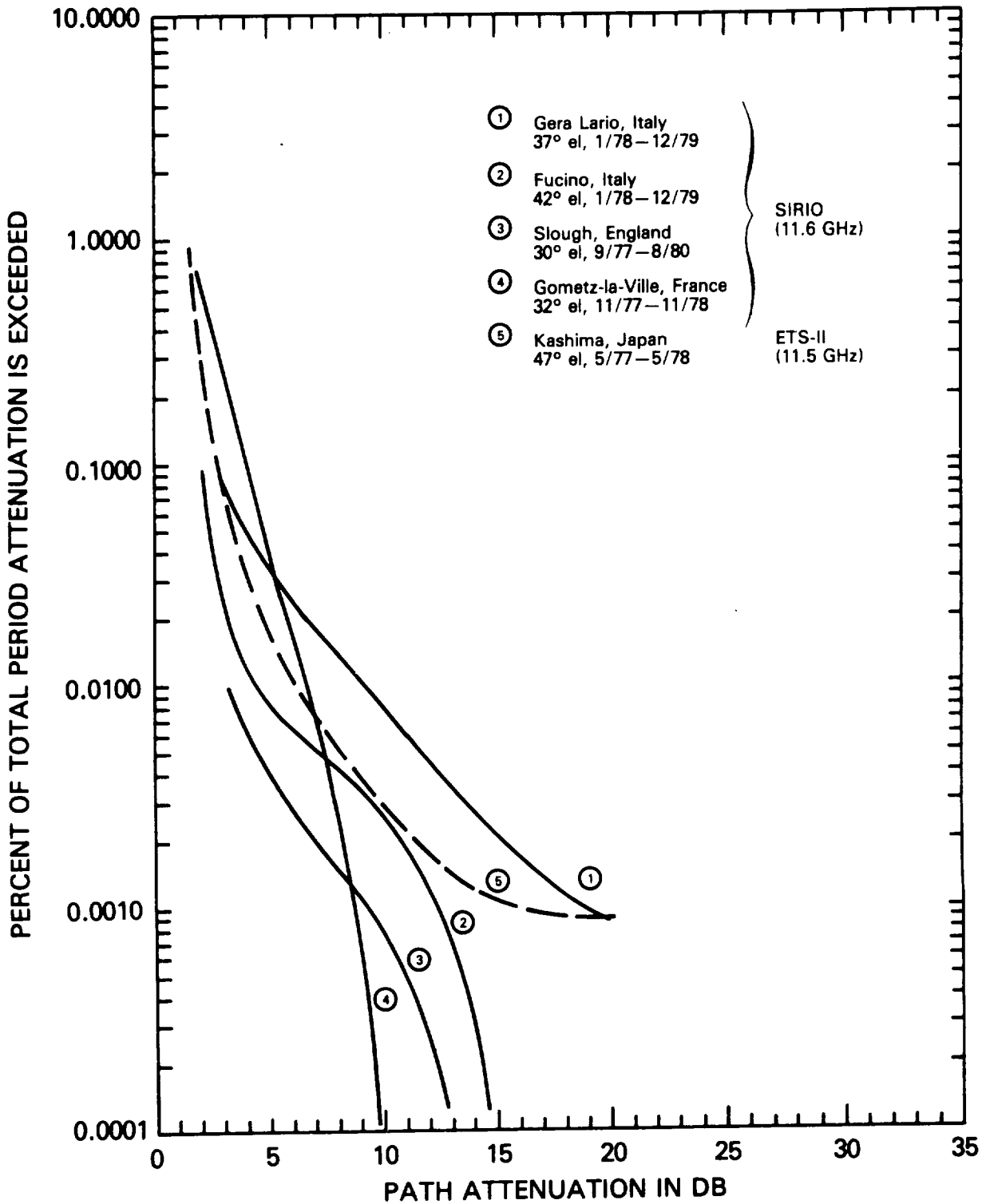


Figure 5.4-8. European and Japanese Attenuation Statistics for 11.5 and 11.6 GHz

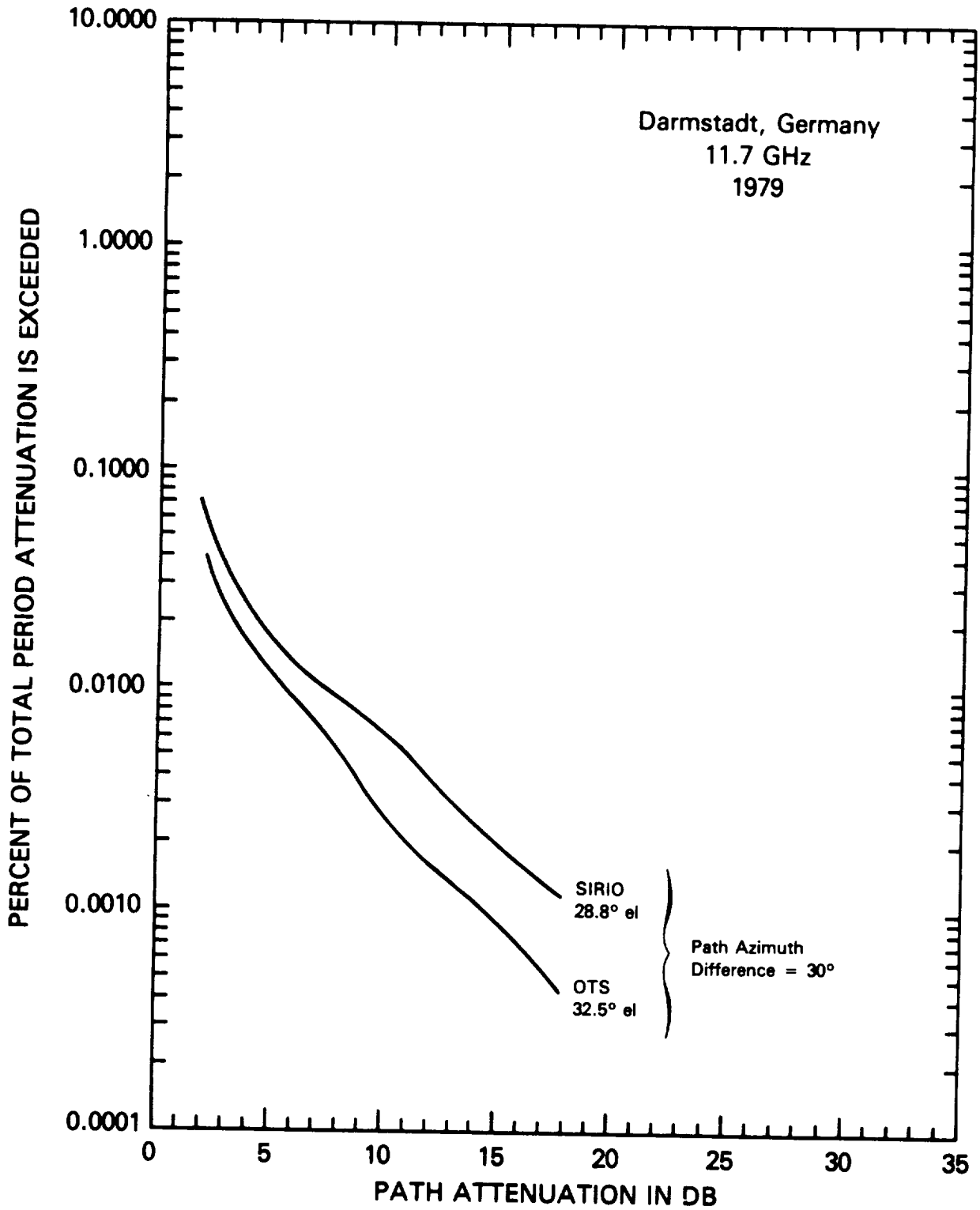


Figure 5.4-9. Simultaneous Attenuation Statistics for Two Paths from Same Earth Station

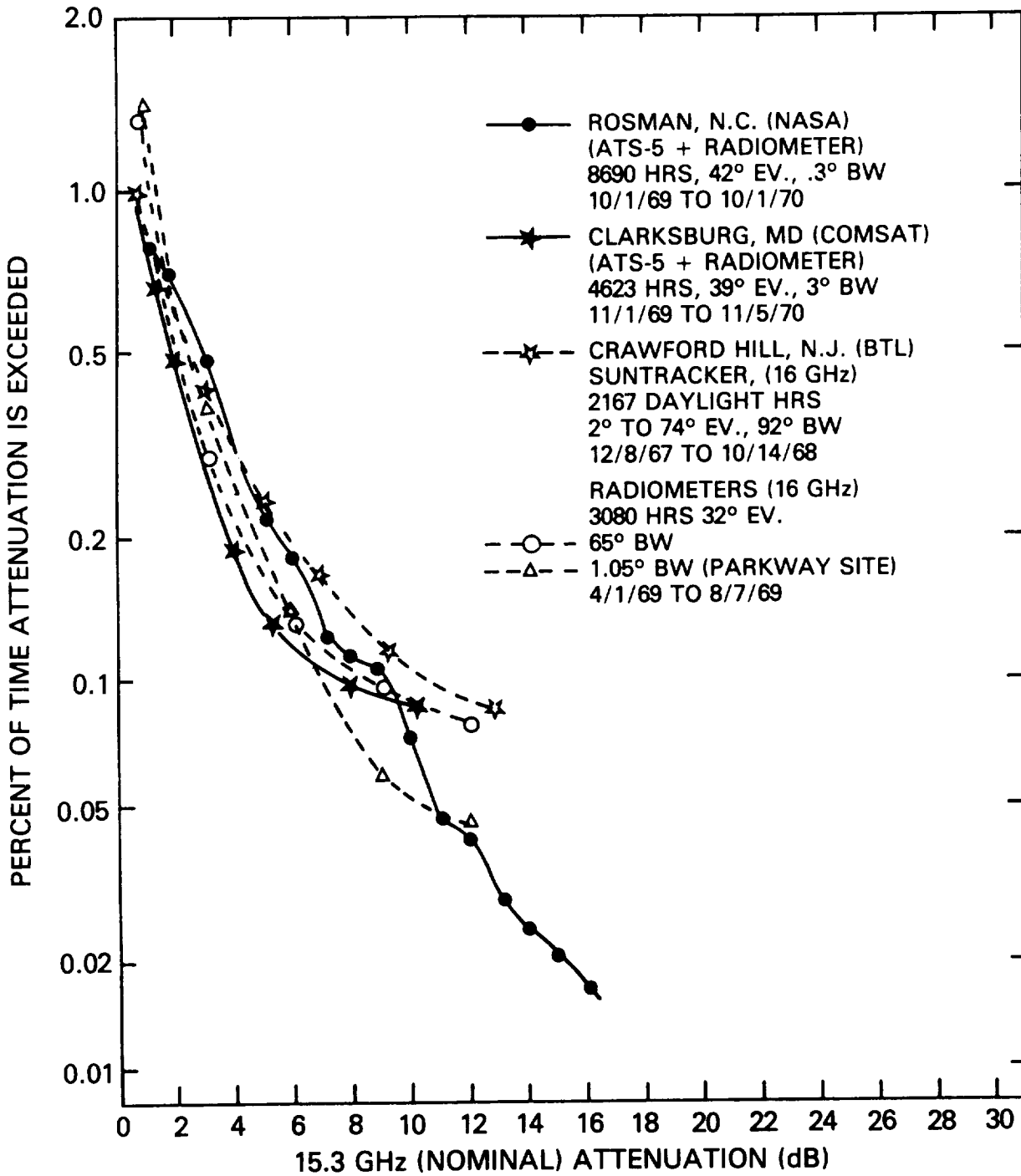


Figure 5.4-10. Summary of 15 GHz Measurements

5.4.3 19-20 GHz Data

Cumulative attenuation data in the 19 to 20 GHz range has been accumulated from both the ATS-6 and the COMSTAR beacons. In addition, the COMSTAR beacon has provided a source for direct measurement of depolarization.

The cumulative attenuation statistics at 19.04 and 20.0 GHz have been plotted in Figure 5.4-11. The Crawford Hill COMSTAR measurements (curve 2) included independent measurement of attenuation on nearly vertical (21 degrees from vertical) and nearly horizontal polarizations. Generally, horizontal and circularly polarized signals are attenuated more than vertically polarized signals. During 0.01% of the time, the COMSTAR measurements showed the horizontal attenuation to be about 2 dB greater than the vertical polarization (Cox, et al - 1979a). The polarization dependence arises because of the shape and general orientation of the raindrops. Also shown are the effects of hurricane Belle on the annual cumulative statistics. Clearly, this single event significantly shifts the curve for the moderate values of attenuation associated with heavy, but not intense, rain rates.

Figure 5.4-12 shows results from Japanese experiments using the 19.45 GHz beacon on the CS spacecraft.

5.4.4 28-35 GHz Data

The 28.56 GHz COMSTAR beacons and the 30 GHz ATS-6 beacon have provided excellent sources for attenuation measurements in the 30 GHz frequency region. The cumulative attenuation statistics for several locations in the U.S. are given in Figure 5.4-13. Japanese researchers have collected annual propagation data at 34.5 GHz with the beacon on the ETS-II satellite, as shown in Figure 5.4-12.

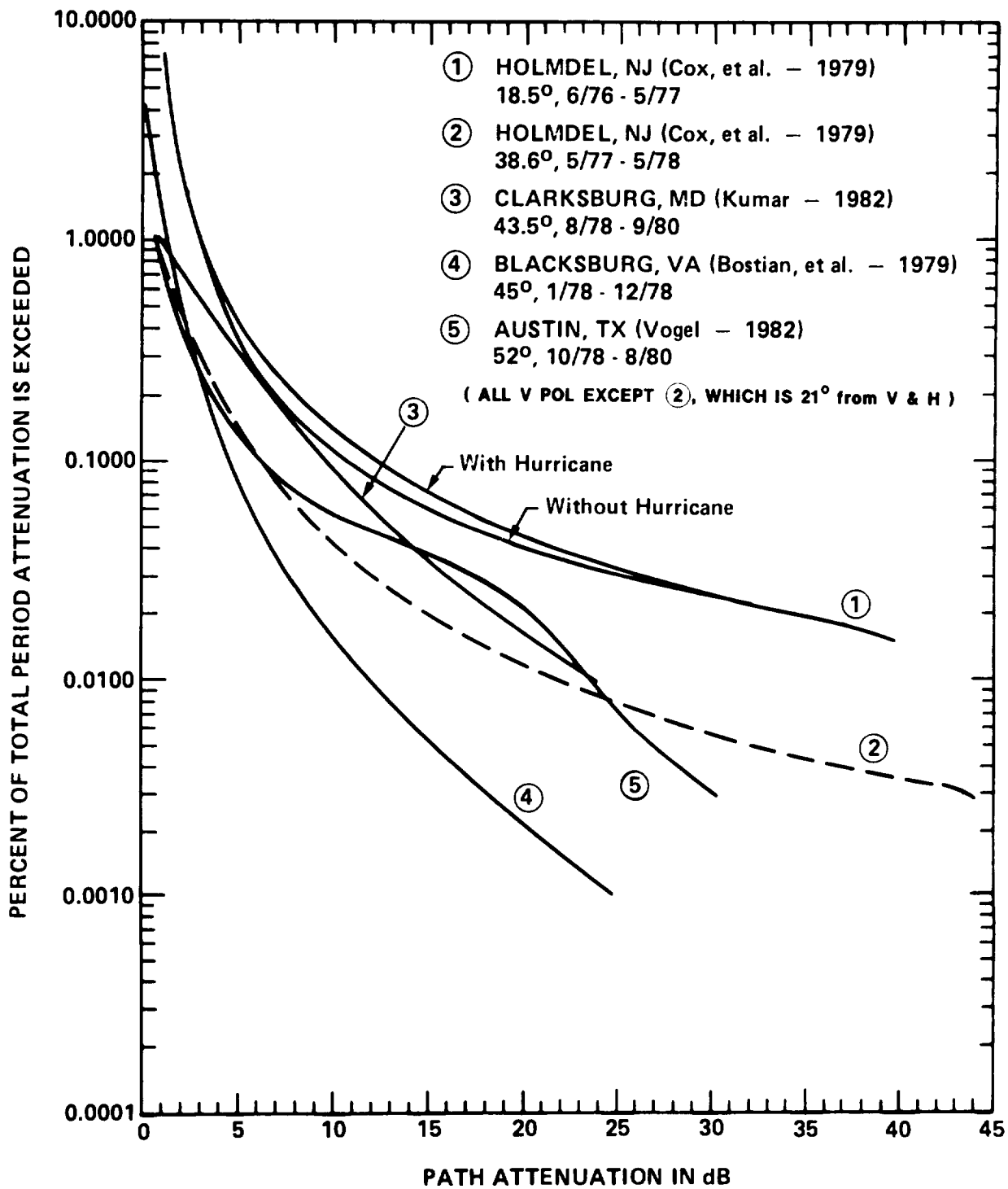


Figure 5.4-11. Summary of 19.04 and 20 GHz Measurements

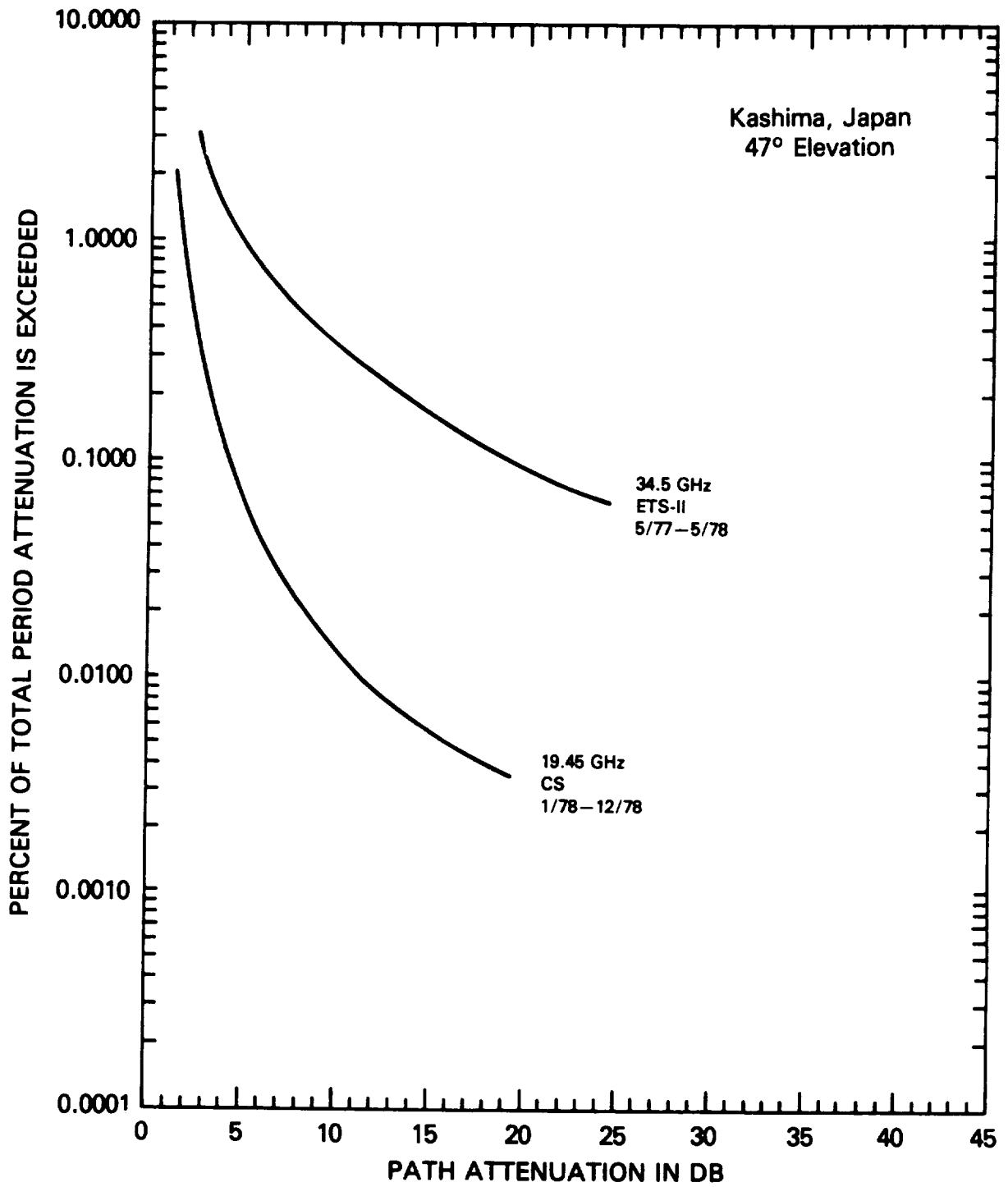


Figure 5.4-12. Results of Experiments with Japanese ETS-II and CS Beacons

5.4.5 Frequency Scaling of Attenuation Data

The relation between measured attenuations may be examined in several ways. The so-called statistical relation is obtained as a set of paired attenuations that are exceeded for equal amounts of time. These points may be obtained from the cumulative attenuation distributions. For the Crawford Hill measurements, for example, (Arnold, et al-1979) 19.5 dB attenuation at 19 GHz and 40.3 dB at 28 GHz were both exceeded for 65 min. This statistical relation is plotted in Figure 5.4-14 as a series of open circles for 19 and 28 GHz data for Crawford Hill.

The instantaneous attenuation relation may be determined from simultaneous data recordings of attenuation at the two frequencies. This instantaneous relation is also shown in Figure 5.4-14. The dashed curve indicates the median 19 GHz attenuation observed for values of 28 GHz attenuation on the abscissa. The bars in the figure indicate the span between the 10% and 90% points in the distribution of 19 GHz attenuations observed for the 28 GHz attenuation values. The quantization is 0.5 dB for the 10% and 90% points and for the median. Note that, while these results are statistical in nature as well, the quantity considered is the instantaneous attenuation for the two frequencies. It is evident from the figure that the statistical relation and the median instantaneous relation are essentially identical.

The dotted line on Figure 5.4-14 is the line for $A_2 = (f_2/f_1)^2 A_1 = 2.25A_1$ where A_1 is the attenuation in dB at frequency $f_1=19.04$ GHz and A_2 is the attenuation in dB at frequency $f_2 = 28.56$ GHz. The relationships between the measured attenuations depart from a frequency squared relation particularly at high attenuation. A straight line, $A_2 = 2.1A_1$ fits the data closely up to $A_1 \approx 20$ dB but the data depart from this line at still higher attenuation. This less than frequency squared attenuation dependence is consistent with the frequency dependence of Chu's theoretical attenuation coefficients (1974) in this frequency range. The further decrease in frequency dependence at higher attenuations is consistent with

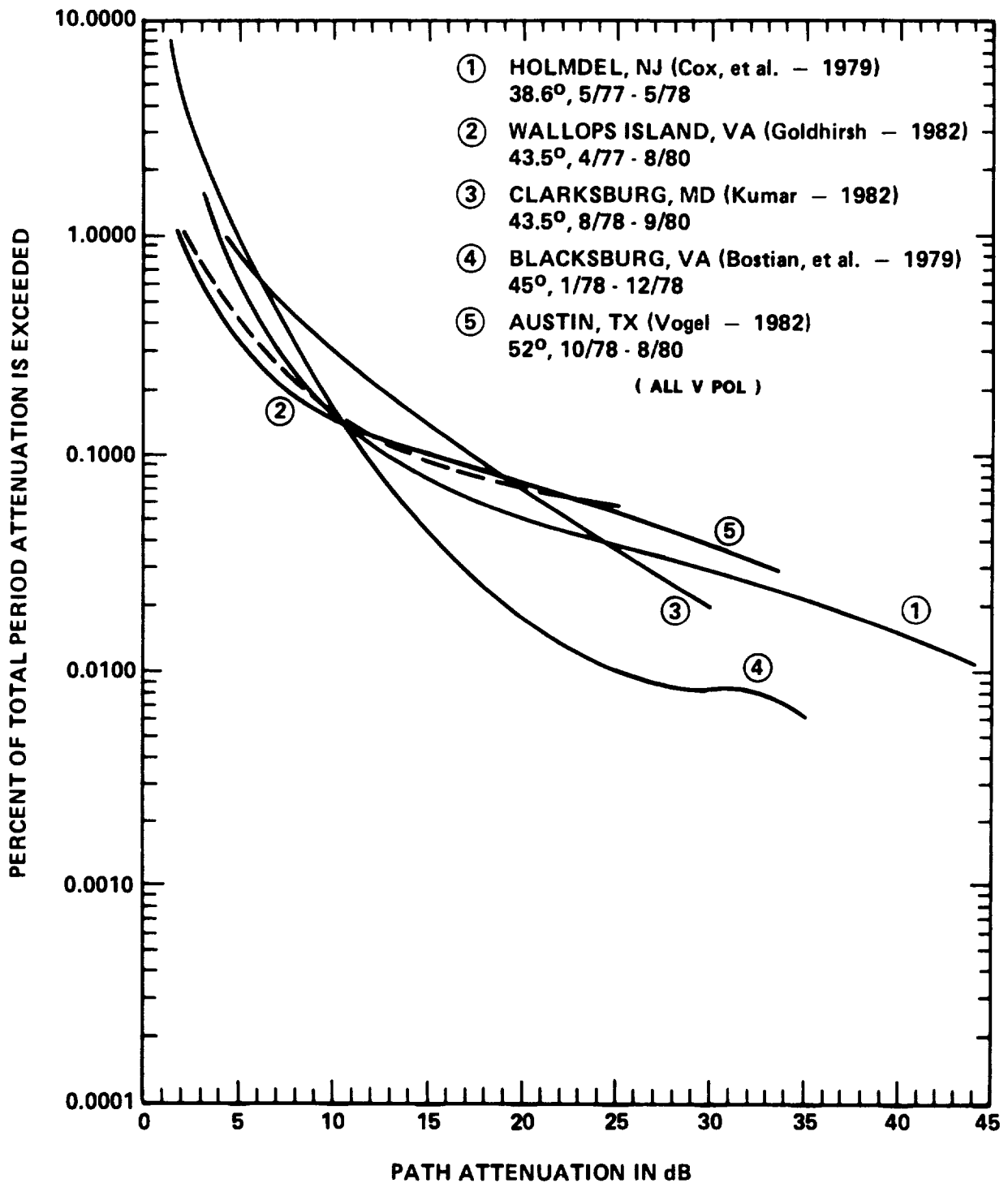


Figure 5.4-13. Summary of 28.56 and 30 GHz Measurements

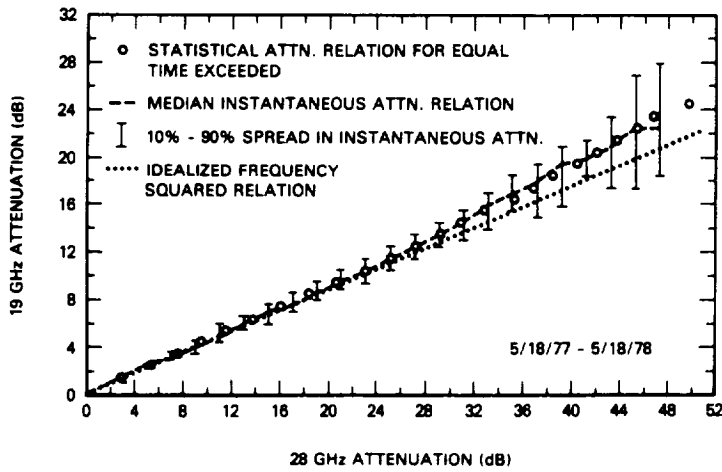


Figure 5.4-14. Relationships between 19 and 28 GHz Attenuation for Earth-Space Radio Propagation

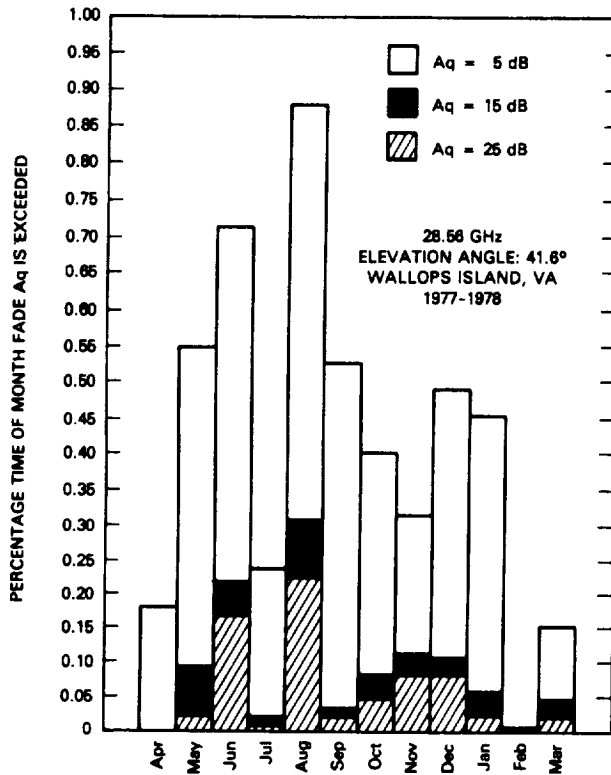


Figure 5.5-1. Histogram Denoting Percentage Times for Various Months the Fades of 5, 15, and 25 dB Were Exceeded

the same effect observed in the theoretical coefficients at higher rain rate since higher attenuation is associated with more intense rain.

In Figure 5.4-14, the increase in the spread between 10% and 90% points as attenuation increases is consistent with constant fractional fluctuation in the ratio of the attenuations at the two frequencies.

5.5 TEMPORAL DISTRIBUTION OF FADES

Systems may be able to accommodate fades during certain months or periods of the day more readily than during other periods. To help assess the magnitude of these effects along the eastern U.S. coast, Goldhirsh (1979, 1980) and others (Rogers and Hyde - 1979, Brussaard - 1977) have prepared histograms and cumulative distributions for various-months and times.

5.5.1 Monthly Distribution of Attenuation

Figure 5.5-1 shows the percentage of time for each month in the period April 1977 to March 1978 that fades of 5, 15, and 25 dB were exceeded. These measurements (Goldhirsh - 1979) were made at 28.56 GHz from the COMSTAR D2 satellite to Wallops Island, VA at an elevation angle of 41.6 degrees. The fades are more excessive during the summer months, except for July. This low value for July is not expected to be representative for that month and demonstrates how data from a single year can misrepresent the long-term average value.

Weather Bureau data may also be utilized to obtain this distribution by month, but this procedure may be inaccurate because the type of rain may vary significantly throughout the year. Some consideration to the amount of rainfall occurring in thunderstorms in a given month is needed to make these estimates more realistic. Ideally the rain rate distribution for each month would be required along with the attenuation models presented in Chapter 3. The variability of the statistics from year to year is demonstrated by a

comparison of the 1977-78 data with that obtained at Wallops Island in the September 1978-August 1979 period, using the COMSTAR D3 satellite (Goldhirsh - 1980). While the overall attenuation exceedance plots for the two periods agreed closely, several monthly exceedance values differed greatly between years. The percentage of July for which 15 dB was exceeded, for example, was about 0.3% in the 78-79 period compared with 0.02% in the 77-78 period. The 15 dB exceedance percentages differed by more than a factor of two between years for six of the twelve months.

5.5.2 Diurnal Distribution of Attenuation

One would expect severe fades to be most likely to occur during the late afternoon and early morning hours, when tropospheric heat exchange is the greatest and convective rains are most frequent. The 28 GHz COMSTAR data taken at Wallops Island, shown in Figures 5.5-2 and 5.5-3 (Goldhirsh - 1979), tends to confirm the expectation for the late afternoon. The figures show the attenuation statistics for the 1977-1978 period in terms of which 4-hour intervals of the day the attenuation was recorded. Figure 5.5-2 is a histogram giving time percentages for exceedance of 5, 15 and 25 dB attenuation values, and Figure 5.5-3 shows the complete cumulative distributions for each interval.

The time-of-day attenuation histogram of Figure 5.5-4 is from 11.7 GHz radiometer-based attenuation data at Etam, West Virginia (Rogers and Hyde - 1979). It shows two periods of the day dominated by deep, long fades, in early morning and late afternoon, as expected. The 11.4 GHz diurnal fade distribution given by Brussaard (1977) for a number of European locations exhibits a marked peak between 1500 and 1800 local time, but no peak in the morning. The 19.5 GHz 1979-80 data for Kashima, Japan shows a very different pattern (Fukuchi, et al - 1981), including a drop in deep fades at around 1700 local time. One-year data compiled at Palmetto, Georgia using the COMSTAR 19 GHz beacon, shows a broad minimum in the diurnal distribution of deep fades between about 0500 and 1000, and a broad peak between 1700 and 2300 (Lin, et al - 1980).

Figure 5.5-2. Diurnal Distribution of Fades Exceeding 5, 15, and 25 dB for Six Contiguous Four-Hour Time Slots of the Day

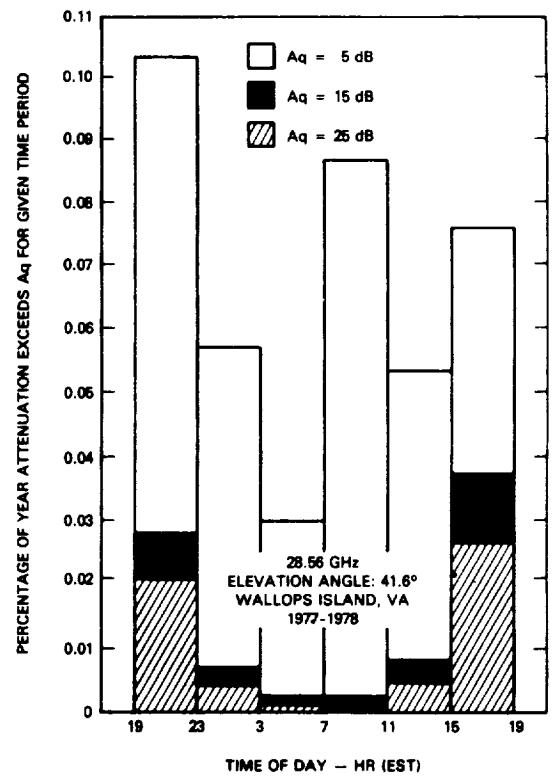
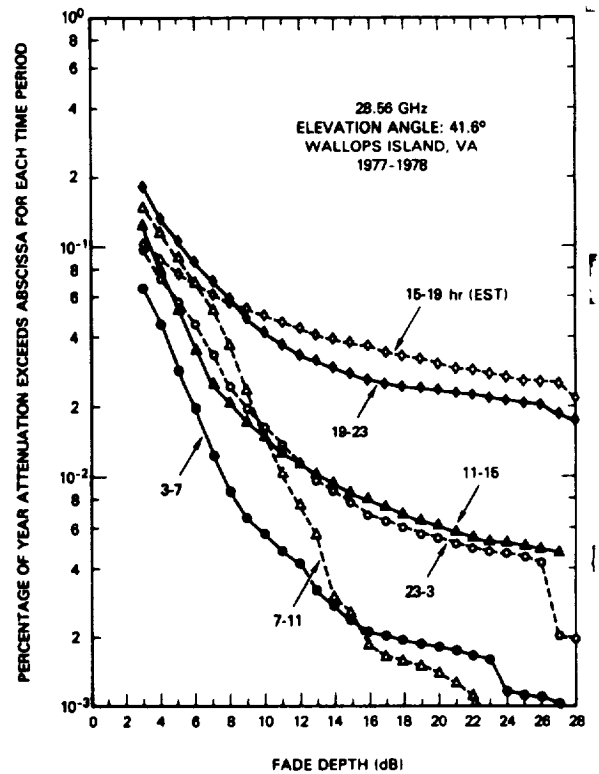


Figure 5.5-3 Cumulative Distributions for Six Contiguous Four-Hour Time Slots of Day



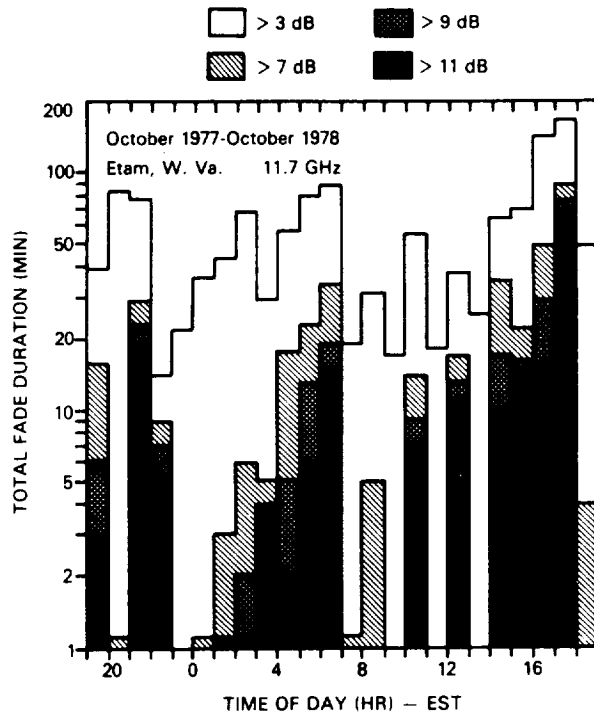


Figure 5.5-4. Diurnal Distribution of Fades Exceeding 3, 7, 9, 11 dB

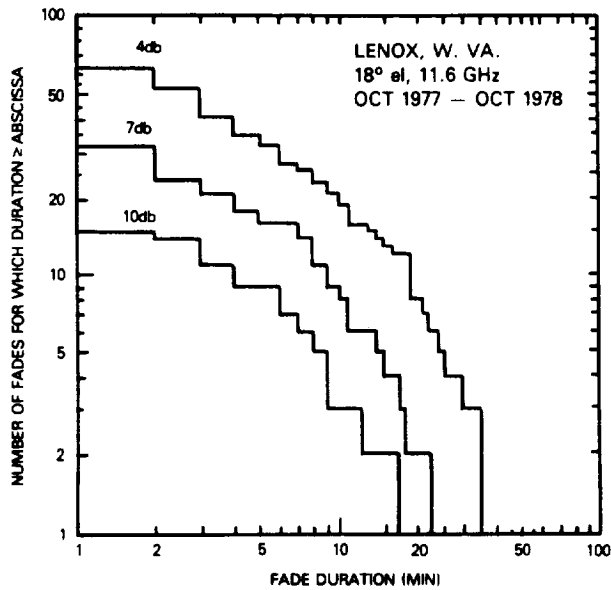


Figure 5.6-1. Histogram of Fade Duration From Radiometer Data

The diurnal distribution, like the monthly distribution, varies widely from year to year. Goldhirsh (1980) presents a comparison of diurnal distributions of the 1977-78 and the 1978-79 periods for 28 GHz attenuation at Wallops Island. In three of the six time intervals, the 15 dB exceedance percentage differed by more than a factor of two between the years.

5.6 FADE DURATION

Several experimenters have derived fade duration statistics for earth-space links. Rogers and Hyde (1979) present histograms of the number of fades exceeding specific depth and duration for 11.6 GHz at Etam and Lenox, West Virginia, based on a year's radiometer measurements. Figure 5.6-1 shows the Lenox histogram. Rogers (1981) gives similar data for Shimotsui, Japan, and in addition shows joint fade duration histograms for pairs of diversity sites in West Virginia and Japan.

Fade duration statistics have been compiled for 19 and 37 Gz at Slough, England, using a sun-tracking radiometer. Figure 5.6-2 shows histograms for fades exceeding 5 and 10 dB from the Slough data. Note that the method of presentation differs from that of Figure 5.6-1. The data in the earlier figure was the number of fades greater than or equal to the abscissa value, and the present figure gives the number with a length falling in one-minute intervals.

The use of a sun-tracking radiometer to estimate long-term path attenuation provides a greater range of measurement than a stationary sky-noise radiometer, but the data by necessity includes no night-time fading events. Also, due to the dependence of rain attenuation on elevation angle, a rainstorm occurring when the sun is low in the sky would produce deeper fades than an identical storm occurring closer to noon. Thus, long-term attenuation data from a sun-tracking radiometer is colored by the time of day that events producing fades tend to occur. One would expect this to limit its accuracy in describing statistics for a fixed elevation angle.

Fade duration statistics from direct attenuation measurements have been compiled by Japanese researchers for 11.5 and 34.5 GHz using the ETS-II satellite, shown in Figure 5.6-3, as well as limited 19.45 and 11.7 GHz statistics from the CS and BS experiments (Hayashi, et al - 1979).

Lin, et al (1980) present a summarization of fade duration data for 19 and 28.5 GHz on the COMSTAR (D2)-to-Palmetto, Georgia path. The durations of fades exceeding each of several attenuation thresholds between 5 and 25 dB at each frequency were normalized and presented on a single plot. The normalization consisted of dividing each fade duration value by the average duration for its frequency and threshold. The combined normalized data was shown to closely fit a log-normal distribution, which confirmed expectations.

5.7 EXPERIMENTAL DEPOLARIZATION DATA

The crosspolarization discrimination not exceeded for a given percentage of time, in decibels, is approximated by a relation (Nowland, et al-1977)

$$XPD = \tilde{a} - \tilde{b} \log_{10} (CPA) \quad (5.7-1)$$

where CPA is the copolarized attenuation value in decibels exceeded for the same percentage of time. This suggests that the data be presented in a semilogarithmic format wherein each parameter is already a logarithm of another parameter. Therefore, in this Handbook we have replotted the results of others in order to present a uniform format of the data and to allow easy comparison with the CCIR approximation (see Eq. 4.3-27).

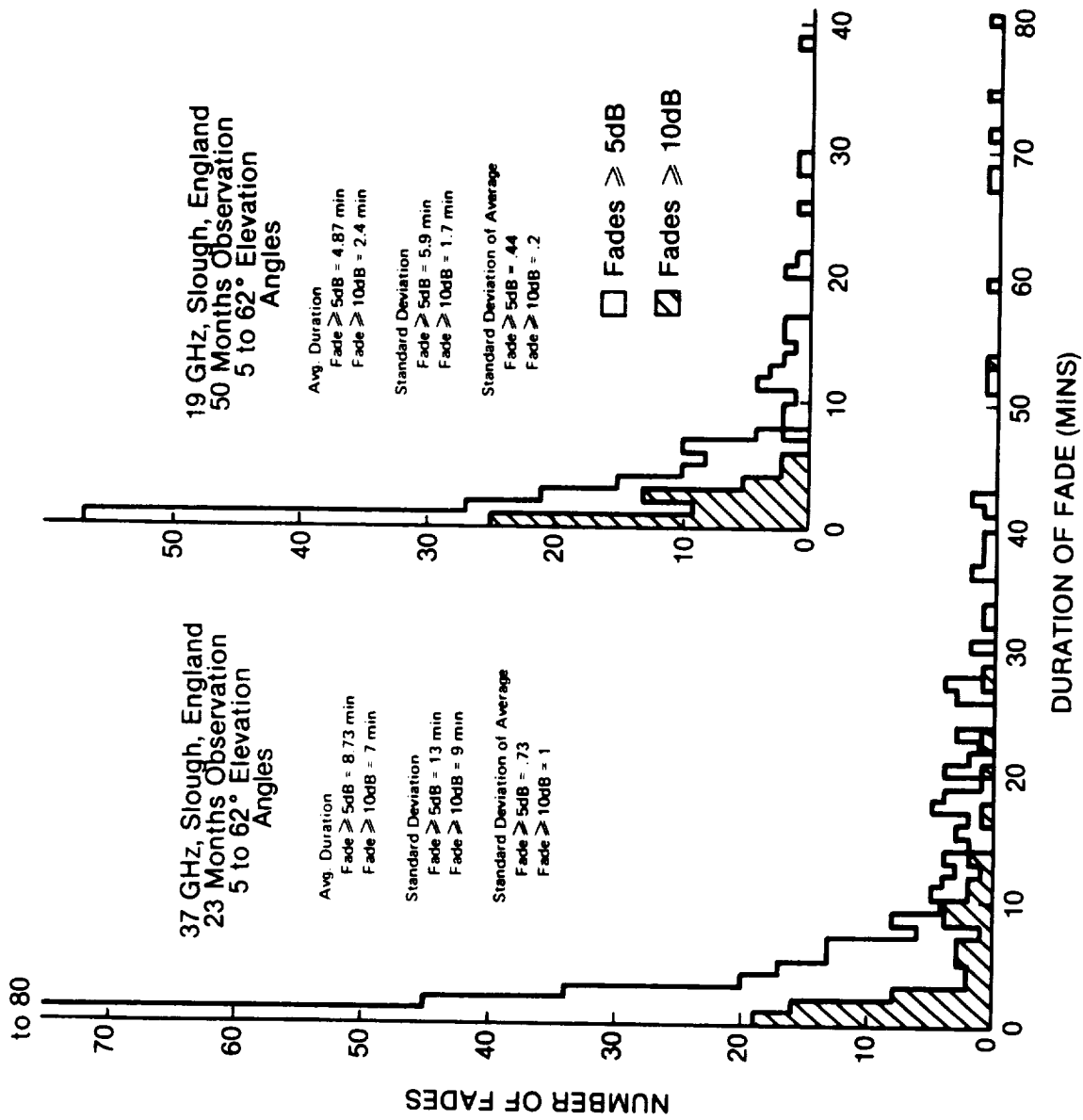


Figure 5.6-2. Histograms of Fades Greater Than 5 and 10 dB at 19 and 37 GHz

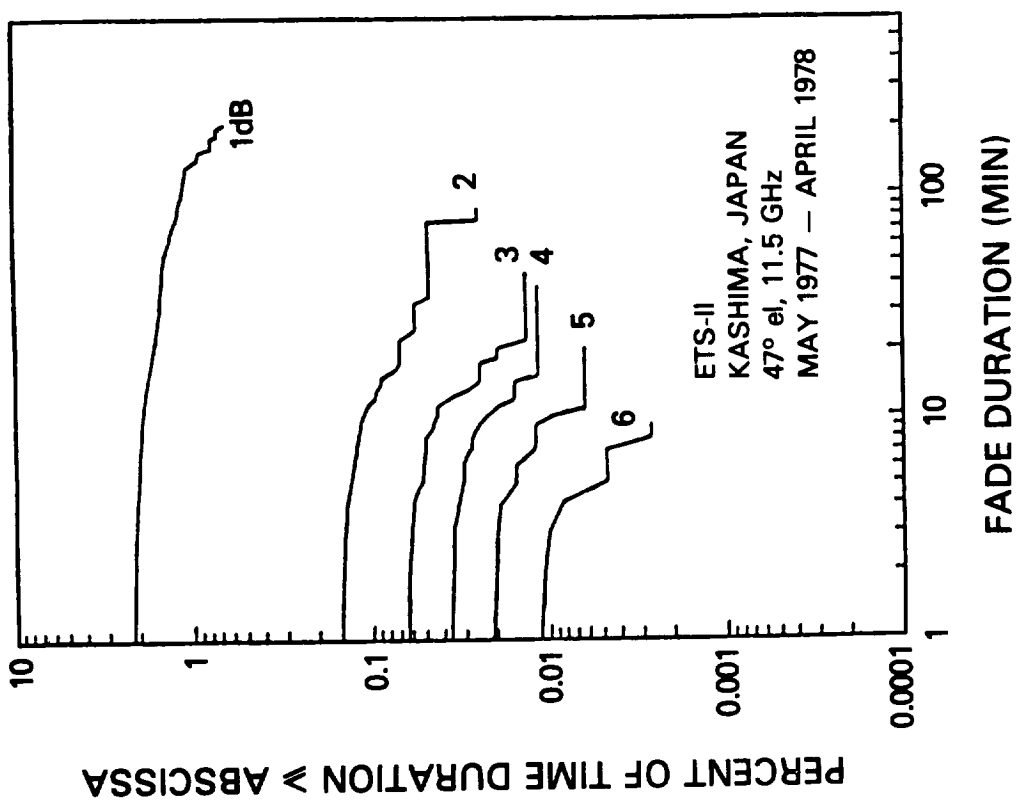
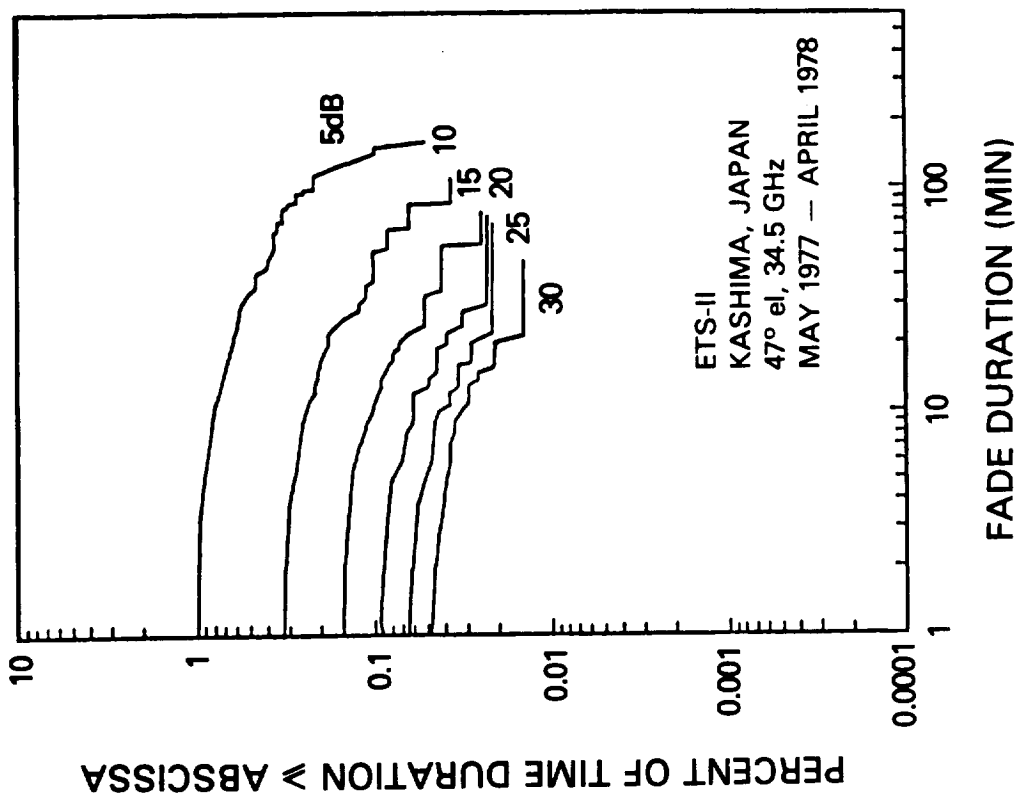


Figure 5.6-3. Fade Duration Statistics for Kashima, Japan, Obtained Using the ETS-II Satellite

5.7.1 19 GHz Data

Figures 5.7-1 and 5.7-2 present the 19 GHz cross-polarization data obtained by the Bell Laboratories experimenters at Crawford Hill, NJ (Arnold, et al - 1979). The near vertical polarization appears to have slightly more cross-polarization discrimination than the horizontal polarization. However, both polarizations show less discrimination than the CCIR estimate. Therefore, in this case, the CCIR approximation appears to be optimistic.

5.7.2 28 GHz Data

The COMSTAR signal at 28 GHz had a fixed polarization, thus allowing measurements at only one orientation with respect to the raindrop anisotropy. The data replotted from Bell measurements (Arnold, et al-1979) is shown in Figure 5.7-3. Again, the CCIR approximation is over-optimistic when compared to the measured data.

5.7.3 Joint Attenuation - Depolarization Data

Systems using orthogonal polarizations for frequency reuse suffer degradation due to crosstalk caused by depolarization in addition to the degradation due to rain attenuation. A full statistical description of the availability of such a system must consider the attenuation and depolarization jointly. Figure 5.7-4 (Arnold, et al - 1979) depicts such joint statistics for attenuation and depolarization on the 28 GHz COMSTAR-Crawford Hill Link. The figure gives the percentage of time that a given attenuation value was exceeded or a given XPD value was not exceeded. Note that the lower bound of all the curves is simply the attenuation exceedance curve, since it corresponds to low values of XPD, which happen a very low percentage of the time. Thus the location of this lower bound is established by attenuation alone. On the other hand, the curves become independent of attenuation for large values of attenuation, since the non-exceedance percentage for XPD far outweighs the exceedance percentage for attenuation.

Figure 5.7-1. 19 GHz Cross-Polarization Measurements - Near Vertical Polarization

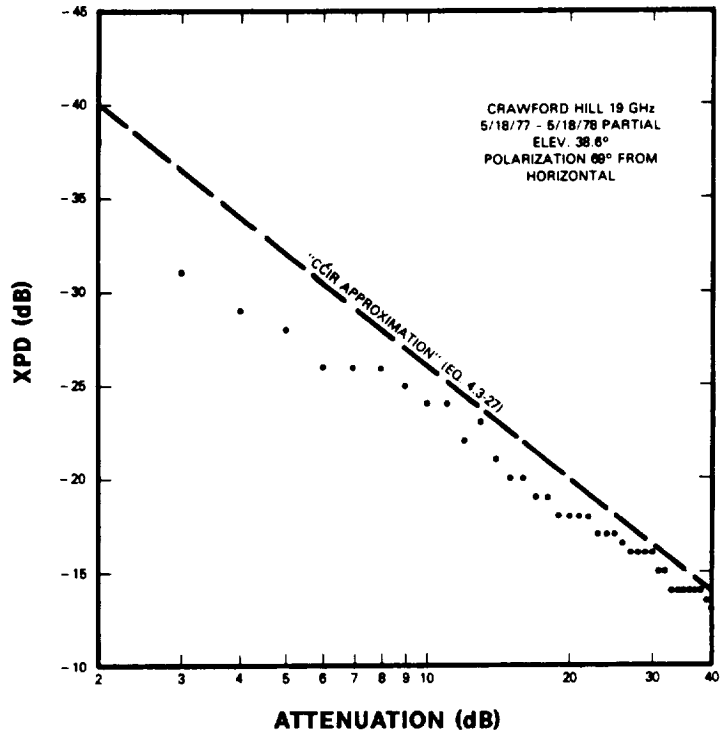


Figure 5.7-2. 19 GHz Cross-Polarization Measurements - Near Horizontal Polarization

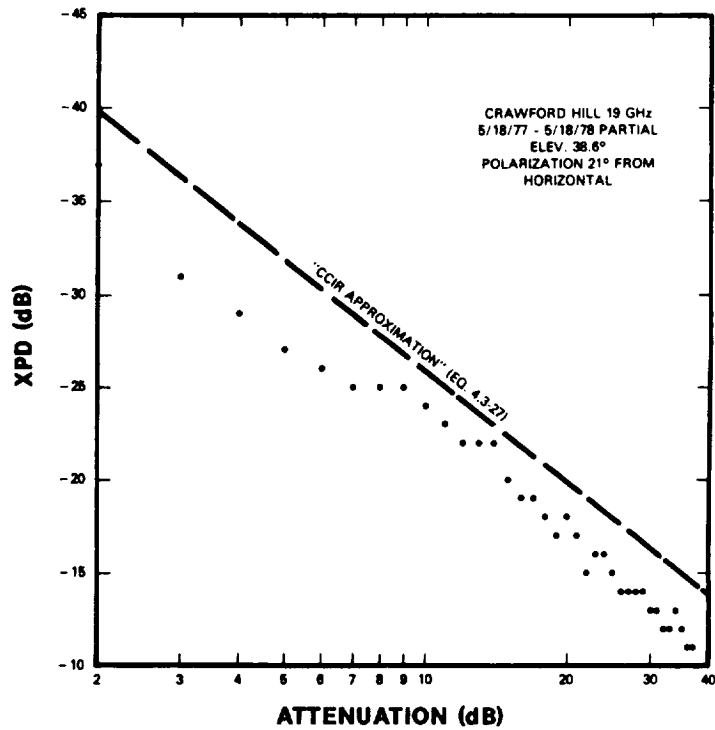


Figure 5.7-3. 28 GHZ
Crosspolarization
Measurements

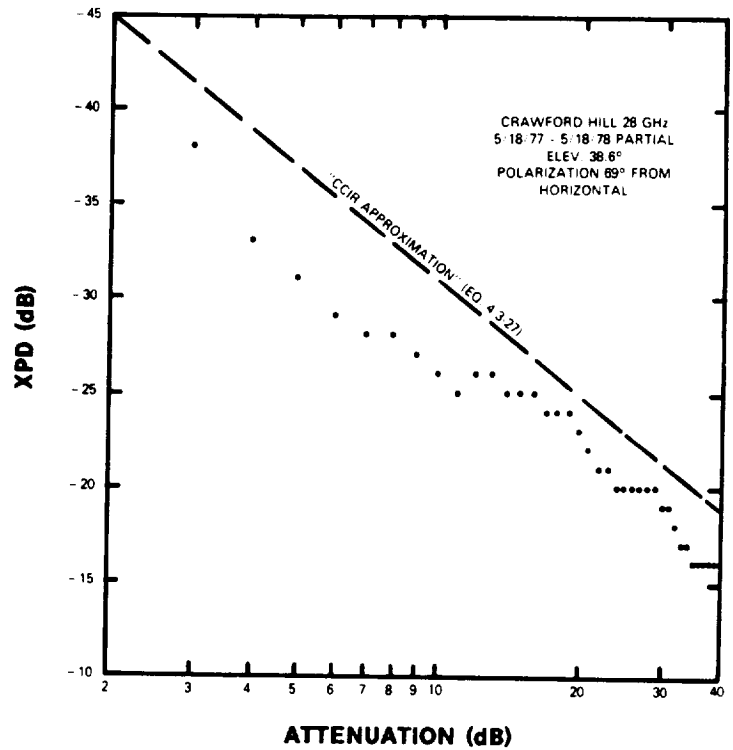
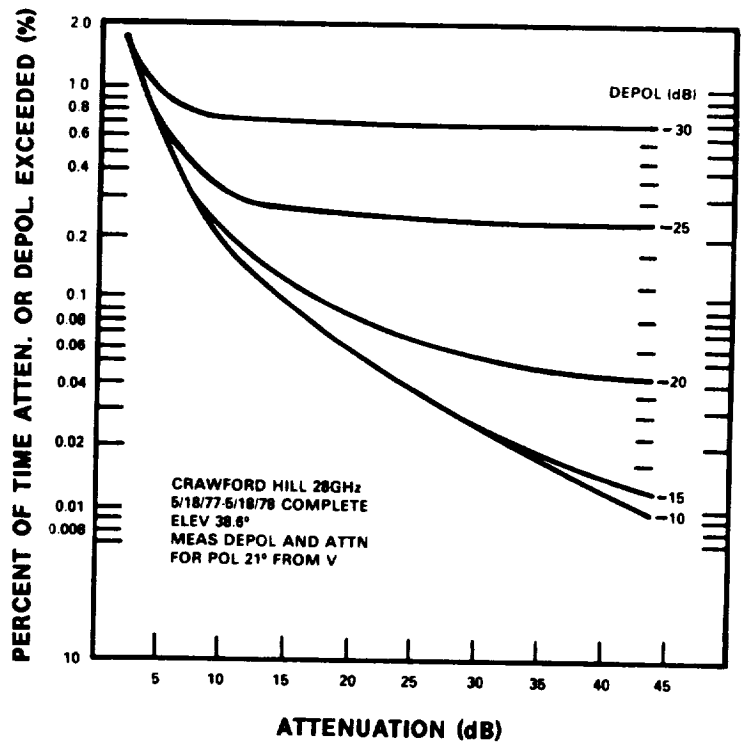


Figure 5.7-4. Joint
Attenuation-Depolarization
Statistics for 28 GHz Link



A family of curves of the type shown in Figure 5.7-4 gives the outage percentage for a hypothetical system that is unavailable when either an attenuation or an XPD threshold is passed. This is a useful approximation, although most systems allow for some tradeoff between XPD and attenuation. When attenuation is low, for example, greater crosstalk may be tolerable than when attenuation is appreciable.

5.8 PHASE AND AMPLITUDE DISPERSION

Experimental measurements of the phase and amplitude dispersion in the lower troposphere made from the COMSTAR D2 satellite have been made at Crawford Hill, NJ (Cox, et al-1979b). The measurements were made across the 528 MHz coherent sidebands at 28 GHz and between the 19 and 28 GHz carriers which were coherent.

The nine-month Crawford Hill data set has been comprehensively searched for evidence of phase dispersion. For all propagation events, the change in average sideband to carrier phase is less than the measurement uncertainty of about 13° for attenuation up to 45 dB. Phase fluctuations are consistent with signal-to-noise ratios over the 45 dB attenuation range. The change in average 19 to 28 GHz phase is on the order of 60° over a 30 dB attenuation range at 28 GHz. This average phase change appears to be due only to the average dispersive properties of the water in the rain along the path. There is no evidence of multipath type dispersion.

Attenuation in dB at 28 GHz is 2.1 times greater than that at 19 GHz for attenuations up to 29 dB at 19 GHz. The small spread observed in the relationship between 19 and 28 GHz attenuations is consistent with the absence of significant phase dispersion over the 528 MHz bandwidth.

5.9 REFERENCES

- Arnold, H.W., D.C. Cox, H.W. Hoffman and R.P. Leck (1979), "Characteristics of Rain and Ice Depolarization for a 19 and 28 GHz Propagation Path from a COMSTAR Satellite," Conference Record, ICC 79, Vol. 3, Boston, MA pp 40.5.1-6.
- Arnold, H.W., D.C. Cox, and A.J. Rustako, Jr. (1980), "Rain Attenuation at 10-30 GHz Along Earth-Space Paths: Elevation Angle, Frequency, Seasonal and Diurnal Effects," Conference Record, ICC 80, Seattle, WA, Vol. 3, pp. 40.3.1-7.
- Bostian, C.W., et al (1979), "A Depolarization and Attenuation Experiment Using the COMSTAR and CTS Satellites," Virg. Poly. Inst. and State Univ., Annual Report, NASA Cont. NAS5-22577.
- Brussaard, G. (1977), "Rain Attenuation on Satellite-Earth Paths at 11.4 and 14 GHz," URSI Commission F Symposium Proceedings, April 28 - May 6, 1977 La Baule, France.
- CCIR (1978) "Rain Attenuation Prediction " Document P/105-E, CCIR Study Groups Special Preparatory Meeting (WARC-79), International Telecommunications Union, Geneva.
- CCIR (1986a), "Propagation Data and Prediction Methods Required for Space Telecommunications Systems," Report 564-3, in Volume V, Recommendations and Reports of the CCIR - 1986, International Telecommunications Union, Geneva, ISBN No. 92-61-02741-5, NTIS Accession No. PB-87-14116-4.
- CCIR (1986b), "Data Banks Used for Testing Prediction Methods in Sections E, F and G of Volume V," Document 5/378 (Rev.1), International Telecommunications Union, Geneva.
- Chu, T.S. (1974), "Rain Induced Cross-Polarization at Centimeter and Millimeter Wavelengths," BSTJ, Vol. 53, pp 1557-79.
- Cox, D.C., H.W. Arnold and A.J. Rustako, Jr. (1979a), "Attenuation and Depolarization by Rain and Ice Along Inclined Radio Paths Through the Atmosphere at Frequencies Above 10 GHz," Conference Record, EASCON 79, Arlington, VA, Vol. 1, pp 56-61.
- Cox, D.C., H.W. Arnold and R.P. Lick (1979b), "Phase and Amplitude Dispersion for Earth-Space Propagation in the 20 to 30 GHz Frequency Range," URSI Program and Abstracts, Spring Meeting, Seattle, Washington, June 18-22, p 253.
- Crane, R.K. (1980), "Prediction of Attenuation by Rain," IEEE Trans. on Comm., Vol. COM-28, No. 9, pp. 1717-1733.

Davies, P.G. (1976), "Diversity Measurements of Attenuation at 37 GHz with Sun-Tracking Radiometers in a 3-site Network," Proc IEEE, Vol. 123, page 765.

Davies, P.G., M.J. Courthold and E.C. MacKenzie (1981), "Measurements of Circularly-Polarized Transmissions from the OTS and SIRIO Satellites in the 11 GHz Band," IEE Conference Publication No. 195, Internat. Conf. Ant. Prop., York, U.K., April 1981.

Fukuchi, H., M. Fujita, K. Nakamura, Y. Furuhamu, and Y. Otsu (1981), "Rain Attenuation Characteristics on Quasi-Millimeter Waves Using Japanese Geostationary Satellites CS and BSE," IEEE Conference Publication No. 195, Internat. Conf. Ant. Prop., York, U.K., April 1981.

Goldhirsh, J. (1979), "Cumulative Slant Path Rain Attenuation Statistics Associated with the Comstar Beacon at 28.56 GHz for Wallops Island, VA," IEEE, Trans. Ant. Prop., Vol. AP-27, No. 6, pp 752-758.

Goldhirsh, J. (1980), "Multiyear Slant-Path Rain Fade Statistics at 28.56 GHz for Wallops Island, VA," IEEE Trans. Ant. Prop., Vol. AP-28, No. 6, pp. 934-941.

Goldhirsh, J. (1982), "Space Diversity Performance Prediction for Earth-Satellite Paths using Radar Modeling Techniques," Radio Science, Vol. 17, No. 6, pp. 1400-1410.

Hayashi, R., Y. Otsu, Y. Furuhamu, and N. Fugono (1979), "Propagation Characteristics on Millimeter and Quasi-Millimeter Waves by Using Three Geostationary Satellites of Japan," paper IAF-79-F-281, XXX Congress, International Astronautical Federation, Munich, Germany.

Ippolito, L.J. (1978), "11.7 GHz Attenuation and Rain Rate Measurements With the Communications Technology Satellite (CTS)," NASA Tech. Memo. 80283, Greenbelt, MD.

Kaul, R., D. Rogers and J. Bremer (1977), "A Compendium of Millimeter Wave Propagation Studies Performed by NASA," ORI Tech. Rpt., NASA Contract NAS5-24252.

Kumar, P.N. (1982), "Precipitation Fade Statistics for 19/29 - GHz Comstar Beacon Signals and 12-GHz Radiometric Measurements," COMSAT Technical Review, Vol. 12, No. 1, pp. 1-27.

Lin, S.H., H.J. Bergmann, and M. V. Pursley (1980) "Rain Attenuation on Earth-Satellite Paths - Summary of 10-Year Experiments and Studies," BSTJ, Vol. 59, No. 2, pp. 183-228.

- Macchiarella, G. and M. Mauri (1981), "Statistical Results on Centimetric Waves Propagation after Two Years of Activity with the Italian Satellite SIRIO," URSI Commission F Open Symposium, Lenoxville, Canada, May 1980.
- Nackoney, O.G. (1979), "CTS 11.7 GHz Propagation Measurements, Third Year's Data and Final Report," GTE Laboratories Report TR-79-471.2, Waltham, MA.
- Nowland, W.L., R.L. Olsen and I.P. Shkarofsky, (1977), "Theoretical Relationship Between Rain Depolarization and Attenuation," Electronics Letters, Vol. 13, No. 22, pp 676-7.
- Ramat, P. (1980), "Propagation Oblique dans les Bandes de Frequences des 11 et 14 GHz," URSI Commission F Open Symposium, Lenoxville, Canada, May 1980.
- Rice, P.L. and N.R. Holmberg (1973), "Cumulative Time Statistics of Surface Point Rainfall Rates," IEEE Trans. Comm., Vol. COM-21 pp 1131-1136.
- Rogers, D. V. (1981), "Diversity- and Single-Site Radiometric Measurements of 12-GHz Rain Attenuation in Different Climates," IEEE Conference Publication No. 195, Internat. Conf. Ant. Prop., York, U.K., April 1981.
- Rogers, D. V. and G. Hyde (1979), "Diversity Measurements of 11.6 GHz Rain Attenuation at Etam and Lenox, West Virginia," COMSAT Tech. Rev., Vol. 9, No. 1, pp. 243-254.
- Rucker, F. (1980), "Simultaneous Propagation Measurements in the 12-GHz Band on the SIRIO and OTS Satellite Links," URSI Commission F Open Symposium, Lenoxville, Canada, May 1980.
- Rustako, A.J., Jr. (1979), "Measurement of Rain Attenuation and Depolarization of the CTS Satellite Beacon at Holmdel, New Jersey," 1979 USNC/URSI Meeting, June 18-22, Seattle WA (abstract).
- Vogel, W.J. (1979), "CTS Attenuation and Cross Polarization Measurements at 11.7 GHz," Univ. Texas Austin, Final Fpt., NASA Contract NAS5-22576.
- Vogel, W.J. (1982), "Measurement of Satellite Beacon Attenuation at 11.7, 1904, and 28.56 GHz and Radiometric Site Diversity at 13.6 GHz," Radio Science, Vol. 17, No. 6, pp. 1511-1520.

CHAPTER VI

PREDICTION TECHNIQUES

6.1 INTRODUCTION

6.1.1 Purpose

This chapter provides a guide to prediction methods and related propagation results for the evaluation of earth-space paths operating above 10 GHz. The topics covered are:

Gaseous Attenuation

Rain Attenuation

Cloud, Fog, Sand and Dust Attenuation

Signal Fluctuations and Low Angle Fading

Depolarization Effects

Bandwidth Coherence

Sky Noise

The techniques described here have been developed from recent ongoing NASA supported studies and from the relevant published literature. These techniques represent the state of knowledge of the adverse effects of the earth's atmosphere on reliable earth-space transmissions above 10 GHz.

This chapter provides propagation data in a format suitable for use by earth-space link system designers operating in the frequency range from 10 to 100 GHz. In this frequency range the troposphere can have a significant effect on the carrier-to-noise ratio of a propagating wave. Typically, the troposphere attenuates and depolarizes the carrier signal and adds broadband amplitude and

phase noise to the signal. The resulting carrier-to-noise ratio reduction reduces the allowable data rate for a given bit error rate (digital systems) and the quality of transmission (analog systems). In the most severe cases the medium will significantly attenuate the carrier and destroy the transmission capabilities of the link (termed a link outage). The frequency of occurrence and average outage time per year are usually of most interest to system designers. Propagation studies to date now allow the predictions to be made with a high degree of certainty and have developed means to reduce the frequency and length of these outages.

6.1.2 Organization of This Chapter

The remainder of this chapter is arranged in six relatively independent sections covering the key topics related to the interaction of the troposphere and earth-space propagation paths. Each section presents a description of selected techniques and provides sample calculations of the techniques applied to typical communications systems parameters. A guide to the sample calculations is given in Table 6.1-1.

6.1.3 Frequency Bands for Earth-Space Communication

Within the guidelines established by the International Telecommunication Union (ITU) for Region 2 (includes U.S. and Canada), the Federal Communications Commission (FCC) in the U.S. and the Department of Communications (DOC) in Canada regulate the earth-space frequency allocations. In most cases, the FCC and DOC regulations are more restrictive than the ITU regulations.

The services which operate via earth-space links are listed in Table 6.1-2. The definitions of each of these services are given in the ITU Radio Regulations. The specific frequency allocations for these services are relatively fixed, but modifications can be enacted at World Administrative Radio Conferences based on the proposals of ITU member countries.

Table 6.1-1. Guide to Sample Calculations

Paragraph Number	Description	Page Number
6.2.4	Relative humidity to water vapor density conversion	6-16
6.2.5	Gaseous Attenuation calculation	6-16
6.3.2.2	Cumulative rain attenuation distribution using the Global Model	6-29
6.3.2.4	Cumulative rain attenuation distribution using the CCIR Model	6-35
6.3.3.2	Cumulative rain attenuation distribution by distribution extension	6-41
6.3.5.1	Fade duration and return period	6-50
6.4.3.3	Estimation of fog attenuation	6-72
6.5.6.1	Variance of signal amplitude fluctuations	6-101
6.5.6.2	Phase and angle-of-arrival variations	6-103
6.5.6.3	Received signal gain reduction	6-103
6.6.2.1.1	CCIR Approximation for rain depolarization	6-106
6.6.3.3	CCIR estimate for ice depolarization	6-119
6.6.5	Prediction of depolarization statistics	6-122
6.7.3.2	Group delay and phase delay	6-131
6.8.3	Sky noise due to clear sky and rain	6-136
6.8.5	Sky noise due to clouds	6-139
6.9.2	Uplink Noise in Satellite Antenna	6-143

A review of the Radio Regulations indicates that most of the frequency spectrum above 10 GHz is assigned to the satellite services or the radio astronomy service. This does not mean that the FCC or DOC will utilize them as such, but it does highlight the potential for use of these frequency bands. Figure 6.1-1 shows those frequency segments not assigned for potential use by the services listed in Table 6.1-2 (ITU-1980).

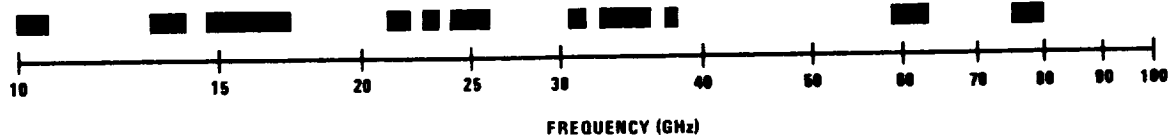


Figure 6.1-1. Frequencies Not Allocated Primarily for Earth-Space Transmissions in Region 2

Table 6.1-2. Telecommunication Services Utilizing Earth-Space Propagation Links

Fixed Satellite
Mobile Satellite
Aeronautical Mobile Satellite
Maritime Mobile Satellite
Land Mobile Satellite
Broadcasting Satellite
Radionavigation Satellite
Earth Exploration Satellite
Meteorological Satellite
Amateur Satellite
Standard Frequency Satellite
Space Research
Space Operations
Radio Astronomy

6.1.4 Other Propagation Effects Not Addressed in This Chapter

6.1.4.1 Ionospheric Effects. The ionosphere generally has a small effect on the propagation of radio waves in the 10 to 100 GHz range, whatever effects do exist (scintillation, absorption, variation in the angle of arrival, delay, and depolarization) arise due to the interaction of the radio wave with the free electrons, electron density irregularities and the earth's magnetic field. The density of electrons in the ionosphere varies as a function of geomagnetic latitude, diurnal cycle, yearly cycle, and solar cycle (among others). Fortunately, most U.S. ground station-satellite paths pass through the midlatitude electron density region, which is the most homogeneous region. This yields only a small effect on propagation. Canadian stations may be affected by the auroral region electron densities which are normally more irregular. A more complete discussion of the effects is included in Report 263-6 of CCIR Volume VI (1986a).

A mean vertical one-way attenuation for the ionosphere at 15 GHz for the daytime is typically 0.0002 dB (Millman-1958), the amplitude scintillations are generally not observable (Crane-1977) and the transit time delay increase over the free space propagation time delay is of the order of 1 nanosecond (Klobuchar-1973). Clearly for most systems operating above 10 GHz these numbers are sufficiently small that other system error budgets will be much larger than the ionospheric contributions.

The one ionospheric effect which might influence wide bandwidth systems operating above 10 GHz is phase dispersion. This topic is discussed in Section 6.7.

6.1.4.2 Tropospheric Delays. Highly accurate satellite range, range-rate and position-location systems will need to remove the propagation group delay effects introduced by the troposphere. Extremely high switching rate TDMA systems require these corrections. The effects arise primarily due to the oxygen and water vapor in the lower troposphere. Typical total additional

propagation delay errors have been measured to be of the order of 8 nanoseconds (Hopfield-1971).

Estimation techniques, based on the measurement of the surface pressure, temperature and relative humidity have been developed (Hopfield-1971, Bean and Dutton-1966, Segal and Barrington-1977) which can readily reduce this error to less than 1 nanosecond. In addition, algorithms for range (Marini-1972a) and range-rate (Marini-1972b) have been prepared to reduce tropospheric contributions to satellite tracking errors.

Since this topic is quite specialized and generally results in an additional one-way delay of less than 10 nanoseconds it is not addressed further in this report. An overview of this subject and additional references are available in CCIR Report 564-3 (1986b), and Flock, Slobin and Smith (1982).

6.2 PREDICTION OF GASEOUS ATTENUATION ON EARTH-SPACE PATHS

The mean attenuation of gases on earth-space paths in the 10 to 100 GHz frequency range has been theoretically modeled and experimentally measured. Above 20 GHz gaseous absorption can have a significant effect on a communication system design depending on the specific frequency of operation. Because of the large frequency dependence of the gaseous absorption, an earth-space communication system designer should avoid the high absorption frequency bands. Alternatively, designers of secure short-haul terrestrial systems can utilize these high attenuation frequency bands to provide system isolation.

6.2.1 Sources of Attenuation

In the frequency range from 10 to 100 GHz the water vapor absorption band centered at 22.235 GHz and the oxygen absorption lines extending from 53.5 to 65.2 GHz are the only significant contributors to gaseous attenuation. The next higher frequency absorption bands occur at 118.8 GHz due to oxygen and 183 GHz due to water vapor. The absorption lines are frequency broadened by

collisions at normal atmospheric pressures (low elevations) and sharpened at high altitudes. Thus the total attenuation due to gaseous absorption is ground station altitude dependent.

6.2.2 Gaseous Attenuation

6.2.2.1 One-Way Attenuation Values Versus Frequency. The Zenith one-way attenuation for a moderately humid atmosphere (7.5 g/m surface water vapor density) at various ground station altitudes (starting heights) above sea level is presented in Figure 6.2-1 and Table 6.2-1. These curves were computed (Crane and Blood, 1979) for temperate latitudes assuming the U.S. Standard Atmosphere, July, 45 N. latitude. The range of values indicated in Figure 6.2-1 refers to the peaks and valleys of the fine absorption lines. The range of values at greater starting heights (not shown) is nearly two orders of magnitude (Leibe-1975).

Table 6.2-1. Typical One-Way Clear Air Total Zenith Attenuation Values, A_c' (dB) (Mean Surface Conditions 21°C, 7.5 g/m³ H₂O; U.S. Std. Atmos. 45°N., July)

Frequency	ALTITUDE				
	0km*	0.5km	1.0km	2.0km	4.0km
10 GHZ	.053	.047	.042	.033	.02
15	.084	.071	.061	.044	.023
20	.28	.23	.18	.12	.05
30	.24	.19	.16	.10	.045
40	.37	.33	.29	.22	.135
80	1.30	1.08	.90	.62	.30
90	1.25	1.01	.81	.52	.22
100	1.41	1.14	.92	.59	.25

*1 km = 3281 feet

Figure 6.2-1 also shows two values for the standard deviation of the clear air zenith attenuation as a function of frequency. The larger value was calculated from 220 measured atmosphere profiles, spanning all seasons and geographical locations (Crane-1976). The smaller value applies after the mean surface temperature and humidity have been taken into account by making the corrections given below.

6.2.2.1.1 Dependence on Ground Station Altitude. The compensation for ground station elevation can be done to first order by linearly interpolating between the curves in Figure 6.2-1. The zenith one-way attenuation for typical ground station altitudes, found in this way, is tabulated in Table 6.2-1 for easy reference.

6.2.2.1.2 Dependence on Water Vapor Content. The water vapor content is the most variable component of the atmosphere. Therefore, for arid or humid regions, a correction should be made based on the expected mean values of water vapor content when utilizing frequencies between 10 and 50 GHz. This correction to the total zenith attenuation is linearly related to the mean local water vapor density at the surface p :

$$\Delta A_{c1} = b_p (\rho_0 - 7.5 \text{ g/m}^3) \quad (6.2-1)$$

where ΔA_{c1} is an additive correction to the zenith clear air attenuation (given by Figure 6.2-1 and Table 6.2-1) that accounts for the difference between the mean local surface water vapor density and 7.5 g/m³. The coefficient b_p is frequency dependent and is given by Figure 6.2-2 and Table 6.2-2 (Crane and Blood, 1979). The accuracy of this correction factor is greatest for sea level altitude.

The US and Canadian weather services generally measure relative humidity or the partial pressure of water vapor. The technique for converting these values to ρ_0 is given in Section 6.2.5.

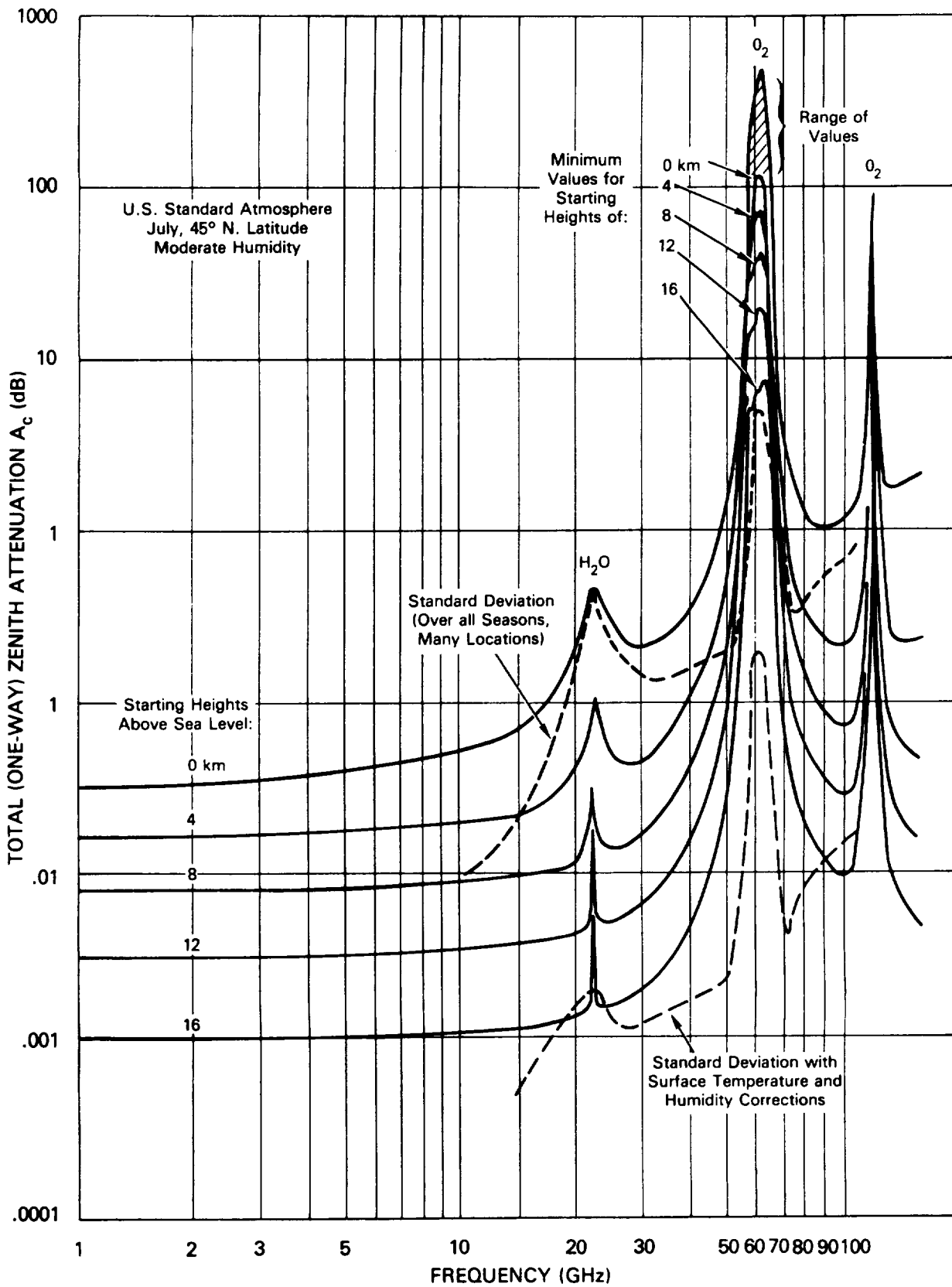


Figure 6.2-1. Total Zenith Attenuation Versus Frequency

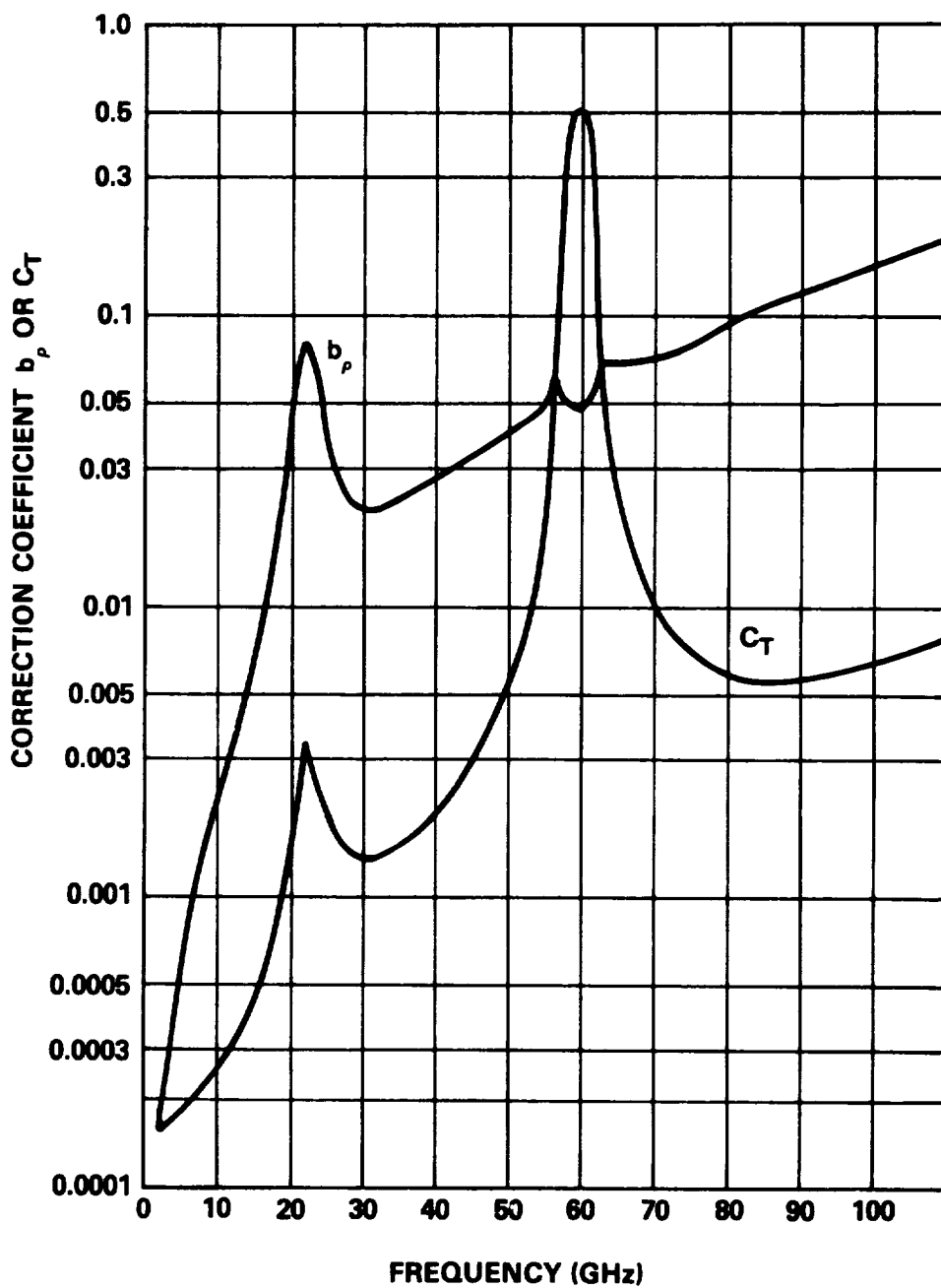


Figure 6.2-2. Water Vapor Density and Temperature Correction Coefficients

Table 6.2-2. Water Vapor Density and Temperature Correction Coefficients

Frequency (GHz)	Water Vapor Density Correction b_p	Temperature Correction C_T
10	2.10×10^{-3}	2.60×10^{-4}
15	6.34×10^{-3}	4.55×10^{-4}
20	3.46×10^{-2}	1.55×10^{-3}
30	2.37×10^{-2}	1.33×10^{-3}
40	2.75×10^{-2}	1.97×10^{-3}
80	9.59×10^{-2}	5.86×10^{-3}
90	1.22×10^{-1}	5.74×10^{-3}
100	1.50×10^{-1}	6.30×10^{-3}

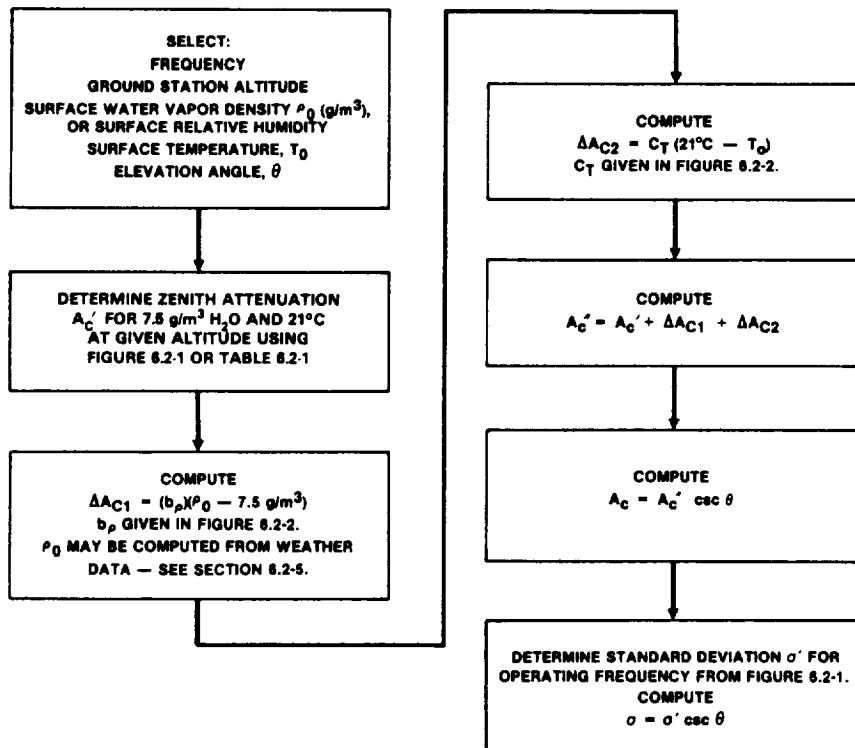


Figure 6.2-3. Technique for Computing Mean Clean Air Attenuation

6.2.2.1.3 Dependence on Surface Temperature. The mean surface temperature T_0 also affects the total attenuation. This relation (Crane and Blood, 1979) is also linear:

$$\Delta A_{c2} = c_T (21^\circ - T_0) \quad (6.2-2)$$

where T_0 is mean local surface temperature in $^\circ\text{C}$.

A_{c2} is an additive correction to the zenith clear air attenuation. Frequency dependent values for c_T are given in Figure 6.2-2 and Table 6.2-2. As with water vapor correction, the accuracy of this factor decreases with altitude.

6.2.2.1.4 Dependence on Elevation Angle. For elevation angles greater than 5 or 6 degrees, the zenith clear air attenuation A_c is multiplied by the cosecant of the elevation angle θ . The total attenuation for arbitrary elevation angle is

$$A_c = A_c' \csc \theta \quad (6.2-3)$$

The standard deviation (see Figure 6.2-1) also is multiplied by the $\csc \theta$ for arbitrary elevation angles.

6.2.3 Estimation Procedure For Gaseous Attenuation

The CCIR has developed an approximate method to calculate the median gaseous absorption loss expected for a given value of surface water vapor density, (CCIR-1986a). The method is applicable up to 350 GHz, except for the high oxygen absorption bands.

Input parameters required for the calculation are:

f - frequency, in GHz

θ - path elevation angle, in degrees,

h_s - height above mean sea level of the earth terminal, in km,
and

ρ_w - water vapor density at the surface, for the location of
interest, in g/m^3 .

If ρ_w is not available from local weather services, representative median values can be obtained from CCIR Report 563-3 (CCIR-1986c).

The specific attenuation at the surface for dry air ($P = 1013$ mb) is then determined from:

$$\gamma_o = \left[7.19 \times 10^{-3} + \frac{6.09}{f^2 + 0.227} + \frac{4.81}{(f - 57)^2 + 1.50} \right] f^2 \times 10^{-4} \text{ dB/km}$$

for $f < 57$ GHz (6.2-4)

$$\gamma_o = \left[3.79 \times 10^{-7} f + \frac{0.265}{(f - 63)^2 + 1.59} + \frac{0.028}{(f - 118)^2 + 1.47} \right] \times \frac{1}{(f^2 + 198)^2 \times 10^{-3}} \text{ dB/km}$$

for $63 < f < 350$ GHz

[The application of the above relationships in the high oxygen absorption bands (50-57 GHz and 63-70 GHz) may introduce errors of up to 15%. More exact relationships are given in CCIR Report 719 (CCIR-1986d)].

The specific attenuation for water vapor, γ_w , is found from:

$$\gamma_w = \left[0.067 + \frac{3}{(f - 22.3)^2 + 7.3} + \frac{9}{(f - 183.3)^2 + 6} + \frac{4.3}{(f - 323.8)^2 + 10} \right] f^2 \rho_w \times 10^{-4} \text{ dB/km}$$

for $f < 350$ GHz (6.2-5)

The above expressions are for an assumed surface air temperature of 15°C. corrections for other temperatures will be described later. Also, the above results are accurate for water vapor densities less than 12 g/m³. [For higher water vapor density values, see CCIR Report 719 (CCIR-1986d), and the following.]

An algorithm for the specific attenuation of water vapor which includes a quadratic dependence on water vapor density and allows

values of water vapor densities $>12 \text{ g/m}^3$, has been proposed by Gibbons (1986) and provisionally accepted by the CCIR (1988),

$$\gamma_w = \left[0.050 + 0.0021\rho_w + \frac{3.6}{(f - 22.2)^2 + 8.5} + \frac{10.6}{(f - 183.3)^2 + 9.0} + \frac{8.9}{(f - 325.4)^2 + 26.3} \right] f^2 \rho_w 10^{-4} \text{ dB/km} \quad (6.2-6)$$

for $T = 15^\circ\text{C}$ and $f < 350 \text{ GHz}$.

Gibbons finds Eq. (6.2-6) to be valid within about $\pm 15\%$ over the range of ρ_w from 0 to 50 g/m^3 . However, in applying Eq. (6.2-6) with water vapor densities greater than 12 g/m^3 it is important to remember that the water vapor density may not exceed the saturation value ρ_s at the temperature considered. This saturation value may be expressed as (Gibbons, 1986),

$$\rho_s = 17.4 \left(\frac{300}{T} \right)^6 10^{\left(10 - \frac{2950.2}{T} \right)} \text{ g/m}^3 \quad (6.2-7)$$

where T is the temperature in $^\circ\text{K}$.

For temperatures in the range -20°C to $+40^\circ\text{C}$ Gibbons proposes a temperature dependence of -1.0% per $^\circ\text{C}$ for dry air in the window regions between absorption lines and -0.6% per $^\circ\text{C}$ for water vapor. The correction factors are therefore

$$\gamma_o = \gamma_o(15^\circ\text{C}) [1 - 0.01(T_o - 15)] \quad (6.2-8)$$

$$\gamma_w = \gamma_w(15^\circ\text{C}) [1 - 0.006(T_o - 15)] \quad (6.2-9)$$

where T_o is the surface temperature in $^\circ\text{C}$.

The equivalent heights for oxygen, h_o , and water vapor, h_w , are determined from:

$$h_o = 6 \quad \text{km} \quad \text{for } f < 57 \text{ GHz} \quad (6.2-10)$$

$$h_o = 6 + \frac{40}{(f - 118.7)^2 + 1} \quad \text{km} \quad \text{for } 63 < f < 350 \text{ GHz}$$

$$h_w = \left[2.2 + \frac{3}{(f - 22.3)^2 + 3} + \frac{1}{(f - 183.3)^2 + 1} + \frac{1}{(f - 323.8)^2 + 1} \right] \quad \text{km} \quad (6.2-11)$$

for $f < 350 \text{ GHz}$

The total slant path gaseous attenuation through the atmosphere, A_g , is then found.

For $\theta \geq 10^\circ$:

$$A_g = \frac{\gamma_o h_o e^{-\frac{h_s}{h_o}} + \gamma_w h_w}{\sin \theta} \quad \text{dB} \quad (6.2-12)$$

For $\theta < 10^\circ$:

$$A_g = \frac{\gamma_o h_o}{g(h_o)} + \frac{\gamma_w h_w}{g(h_w)} \quad \text{dB} \quad (6.2-13)$$

with

$$g(h) = 0.661x + 0.339 \sqrt{x^2 + \frac{h}{1545.5}} \quad (6.2-14)$$

$$x = \sqrt{\sin^2 \theta + \frac{h_s}{4250}} \quad (6.2-15)$$

where h is replaced by h_o or h_w as appropriate.

The above procedure does not account for contributions from trace gases. These contributions are negligible except in cases of very low water vapor densities ($\leq 1 \text{ g/m}^3$) at frequencies above about 70 GHz.

6.2.4 Conversion of Relative Humidity to Water Vapor Density

The surface water vapor density ρ_o (g/m^3) at a given surface temperature T_o may be found from the ideal gas law

$$\rho_o = (\text{R.H.}) e_s / R_w (T_o + 373) \quad (6.2-16)$$

where R.H. is the relative humidity, e_s (N/m^2) is the saturated partial pressure of water vapor corresponding to the surface temperature T_o ($^{\circ}\text{C}$) and $R_w = 461 \text{ joule/kgK} = 0.461 \text{ joule/gK}$. A plot of e_s in various units is given in Figure 6.2-4. For example, with

$$\text{R.H.} = 50\% = 0.5$$

$$T_o = 20^{\circ}\text{C}$$

$$e_s \approx 2400 \text{ n/m}^2 \text{ at } 20^{\circ}\text{C} \text{ from Figure 6.2-4}$$

then

$$\rho_o = 8.9 \text{ g/m}^3.$$

The relative humidity corresponding to 7.5 g/m^3 at 20°C (68°F) is $\text{R.H.} = 0.42 = 42\%$.

6.2.5 A Sample Calculation for Gaseous Attenuation

This section presents an example calculation for the total path gaseous attenuation, using the CCIR procedure described in Section 6.2.3.

Assume the following input parameters for a K_a band link:

Frequency, $f = 29.3 \text{ GHz}$

Path Elevation Angle, $\theta = 38^{\circ}$

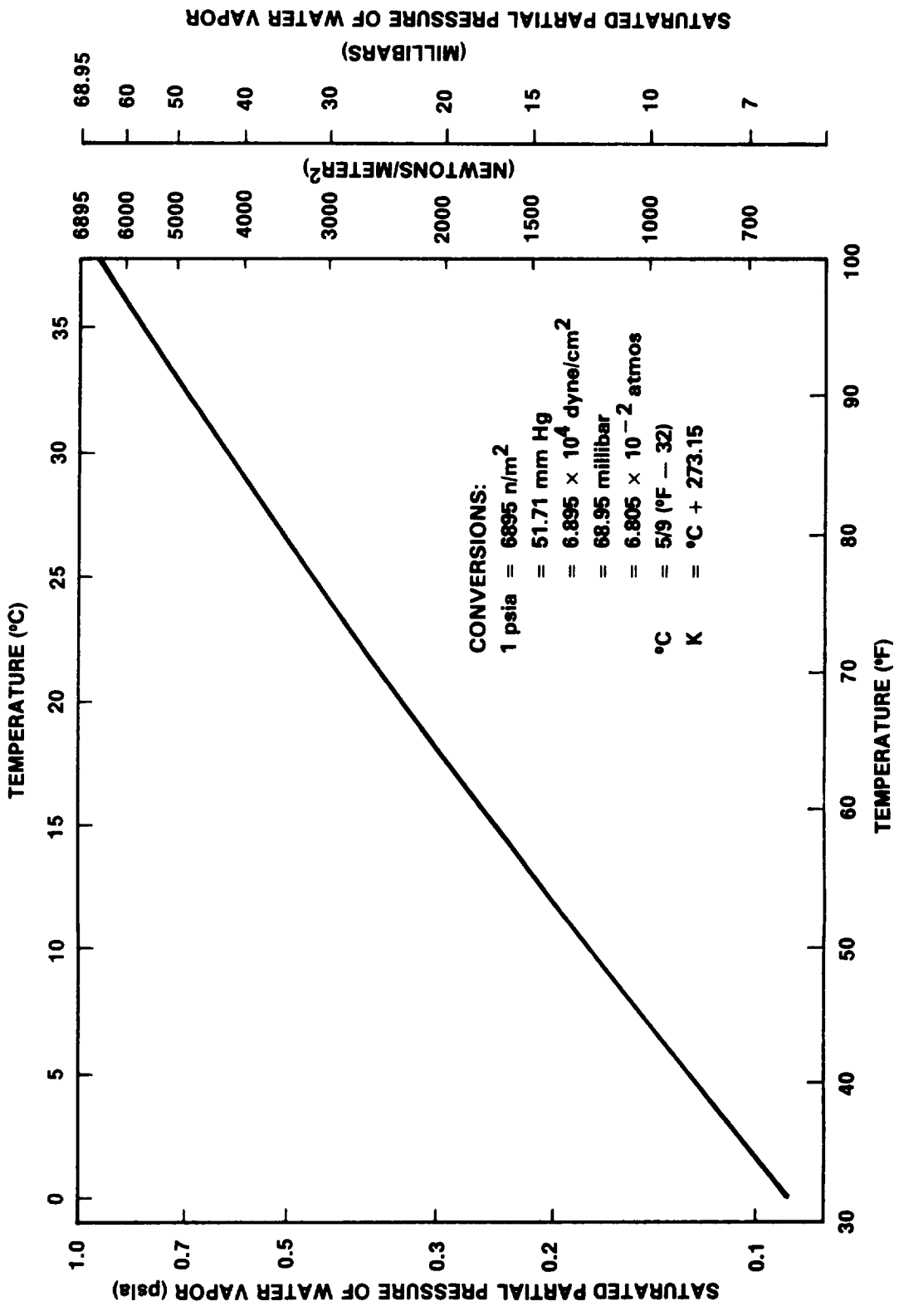


Figure 6.2-4. The Saturated Partial Pressure of Water Vapor Versus Temperature

Height above mean sea level, $h_s = .2$ km

Surface water vapor density, $\rho_w = 7.5$ g/m³

Surface temperature, $T_o = 20^\circ\text{C}$

Step 1. Calculate the specific attenuation coefficients for oxygen, γ_o , and for water vapor, γ_w , from Equations (6.2-4) and (6.2-6) respectively;

$$\gamma_o = 0.01763 \text{ dB/km} \quad (\text{from } f < 57 \text{ GHz relationship})$$

$$\gamma_w = 0.0777 \text{ dB/km}$$

Step 2. Correct γ_o and γ_w for 20°C , using equations (6.2-8) and (6.2-9) respectively;

$$\gamma_o = 0.01763 [1 - 0.01(20 - 15)] = 0.01675 \text{ dB/Km}$$

$$\gamma_w = 0.0777 [1 - 0.006(20 - 15)] = 0.07537 \text{ dB/Km}$$

Step 3. Calculate the equivalent heights for oxygen, h_o , and for water vapor, h_w , from Equations (6.2-10) and (6.2-11) respectively;

$$h_o = 6 \text{ km}$$

$$h_w = 2.258 \text{ km}$$

Step 4. The total slant path gaseous attenuation is determined from Equation (6.2-8);

$$\begin{aligned} A_g &= [(0.018) (6)e^{-(0.2)/(6)} + (0.078) (2.258)]/\sin (38) \\ &= 0.1579 + 0.2764 = 0.4343 \text{ dB} \end{aligned}$$

The results show that the contribution from oxygen absorption is 0.1579 dB, and the contribution from water vapor is 0.2764 dB, for a total of 0.4343 dB.

.3 PREDICTION OF CUMULATIVE STATISTICS FOR RAIN ATTENUATION

.3.1 General Approaches

.3.1.1 Introduction to Cumulative Statistics. Cumulative statistics give an estimate of the total time, over a long period, that rain attenuation or rate can be expected to exceed a given amount. They are normally presented with parameter values (rain rate or attenuation) along the abscissa and the total percentage of time that the parameter value was exceeded (the "exceedance time") along the ordinate. The ordinate normally has a logarithmic scale to most clearly show the exceedance times for large values of the parameter, which are often most important. Usually, the percentage exceedance time is interpreted as a probability and the statistical exceedance curve is taken to be a cumulative probability distribution function. Because of the general periodicity of meteorological phenomena, cumulative statistics covering several full years, or like periods of several successive years, are the most directly useful. (A technique exists, however, for extending statistics to apply to periods greater than those actually covered. This is described in Section 6.3.4.) Statistics covering single years or periods would be expected to exhibit large fluctuations from year to year, because of the great variability of the weather. In most geographic regions, data covering ten years or more is usually required to develop stable and reliable statistics.

Cumulative rain rate or attenuation exceedance statistics alone give no information about the frequency and duration of the periods of exceedance. Rather, only the total time is given. The nature of rain attenuation, however, is such that the exceedance periods are usually on the order of minutes in length. Different phenomena besides rain give rise to attenuation variations occurring on a time scale of seconds. These amplitude scintillations, as they are called, are not considered in this section, but are discussed in Section 6.5.

6.3.1.2 Procedures for Calculating Cumulative Rain Attenuation Statistics. The system designer needs reliable cumulative attenuation statistics to realistically trade off link margins, availability, siting and other factors. Needless to say, applicable millimeter-wave attenuation measurements spanning many years seldom exist. It is therefore necessary to estimate statistics, using whatever information is available.

An estimate of the rain attenuation cumulative statistics may be determined in several ways. The optimum way depends on the amount of rain and/or attenuation data available, and on the level of sophistication desired. However, it is recommended that the simplest calculations be carried out first to provide an approximation for the statistics and also to act as a check on the results of more sophisticated calculations.

The flow charts in Figures 6.3-1, 6.3-7 and 6.3-13 will assist in applying selected calculation procedures. The steps are numbered sequentially to allow easy reference with the accompanying discussions in Sections 6.3.2, 6.3.3 and 6.3.4. These are the procedures given:

- Analytical Estimates using the Global Model (Section 6.3.2, Figure 6.3-1). Requires only Earth station location, elevation angle, and frequency.
- Analytical Estimates using the CCIR Model (Section 6.3.2, Figure 6.3-7). Requires only Earth station location, elevation angle, and frequency.
- Estimates Given Rain Rate Statistics (Section 6.3.3, Figure 6.3-1). Requires cumulative rain rate exceedance statistics for vicinity of the Earth station location, elevation angle, and frequency.
- Estimates Given Rain Rate and Attenuation Statistics (Section 6.3.4, Figure 6.3-13). Requires attenuation statistics which

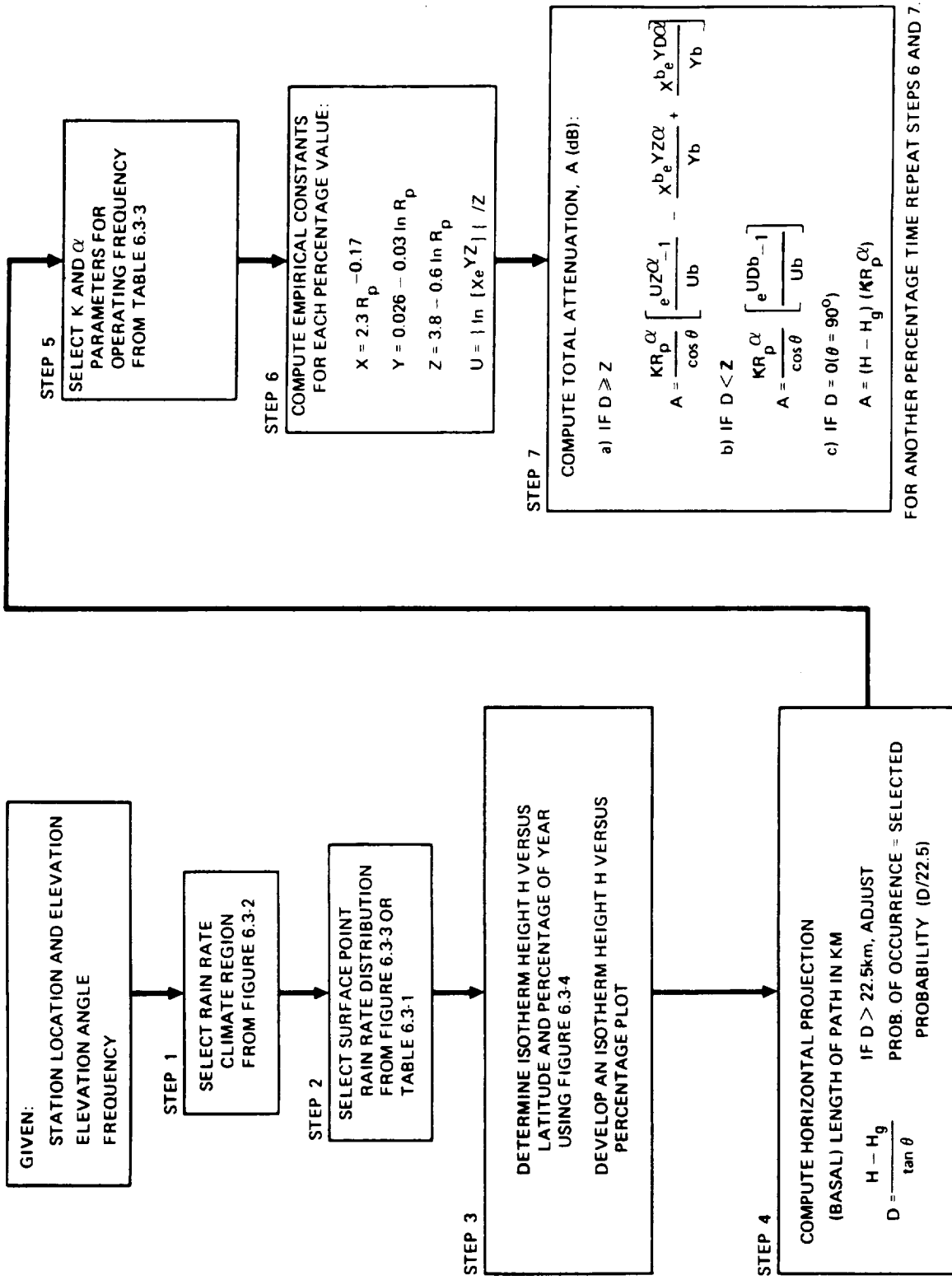


Figure 6.3-1. Analytic Estimate Procedure for Cumulative Rain Rate and Attenuation Statistics Using the Global Model

may be for frequency and elevation angle different from those needed.

6.3.1.3 Other Considerations. Generally the yearly cumulative statistics are desired. The worst-month or 30-day statistics are sometimes also needed, but are not derivable from the data presented here. Worst 30-day statistics are discussed in Section 6.3.7.

The attenuation events due to liquid rain only are considered here. Liquid rain is the dominate attenuation-producing precipitation because its specific attenuation is considerably higher than snow, ice, fog, etc. The contribution of these other hydrometeors is estimated in later sections.

The cumulative statistics are appropriate for earth-space paths for geostationary or near-geostationary satellites with relatively stable orbital positions. The modifications required to develop statistics for low-orbiting satellites is unclear because of the possibly nonuniform spatial distribution of rain events arising from local topography (lakes, mountains, etc.). However, if one assumes these effects are of second-order, low orbiting satellites may simply be considered to have time-dependent elevation angles.

6.3.2 Analytic Estimates of Rain Attenuation from Location and Link Parameters

The following analytic estimation techniques provide reasonably precise estimates of rain attenuation statistics. The first technique is based on the modified Global Prediction Model (Crane and Blood- 1979, Crane- 1980, 1980a). Only parts of the model relevant to the contiguous US and Canada, and elevation angles greater than 10° , are presented here. The second technique uses the CCIR Model and is perhaps the simplest prediction approach. Example applications of both techniques are given. The analytical developments for the global model and the CCIR model are presented in Sections 3.4 and 3.6, respectively.

The models require the following inputs:

- a) Ground station latitude, longitude and height above mean sea level
- b) The earth-space path elevation angle
- c) The operating frequency

6.3.2.1 Global Model Rain Attenuation Prediction Technique. Figure 6.3-1 gives the step-by-step procedure for applying the Global Model. The steps are described in detail below.

Step 1 - At the Earth terminal's geographic latitude and longitude, obtain the appropriate climate region using Figure 6.3-2. For locations outside the Continental U.S. and Canada, see Section 3.4.1. If long term rain rate statistics are available for the location of the ground terminal, they should be used instead of the model distribution functions and the procedure of Section 6.3.3 should be employed.

Step 2 - Select probabilities of exceedance (P) covering the range of interest (e.g., .01, .1 or 1%). Obtain the terminal point rain rate R (mm/hour) corresponding to the selected values of P using Figure 6.3.3, Table 6.3-1 or long term measured values if available.

Step 3 - For an Earth-to-space link through the entire atmosphere, obtain the rain layer height from the height of the 0° isotherm (melting layer) H_0 at the path latitude (Figure 6.3-4). The heights will vary correspondingly with the probabilities of exceedance, P. To interpolate for values of P not given, plot H_0 (P) vs Log P and sketch a best-fit curve.

Step 4 - Obtain the horizontal path projection D of the oblique path through the rain volume:

$$D = \frac{H_0 - H_g}{\tan\theta} ; \theta \geq 10^\circ \quad (6.3-1)$$

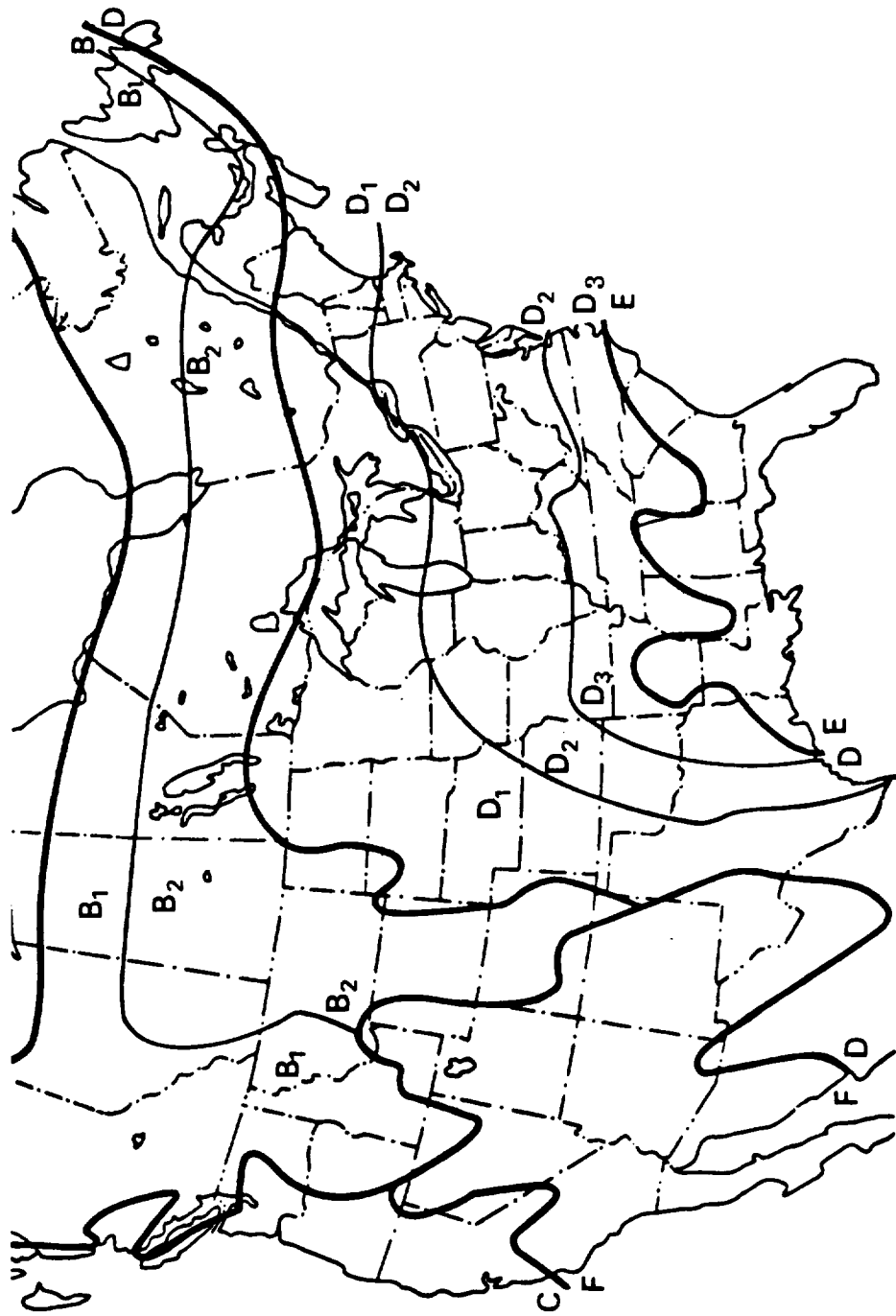


Figure 6.3-2. Rain Rate Climate Regions for the Continental U.S. and Southern Canada

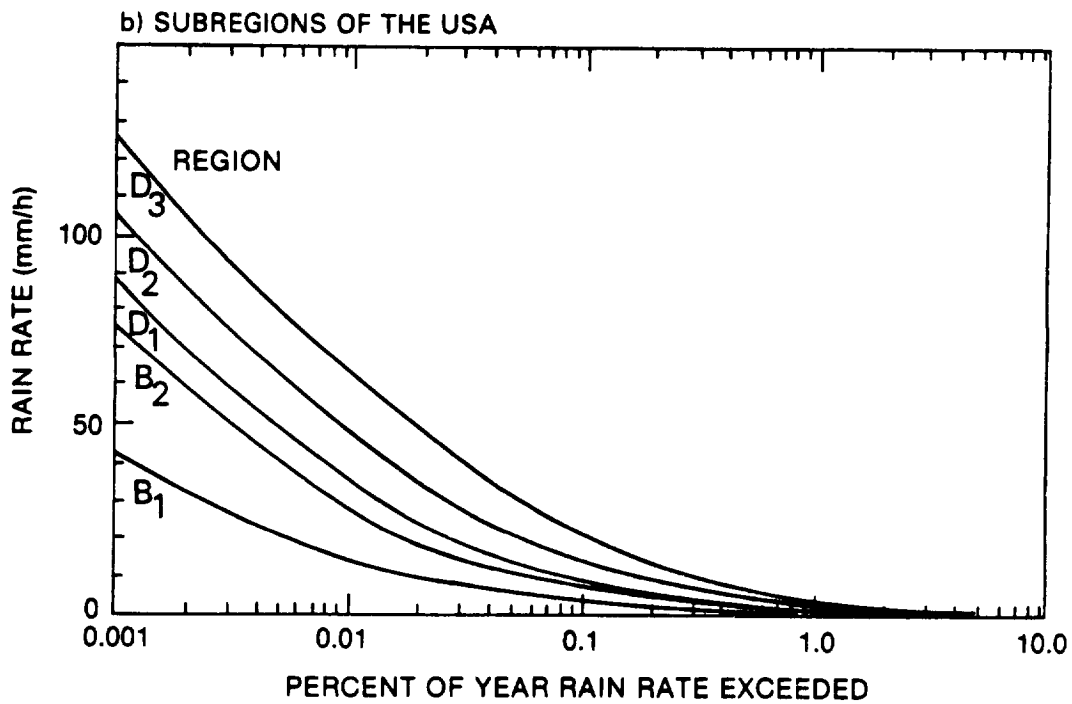
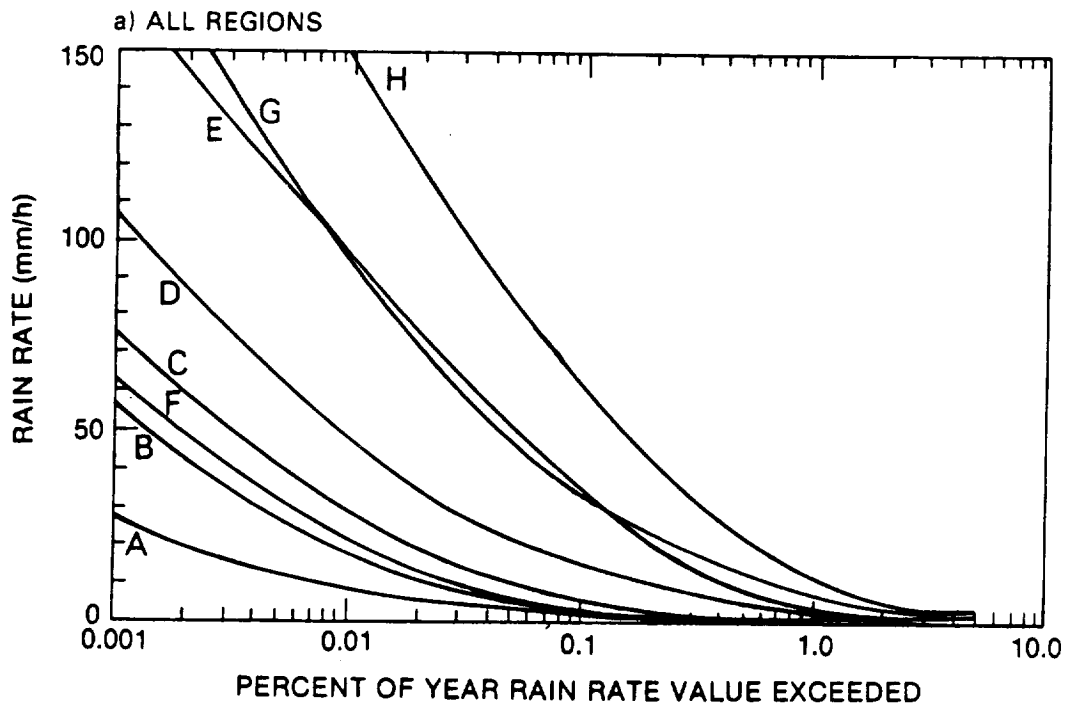


Figure 6.3-3. Point Rain Rate Distributions as a Function of Percent of Year Exceeded

Table 6.3-1. Point Rain Rate Distribution Values (mm/hr) Versus Percent of Year Rain Rate is Exceeded

Percent of Year	RAIN CLIMATE REGION													Minutes per Year	Hours per Year
	A	B ₁	B	B ₂	C	D ₁	D=D ₂	D ₃	E	F	G	H			
0.001	28.5	45	57.5	70	78	90	108	126	165	66	185	253	5.26	0.09	
0.002	21	34	44	54	62	72	89	106	144	51	157	220.5	10.5	0.18	
0.005	13.5	22	28.5	35	41	50	64.5	80.5	118	34	120.5	178	26.3	0.44	
0.01	10.0	15.5	19.5	23.5	28	35.5	49	63	98	23	94	147	52.6	0.88	
0.02	7.0	11.0	13.5	16	18	24	35	48	78	15	72	119	105	1.75	
0.05	4.0	6.4	8.0	9.5	11	14.5	22	32	52	8.3	47	86.5	263	4.38	
0.1	2.5	4.2	5.2	6.1	7.2	9.8	14.5	22	35	5.2	32	64	526	8.77	
0.2	1.5	2.8	3.4	4.0	4.8	6.4	9.5	14.5	21	3.1	21.8	43.5	1052	17.5	
0.5	0.7	1.5	1.9	2.3	2.7	3.6	5.2	7.8	10.6	1.4	12.2	22.5	2630	43.8	
1.0	0.4	1.0	1.3	1.5	1.8	2.2	3.0	4.7	6.0	0.7	8.0	12.0	5260	87.7	
2.0	0.1	0.5	0.7	0.8	1.1	1.2	1.5	1.9	2.9	0.2	5.0	5.2	10520	175	
5.0	0.0	0.2	0.3	0.3	0.5	0.0	0.0	0.0	0.5	0.0	1.8	1.2	26298	438	

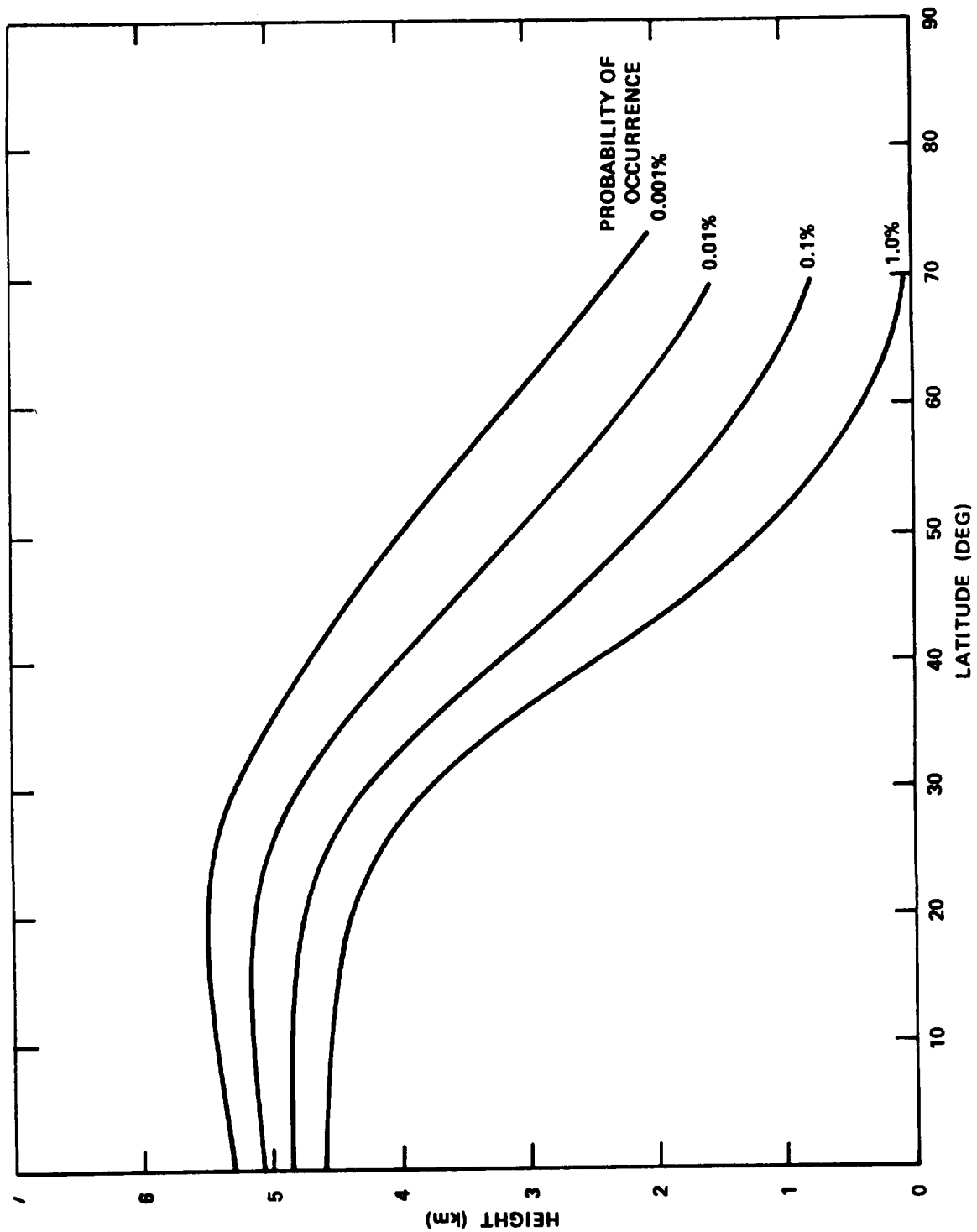


Figure 6.3-4. Latitude Dependence of the Rain Layer 0°C Isotherm Height (H) as a Function of Probability of Occurrence

$H_o = H_o(P)$ = height (km) of isotherm for probability P

H_g = height of ground terminal (km)

θ = path elevation angle

Test $D \leq 22.5$ km; if true, proceed to the next step. If $D \geq 22.5$ km, the path is assumed to have the same attenuation value as for a 22.5 km path but the probability of exceedance is adjusted by the ratio of 22.5 km to the path length:

$$\text{New probability of exceedance, } P' = P \left(\frac{22.5 \text{ km}}{D} \right) \quad (6.3-2)$$

where D = path length projected on surface. This correction accounts for the effects of traversing multiple rain cells at low elevation angles.

Step 5 - Obtain the specific attenuation coefficients, k and α , at the frequency and polarization angle of interest, from Table 6.3-3. For frequencies not in the table, use logarithmic interpolation for K and linear interpolation for α . The subscript H columns are for horizontal linear polarization, and the subscript V columns are for vertical linear polarization. [For polarization tilt angles other than horizontal or vertical, use the relationships on Figure 6.3-6, Step 4, to obtain K and α].

Step 6 - Using the R_p values corresponding to each exceedance probability of interest, calculate the empirical constants X , Y , Z and U using

$$X = 2.3 R_p^{-0.17} \quad (6.3-4)$$

$$Y = 0.026 - 0.03 \ln R_p \quad (6.3-5)$$

$$Z = 3.8 - 0.7 \ln R_p \quad (6.3-6)$$

$$U = [\ln(Xe^{YZ})]/z \quad (6.3-7)$$

Step 7 - If $Z \leq D$, compute the total attenuation due to rain exceeded for P % of the time using

$$A = \frac{k R_p^\alpha}{\cos \theta} \left[\frac{e^{UZ\alpha} - 1}{U\alpha} - \frac{X^\alpha e^{YZ\alpha}}{Y\alpha} + \frac{X^\alpha e^{YD\alpha}}{Y\alpha} \right]; \theta \geq 10^\circ \quad (6.3-8)$$

where A = Total path attenuation due to rain (dB)

k, α = parameters relating the specific attenuation to rain rate (from Step 5).

R_p = point rain rate

θ = elevation angle of path

D = horizontal path projection length (from step 4)

If $D < Z$,

$$A = \frac{k R_p^\alpha}{\cos \theta} \left[\frac{e^{UD\alpha} - 1}{U\alpha} \right] \quad (6.3-9)$$

If $D = 0, \theta = 90^\circ$,

$$A = (H - H_g)(K R_p^\alpha) \quad (6.3-10)$$

This procedure results in an analytical estimate for the attenuation, A, exceeded for P percent of an average year. The use of a programmable calculator or computer for performing these calculations is highly recommended.

6.3.2.2 A Sample Calculation for the Global Model. The following information is given for the Rosman, NC Earth Station operating with the ATS-6 satellite.

Earth station latitude :. 35°N
 Earth station longitude: 277°E.
 Earth station elevation: 0.9 km

Antenna elevation Angle: 47°

Operating frequency: 20 GHz

We wish to find an analytic estimate for the cumulative attenuation statistics using the procedure of Figure 6.3-1.

1. Select rain rate climate region for Rosman, NC:

From Figure 6.3-2, Rosman is located in region D₃.

2. Select surface point rain rate distribution:

From Table 6.3-1, region D₃ has the following distribution:

<u>%</u>	<u>R_p</u>
0.01	63
0.02	48
0.05	32
0.10	22
0.20	14.5
0.50	7.8
1.0	4.7

3. Determine isotherm height H:

From Figure 6.3-4, the following isotherm height estimates apply at 35° latitude.

<u>%</u>	<u>H</u>
0.01	4.4 km
0.1	3.75
1.0	3.2

By plotting these, the following additional points may be interpolated

0.02	4.2
0.05	3.95
0.2	3.55
0.5	3.3

4. Compute D:

Using $\theta = 47^\circ$ and $H_g = 0.9$ km, we obtain

<u>z</u>	<u>D</u>
0.01	3.25 km
0.02	3.1
0.05	2.85
0.1	2.65
0.2	2.45
0.5	2.25
1.0	2.15

5. Select K and α :

The specific attenuation coefficients, K and α are selected from Table 6.3-3 at 20 GHz, horizontal polarization.

$$K = 0.0751$$

$$\alpha = 1.10$$

6. Compute empirical constants:

For example,

<u>z</u>	<u>X</u>	<u>Y</u>	<u>Z</u>	<u>U</u>
0.1	1.36	-0.067	1.95	0.091
0.2	1.46	-0.054	2.20	0.118

0.5 1.62 -0.036 2.57 0.153

7. Compute attenuation, A:

We note from step 6 that at 0.2%, D is greater than Z. This also holds for percentages less than 0.1%. Thus the formula of Step 7 (a) is used to find the attenuation for $\% \leq 0.1$.

For $\% \geq 0.5$, D is less than Z, so the formula of Step 7 (b) applies. The attenuation values found in this way are plotted versus percentage exceedance in Figure 6.3-5. The figure includes statistics derived from 20 GHz attenuation measurements made at Rosman with the ATS-6 over a 6-month period.

6.3.2.3 CCIR Model Rain Attenuation Prediction Technique

This section presents the step by step procedure for application of the CCIR rain attenuation prediction model, described in detail in Section 3.6. The procedure is outlined in Figure 6.3-6.

Step 1 Obtain the rain rate, $R_{0.01}$, exceeded for 0.01% of an average year for the ground terminal location of interest. If this information is not available from local data sources, an estimate can be obtained by selecting the climate zone of the ground terminal location from Figure 6.3-7, and the corresponding rain rate value for that climate zone from Table 6.3-2. (For locations not found on Figure 6.3-7, see Figures 3.6-1 and 3.6-2).

[Important Note: The CCIR rain climate zones are not the same as the climate regions of the Global Model described earlier.]

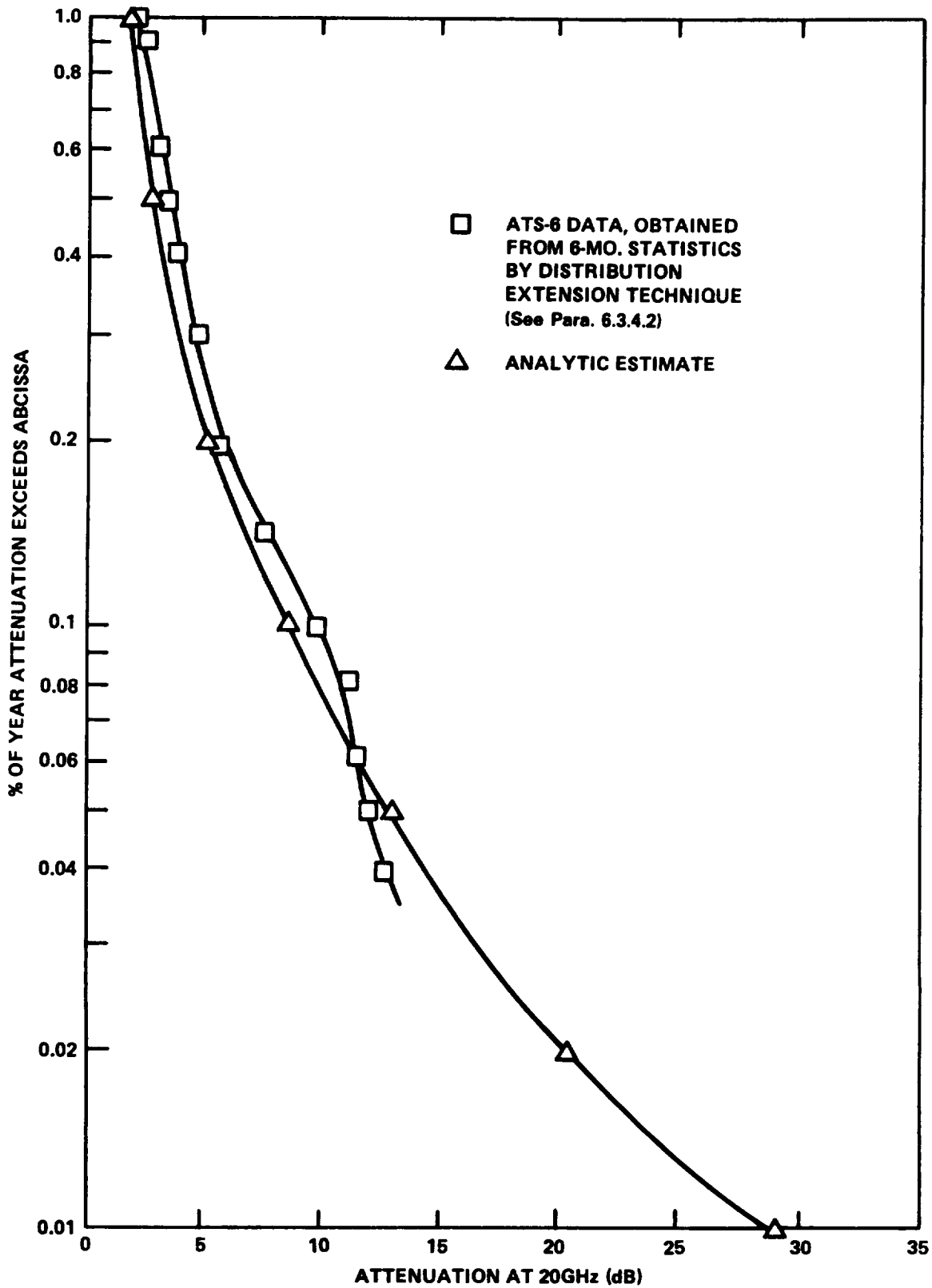


Figure 6.3-5. Analytic Attenuation Estimate and Actual Measurements

Table 6.3-2. Rain Rates Exceeded for 0.01% of the Time

Climate	A	B	C	D	E	F	G	H	J	K	L	M	N	P
Rate	8	12	15	19	22	28	30	32	35	42	60	63	95	145

Step 2 Determine the effective rain height, h_r , from;

$$\begin{aligned}
 h_r &= 4.0 & 0 < \phi < 36^\circ \\
 &= 4.0 - 0.075 (\phi - 36) & \phi \geq 36^\circ
 \end{aligned}
 \tag{6.3-11}$$

where ϕ is the latitude of the ground station, in degrees N or S.

Step 3 Calculate the slant path length, L_s , horizontal projection, L_G , and reduction factor, r_p , from:

For $\Theta \geq 5^\circ$,

$$L_s = (h_r - h_o) / \sin (\Theta) \tag{6.3-12}$$

$$L_G = L_s \cos (\Theta) \tag{6.3-13}$$

$$r_p = \frac{1}{1 + 0.045L_G} \tag{6.3-14}$$

where Θ is the elevation angle to the satellite, in degrees, and h_o is the height above mean sea level of the ground terminal location, in km. (For elevation angles less than 5° , see Section 3.6).

Step 4 Obtain the specific attenuation coefficients, K and α , at the frequency and polarization angle of interest from Table 6.3-3. For frequencies not on the table, use logarithmic interpolation for K and linear interpolation for α . For polarization tilt angles other than linear horizontal or vertical, use the relationships on Figure 6.3-6, Step 4, to obtain K and α .

Step 5 Calculate the attenuation exceeded for 0.01% of an average year from;

$$A_{0.01} = K R_{0.01}^\alpha L_s r_p \tag{6.3-15}$$

Step 6 Calculate the attenuation exceeded for other percentage values of an average year from:

$$A_p = 0.12 A_{0.01} p^{-(0.546 + 0.043 \log p)} \quad (6.3-16)$$

This relationship is valid for annual percentages from 0.001% to 1.0%.

6.3.2.4 Sample Calculation for the CCIR Model

In this section the CCIR model is applied to a specific ground terminal case. Consider a terminal located at Greenbelt, MD., at a latitude of 38°N, and elevation above sea level of 0.2 km. The characteristics of the link are as follows:

Frequency: 11.7 GHz

Elevation Angle: 29°

Polarization: Circular

Step 1 Figure 6.3-7 indicates that the terminal is in climate zone K, with a corresponding $R_{0.01}$ of 42 mm/h (Table 6.3-2).

Step 2 The effective rain height, from Eq (6.3-11), is

$$h_r = 4.0 - 0.075(38 - 36) = 3.85$$

Step 3 The slant path length, horizontal projection, and reduction factor are determined from Eq.'s (6.3-12, -13, -14) respectively;

$$L_s = (3.85 - 0.2) / \sin(29^\circ) = 7.53$$

$$L_G = (7.53) \cos(29^\circ) = 6.58$$

$$r_p = 1 / [1 + (0.045)(6.58)] = 0.771$$

Step 4 The specific attenuation coefficients are determined by interpolation from Table 6.3-3, with a polarizaiton tilt angle of 45° (circular polarization);

$$K = 0.0163, \quad \alpha = 1.2175$$

Step 5 The attenuation exceeded for 0.01% of an average year, from Eq. (6.3-15), is;

$$\begin{aligned} A_{0.01} &= (0.0163)(42)^{1.2175}(7.53)(0.771) \\ &= 8.96 \text{ dB} \end{aligned}$$

Step 6 The attenuation exceeded for other percentages is then determined from Eq. (3.6-16);

<u>%</u>	<u>Attenuation (dB)</u>
1.0	1.08
0.5	1.56
0.3	2.02
0.1	3.42
0.05	4.67
0.03	5.80
0.01	8.96
0.005	11.48
0.003	13.65
0.001	19.16

Figure 6.3-8 shows a plot of the resulting attenuation prediction distribution, compared with three years of measured distributions obtained with the CTS satellite (Ippolito 1979). The CCIR prediction is seen to over-predict slightly for higher percentage values, and to vastly under-predict for percentages below about 0.01%.

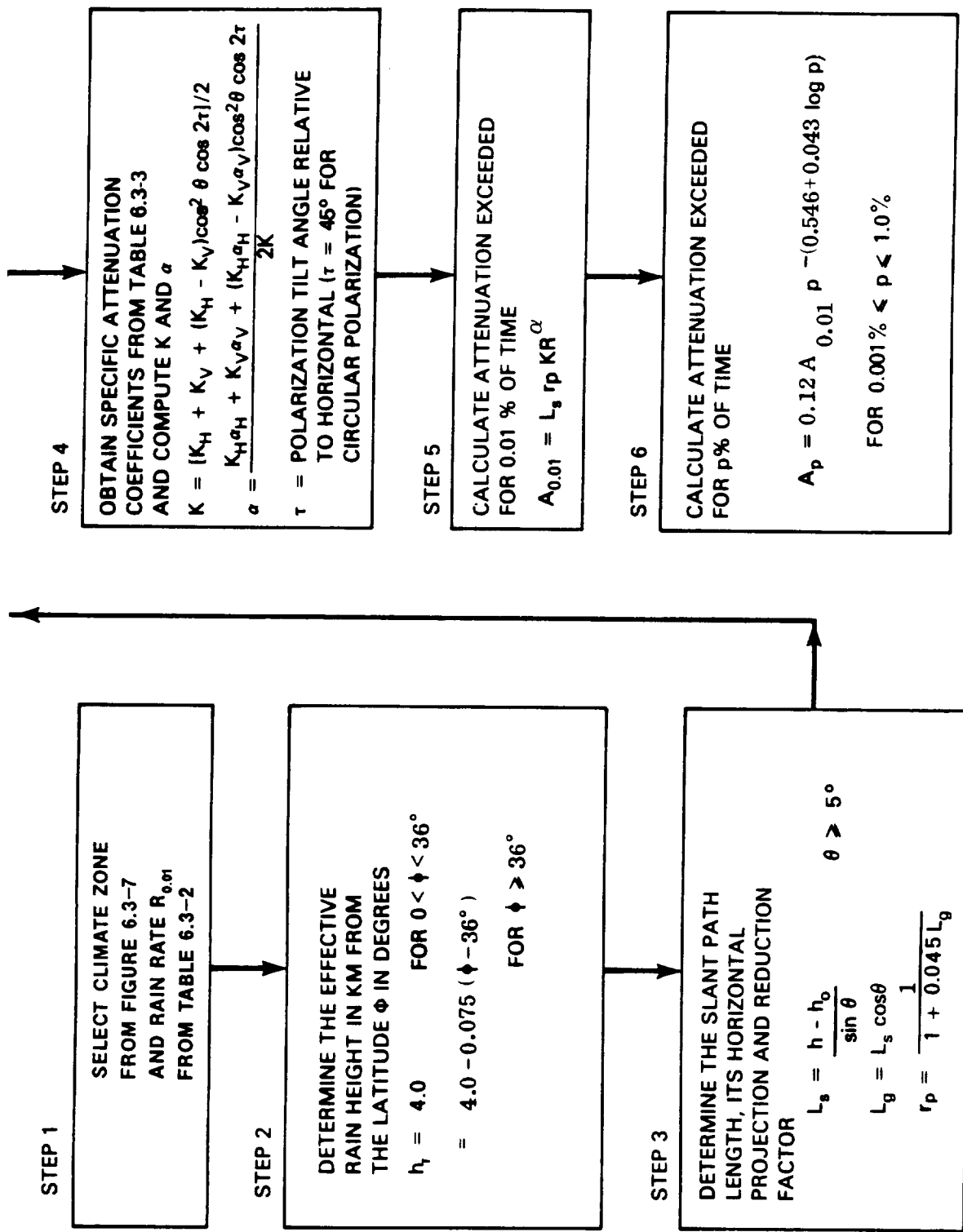


Figure 6.3-6. Analytical Estimate Procedure for Cumulative Rain Rate and Attenuation Statistics Using the CCIR Model

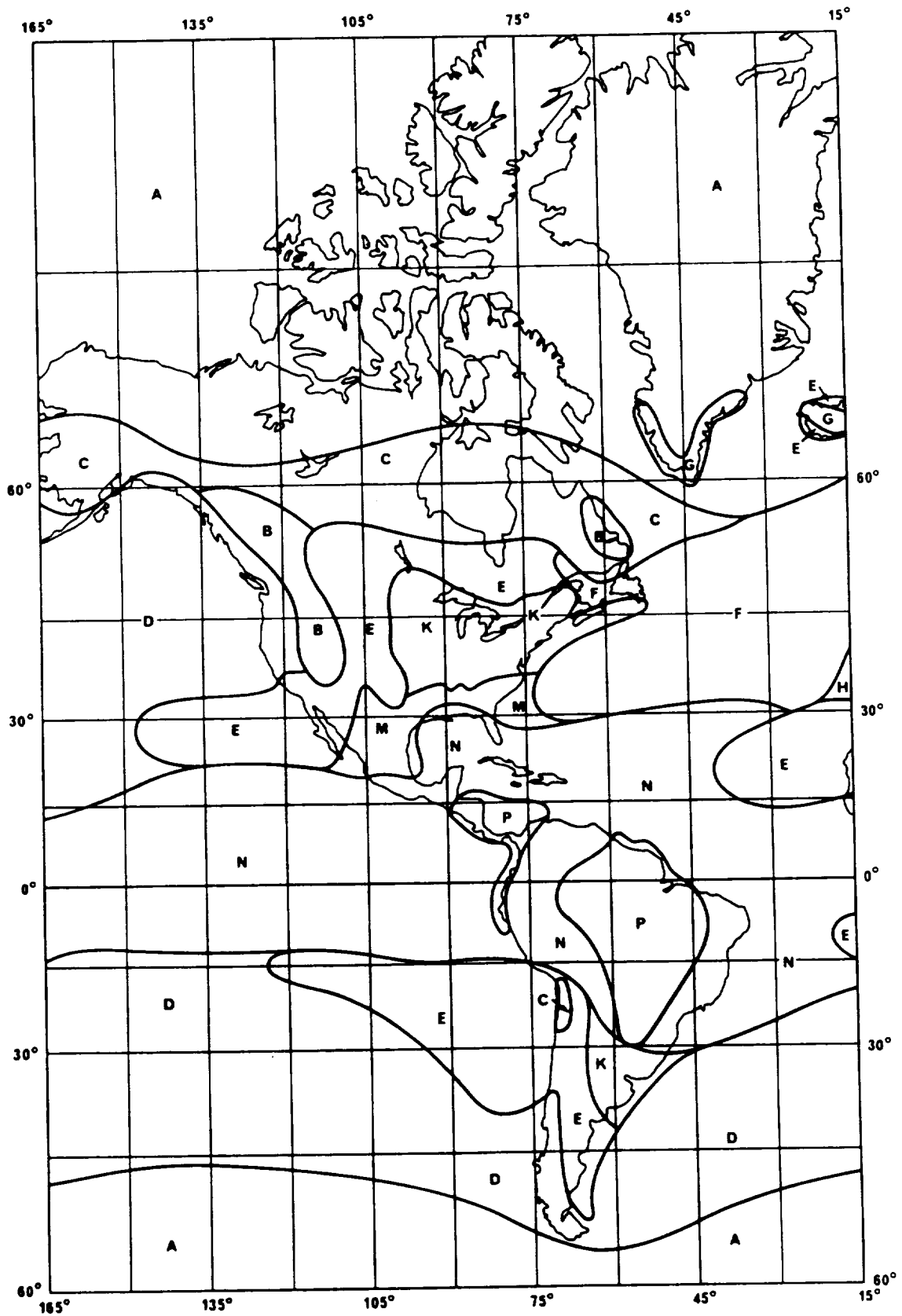


Figure 6.3-7. CCIR Rain Climate Zones for ITU Region 2

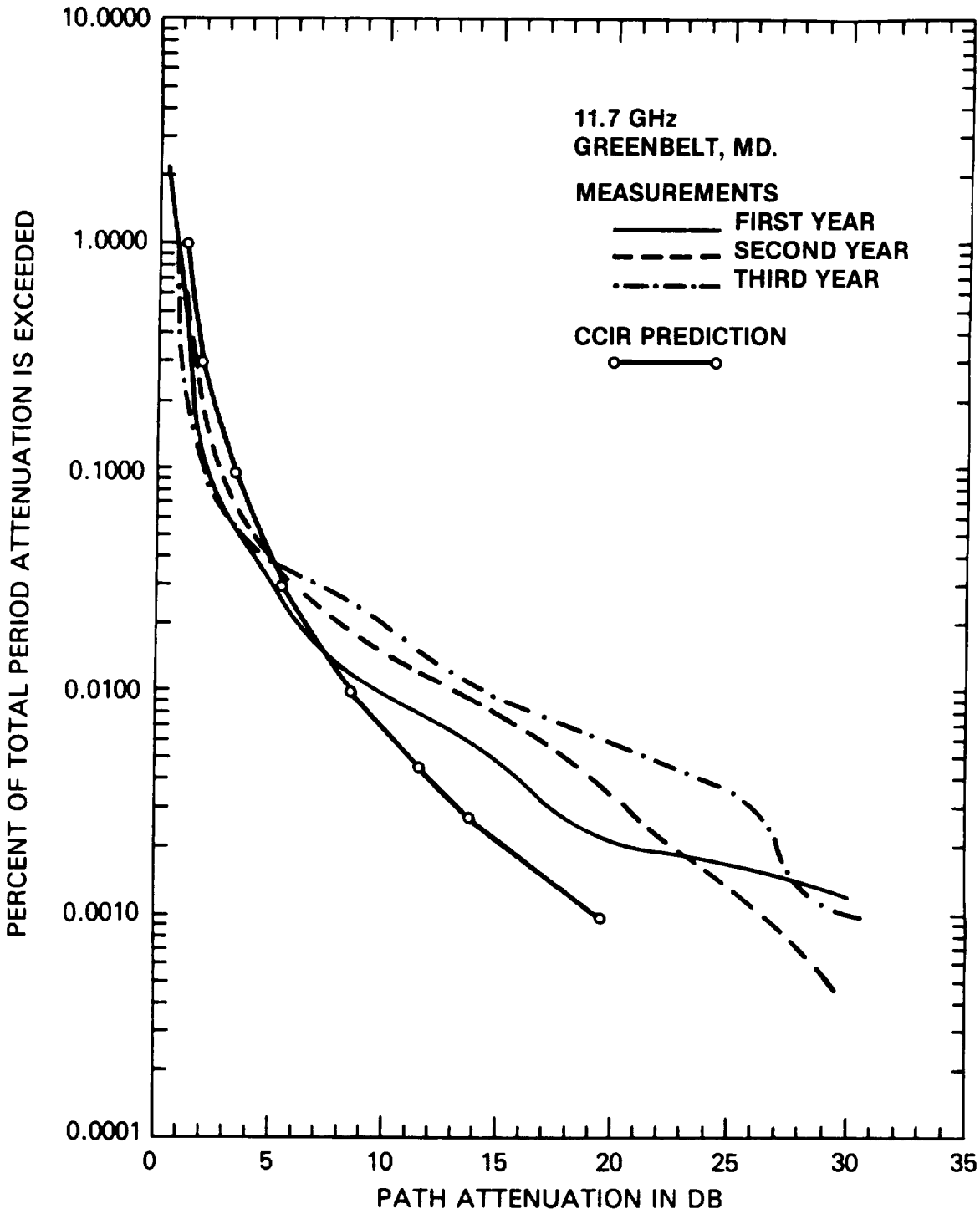


Figure 6.3-8. Comparison of CCIR Prediction with Measured Data, Greenbelt, MD. 11.7 GHz

Table 6.3-3. Regression Coefficients for Estimating Specific Attenuation in Step 4 of Figure 6.3-6

Frequency (GHz)	k_H	k_V	α_H	α_V
1	0.0000387	0.0000352	0.912	0.880
2	0.000154	0.000138	0.963	0.923
4	0.000650	0.000591	1.12	1.07
6	0.00175	0.00155	1.31	1.27
8	0.00454	0.00395	1.33	1.31
10	0.0101	0.00887	1.28	1.26
12	0.0188	0.0168	1.22	1.20
15	0.0367	0.0347	1.15	1.13
20	0.0751	0.0691	1.10	1.07
25	0.124	0.113	1.06	1.03
30	0.187	0.167	1.02	1.00
35	0.263	0.233	0.979	0.963
40	0.350	0.310	0.939	0.929
45	0.442	0.393	0.903	0.897
50	0.536	0.479	0.873	0.868
60	0.707	0.642	0.826	0.824
70	0.851	0.784	0.793	0.793
80	0.975	0.906	0.769	0.769
90	1.06	0.999	0.753	0.754
100	1.12	1.06	0.743	0.744
120	1.18	1.13	0.731	0.732
150	1.31	1.27	0.710	0.711
200	1.45	1.42	0.689	0.690
300	1.36	1.35	0.688	0.689
400	1.32	1.31	0.683	0.684

* Values for k and α at other frequencies can be obtained by interpolation using a logarithmic scale for k and frequency and a linear scale for α

6.3.3 Estimates of Attenuation Given Rain Rate Statistics

6.3.3.1 Discussion and Procedures. If the rainfall statistics can be reconstructed from Weather Service data or actual site measurements exist for a period of at least 10 years near the ground station site, these may be utilized to provide R_p versus percentage exceedance. The temporal resolution required of these measurements is dependent on the smallest percentage resolution required. For example, if 0.001% of a year (5.3 minutes) statistics are desired, it is recommended that the rain rate be resolved to increments of no more than 1-minute to provide sufficient accuracy. This can be done utilizing techniques described in Chapter 2 of this handbook, but 5-minute data is more easily obtained.

The cumulative statistics measured near the ground station site replaces Steps 1 and 2 of Figure 6.3-1. The attenuation statistics are generated using the procedures in Steps 3 through 7 of Figure 6.3-1.

6.3.3.2 Example. Again we take the case of the 20 GHz ATS-6 link to Rosman, NC. We have cumulative rain rate statistics for Rosman for a six-month period as shown in Figure 6.3-9. (Data spanning such a short period should not be used to estimate long-term statistics. The use here is for demonstration purposes only.) We first select values of rain rate R corresponding to several values of percentage exceedance.:

<u>%</u>	<u>R_p</u>
0.01	66
0.02	55
0.05	34
0.10	16.5
0.20	10.5
0.50	4.5
1.0	2.3

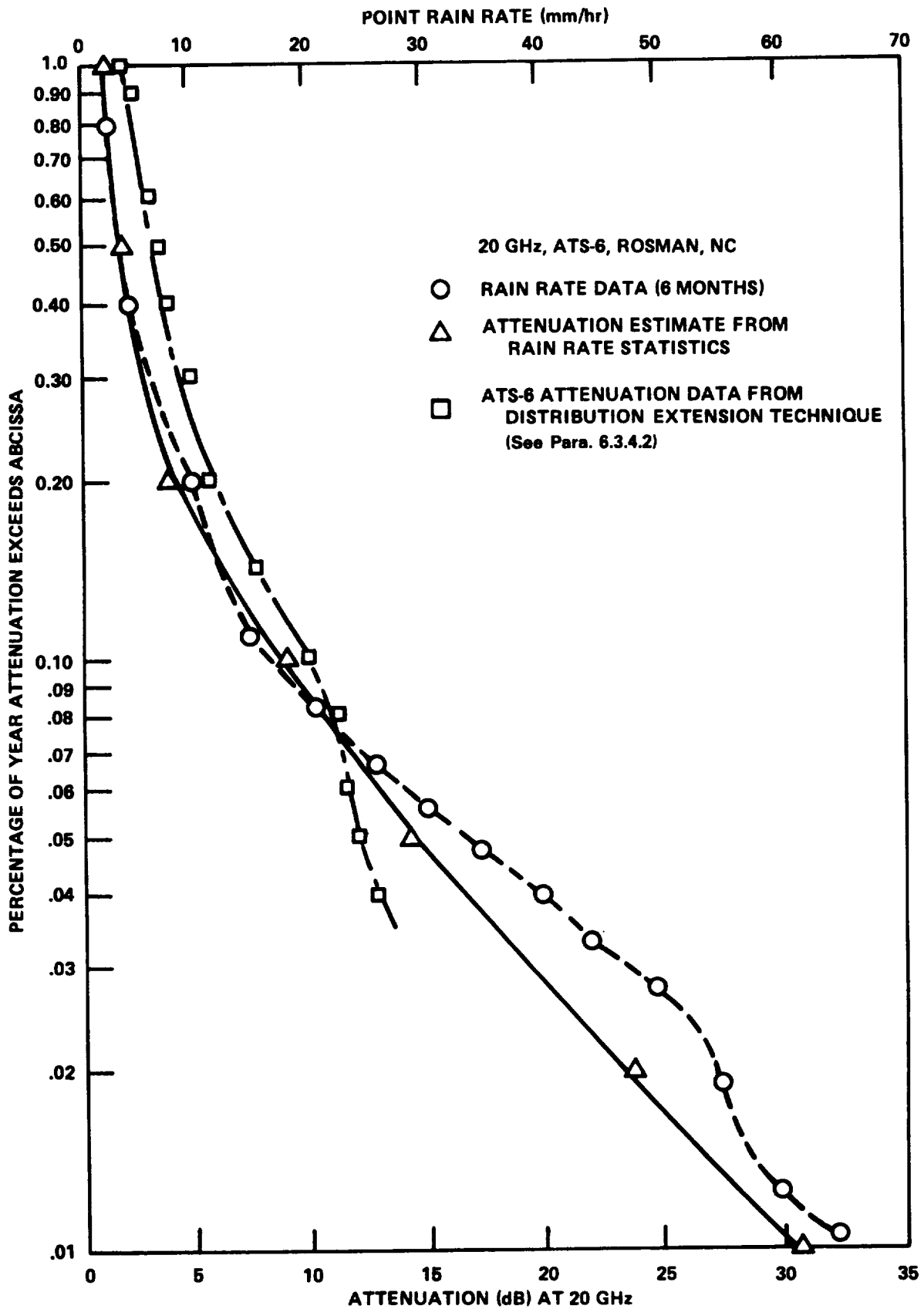


Figure 6.3-9. Attenuation Statistics Estimate Based on Measured Rainfall Statistics

We now proceed exactly as in the Global Model application example (Section 6.3.2.2), using these values of R_p instead of those in Table 6.3-1 or Figure 6.3-3.

The results of these calculations are shown in Figure 6.3-9, along with the measured attenuation statistics. This data is presented to demonstrate the technique. More accurate data, covering a longer period, is presented in Chapter 5.

6.3.4 Attenuation Estimates Given Limited Rain Rate and Attenuation Statistics

6.3.4.1 Discussion and Procedures. The system designer will virtually never find attenuation statistics spanning a number of years for his desired location, operating frequency and elevation angle. But by applying distribution extension and scaling procedures to the limited statistics available, the designer may make useful estimates of the statistics for the situation at hand.

Distribution extension allows one to take concurrent rain rate and attenuation measurements intermittently over a limited period of time, then convert the data into cumulative attenuation statistics covering the entire year. The conversion requires stable cumulative rain rate statistics for the site or a nearby weather station, and measurements taken over a statistically significant fraction of the year. Distribution extension is required in practice because it is often costly to make continuous attenuation measurements over extended periods. Rather, data are taken only during rainy periods.

Scaling is required to account for differences between the frequency and elevation angle applying to the available statistics, and those applying to the actual system under consideration. This scaling is based on empirical formulas which, to the first order approximation, depend only on the frequencies or the elevation angle and apply equally to all attenuation values. To a better approximation, however, the rain rate corresponding to the attenuation and other factors must be considered as well.

Figure 6.3-10 shows a generalized procedure for applying the distribution extension and scaling techniques described in this section.

6.3.4.2 Attenuation Distribution Extension. The technique is illustrated in Figure 6.3-11. The upper two curves represent cumulative rain rate and attenuation statistics derived from measurements taken over some limited period of time. The measurement time may consist for example, of only the rainy periods from April through September. The exceedance curves are plotted as functions of the percentage of the total measurement time. The lower solid curve represents the cumulative rain rate statistics, measured over an extended period at the same location as the attenuation measurements, or derived from multi-year rainfall records from a nearby weather station.

A curve approximating the long-term cumulative attenuation distribution (the bottom curve in Figure 6.3-11) is derived from the three upper curves by the following graphical procedure:

1. Select a percent exceedance value, E_1 , and draw a horizontal line at that value intersecting the limited-time rain rate and attenuation distribution curves at points a and b, respectively.
2. At the rain rate value R corresponding to E_1 , project a line down to intersect (at point c) the long-term rain rate curve at the exceedance value E_2 .
3. At the attenuation value A corresponding to E_1 , project a line down to the exceedance value E_2 . This (point d) is a point on the long-term attenuation curve.

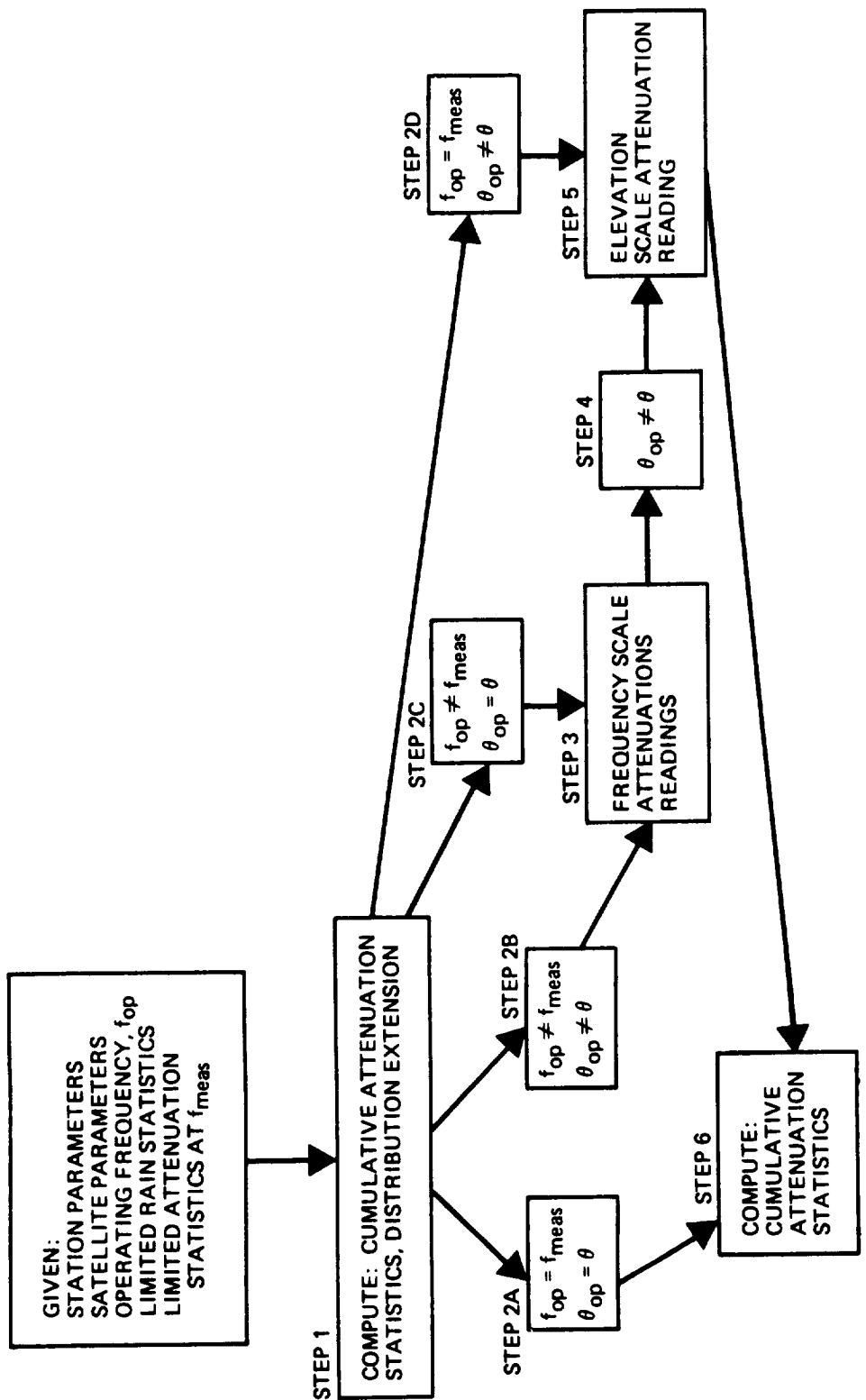


Figure 6.3-10. Procedure for Generation of Cumulative Attenuation Statistics Given Limited Rain Rate and Attenuation Statistics

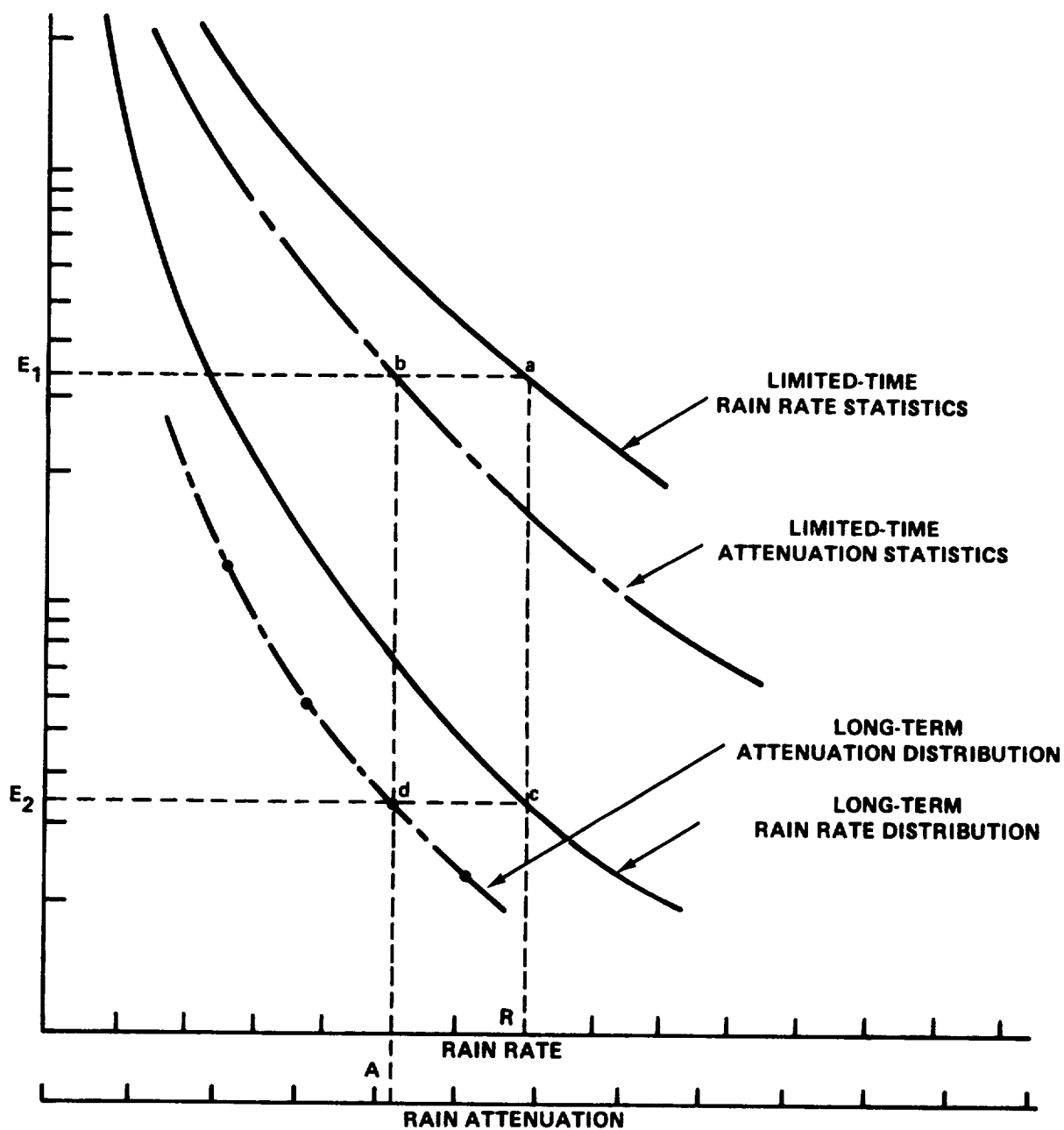


Figure 6.3-11. Construction of Cumulative Attenuation Statistics Using the Distribution Extension Technique

4. Repeat the process for several points and join them with a smooth curve.

Distribution extension in this manner assumes that the values of rain rate and attenuation remain the same as the measured values, on the average, for times of the year different than the measurement period. This is not necessarily so. The physical distribution of raindrops along the propagation path in a stratiform rain, for example, differs from the distribution in a mild convective storm. Both conditions could produce local rainfall at the same rate, but the attenuation produced could be quite different. Thus in regions where there is wide seasonal variation in how rain falls, distribution extension should be used with caution. The reliability of the extended distribution depends on how "typical" of the whole year the rainfall was during the measurement period. If the shapes of the limited-time and the long-term distribution curves are similar, the limited-time sample is statistically significant and the distribution extension will be valid.

6.3.4.3 Frequency Scaling. If frequency scaling of measured rain attenuation (Step 3 of Figure 6.3-10) is required, the specific attenuation scaling technique is recommended. In this technique specific attenuation data is utilized to scale the attenuation A from frequency f_1 to frequency f_2 . Referring to the equation for rain attenuation in Step 7 of Figure 6.3-1, the result is

$$\frac{A_2}{A_1} = \frac{k_2}{k_1} R_p^{\alpha_2 - \alpha_1} \cong \frac{k_2}{k_1} \quad (\text{for } \alpha_1 \cong \alpha_2) \quad (6.3-17)$$

where

$$A_1 = A_1(f_1), \quad A_2 = A_2(f_2), \quad k_1 = k_1(f_1), \quad . . . , \quad \text{etc.} \quad (6.3-18)$$

This is a fair estimate for small frequency ratios (e.g., less than 1.5:1), and moderate rain rates, but errors can be large otherwise. This is because the above equation implicitly assumes that rainfall

is homogeneous over the propagation path, which is usually not true. By assuming a simple Gaussian model for the rain rate with distance along the path, Hodge (1977) derived an expression for attenuation ratio that includes an inhomogeneity correction factor, and uses the high correlation between attenuation and peak rain rate to eliminate the rain rate:

$$\frac{A_2}{A_1} = \frac{k_2}{k_1} \left(\frac{A_1}{k_1} \sqrt{\frac{\alpha_1}{\pi}} \right)^{\frac{\alpha_2}{\alpha_1} - 1} \sqrt{\frac{\alpha_1}{\alpha_2}} \quad (6.3-19)$$

This yields a better fit to empirical data.

6.3.4.4 Elevation Angle Scaling. Step 5, the elevation angle scaling between the operational elevation angle θ_{op} and the measured data angle θ_{meas} is somewhat complex. The first order approximation, the cosecant rule, is recommended, namely

$$\frac{A(\theta_2)}{A(\theta_1)} = \frac{\csc \theta_2}{\csc \theta_1} = \frac{\sin \theta_1}{\sin \theta_2} \quad (6.3-20)$$

If more detailed calculations are desired the full formulas in Figure 6.3-1 are utilized.

6.3.4.5 Example of Distribution Extension. Figure 6.3-12 shows an example of applying the distribution extension technique. The upper two curves are cumulative rain-rate and attenuation statistics derived from more than 600 total minutes of measurements over the July through December 1974 period. The bottom curve in the figure is the measured distribution of rain rate for the entire six-month period (263,000 minutes). Comparison of the two rain rate distributions shows that they are very similar in shape. This indicates that the rain rate measurements made during attenuation measurements are a statistically significant sample of the total rainfall, and that using the distribution extension technique is

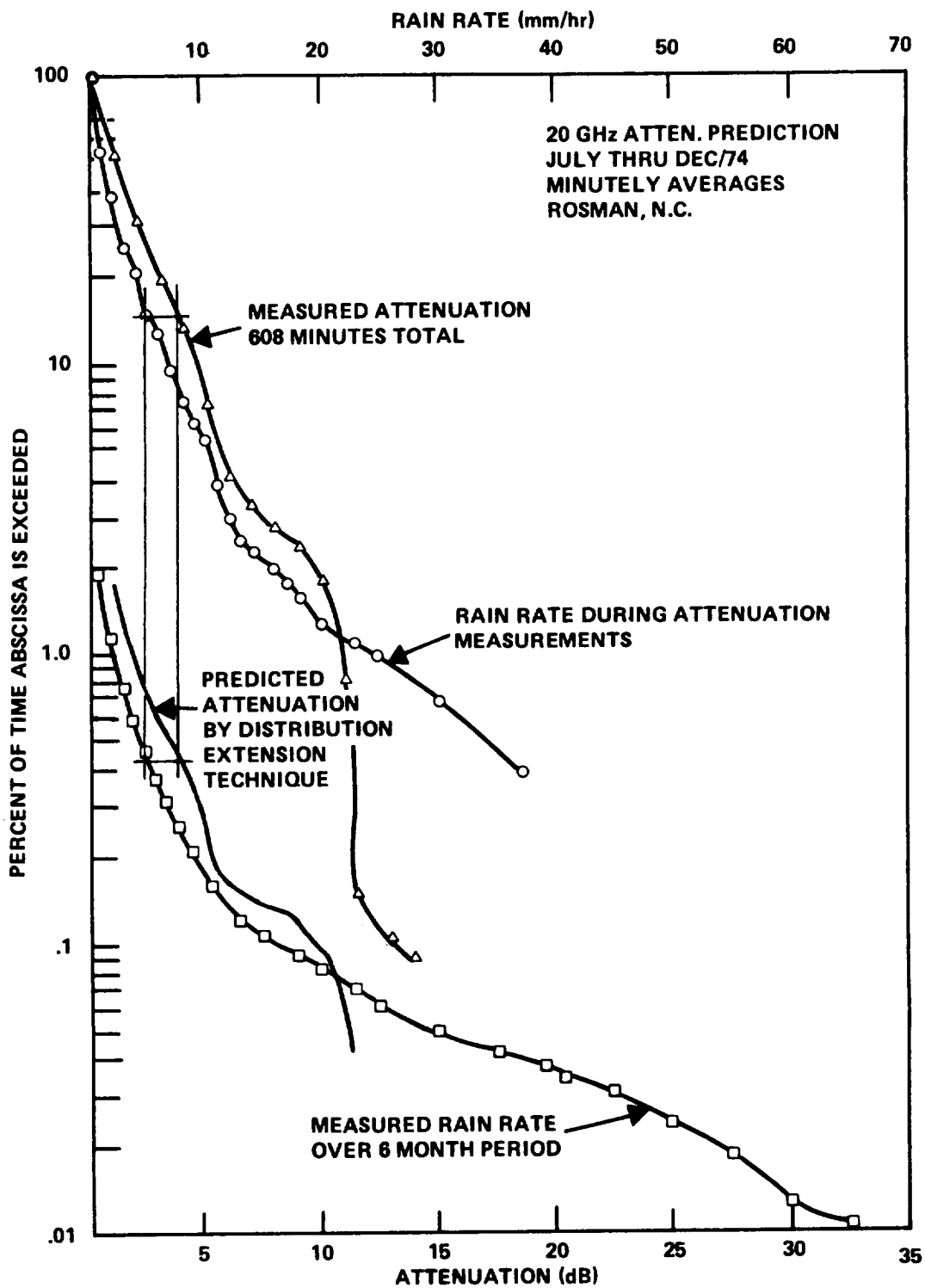


Figure 6.3-12. Example of Distribution Extension Technique

valid. The extended attenuation distribution, constructed as described in paragraph 6.3.4.2, is shown in the figure.

6.3.5 Fading Duration

System designers recognize that at some level of rain rate R_m the entire system margin will be utilized. The cumulative rain rate statistics indicate the percentage of time the rain rate exceeds R_m . In this section, a technique is presented for estimating an upper bound on the duration of the periods that the rain rate exceeds a given R_m . This is equivalent to the duration of fades exceeding the depth corresponding to R_m .

Experimental fade duration statistics are presented in Chapter 5 (Section 5.6). As mentioned in that section, experimental data has confirmed that the duration of a fade greater than a given threshold tends to have a log-normal probability distribution. This is equivalent to the logarithm of the duration having a normal distribution. Given sufficient experimental data, one may determine the parameters of the best-fitting log-normal distribution, and use these to extrapolate from the empirical distribution. Such extrapolation could be used in lieu of, or in addition to, the technique described here when fade duration data is available.

6.3.5.1 Estimating Fade Duration Versus Frequency of Occurrence.

The US and Canadian weather services have published maximum rainfall intensity (rain rate) - duration - frequency curves which provide the point rain rates for several hundred locations on the North American continent (U.S. Dept. Comm.-1955 and Canada Atmos. Env.-1973). Two typical sets of curves for the close-proximity cities of Baltimore, MD and Washington, D.C. are shown in Figure 6.3-13. The return periods are computed using the analysis of Gumbel (1958) since data is not always available for the 100-year return period. These curves are derived from the single maximum rain-rate event in a given year and are termed the annual series. For microwave propagation studies, curves that consider all high rain rate events are necessary. Such curves, called the partial-duration series, are

not normally available, but empirical multipliers have been found for adjusting the annual series curves to approximate the partial-duration series (Dept. Commerce-1955). To obtain the partial-duration curve, the rain rates on the annual series curve for the desired return period are multiplied by the appropriate factors, given in Table 6.3-4.

Table 6.3-4. Multiplicative Factors to Convert Annual to Partial-Duration Series

RETURN PERIOD (YEARS)	MULTIPLY ANNUAL SERIES RAIN RATE BY
2	1.13
5	1.04
10	1.01
25, 50, 100	1.00

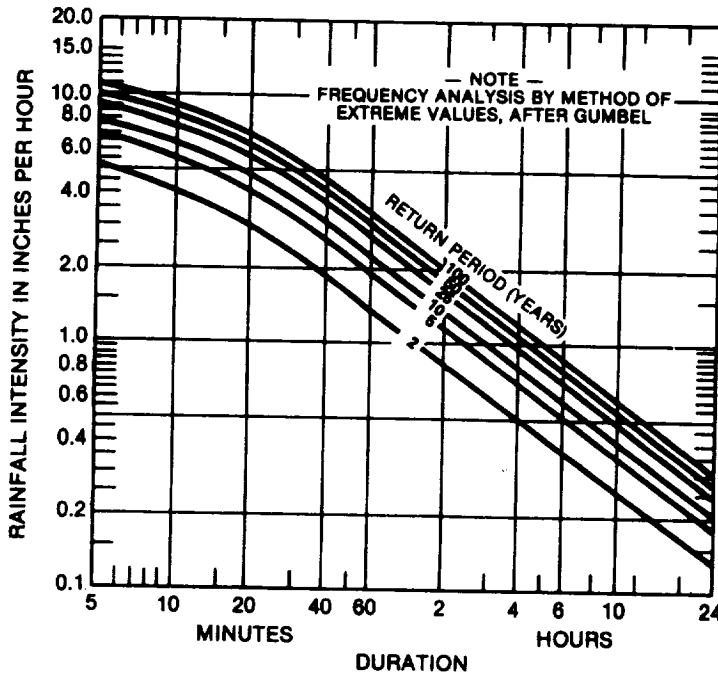
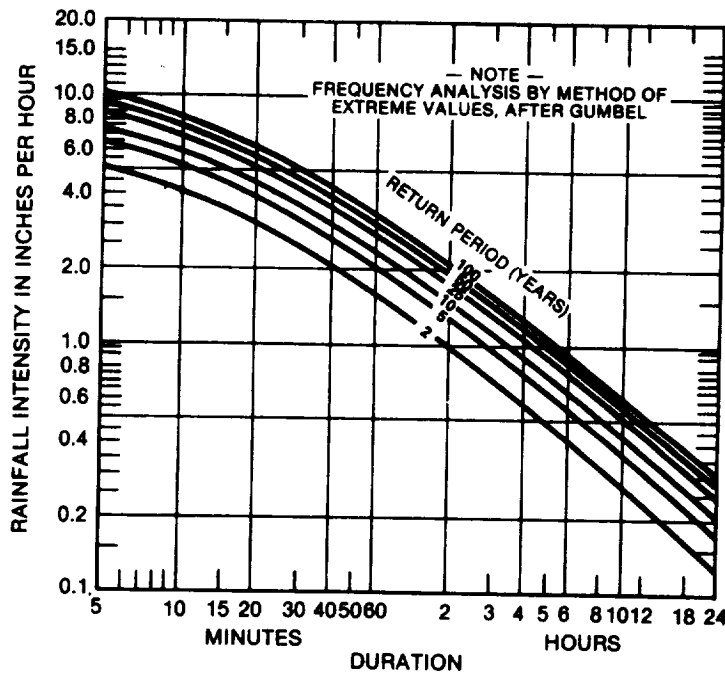


Figure 6.3-13. Typical Rain Rate-Duration-Frequency Curves From U.S. Weather Service, Annual Series

The intensity-duration-frequency curves actually give the average rain rate over the duration period, whereas the instantaneous rain rate is of interest from a propagation standpoint. The curves therefore do not directly give the frequency versus duration of fades of a given depth. However, for short averaging periods (e.g., five minutes), the instantaneous rain rate would be expected to stay fairly close to the average rain rate, and would certainly never exceed it for the entire period. The curves then can be used to approximate the frequency of short-duration fades, and to place an upper bound on the frequency in any case.

The minimum return period shown on Figure 6.3-13 is two years. It is desirable to be able to extrapolate to one year. This can be done using the Gumbel frequency analysis technique for extreme values. This has been accomplished graphically, for durations of 5 through 60 minutes as shown in Figure 6.3-14. The data used in the curves has been adjusted using the multipliers of Table 6.3-4 to correspond to the partial-duration series. For example, the rain rate expected in Baltimore in a 5-minute period once in 2 years is $5.2 \times 1.13 = 5.9$ inches per hour. Extrapolating to one year yields 4.8 inches per hour (122 mm/h). Similar calculations may be done for other duration periods to generate a 1-year return period curve for the partial-duration series.

The recommended technique for estimating the maximum fade period to be expected in an N-year rain event is described in Figure 6.3-15. Here the station parameters (latitude, longitude, etc.), operating frequency and link margin (after clear air attenuation is removed) are required inputs. By iteratively solving the attenuation equation in Figure 6.3-1 the maximum allowable point rain rate R_{pm} is obtained. The estimate of the maximum fade duration for the worst rain in 1,2,5,10 or more years is then obtained from data for the partial-duration series rain rate-duration-frequency curves (see Figure 6.3-9). For example, if the system maximum allowable rain rate R_{pm} is 5 inches/hour (125 mm/hr), a system in

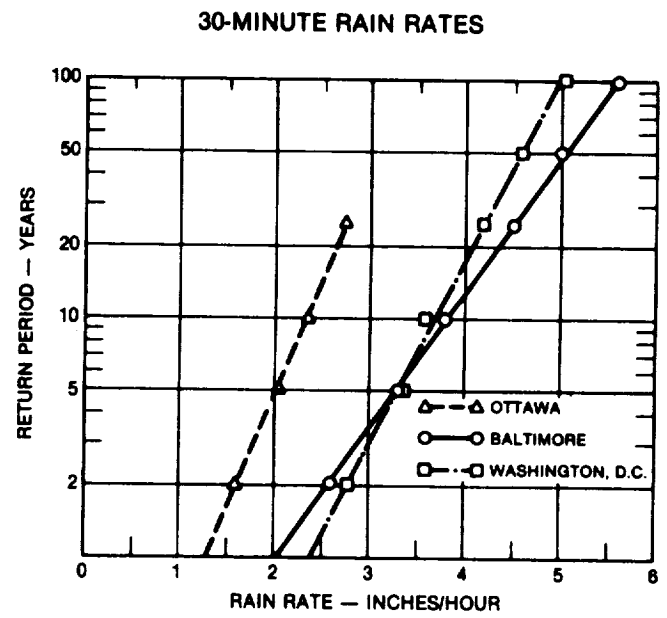
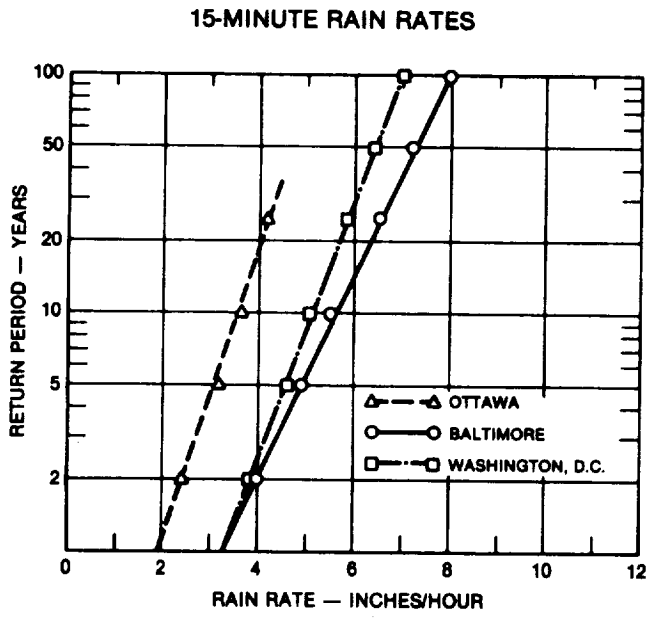
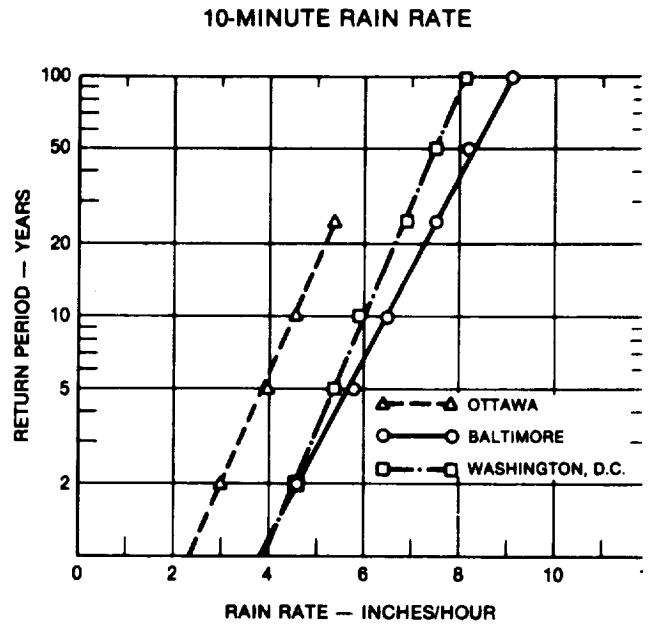
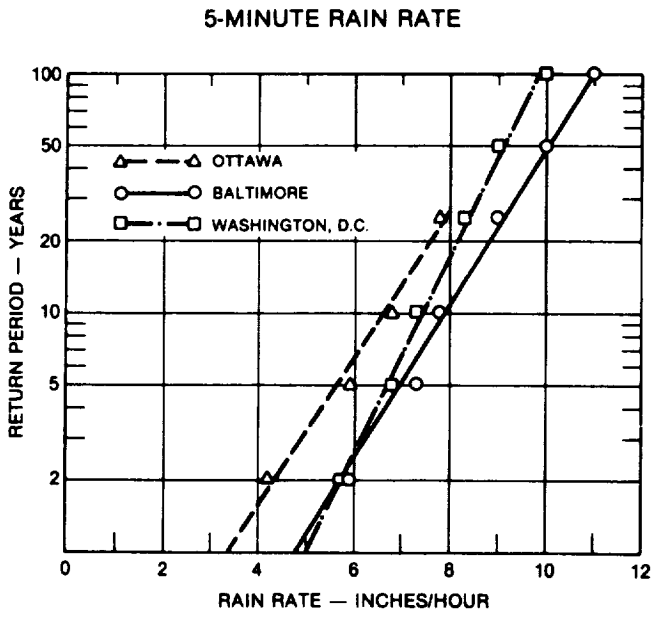


Figure 6.3-14. Extrapolated Partial-Duration Rain Rate-Duration-Frequency Curves

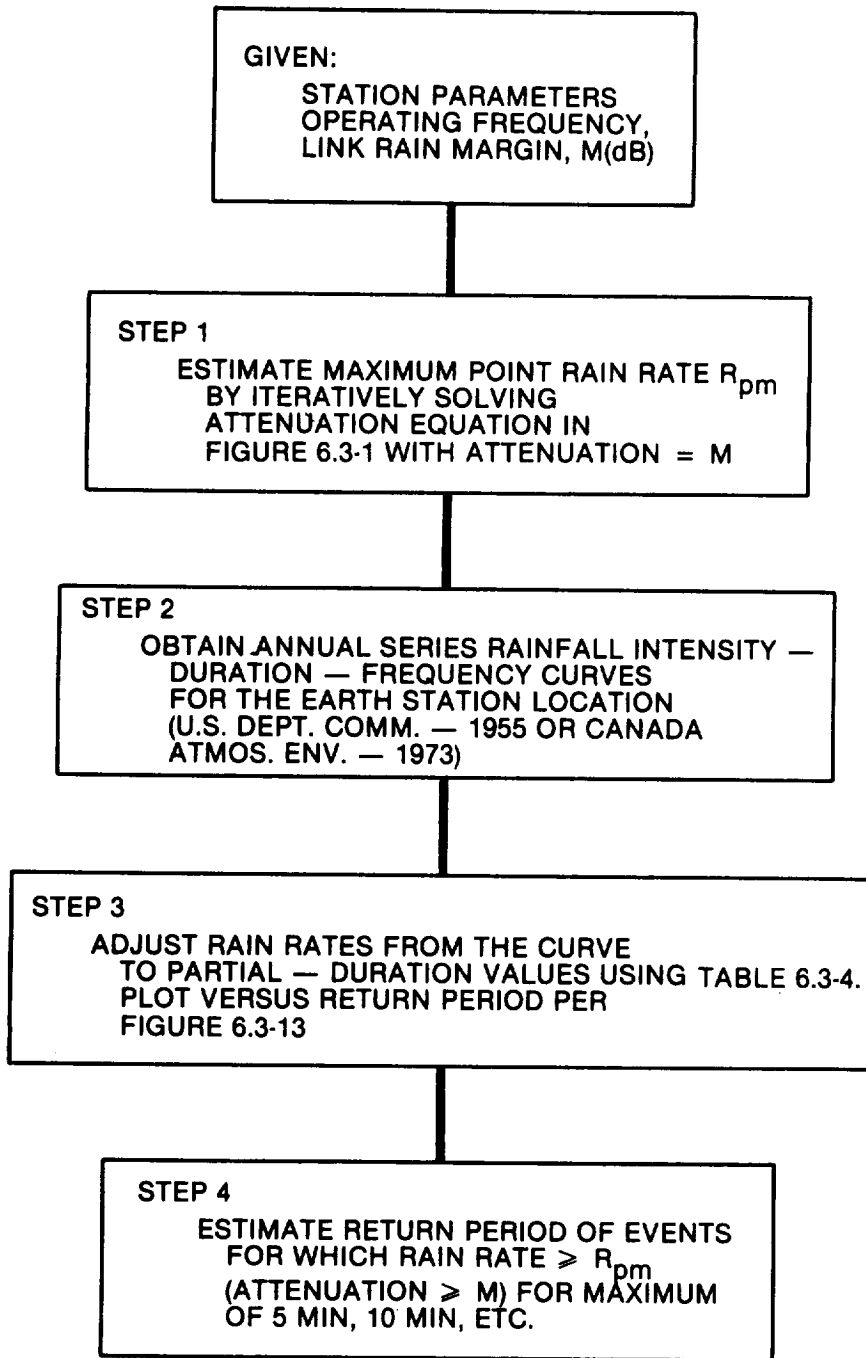


Figure 6.3-15. Technique for Estimating Frequency of Occurrence of Fades of Given Duration

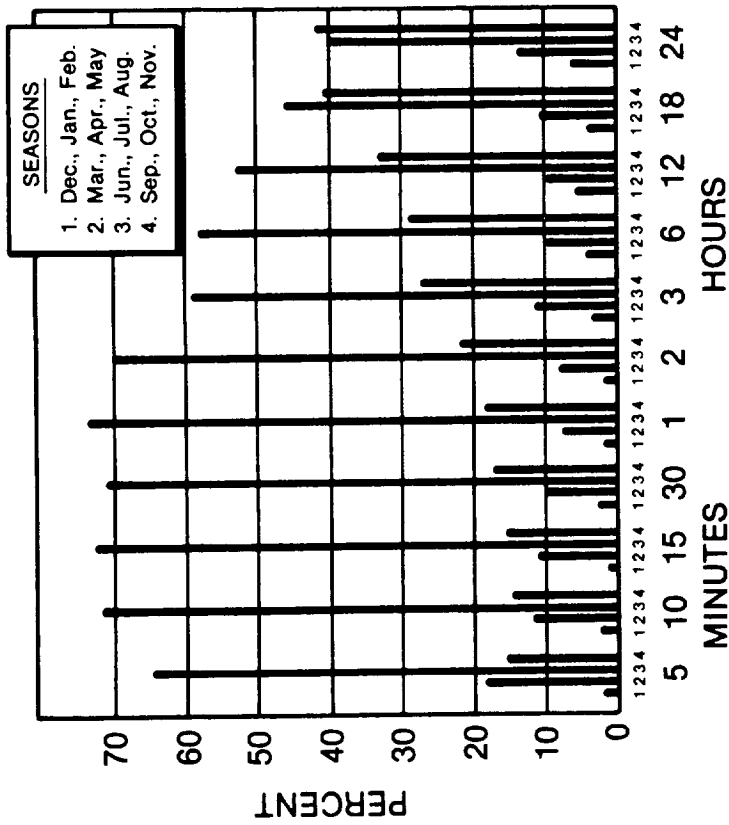
Washington, D.C. should on the average expect one maximum 5-minute fade each year, one maximum 10-minute fade every three years, etc.

6.3.5.2 Annual and Daily Temporal Distribution of Intense Rain Events. The temporal distribution of rain-induced fade events can be important to a designer since loss of a link during low utilization periods may be tolerable. Figure 6.3-16a shows the distribution, by season, of "record" rainfall events at 207 weather stations throughout the U.S. The events are measured in terms of depth-duration, which specifies the total number of inches of rain and the time over which it fell. The durations are shown in the figure, and range from 5 minutes to 24 hours. Figure 6.3-16b shows the distribution of the maximum events by the times when they start. It is clear that the short-duration events, having the most intense rain (and the deepest fades) occur predominantly in the summer months and during the afternoon hours. There are regional variations, of course: throughout much of the west coast, summer rains are insignificant. In the midwest, nocturnal thunderstorms are common. The figure also shows that more than 40% of the record 24-hour rainfall events happen in the fall, when steady stratiform rains are the rule. The regional variations in the time distribution of heavy rains is clearly shown in Figure 6.3-17 (Rasmusson- 1971). It gives the time of day of the maximum thunderstorm frequency, based on 10 years' observations. A phenomenon not indicated by the map is the existence of secondary peaks in thunderstorm frequency in many regions.

6.3.6 Rate of Change of Attenuation

Experimental data related to the rate-of-change of attenuation is relatively sparse. Apparently experimenters have not analyzed their measurements to obtain this information except during some extreme attenuation occurrences. Some measurements made at Rosman, NC of the CTS 11.7 GHz beacon showed a maximum rate-of-change of 2 dB/sec on April 24, 1977 (Ippolito-1979). This translates to change of rain rate from 50 mm/hr to 57 mm/hr in one second. Assuming this

a) BY SEASONS



b) BY QUARTER DAYS
(Time of Beginning)

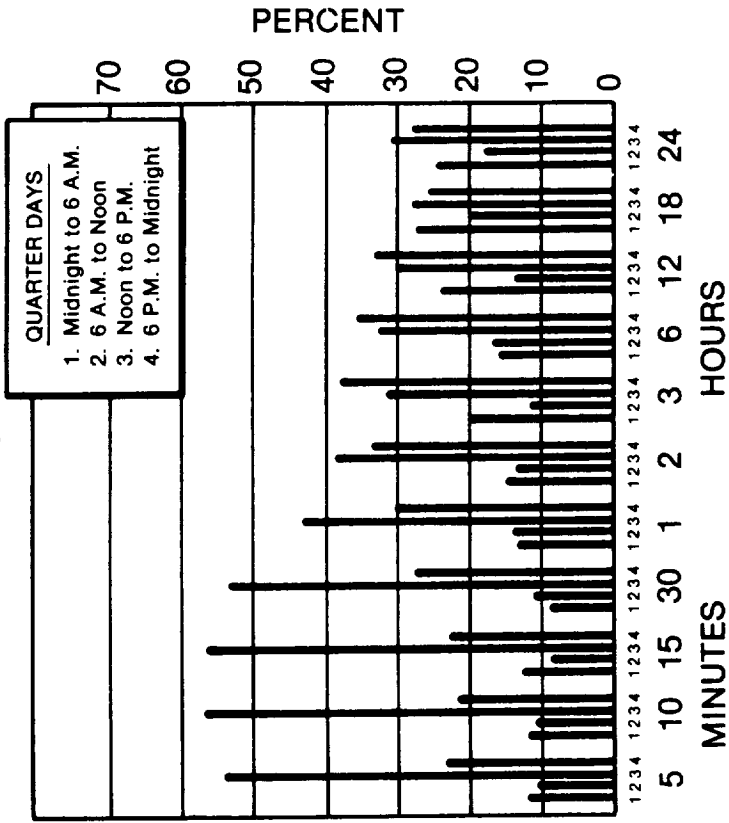


Figure 6.3-16. Distribution of Maximum Rainfall Occurrences at U.S. First-Order Stations (U.S. Dept. Comm.-1947)

HOUR OF MAXIMUM FREQUENCY OF THUNDERSTORMS (LST)

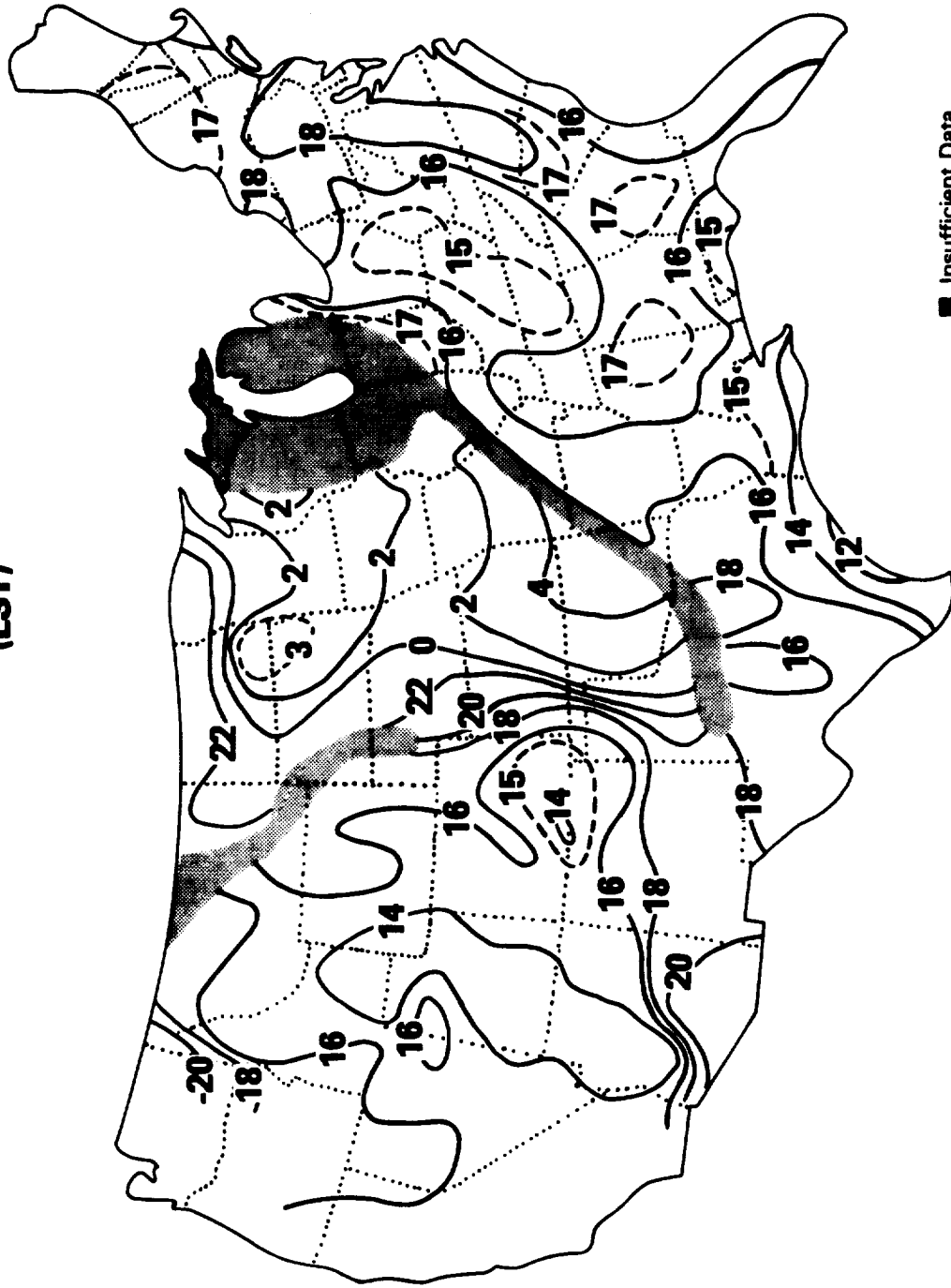


Figure 6.3-17. Time of Day When Maximum Thunderstorm Frequency Occurs (Rasmusson - 1971)

change in rain rate, the rate of change of attenuation would have been 4 dB/sec at 20 GHz.

Maximum fade rates of 0.1 dB/sec at 15 GHz are reported by Hodge (1974) and Strickland (1977). Dintelmann (1981) reports fade rates of up to 0.6 dB/sec in Europe at 11.7 GHz.

6.3.7 Worst-Month Statistics

Worst-month statistics are of interest to those faced with designing a system to meet performance criteria expressed in terms of a percentage of any calendar month, or of any contiguous 30-day period. The system designer in this case needs to find the percentage of time that some threshold value of attenuation or rain rate will be exceeded within a given month. For every threshold value, there corresponds a month of the year having the highest percentage of time exceeding the threshold (i.e., the percentage exceedance). This is designated the "worst-month" for that threshold. The percentage exceedance in this month, to be expected once every year or every given number of years, is of most interest. For high rain rates, the worst-month would probably correspond to the period of highest thunderstorm intensity or frequency, whereas the worst-month for lower rain rates might be when most rainfall is of the steady, stratiform variety.

An exponential model has been devised (Crane and Debrunner-1978 and CCIR-1978, Rpt 723) for estimating the ratio of the percentage exceedance for a given threshold value in the worst-month to the average annual percentage exceedance for the same threshold. This exponential relationship is expected for statistics of rare events (Gumbel-1958).

Let X_{ij} be the percentage exceedance in month i corresponding to a threshold rain rate j . In a given year, there is for each value j a month h with the highest X_{ij} , denoted X_{hj} . The worst-month statistic is the value of X_{hj} that is equalled or exceeded, on average, once in N years where N (the return period) is specified.

The probability that the worst month percentage exceedance is equal to or greater than X_{hj} is given by:

$$P(X_{hj}) = \frac{1}{12N} \quad (6.3-21)$$

The exponential model, which applies when X_{hj} is small, states:

$$P(X_{hj}) = C_{0j} \exp(-X_{hj}/C_{1j}) \quad (6.3-22)$$

where C_{0j} and C_{1j} are empirical constants. Inverting this equation yields:

$$X_{hj} = C_{1j} \ln C_{0j} - \ln P(X_{hj}) \quad (6.3-23)$$

Figure 6.3-18 is a plot of monthly probabilities of exceeding preselected thresholds X_{ij} for 44 consecutive months of attenuation measurements. It clearly follows the straight-line relation of the model, with $C_{0j} = 0.19$ and $C_{1j} = 7.8 \times 10^{-4}$.

The ratio of the N-year worst-month percentage exceedance X_{hj} to Y_j , the average annual percentage exceedance for the same threshold j , is given by

$$Q_{jN} = \frac{X_{hj}}{Y_j} = \frac{\ln(12 N C_{0j})}{C_{0j}} \quad (6.3-24)$$

For the case of $N=1$ year, this is bounded by:

$$\frac{12}{M} \leq Q_{j1} \leq 12 \quad (6.3-24)$$

Where M is the number of months in the year that intense rains typically fall. If $M < 3$, the exponential model should be questioned. The lower bound has been shown to be a fair estimate of Q_{j1} for rain rates with annual percentage exceedances in the .001% to .01% range.

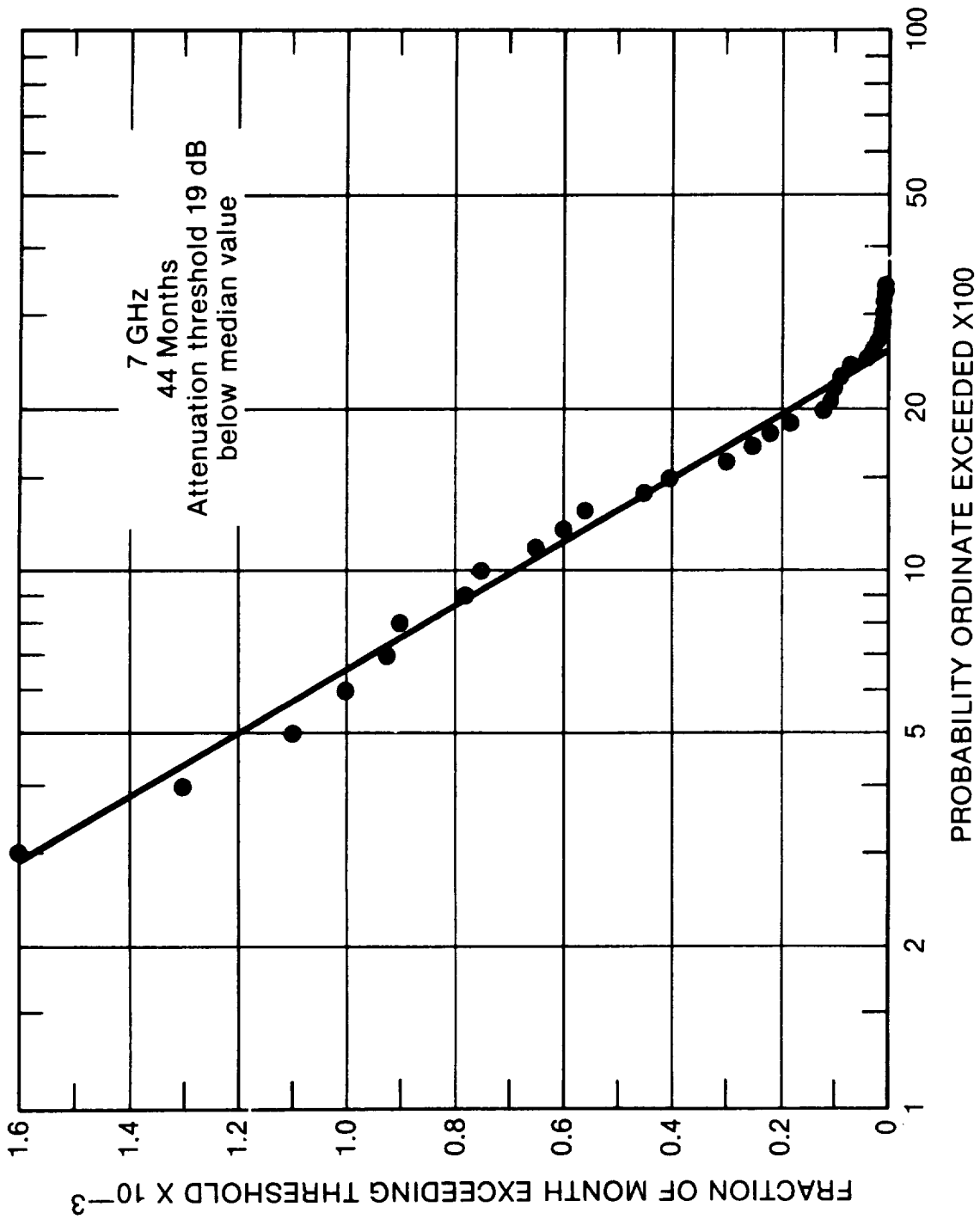


Figure 6.3-18. Probability of Attenuation Threshold Being Exceeded for the Indicated Fraction of Time Per Month (CCIR-1978, Rpt 723)

The worst-month versus annual probability relationship has been found to be closely approximated by a power law of the form

$$\bar{Q} = A\bar{Y}^{-\beta} \quad (6.3-25)$$

where Q is the ratio of the average worst-month probability to the average annual probability (Y) and A and β are coefficients. The observed ranges of coefficient values are $1.2 \leq A \leq 3.3$ and $0.167 \leq \beta \leq 0.074$ (CCIR Rep. 723-1, 1982a). A useful approximate relationship between worst-month exceedance time percentages (p) and annual time percentages (p_w) is (CCIR, 1982a):

$$p = 0.29 p_w^{1.15} \quad (6.3-26)$$

where p and p_w are in percent. The corresponding coefficient values for the previous power law relationship are $A = 1.64$ and $\beta = 0.13$. These values yielded Q ratios in good agreement with average values for different locations in North America and Europe. For current CCIR recommendations, the reader is referred to CCIR report 723-2, "Worst Month Statistics", (CCIR, 1986e).

6.4 CLOUD, FOG, SAND AND DUST ATTENUATION

6.4.1 Specific Attenuation of Water Droplets

The water droplets that constitute clouds and fog are generally smaller than about .01 cm in diameter. This allows the Rayleigh approximation to be used to calculate specific attenuation in clouds and fog for frequencies up to 100 GHz. Using this approximation, the specific attenuation α_c is, unlike the case of rain, independent of the droplet size distribution. It is proportional to the liquid water content ρ_l :

$$\alpha_c = K_c \rho_l \text{ dB/km} \quad (6.4-1)$$

ρ_l is normally expressed in units of g/m^3 . The attenuation constant K_c is a function of frequency and temperature and is given by Figure 6.4.1 (CCIR Rpt. 721-1, 1982a). The curves given in the figure assume pure water droplets. The values for salt-water droplets, corresponding to ocean fogs and mists, are higher by approximately 25% at 20°C and 5% at 0°C (Koester and Kosowsky-1978).

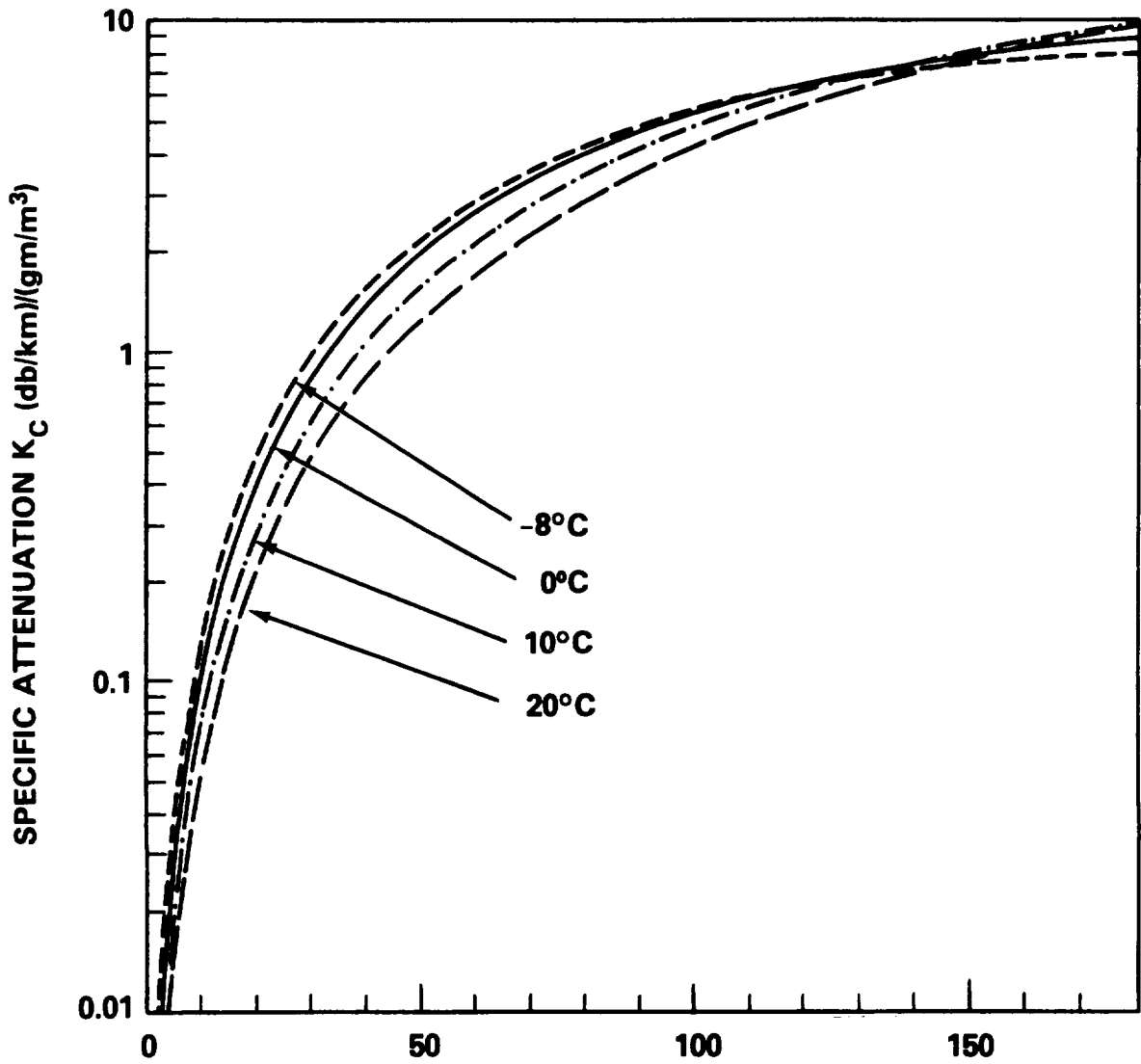


Figure 6.4-1. Attenuation Coefficient K_C Due to Water Droplets
(from CCIR 1982a, Rpt 721-1)

6.4.2 Clouds

6.4.2.1 Water Content of Clouds. The liquid water content of clouds varies widely. For stratiform, or layered, clouds, the value was observed to most often fall in the range of 0.05 to 0.25 g/m³. For the most dense of this type of cloud, stratocumulus, maximum values from 0.3 to 1.3 g/m³ have been measured (Mason-1971). Cumulus clouds, especially the large cumulonimbus and cumulus congestus that accompany thunderstorms, have the highest values of liquid water content. Fair weather cumulus were found to have liquid water contents generally less than 1 g/m³. Peak values exceeding 5 g/m were found in cumulus congestus clouds by Weickmann and aufm Kampe (1953). They estimated an average value of 2 g/m³ for cumulus congestus and 2.5 g/m³ for cumulonimbus. A review of typical values is given in Slobin (1982).

Clouds are not homogeneous masses of air containing evenly distributed droplets of water. Rather, the liquid water content can vary widely with location within a single cloud. On the average, the liquid water content in smaller cumulus congestus clouds increases fairly steadily with distance up from the base, then begins to drop off somewhere in the mid-to-upper parts. It also generally decreases with horizontal distance from the center toward the edges. Small-scale variations are also present, however. Sharp differences have been observed in localized regions on the order of 100 m across. One would expect fairly rapid local variation with time as well, due to the complex patterns of air movement taking place within cumulus clouds. Updraft wind velocities greater than 10 m/s exist within cumulonimbus clouds (Rogers-1976).

6.4.2.2 Measured Attenuation of Clouds. Typical path lengths through cumulus congestus clouds probably fall between about 2 and 8 km. Using the estimated average liquid water content from above (2 g/m³), and the attenuation coefficient from Figure 6.4.1, this implies an added path loss at 35 GHz of about 4 to 16 dB. Fortunately, this calculation grossly overestimates the actual attenuation that has been observed through these clouds. This

appears to be generally true, as seen in Tables 6.4-1 and 6.4-2, which present measurements from two sources.

Table 6.4-1. Zenith Cloud Attenuation Measurements, From Lo, Fannin and Straiton (1975)

Cloud Type	Number of Observations	Mean Cloud Attenuation (dB)		Mean Gaseous Attenuation (dB)	
		35 GHz	95 GHz	35 GHz	95 GHz
Altostratus	7	.02	.23	.38	1.93
Altostratus	2	.15	.30	.34	1.73
Stratocumulus	22	.18	.61	.43	2.14
Stratus	8	.13	.12	.42	2.14
Nimbostratus	5	.14	.11	.44	2.32
Cumulus	20	.12	.34	.41	2.12
Cumulonimbus	6	.34	2.36	.40	2.07

Table 6.4-2. Zenith Cloud Attenuation Measurements, CCIR Rpt. 721-2 (1986f)

Cloud Type	Cloud Attenuation (dB)	
	95 GHz	150 GHz
Stratocumulus	0.5 - 1	0.5 - 1
Small, Fine Weather Cumulus	0.5	0.5
Large Cumulus	1.5	2
Cumulonimbus	2 - 7	3 - 8
Nimbostratus (Rain Cloud)	2 - 4	5 - 7

In Table 6.4-1, the gaseous attenuation, calculated for the measured surface relative humidity, is given for comparison. The cloud attenuation is in most cases 40% or less of the gaseous attenuation. For frequencies removed from the 35 and 95 GHz "windows," the cloud attenuation would be a smaller fraction of gaseous attenuation. In Table 6.4-1, the number of observations is rather small for all but two types of clouds. The numbers given should therefore not be given undue statistical significance. Also, in using both tables, one should bear in mind the great variability in size and state of development of the clouds observed.

The 35 and 95 GHz data of Table 6.4-1 or 6.4-2 may be roughly scaled in frequency, using the frequency dependence of attenuation coefficient from Figure 6.4-1. Scaling in this manner is quite approximate, as is seen from Table 6.4-1. The ratio of attenuation coefficients at 35 and 95 GHz varies between about 3.9 for -8°C to 6.3 for 20°C . The ratio of average cloud attenuations measured at those frequencies is, from the table, 3.4 for stratocumulus, 2.8 for cumulus, and 6.9 for cumulonimbus. In another series of measurements on individual fair weather cumulus clouds (Lo, et al-1975) this ratio was usually between 3.7 and 5.5.

There appears to be a large discrepancy between tables 6.4-1 and 6.4-2 in the attenuation of nimbostratus clouds at 95 GHz. The large values of Table 6.4-2 may be due to the inclusion of precipitation in the path, however, because the presence of nimbostratus clouds would usually be accompanied, sooner or later, by precipitation at the ground station, the higher values of attenuation would be expected. This does not necessarily apply to cumulonimbus clouds, however. Because of the large vertical development and limited horizontal extent of these clouds, a typical ($30-40^{\circ}$ elevation angle) propagation path may be intercepted by them without significant rainfall at the ground station.

6.4.2.3 Statistics of Microwave Effects of Clouds. A JPL study (Slobin 1982), has made estimates of the statistics of cloud effects for the continental U.S., Alaska and Hawaii. The presence of clouds in space-earth downlink antenna beams has two primary effects: signal attenuation, and an increase in system noise temperature. For very low-noise receiving systems, such as those used for deep-space communications, the noise effect can be quite significant. Cloud noise statistics may therefore be important in siting such systems and in scheduling their use. Cloud effects can normally be ignored in a high-reliability system designed with a rain margin. However, clouds must be considered for systems with minimal margin that are intended for continuous use, such as a deep-space link receiving unrepeatable spacecraft data.

The JPL study determined that the U.S. could be divided into fifteen regions of statistically "consistent" clouds, as shown in Figure 6.4-2. The region boundaries shown in the figure are highly stylized and should be interpreted liberally. Some boundaries coincide with major mountain ranges (Cascades, Rockies, and Sierra Nevada), and similarities may be noted between the cloud regions and the rain rate regions of the Global Model. Each cloud region is considered to be characterized by observations at a particular National Weather Service observation station. The locations and three-letter identifiers of these stations are shown in the figure. For each of these stations, an "average year" was selected on the basis of rainfall measurements. The "average year" was taken to be the one in which the year's monthly rainfall distribution best matched the 30-year average monthly distribution. Hourly surface observations for the "average year" for each station were used to derive cumulative distributions of zenith attenuation and noise temperature due to oxygen, water vapor, and clouds, for a number of frequencies ranging from 8.5 to 90 GHz.

The following method was employed to calculate the cumulative distributions.

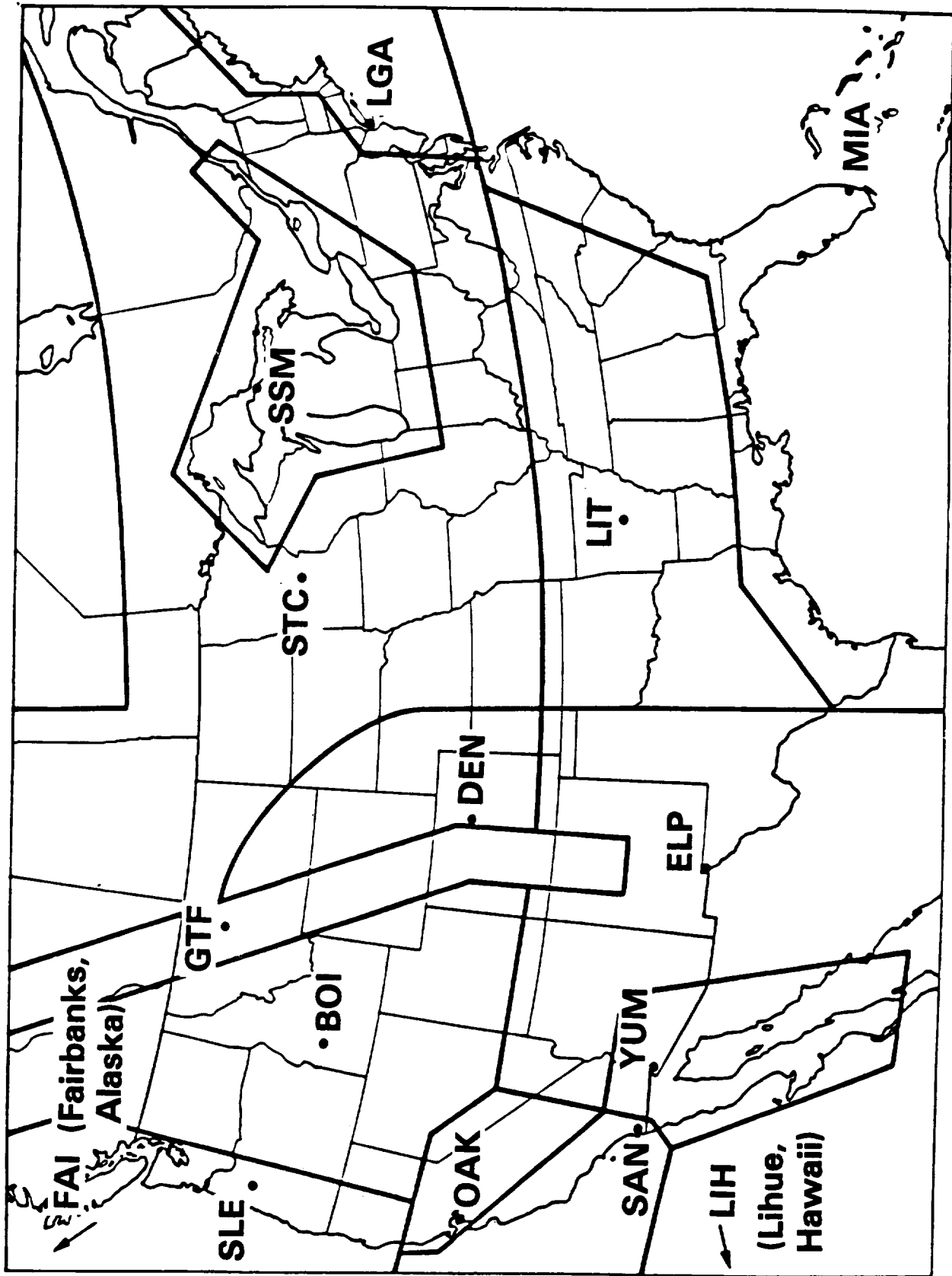


Figure 6.4-2. Consistent Cloud Regions

- For each hour's observations, the attenuation of each reported cloud layer (up to four) was calculated based on the layer's water particle density, thickness, and temperature. The attenuation due to water vapor and oxygen was also found using the reported surface conditions.
- Total attenuation and noise temperature due to all cloud layers and gases were calculated for sixteen possible cloud configurations, corresponding to all combinations of cloud presence or absence at the four layer heights.
- Cumulative probability distributions for attenuation and noise temperature were calculated using the reported percent-coverage values corresponding to each cloud layer. For example, if the percentage of coverage was 60 percent for layer 1 and 20 percent for layer 2, then the probability of various configurations of clouds present in the antenna beam would be as follows:

no clouds present:	$(1-.6) (1-.2) = 0.32$
layer 1 clouds only present:	$(.6) (1-.2) = 0.48$
layer 2 clouds only present:	$(1-.6) (.2) = 0.08$
clouds in both layers present:	$(.6) (.2) = 0.12$

Typical cumulative attenuation and noise temperature distributions calculated in this way are shown in Figure 6.4-3. The curves apply to zenith paths only, but can be extended to slant paths using a cosecant law. Such extension will probably lead to overestimation at low elevation angles and small time percentages. This is because clouds with large vertical development have less thickness for slant paths than for zenith paths. At time percentages where rain effects become significant (cumulative distributions greater than 95%), the attenuation and noise temperature due to the rain should be considered also.

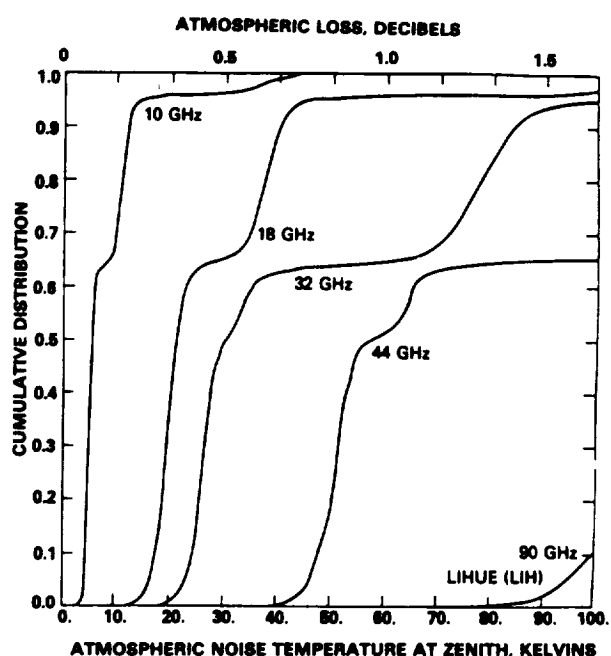
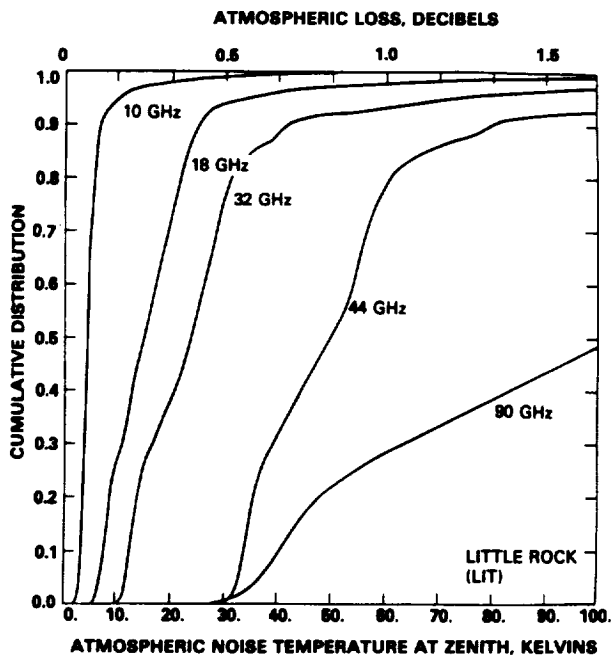
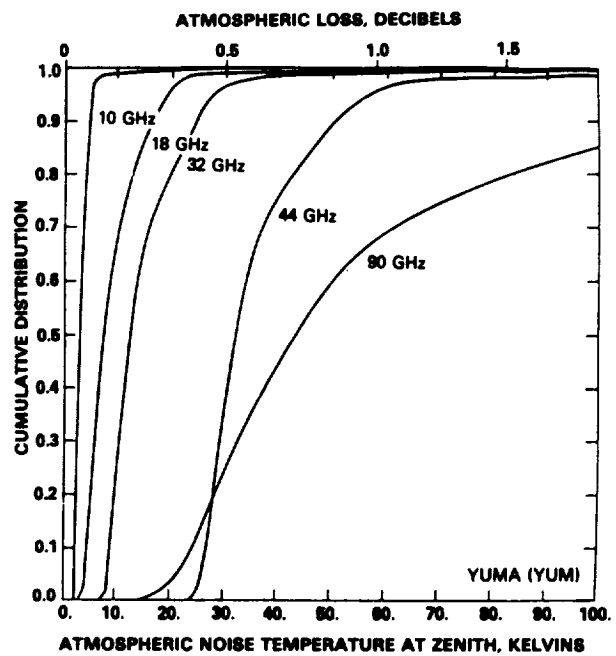
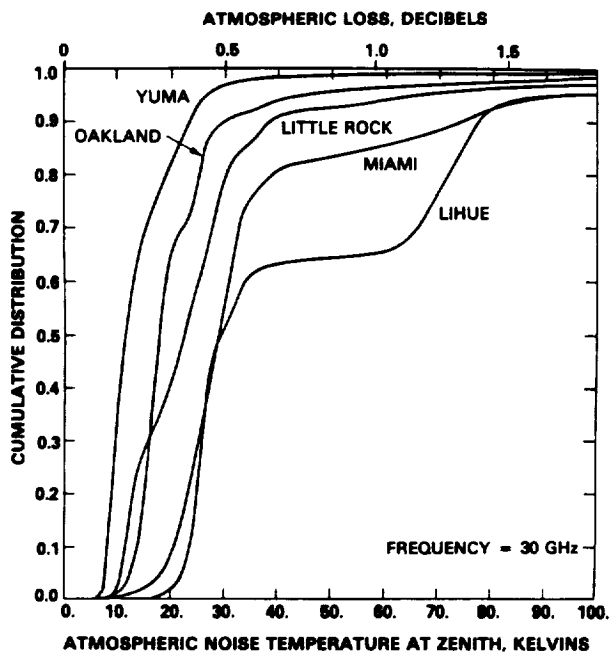


Figure 6.4-3. Examples of Cloud and Gaseous Effects Statistics

Plots of noise temperature and attenuation statistics, both full-year and quarter-year, are available for the 15 regions at 15 frequencies (8.5, 10, 12, 15, 18, 20, 25, 28, 30, 32, 35, 39, 44, 49 and 90 GHz). Interested persons should contact Stephen Slobin, Jet Propulsion Laboratory, Pasadena, CA 91109.

6.4.3 Fog

6.4.3.1 Water Content of Fog. Fog results from the condensation of atmospheric water vapor into water droplets that remain suspended in air. Fog is characterized by optical visibility, which is defined as the distance over which a black target against the sky horizon background can just be discerned by the human eye. The international definition of fog is satisfied when visibility is less than one kilometer (Koester and Kosowsky-1970).

There are two main types of fog, differing in the locale and method of formation. Advection fog is coastal fog that forms when warm, moist air moves over colder water. The liquid water content of advection fog does not normally exceed 0.4 g/m^3 . Radiation fog forms inland at night, usually in valleys and low marshes, and along rivers. Radiation fog can have a liquid water content up to 1 g/m^3 . Empirical relations have been found (Koester and Kosowsky-1970) between the liquid water content, ρ_l , and the visibility, $V(\text{km})$:

$$\rho_l = (18.35 V)^{-1.43} \text{ for advection fog} \quad (6.4-2)$$

$$\rho_l = (42.0 V)^{-1.54} \text{ for radiation fog} \quad (6.4-3)$$

6.4.3.2 Attenuation of Fog. The specific attenuation of fog (in dB/km) is estimated using the curves in Figure 6.4-1. The 10°C curve is recommended for the summer, and the 0°C curve should be used for other seasons. Typical liquid water content values for both types of fog vary between about 0.1 and 0.2 g/m^3 . The specific attenuation of this, assuming a temperature of 10° , would be about 0.08 to 0.16 dB/km at 35 GHz , or 0.45 to 0.9 dB/km at 95 GHz . (See Figure 6.4-1.) In a typical fog layer 50 m thick, a path at a 30° elevation angle would be in the fog only 100 m , producing less than 0.1 dB of

attenuation at 95 GHz. This suggests that fog attenuation would, in most cases, be negligible.

6.4.3.3 Fog Attenuation Estimation Method. A relatively simple procedure for the estimation of fog attenuation from fog density or fog visibility data has been developed by Altshuler (1984). A regression analysis was performed on a large set of fog attenuation data over a wide range of frequencies (10 to 100 GHz) and temperatures (-8 to 25°C), using tabulated values of indices of refraction. The resulting analysis produced the following expression:

$$a_f = -1.347 + 11.152/f + 0.060f - 0.022T \quad (6.4-4)$$

where

a_f is the normalized fog attenuation, in dB/km/g/m³

f is the frequency in GHz, and

T is the temperature in °C

The total fog attenuation is found by multiplying a_f by the fog density, in g/m³, and the fog extent, in km. Unfortunately, the fog density is not easily obtainable, and can vary greatly. Fog, however, is often characterized by visibility, which is much easier to measure than fog density.

The fog density, M , is empirically related to the visibility, V by;

$$M = (0.024/V)^{1.54} \quad (6.4-5)$$

where V is in km, and M is in g/m³.

The total fog attenuation, A_f (dB), is then available from;

$$A_f(\text{dB}) = a_f * M * L_f \quad (6.4-4)$$

where L_f is the fog extent, in km.

The standard error of the estimation procedure described above is 0.14 db. The author recommends in a later publication that the procedure should not be used for frequencies below 30 GHz, since the error is comparable in magnitude to the fog attenuation itself (Altshuler-1986).

As an example of an application of the procedure, consider a link at 44 GHz, with a fog visibility of 120 m (0.12 km). The fog density is then

$$M = (0.024/0.12)^{1.54} = 0.0839$$

The normalized fog attenuation, at a temperature of 25°C, will be, from Eq. (6.4-4);

$$a_f = 0.996 \text{ dB/km/g/m}^3$$

The total fog attenuation, assuming a fog extent of 2 km, will then be, from Eq. (6.4-6)

$$A_f \text{ (dB)} = (0.996)(0.0839)(2) = 0.167 \text{ dB}$$

The fog attenuation, as expected, is very low, and is not usually a factor in satellite link system design for frequencies below 100 GHz.

6.4.4 Sand and Dust Attenuation

Sand and dust scatter electromagnetic energy and their effect may be evaluated via Mie scattering. To date simulated measurements have been carried out in the laboratory (Ahmed and Auchterlouis-1976). At 10 GHz and concentrations of sand and dust less than 10^{-5} g/m³ the measured specific attenuation was less than 0.1 dB/km for sand and 0.4 dB/km for clay. Severe storms have concentrations exceeding these values.

Ghobrial, et al (1978) have calculated a theoretical specific attenuation for sand. Based on the characteristics of particles collected during sandstorms, they conclude that negligible attenuation is suffered by X-band transmissions through sandstorms. This is due to the small particle size compared to the wavelength and the low loss tangent for sand.

Chu (1979) reported that attenuation coefficients from sand particles at microwave frequencies were linearly proportional to frequency, and inversely proportional to optical visibility. The attenuation coefficients for distributions of identical particles were linearly proportional to particle radius. Other theoretical analyses have shown that sand and dust particle attenuation at microwave frequencies tends to be significant at very high particle concentrations (visibilities of less than 20m), or at high moisture contents, or both [Bashir et al. (1980), Ansari and Evans (1982), Goldhirsh (1982)].

Blowing sand and dust storms occur in some regions of the U.S. These are recorded by the Weather Service as part of the Local Climatological Data (LCD) at the 291 stations. Ground stations needing this information should review the data recorded by a nearby LCD recording station.

The vertical extent of these sand storms is unknown, but it seems unlikely that high concentrations would exceed 1 km. The path length is expected to vary between 1/2 and 3 km, generally resulting in a total additional attenuation due to sand of the order of 1 dB or less. No measured satellite beacon link data is available to confirm these results.

6.5 PREDICTION OF SIGNAL FLUCTUATIONS AND LOW-ANGLE FADING ON EARTH-SPACE PATHS

The amplitude, phase, and angle-of-arrival of a microwave signal passing through the troposphere vary due to inhomogeneities in the refractivity (clear air). The effects occur on time scales shorter

than a minute and on spatial scales shorter than a kilometer. At low elevation angles, the amount of troposphere traversed is significant, and so, below approximately 10 degree elevation angles, low-angle fading must be considered.

6.5.1 Antenna Aperture Effects

The effects of tropospheric turbulences and the antenna can not be totally decoupled because, of course, the measurements and operating systems utilize antennas. The antenna aperture processes the incident wavefront with its spatial and temporal fluctuations into a received signal with only temporal variations.

Wavefront tilt due to inhomogeneities and gradients in the refractivity appear to the antenna as an angle-of-arrival variation. Average elevation angle ray bending is usually 10 times more pronounced than azimuthal ray bending. However, wave tilt fluctuations tend to be randomly distributed in angle relative to the slant path propagation direction, at least when the majority of the path is above the regime of surface effects (surface effects extend upwards several hundred meters).

Fluctuations occurring on spatial scales smaller than the size of the aperture are often referred to as wavefront ripple. This phase incoherence results in an instantaneous gain loss or degradation.

The fluctuations described herein apply to the ground station downlink because its antenna is in close proximity to the turbulent medium. An uplink satellite path will suffer fluctuation gain degradation only due to scattering of energy out of the path. Because of the large distance traversed by the wave since leaving the troposphere, the wave arrives at the satellite antenna as a plane wave (no ripple) and with only minute angle-of-arrival effects. Interference to satellites on the geostationary arc can occur due to the refraction and diffraction of radio relay links oriented toward the satellite.

6.5.2 Amplitude Fluctuations

6.5.2.1 Overview. The phenomena of amplitude and angle-of-arrival fluctuations combine to form received signal amplitude fluctuations. For many cases of propagation one or more of these effects may often be neglected. For example, a receiving system which employs an antenna with a wide beamwidth will not experience angle-of-arrival-induced amplitude fluctuations for most elevation angles. However, such simplification is not always possible. The theory of wave propagation and scattering in random media allows a combination of the turbulence induced effects to be performed in the context of weak fluctuations along a line-of-sight path. The work of Ishimaru (1978), which defines coherent and incoherent field components as a plane wave propagates through a random medium, provides a method of combining amplitude and angle-of-arrival effects into a model of received signal amplitude fluctuation. A model utilizing the concept of incident plane wave decomposition (see Figure 6.6-1) has been proposed by Theobald and Hodge (1978).

6.5.2.2 Variance of Received Signal Amplitude. The assumption of weak turbulence is invoked for a plane wave incident on a region of turbulence, propagating a distance L_t (km) and impinging on a circular aperture of diameter d_a (meters). The antenna is assumed to have a Gaussian pattern function with half-power beamwidth B (degrees). If v_d is the received signal voltage, assuming a square-law first mixer, an expression for signal variance relative to average power is

$$S^2 = 10 \log_{10} \left(\frac{\langle v_d^2 \rangle - \langle v_d \rangle^2}{\langle v_d \rangle^2} \right) \quad (6.5-1)$$

$$= 10 \log_{10} \left(\frac{I_c \sigma_1^2 + \frac{I_i B^2}{5.55 \alpha_2^2 + B^2} - I_i \left(\frac{B^2}{2.77 \alpha_2^2 + B^2} \right)^2}{I_c + I_i \left(\frac{B^2}{2.77 \alpha_2^2 + B^2} \right)} \right)$$

where

$$I_i = 1 - \exp [-L_t/L_0]$$

$$I_c = (1 - I_i) / (1 + \sigma_1^2)$$

$$\sigma_1^2 = \text{electric field amplitude variance}$$

σ^2_2 = angle-of-arrival variance (deg²)

L_t = path length

L_o = a function of density and crosssection of scattering along the path.

Measurements at The Ohio State University of the ATS-6, 20 and 30 GHz beacons as the satellite underwent synchronous orbit transition were used to derive empirical constants for this model. The path length, L_t , was determined as a function of elevation angle, θ , using an effective turbulence height, h_t , of 6 km in the formula

$$L_t = \left[h_t^2 + 2r_e h_t + (r_e \sin \theta)^2 \right]^{1/2} - r_e \sin \theta \quad (6.5-2)$$

where r_e = mean earth radius = 6371 km.

The constants were

$$L_o = 180 \text{ km}$$

$$\sigma^2_1 = 2.6 \times 10^{-7} f(\text{GHz})^{7/12} L_t(\text{km})^{11/6}$$

$$\sigma^2_2 = 5.67 \times 10^{-6} L_t(\text{km})^{1.56} d_a(\text{m})^{-1/3}$$

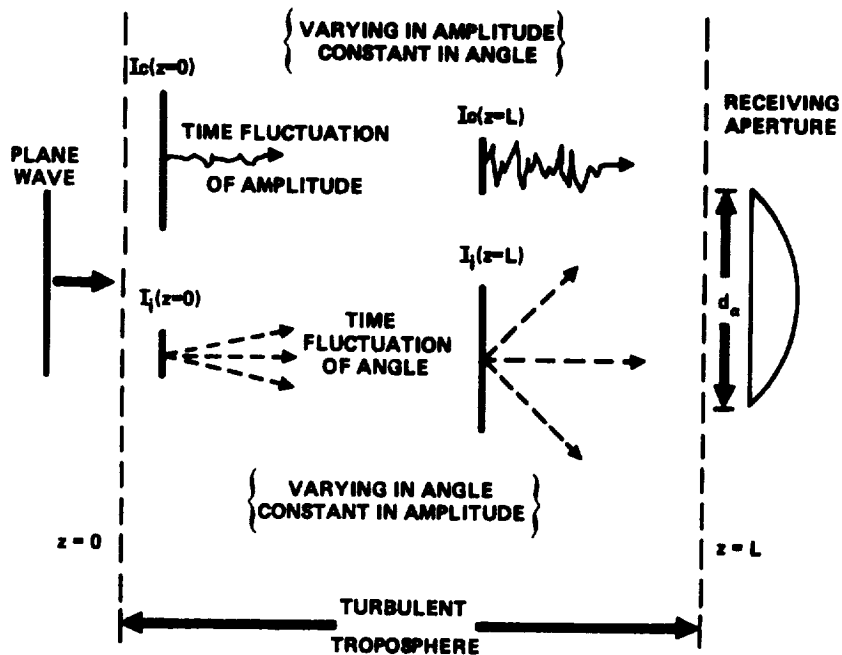


Figure 6.5-1. Decomposition into Coherent and Incoherent Components

A plot of the variance measurement, S^2 , expressed in dB, is shown in Figure 6.5-2 for four representative frequencies for a 4.6 m diameter aperture. S^2 is plotted as a function of elevation angle and equivalent path length for a 6 km high region of turbulence.

Figure 6.5-2 represents the average S^2 as derived from the O.S.U. empirical constants. However, since both σ^2_1 , and σ^2_2 may be represented in closed form as a function of C^2_n (Tatarski-1961), instantaneous, diurnal, or seasonal values for S^2 may be found from this model given an estimate of the appropriate C^2_n .

6.5.2.2.1 Applicability of the Model. The empirical constants which were found from observed data are applicable for the prediction of average turbulence-induced propagation effects in a temperate climate, during the warmer seasons of the year, and under non-precipitating clear-air conditions. It is necessary to derive local estimates of C^2_n for the model if these conditions are not the same.

6.5.2.2.2 Distribution of Amplitude Variance. It is known that peak-to-peak variations of 30 N-units in the refractive index are expected on a time scale of days and hours (Theobald-1978). Corresponding fluctuations in received signal amplitude variance expressed in dB would be expected to be about 20 dB peak-to-peak for a fluctuation of 30 N-units out of an average of 345. Figure 6.5-3 shows a representative case of average amplitude variance at 30 GHz for a 4.6 m diameter aperture as a function of elevation angle. Curves for plus or minus 10 dB variation in C^2_n about the average are shown for comparison.

A more exact representation of the expected distribution of amplitude variance may be obtained given measured statistics of variance variability about the average. Figures 6.5-4a and b present probability distribution functions of variance differences for 2 and 30 GHz earth-space signals measured over a period of 26 days. The satellite was undergoing transition in elevation from 0.38° to 45° and the mean variance was removed as a function of elevation angle. The 90% confidence limits of 14.6 and 14.7 dB, respectively, are in good agreement with the statistics of expected refractive index variation.

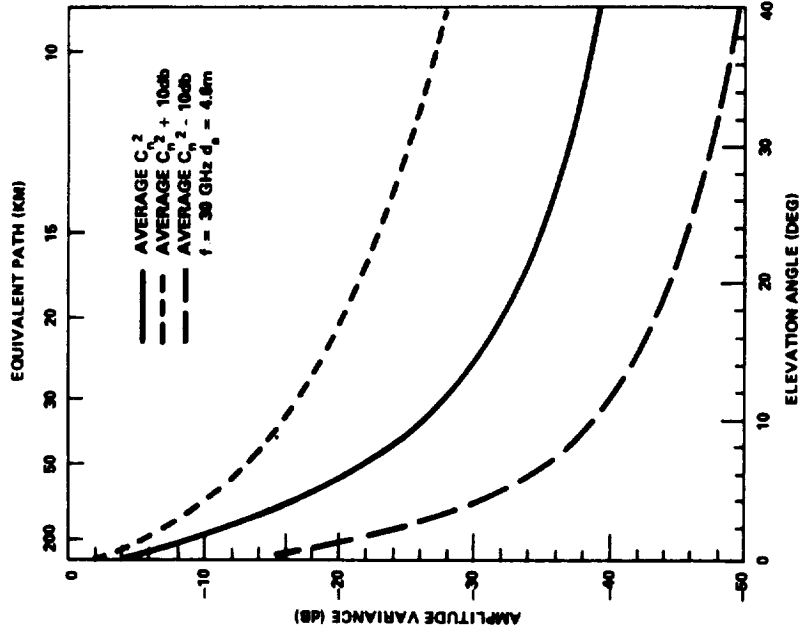


Figure 6.5-2. Amplitude Variance for a 4.6M Diameter Aperture for 1 to 100 GHz

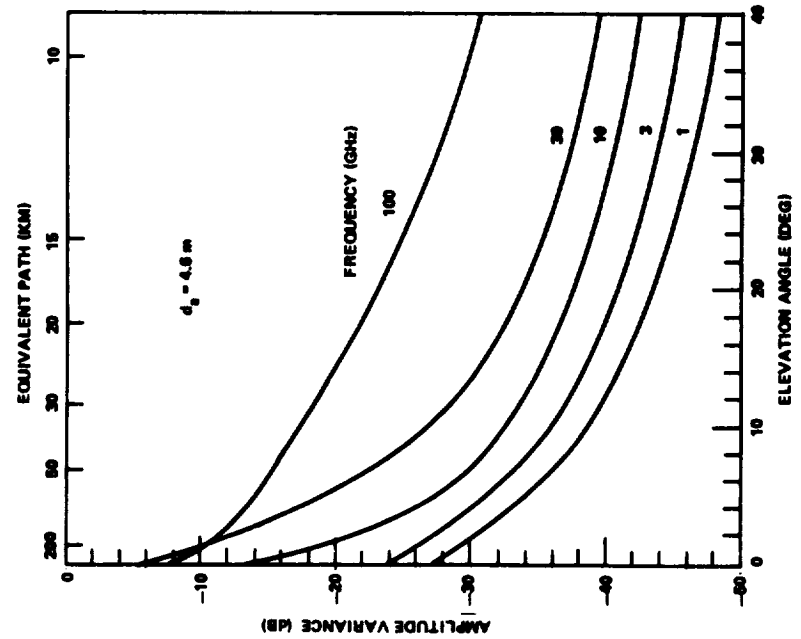


Figure 6.5-3. Effect of 20 dB Peak-to-Peak (30 N-units) Variation of C_n^2 on Amplitude Variance

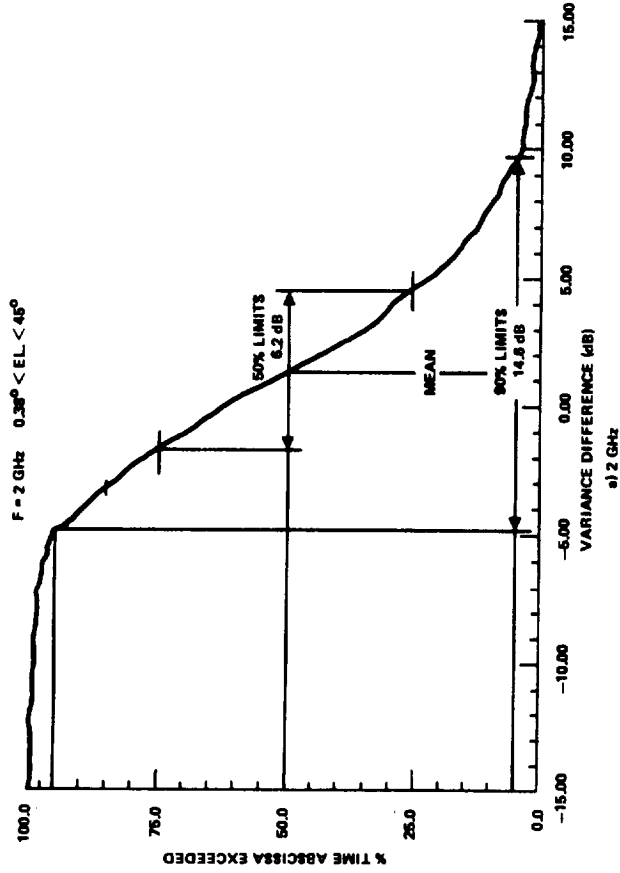
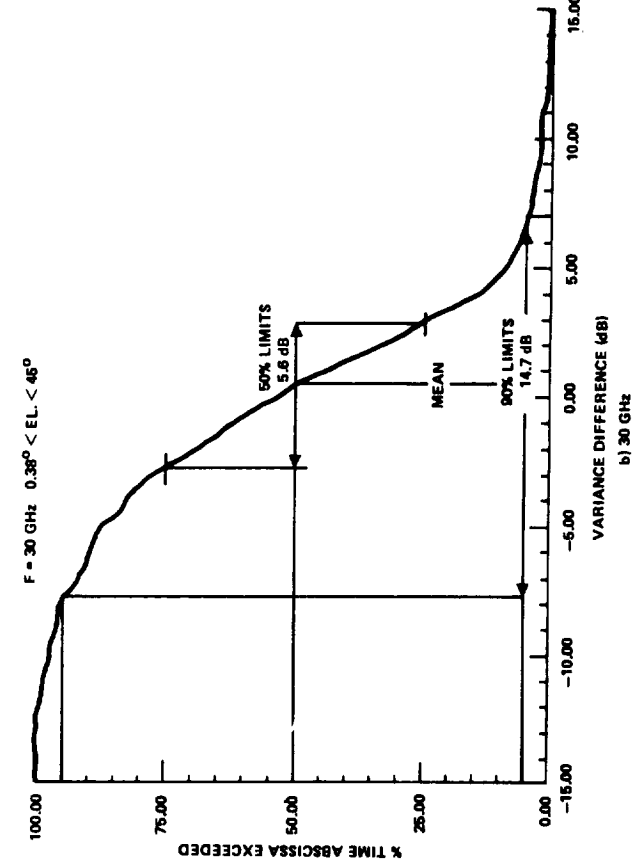


Figure 6.5-4. Distribution of Amplitude Variance from that Predicted from Average Turbulence-Induced Fluctuation Theory

6.5.2.2.3 Power Spectral Density. The formulation of the structure of the power spectral density of turbulence-induced amplitude fluctuations has been derived from classical turbulence theory (Tatarski-1961). The theoretical spectrum of amplitude fluctuations in a medium characterized by a real refractive index is found to roll off as $f_f^{-8/3}$, or -26.6 dB/decade, in fluctuation frequency f_f . This behavior is not a function of operating frequency, as long as the wavelength is small or on the order of the smallest refractive inhomogeneities. Deviation from this slope will occur due to non-stationarity of the scintillation process.

The spectral slope was calculated for time records of 102.4 seconds at 2 and 30 GHz on the ATS-6 CW beacons as the satellites moved in elevation angle from 0.38 to 25 degrees (Baxter and Hodge-1978). Spectral slope was found to be essentially independent of equivalent path length and measured statistics were well centered about the theoretical value of -26 dB/decade. Figures 6.5-5a and b present the probability distribution functions of the 2 and 30 GHz spectral slopes, respectively. Figure 6.5-6 presents the worst-case confidence limits of distribution of spectral slope from an average -26.6 dB/decade, for 50% and 90% of total time. Such an estimate may be used to directly find the expected fading rates and spectral components due to turbulence-induced amplitude scintillation. The data represents clear air statistics over a period of 26 days.

6.5.2.2.4 Estimation of Gain Degradation. The model for received signal amplitude variance has also been used to derive an expression for gain reduction, R, defined by (Theobald and Hodge - 1978)

$$R = 10 \log_{10} \frac{\langle v_d^2 \rangle}{\langle v_d^2 \rangle_{\text{no angle fluctuations}}} \quad (6.5-3)$$

$$R = 10 \log_{10} \frac{l_c + l_i \left[\frac{B^2}{2.77 \sigma_2^2 + B^2} \right]^2}{l_c + l_i}$$

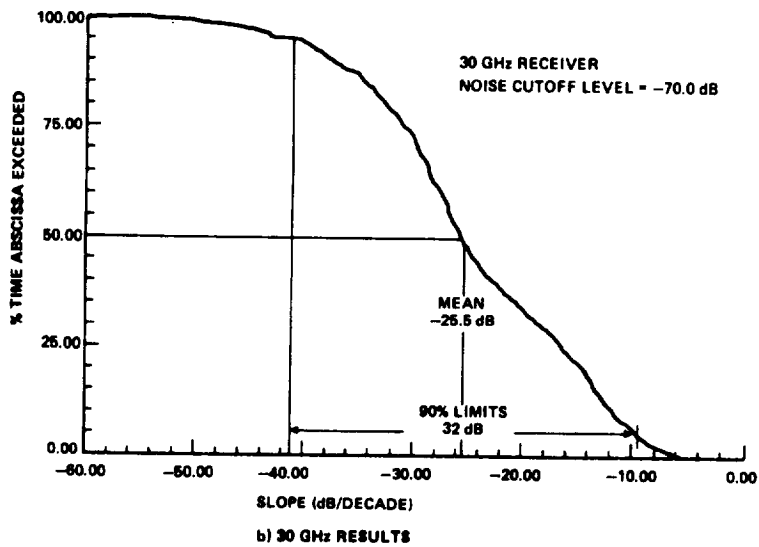
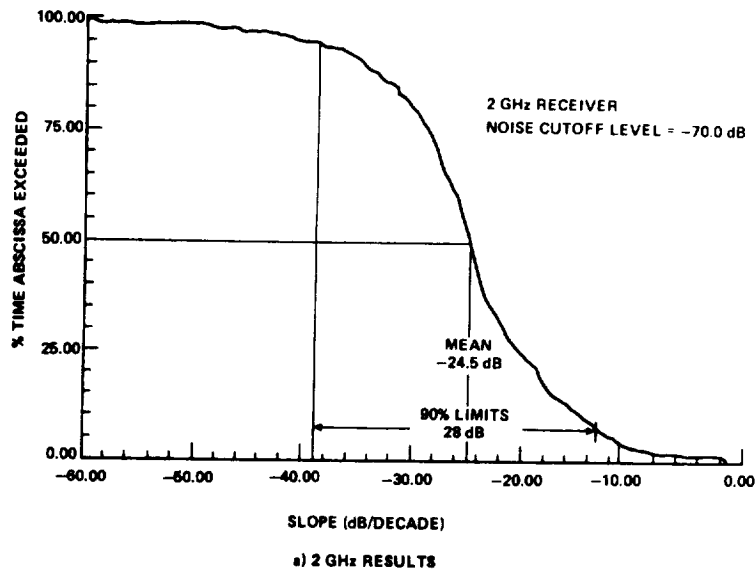


Figure 6.5-5. Probability Density Function of Spectral Slope

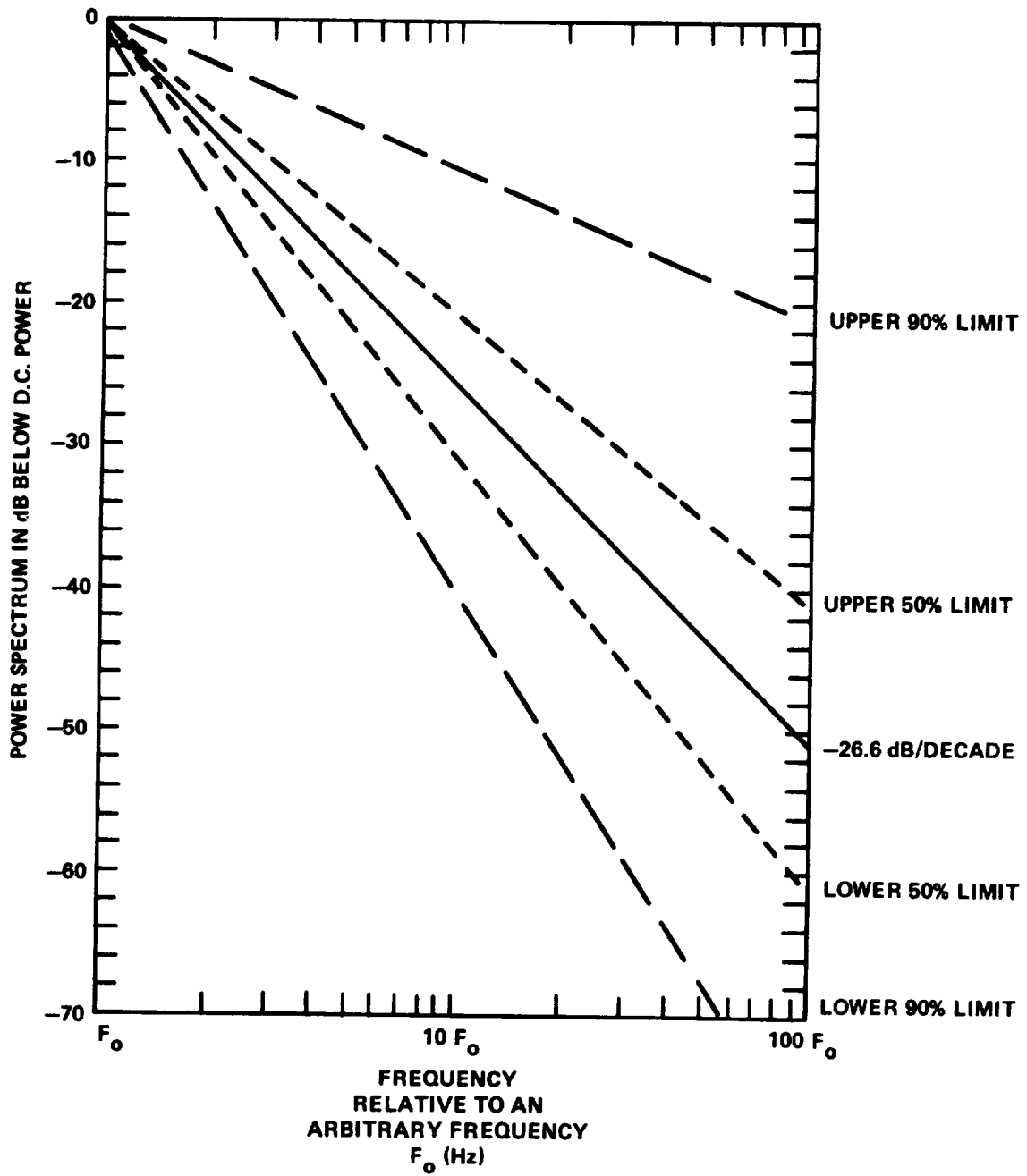


Figure 6.5-6. Confidence Limits of Distribution of Spectral Slope from Average -26dB/Decade

where the constants are the same as those defined for the variance expression, S^2 . This value for R may then be combined with atmospheric gas loss in order to obtain an estimate of average received signal level for an earth-space path. Figure 6.5-7 presents an example of predicted signal levels for 2, 7.3 and 30 GHz for antenna beam widths of 1.8° , 0.3° , and 0.15° , respectively. Also included are measured signal levels, relative to zenith, from the ATS-6 2 and 30 GHz (Devasirvatham and Hodge-1977) transmissions and TACSATCOM 7.3 GHz (McCormick and Maynard-1972) beacons as the satellites were moving in elevation angle.

6.5.2.3 Low Angle Scintillations/Fading. At low elevations (typically less than 10 degrees) scintillations and fades occur due to refractive effects and multipath effects in the troposphere. In addition for stations utilizing antennas with significant sidelobe levels intercepting the ground, classic multipath is possible and should be considered. However, the effects reported here are generally thought to not include the effects of ground-reflected multipath.

Because no unified theory for low-angle fading exists, the design of future systems must be done by similarity. As more data becomes available and more systems require low elevation angle operation, undoubtedly a low-angle fading theory will be developed.

6.5.2.3.1 Presentation of Selected Experimental Results. Concise summaries of low-angle fading data and long term statistics for a variety of locations is presented in Tables 6.5-1 and 6.5-2, respectively. These results are typical of the magnitude of the effect, however to date no comprehensive model attempts to explain these effects. A typical plot of the signal amplitude variance at 20 and 30 GHz as observed in Columbus, Ohio between 42° and 2° is shown in Figure 6.5-8 (compare with Figure 6.5-2). Because the distribution suggested a cosecant behavior, a minimum mean-square-error curve was fit to the data as noted in Figure 6.5-8.

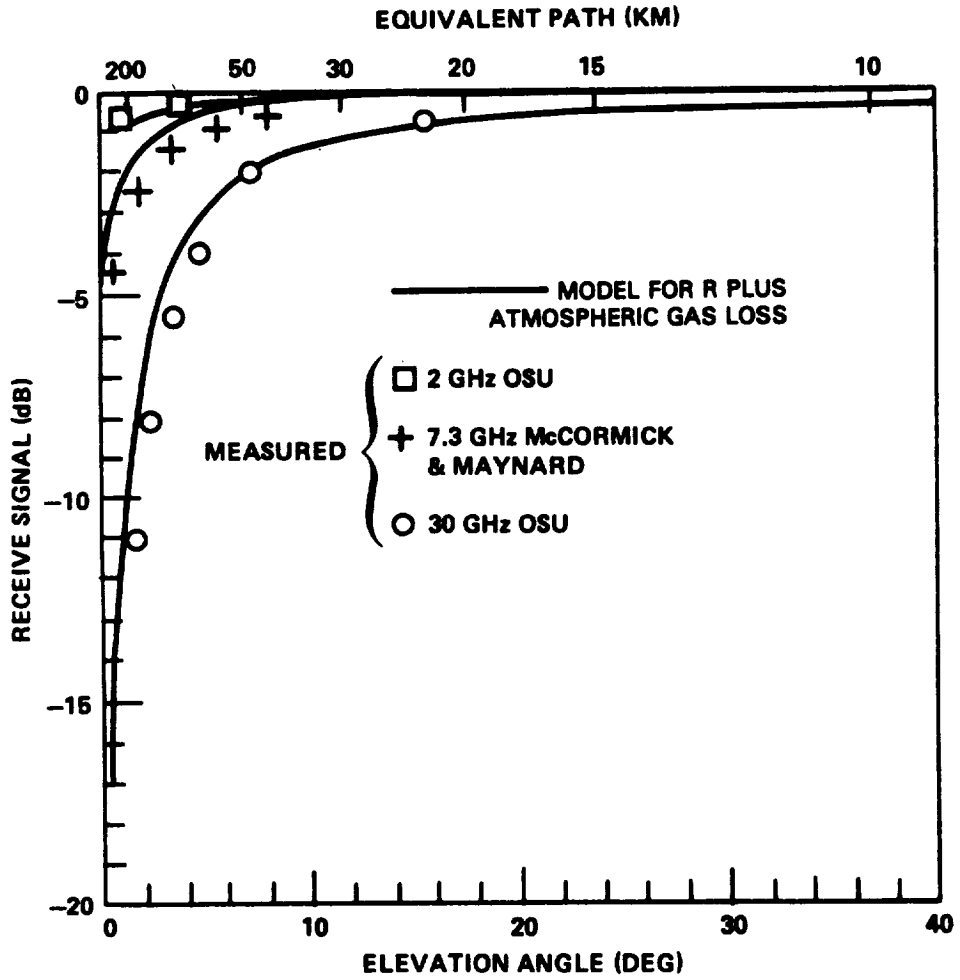


Figure 6.5-7. Predicted and Measured Signal Level as a Function of Elevation Angle

Table 6.5-1. Fading Data Predominantly Due to Scintillation from Satellites at Low Angles of Elevation

[CCIR Report 564-1, 1978]

Location	Satellite	θ (degrees)	Fading data
United Kingdom; Martlesham, Suffolk	ATS-6; 30 GHz	6.5	6.5 (dB) (peak-to-peak) } Maximum in 10 (dB) (peak-to-peak) } turbulent windy 18 (dB) (peak-to-peak) } conditions
		3.3	
		2.4	
United Kingdom; Birmingham	ATS-6; 30 GHz	0.3-1.2	Occasional deep fades of 20 dB
		1-2	Slow enhancements and sudden fades of 20 dB
USA; Virginia [Stutzman <i>et al.</i> , 1975]	ATS-6; 20 GHz	9	2-3 dB Before and after light rain 2-7 dB Hazy conditions 8-15 dB Partly cloudy conditions
		4.7-5.1	
		4.5	
USA; Ohio	ATS-6; 2 and 30 GHz	2.8	3 dB at 2 GHz } Maximum effect in 15 dB at 30 GHz } cumulus 7 dB at 2 GHz } clouds 20 dB at 30 GHz }
		0.38	
USA; Massachusetts	IDCSP; 7 GHz	10	0.03-0.2 dB r.m.s. 10 dB r.m.s. was observed occasionally in summer. Elevation angle fluctuations of up to 0.01° at 3° elevation and 0.002° at 10° elevation (r.m.s. values in 5-min period).
		3	
Canada; Eureka [Strickland <i>et al.</i> , 1977]	Anik II; 4 and 6 GHz	1	Data similar at the two frequencies. Fades of 11 and 20 dB predicted for 1% and 0.1% of worst month.
United Kingdom; Goonhilly [Harris, 1977]	Indian Ocean Satellite, (INTELSAT IV) 4 and 6 GHz	6.5	3 dB (peak-to-peak) exceeded for 0.3% of time on 4 GHz down-link, in a 9-month continuous measurement.
USA; Maryland [Ippolito, 1976]	ATS-6; 20 and 30 GHz	2.5-9	1.5 dB (peak-to-peak) at 9°, increasing to 11 dB at 2.5° at 30 GHz. Values at 20 GHz about 40-70% of those at 30 GHz. Occasional deep fades during light rain.

Table 6.5-2. Statistical Fading Data Predominantly Due to Scintillation and Clear Air Low Elevation Angle Fading

[CCIR Report 564-3, 1986b]

Satellite and frequency	Location of measurements	Antenna diameter (m)	Elevation angle	Peak-to-peak amplitude exceeded for given percentages (dB)						Period of measurement	Reference	
				Whole period			Worst month					
				0.1%	0.3%	1%	0.1%	0.1%	1%			
Intelsat IV-A 3.8 GHz	Oulu, Finland	3	5.4°	3.7	3.2	2.6	4.2	3.2	3.2	3.2	May 1977-May 1978	[Alnutt, 1985]
Intelsat IV-A 3.9 GHz	Oulu, Finland	3	3.5°	3.7	3.2	2.6	4.5	3.3	3.3	3.3	July 1979-July 1980	[Alnutt, 1985]
Anik-A 4 and 6 GHz	Eureka, Canada	4.6	1°	-	-	-	20	11	11	-	-	[Strickland <i>et al.</i> , 1977]
Intelsat-IV 4 and 6 GHz combined	Goonhilly, United Kingdom (to Bahrain)	30	6.5° (57°)	3.7	3	2.6	4	3	3	3	9 months	[Harris, 1977]
Intelsat-IV, 4 and 6 GHz combined	Goonhilly, United Kingdom Yamaguchi, Japan	27.5	6.5° 9°	4.6	4.3	3.6	6	5.2	5.2	5.2	-	-
7 GHz	Ottawa, Canada	9.1	1° 2-3° 5°	-	-	15	-	-	-	-	Summer period	[Webber and McCormick, 1980]
OTS 11.8 GHz	Svalbard Norway	3	3.2°	-	-	-	6.5	3.4	3.4	3.4	April-December 1979 June-August 1980	[Gutierrez, 1981a]
Intelsat-V 11.45 GHz	Chilbolton, United Kingdom	3	8.9°	4	3.4	2.7	-	-	-	-	July-September 1983	[Lo <i>et al.</i> , 1984]

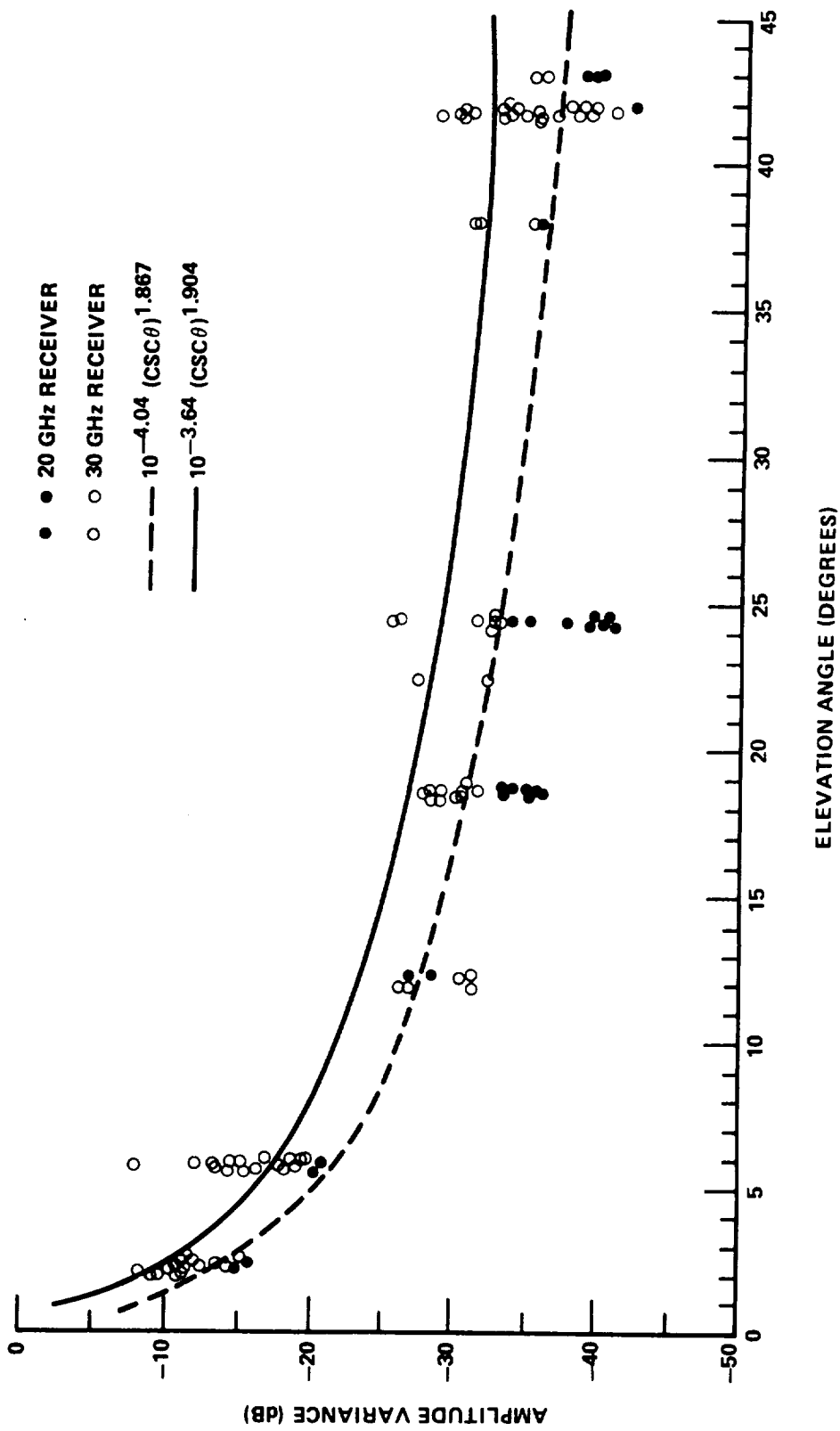


Figure 6.5-8. Measured Amplitude Variance Versus Elevation Angle
(Columbus, Ohio)

Experimental measurements of the fade durations at 6 GHz for fades from 0 to 21 dB below the long term median are shown in Figure 6.5.9 (Strickland, et al-1977). These measurements were made at Eureka, Canada during the month of July 1974 when the moisture content (N-value) is above the yearly average. This data is probably typical of continental air mass data. The frequency and elevation angle scaling factors for this data are not thoroughly confirmed, but the Tatarski (1961) model appears to model experimental results (CCIR-1978, Rpt 718). The variance appears to scale proportional to frequency according to the relation:

$$\text{variance} = 42.25 \left(\frac{2\pi}{\lambda} \right)^{5/6} \int C_n^2(p) p^{5/6} dp \quad (6.5-4)$$

where p is the distance along the path.

The cumulative distribution for the rate of change of signal amplitude between 0.4 second samples was found to be identical for positive and negative-going signals (Strickland, et al-1977). The measured distribution is given in Figure 6.5-10, but again the frequency and elevation angle scaling factors are unknown.

6.5.3 Phase Variations

Phase variations arise due to the variable delay as the wave passes through a medium with variable refractivity and also due to wavefront ripple introduced by the "lumpy" medium. The former is termed phase delay fluctuations, while the latter effect is called phase scintillations.

6.5.3.1 Estimation of Phase Delay Fluctuations on Earth-Space Paths.

An expression for the rms phase fluctuation for a finite circular aperture antenna of diameter d_a ,

$$\sigma_\phi = \left(1 - \frac{d_a^2}{4L^2} \right) \left(2L \sqrt{\overline{\Delta N^2}} \right)^{1/2} \frac{2\pi \times 10^{-6}}{\lambda} \quad (6.5-5)$$

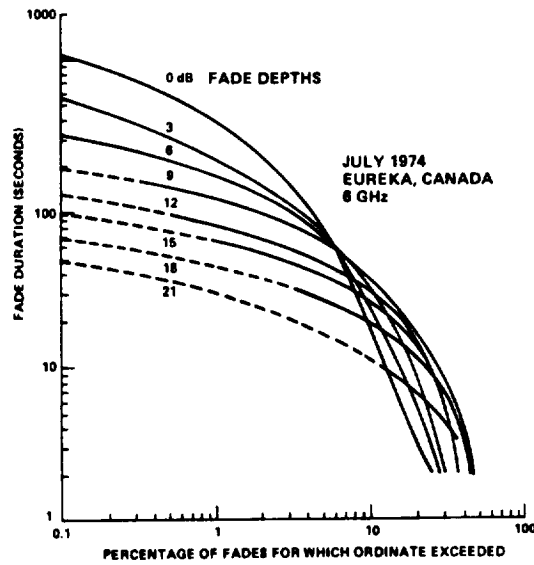


Figure 6.5-9. Cumulative Distributions of Fade Durations at 6 GHz

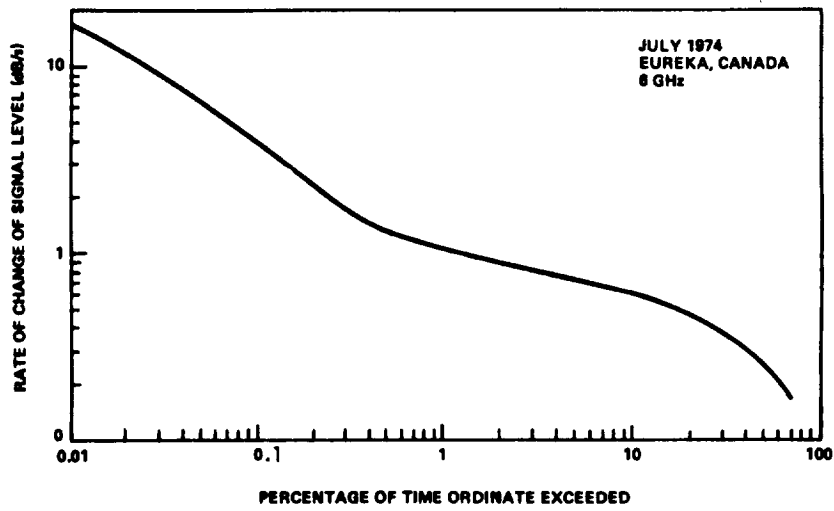


Figure 6.5-10. Cumulative Distribution of Rate of Change of 6 GHz Signal

has been presented by Muchmore and Wheelon (1955). The derivation employs a ray theory approach and assumes an exponential spatial correlation for the turbulence scale. σ_θ is in radians, ℓ is the scale length of the turbulent eddy, L_t is the path length through the turbulence, λ is wavelength, and $\overline{\Delta N^2}$ is the mean-square fluctuation in the refractivity N. When using this expression, one should only assume values of ℓ and $\overline{\Delta N^2}$ such that

$$5\text{m} \leq \ell \overline{\Delta N^2} \leq 500\text{m}. \quad (6.5-6)$$

The results of using this relation at the limiting values of $\ell \overline{\Delta N^2}$ for 3 and 10 GHz are presented in Figure 6.5-11. Typical values of ℓ are 60 meters and $\overline{\Delta N^2} = 1/2$. This modeVL indicates that the phase delay fluctuations increase linearly with frequency and become significantly less if the antenna diameter approaches the scale length.

Another technique for estimating these phase delay fluctuations based on the monthly variance of the surface refractivity and estimates of the frequency spectrum of the delay fluctuation have been made by Nusple, et al (1975).

6.5.3.2 Estimate of Phase Ripple Effects on Earth-Space Paths.

Accompanying the amplitude scintillations of a plane wave propagating through tropospheric turbulence are transverse phase ripple variations. According to the theory of Tatarski (1961) the mean-square phase variation over a distance transverse to the propagation path is.:

$$D_\theta(\rho_\theta) = K_\theta C_{n0}^2 (2\pi/\lambda)^2 L_T \rho_\theta^{5/3} \quad (6.5-7)$$

where λ is wavelength, L_t is the propagation path length through the region of turbulence, and C_{n0} is the surface structure constant. The constant K is equal to 2.91 for the exponential C_n^2 model (Tatarski-1961) and equal to 4.57 from Ohio data (Theobald and Hodge-1978). This expression may be used to estimate the expected mean-square

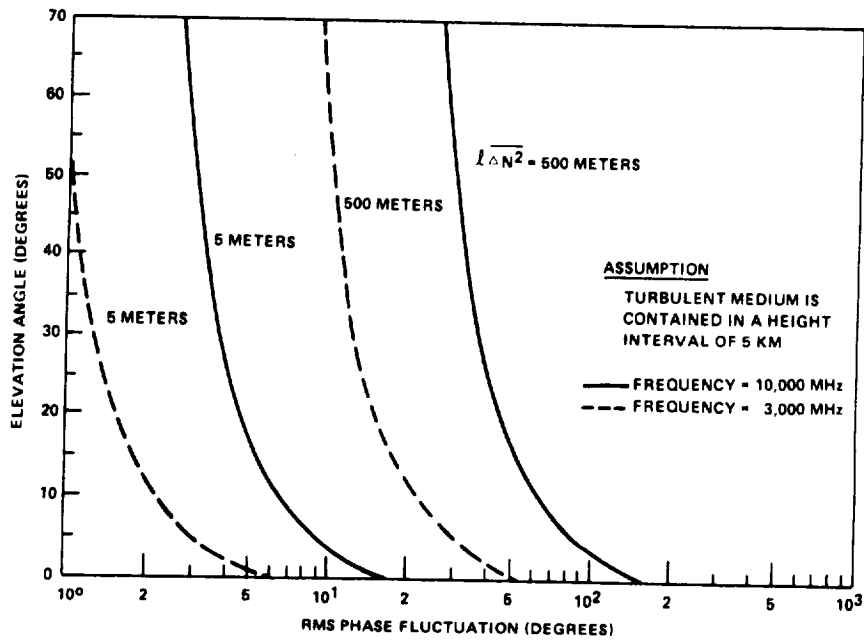


Figure 6.5-11. R.M.S. Phase Fluctuations for an Earth-Space Path

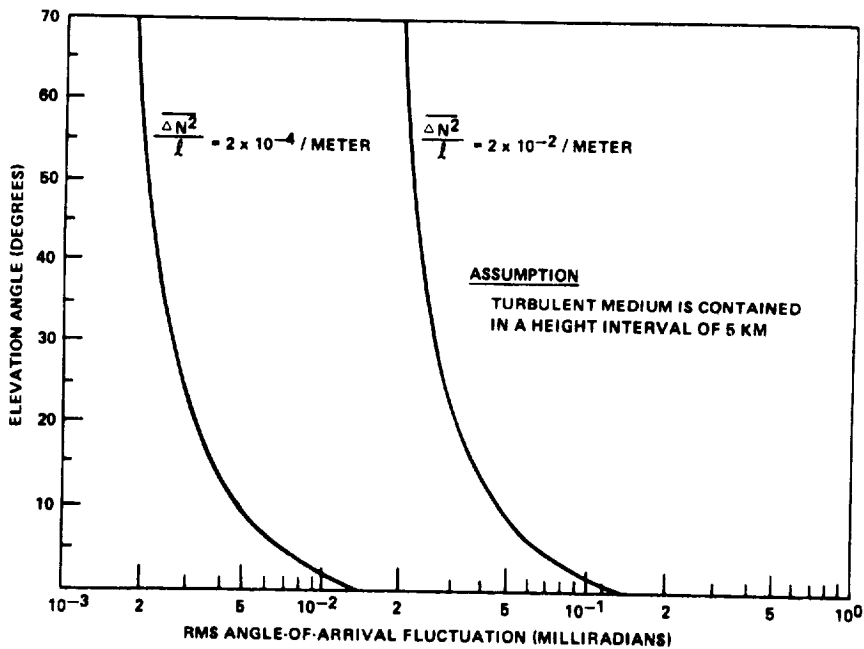


Figure 6.5-12. R.M.S. Angle-of-Arrival Fluctuations for an Earth-Space Path

phase variation between two points separated by a distance ρ_0 normal to the direction of propagation, given an estimate of C_{no} .

Clearly, this phase incoherence appears as an apparent antenna gain degradation. Measurements made with a 22 m diameter antenna at 5 degrees elevation angle and 4 and 6 GHz indicate a 0.2 to 0.4 dB degradation (Yokoi, et al-1970). A 7 meter diameter antenna at 5 degrees elevation angle and 15.5 and 31.6 GHz yielded a gain degradation of 0.3 and 0.6 dB, respectively (Yamada and Yokoi-1974). This effect is clearly most pronounced for large antennas, high frequencies and elevation angles below 5 degrees (CCIR 1986b, Rpt. 564-3).

6.5.4 Angle-of-Arrival Variation

The average ray bending (mean deviation from the geometric or vacuum line-of-sight) along a slant path has been estimated by a linear relation to the surface refractivity (Crane-1976a). Estimates of the apparent fluctuations of ray direction or the angle-of-arrival are given below. Because they are assumed to arise solely due to refractive effects the variations are symmetrical about the direction of propagation and the fluctuation frequency is of the order of the time for the turbulence length to pass through the beam.

The Muchmore and Wheelon expression for the rms angle-of-arrival fluctuation in radians is

$$\sigma_{\theta} = \left[\frac{2\sqrt{\pi} L_r \overline{\Delta N^2}}{l} \right]^{1/2} \times 10^{-6} \quad (6.5-8)$$

where all parameters are as previously defined. A Gaussian correlation function for the scale of turbulence was assumed and one should impose the limits

$$2 \times 10^{-4} \text{ m}^{-1} \leq \overline{\Delta N^2} / l \leq 2 \times 10^{-2} \text{ m}^{-1} \quad (6.5-9)$$

Figure 6.5-12 is an example for this expression, within the stated range of $\overline{\Delta N^2}/\ell$, for an earth-space propagation path through a turbulent region of height 5 km. Note that σ_θ^2 is directly proportional to path length and independent of operating frequency. Also, σ_θ decreases with increasing eddy size, ℓ , while phase fluctuation σ_ϕ increases with increasing eddy size.

Estimates (CCIR-1986b, Rpt. 564-3) indicate that the short-term variations in the angle-of-arrival may be of the order of 0.02 degrees (0.37 milliradians) at 1 degree elevation. This is higher than the theory predicts (see Figure 6.5-12), but the effect does decrease rapidly with increasing elevation angle. Crane (1976) reports values of σ_θ within the bounds of Figure 6.5-12 for 7 GHz measurements made at varying elevation angles with a 37 m diameter antenna.

Generally, for beamwidths greater than 0.01 degree and elevation angles above 10 degrees, the angle-of-arrival fluctuations are masked by other fluctuations.

6.5.5 Fading and Gain Degradation Design Information

6.5.5.1 Fade Distribution Function Estimation. The estimates of gain reduction and signal variance parameters, R and S^2 , have been presented. These quantities may be incorporated into distribution functions which are of the form used in link design. They represent the long term average fade statistics due to clear air amplitude and angle-of-arrival fluctuations. The estimates of R and S^2 may be more closely matched to local and seasonal conditions if a local estimate of C_n^2 is available. A hypothetical low elevation angle fade distribution is presented in Figure 6.5-13. The abscissa is referenced to the signal level received in the absence of turbulence, i.e., including free space loss and gaseous absorption. The point at which the signal level is R dB is also the mean of the received signal; thus, one point on the fade distribution is established. The fade distribution for turbulence-induced fluctuations is assumed to be log-normal, with mean and median being

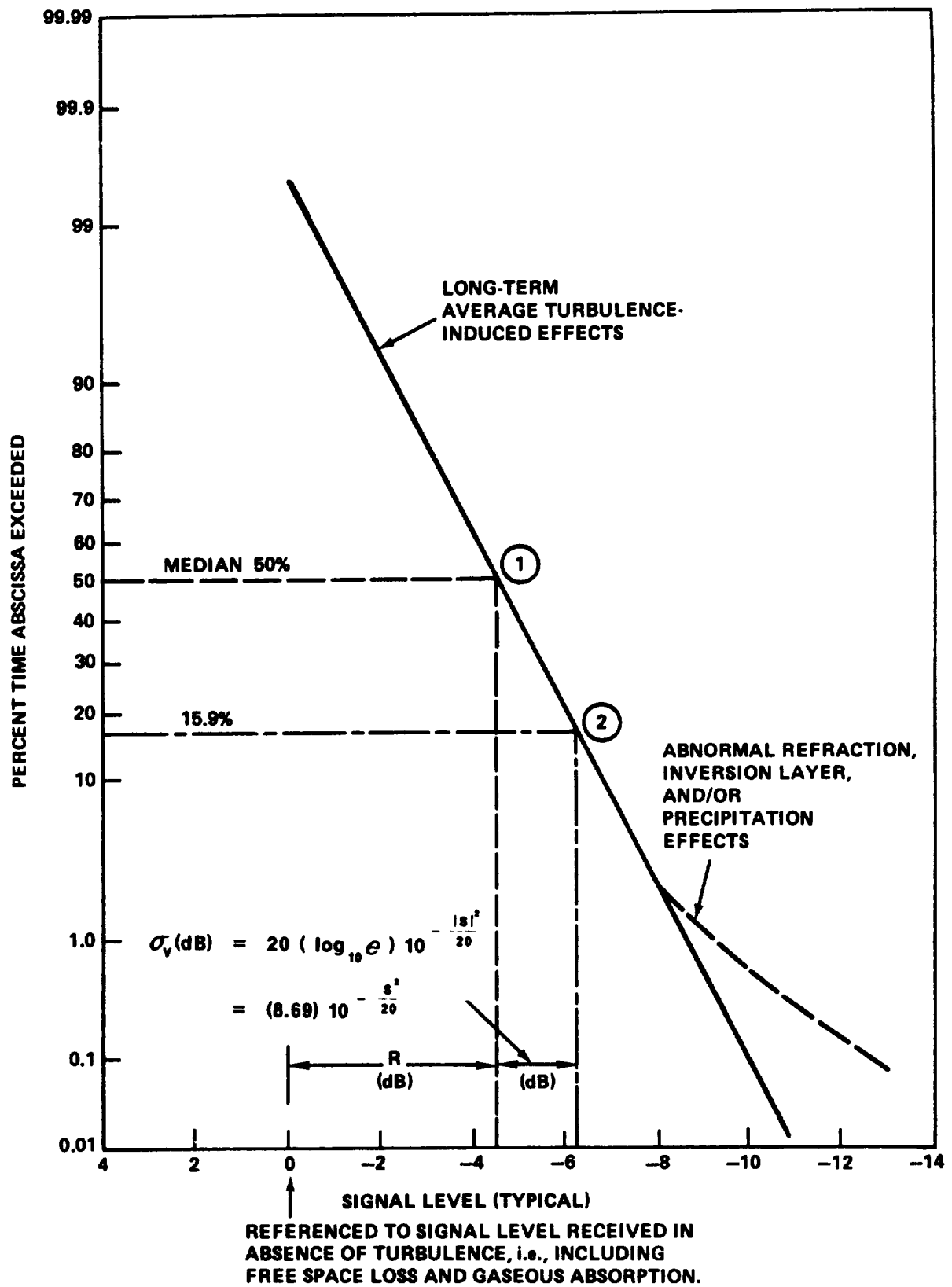


Figure 6.5-13. Hypothetical Fade Distribution Function for Low Elevation Angles

equal. The fade distributions resulting from the Ohio State University ATS-6 30 GHz beacon measurements (Devasirvatham and Hodge-1977) indicate that this log-normal assumption is valid for elevation angles above approximately 2° . A similar observation was made concerning the 7.3 GHz fade distribution above 4° elevation angle observed by McCormick and Maynard (1972).

A fade distribution may now be produced using this assumption of linearity. Referring to Figure 6.5-13, it was noted that the point at which the received signal level is R dB represents the mean signal level. For a normal distribution, the mean is plotted at the 50% time abscissa exceeded point, indicated by 1 in the figure. One standard deviation to the right of the mean on a normal distribution occurs at the 15.9% time abscissa exceeded level. It may be easily shown that the standard deviation of received signal level, expressed in dB and denoted $\sigma_{v_{dB}}$, may be written in terms of the signal variances S^2 . This point, $\sigma_{v_{dB}}$, to the right of R , is denoted by 2 in the figure. A straight line drawn between points 1 and 2 now approximately represents the fade distribution, referenced to the mean signal level in the absence of turbulence induced fluctuations. This distribution was based on small fluctuation arguments and should be employed as a lower bound when estimating a particular fade distribution.

Deviation of this fade distribution from the expected form will occur at small time percentages. Additional fading due to precipitation, abnormal refraction, or inversions in the atmosphere will cause greater fade depths for the small time percentages. However, the turbulence effects, which are always present, are still dominant for larger time percentages. For high elevation angles, i.e., short path lengths, S^2 will be very small and the line drawn through points 1 and 2 will be virtually vertical.

However, the precipitation effects at the lower percentages will still be present for short path length cases and will become the dominant feature of the fade distribution.

6.5.5.2 Gain Degradation Design Information.

6.5.5.2.1 Estimation of Domains. The effects of amplitude and angle-of-arrival fluctuations are, of course, most prominent for very long path lengths and/or very narrow beamwidths. One may estimate whether or not gain degradation need be considered in a path design if elevation angle (or equivalent path length) and antenna beamwidth are known. Figure 6.5-14 presents regimes of average gain degradation between 0.5 and 3 dB and where they must be considered as a function of elevation angle and antenna beamwidth.

Realized gain, or expected gain less gain degradation, is plotted as a function of antenna beamwidth (for any frequency) or equivalent aperture diameter at 30 GHz in Figure 6.5-15. All equivalent aperture diameters are presented for an antenna aperture efficiency of 0.6. The curve representing zero path length L_t is simply the common gain approximation $G = 41253/B^2$ where B is the half power beamwidth in degrees. Realized gain curves for path lengths of 50 to 300 km are plotted using the model. Equivalent earth-space path elevation angles assuming a 6 km high homogeneous atmosphere are presented in parentheses.

Notice that gain degradation due to turbulence-induced fluctuation is negligible for beamwidths wider than about 0.7° for all path lengths. Degradation effects then gradually increase as beamwidth narrows from 0.7° to 0.05° and at any particular beamwidth are approximately directly proportional, in dB, to path length. As beamwidth narrows beyond 0.05° , a saturation effect occurs and the degradation becomes constant for any one path length.

All design figures of Section 6.5.5 represent estimates for clear air effects in a temperate climate during daytime and in the warmer months of the year. If a local value of C^2_n is known, more accurate values of R and S^2 may be obtained. If local statistics of C^2_n are known, statistics of R and S^2 may be obtained.

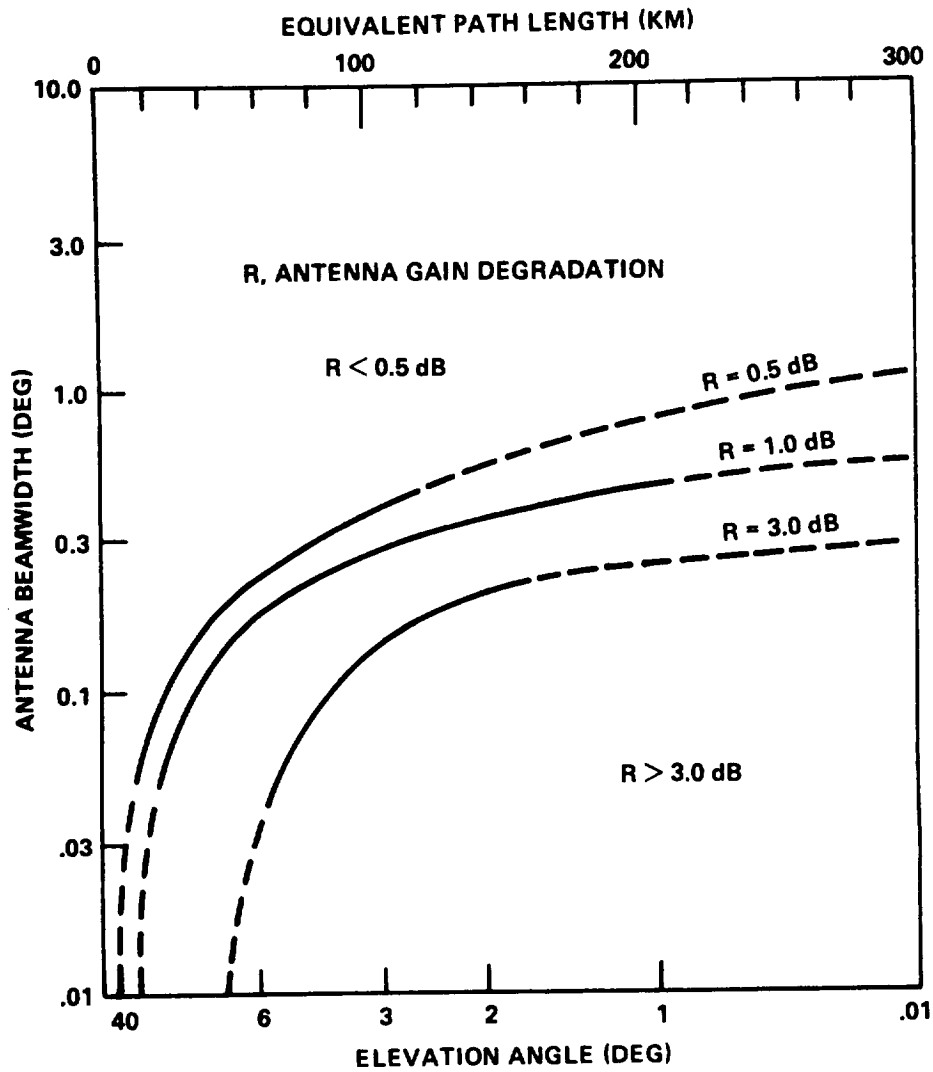


Figure 6.5-14. Gain Degradation Regimes as a Function of Beamwidth and Elevation Angle

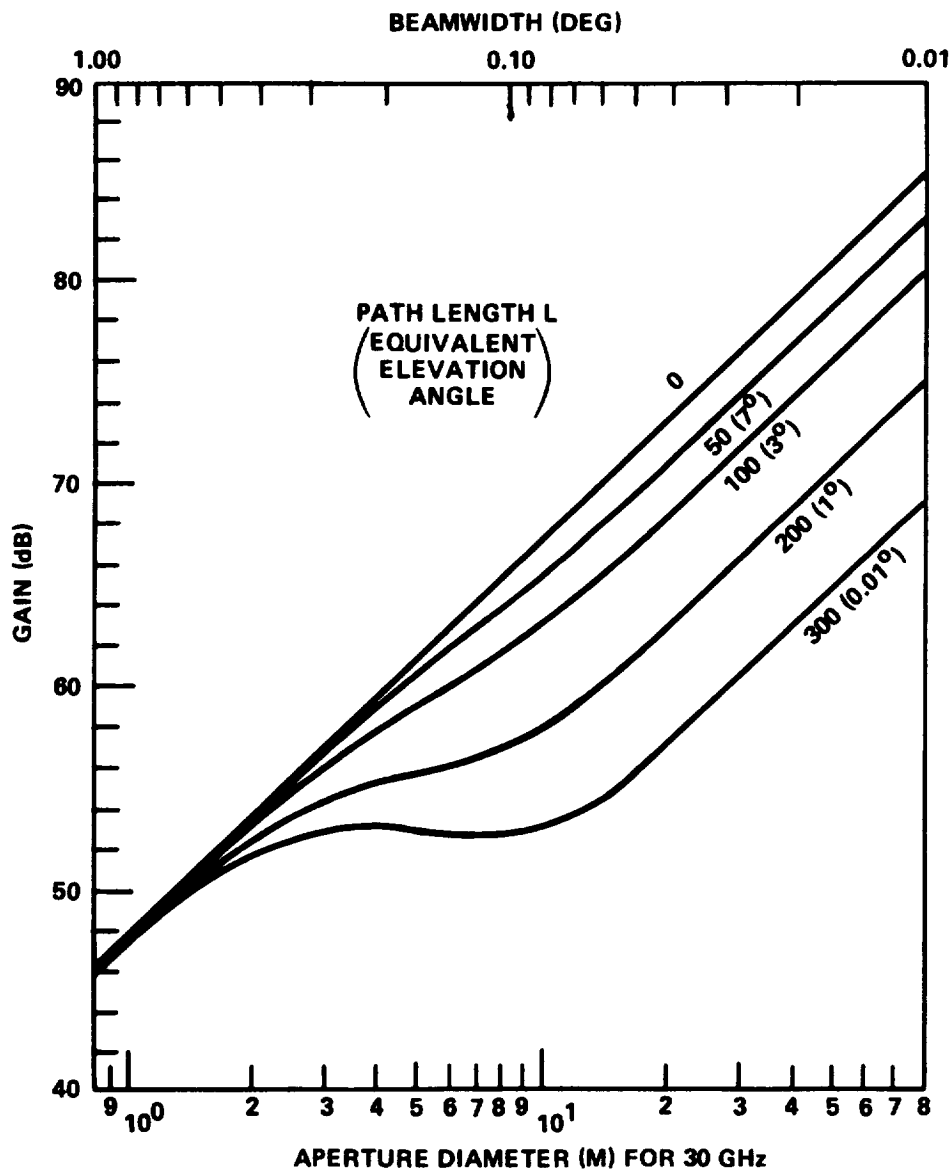


Figure 6.5-15. Realized Gain Versus Beamwidth or Aperture Diameter at 30 GHz

6.5.5.2.2 Spatial Diversity. Paths operating at very low elevation angles with narrow beamwidth antennas may experience unacceptable fading due to scintillation and multipath effects. The required reliability may be regained by the use of spaced site diversity. A site separation greater than 300 m transverse to the propagation path has been suggested (CCIR-1986b, Rpt 564-3) as necessary to alleviate severe turbulence-induced effects. In effect, separation on the order of or larger than the scale size of the largest inhomogeneities in refractive index along the propagation path, and especially near the surface where refraction is greatest, results in decorrelation of the instantaneous signal fluctuations and hence improved performance.

The aperture effects of large antennas may be circumvented if several phase-locked antennas, each with relatively wide beamwidth, are employed in an array to achieve the desired system gain. Of course, overall fade margins will be on the order of that for a single element, but angle-of-arrival effects are eliminated. In addition, such an array alleviates the need to mechanically track a geosynchronous satellite, as is necessary with large aperture, narrow beamwidth antennas.

6.5.6 A Sample Computation of Signal Fluctuations and Gain Degradation

In this section examples of the parameters described in Section 6.5 are worked out for a hypothetical ground station located at Columbus, Ohio with a 4.6m (15 ft) diameter parabolic antenna observing a 28.56 GHz COMSTAR beacon at 10 degrees elevation angle. Actually, the COMSTAR satellites are not at that low an angle, but in order to demonstrate the effects of gain reduction this value has been arbitrarily selected.

6.5.6.1 Amplitude Fluctuations. The variance of the received signal amplitude is calculated using the expression in Section 6.5.2.2. The full half-power beamwidth B in degrees is $70\lambda / d_a = 70 c / f d_a = (70)(3 \times 10^8 \text{m/sec}) / (28.56 \times 10^9 \text{sec}^{-1})(4.6 \text{m}) = 0.16$ degrees. The

path length of the turbulence L_t is computed from $h_t = 6$ km, $r_e = 6371$ km and $\theta = 10$ degrees using the equation

$$L_t = \left[h_t^2 + 2r_e h_t + (r_e \sin\theta)^2 \right]^{1/2} - r_e \sin\theta = 34 \text{ km} \quad (6.5-10)$$

The other constants are:

$$L_o = 180 \text{ km}$$

$$\delta^2_1 = 1.18 \times 10^{-3}$$

$$\delta^2_2 = 8.35 \times 10^{-4}$$

$$I_i = 0.17$$

$$I_c = 0.83$$

and the signal variance relative to the average power is

$$S^2 = 10 \log_{10} \frac{9.79 \times 10^{-4} + 0.14396 - 0.14297}{0.83 + 0.14}$$
$$= 10 \log_{10} (2.03 \times 10^{-3}) \approx -27 \text{ dB}$$

Note that this agrees well with the results in Figure 6.5-2. Reference to Tatarski (1961) would have allowed evaluation in terms of C^2_n rather than the formulation by Theobald and Hodge (1978) utilized here.

Reference to Figure 6.5-4b indicates that 50% of the time the S^2 would be between -24 and -30 dB, while 90% of the time S^2 would be between -20 and -34 dB.

The power spectrum density of the fluctuations decreases at 26.5 dB/decade (see Figure 6.5-6). If one considers some lower frequency cutoff for the amplitude fluctuations (say 0.1 Hz) the

fluctuation power at 1 Hz is on the average 26.5 dB below the value of 0.1 Hz. Only 10% of the time will the 1 Hz fluctuation power be only 10 dB below the 0.1 Hz fluctuation power. Clearly, most of the fluctuation power for clear air fluctuations is at the low frequencies (less than 1 Hz).

6.5.6.2 Phase and Angle-Of-Arrival Variations. Phase fluctuations are estimated from the model of Muchmore and Wheelon (1955) presented in Section 6.5.3. Data quoted in Muchmore and Wheelon indicate typical values for $\ell \approx 60\text{m} \approx 200$ feet and $\overline{\Delta N^2} = 1/2$. Thus $\overline{\ell \Delta N^2} = 30$ meters.

For a finite circular antenna of 4.6 m diameter, the rms phase delay fluctuation is 0.85 radians = 48 degrees. For a $C_{no} = 10^{-14}$, the phase ripple fluctuation across the antenna is very small.

The estimate of the angle-of-arrival fluctuations in radians (see Section 6.5.4) is calculated to be 3.2×10^{-5} radians = 1.8×10^{-3} degrees. This is a small number compared to 0.16 degree half-power beamwidth of the antenna. Also note that the limits on $\Delta N^2/\ell = 8.3 \times 10^{-3}\text{m}^{-1}$ are not exceeded.

6.5.6.3 Prediction of the Average Received Signal Gain Reduction. The average received signal reduction is calculated using the same parameters required for calculation of the amplitude fluctuations. Using the relation in Section 6.5.2.2.4.

$$R = 10 \log_{10} \frac{(0.83 + 0.17(0.84))}{1.0} = -0.12 \text{ dB}$$

Thus during clear weather this COMSTAR beacon will on the average be 0.12 dB below the value calculated considering clear air attenuation only. This same value could be estimated from Figure 6.5-15.

The long-term average distribution in Figure 6.5-13 is now constructed from R and S². The point 2 (15.9% point) is found to be $20(\log_{10}e) 10^{-|S^2|/20} = 0.39$ dB which is the standard deviation of the receiver voltage taken from a square law detector.

6.6 PREDICTION OF DEPOLARIZATION ON EARTH-SPACE PATHS

6.6.1 Introduction

Depolarization refers to that effect wherein an earth-space wave's polarization is altered in the troposphere. Depolarization is also referred to as cross-polarization. For linearly polarized waves a vertically (horizontally) polarized wave will, after passing through a medium, have a horizontally (vertically) polarized component in addition to the initial wave. For circularly polarized waves a RHCP (LHCP) wave will develop into an elliptical wave. For frequency reuse systems based on polarization isolation this coupling reduces isolation and increases "cross-talk."

6.6.1.1 Sources of Depolarization. The major source of depolarization at frequencies below 10 GHz is Faraday rotation of the plane of polarization by the Earth's ionosphere. Faraday rotation may be as much as 1° of rotation at 10 GHz. It is discussed in a companion publication of propagation effects at frequencies below 10GHz (Flock, 1987).

At frequencies above 10 GHz, the primary sources of depolarization are tropospheric and are due to the presence of

- hydrometeors (rain, ice, snow)
- multipath
- refractive effects

These hydrometeor and scattering effects generate depolarization because of the non-spherical shapes of the hydrometer particles. For example, as raindrop sizes increase their shape departs from spherical and becomes an oblate spheroid with an increasingly pronounced flat bottom. For large drop sizes a concave depression

develops (Pruppacher and Pitter-1971). Polarized microwave energy scattered from these particles can easily be converted into an orthogonal polarization.

6.6.1.2 Measures of Depolarization. The measurement of depolarization by propagation researchers usually has been done utilizing orthogonally-polarized feeds on a single antenna while observing singly-polarized satellite signals. This parameter is called the cross-polarization discrimination (XPD) or cross-polarization ratio (XPR) defined as (Bostian, et al-1977)

$$\begin{aligned} \text{XPD} &= \frac{\text{power output from co-polarized port}}{\text{power output from cross-polarized port}} \\ &= (\text{XPR})^{-1} \end{aligned}$$

For perfect transmitting and receiving antennas and a perfect medium this isolation could become infinite, but with practical components some leakage is always present. Definitions and sample calculations of depolarization terms have been well documented in a tutorial report by Stutzman (1977).

Unfortunately, the system designer desires the cross-polarization isolation (XPI) term defined as

$$\begin{aligned} \text{XPI (dB)} &= \text{co-polarized signal power (dB)} \\ &\quad - \text{cross-polarized signal power (dB) on the same channel} \end{aligned}$$

Fortunately, for most levels of attenuation observed, $\text{XPI} \approx \text{XPD} = (\text{XPR})^{-1}$ (Watson and Arbabi-1973).

6.6.1.3 Depolarization Measurements. Most experimental depolarization data has been obtained from the 11.7 GHz right-hand circularly polarized Communications Technology Satellite (CTS) beacon, the 19.04 and 28.56 GHz linear polarized AT&T COMSTAR satellite beacons, and the 11.6 GHz circularly polarized SIRIO beacon.

6.6.2 Rain Depolarization

6.6.2.1 Depolarization Versus Attenuation Relations. Correlation of depolarization with rain rate has not been too successful because of the many parameters required for these calculations. However, experimentally and analytically (Nowland, et al-1977a) it has been observed that rain-induced depolarization can be related to total attenuation by the formula

$$\text{XPD} = \tilde{a} - \tilde{b} \log_{10} (A) \quad (6.6-1)$$

where XPD is the cross-polarization discrimination in dB and A is the total attenuation in dB due to rain (not including the clear air attenuation). \tilde{a} and \tilde{b} are empirical constants.

6.6.2.1.1 CCIR Approximation. The CCIR (1986b, Rpt. 564-3) has developed analytical approximations for the empirical constants \tilde{a} and \tilde{b} which give reasonable agreement for the XPD with existing theory and available data. The relationships are,

$$\begin{aligned} \tilde{a} = & 30 \log(f) - 10 \log_{10}[0.516 - 0.484 \cos(4\tau)] \\ & - 40 \log_{10}(\cos\theta) + 0.0052\sigma^2 \end{aligned} \quad (6.6-2)$$

and

$$\begin{aligned} \tilde{b} = & 20 \quad \text{for } 8 \leq f \leq 15 \text{ GHz} \\ & = 23 \quad \text{for } 15 < f \leq 35 \text{ GHz} \end{aligned} \quad (6.6-3)$$

where:

f = frequency, in GHz

τ = polarization tilt angle with respect to the horizontal, in degrees ($\tau = 45^\circ$ for circular polarization)

θ = path elevation angle, in degrees

σ = standard deviation of the raindrop canting angle, in degrees

The above relationships are valid over the ranges:

$$8 \leq f \leq 35 \text{ GHz}$$

$$\theta \leq 60^\circ$$

$$0^\circ \leq \tau \leq 90^\circ$$

Recommended values for the standard deviation σ are:

<u>Percent of Time</u>	<u>σ</u>
1.0%	0°
0.1%	5°
0.1%	10°
0.001%	15°

The above results do not include the effects of ice depolarization. A CCIR factor for ice induced XPD is discussed later in Section 6.6.3.3.

6.6.2.1.2 VPI & SU and Univ. of Texas Results. The Virginia Polytechnic Institute and State University (VPI&SU) have analyzed their CTS (11.7 GHz) and COMSTAR (16.04 and 28.56 GHz) beacon depolarization data in two manners. The first technique is to compare the measured cumulative XPD with the measured cumulative rain attenuation statistics. These results are termed the statistical depolarization results. The second technique pairs "instantaneous" (half-minute) intervals of data for both parameters and smooths the data to obtain \tilde{a} and \tilde{b} .

The results of these two techniques for 11.7 GHz data both from VPI&SU and the University of Texas (C.W. Bostian, et al-1979) are shown in Figure 6.6-1. Clearly these results indicate a wide spread of values have been obtained to date even though they are averaged over an entire year. The attenuation has been truncated at 5 dB because of the effects of ice depolarization (see Section 6.6.3).

VPI&SU has also related the XPD to attenuation for each month of 1978 for which 5 dB or greater fades occurred. These \tilde{a} and \tilde{b} results are shown in Table 6.6-1 for the number of half-minute samples indicated. The R^2 term, a correlation coefficient, is a measure of the goodness of the fit. The wide variations noted are similar to those observed by other investigators.

Additional data from the University of Texas at Austin (Vogel - 1979) incorporating exceedance values is presented in Figure 6.6-2. These curves show the 10%, 50% (median) and 90% expectation of exceeded isolation for each attenuation. For example at 5 dB (meaning $4 \text{ dB} \leq A \leq 5 \text{ dB}$) the XPD exceeded 23 dB for 90%, exceeded 28 dB for 50% and exceeded 33 dB for 10% of the data. The logarithmic fit to these three curves is

$$\begin{aligned} 10\% & : \text{XPD} - 42.9 - 17.5 \log_{10}A \\ 50\% & : \text{XPD} - 35.8 - 13.4 \log_{10}A \\ 90\% & : \text{XPD} - 31.5 - 12.6 \log_{10}A \end{aligned}$$

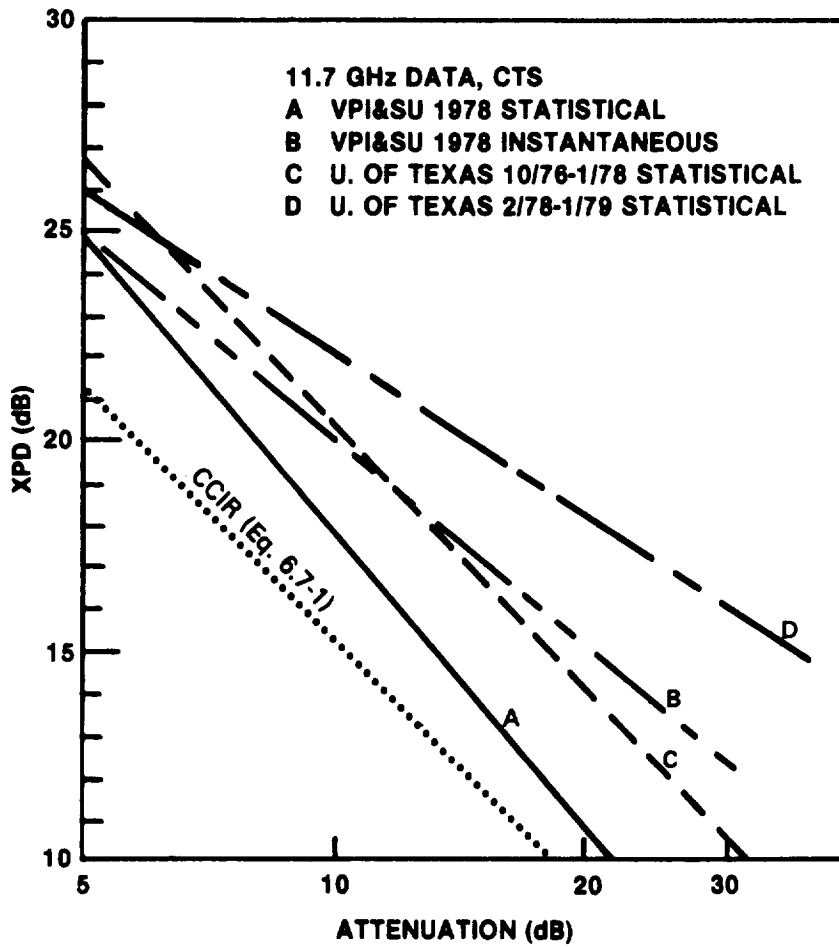


Figure 6.6-1. Cross-Polarization Discrimination Versus Attenuation for Statistical and Instantaneous Data

Table 6.6-1. Least-Mean Square Fits of Depolarization Coefficients by Month

$XPD = \tilde{a} - \tilde{b} \log_{10} A$ $5 < A < 30$ dB VPI&SU 1978 CTS DATA

MONTH	\tilde{a}	\tilde{b}	R ²	NO. OF 1/2 MINUTE INTERVALS
JAN	30.79	2.62	.00	22
MAR	51.18	38.18	.63	309
MAY	49.01	27.93	.90	30
JUNE	38.42	17.53	.56	38
JULY	42.23	21.94	.80	74
AUG	47.31	25.99	.47	28
SEPT	64.20	51.93	.32	50
NOV	27.59	4.11	.04	7
YEAR	36.29	16.22	.36	574

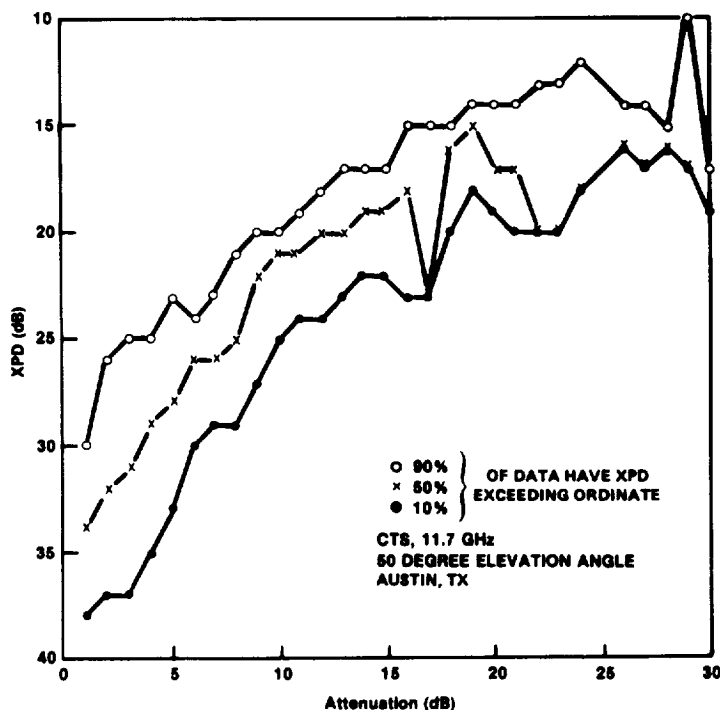


Figure 6.6-2. Twelve Month Isolation Versus Attenuation Data

for the 11.7 GHz CTS beacon at 50 degrees elevation angle.

6.6.2.2 Frequency Scaling Depolarization Measurements. The Virginia Polytechnic Institute and State University (Bostian, et al-1978, 1979) has also made simultaneous measurements of the depolarization at 19 GHz vertical and horizontal and 28.56 GHz using the COMSTAR beacons. Their results for 1977 and 1978 are given in Table 6.6-2.

Table 6.6-2. Cross-Polarization Discrimination Versus Attenuation (Least-Mean-Square Fits)

Blacksburg, VA		Elevation Angle = θ
Period	Frequency/Polarization	$XPD = \tilde{a} - \tilde{b} \log_{10}(A)$
Aug 1977	11 GHz, RHCP (CTS, $\theta = 33^\circ$)	$XPD = 44.7 - 22.6 \log_{10}(A)$
1978	11 GHz, RHCP (CTS)	$XPD = 36.3 - 16.2 \log_{10}(A)$
Aug 1977	19 GHz, vertical (COMSTAR, $\theta = 44^\circ$)	$XPD = 47 - 24.5 \log_{10}(A)$
Sept 1977	19 GHz, horizontal (COMSTAR)	$XPD = 37.1 - 20.0 \log_{10}(A)$
1978	19 GHz, vertical (COMSTAR)	$XPD = 43.9 - 16.6 \log_{10}(A)$
Aug 1977	28 GHz, vertical (COMSTAR)	$XPD = 36.4 - 15.4 \log_{10}(A)$
1978	28 GHz, vertical (COMSTAR)	$XPD = 31.2 - 7 \log_{10}(A)$

The analysis of Nowland, et al (1977a) may be utilized to show the expected frequency dependence of the coefficients \tilde{a} and \tilde{b} in $XPD = \tilde{a} - \tilde{b} \log_{10}(A)$. Using Equations 11 and 12 of Nowland, et al (1977a) and many of the constants in the paper, the solid curve was derived in Figure 6.6-3. The dashed curve was derived using the effective path length $L_e = 12.82 R^{-0.3}$ and the specific attenuation in Section 6.3. Several experimental data points are shown, but

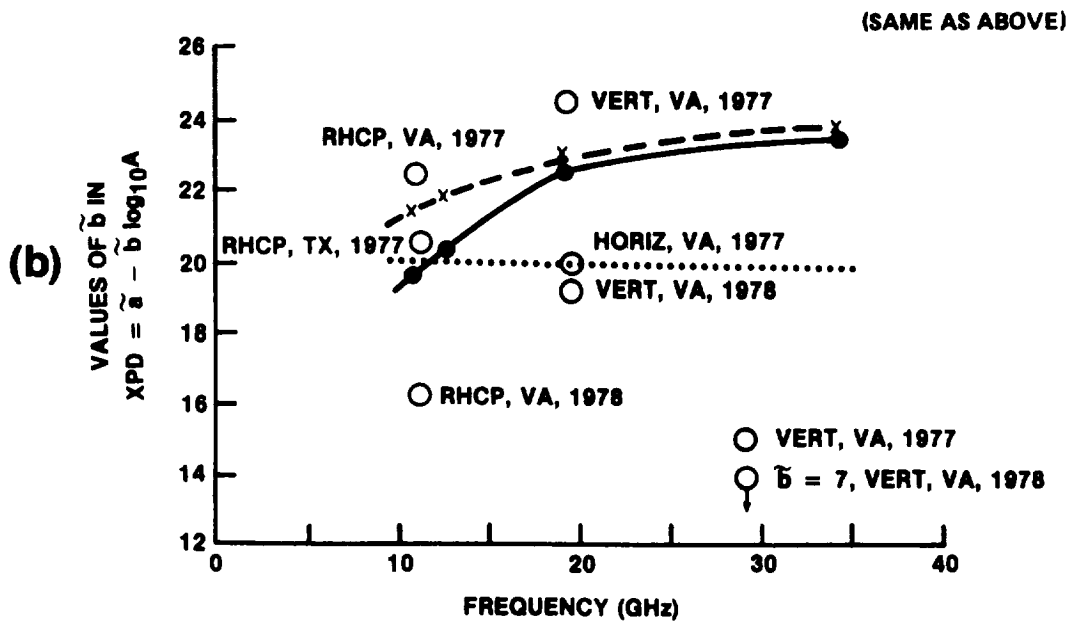
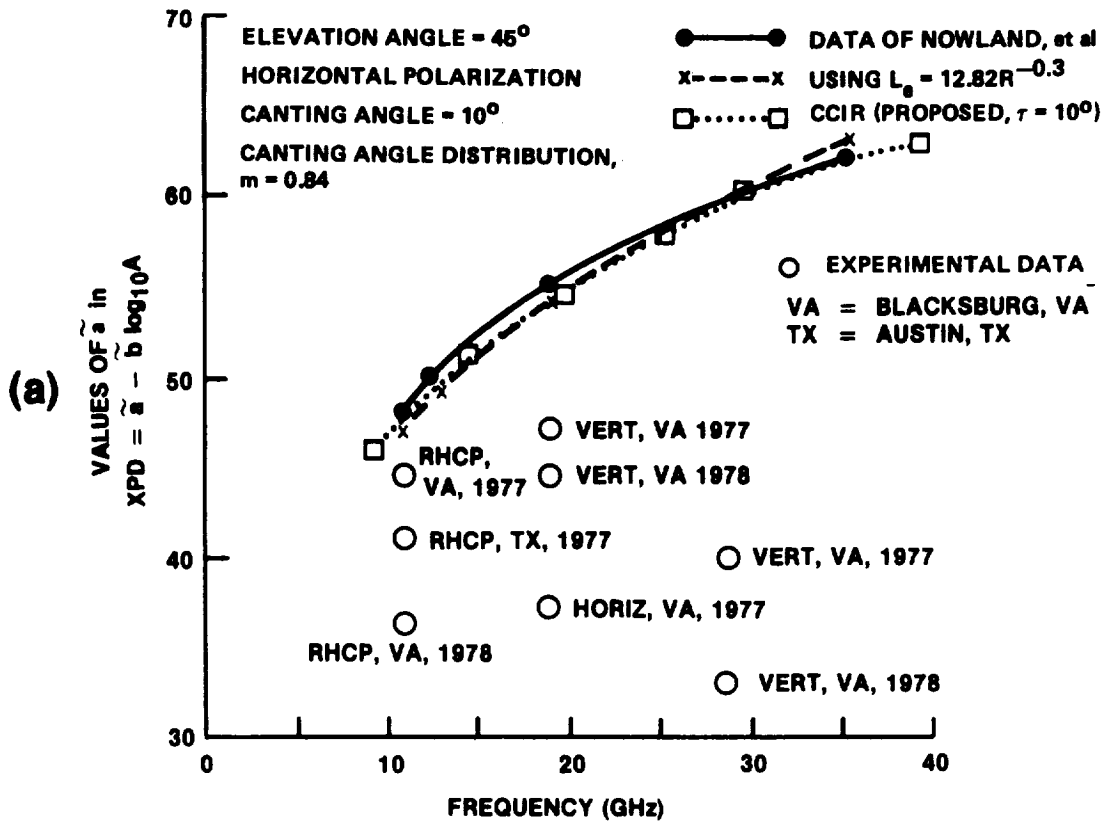


Figure 6.6-3. Frequency Dependence of the Coefficients in the Cross-Polarization Discrimination Relation

these do not correlate well with the theory (possibly because of the polarization dependence of \tilde{a}). The important results of these figures are that \tilde{a} increases with increasing frequency, while \tilde{b} appears to be relatively constant. In the relation $XPD = \tilde{a} - \tilde{b} \log_{10}(A)$ this would imply that the XPD increases with increasing frequency, but because of the rapid increase in A with frequency, XPD will actually decrease for increasing frequency and moderate rain rates.

Chu (1980) has found linear relations between the XPD and frequency throughout the 10 to 30 GHz frequency range. Specifically, XPD (expressed as a numerical ratio) is directly proportional to frequency for a fixed rain rate, and is inversely proportional to frequency for a fixed value of rain attenuation. Bostian (1979b) confirms this linear relation between the XPD (f_1) and XPD(f_2) from his monthly COMSTAR data for 1978, but, the value $XPD(f_2)/XPD(f_1)$ varies from month to month.

6.6.2.3 Elevation Angle Dependence of Depolarization. In the U.S. and Canada depolarization measurements have been obtained at elevation angles from 10.7° in Blacksburg, VA (Bostian, et al-1986) to 49° at Austin, Texas (Vogel-1978). The general dependence of XPD versus A on elevation angle θ can be obtained from the theoretical results of Nowland, et al (1977a). Note that both the coefficient a and the total attenuation A depend on elevation angle.

The elevation angle dependent results of Nowland, et al (1977b) 11.7 GHz (experimental data) are shown in Figure 6.6-4. Clearly the a coefficient is elevation angle dependent, however the experimental data does not confirm this fact. The b coefficient appears to be nearly independent of elevation angle and does appear to agree with the limited data base.

Chu (1980) has observed that the differential propagation constant for depolarization is governed by a $\cos^2\theta$ relation.

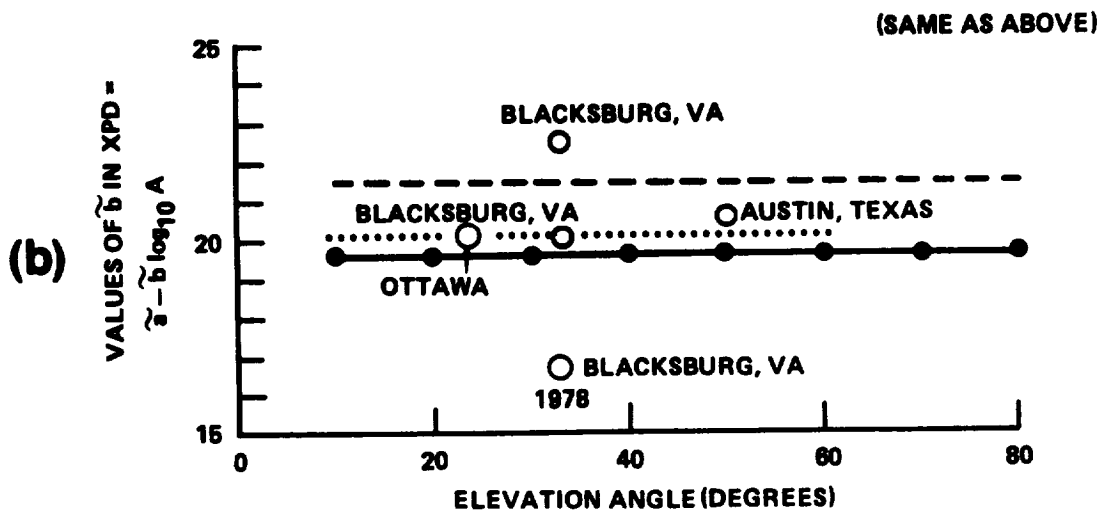
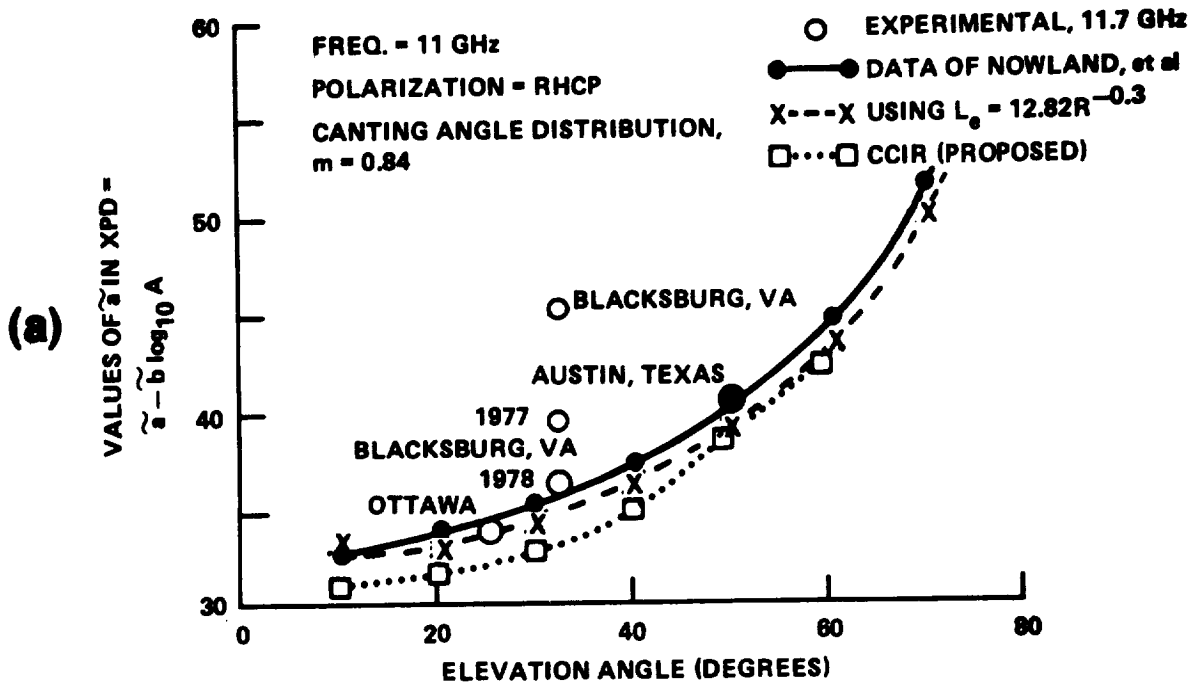


Figure 6.6-4. Elevation Angle Dependence of the Coefficients in the Cross-Polarization Discrimination Relation

However the XPD dependence on elevation angle must also take the effective path length effect into account (Chu-1974).

6.6.2.4 Phase Variations During Rain-Induced Depolarization Events.

At Blacksburg, VA (Bostian, et al-1977) measurements have been made of the phase difference between the co-polarized signal components. This phase difference has been observed to both decrease and increase by about 150 degrees for 3 dB fades and then not change significantly for higher attenuations: The phase difference has also been observed to increase and then decrease in the same storm. The mechanism for this plateau at 150 degrees and why the sign changes remains unexplained.

6.6.3 Ice-Crystal Depolarization

6.6.3.1 Meteorological Presence of Ice. Ice crystals form around dust particles in shapes influenced by the ambient temperature. In cirrus clouds they may exist for an indefinite time, but in cumulonimbus clouds they follow a cycle of growth by sublimation, falling and melting in the lower reaches of the cloud (Bostian and Allnutt-1971b). Radio, radar and optical observations all confirm that cloud ice crystals possess some degree of preferred orientation related to the orientation of the electrostatic field. The crystals range in size from 0.1 to 1 mm and concentrations range from 10^3 to 10^6 crystals/ m^3 . The variation in concentration and occurrence of events may be due to the variation of "seed" nuclei in various air masses. For example continental air masses contain more dust nuclei than maritime air masses and so occurrences of ice-crystal depolarization occur more frequently at inland ground stations. This general trend has been observed between observations at the Virginia Polytechnic Institute and State University (inland, most frequent), University of Texas at Austin (intermediate) and Bell Telephone Laboratories (maritime, least frequent).

6.6.3.2 Ice-Crystal Depolarization Measurements. Ice particles well above the height of the melting layer may have significant cross-polarization effects even for small values of attenuation

(typically below 3 to 5 dB at 11.7 GHz). This effect is believed to contribute to the poor correlation between the excess attenuation and the cross-polarization discrimination at these low values of attenuation.

In Austin, TX (Vogel-1978, 1979) ice depolarization was associated with either thunderstorms during the summer months or with clouds in the presence of polar air masses during the winter. An example of the percentage of time that XPD was less than or equal to the abscissa given that the excess attenuation was less than or equal to 1 dB is shown for the 18 month period from 12 June 1976 to 31 January 1978 and the period February 1978 to January 1979 in Figure 6.6-5. This curve shows that during 1976-78 45 per cent of the time that the XPD was less than or equal to 35 dB, there was less than 1 dB of attenuation; 24 per cent of the time that the XPD = 30 dB the A = 1 dB and 12 per cent of the time that XPD = 25 dB the A ; 1 dB. In contrast, using the rain depolarization relation for 1 dB yields XPD = 40 dB. Therefore systems requiring 30 dB or more XPD should expect a significant number of depolarization events due to ice.

Also, it has been observed (Shutie, et al-1978) that at 30 GHz ice crystals yield a constant value (typically 90 degrees) of the relative phase angle between the crosspolar and copolar signals as a function of XPD as shown in Figure 6.6-6. The corresponding polar plot for a heavy rain event is shown in Figure 6.6-7. In this case the XPD was reduced by signal attenuation and the signal to noise ratio of the relative phase measurement decreased as the XPD decreased. This effect appears to increase the scatter of the phase angle with decrease in XPD.

English investigators have also noted that rapid changes in relative phase and XPD are observed in thunderstorms and are associated with realignment of the ice crystal orientation by the electrostatic fields. In electrically-active storms, these

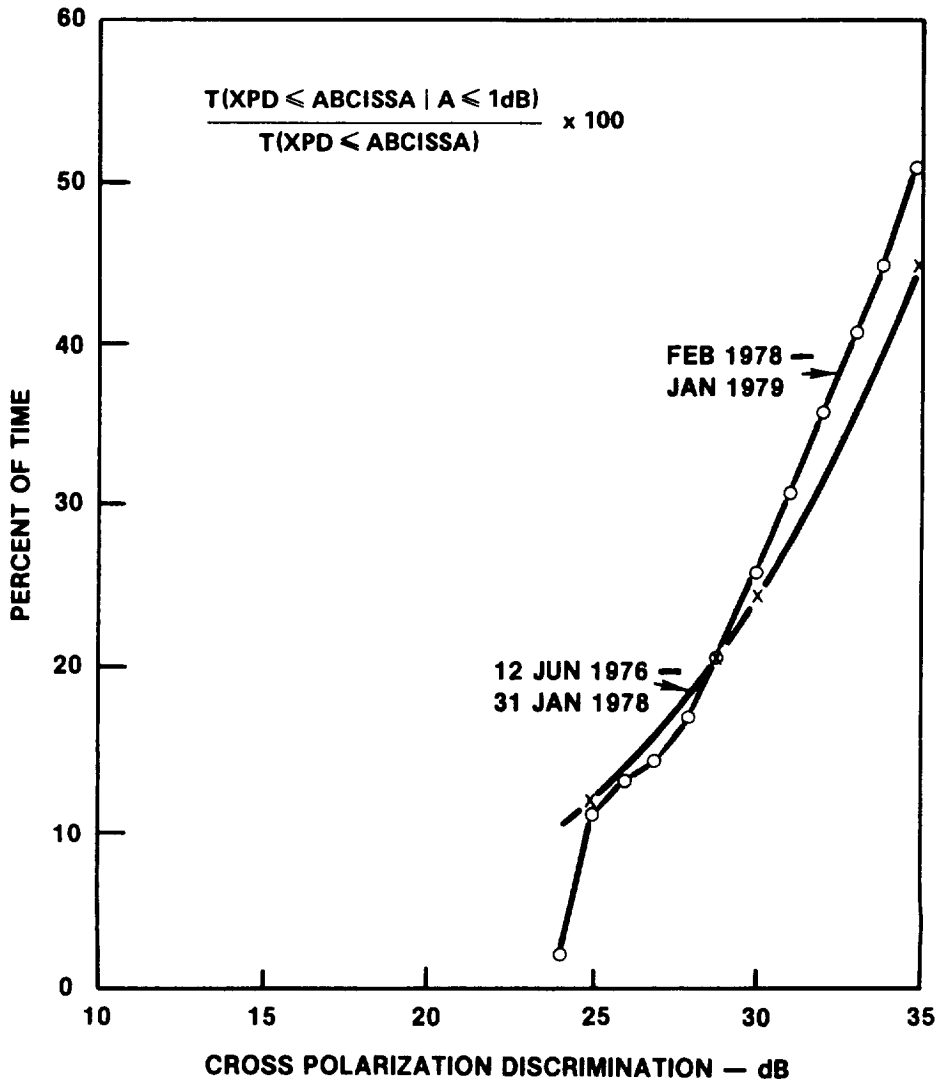


Figure 6.6-5. Contribution of Ice Depolarization to all Depolarization Events

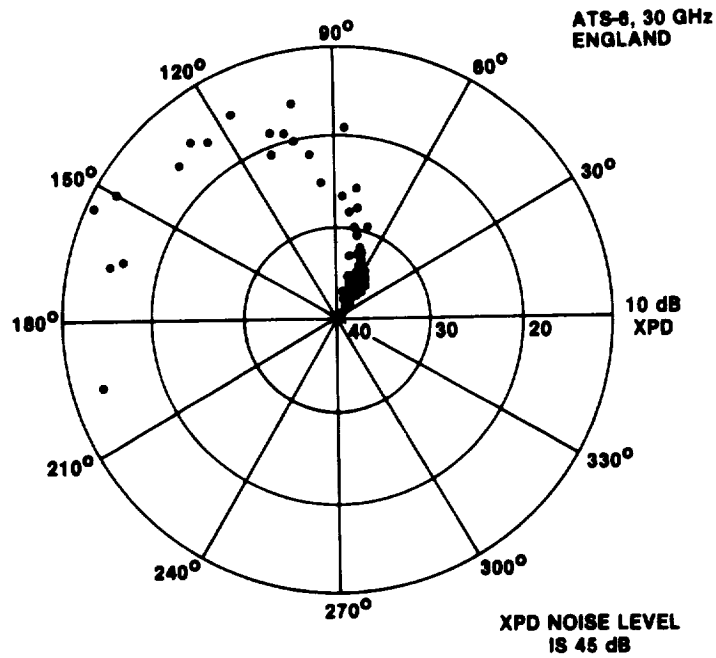


Figure 6.6-6. Polar Plot of the Cross Polarization Discrimination Arising from an Ice Cloud

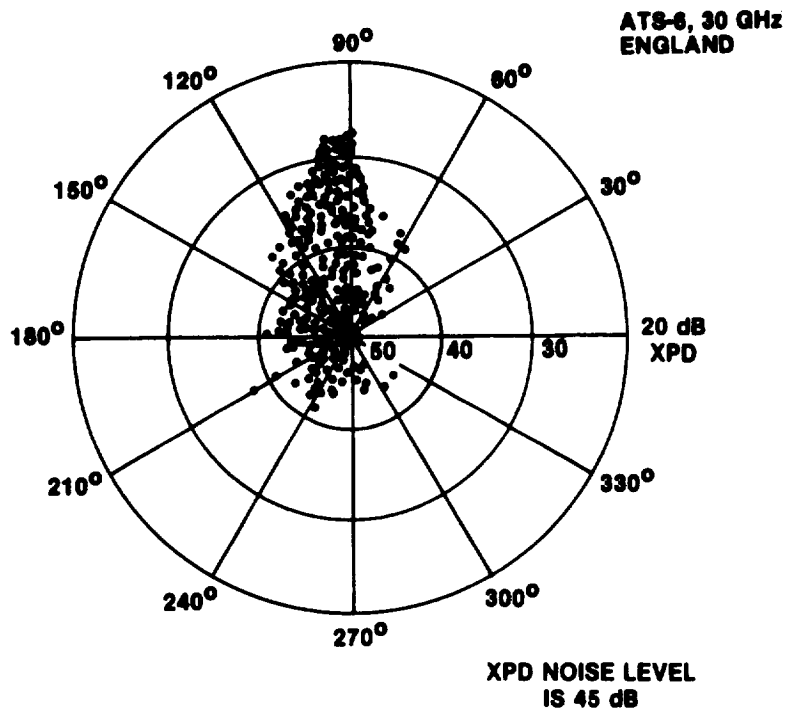


Figure 6.6-7. Polar Plot of the Cross Polarization Discrimination Arising from a Heavy Rain Event

electrostatic fields discharge rapidly resulting in rapid relative phase shifts of 180° , and rapid decreases in XPD of 27 dB in 20 seconds (Shutie, et al-1977) have been observed at the occurrence of a lightning flash. An example of this is shown in Figure 6.6-8 where the spikes in the relative phase occur for increasing XPD and result in large phase changes.

The spectra of rain and ice-induced crosspolarized signals have been analyzed (Hayworth, et al-1977) and it appears that a cancellation system with a 10 Hz bandwidth would track the majority of depolarizing events. However this bandwidth is probably insufficient during the sudden realignment of ice crystals in thunderstorms and in nonelectrically active precipitation. A suggestion has been made to consider use of a dual time constant system to accommodate all likely events.

For ice crystal depolarization the crosspolar phase shift is usually ± 90 degrees of the copolarized signal and so differential attenuation dominates the XPD variations. This effect was displayed in Figure 6.6-6. However depending on the frequency, rain-induced XPD variations predominantly shift the phase near 20 GHz and below and induce differential attenuation from 20 to 60 GHz (Hogg and Chu-1975).

6.6.3.3 CCIR Estimation for Ice Depolarization. The CCIR (1986b, Rpt. 564-3) has provided an empirical factor, $C_{ice}(p)$, for estimating the contribution of ice depolarization at the percent of time p in terms of $XPD_{rain}(p)$, the cross polarization caused by rain. The resulting rain + ice XPD at the percent of time p , $XPD_T(p)$, is then determined from:

$$XPD_T(p) = XPD_{rain}(p) - C_{ice}(p) \quad , \text{in dB} \quad (6.6-4)$$

where,

$$C_{ice}(p) = \frac{0.3 + 0.1 \log_{10} p}{2} XPD_{rain}(p) \quad (6.6-5)$$

Therefore,

$$\text{XPD}_T(p) = (0.85 - 0.05 \log_{10} p) \text{XPD}_{\text{rain}}(p) \quad (6.6-6)$$

This result, in conjunction with the CCIR estimation procedure for rain depolarization presented in Section 6.6.2.1.1, can be used to determine a total XPD distribution for a given set of link parameters.

6.6.4 Other Sources of Depolarization

6.6.4.1 Snow Depolarization. Snow depolarization occurs during both the winter and summer months. During the summer months snow exists above the 0°C isotherm. During winter, as the isotherm lowers, the thickness of the snow layer increases and the depolarization due to rain decreases.

In Canada (Hendry, et al-1976) tests using circularly polarized diversity radars at frequencies near 2.9 GHz (10.4 cm wavelength) and 16.7 GHz (1.8 cm wavelength) at an elevation angle of 3.2 degrees have diagnosed storms during both summer and winter. During June snow occurred during a storm from 2.6 to 8.2 km altitude and yielded a differential phase shift of 0.36 deg/km at 2.9 GHz. Winter data taken at 16.7 GHz gave more variable results of 0.16 to 1.17 deg/km for moderate to heavy snowstorms ranging in altitude from 70 m to 2.6 km. The mean value of differential phase shift was 0.69 deg/km at 16.7 GHz.

6.6.4.2 Multipath Depolarization. The cross-polarized pattern of a parabolic reflector antenna normally has its peak at small angles off-axis. This allows oblique indirect rays, which may be present on earth-space paths at low elevation angles, to produce a significant cross-polarized component. Measurements have been made on terrestrial links at 11 GHz (Watson, et al-1973) and 22 GHz (Turner-1973). The magnitude of the indirect signal reflected from the earth can be roughly estimated from the data in Lord and Oliver (1946) taken near 3 GHz.

ENGLAND

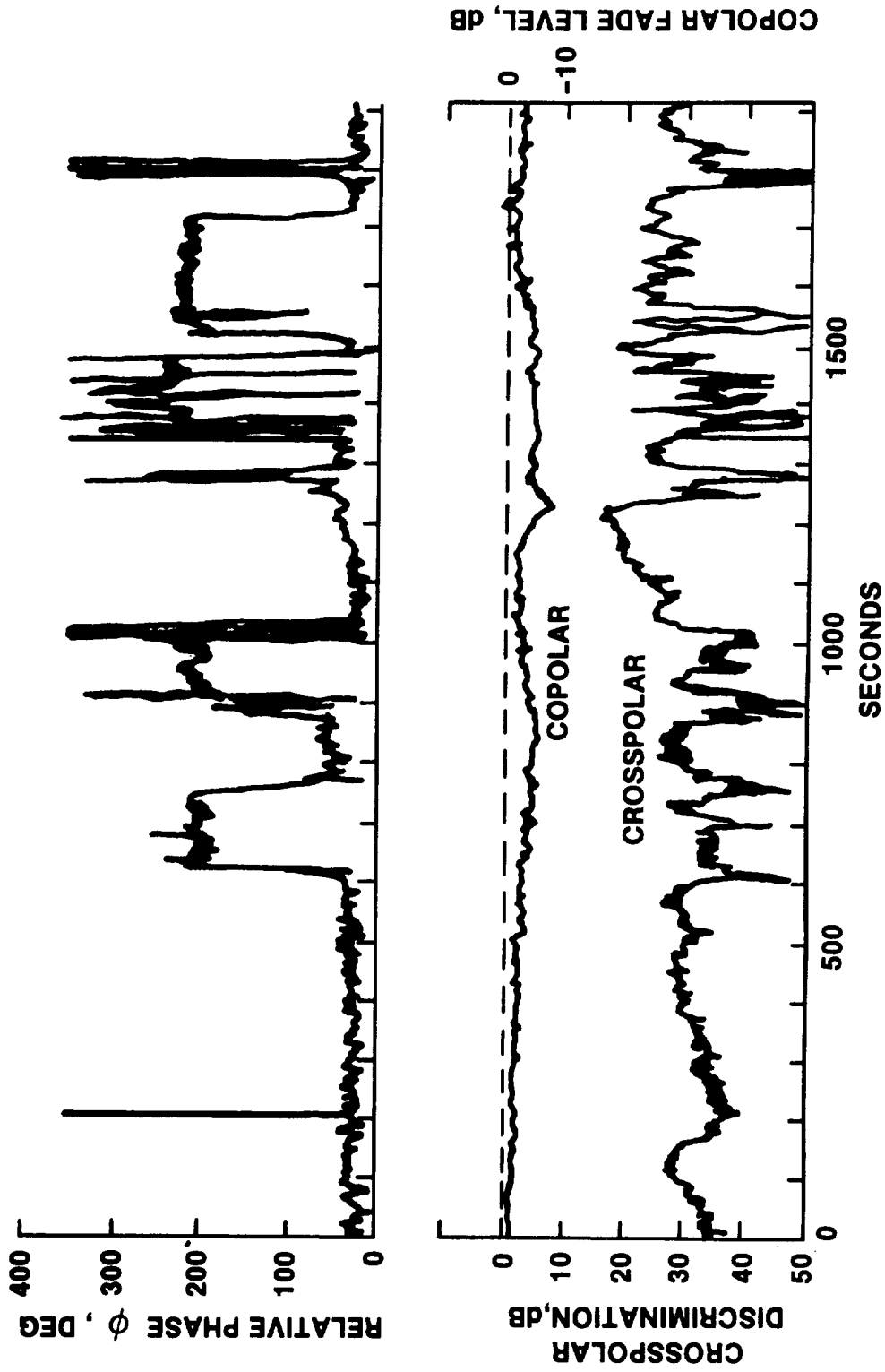


Figure 6.6-8. Phase, Copolar Fade and Crosspolar Discrimination for an Electrically Active Thunderstorm (15th July 1976)

6.6.4.3 Refractive Effects. Variations in the radio refractivity (dielectric constant of tropospheric layers) can cause rotation of the polarization plane of the rays refracting through the layers. This condition will occur for layers which are not perpendicular to the vertical plane containing the transmitter and receiver as described by LeFrancois, et al (1973).

6.6.5 Prediction of Depolarization Statistics

This section presents a summary of the procedure for developing a prediction of depolarization statistics, in the form of the cumulative distribution of XPD, for rain and ice-particle induced depolarization on a slant path. Figure 6.6-9 shows the methodology for developing the statistics. The XPD prediction requires the cumulative distribution of rain attenuation, either as measured or calculated from one of the methods described in Section 6.3.

The coefficients \tilde{a} and \tilde{b} are determined at each percent p from the CCIR procedure, Eq.'s 6.6-2 and 6.6-3, for the given frequency, elevation angle, and polarization tilt angle (STEP 1). The rain induced XPD is then determined from the coefficients and from the rain attenuation distribution by Eq. 6.6-1 (STEP 2). The contribution from ice particles is determined from the CCIR relationship, Eq. 6.6-6 (STEP 3).

The procedure is valid in the frequency range $8 \leq f \leq 35$ GHz. Outside of this frequency range, attenuation statistics are not useful in predicting XPD statistics. For frequencies below 8 GHz, relationships between XPD, point rain rate, and effective path length have been employed (see Oguchi-1977, Kobayashi-1977).

Long term XPD statistics obtained at one frequency and polarization tilt angle can be scaled (STEP 4) to another frequency and polarization tilt angle using the semi-empirical relation (CCIR Rpt. 564-3, 1986b),

$$XPD_2 = XPD_1 - 20 \log_{10} \left[\frac{f_2 \sqrt{1 - 0.484(1 + \cos 4\tau_2)}}{f_1 \sqrt{1 - 0.484(1 + \cos 4\tau_1)}} \right] \quad (6.6-7)$$

for $4 \leq f_1, f_2 \leq 30$ GHz

where XPD_1 and XPD_2 are the XPD values not exceeded for the same percentage of time at frequencies f_1 and f_2 and polarization tilt angles τ_1 and τ_2 , respectively. The above can be used to scale both rain and ice depolarization, since it has been observed that both phenomena have approximately the same frequency dependence at frequencies less than about 30 GHz.

Figure 6.6-10 show a sample calculation of the XPD procedure developed from cumulative attenuation statistics for Rosman, NC with the ATS-6 20 GHz satellite beacon. The attenuation statistics were obtained from the distribution extension technique described in Section 6.3. The curve labeled DEPOLARIZATION presents the XPD calculated from the procedure of Figure 6.6-9, with both the rain and rain + ice predictions shown.

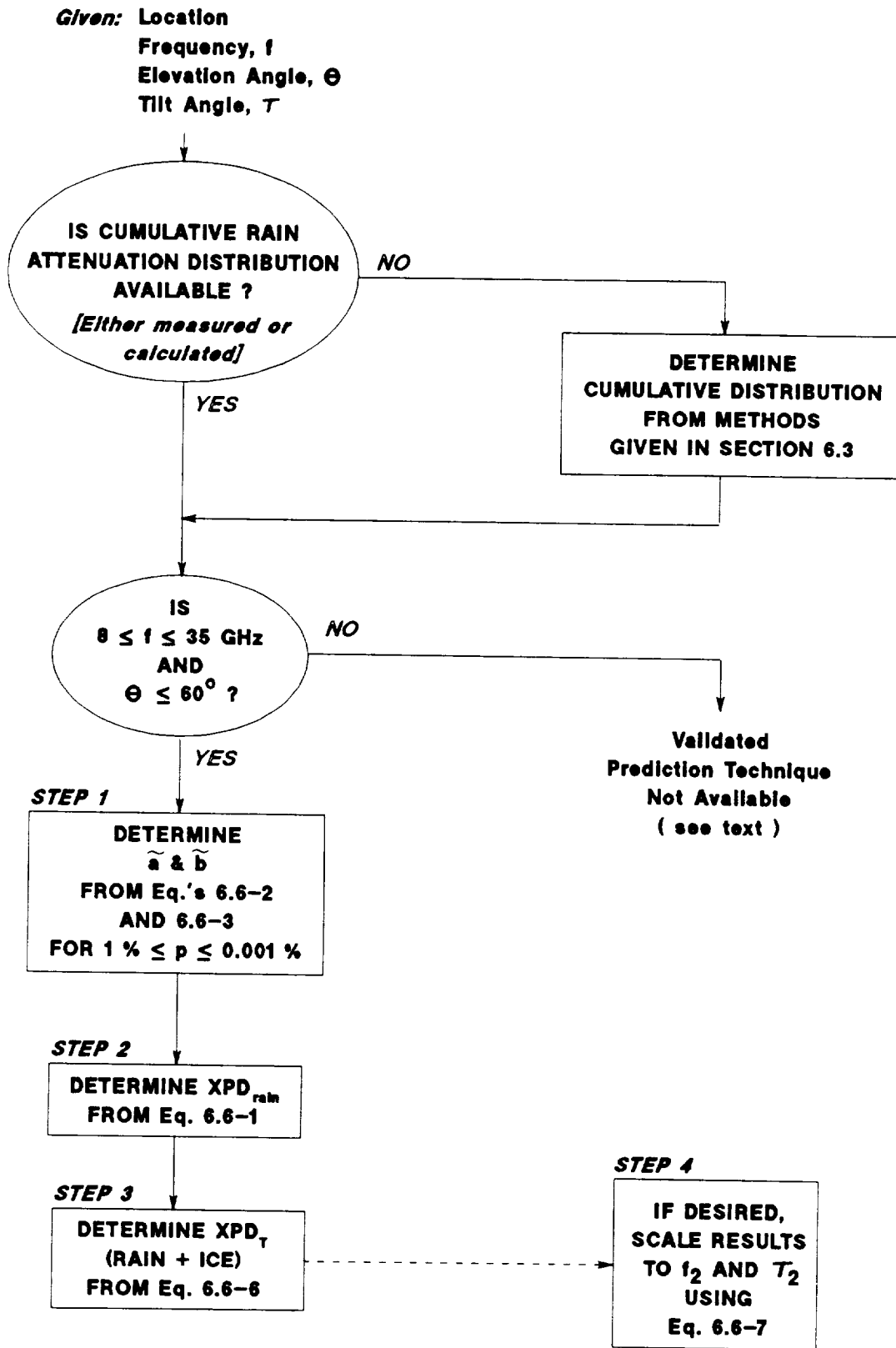


Figure 6.6-9. Technique for Prediction of Depolarization Statistics

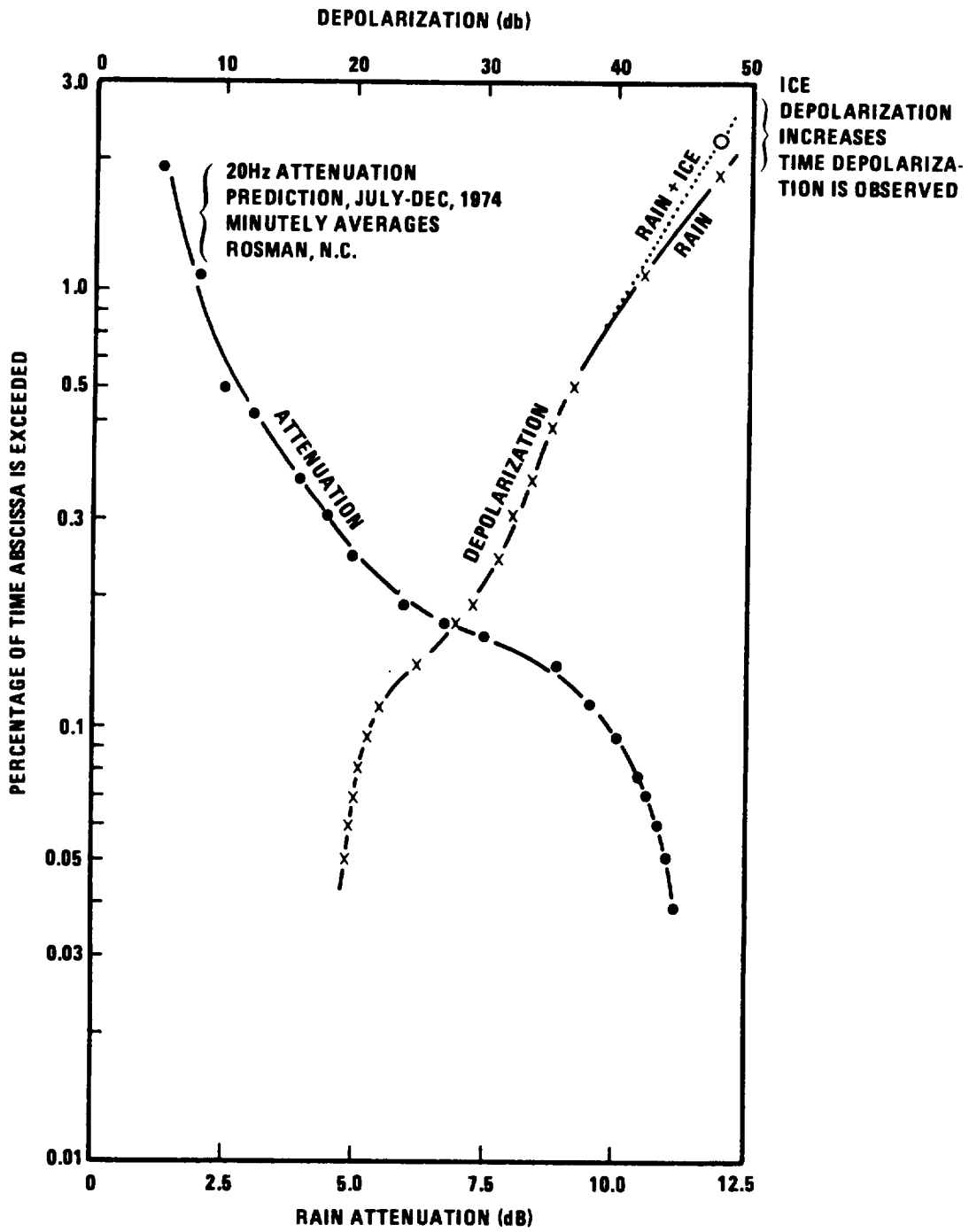


Figure 6.6-10. Attenuation and Depolarization Statistics for Rosman, N.E.

6.7 DISPERSION AND BANDWIDTH COHERENCE EFFECTS

When the dispersion of the propagating medium is sufficiently high, the phase and/or amplitude of wide-bandwidth transmissions may be selectively altered, causing a variation or reduction in the coherence bandwidth of the transmitted signal. Both tropospheric and ionospheric effects have been predicted and observed. This section reviews the analytical and experimental results for both tropospheric and ionospheric induced effects on radiowave paths operating above 10 GHz.

6.7.1 Tropospheric Effects on Bandwidth Coherence

6.7.1.1 Amplitude Variations

Theoretical estimates of the degradation of pulse shapes through rain have indicated that only minor effects are observed. The calculations (Crane-1967) indicated that pulse distortion does not become significant until total rain attenuations of the order of 100 dB are encountered. Since current link margins do not allow such high attenuations, the link will fail due to signal attenuation before pulse shape degradation affects transmission.

Amplitude variation with frequency becomes significant at frequencies in the vicinity of molecular absorption bands, such as the 50-70 GHz oxygen absorption band. The greatest dispersive effect would occur at the individual absorption lines which are quite narrow (Liebe -1955). However, due to the great path attenuation present at these frequencies, it is not likely they would be used for earth-space communications.

For rain the frequency dependence of the specific attenuation (db/km) is

$$\frac{\partial \alpha}{\partial f} = \frac{\partial (aR^b)}{\partial f} \propto \left[\frac{1}{a} \frac{\partial a}{\partial f} + (\ln R) \frac{\partial b}{\partial f} \right] \quad (6.7-1)$$

where, for example, for the frequency range from 8.5 to 25 GHz
(Olsen et al-1977)

$$\frac{\partial a}{\partial f} = 1.02 \times 10^{-4} f^{1.42} \quad (6.7-2)$$

$$\frac{\partial b}{\partial f} = -0.11 f^{-1.0779} \quad (6.7-3)$$

For example, at 20 GHz and R = 25 mm/hr,

$$a = 5.93 \times 10^{-2}$$

$$b=1.12$$

$$\frac{\partial a}{\partial f} = 7.18 \times 10^{-3}$$

$$\frac{\partial b}{\partial f} = -4.36 \times 10^{-3}$$

$$\alpha = 2.18 \text{ db/km}$$

so

$$\frac{\partial \alpha}{\partial f} = 0.23 \text{ dB/(km-GHz)}$$

or for a typical effective path length $L_e = 6 \text{ km}$

$$\frac{\partial(\alpha L_e)}{\partial f} = L_e \frac{\partial \alpha}{\partial f} = 1.38 \text{ dB/GHz}$$

6.7.1.1.1 Experimental Results. The ATS-6 beacons at 20 and 30 GHz were both capable of being modulated with ± 180 , 360, 540 and ± 720 MHz sidetone signals. Typical selective fading events across the 1.44 GHz bands are shown in Figures 6.7-1 and 6.7-2, respectively (WEC-1975). These are four-second averages taken on day 270 of 1974 just before the onset of a fade event (230000Z) at the beginning of the fade event (232352Z), and before receiver lock was lost during the fade event (232428Z). Except for fade depths in excess of 20 dB, the accuracy of the attenuation measurements is ± 1 dB. These rain fade results, while representative of those taken at Rosman, do

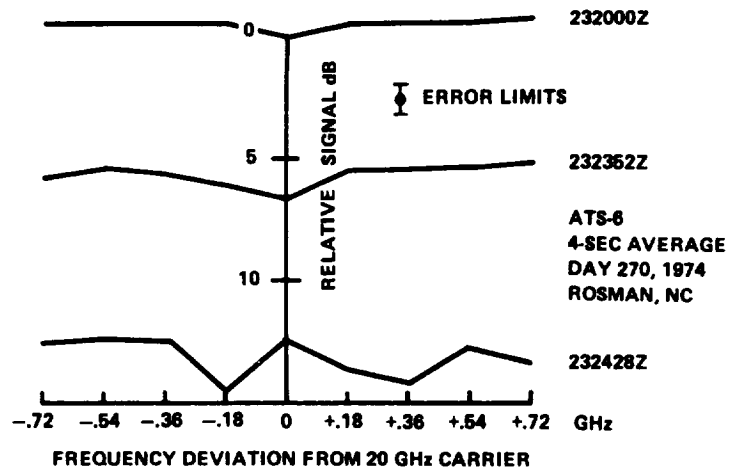


Figure 6.7-1. Selective Fading Near 20 GHz

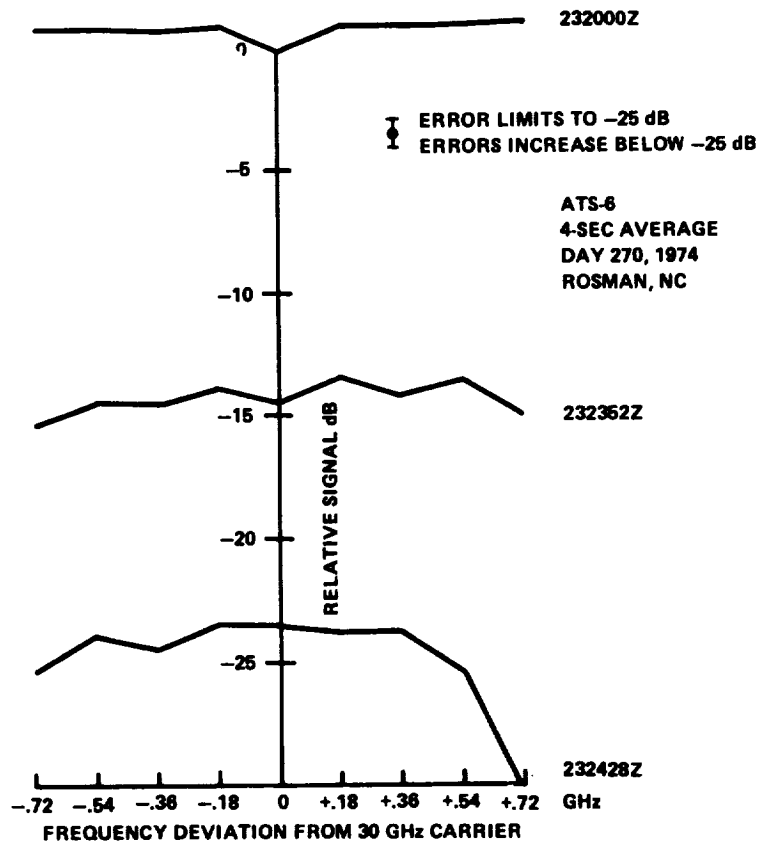


Figure 6.7-2. Selective Fading Near 30 GHz

not appear to be sufficiently accurate for deep fades because the signal levels approach the noise floor of the receiver. For one-minute averages, no measurable selective fading was observed (WEC-1975).

The cross-correlation of 4 and 6 GHz signals due to low angle fading in the Canadian arctic was found to be low (Strickland, et al-1977). During a 2.5 hour period on the day when the fading was most severe the correlation coefficient was 0.34 since the 6 GHz signal experienced 55% more fades than the 4 GHz signal. This would indicate significant dispersion was present, but the mechanism for this effect is tropospheric refraction and not rain. Frequency selective fading may be significant at low elevation angles.

6.7.1.2 Phase Variations. Phase measurements have not yielded significant results for frequencies above 10 GHz. The phase coherent sidetone signals on ATS-6 showed only minor variations across the 1.44 GHz bandwidths. These variations were most evident for the shorter (one and four second) averaging periods compared to the one-minute period (WEC-1975).

Phase measurements have been attempted for the one degree elevation angle satellites observed from the arctic (Strickland et al-1977). Unfortunately, no significant fade events occurred and no differential phase variations were recorded.

Phase effects are produced by the molecular absorption mechanism along with amplitude effects. Large values of phase dispersion would therefore be expected in the absorption bands.

6.7.2 Ionospheric Effects on Bandwidth Coherence

6.7.2.1 Amplitude Variations. Ionospheric attenuation at microwave frequencies is inversely proportional to the frequency squared (Flock, 1987) and is generally less than 0.001 dB at 15 GHz and an elevation angle $\theta = 90^\circ$. The variation is approximately related to cosecant θ . The attenuation is therefore usually less

than 0.01 dB above 10 GHz.

6.7.2.2 Phase Variations. The group delay due to the free electrons in the ionosphere is (Flock, 1987)

$$\Delta\tau = 40.3 \frac{N_e}{cf^2} = \frac{1.33 \times 10^{-7}}{f^2} N_e, \text{sec} \quad (6.7-4)$$

where N_e is the total electron content in electrons/m², $c = 3 \times 10^8$ m/sec and f is in Hertz. This delay is equivalent to a phase delay (in radians)

$$\Delta\tau = \frac{\Delta\phi}{2\pi f} \quad (6.7-5)$$

so that

$$\Delta\phi = (2\pi)(40.3) \frac{N_e}{cf} \quad (6.7-6)$$

For a typical value of $N_e = 10^{17}$ m⁻², the total phase delay at 11.7 GHz is only 7.21 radians. The frequency dependence of this is only

$$\begin{aligned} \frac{\partial(\Delta\phi)}{\partial f} &= - \frac{2\pi(40.3) N_e}{cf^2} \\ &= -6.2 \times 10^{-10} \text{ radian/Hertz} \\ &= -0.62 \text{ radian/GHz} \\ &= -35 \text{ degrees/GHz.} \end{aligned}$$

For higher frequencies, the rate of change of phase with frequency decreases.

6.8 DOWNLINK NOISE AT EARTH STATIONS

6.8.1 Introduction

An Earth station observing a satellite at a high elevation angle

may be considered to be receiving sky noise from the antenna boresight direction. As the elevation angle of the satellite decreases, thermal noise emission from the Earth's surface will be increasingly observed in the antenna's sidelobes. This section reviews the sky noise component and its contribution to satellite communications system performance.

Antenna noise is conveniently treated in terms of noise temperature, since the two parameters are linearly related. In circuit theory the noise power, p_n , which is transferred to a matched load is

$$p_n = kTB \quad \text{watts} \quad (6.8-1)$$

where k is Boltzmann's constant, T is noise temperature in (degrees) Kelvin, and B is the bandwidth in Hertz. Thermal radiation from the gaseous atmosphere is given by the Rayleigh-Jeans longwave approximation to Plank's equation

$$p_n' = \frac{2kT}{\lambda^2} = 22.2kTf^2 \quad (6.8-2)$$

where f is the frequency in GHz. Note the ambiguity in the frequency dependence of the two relations. However, we will be considering noise temperature in its circuit theory usage so the difference is not of prime concern.

6.8.2 Clear Air Sky Noise

The thermal noise emission from a gas in thermodynamic equilibrium, from Kirchhoff's law, must equal its absorption, and this equality must be true at all frequencies.

The noise temperature T_b in a given direction through the atmosphere (also called the brightness temperature) is given by radiative transfer theory (Waters-1976, Wulfsberg-1964)

$$T_b = \int_0^{\infty} T_m \gamma e^{-\tau} dl + T_{\infty} e^{-\tau_{\infty}} \quad (6.8-3)$$

where T_m is the ambient temperature, γ is the absorption coefficient, and τ is the optical depth to the point under consideration. In radio engineering terms

$$\tau = 4.343 A \quad \text{dB} \quad (6.8-4)$$

where A is the absorption over the path in question, in dB. For frequencies above 10 GHz, the second term on the righthand side of Eq. (6.8-3) reduces to 2.7 K, the cosmic background component, unless the Sun is in the antenna beam, as illustrated in Figure 6.8-1.

For an isothermal atmosphere (T_m constant with height), substituting $\gamma dl = d\tau$ in Eq. (6.8-3) yields

$$T_b = T_m(1 - e^{-\tau}) = T_m \left(1 - 10^{-\frac{A}{10}} \right) \quad \text{K} \quad (6.8-5)$$

where A is again atmospheric absorption in dB. The value of T_m taken in Eq. (6.8-4) ranges from 260 to 280 K. One relationship used to determine a value of T_m from surface measured temperature is (Wulfsberg-1964)

$$T_m = 1.12 T_s - 50 \quad \text{K} \quad (6.8-6)$$

where T_s is the surface temperature in K.

Noise temperature (or brightness temperature) curves for 3, 7.5, and 17 g/m³ surface water vapor content, with the US Standard Atmosphere for the two lower values and the Tropical Atmosphere for the highest value, have been published by Smith (1982) and reproduced in CCIR Report 720-2 (CCIR-1986h). Examples for an average humidity state (7.5 g/m³ at the surface) are reproduced as Figures 6-8-2 and 6.8-3.

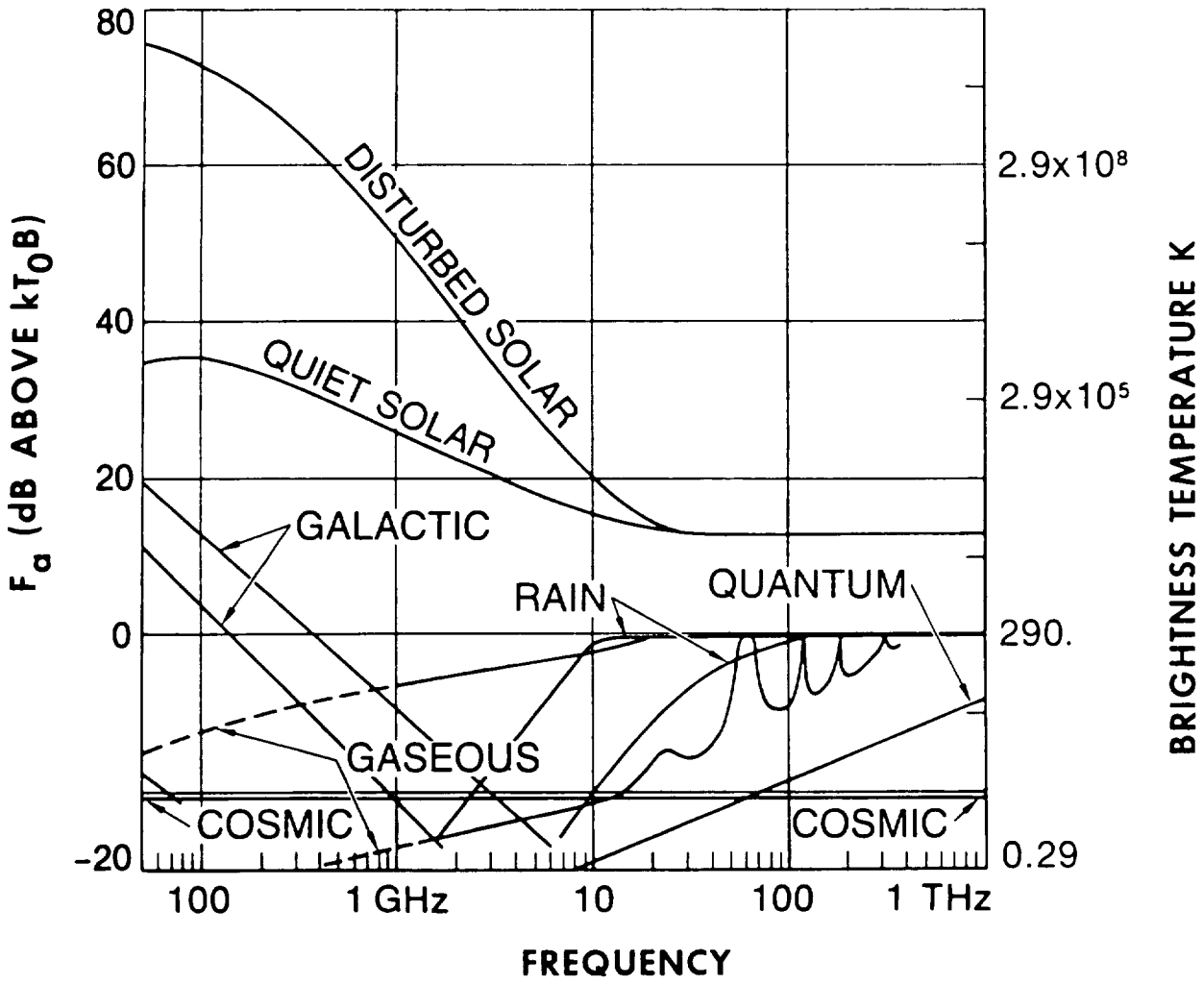


Figure 6.8-1. Noise Factor and Brightness Temperature from Natural Sources observed on Satellite Downlinks [Source: Spaulding and Hagn - 1978]

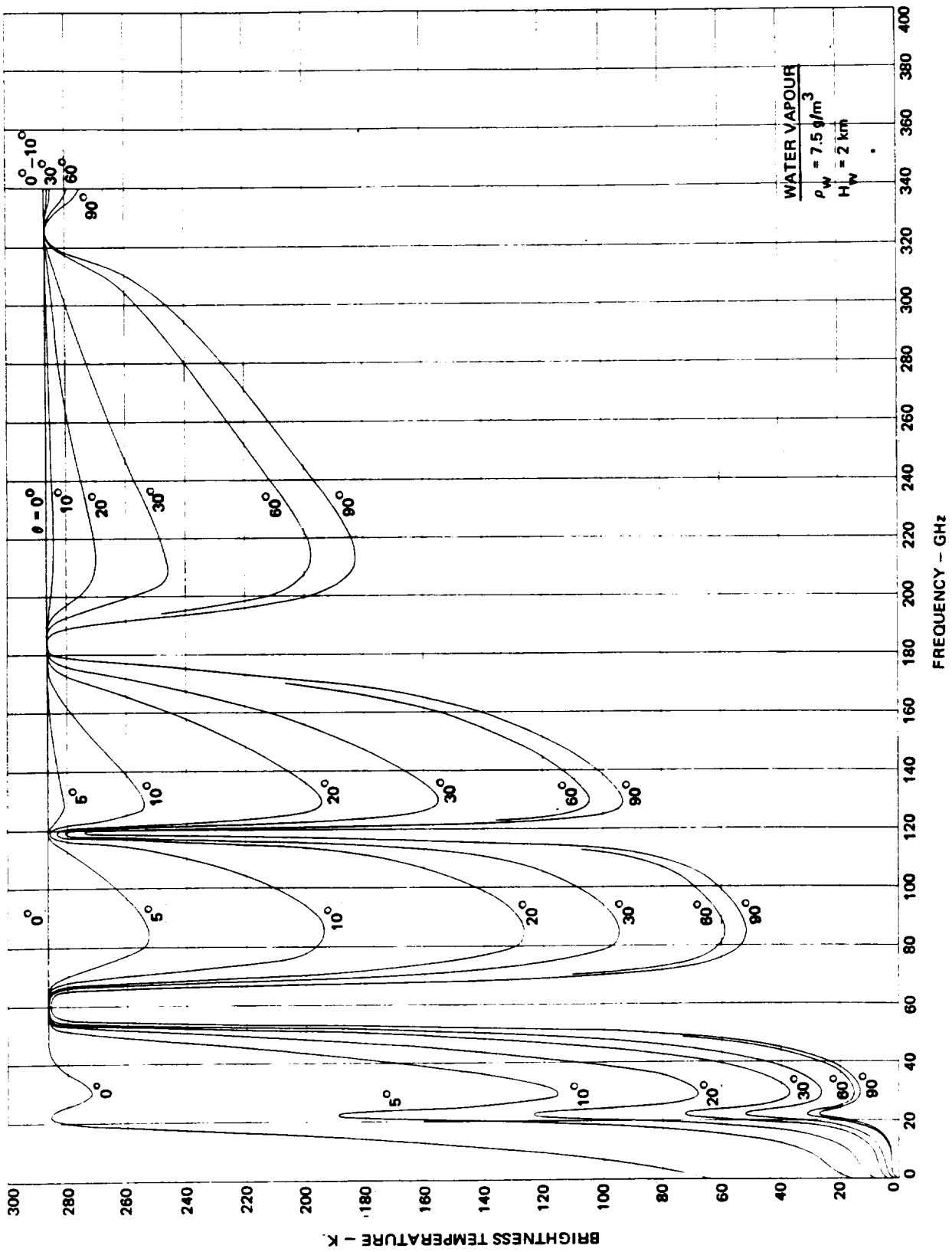


Figure 6.8-2. Brightness Temperature (Clear Air) for a Water Vapor Concentration of 7.5 g/m^3 , 1 to 350 GHz. [Smith - 1982]

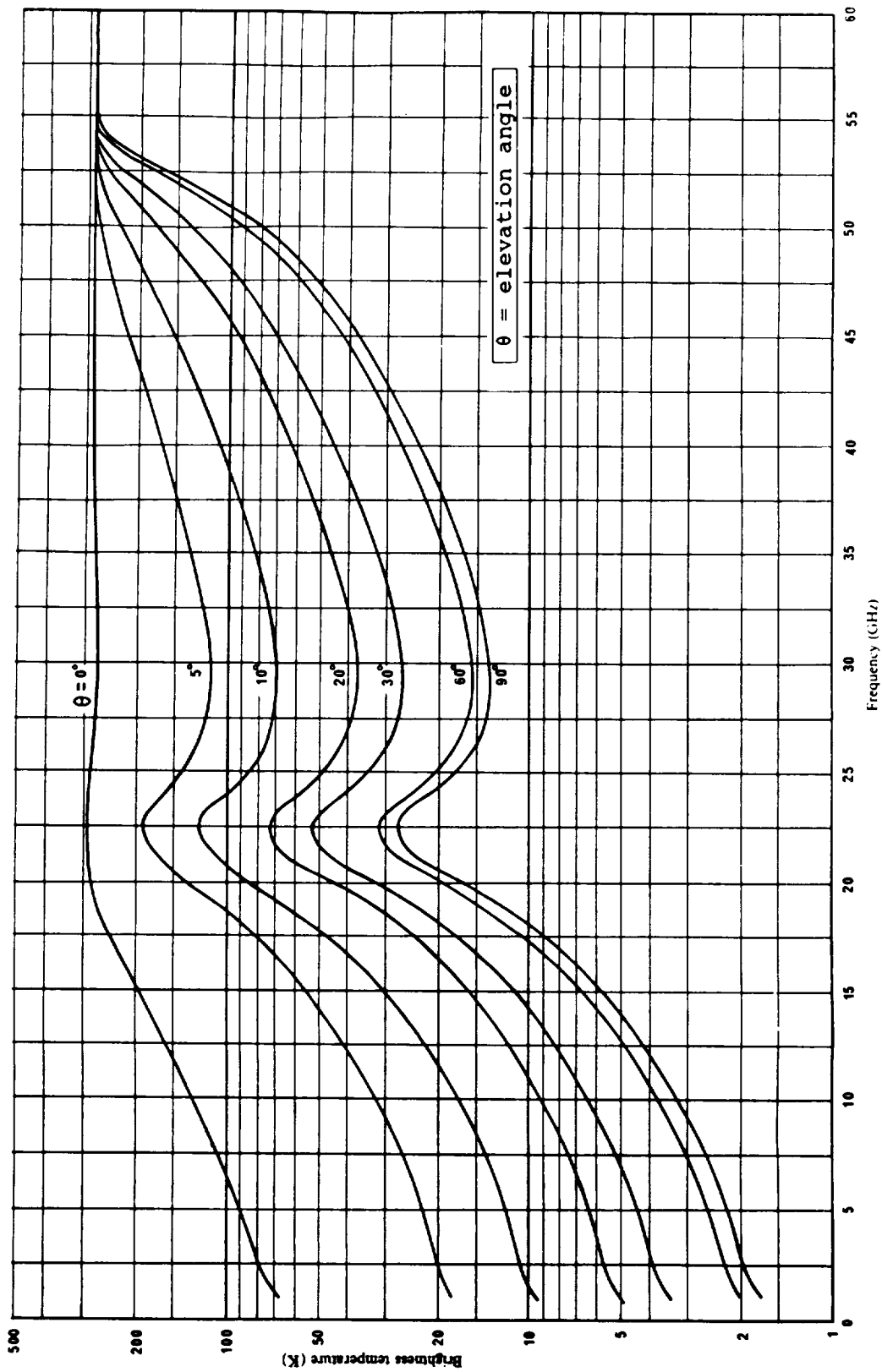


Figure 6.8-3. Brightness Temperature (Clear Air) for a Water Vapor Concentration of 7.5 g/m³, Expanded Scale, [Smith - 1982]

6.8.3 Sky Noise Due to Rain

Kirchhoff's law applies to noise emission from rain as well as from atmospheric gases, but only to the absorption component of the rain attenuation and not to the scattered component. The scattered component increases with frequency, so that while Eq. (6.8-5) may be appropriate at 10 GHz, it will give too high a value at 70 GHz.

Values of T_s due to rain may be estimated from the rain attenuation calculation techniques presented in Section 6.3. For example, to compute the cumulative statistics of T_s , first compute the cumulative attenuation statistics due to rain, and then use Eq. 6.8.5 to convert attenuation to apparent sky noise temperature. An example of this process has been done for Rosman, NC at 20 GHz. The results are given in Table 6.8-1.

The sky noise temperature (see last column of Table 6.8-1) will degrade the overall system noise figure of the receiver system. For example, for a receiver with a 4 dB noise figure, the resultant noise figure for the rain rate corresponding to 0.01% of the year will be 5.4 dB, i.e., an increase of 1.4 dB.

6.8.4 Sample Calculations

Two illustrative examples of application of the sky noise relationships for clear air and for rain are presented below.

Example 1. A land mobile satellite system downlink is to operate at 20 GHz with a service reliability of 95 % of the time. The receiver system noise temperature, exclusive of antenna noise, is 100 K. The elevation angle to the satellite is 60° . The median surface humidity is estimated at 7.5 g/m^3 . What is the required propagation margin?

From Figure 6.8-3 we read $T = 20 \text{ K}$ for the parameters given above. For the worst 5 % of the time we arbitrarily double this value to $T = 40 \text{ K}$.

The gaseous attenuation for the link can be determined from the

Table 6.8-1. Cumulative Statistics of Sky Temperature Due to Rain for Rosman, N.C. at 20 GHz. $T_m = 275$ K.

PERCENT OF YEAR	POINT RAIN RATE VALUES	AVERAGE RAIN RATE	TOTAL RAIN ATTENUATION*	SKY NOISE TEMPERATURE†
0.001	102 mm/hr	89 mm/hr	47 dB	275 K
0.002	86	77	40	275
0.005	64	60	30	275
0.01	49	47	23	274
0.02	35	35	16	269
0.05	22	24	11	252
0.1	15	17	7	224
0.2	9.5	11.3	4.6	180
0.5	5.2	6.7	2.6	123
1.0	3.0	4.2	1.5	82
2.0	1.8	2.7	0.93	53

NOTES:

* At 20 GHz the specific attenuation $A = 0.06 R_{ave}^{1.12}$ dB/km and for Rosman, N.C. the effective path length is 5.1 km to ATS-6.

† For a ground temperature of $17^{\circ}\text{C} = 63^{\circ}\text{F}$ the $T_m = 275$ K.

CCIR estimation procedure given in Section 6.2.3. The resulting total (oxygen + water vapor) attenuation is found as

$$A_g = 0.34 \text{ dB}$$

Doubling the value for the worst 5 % of the time, the attenuation is 0.68 dB.

At the 95 % reliability level, attenuation caused by rain may be ignored, since rain occurs only 2-3 % of the total time for most regions.

The propagation margin is then computed as follows:

Decrease in signal level = 0.68 dB.

$$\begin{aligned} \text{Increase in noise temperature} &= 10 \log[(100 + 40 + 2.7)/100] \\ &= 1.54 \text{ dB} \end{aligned}$$

$$\text{Required propagation margin} = 0.68 + 1.54 = 2.22 \text{ dB.}$$

Note that for this case the sky noise increase contribution is more than double the contribution due to the decrease in signal level to the total margin required.

Example 2. A satellite system is to operate in the fixed service with a downlink at 20 GHz. The required service reliability is 99.99 % of the time. The 0.01 % of the time rain rate has been measured to produce an attenuation of 30 dB in the direction of the satellite. The receiver system noise temperature, exclusive of antenna noise, is 300 K. What is the required propagation margin?

The clear air component is assumed to be the 95 % value from example 1, i.e. $T = 40 \text{ K}$, $A = 0.68 \text{ dB}$.

The sky noise increase due to a rain attenuation of 30 dB is determined from Eq. (6.8-5)

$$T_r = 280(1 - 10^{-30/10}) = 279.7 \text{ K}$$

The propagation margin is then computed as follows:

$$\text{Decrease in signal level} = 30 + 0.68 = 30.68 \text{ dB.}$$

$$\begin{aligned} \text{Increase in noise temperature} &= 10 \log[(279.7 + 300)/300] \\ &= 2.86 \text{ dB.} \end{aligned}$$

$$\text{Required propagation margin} = 30.68 + 2.86 = 33.54 \text{ dB.}$$

For this example the signal level decrease is the predominate factor in the margin requirement.

Note that the reliability criterion plays a significant role in propagation margins for the two above examples (2.22 vs 33.54 dB). The relative difference in receiver noise temperature, however, also accounts for the greater importance of noise over attenuation in the first example.

6.8.5 Sky Noise Due to Clouds, Fog, Sand and Dust. The major contributor to the sky noise temperature is the medium with the highest attenuation. Generally, clouds will present higher attenuations than fog, sand or dust. For example, for cumulus clouds with no precipitation the water density will be approximately 0.5 g/m^3 . For the Rosman example described earlier (20 GHz),

$$A = K_c \rho_1 t_c \csc \theta \quad (6.8-7)$$

where t_c is the thickness of the clouds (typically 2 kilometers). Using typical numbers

$$\begin{aligned} A &= (0.4 \text{ dB m}^3/\text{gm km}) (0.5 \text{ gm/m}^3) (2 \text{ km}) \csc (47^\circ) \\ &= 0.55 \text{ dB} \end{aligned}$$

The corresponding sky noise contribution is then

$$T_s = T_{mc} [1 - 10^{-(0.55/10)}]$$

With T_{mc} equal to the temperature of the cloud (i.e., $T_{mc} =$

0°C = 273 K), T_s is 32 K. Clearly, at 20 GHz, rain represents a much more significant contributor to the sky noise temperature than clouds.

6.8.6 Total Sky Noise Temperature Arising from Several

Contributors. The sky noise temperatures from several sources do not add linearly. Rather, the attenuation from each contributor must be added and the total result substituted into the sky noise versus attenuation relation. For example, for the Rosman ground station observing the ATS-6, the clear air attenuation is 1.2 dB yielding a T_s (clear air) = 66 K. From Table 6.8-1 for 0.2% of the year (105 minutes) the rain induced sky temperature due to clear air and rain is 203 K which is significantly less than the sum of each contributor (246 K). During rain conditions the cloud contributions should also be added, but these will generally be even a smaller contribution than the clear air attenuation.

6.8.7 Extraterrestrial Sources of Sky Noise

6.8.7.1 Solar Noise. The sun generates very high noise levels when it is collinear with the Earth station-satellite path. For geostationary satellites, this occurs near the equinoxes, for a short period each day. The power flux density generated by the sun is given as a function of frequency in Figure 6.8-4 (Perlman, et al-1960). Above about 20 GHz, it is practically constant at -188 dBW/Hz-m² for "quiet sun" conditions.

Reception of solar noise can be viewed as an equivalent increase in the antenna noise temperature by an amount T_s . T_s depends on the relative magnitude of the antenna beamwidth compared with the apparent diameter of the sun (0.48°), and how close the sun approaches the antenna boresight. The following formula, after Baars (1973), gives an estimate of T_s (in Kelvins) when the sun, or another extraterrestrial noise source, is centered in the beam.

$$T_s = \frac{1 - e^{-\left(\frac{D}{1.26}\right)^2}}{f^2 D^2} \log^{-1}\left(\frac{S + 250}{10}\right) \quad (6.8-9)$$

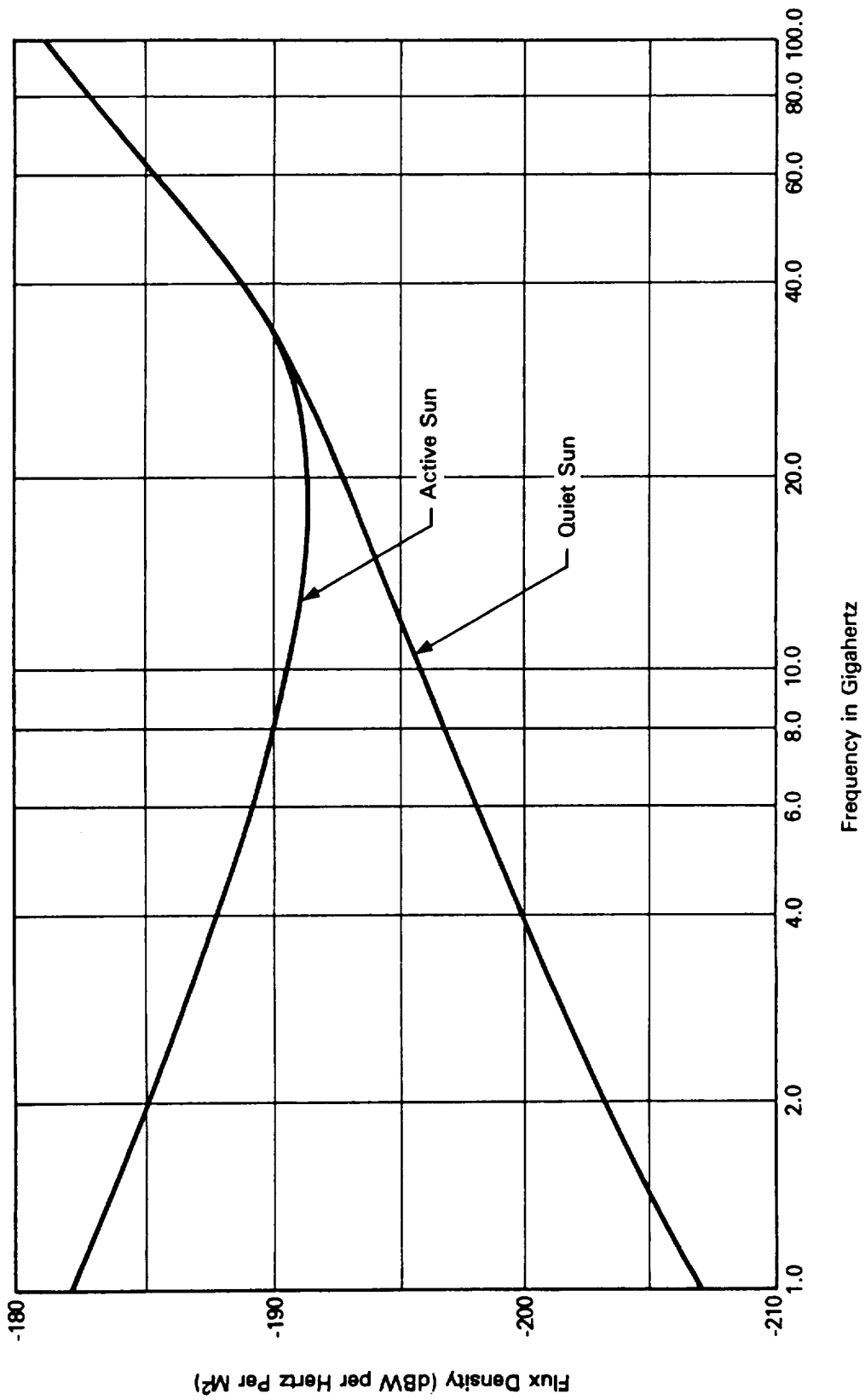


Figure 6.8-4. Values of Noise from Quiet and Active Sun

where D = apparent diameter of the sun, deg
 f = frequency, GHz
 S = power flux density, dBW/Hz-m²
 θ = antenna half-power beamwidth, deg

For an Earth station operating at 20 GHz with a 2 m diameter antenna (beamwidth about 0.5°), the maximum increase in antenna temperature that would be caused by a ("quiet") sun transit is about 8100 K, according to the formula.

The sun's flux has been used extensively for measuring tropospheric attenuation. This is done with a sun-tracking radiometer, which monitors the noise temperature of an antenna that is devised to automatically remain pointed at the sun.

6.8.7.2 Lunar Noise. The moon reflects solar radio energy back to the Earth. Its apparent size is approximately 1/2 degree in diameter, like the sun. The noise power flux density from the moon varies directly as the square of frequency, which is characteristic of radiation from a "black body." The power flux density from the full moon is about -202 dBW/Hz-m² at 20 GHz. The maximum antenna temperature increase due to the moon, for the 20 GHz 2m antenna considered earlier, would be only about 320K. Because of the phases of the moon and the ellipticity of its orbit, the apparent size and flux vary widely, but in a regular and predictable manner. The moon has been used in measuring Earth station G/T (Johannsen and Koury-1974).

6.8.7.3 Radio Stars. The strongest radio stars are ten times weaker than the lunar emission. The strongest stars (Wait, et al-1974) emit typically -230 dBW/Hz-m² in the 10 to 100 GHz frequency range. Three of these strong sources are Cassiopeia A, Taurus A and Orion A. These sources are sometimes utilized for calibration of the ground station G/T. During the calibrations the attenuation due to the troposphere is usually cancelled out by comparing the sky noise on the star and subtracting the adjacent (dark) sky noise.

6.9 UPLINK NOISE IN SATELLITE ANTENNAS

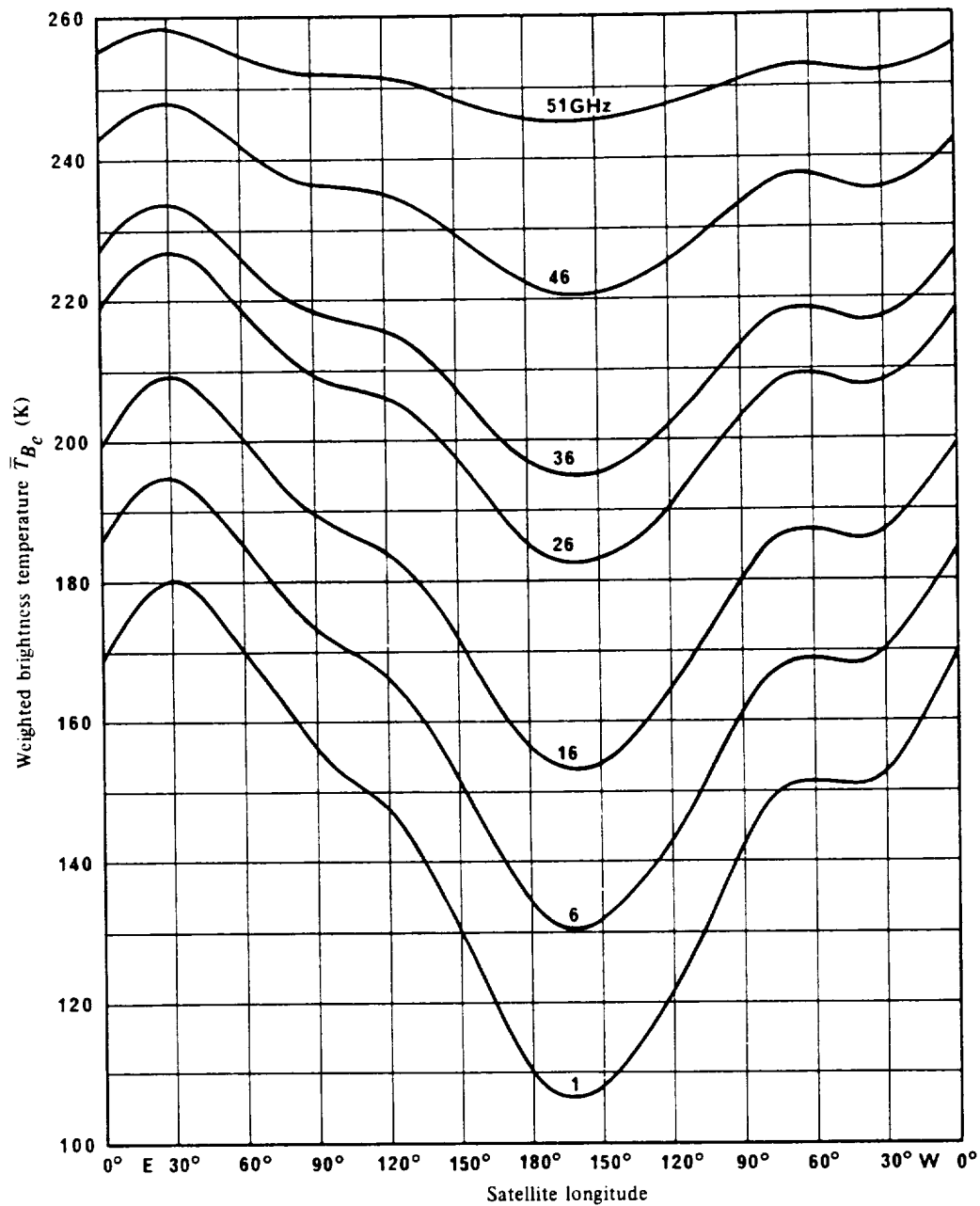
6.9.1 Components of Uplink Noise

The earth viewing (uplink) antenna of an orbiting satellite typically includes only a portion of the earth's surface within its half-power beamwidth. The observed noise is a complex function of atmospheric and surface temperature, elevation angle, frequency, and antenna gain (see, for example, Report 720-2, CCIR-1986h). A major factor in the observed noise temperature is the fraction of land (high brightness temperature) to sea (low brightness temperature) in the main antenna beam. This factor is illustrated in Figure 6.9-1, which shows the variation in antenna temperature at a geostationary satellite using an earth-coverage antenna with a gaussian beam as it is moved around the geostationary orbit (Njoku and Smith - 1985). At the lowest frequency (1 GHz) the variation with subsatellite longitude is entirely due to the land/sea fraction. As the frequency increases, the effects of the atmosphere come into play. The brightness temperature values used to compute Figure 6.9-1 are given in Figure 6.9-2, as a function of frequency and location (latitude), and they may be used for computation of more specialized satellite antenna coverage systems.

6.9.2 Sample Calculation

Consider a satellite in geostationary orbit that has a spot beam directed at the Washington D.C. area such that 60 % of the area within the 3 dB contour is land and 40 % is sea. The great-circle distance from the sub-satellite point to the center of the spot beam is 60° in equivalent latitude and the frequency is 40 GHz. What is the uplink antenna noise temperature at the satellite?

The satellite antenna noise temperature T_s may be approximated from Figure 6.9-2. The land portion will have a brightness temperature of 275 K, and the sea portion will be 185 K. Therefore



Curves are for US Standard Atmosphere with 7.5 g/cm^3 water vapor and 50 % cloud cover. The Earth Coverage antenna pattern is given by

$$G(\phi) = -3 \left(\frac{\phi}{8.715} \right)^2 \text{ dB} \quad \text{for } 0 \leq \phi \leq 8.715$$

where ϕ is the angle off of boresight. (Njoku and Smith - 1985)

Figure 6.9-1. Weighted Brightness Temperature of the Earth as a Function of Longitude, Viewed from Geostationary Orbit at Frequencies between 1 and 51 GHz.

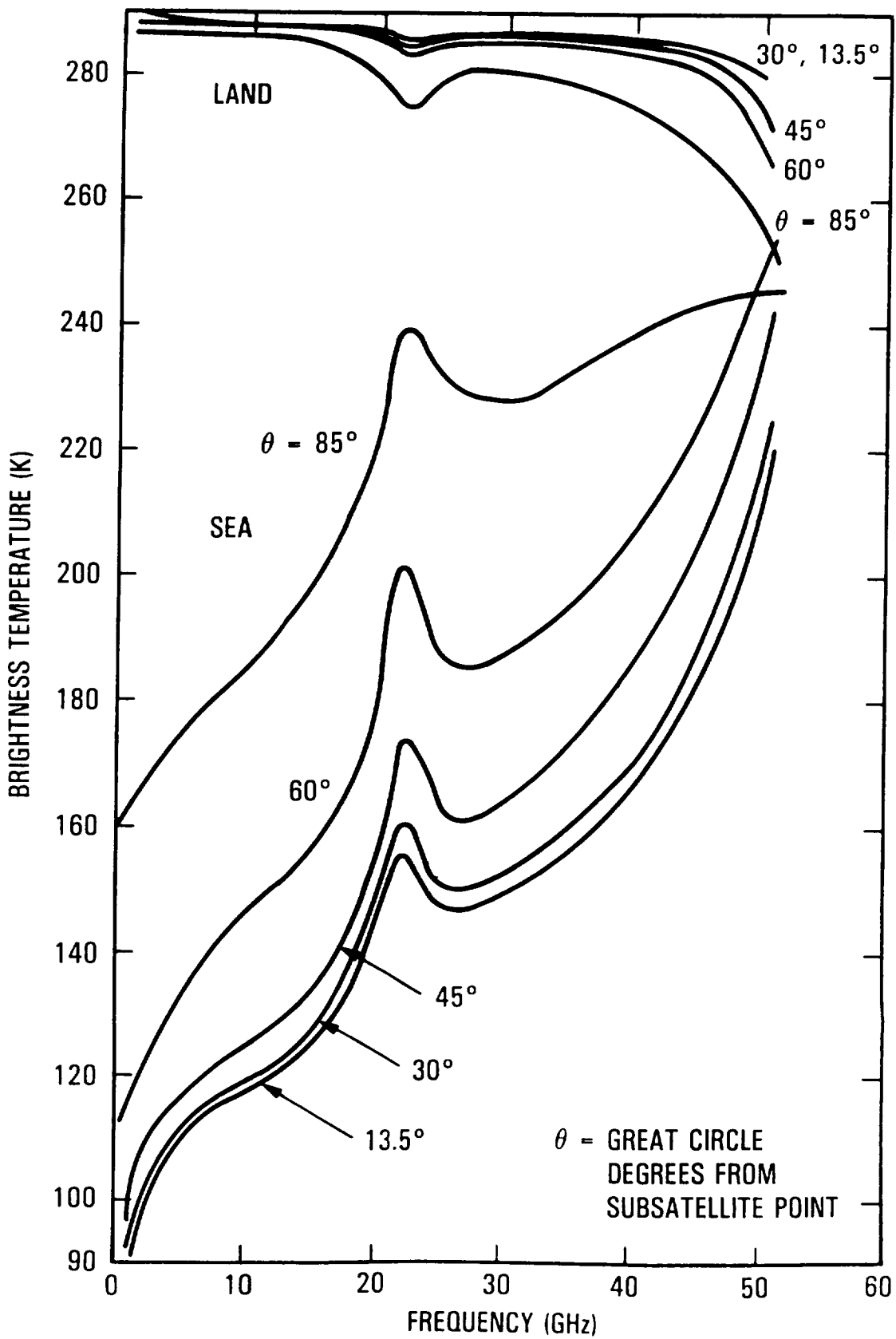


Figure 6.9-2. Brightness Temperature Contributions for Land and Sea, as a Function of Frequency and Latitude.

$$T_s = 0.6(275) + 0.4(185) = 239 \text{ K}$$

A more exact determination involves weighting each incremental area in the antenna beam by the appropriate off-boresight antenna gain. The additional accuracy is usually not necessary, however, since current satellite receiver noise temperatures are typically 1000 K or higher, and the incremental difference in the total system noise temperature would likely be very small.

6.10 REFERENCES

- Ahmed, I.Y. and L.J. Auchterlouie (1976), "Microwave Measurements of Dust Using an Open Resonator," Electronics Letters, Vol. 12, No. 17, p. 445.
- Allnutt, J.E. (1976), "Slant Path Attenuation and Space Diversity Results using 11.6 GHz Radiometers," Proceedings IEE, Vol. 123, p. 1197.
- Allnutt, J.E. (1985), "Low Elevation Angle Propagation Measurements in the 6/4 GHz and 14/11 GHz Band," IEE Conf. Publ. No. 248, IEE Fourth International Conf. On Antennas and Propagation, (ICAP 85), U. of Warwick, Coventry, U.K., 16-19 April, 1985, pp. 57-61.
- Altshuler, E.A. (1984), "A Simple Expression for Estimating Attenuation by Fog at Millimeter Wavelengths," IEEE Trans. Ant. & Prop., Vol. AP-32, No. 7, pp. 757-758.
- Altshuler, E.A. (1986), "Addendum to A Simple Expression for Estimating Attenuation by Fog at Millimeter Wavelengths," IEEE Trans. Ant. & Prop., Vol. AP-34, No. 8, pp. 1067.
- Ansari, A.J., and B.G. Evans, (1982), "Microwave Propagation in Sand and Dust Storms," Proc. IEE, Vol. 129, Part 5, No. 5, pp. 315-322.
- Baars, J.W.M. (1973), "The Measurement of Large Antennas with Cosmic Radio Sources," IEEE Trans. Ant. Prop., Vol. AP-21, No. 4, pp. 461-474.
- Bashir, S.O., A.W. Dissanayke, and N.J. McEwan (1980), "Prediction of forward scattering and cross-polarization due to dry and moist haboob and sandstorms in Sudan in the 9.4 GHz band," Telecom. J., Vol 47, No. VII, pp. 462-467.
- Bean, B.R. and E.J. Dutton (1966), "Radio Meteorology," National Bureau of Standards Monograph 92, republished in paperback by Dover.
- Bergmann, H.J. (1977), "Satellite Site Diversity: Results of a Radiometer Experiment at 13 and 18 GHz," IEEE Trans. Ant. Prop., Vol. AP-25, p. 483.
- Bostian, C.W. and J.E. Allnutt (1979), "Ice-Crystal Depolarization on Satellite-Earth Microwave Radio Paths," Proc. IEE, Vol. 126, p. 951.
- Bostian, C.W., S.B. Holt, Jr., S.R. Kauffman, E.A. Manus, R.E. Marshall, W.L. Stutzman and P.H. Wiley (1977), "Rain Depolarization and Attenuation Measurements at 11.7, 19.04 and 28.56 GHz: A Description of the Experiment and Some

Preliminary Results," URSI Comm. F Proc., April 28 - May 6, La Baule, France, pp. 403-408.

- Bostian, C.W., W.L. Stutzman, E.A. Manus, P.H. Wiley, R.E. Marshall and P. Santago (1979), "Summary of 1978 Attenuation and Depolarization Measurements Made With the CTS (11.7 GHz) and COMSTAR (19.04 and 28.56 GHz) Beacons," Invited Paper for the USNC/URSI Special Sessions on Propagation Above 10 GHz, June 18-20, Seattle, Washington.
- Bostian, C.W., Pratt, T., & Stutzman, W.L. (1986), "Results of a Three-Year 11.6 GHz Low-Angle Propagation Experiment Using the SIRIO Satellite," IEEE Trans. Ant. & Prop., Vol. AP-34, No. 1, pp. 58-65.
- Bostian, C.W., Stutzman, W.L., & Pratt, T. (1987), "SIRIO Results at Virginia Tech," Alta Frequenza, Vol LVI, N. 1-2, pp. 95-99.
- CCIR (1978), "Propagation In Non-Ionized Media," Volume V, Recommendations and Reports of the CCIR - 1978, International Telecommunication Union, Geneva.
- CCIR (1981a), Propagation Data Required for Space Telecommunication Systems, Report 564-1 (MOD F), Doc. 5/1044, Geneva, Switzerland.
- CCIR (1981b), Radiometeorological Data, Report 563-1 (MOD F), Doc. 5/5049, Geneva, Switzerland.
- CCIR (1981c), Attenuation by Precipitation and Other Atmospheric Particles, Report 721 (MOD F) Doc. 5/5026, Geneva, Switzerland.
- CCIR (1981), "Draft Revision of Report 720(MOD #I)," Document USSG 5/31, 12 March.
- CCIR (1982), Radio Propagation Factors Relating to Frequencies Near 12.5 and 17.5 GHz, Doc. A/68, 2 July 1982, Preparatory Meeting SAT-R2, Geneva, Switzerland.
- CCIR (1986a), Propagation in Ionized Media, Volume VI, Recommendations and Reports of the CCIR - 1986, International Telecommunication Union, Geneva.
- CCIR (1986b), "Propagation Data and Prediction Methods Required for Earth-Space Telecommunications Systems," Report 564-3, in Volume V, Recommendations and Reports of the CCIR - 1986, International Telecommunication Union, Geneva.
- CCIR (1986c), "Radiometerological Data," Report 563-3, in Volume V, Recommendations and Reports of the CCIR - 1986, International Telecommunication Union, Geneva.
- CCIR (1986d), "Attenuation By Atmospheric Gases," Report 719-2, in Volume V, Recommendations and Reports of the CCIR - 1986,

International Telecommunication Union, Geneva.

- CCIR (1986e), "Worst Month Statistics," Report 723-2, in Volume V, Recommendations and Reports of the CCIR - 1986, International Telecommunication Union, Geneva.
- CCIR (1986f), "Attenuation by Hydrometeors, In Particular Precipitation and Other Atmospheric Particles," Report 721-2, in Volume V, Recommendations and Reports of the CCIR - 1986, International Telecommunication Union, Geneva.
- CCIR (1986g), "Cross-polarization Due to the Atmosphere," Report 722-2, in Volume V, Recommendations and Reports of the CCIR - 1986, International Telecommunication Union, Geneva.
- CCIR (1986h), "Radio Emissions from Natural Sources in the Frequency Range Above About 50 Mhz," Report 720-2, in Volume V, Recommendations and Reports of the CCIR - 1986, International Telecommunication Union, Geneva.
- CCIR (1988), "Attenuation by Atmospheric Gases," Report 719-2, Doc. 5/156, International Telecommunication Union, Geneva, 18 April, 1988.
- Canada Atmospheric Environment (1973), Short Duration Rainfall Intensity-Duration-Frequency Graphs, Downsview, Ontario, Canada.
- Chu, T.S. (1974), "Rain-Induced Cross-Polarization at Centimeter and Millimeter Wavelengths," Bell Syst. Tech. Jrnl., Vol. 58, No. 8, pp. 1557-1579.
- Chu, T.S. (1979), "Effects of Sandstorms on Microwave Propagation," Bell System Tech. J., Vol. 58, pp. 549-555.
- Chu, T.S. (1980), "Microwave Depolarization of an Earth-Space Path," Bell System Technical Journal, Vol. 59, No. 6, pp. 987-1007.
- Crane, R.K. (1967), "Coherent Pulse Transmission through Rain," IEEE. Trans. Ant. Prop., Vol. AP-15, p. 252.
- Crane, R.K. (1976), An Algorithm to Retrieve Water Vapor Information from Satellite Measurements, NEPRF Tech-Rept. 7-76, Final Report, Project No. 1423, Environmental Research & Technology, Inc., Concord, Mass.
- Crane, R.K. (1976a), "Refraction Effects in the Neutral Atmosphere," Astrophysics, Part B. Radiotelescopes, Vol. 12 of Methods of Experimental Physics, M. C.. Weeks, ed., Academic Press, N. Y.
- Crane, R.K. (1977), "Ionospheric Scintillations," Proc. IEEE, Vol. 65, pp. 180-199.
- Crane, R.K. (1980), "Prediction of Attenuation by Rain," IEEE Trans.

- Crane, R.K. (1980a), "Earth-Space and Terrestrial Microwave Propagation - Estimation of Rain Attenuation with the Global Model," ERT Technical Report P-A414-TR, prepared for NASA Headquarters under Contract NASW-3337 (October 1980).
- Crane, R.K. and D.W. Blood (1979), Handbook for the Estimation of Microwave Propagation Effects-Link Calculations for the Earth Space Paths, Environmental Research & Technology, Inc., Concord, Mass., report to NASA/GSFC under Contract NAS5-25341.
- Crane, R.K. and W.E. DeBrunner (1978), "Worst-Month Statistics," Electronics Letters, Vol. 14, No. 2, pp. 38-40.
- Davies, P.G. (1976), "Diversity Measurements of Attenuation at 37 GHz with Sun-Tracking Radiometers in a 3-site Network," Proceedings IEE, Vol. 123, p. 765.
- Davies, P.G. and D.L. Croom (1974), "Diversity Measurements of Attenuation at 37 GHz with Solar-Tracking Radiometers," Electronics Letters, Vol. 10, p. 482.
- Devasirvatham, D. and D.B. Hodge (1977), "Amplitude Scintillations on Earth-Space Propagation Paths at 2 and 30 GHz," The Ohio State University ElectroScience Lab., Tech. Rpt. 4299-4.
- Dintelmann, F. (1981), "Analysis of 11 GHz Slant Path Fade Duration and Fade Slope," Electronics Letters, Vol. 11, No. 22, pp. 547-548.
- Engelbrecht, R.S. (1979), "The Effect of Rain on Satellite Communications Above 10 GHz," RCA Review, Vol. 40, p. 191.
- Ferguson, A. and R.R. Rogers (1978), "Joint Statistics of Rain Attenuation on Terrestrial and Earth-Space Propagation Paths," Radio Science, Vol. 13, p. 471.
- Flock, W.L. (1987), "Propagation Effects on Satellite Systems at Frequencies Below 10 GHz - A Handbook for Satellite Systems Design," Second Edition, NASA Reference Publication 1108 (02), December 1987.
- Flock, W.L., S.D. Slobin, and E.K. Smith (1982), "Propagation Effects on Radio Range and Noise in Earth-Space Telecommunications," Radio Science, Vol. 17, pp. 1141-1144, Nov.-Dec. 1982.
- Freeny, A.E. and J.D. Gabbe (1969), "A Statistical Description of Intense Rainfall," Bell System Technical Journal, Vol. 48, p. 1789.
- Funakawa K. and Y. Otsu (1974), "Characteristics of Slant Path Rain Attenuation at 35 GHz Obtained by Solar Radiation and

Atmospheric Emission Observations," Journal de Reserches Atmospherique, Vol. 8, p. 339.

- Ghobrial, S.I., I.A. Ali, and H.M. Hussein (1978), "Microwave Attenuation in Sandstorms," Summaries of Papers, 1978 International Symposium on Antennas and Propagation, Sendai, Japan.
- Gibbins, C.J. (1986), "Improved Algorithms for the Determination of Specific Attenuation as Sea Level by Dry Air and Water Vapor, in the Frequency Range 1-350 GHz," Radio Science, Vol. 21, pp. 949-954, Nov.-Dec. 1986.
- Goldhirsh, J. (1976), "Path Attenuation Statistics Influenced by Orientation of Rain Cells (1976)," IEEE Trans. Ant. Prop., Vol. AP-24, p. 792.
- Goldhirsh, J. (1982), "A parameter review and assesment of attenuation and backscatter properties associated with dust storms over desert regions in the frequency range of 1 to 10 GHz," IEEE Trans. on Ant. and Prop., Vol. AP-30, pp. 1121-1127.
- Gumbel, E.J. (1958), Statistics of Extremes, Columbia Univ. Press, New York, New York.
- Gutteberg, O. (1981), "Measurement of Tropospheric Fading and Cross-polarization in the Artic using Orbital Test Satellite," IEE Conf. Publ. No. 195, Part 2, IEE Second Int. Conf. on Antennas and Propagation, Heslington, York, U.K., pp. 71-75.
- Hall, J.E. and J.E. Allnutt (1975), "Results of Site Diversity Tests Applicable to 12 GHZ Satellite Communications," IEE Conference Publication No. 126, Satellite Communication Systems Technology, London.
- Harris, J.M. (1977), "Tropospheric Scintillation of Microwaves Propagated on Low Elevation Angle Earth-space Path," COMSAT Tech. Memo CL-54-77.
- Hendry, A., G.C. McCormick and B.L. Barge (1976), "Ku-Band and S-Band Observations of the Differential Propagation Constant in Snow," IEEE Trans. Ant. Prop., Vol. AP-24, No. 4, pp. 521-525.
- Hodge, D.B., D.M. Theobald, and R.C. Taylor (1976b), "ATS-6 Millimeter Wavelength Propagation Experiment," Ohio State University, ElectroScience Laboratory, Rept. 3863-6.
- Hogg, D.C. (1968), "Millimeter Wave Communication through the Atmosphere," Science, Vol. 159, p. 39.
- Hogg, D.C. and T.S. Chu (1975), "The Role of Rain in Satellite Communications," Proc. IEEE, Vol. 63, No. 9, pp. 1307-1331.

- Hopfield, H.S. (1971), "Tropospheric Effect on Electromagnetically Measure Range: Prediction from Surface Weather Data," Radio Science, Vol. 6, pp. 357-367.
- Hyde, G. (1976), "Data Analysis Report - ATS-F Comsat Millimeter Wave Propagation Experiment," Comsat Laboratories, Clarksburg, Maryland.
- Ippolito, L.J. (1976), "20 and 30 GHz Millimeter Wave Experiments with the ATS-6 Satellite," NASA Tech. Note TN D-8197, April 1976.
- Ippolito, L. J. (1979), "11.7 GHz Attenuation and Rain Rate Measurements with the Communications Technology Satellite (CTS), NASA TM 80283, Goddard Space Flight Center, Greenbelt, MD.
- Ippolito, L.J. (1986), Radiowave Propagation in Satellite Communications, Van Nostrand Reinhold, New York.
- Ishimaru, A. (1978), Wave Propagation and Scattering in Random Media, Single Scattering and Transport Theory, Vol. 1, Academic Press, New York, N. Y.
- Johannsen, K.G. and A. Koury (1974), "The Moon as a Source for G/T Measurements," IEEE Trans. Aerosp. Elect. Syst., Vol. AES-10, No. 5, pp. 718-727.
- Kaul, R. (1980), "Extension of an Empirical Site Diversity Relation to Varying Rain Regions and Frequencies," URSI Commission F Symposium, Lennoxville, Quebec.
- Kobayashi, T. (1977), "Degradation of cross-polarization isolation due to rain," J. of Radio Research Labs. (Japan), Vol. 24, No. 114, pp. 101-107.
- Koester K L and L H Kosowsky (1970), "Attenuation of Millimeter Waves in Fog," Fourteenth Radar Meteorology Conference, November 17-20, Tuscon, Arizona.
- Koester, K.L. and L.H. Kosowsky (1978), "Millimeter Wave Propagation in Ocean Fogs and Mists," Proceedings IEEE Ant. Prop. Symposium.
- Kraus, J.D. (1966), Radio Astronomy, McGraw-Hill Book Co., New York. LeFrancois, G.L., Martin and M.: Rooryck (1973), "Influence de la Propagation Sur la Valeur de Decouplage de Deux Polarisations Orthogonales," Ann. des Telecomm., Vol. 28, July-August, in French.
- Liebe, H.J. (1975), "Molecular Transfer Characteristics of Air Between 40 and 140 GHz," IEEE Trans. Microwave Theory and Techniques, MTT-23, No. 4.
- Lo, Lai-Inn, B.M. Fannin and A.W. Straiton (1975), "Attenuation of

8.6 and 3.2 mm Radio Waves by Clouds," IEEE Trans. Ant. Prop., Vol. AP-23, No. 6.

- Lo, P.S.L., O.P. Banjo, and E. Vilar (1984), "Observations of Amplitude Scintillations on a Low Elevation Earth-space Path," Electronics Letters, Vol. 20, No. 7, pp. 307-308.
- Lord, L.H. and R. Oliver (1946), "An Experimental Investigation of the Reflection and Absorption of Radiation of 9-cm Wavelength," Proc. Phys. Soc., Vol. 58, pp. 265-280.
- Marini, J.W. (1972a), "Correction of Satellite Tracking Data for an Arbitrary Tropospheric Profile," Radio Science, Vol. 7, pp. 223-231.
- Marini, J.W. (1972b), "Tropospheric Range-Rate Tracking Data Correction," NASA/Goddard Space Flight Center, Doc. X-551-72-277.
- Mason, B.J. (1971), The Physics of Clouds, Clarendon Press, Oxford, pp.119-121.
- McCormick, K.S. and L.A. Maynard (1972), "Measurements of SHF Tropospheric Fading Along Earth Paths at Low Elevation Angles," Electronics Letters, Vol. 8, No. 10.
- McEwan, N.J., P.A. Watson, A.W. Dissanayake, D.P. Haworth and V.T. Vakili (1977), "Crosspolarization from High Altitude Hydrometeors on a 20 GHz Satellite Radio Path," Electronics Letters, Vol. 13, pp. 13-14.
- Muchmore, R.B. and A.D. Wheelon (1955), "Line-of-Sight Propagation Phenomena - I. Ray Treatment," Proc. IRE. Vol. 43, pp. 1437-1449.
- Njoku, E.G. and E.K. Smith (1985), "Microwave Antenna Temperature of the Earth from Geostationary Orbit," Radio Science, Vol. 20, No. 3, pp. 591-599.
- Nowland, W.L., R.L. Olsen and I.P. Shkarofsky (1977a), "Theoretical Relationship Between Rain Depolarization and Attenuation," Electronics Letters, Vol. 13, No. 22, pp. 676-677.
- Nowland, W.L., I.I. Strickland, J. Schlesak and R.L. Olsen (1977b), "Measurements of Depolarization and Attenuation at 11.7 GHz by Using the Communications Technology Satellite," Electronics Letters, Vol. 13, No. 24, pp. 750-751.
- Nusple, P.P., N.G. Davies and R.L. Olsen (1975), "Ranging and Synchronization Accuracies in a Regional TDMA Experiment," Proc. Third Intl. Digital Satellite Comm. Conf., Kyoto, Japan.
- Oguchi, T. (1977), "Scattering Properties of Pruppacher and Pitter Form Raindrops and Cross Polarization Due to Rain:

- Calculations at 11, 13, 19.3 and 34.8 GHz," Radio Science, Vol. 12, No. 1, pp. 41-51, Jan.-Feb. 1977.
- Olsen, R.L., D.V. Rogers and D.B. Hodge (1978), "The aR^b Relation in the Calculation of Rain Attenuation," IEEE Trans. Ant. Prop., AP-26, pp. 318-329.
- Pruppacher, H.R. and R.L. Pitter (1971), "A Semi-empirical Determination of the Shape of Cloud and Rain Drops," J. Atmos. Science, Vol. 28, pp. 86-94.
- Radio Regulations, International Telecommunication Union, Geneva.
- Rice, P.L. and N.R. Holmberg (1973), "Cumulative Time Statistics of Surface Point Rainfall Rates," IEEE Trans. Comm., Vol. COM-21, No. 10, pp. 1131-1136.
- Rogers, D.V. (1981), "Diversity- and Single-Site Radiometric Measurements of 12-GHz Rain Attenuation in Different Climates," IEE Conference Publication No. 195, International Conf. on Ant. & Prop., AP-26 U.K. pp. 118-123.
- Rogers, R.R. 1976, A Short Course in Cloud Physics, Chapter 12, Pergamon Press, London.
- Segal, B. and R.E. Barrington (1977), Tropospheric Refractivity Atlas for Canada, Dept. of Communications, CRC Report No. 1315-E, Ottawa.
- Shutie, P.F., J.E. Allnutt and E.C. MacKenzie (1977), "Depolarization Results at 30 GHz Using Transmissions from the ATS-6 Satellite," Proc. URSI Symposium on Propagation in Non-Ionized Media, La Baule, France, April 28 - May 6, pp. 367-369.
- Shutie, P.F., E.C. MacKenzie and J.E. Allnutt (1978), "Relative Phase Measurement at 30 GHz Between Copolar and Induced Crosspolar Signals Produced by Ice Particles on a Satellite-to-Ground Link," Electronics Letters, Vol. 14, No. 4, pp. 105-107.
- Slobin, S.D. (1982), "Microwave noise temperature and attenuation in clouds: Statistics of these effects at various sites in the United States, Alaska, and Hawaii," Radio Science, Vol. 17, pp. 1443-1454, Nov.-Dec. 1982.
- Smith, E.K. (1982), "Centimeter and Millimeter Wave Attenuation and Brightness Temperature due to Atmospheric Oxygen and Water Vapor," Radio Science, Vol. 17, No. 6, pp. 1455-1464.
- Spaulding, A.D., G.H. Hagn (1978), "Worldwide Minimum Environmental Radio Noise Levels (0.1 Hz to 100 GHz)," Symposium Proceedings, Effects of the Ionosphere on Space and Terrestrial Systems, J.M. Goodwin, Ed., ONR/NRL, pp. 177-182, Jan. 24-26, 1978.

- Strickland, J.I. (1974), "Radar Measurements of Site Diversity Improvement During Precipitation," Journal de Recherches Atmospherique, Vol. 8, p. 45.
- Strickland, J.I., R.I. Olsen and H.L. Werstiuk (1977), "Measurements of Low Angle Fading in the Canadian Arctic," Ann. Telecomm., Vol. 32, Nos. 11-12, pp. 530-535.
- Strickland, R.I., R.O. Olsen, and H.L. Werstiuk, (1977), "Measurements of Low Angle Fading in the Canadian Arctic," Ann. des Telecomm., Vol. 11-12, pp. 530-535.
- Stutzman, W.L., C.W. Bostian, C.W. Manus, E.A. Marshall, and P.H. Wiley (1975), "ATS-6 Satellite 20 GHz Propagation Measurements at Low Elevation Angles," Electronics Letters, Vol. 11, pp. 635-636.
- Stutzman, W.L. (1977), "Mathematical Formulations and Definitions for Dual Polarized Reception of a Wave Passing Through a Depolarizing Medium (A Polarization Primer)," Virginia Polytechnic & State Univ., prepared under NASA Contract NAS5-22577.
- Suzuki, Y., T. Shinozuka, H. Kuroiwa, H. Inomata (1982), "TDMA Site Diversity Switching Experiments with Japanese CS," Record, International Conference on Communication, Philadelphia, PA.
- Tang, D.D., D. Davidson, and S.C. Bloch (1982), "Diversity Reception of COMSTAR Satellite 19/29 - GHz Beacons with the Tampa Triad, 1978-1981," Radio Science, Vol. 17, No. 6, pp. 1477-1488.
- Tatarski, V.I. (1961), Wave Propagation in a Turbulent Medium, McGraw-Hill Book Co., New York N. Y.
- Theobald, D.M. (1978), "Tropospheric Refraction," report prepared for ORI, Inc. under NASA Contract NASS-23438.
- Theobald, D.M. and D.B. Hodge (1978), "Gain Degradation and Amplitude Scintillation Due to Tropospheric Turbulence," The Ohio State University ElectroScience Lab., Tech. Rpt. 784229-6, Revision 1.
- Thompson, M.C., Jr., L.E. Woods, H.B. Janes and D. Smith (1975), "Phase and Amplitude Scintillations in the 10 to 40 GHz Band," IEEE Trans. Ant. Prop., Vol. AP-23, pp. 792-797.
- Towner, G.C., R.E. Marshall, W.L. Stutzmann, C.W. Bostian, T. Pratt, E.A. Manus, P.H. Wiley (1982), "Initial Results from the VPI and SU SIRIO Diversity Experiment," Radio Science, Vol. 17, No. 6, pp. 1489-1494.
- Turner, D.J.W. (1973), "Measurements of Cross-Polar Discrimination at 22 and 37 GHz," IEE Conf. Proc. No. 98.

- U.S. Dept. of Commerce (1947), Weather Bureau, "Maximum Recorded United States Point Rainfall," Tech. Paper No. 2, Washington, D.C.
- U.S. Dept. of Commerce (1955), Weather Bureau, "Rainfall Intensity-Duration-Frequency Curves," Tech. Paper No. 25, Washington, D.C.
- Vogel, W.J. (1978), CTS Attenuation and Cross-Polarization Measurements at 11.7 GHz, Final Report, Elect. Eng. Res. Lab., Univ. Texas at Austin, prepared under NASA Contract NAS5-22576.
- Vogel, W.J., A.W. Straiton, B.M. Fannin and N.K. Wagner (1976), "Attenuation Diversity Measurements at 20 and 30 GHz," Radio Science, Vol. 11, p. 167.
- Vogel, W.J., A.W. Straiton and B.M. Fannin (1977), "ATS-6 Ascending: Near Horizon Measurements Over Water at 30 GHz," Radio Science, Vol. 12, September-October, pp. 757-765.
- Wait, D.F., W.C. Daywitt, M. Kanda and C.K.S. Miller (1974), A Study of the Measurement of G/T Using Casseopeia A, National Bureau of Standards, Rept. No. NBSIR 74-382.
- Waters, J.W. (1976), "Absorption and Emissions by Atmospheric Gases," Methods of Experimental Physics, Vol. 12B, Radio Telescopes, Ed. M. L. Meeks, Academic Press, New York, NY.
- Watson, P.A. and M. Arbabi (1973), "Cross-polarization Isolation and Discrimination," Electronics Letters, Vol. 9, No. 22, pp. 516-517.
- Watson, P.A., F. Goodall and M. Arbabi (1973), "Linear Cross-Polarization and Attenuation Measurements at 11 and 36 GHz," IEE Conf. Proc. No. 98.
- Webber, R.V., and K.S. McCormick (1980), "Low Angle Measurements of the ATS-6 Beacons at 4 and 30 GHz," Proc. URSI (Commission F) International Symposium on Effects of the Lower Atmosphere on Radio Propagation at Frequencies Above 1 GHz, Lennoxville, Canada.
- Webster, W.J., Jr., T.T. Wilheit, T.C. Chang, P. Gloersen and T.J. Schmugge (1975), "A Radio Picture of the Earth," Sky and Telescope, Vol. 49, No. 1, pp. 14-16.
- WEC (Westinghouse Electric Corporation) (1975), ATS-6 Millimeter Wave Propagation Experiment - Final Data Analysis Report, Baltimore, Md., prepared under NASA/GSFC Contract NAS5-20904.
- Weickmann, H.K. and H.J. aufm Kampe (1953), "Physical Properties of Cumulus Clouds," Journal of Meteorology, Vol. 10.

Wulfsberg, K.N. (1964), "Apparent Sky Temperatures at Millimeter-Wave-Frequencies," Phys. Science Res. Paper No. 38, Air Force Cambridge Res. Lab., No. 64-590.

Wulfsberg, K.N. (1973), "Path Diversity for mm-wave Earth-to-Satellite Links," Radio Science, Vol. 8, p. 1.

Yamada, M. and H. Yokoi (1974), "Measurements of Earth-Space Propagation Characteristics at 15.5 and 31.6 GHz Using Celestial Radio Sources," Elect. and Comm. in Japan, Vol. 57-B, p. 2.

Yokoi, H., M. Yamada and T. Satoh (1970), "Atmospheric Attenuation and Scintillation of Microwaves from Outer Space," Astronomical Society, Japan, Vol. 22, pp. 511-524.

1

2

3

4

5

6

7

CHAPTER VII

APPLICATION OF PROPAGATION PREDICTIONS TO EARTH/SPACE TELECOMMUNICATIONS SYSTEM DESIGN

7.1 INTRODUCTION

A function of the satellite communication system designer, or system engineer, is to interface between the source of system requirements (i.e., the user) and the sources of performance data. Stated in terms of the present problem, the system engineer uses propagation and other technical data to achieve a system design that will meet the requirements specified by the user. These requirements are specified in terms of a gross quantitative need (e.g., number of channels), a quantitative expression of performance (e.g., percent of time available), and, sometimes, more qualitative expressions (e.g., "highly reliable"). Even though both the propagation data and the requirements are often expressed in terms of cumulative probability distributions, it is not always straightforward to relate one distribution to the other. The correspondence between a given propagation phenomenon and system performance may be complex. The purpose of this chapter is to relate propagation data to system performance parameters. It should allow the system engineer to perform the analyses telling how well requirements are met by a given system design, thereupon enabling the system engineer to modify that design if necessary. First (in Section 7.2), the various ways of specifying performance criteria for different kinds of systems are discussed. In addition, examples of specific satellite communication systems are discussed. Procedures for designing such systems are then described in section 7.3.

There are engineering disciplines for which true synthesis procedures exist, but the design of complex systems with interactive elements is usually not a true synthesis. Instead, iterative

analyses are performed, starting with a preliminary design choice, until the refined design can be shown by analysis to meet the requirements. The application of this philosophy of system design or synthesis to satellite communications is summarized here and detailed in Section 7.3.

The system design procedure is based on criteria that take the form of discrete cumulative probability distribution functions of performance. The steps necessary to go from this set of performance requirements and propagation statistics to a system design are (see Figure 7.1-1):

INITIAL PHASE

- 1) Establish system performance requirements (discrete distribution of baseband/digital performance).
- 2) Apply modulation equations to convert system performance requirements to discrete distribution of the received composite CNR (carrier-to-noise ratio).
- 3) Prepare initial design with parameters sized according to free space propagation conditions (apply power budget equations).

DESIGN SYNTHESIS AND TRADE OFF PHASE

- 4) Employ
 - a) Composite CNR distribution from step 2
 - b) System architecture
 - c) Multiple Access equations
 - d) Availability sub-allocation philosophyto develop distribution functions for CNR on each path.

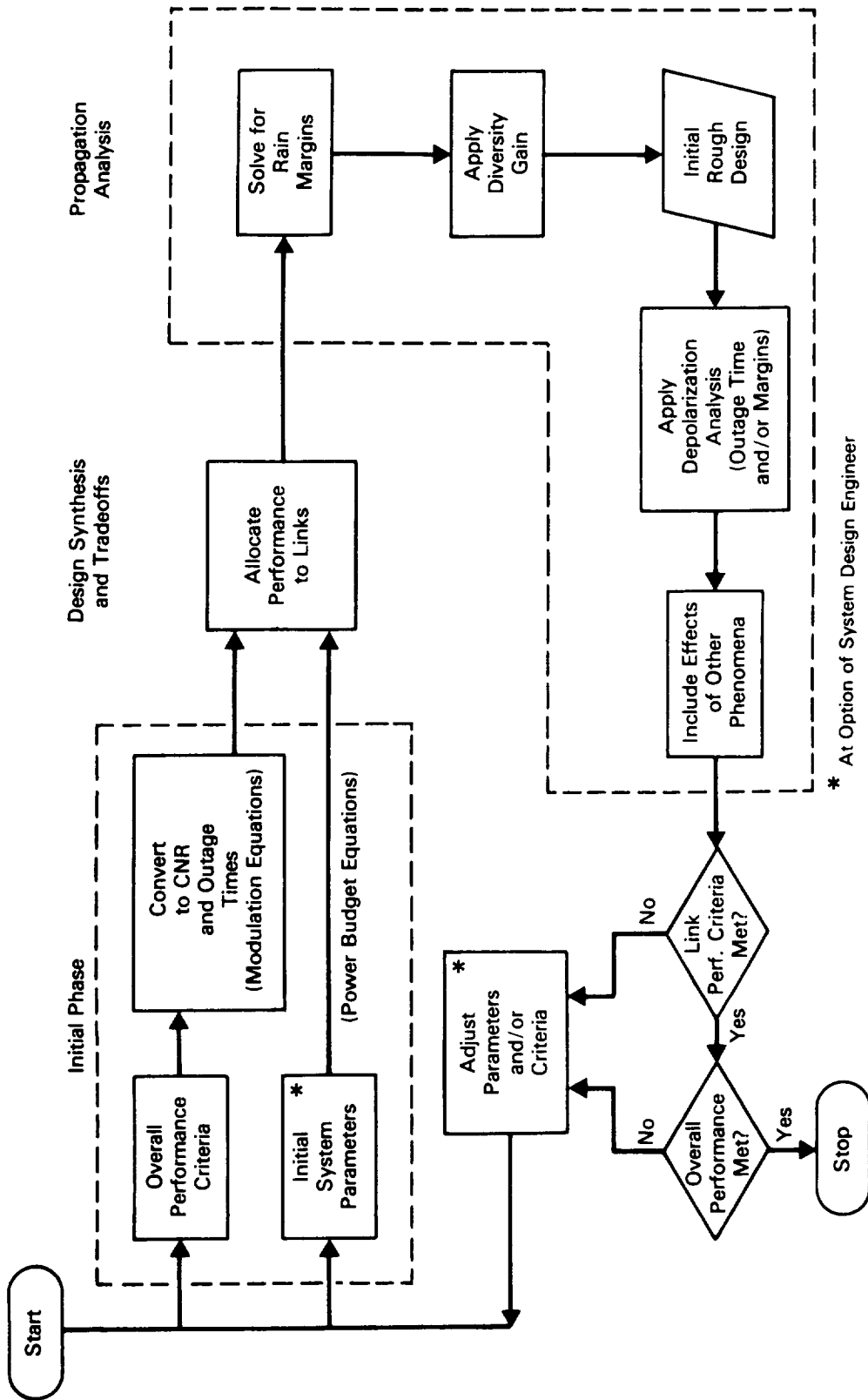


Figure 7.1-1. System Design Process

PROPAGATION ANALYSIS AND ITERATION PHASE

- 5) Compute rain margins, as reduced by diversity gain, for each path.
- 6) Adjust system parameters according to margins given by step 5. This gives a preliminary design at the feasibility concept level.
- 7) Apply depolarization analysis to adjust margins and/or increase the outage time values (% of time for the worst-performance level of the distributions).
- 8) Consider other propagation effects such as cloud and fog attenuation, signal fluctuations, and antenna gain degradations and add margin to design as necessary.
- 9) Adjust system parameters to include all additive margins. Analyze system performance, first at the path level, then on the end-to-end performance level.
- 10) If performance meets requirements closely, stop. Otherwise, adjust design and repeat analysis. If design cannot be made to meet requirements, consider changing requirements.

Performance criteria typically deal with baseband quality, or digital error rates, whereas the power budgets relate physical system parameters to signal-to-noise ratio, CNR, (or equivalents such as S/N , E_b/N_0 , C/kT , etc.). Therefore, the baseband or digital performance criteria must be functionally related to CNR by means of modulation performance equations.

Gross design is performed by means of elementary power budget analysis and free-space (or clear air) propagation characteristics. Basic choices are made at this point, such as selection of modulation and multiple access techniques. It is assumed that the reader is familiar with these techniques and power budget analysis (Northrop-1966). This analysis establishes a relationship between

basic system parameters and the signal- or carrier-to-noise ratio (CNR) on a given transmission path.

The system performance requirements, which apply to end-to-end performance, are suballocated to various system components. Most important, the relationship of the end-to-end communication performance to that of each of the links must be determined. For example, the actual received CNR is a composite which may include both uplink and downlink noise contributions. The end-to-end availability involves availabilities of each path.

Since rain induced attenuation is the most severe propagation effect for the frequencies of interest, the next step in the procedure is to calculate a rain margin. If the system uses site diversity, some of this rain margin may be offset by "diversity gain." The remaining margin is then applied to the initial system parameters. Typically, the margin is applied as an increase in power; but it is also possible to increase antenna gains or modify the modulation parameters. At this point, a rough design has been achieved. This level of detail and accuracy may be sufficient if the objective is only to determine system feasibility. For more accurate results, the effects of other propagation phenomena must be considered. Except for depolarization, these effects are generally additive in terms of margin. Loss in crosspolarization isolation (usually termed "depolarization") can be accommodated as an additive term whenever the interference component is small relative to thermal noise and other interference sources. Thus, small degradations such as those due to depolarization from ice are treated as part of the system margin computation*. The more severe degradations in cross polarization such as those caused by rain cannot be counteracted by margin increases. These events will

*It is not necessary to add margins on a worst case basis. Where large margins have already been included for rain, the ice depolarization event can be assumed to "share" the same margin.

usually be severe enough to cause an outage. Therefore, in systems employing cross polarization isolation, the depolarization phenomenon may reduce or limit the system availability.

Having thus adjusted the system parameters and the performance analyses, the system design engineer can determine whether performance criteria are met, first for the individual link, and then for the overall system. If so, the design process is essentially completed*. If not, the system parameters and/or the performance criteria are modified, and the analysis procedure is repeated. To some, the idea that the criteria are subject to change is disturbing. Within physical (and economic) constraints, it is preferable to modify only the technical system parameters. But there may be cases where the initial performance goals are unrealistic. For example, it simply may not be worth the expense of a large increase in EIRP in order to get a circuit availability of 99.99% for small earth terminals at 44 GHz.

Section 7.2 addresses system performance criteria and examples of representative satellite communication systems, while paragraphs 7.3.1 through 7.3.3 are introductions to general system design procedures. The experienced communication system engineer will probably be familiar with the material covered in these paragraphs, and may therefore skip them without loss of continuity, and concentrate on paragraphs 7.3.4 through 7.3.6, which are addressed to the main issue at hand, namely the specific application of propagation data. Section 7.4 describes several methods for overcoming the effects of rain fades. Diversity schemes and signalling techniques are described that can significantly improve communication performance. Table 7.1-1 is a guide to specific examples contained in this chapter.

*A fine-tuning iteration may be desirable if the design exceeds requirements.

Table 7.1-1. Guide to Systems Analysis Procedures

<u>Paragraph Number</u>	<u>Description</u>	<u>Page Number</u>
7.3.4	Performance specification of digital and analog systems	7-43
7.3.5	Analog and digital system synthesis and tradeoffs	7-46
7.3.6	Analog and digital system propagation analysis and link budgets	7-55
7.3.7	Calculation of composite margin	7-70
7.4.2.1.3	Estimates of parameters required for empirical diversity model	7-93
7.4.2.1.4	Analytic estimate of site diversity gain	7-102

7.2 COMMUNICATION SYSTEM PERFORMANCE CRITERIA AND SPECIFIC SATELLITE SYSTEMS

7.2.1 Performance Criteria

7.2.1.1 Introduction

Criteria for communication system performance represent attempts to quantify the "reliability or "quality" of the service. Two methods, applying different probabilistic notions, are generally used. The first method is to regard some indicator of communication quality (e.g., CNR) as a random variable and specify values of its inverse cumulative distribution function, or the probability that a given value is exceeded. With the second method of specifying performance criterion, the quality indicator is taken as a random process, and some statistic of this time-varying process is used. A

typical statistic in this case might be the median, mean, or "three-sigma" duration of the periods during which the value stays below a given threshold. If a period during which the CNR is below some threshold is regarded as an "outage", then the criterion would specify outage duration statistics.

The first type of performance criterion, which will be termed availability criterion, is generally specified as the percentage of time that a threshold value is exceeded (or not exceeded), rather than a probability. This is natural, since what we can measure is percentage of time, and not probability. (Ergodicity allows these to be assumed equivalent). Availability criteria are in wide use, and the bulk of long-term performance data analysis has been done from an availability standpoint. However, such criteria and data do not give any information about the time-variation of performance. In many situations, it is desirable to know something about how fast the performance may change. Some temporal information is given by a slightly modified availability criterion, in which a time period is specified. For example, the criterion could state that a given level of noise will not be exceeded for more than a certain percentage of any month. However, the connection between such a criterion and any quantitative temporal description is obscure.

The second type of performance criterion, which expressly describes the temporal behavior, such as mean outage duration, will be termed outage statistics. Besides the outage duration, such statistics might include the distribution function for the time until the next outage, given that an outage is just over. Or they might probabilistically describe diurnal or seasonal performance variations. In the limit, such statistics would give the autocorrelation function or the spectral density of the process. As yet, the available data does not cover a long enough time span to be statistically reliable. We will therefore confine our attention primarily to performance criteria that specify availability, rather than outage statistics.

There are several sources of performance criteria. Among the more generally accepted standards are those promulgated by the International Radio Consultative Committee (CCIR). Telecommunication systems for U.S. commercial use conform to standards similar but not identical to the CCIR's. These criteria are expressed in terms of a baseband noise level (analog) or an error rate degradation (digital) not to be exceeded more than some small percentage of the time in any month (typically, .001 to 0.3%). The Defense Communications Agency has more recently advanced (Kirk and Osterholz-1976 and Parker-1977) criteria based on the probability of occurrence of outage on a five minute call (voice channels), or the error free block probability for a 1000 bit block (data channels).

7.2.1.2 Digital Transmission Performance

7.2.1.2.1 Short Term Bit Error Rate. The primary measure of circuit or transmission quality for digital systems is the bit error rate (BER). Semantically, we use "bit" error rate because the overwhelming majority of digital communications systems transfer binary data streams.* Bit error rate usually applies over a moderately short term, and normally does not incorporate "errors" or outages of duration longer than a few tens of bits.

For most digital systems, the bit error probability can be expressed as a function of the energy-per-bit to noise power spectral density ratio (E_b/N_0). These relationships are available for the theoretical performance of commonly used modulation and coding systems from any good communication theory reference (e.g., Schwartz, et al-1966 and Spilker-1977). The theoretical BEP vs. E_b/N_0 relations usually assume white, Gaussian noise. In the presence of

*We should also distinguish between bit error rate, which defines the actual performance, and must be measured by averaging over a sequence of bits communicated, and the bit error probability (BEP), which is a theoretical concept that can apply even to a single bit. BER will be used here, since it is more common, even though BEP is technically more correct.

non-white or non-Gaussian noise, or interference, these relations are not accurate. It is now becoming common to express the performance of actual systems in terms of the E_b/N_0 rather than CNR. E_b/N_0 is numerically equal to the ratio of signal power to noise power within a (noise) bandwidth equal in hertz to the digital bit rate in bits per second. (Note that bit rate is not in general the same as symbol rate.) For example, the (theoretically ideal) performance of binary PSK modulation requires an E_b/N_0 of 9.6 dB for a BER of 10^{-5} .

In the case of digital systems used to accommodate fundamentally analog requirements (e.g., PCM voice channels), there exists a threshold error rate at which circuit quality is considered unacceptable. This threshold value then determines the point at which an "outage" exists. Because error rate is a sensitive function of E_b/N_0 , circuit quality degrades quite drastically when E_b/N_0 falls below the value corresponding to the threshold error rate. Degradation is not "graceful."

7.2.1.2.2 Digital Transmission Performance. Data communications systems rarely transmit uniform, homogeneous, continuous bit streams. Rather, the data is often formatted in blocks or packets. In many cases, then, the performance requirement is specified in terms of the probability of an error free block, which might typically contain 1000 or more bits. If the only type of transmission imperfection is the randomly occurring bit error process, then the block error performance can be calculated from the bit error rate: Probability of error free block of n bits = $P(\geq 1, n) = (1 - \text{BER})^n$. However, the block error performance may be influenced by the probability of longer outages, losses of synchronization, and the like, which are not usually included in the BER.

In systems used to transfer well-defined messages, other performance criteria may be required. In the most general case where a block is composed of many messages, the system performance requirements could include a message performance criterion, a block transmission performance criterion and a bit error rate. Note that

consistency among the various criteria is mandatory. For example, a block error performance of 99% (i.e., 99 out of 100 blocks are error free) for 1000-bit blocks could not be achieved when the bit error rate is 10^{-4} .

In data communications systems where real time delivery is not critical, the concept of throughput is often used. It is implicit that the system involves a return channel path over which acknowledgments and/or requests for retransmission are made. The throughput is defined (Brayer - 1978) as the ratio of the number of information bits transmitted (K) to the total number of bits (including overhead and re-transmissions), n , before the block is accepted. The throughput is approximately

$$K[1-P(\geq 1, n)]/n \quad (7.2-1)$$

This approximation for throughput as a function of block error rate applies only when the return channel is error free. Brayer (1978) makes a case for using message delivery delay as the most important criterion, rather than throughput itself. However, they are related closely.

In summary it can be seen that throughput and block error rate are directly related. Bit error rate contributes a major, but not always the only, portion of the block error rate. In communication system design, the (short term) bit error rate or bit error probability is taken as a parameter of analysis and preliminary design. Final performance estimates must, however, take into account both the nominal BER performance, and some consideration of outages. The qualitative relationships among the various criteria are shown in Figure 7.2-1. Notice that the fundamental, or user-requirement-oriented, criteria are on the right side of the diagram, yet the correct logical path for analysis is from left to right. Thus, analysis is employed to demonstrate that a set of system and environmental conditions will meet the performance requirements.

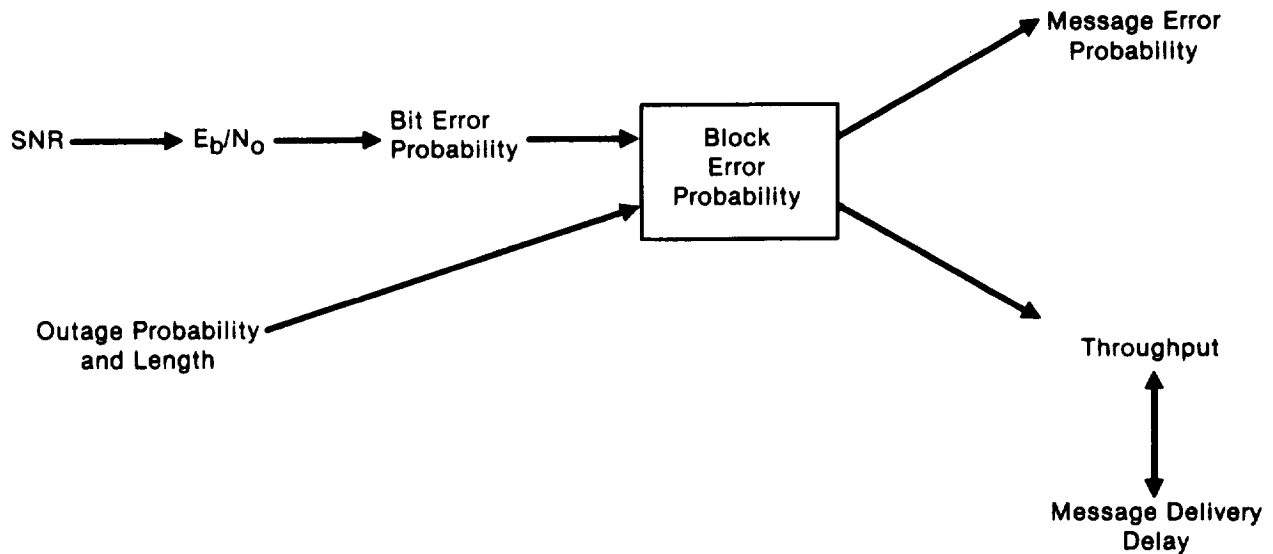


Figure 7.2-1. Data System Performance

7.2.1.3 Analog Transmission Performance

The establishment of performance criteria for analog systems is a complex issue. Transmission system criteria are usually defined on an end-to-end, reference circuit basis. If the satellite system is only a portion of this end-to-end path, a sub-allocation must be made to the satellite segment. Also, when the system is used for relay of multichannel voice trunks, the conversion from baseband (voice channel) performance criteria to the radio frequency criteria (i.e., C/N) involves assumptions about channel loading and modulation parameters. For example, for an FDM-FM system, the noise in picowatts, psophometrically weighted (pWOp), in a voice channel is (GTE-1972)

$$pWOp = \log_{10}^{-1} \left\{ 1/10[-C - 48.1 + F - 20 \log(\Delta f/f_{ch})] \right\} \quad (7.2-2)$$

where

C = RF input power in dBm

F = receiver noise figure, dB

Δf = peak deviation of the channel for a 1 kHz test tone signal

f_{ch} = center frequency of the channel in the baseband

Similar equations apply to single channel FM voice and FM video, and to other modulation structures.

pW0p is one of many noise measures in use. Specifically,

dBrnc (dB above reference noise, C-message weighting.
Reference noise is equivalent in power to a 1,000 hertz tone at -90 dBm.)

dBa (dB above reference noise-adjusted, FlA weighting.
Reference noise adjusted is equivalent in power to a 1,000 hertz tone at -85 dBm.)

pWp (picowatts of noise power, psophometrically weighted.)

dBm0p (psophometrically weighted noise power in dB, with respect to a power level of 0 dBm.)

These units represent absolute values of noise. By appending a "0" to each (e.g., pW0p), the same units serve as measure of noise relative to 0 level signal (i.e., 0 dBm). Then the following approximate conversions apply (GTE-1972):

$$dBrnc0 = 10 \log_{10} pW0p + 0.8 = dBa0 + 6.8 = dBm0p + 90.8 = 88.3 - S/N$$

In general, most standards involve long term nominal objectives and short term or worst case threshold values. Below this threshold, an "outage" exists. FM links are often engineered so that the receiver FM threshold value of C/N is at or within a few dB of that value which gives the absolutely minimum acceptable

performance. That is, the receiver RF performance threshold and the baseband (acceptable) performance threshold are matched.

As an example of a long-term performance objective, the latest CCIR position (reflected in Recommendation 353-3, CCIR-1978) is that 10,000 pW0p one-minute mean noise power should not be exceeded more than 20% of any month. The old U.S. criterion for long intertoll trunks required 20,000 pW0p or less nominal (in the absence of a fade). In the case of television signals, various criteria require a weighted baseband S/N of from 50 to 59 dB to exist under nominal conditions.

Noise performance requirements for small percentages can be thought of as "outage" conditions. The CCIR recommendation is that 1,000,000 pW0 (unweighted) measured with a 5 ms. integration time, exist not more than 0.01% of any year. An intermediate requirement is also established: that 50,000 pW0p one-minute mean power not be exceeded for more than 0.3% of any month. In the U.S., a criterion of 316,000 pW0p for .02% of the time is often employed. DCA standards similarly require that 316,000 pW0p not be exceeded for more than 2 minutes in any month nor for one minute in any hour. Video threshold requirements are typically in the 33 to 37 dB weighted signal to noise ratio range.

Criteria are under constant revision. Indeed, there are arguments suggesting that new applications require specialized criteria. Current criteria, developed for terrestrial systems or for satellite communications systems below 10 GHz, may not be applicable for millimeter wave systems where the statistics differ appreciably.

Note that outage criteria, such as the one DCA has promulgated (probability of outage on a five minute call), are very different from nominal or long-term availability criteria. Because propagation outages in the frequency range of interest typically have durations on the order of magnitude of minutes, it is not straightforward to relate availability statistics to outage

probability statistics. Some approximations may be made from rain statistical data and limited data on fade depth vs. duration, but more theoretical and experimental work appears to be necessary before such outage criteria can be reliably applied in design. In this Handbook, therefore, we have found it necessary to emphasize availability criteria. Where duration data is available, it may be employed as a subsidiary, or second order, check on whether system requirements are met.

7.2.1.4 Summary of Nominal Criteria and Their Application

The nominal performance criteria for digital and analog systems are substantially different. However, these can be related by analysis to corresponding values of CNR, which communication engineers prefer to work with. There is, usually, a long term or nominal performance standard, as well as some definition of short term event behavior (outage criterion). With data systems, the long and short term phenomena may be statistically combined, so that it is possible to define combined performance criteria. These similarities, differences, and relationships are shown in Table 7.2-1.

Table 7.2-1. Performance Criteria and Relationships

System	Fundamental Quality Parameter	Nominal (Long Term) Performance	Short-Term (Outage) Criterion	Combined Criterion
Analog	Baseband noise or signal to noise	Mean or Median CNR	CNR equalled or exceeded except for p%	—
Digitized Analog	Baseband quality	Bit Error Rate	Same as above	—
Data	Error free block probability	Bit Error Rate	Outage probability	Error free block probability Throughput Delivery Delay

7.2.1.5 Additional Performance Criteria

In some applications, more specific control of the transmission quality is necessary and criteria such as those cited above are inadequate. In these situations a number of linear and nonlinear distortion parameters may be specified. Most of these relate to the system (hardware) components. It appears that the only significant distortion parameter introduced by the propagation path is phase fluctuation (scintillation)*. Small amounts can be accommodated in the power budget analysis as equivalent S/N or E_b/N_0 degradations. (By "small amounts," we mean values which lead to no more than, say, 1 dB in equivalent S/N degradation.) On the other hand, large phase scintillations that occur infrequently will add to the outage time calculation, providing:

- 1) these events are not concurrent with the predominant cause of outage, namely amplitude fades (attenuation), and
- 2) the rate of phase variation is high enough that it will not be tracked by a digital system, or be filtered out in an analog system.

7.2.2 Recent Satellite Technology

The ever increasing demand for worldwide satellite telecommunication will saturate the available frequency spectrum allocated to current C-band and Ku-band services by the early 1990's. To meet future demands, the systems designer is exploring higher frequency bands (such as Ka) to relieve the congestion in orbit and developing new technologies enabling higher degrees of frequency reuse for a more efficient utilization of the orbital arc.

*A possible exception is dispersion at frequencies near the absorption bands, but these bands will usually be avoided.

Most communications satellite designs include methods for frequency reuse. Polarization isolation is currently used on most C-band and Ku-band systems to effectively double the bandwidth and capacity of a satellite system. Another attractive method is to use multibeam (or spot beam) antennas, provided the beams are sufficiently separated to avoid beam-to-beam interference. Multibeam antennas are appropriate for satellite systems operating in the higher frequency bands because narrow spot beams can be achieved with moderate antenna sizes.

The principle of multibeam frequency reuse and its advanced technologies will enhance satellite capacity and orbital arc/spectrum utilization.

In satellite communication employing digital modulation, on-board processing (demodulation/remodulation) is becoming more widely used. Benefits include improved end-to-end bit error rate performance as well as improved terminal interconnectivity.

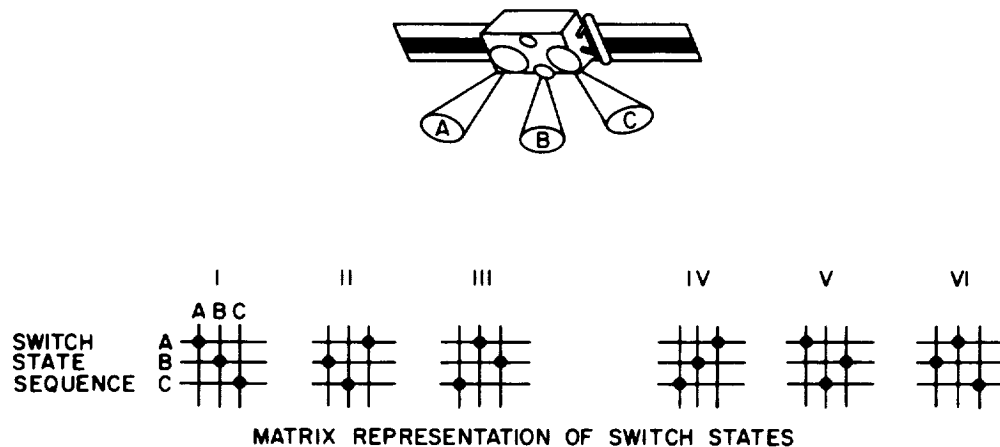
These relatively recent technologies are discussed in the following paragraphs. Section 7.3 discusses propagation considerations peculiar to the newer systems.

7.2.2.1 SS/TDMA

One way to increase the capacity of satellite communication systems is to employ multiple beams with time division multiple access (TDMA) techniques. This is especially attractive at Ka-band since the higher the frequency, the more workable the multi-spot antennas are. However, this approach makes it difficult to ensure proper connectivity between uplink and downlink beams that cover different geographical locations. In order to reduce the number of required transponders, satellite-switched/time division multiple access (SS/TDMA) can be used.

In an SS/TDMA system the satellite uses several spot beam antennas and a microwave switch matrix (MSM) to route TDMA bursts arriving on different uplink beams to different downlink beams.

Figure 7.2-2 shows a simplified example of an SS/TDMA system that will be used for NASA's Advanced Communications Technology Satellite (ACTS).



SWITCH STATE NUMBER		I	II	III	IV	V	VI
SWITCHING MODE ALLOCATION	FROM BEAM A	TO A	TO C	TO B	TO C	TO A	TO B
	FROM BEAM B	TO B	TO A	TO C	TO B	TO C	TO A
	FROM BEAM C	TO C	TO B	TO A	TO A	TO B	TO C

Figure 7.2-2. Diagram of the MSM interconnecting the three beams

The on-board Distribution Control Unit (DCU) programs the switch matrix to execute a cyclic set of switch states, each consisting of a set of connections between the uplink and down link beams, so that the traffic from various regions is routed to designated regions without conflict. A switch state sequence is a succession of switch states during a frame period. To accommodate all of the traffic presented to a system, a sequence of different switch states occurring in a periodic frame is required. For example, for complete interconnectivity between N beams, a total of N! different switch state sequences is needed.

The switching mode allocation describes both the succession and the duration of each switch state so as to route the desired amount of traffic among the beams. The first state shown at the bottom of Figure 7.2-2 provides the connections A to A, B to B, and C to C; the second state provides the connections A to C, B to A, and C to B, and so on.

Figure 7.2-3 illustrates a 3-beam SS/TDMA frame which consists of a synchronization field and a traffic field. The first state of the synchronization field provides loop-back connections to the origination beams. This provides for synchronization between the satellite switch and a TDMA reference station. The reference station in each beam observes synchronization errors of the stations in other beams and sends them necessary corrections. Subsequent states in the synchronization field provide for the distribution of reference bursts and location of synchronization bursts from the traffic stations. The traffic field consists of a number of switching modes and a growth space. The growth space is allocated to cope with traffic pattern changes, since unbalanced traffic between pairs of uplink and downlink beams are likely to occur. The satellite transponder utilization is maximum when the traffic field is fully occupied with a number of switching modes and the growth space is zero.

The Microwave Switch Matrix (MSM) is the key element of SS/TDMA system. ACTS MSM provides connectivity for the three stationary beams. The MSM is a solid state (dual-gate GaAs FET), programmable crossbar switch with a switching time of less than 100ns; it is a 4x4 IF switch, but only 3 input and 3 output ports are used at any given time (Naderi, Campanella - 1988). The INTELSAT VI satellite incorporates a 6x6 dynamic switch and a 8x8 static switch. The 6x6 switch provides interconnectivity between the two hemisphere beams, and the four overlaid zone beams, two in each hemisphere. The 8x8 static switch provides interconnectivity between the two 14/11 GHz spots and six 6/4 GHz beams. The static switch also provides

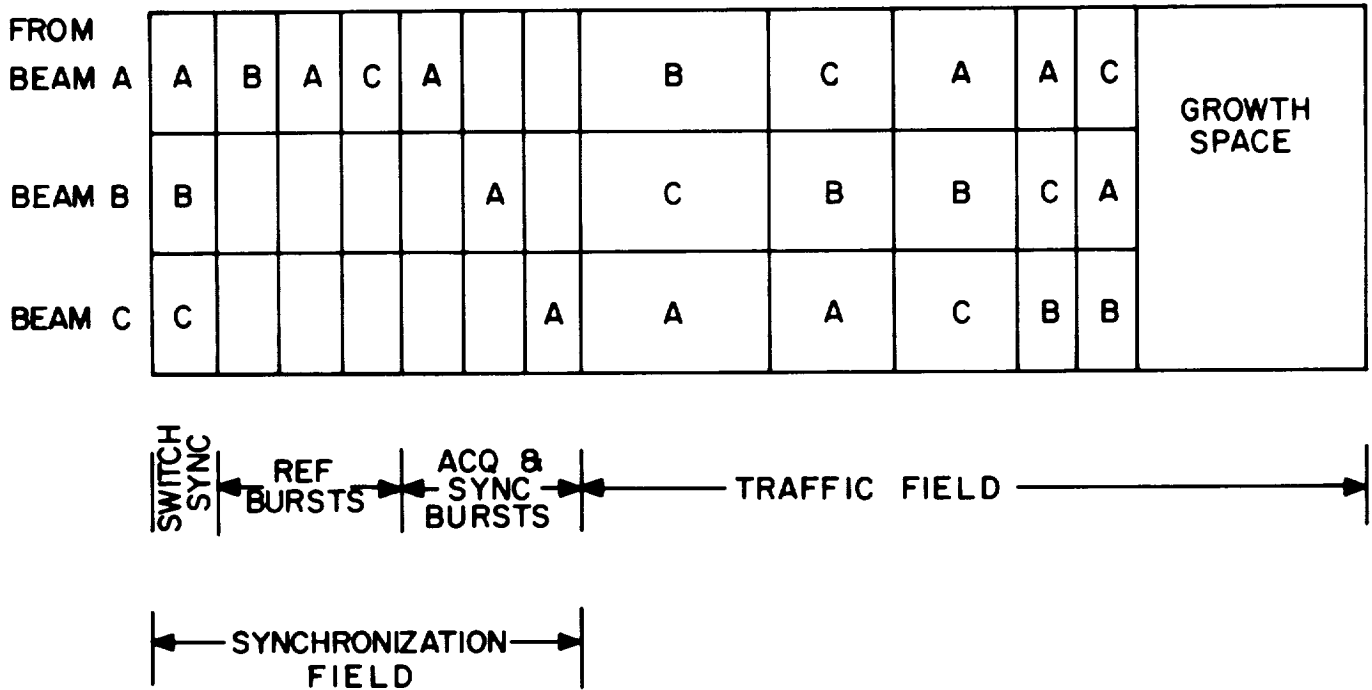


Figure 7.2-3. Typical SS/TDMA frame for a 3-beam system

interconnectivity between the two global beams (Scarcella and Abbott - 1983). The architecture the INTELSAT VI satellite switch matrix is a coupler crossbar with dual-gate GaAs FET switching elements.

7.2.2.2 On-board Processing

The difficulty with some of the more common means of satellite access, such as frequency division multiple access (FDMA) and code division multiple access (CDMA), is that the power in each of the downlink signals is controlled by the relative power in each of the satellite uplink signals. Thus, downlink power cannot be allocated to user requirements independent of the uplink. Furthermore, uplink power from each user must be carefully controlled to prevent saturation of the satellite power amplifier. Saturation distorts the signal modulation and generates undesired intermodulation products.

Time division multiple access (TDMA) to a satellite repeater avoids saturation of the power amplifier, but there is still an effective downlink power sharing (really, time sharing) problem because of the uplink time sharing. Moreover, linear and nonlinear distortion (intersymbol interference and AM-to-PM conversion) still occur because of required bandlimiting and amplification on the satellite. In addition, all users must operate at high data rates on both the uplink and downlink because of the burst transmissions.

On-board processing circumvents many of these difficulties first of all because uplink signal distortion and interference are not retransmitted on the downlink, and secondly because downlink power can be allocated in accordance with downlink user needs, independent of uplink transmissions. This allows interconnection of terminals that use different modulation and coding schemes. In addition, all downlink users will then have a common frequency standard and symbol clock on the satellite, which is useful for network synchronization.

On the other hand, on-board processing requires carrier and clock synchronization of the uplink signals, which functions are not required on a conventional frequency translation satellite.

To get an idea of the performance improvement achievable with on-board processing, Figure 7.2-4 shows a comparison between conventional and on-board processing satellites, in terms of uplink and downlink carrier/noise power ratios, considering a specified bit error rate of $10e-4$. Ideal error rate ($P_e = 1/2 \operatorname{erfc} \sqrt{E_b/N_0}$) conditions are assumed, that is no degradation resulting from filtering or non-linear distortions.

Link analysis for an on-board processing satellite treats the uplink and downlink as two separate point-to-point analyses. To estimate the performance, it is necessary to determine separately the bit error probability on the uplink and downlink. The overall error rate is obtained by combining uplink and downlink error rates as follows:

$$BER_C = BER_U (1-BER_D) + BER_D(1-BER_U) \approx BER_U + BER_D \quad (7.2-3)$$

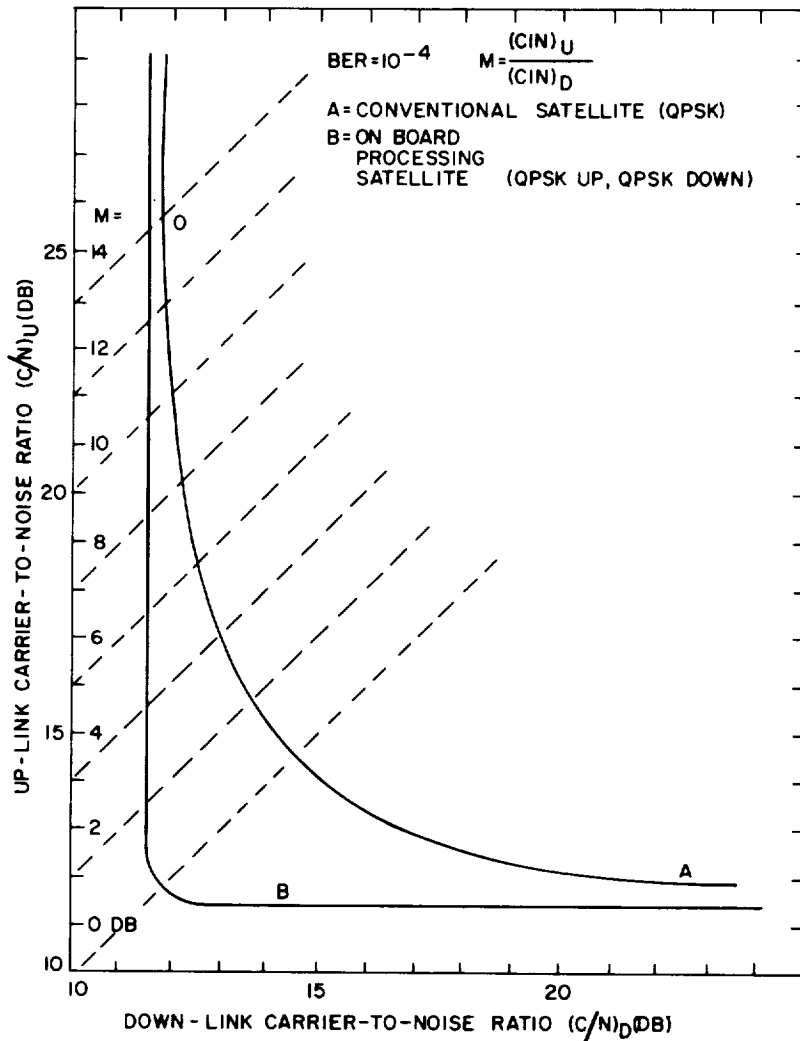


Figure 7.2-4. Comparison of conventional and processing satellite performances (linear channel)

By comparison, link analysis for a conventional satellite generally treats the entire "round-trip" (uplink transmission to the satellite and downlink retransmissions to an earth station) as a single analysis. To estimate performance, the uplink and downlink values of E_b/N_0 (or C/N) are combined as follows:

$$(E_b/N_0)^{-1}_C = (E_b/N_0)^{-1}_U + (E_b/N_0)^{-1}_D \quad (7.2-4)$$

where the subscripts U, D, and C denote uplink, downlink and composite values respectively.

One can see from Figure 7.2-4 that the maximum power gain saving is obtained when uplink and downlink are the same. In that case the advantage of an on-board processing satellite compared with a conventional one is a saving of 3 dB on both uplink and downlink transmitted power. However, when the uplink power is much larger than the downlink power the saved power is much smaller (about 0.5 dB).

7.2.3 Representative Systems

Several systems that exploit expanded satellite capacity and efficient utilization of the orbital arc have recently been developed. These systems generally use higher carrier frequencies, such as Ka-band. This leads to the possibility of smaller earth stations, but at a cost of larger rain attenuation. Many of these systems use multiple beams, on-board processing and switching, and intersatellite links, as discussed in paragraph 7.2.2.

The proliferation of microterminals and VSAT systems provides a means for bypassing terrestrial communication networks. The Ku- and Ka-bands are particularly suitable for the VSAT application. Typical examples of current U.S. and European satellite communication systems are discussed in the following paragraphs.

7.2.3.1 VSAT Networks. The capability of satellite data communication networks has improved significantly because of recent advances in technology, especially in the area of microwave integrated circuits. This includes the development of solid-state power amplifiers (SSPA) with up to 5 watts of output power at C-band and 2 watts at Ku-band, low cost up-converters, and low noise down-converters. Current digital technology, which allows significant processing power in a small size and at low cost, led to the introduction of Very Small Aperture Terminal (VSAT) Networks for data communications.

VSAT networks are rapidly gaining in importance as a means of providing private voice and data communications for corporations that operate in widely dispersed sites. Currently two frequency bands are being used for VSAT networks: C-band and Ku-band. In general, VSAT networks operate at Ku-band because the higher frequency provides about 7 dB more gain than C-band for the same aperture size. On the other hand, Ku-band suffers significant rain attenuation, so consequently more system outages occur (Lyon-1985).

The networks are configured as hub-based systems, with a large earth station commonly referred as "hub," located at or near corporate headquarters and numerous small terminals (VSATs) located at remote sites. Since terminals are small, typically between 1.2 meters and 1.8 meters in diameter, it is usual to use a large earth station to receive and regenerate the transmitted data signals before distribution to other terminals. Hence, VSAT's communicate with the hub over the VSAT-to-hub satellite link and the hub station communicates with the VSAT usually by terrestrial links. Consequently, such communication involves double hops, which can present considerable difficulty for voice communication and is not used except in extreme cases.

With the use of a baseband processor on the satellite, the function of the major earth station can be replicated and the double hop eliminated. With this technology, voice communication would also be acceptable, because of the smaller time delays. This concept was recently proposed as an application of the NASA ACTS baseband processor technology (Naderi, Campenella-1988). The ACTS baseband processor will provide small customer premise services, allowing low data rate users direct and efficient access to the satellite. The use of spot beams and switching technologies will provide multiple voice channels to VSATs in a single satellite hop, neither of which is possible with current VSAT networks.

The range of possible applications for VSAT networks is widespread, particularly since rapid one-and two-way communications can be supported. Typical VSAT network applications include:

inventory management between retail stores and head-quarters, express mail and facsimile, travel and financial related services, meteorological data gathering, and corporate video distribution. Such variety in applications for VSAT technology is one force behind the growing number of companies installing VSAT networks to satisfy their ever increasing telecommunications needs. The emergence of these networks was stimulated by the U.S. industry investment in DBS-TV technology, the success of Equatorial Communications with over 25,000 receive-only and 1,000 transmit/receive VSATs installed, and the decision of Federal Express to purchase 50,000 small two-way earth stations for networking their field centers.

7.2.3.2 ACTS. The Advanced Communications Technology Satellite (ACTS), currently under development by NASA, will contain several new technologies and features which have the potential to dramatically enhance the capabilities of future satellite systems. ACTS will be one of the first satellites to operate a K_a-band (30 GHz uplink/20 GHz downlink), and will include electronically hopping multiple spot-beam antennas, on-board processing with baseband message routing, and adaptive rain fade compensation. These capabilities enable ACTS to provide multiple voice/data channels to VSAT type ground terminals in a single satellite hop, which is not possible with current VSAT networks at C- and Ku-bands (Naderi and Campanella-1988).

The ACTS system has two modes of access and operation:

- 1) On-board stored baseband switched TDMA, OSBS/TDMA, and
- 2) A SS/TDMA system based on IF switching, with no on-board processing. System access and control is accomplished by the network's master control station, located at NASA Lewis Research Center, in Cleveland, Ohio.

The OSBS/TDMA (on-board processor) mode demodulates and stores the received signal, reroutes data from input to output storage locations, then remodulates and transmits on the downlink beam.

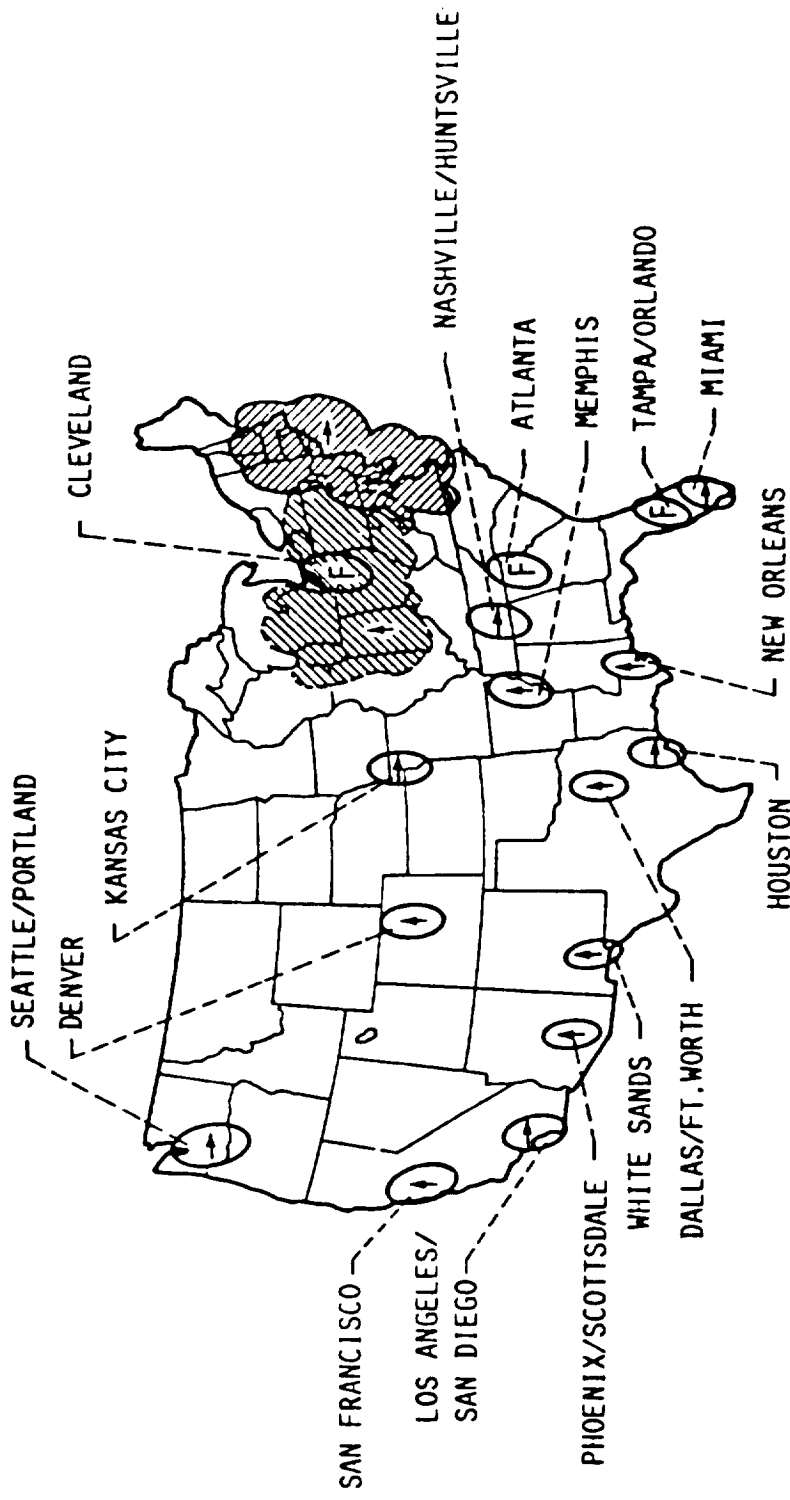
Serial minimum shift keying (SMSK) modulation is employed, with transmission rates of 110 or 27.5 Mbps on the uplink and 110 Mbps on the downlink

The SS/TDMA mode has no on-board storage or processing, other than switching. The system is designed to operate at a nominal burst rate of 220 Mbps, but other rates are possible. Since this mode is non-regenerative, ground terminals are not restricted in the modulation technique utilized for transmission.

Figure 7.2-5 shows the antenna beam coverage areas for ACTS. There are three fixed beams, focused on Cleveland, Atlanta, and Tampa, and two hopping beams. One of the hopping beams (vertically polarized) can hop to anywhere in the west sector (cross-hatched area on the figure indicated by a vertical arrow), or to any of the six fixed beam locations indicated by the vertical arrows. The second hopping beam (horizontally polarized) covers the east sector, and any of the seven fixed beam locations shown with horizontal arrows. A mechanically steerable antenna, not represented on the figure, is also included, which will provide a spot beam to anywhere in the disk of the earth as seen from the 100° West longitude location of ACTS.

Propagation measurements are an important element in the ACTS program, and will be accomplished both through the communications channels and with a set of three beacons available on the satellite. Table 7.2-2 summarizes the characteristics of the beacons on ACTS. The 27.5 GHz beacon and 20 GHz beacon pair operate through CONUS coverage antennas, providing a nominal E.I.R.P. of 13 dBw at edge of beam. The 27.5 GHz beacon is unmodulated, while one of the 20 GHz beacons will contain low rate telemetry data. The beacons will allow measurements of the classical propagation parameters, such as rain attenuation, depolarization, gaseous and cloud attenuation, diversity, and fade rate/duration.

Links operating in the OSBS/TDMA mode are designed for about a 5 dB clear weather margin, but terminals experiencing a fade can be



- SPOT BEAM
- F FIXED BEAM
- ↑ POLARIZATION

ACTS AT 0° LATITUDE, 100° W
 STEERABLE ANTENNA WILL COVER ALL OF U.S. INCLUDING ALASKA & HAWAII

Figure 7.2-5. ACTS Antenna Beam Coverage Areas

Table 7.2-2. ACTS Beacon Parameters

Item	27.5 GHz Beacon	20 GHz Beacons
Number of Beacons	1	2
Frequency (Polarization)	27.505 GHz \pm 0.5 MHz (Vertical)	20.185 GHz \pm 0.5 MHz (Vertical) 20.195 GHz \pm 0.5 MHz (Horizontal)
Modulation	None	FM and PCM (telemetry)
R.F. Power	20.0 dBm	23.0 dBm
Operating Temperature	-10 to +55 °C	
Frequency Stability	\pm 10 PPM over 2 yrs at constant temperature \pm 1.5 PPM over 24 hrs for -10 to +55°C	
Output Power Stability	\pm 1.0 dB over 24 hrs \pm 2.0 dB over full mission	

provided an additional 10 dB margin by a dynamic rain fade compensation method incorporated in the processor. Fade levels are monitored at the terminals either by the ACTS beacons, or by direct monitoring of the communications signal. Once a predetermined fade threshold is exceeded and the master control station is informed, two corrective actions are implemented; forward error correction (FEC) coding and burst rate reduction. Viterbi convolutional coding with a reduction of the burst rate to 1/2 is employed.

Fade compensation in the SS/TDMA mode is accomplished by a dual mode traveling wave tube amplifier (TWTA), which can operate with output powers of 11 or 46 watts. Locations undergoing a fade can be switched to the high power mode, resulting in over a 6 dB improvement in margin.

ACTS, scheduled for launch in 1992, will be used for a series of technology verification experiments over a period of two to four years. NASA has issued information on the requirements for participation as an experimenter with ACTS and has encouraged participation in a wide range of technology areas (NASA-1987).

7.2.3.3 INTELSAT VI The first commercial satellite, Intelsat I, initially known as the Early Bird, was launched in a geosynchronous orbit above the Atlantic in 1965, providing 240 two-way telephone circuits and one TV transatlantic channel. It weighed only 38 Kg in orbit and was spin stabilized. Since 1965 over 100 commercial communications satellites have been launched to provide both domestic and international communications.

The latest addition to Intelsat's fleet of satellites will be the Intelsat VI. Intelsat VI is a dual-spin stabilized spacecraft, compatible for launch by either the Space Shuttle or Ariane IV. The major technological advancements of Intelsat VI include a sixfold reuse of the 6/4 GHz bands, the dynamic interconnection of six of the satellite's antenna beams for use with satellite-switched TDMA (paragraph 7.2.2.1), and a 10 year design life. The spacecraft provides a capacity of approximately 40,000 two-way telephone circuits plus two color-TV channels.

The antenna system consists of a 2 m diameter receive (6 GHz) and a 3.2 m diameter transmit (4 GHz) reflector; 1.12 m and 1.0 m diameter east and west spot beam steerable reflector antennas (14/11 GHz); and transmit and receive global horn antennas (6/4 GHz). The repeater system consists of 48 distinct transponders operating over the 6/4 GHz and 14/11 GHz bands. Frequency reuse through beam isolation and orthogonal polarization is employed at both frequency bands. The spacecraft thus has available a useful bandwidth of 3,200 MHz. Two 150 MHz, six 72 MHz, and two 77 MHz channels are assigned to 14/11 GHz. Twenty-six 72 MHz, two 41 MHz, and a maximum of ten 36 MHz channels are assigned to 6/4 GHz. Four of the 6/4 GHz, 36 MHz channels, as well as the two 41 MHz channels, provide permanent global coverage. Additional bandwidth of up to 72 MHz may

be switched to global coverage. Finally, considering the availability of the hemi, zone, spot, and global coverages, up to 1,389 MHz of bandwidth can be assigned to earth stations in the geographic areas of highest traffic density (A. Ghais, and et. al., 1982).

The Intelsat VI provides static and dynamic interconnection capabilities to achieve the required signal paths from the receive to the transmit coverages. The spacecraft incorporates a 6x6 dynamic switch matrix which switches through a sequence of modes each frame and an 8x8 static switch which maintains a constant configuration for relatively long periods of time until changed by a new set of ground commands. The 6x6 dynamic switch provides full interconnectivity between two hemisphere beams and four overlaid zone beams. The 8x8 static switch provides full interconnectivity between the two 14/11 GHz spots, the six 6/4 GHz beams, and the two global beams.

The communications capability from Early Bird through Intelsat VI represents an increase in capacity by a factor of more than 150. The Intelsat system has maintained an amazing reliability factor of greater than 99.9 percent. Furthermore, it has achieved significant reduction in utilization charges.

7.2.3.4 DoD Missions The major role of the military in space activities today is for communication, navigation and observation. The Defense Satellite Communications Systems (DSCS) III and the Fleet Satellite Communication (FLTSATCOM) satellites are currently operational in worldwide military communications missions.

The DSCS III satellites consist of four synchronous satellites that provide reliable world wide communications to the United States defense forces throughout the 1980's and 1990's. Each three-axis stabilized satellite contains a Super High Frequency (SHF) communication payload consisting of multi-beam antennas and a six channel transponder designed for both FDMA and TDMA operation and real-time commandable uplink and downlink. By the early 1990's new

payloads enhancing mission capabilities are feasible. Possibilities include advanced wideband user and AFSATCOM payloads. The new wideband payload features EHF links, adaptive nulling, on-board despreading, and an active transmit array giving higher capacity and jammer protection. The AFSATCOM payload includes EHF and UHF links plus multichannel digital demodulation to give higher jamming protection and capacity in a MILSTAR backup role and to provide EHF telemetry/commanding. Both payloads will utilize satellite crosslinks to improve global netting.

The Fleet Satellite Communications (FLTSATCOM) satellites are a powerful addition to the world-wide Navy, Air Force, and Department of Defense (DoD) network for communications between naval aircraft, surface ships, and submarines, ground stations, Strategic Air Command and the Presidential command networks. Each satellite provides twenty-three communication channels in the 240 to 400 MHz UHF band and at SHF. The communications transponder features channelized, limiting repeaters to facilitate access to low-power users and on-board processing for anti-jam protection. Four FLTSATCOM satellites are needed in geosynchronous orbit to provide visible-earth coverage for the DoD strategic and tactical users. FLTSATCOM 7 and 8 are modified with additional EHF transition packages to upgrade anti-jam protection. FLTSATCOM 6, 7, and 8 now provide world wide service until the early 1990's, at which time the new MILSTAR spacecraft will take over strategic and tactical service, both at UHF and at EHF.

The trend in DoD satellite communications systems, as with commercial and international systems, is to higher operational frequency bands. The ~~EHF~~ bands, (44 GHz up/20 GHz down), will see extensive service commence in the early 1990's, with MILSTAR, DSCS III, FLTSATCOM, and SDI (Strategic Defense Initiative) baseline communications elements.

7.2.3.5 OLYMPUS-1 Olympus-1, formerly known as L-SAT (Large Satellite), is an experimental 3-axis stabilized satellite being developed by the European Space Agency (ESA) for advanced satellite

communications applications. It is a very large satellite, with a total span of 60 meters between solar panels, a transfer orbit mass of 2,300 kg, and a solar array power of 2.9 kW. Satellite location is at 19° W latitude, with its control center at Fucino, Italy.

Olympus-1 consists of four separate payloads:

- 1) 12/20/30 GHz Propagation Package - for propagation measurements and experiments,
- 2) 14/12 GHz Specialized Services Payload - for business services experiments involving small customer premises earth terminals,
- 3) 17/12 GHz Direct Broadcast Satellite (DBS) Payload - for two channels of direct broadcasting services, and
- 4) 30/20 GHz Communications Payload - for point-to-point and multipoint communications applications.

Table 7.2-3 summarizes the characteristics of the Olympus-1 beacon package. All three beacons are coherently derived from a single frequency source. The 12.5 GHz beacon is transmitted through a full earth coverage antenna, which provides a signal to the entire earth sphere as observed from the satellite location. This provides coverage to all of Europe, South America and Africa, and to the east coast of North America. The 20 and 30 GHz beacons provide coverage through regional spot beams to Europe and North Africa only.

The 14/12 GHz Specialized Service Payload consists of four 30 watt transponders with an EIRP of 44 dBW. Each transponder can be subdivided into two TDMA data streams of 25 Mbps each, serving five spot beams covering most of Europe. Four of the five beams can be utilized in an IF switched SS/TDMA mode of operation.

The DBS Payload provides two channels, one for use by Italy, the other for the European Broadcasting Union (EBO). A 230 watt TWTA is employed, with a peak EIRP of 63 dBW available.

Table 7.2-3. OLYMPUS-1 Propagation Beacons

Frequency	12.502 GHz	19.770 GHz	29.656 GHz
Polarization	Vert.	Vert. or Hor. or switched (1866 Hz rate)	Vert.
EIRP (min.)	10 dBW	24 dBW	24 dBW
Frequency Stability: Over 24 hrs Over any 1 yr Over 7 yrs	±1.2 KHz ±36 KHz ±120 KHz	±2 KHz ±60 KHz ±200 KHz	±3 KHz ±90 KHz ±300 KHz
EIRP Stability: Over 1 sec Over 24 hrs Over any 1 yr Over 7 yrs	±0.05 dB ±0.5 dB ±1.0 dB ±2.0 dB		

The 30/20 GHz Payload consists of two 40 MHz transponders and one 700 MHz transponder operating through two independently steerable 0.6° spot beams. Each TWTA is 30 watts, resulting in an EIRP of 51 dBW for each of the spot beams. Videoconferencing, tele-education and wideband communications experiments, both point-to-point and multipoint, are planned.

Olympus-1 is scheduled for launch in 1989 on an Ariane launch vehicle, with an expected mission life of 5 to 10 years.

7.2.3.6 ITALSAT ITALSAT, the first satellite to be launched by the Italian Space Agency (ASI), is a wideband regenerative SS/TDMA system to be integrated into the existing Italian terrestrial telephone network, to improve performance and provide advanced access and routing techniques (Morelli, et al-1988). The satellite, to be located at 13° E latitude, is three-axis stabilized, with a payload mass of 255 kg, prime power of 1.565 Kw.

ITALSAT consists of three payloads:

- 1) 30/20 GHz Multibeam Payload - employing on-board baseband processing, for point-to-point and point-to-multipoint communications,
- 2) 30/20 GHz Global Payload - three non-regenerative transponders, for video and digital user services, and,
- 3) 20/40/50 GHz Propagation Beacon Package - for propagation measurements and experiments.

The multibeam package provides on-board demodulation at 12 GHz, and direct 4 phase QPSK remodulation at 20 GHz. The data rate is 147.5 Mbps, and the system operates with six 0.5° spot beams providing coverage throughout Italy and its islands. Six active repeaters provide a total capacity of 885 Mbps, equivalent to about 12,000 digital telephony circuits. 20 watt TWTA's are employed, resulting in an EIRP for each beam of 57 dBW.

The global payload consists of 3 frequency translation transponders, each with a 36 MHz useable bandwidth, operating through a single 1.8° x 1.3° beam. EIRP is 46.2 dBW, with 20 GHz TWTA's also employed.

Table 7.2-4 summarizes the characteristics of the ITALSAT propagation beacon package. All three beacons are generated from the same master oscillator. The 18.7 GHz beacon is used as a telemetry relay, and is radiated on the global antenna. The 40 GHz beacon is phase modulated at 505 MHz to provide two sidebands for differential attenuation and phase measurements over a 1.01 GHz bandwidth. The 50 GHz beacon is switched between polarizations at an 1866 Hz rate, similar to OLYMPUS-1, to measure cross-polarization characteristics. The 40 and 50 GHz beacons are radiated from 3° horns, to provide coverage over most of Europe.

Table 7.2-4. ITALSAT Propagation Beacons

Frequency	18.685 GHz	39.592 GHz	49.490 GHz
Polarization	Vert.	Vert.	Vert or Hor. or switched @ 1866 Hz rate
Modulation	PSK (512 bps)	PM (505 MHz)	None
EIRP (min)	23.7 dBW	27.8 dBW 24.8 dBW (mod.)	25 dBW
Frequency Stability: Over 24 hrs Over 5 yrs	$\pm 3 \times 10^{-7}$ $\pm 3 \times 10^{-6}$		

The ITALSAT propagation measurements program is an ambitious effort involving a wide range of experiments and experimenters, and it will provide the first direct satellite path measurements at frequencies above 40 GHz (Giannone, et al-1986). ITALSAT is scheduled for launch in early 1991 on an Ariane 4 launch vehicle.

7.2.3.7 ATDRSS The current Tracking and Data Relay Satellite System (TDRSS) has for its main purpose the relaying of digital data from low-orbiting satellites to a single ground station, from where the data is distributed to the users that require it. The TDRS satellites themselves are geostationary bent-pipe satellites that will eventually replace the existing ground network of tracking and data relay stations. The Advanced TDRSS (ATDRSS) will upgrade the current system to satisfy user data relay requirements into the next century. This upgrade will include the capability of TDRS-to-TDRS crosslinks either at 60 GHz or at optical frequencies, together with the capability of relaying data directly to several ground stations, using K_A band links.

The capability of downlinking data to more than one ground station provides the opportunity to mitigate downlink rain fades by

the use of site diversity (paragraph 7.4.2.1), thereby improving system availability. In addition, other fade mitigation techniques such as adaptive FEC coding (paragraph 7.4.3.2) are being investigated for use with ATDRSS. The goal is to achieve a 99.9 percent system availability. This will involve consideration of service scheduling (Schwartz and Schuchman-1982) that will allocate downlink power in accordance with user needs rather than simply the transmission of fixed power levels. Because of the multiple ground stations, on-board beam switching will be used for downlink data transmission, which, together with downlink power control, provides an opportunity for significant downlink rain fade mitigation (paragraph 7.4.3.1.2) not possible with the current TDRSS.

7.3 DESIGN PROCEDURE

7.3.1 Introduction

The procedure presented in this Section is a general one, applicable to satellite communication systems of conventional design and application. Special purpose systems, unusual variants, or unusual system architectures will require modifications to the procedure. For example, those systems which employ adaptive power control or adaptive antenna beam control fall into the "unusual" category. Power budgets for some of the newer satellite communication systems are presented at the end of this section.

The procedure is based on time percentage availability or outage as the primary and initial design criterion. Emphasis on this approach is necessitated by the fact that the largest amount of reliable propagation data is presented in time percentage terms. Where other criteria are important, different procedures may be necessary. But even where other criteria are employed, it is expedient to perform initial gross sizing calculations according to time percentage criteria.

As previously noted, the system design process is not a true synthesis. It consists rather of iterative analyses. The designer

begins with some rough "guesstimates" of parameters such as earth terminal antenna size, satellite RF power, along with a set of system requirements (coverage area or locations, capacity, connectivity, and service criteria). By employing analytic (not synthetic) procedures, the designer determines whether the initial parameters and the requirements/criteria are consistent. If not, additional iterations are made, with adjustments either to the parameters or to the requirements. This last point is not trivial: if there is a large disparity between calculated system performance and the requirements, it may be necessary to consult with the source of the requirements and agree to a change (e.g., lower capacity or availability). The final system design parameters should always be verified in as many variables as possible according to available data. Thus, although the initial design may have been performed using an availability criterion, it may be of interest and importance to predict outage duration statistics, if the necessary data are available.

7.3.2 Path Performance Versus Overall Channel Performance:. Availability Allocation

The typical satellite communication application involves two or four distinct links. For example, a telephone trunk system between Los Angeles (LA) and New York (NY) will involve these links:.

LA to Satellite
Satellite to NY
NY to Satellite
Satellite to LA

If the performance requirements for this example specify the availability of a duplex telephone circuit between NY and LA, the system designer may be faced with a difficult problem. In general, finding the simplex, duplex, or (worst of all) system-wide availability with multiple earth terminal locations is a problem of considerable statistical complexity. Significantly, this problem is

unique to satellite systems, and is particularly aggravated at the higher frequencies. Also, symmetry applies in these systems. Statistical assumptions made and procedures developed for terrestrial systems, and for satellite systems below 10 GHz, may not be adequate for the applications to which this Handbook is directed.

Some sort of availability allocation is necessary, since most of the propagation data and procedures for applying them are oriented towards single path availability. The composite availability calculations involved are similar to multiple and redundant part reliability calculations. Each application will involve its own special considerations in the allocation process. Often, a worst case philosophy is applied in an attempt to simplify the problem. The following factors are relevant:

- One end (terminal location) often has considerably worse rain statistics than the other.
- Satellite systems are limited in downlink power; uplink power margin at the earth terminal is more readily obtainable.*
- Uplink and downlink effects are quantitatively similar except for widely separated uplink/downlink frequencies (e.g., 30/20, 43/20), where attenuation factors in particular can differ substantially.
- The uplink and downlink connecting to a given earth terminal have highly correlated propagation outage statistics.
- The propagation effects on paths between the satellite and two different earth terminals are uncorrelated.

Because of the variety of system concepts and frequency bands possible, general rules for allocation of availability cannot be given. The following may be of help in many cases of interest:

*A very important exception involves mobile or portable terminals.

- In a one-way (simplex) system, availability can be suballocated or split between the up and downlink with considerable freedom.

Frequently, however, the downlink is the dominant (weaker) link. In other words, the working assumption is that the uplink non-availability is an order of magnitude smaller than the downlink's.

- For a two-way (duplex) system, one of the following simplifications may be applied:
 - One end has much worse rain statistics than the other. Then, this duplex circuit can be treated as two simplex circuits with the majority of the outages on that end. On each of these simplex circuits, either the uplink or the downlink, whichever is worse, dominates the availability.
 - Assume initially that uplink margin is liberally available. The duplex link availability is then determined by the composite availability of both downlinks (or, the circuit outage time is the sum of the outages of each of the two downlinks).

Because the designer is forced by the procedure to iterate the design, errors introduced by simplifying assumptions made during the availability suballocation phase are corrected when performance verification analyses are made. For example, suppose the initial downlink design parameters were selected under the assumption that ample uplink margin exists, and that the uplink parameters were chosen to be as good as possible within economic constraints. In the final performance computation, the slightly less than perfect availability of the uplink is factored into the overall availability. Any shortfall relative to requirements can then be met by a small adjustment to the downlink parameters, in the next iteration of the design.

7.3.3 Summary of Procedures for Application of Propagation Data

The system design procedure presented here is based on criteria that take the form of discrete cumulative probability distribution functions of performance. In practice, three, two, or just one point on this distribution are given, for example, 99.9% probability that the baseband signal to noise ratio exceeds 20 dB. The worst (lowest probability) point of this set is usually considered to be the outage point or the non-availability threshold. In addition, a statement might be made about the time characteristics of the outage events, for example, the maximum acceptable value for the average duration. These criteria are usually for the baseband (e.g., voice channel) noise performance, or for the digital channel performance (e.g., error rate). The steps necessary to go from this set of requirements and propagation statistics to a system design are (see Figure 7.3-1):

INITIAL PHASE

- 1) Establish system performance requirements (discrete distribution of baseband/digital performance)
- 2) Apply modulation equations to convert system performance requirements to discrete distribution of the received composite CNR
- 3) Prepare initial design with parameters sized according to free space propagation conditions (apply power budget equations).

DESIGN SYNTHESIS AND TRADEOFF PHASE

- 4) Employ
 - a) Composite CNR distribution from step 2
 - b) System Architecture
 - c) Multiple Access Equations

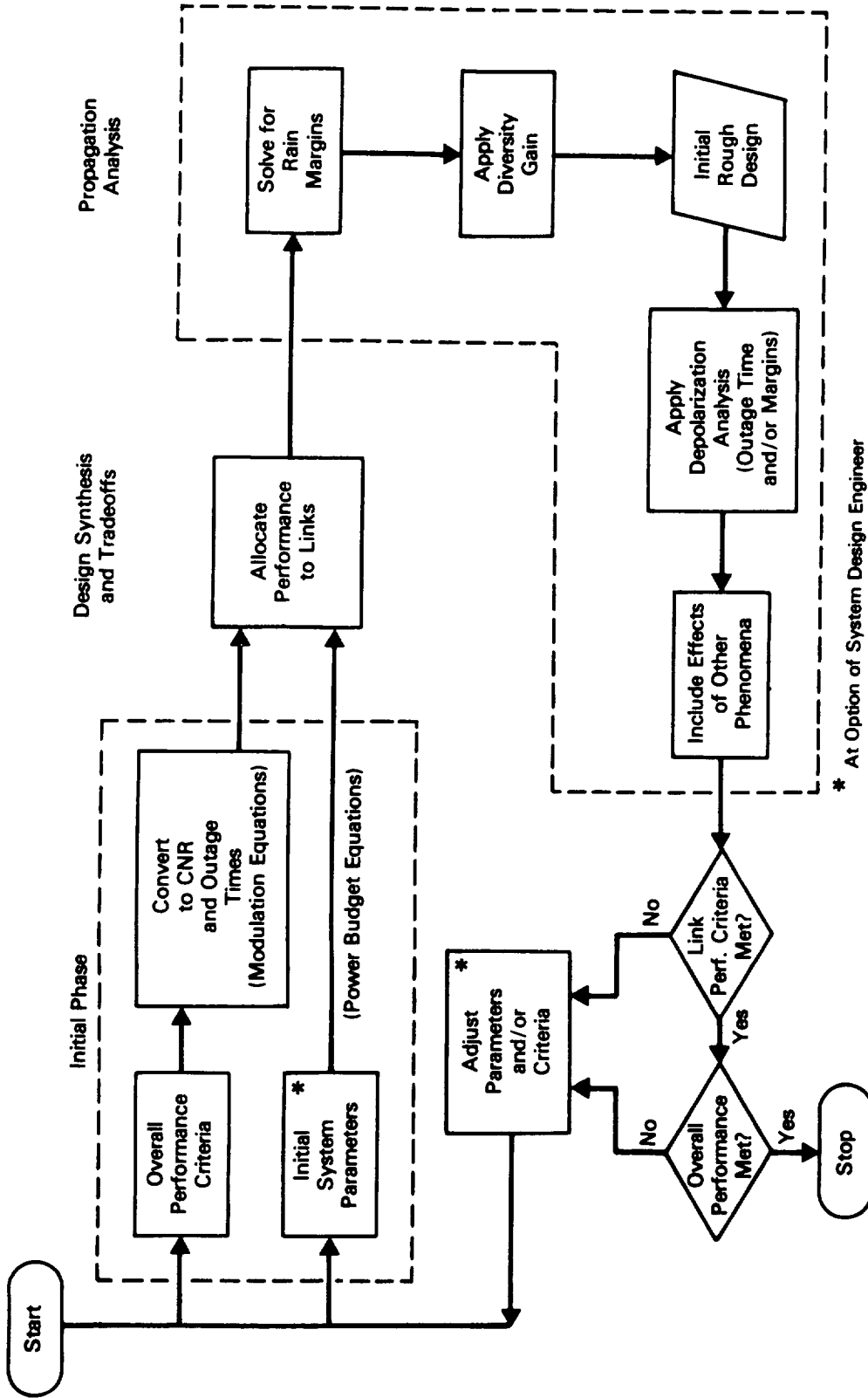


Figure 7.3-1. System Design Process

- d) Availability sub-allocation philosophy to develop distribution functions for CNR on each path.

PROPAGATION ANALYSIS AND ITERATION PHASE

- 5) Compute rain margins, as reduced by diversity gain, for each path.
- 6) Adjust system parameters according to margins given by step 5. This gives a preliminary design at the feasibility concept level.
- 7) Apply depolarization analysis to adjust margins and/or increase the outage time values (% of time for the worst-performance level of the distributions).
- 8) Consider other propagation effects, adding margin to design as necessary.
- 9) Adjust system parameters to include all additive margins. Analyze system performance, first at the path level, then at the end-to-end performance level.
- 10) If performance meets requirements closely, stop. Otherwise, adjust design and repeat analysis. If design cannot be made to meet requirements, consider changing requirements.

These steps will be considered in more detail in the remainder of this chapter. The most difficult step is 4 above. It is not possible to define a step-by-step "cookbook" procedure for this phase of the design process.

As indicated above, these steps may be grouped into three major phases. It is in the third phase that propagation phenomena and data are explicitly considered. Since the emphasis of this Handbook is propagation, a detailed exposition of the first two phases is not appropriate. However, some discussion is required because both performance criteria and the system engineering are profoundly

influenced by the pronounced propagation effects which apply above 10 GHz.

7.3.4 Specifics of Applications Initial Phase - Performance Specification of Digital and Analog Systems

The initial phase contains three steps:

- 1) performance requirements
- 2) conversion to received CNR requirement
- 3) initial design choices

Two examples will be used to illustrate the design procedure. The first step, to specify performance requirements, is now carried out for the examples. Additional information will be given for the systems in the example as they are developed further.

EXAMPLE 1 (Digital transmission system)

Requirement: One-way bit error rate of 10^{-6} or better for at least 80% of the time, and 10^{-4} or worse for a maximum of 1% of the time.

EXAMPLE 2 (Analog, duplex telephone trunking system)

Requirement: No more than 10,000 pW0p for at least 80% of the worst month, and no more than 100,000 pW0p, except for 0.3% of the time or less. (More than 500,000 pW0p is outage condition.)

The second and third steps are performed in parallel. Conversion from the basic performance criteria to receiver CNR requirements involves application of modulation equations. To apply the equations, the type of modulation* and other system parameters such as total link capacity need to have been selected. For the above two examples:

*"Modulation" is used in a generic sense here, to include coding, baseband processing, and the like.

- 1) The digital system is considered to operate at a link data rate of 40 Mbps, employing quaternary phase shift keying (QPSK) and Rate 3/4 convolutional encoding with Viterbi decoding. This combination is assumed to operate with an E_b/N_o of 10.3 dB for a BER of 10^{-4} , and 12 dB for 10^{-6} . The values of C/kT required are 86.3 and 88 dB-Hz, respectively. Because of the rate 3/4 coding, the symbol rate is $4/3 \times 40 = 53.5$ Ms/s and the CNR values in the symbol rate bandwidth are 9 and 10.7 dB for 10^{-4} and 10^{-6} BER, respectively.
- 2) The analog system is assumed to use FDM-FM with 120 channels and CCIR pre-emphasis characteristics. The following is a simplified version of the FM modulation performance equation (see Section 7.2.1.3):

$$(C/kT)_{dB} = 125.8 - 20 \log (\Delta f/f_{ch}) - 10 \log (pW0p)$$

From this, and the typical parameters $\Delta f/f_{ch} = 1.22$, the required values of C/kT are:

<u>pW0p</u>	<u>C/kT</u>	<u>%</u>
10,000	84.1	80
100,000	74.1	99.7
500,000	67.1	N/A (defines outage)

Note however that the FM equation only applies above "threshold." The threshold values of C/kT must also be determined. Since this system has a bandwidth of about 62 dB-Hz, the threshold values of C/kT and the threshold C/kTB are related:

$$(C/kTB)_{dB} = C/kT - 62$$

Thus, if this system is implemented with a conventional FM receiver of 12 dB C/kTB threshold, a C/kT of 74 dB will be at threshold, and this becomes the outage point. With an extended threshold demodulator (6 dB threshold), the 500,000 pW0p outage noise level and the demodulator threshold occur at about the same point, which is desirable.

To complete the first phase of design, it remains to select initial values, ranges, or limits of system parameters. Many of these may be implied by overall system requirements, such as coverage area or total number of channels. Others may be constrained by cost considerations or achievable levels of hardware performance. The primary parameters that must all eventually be specified are the frequencies of operation, and the receive and transmit antenna gain, transmitted power, and receiver noise temperature of both the satellite and the earth terminal. We start by specifying as many of these as possible. In the subsequent design synthesis and trade-off phase, the parameter values are adjusted for consistency and the missing parameters are determined.

The initial parameters assumed for the digital example are the following:.

- 1) 12 GHz downlink, 14 GHz uplink
- 2) 3-meter earth terminal antenna, if possible, but no greater than 5 meters in any case
- 3) Satellite EIRP (equivalent isotropic radiated power, power times gain) on the order of 40 dBW
- 4) Ground terminal noise temperature no less than 300K
- 5) Satellite antenna receive gain - 33 dBi
- 6) Satellite receiver noise temperature - 1000 K.

For the analog example, we start with the following parameter values:

- 1) 30 GHz uplink, 20 GHz downlink
- 2) Ground terminal figure of merit (G/T: ratio of antenna gain over noise temperature) = 40 dB/K
- 3) Earth terminal receiver noise temperature = 200 K
- 4) Satellite antenna transmit gain = 36 dBi

- 5) Satellite antenna receive gain = 33 dBi
- 6) Satellite figure of merit (G/T) = 3 dB/K.

7.3.5 Design Synthesis and Tradeoff Phase

A general method of translating overall performance objectives into individual link objectives does not exist at this time for satellite systems operating above 10 GHz. Techniques have been developed for line-of-sight systems (Parker-1977 and GTE-1972), and satellite systems at lower frequencies (CSC-1971), but these have limited application in the present case. We present here some design tools that have been used in millimeter-wave system design. They include rules-of-thumb and simplifications that often apply, and more detailed procedures useful when the simplifying assumptions cannot be made.

At this point in the design procedure we have two functionally related parameters: a required composite C/N value, and the percentage of time for which this C/N applies. There may be several points of this function (the cumulative probability distribution function of C/N) specified. At some small percentage of time, the system is considered to be unavailable. At some larger percentage of time, a form of "degraded" operation might be defined, corresponding to a higher C/N value than the outage C/N. The present problem is one of assigning to each link of the system values of C/N and corresponding time percentages for which the values must be exceeded. Practically, this usually reduces to allocating outage time or availabilities among the links comprising the system, and allocating C/N values to the links in a way that is both compatible with the link outage time allocation, and achieves the required overall system performance.

7.3.5.1 Suballocation of Outages and Signal-to-Noise Ratio. One important element in this phase is the sub-allocation of outages. We have a specification on the permitted outage time for a service

or circuit, which comprises 2, 4, or perhaps more links. It is clear that in general

$$\text{Outage}_{\text{total}} = \sum \text{link outages} + \left(\begin{array}{c} \text{jointly} \\ \text{determined} \\ \text{outages} \end{array} \right) \quad (7.3-1)$$

The definitions of link outages are usually obvious once the system architecture has been defined. If the permitted total outage time is small (<1%), the jointly determined outages are extremely small and can be ignored. For example, if $(S/N)_{\text{composite}} < 10$ dB is an outage, then for a bent pipe repeater either $(S/N)_{\text{up}} < 10$ dB or $(S/N)_{\text{down}} < 10$ dB would constitute link outage events. Now, a variety of combinations (e.g., $(S/N)_{\text{up}} = 13$ dB and $(S/N)_{\text{down}} < 13$ dB) can also result in an outage condition. However, assuming uncorrelated statistics and a small percentage of time criterion, these joint contributions can be ignored with only slight error, since they are very small. Therefore it is reasonable for the initial design, even with bent pipe repeaters, to suballocate the total outage time to up- and downlinks according to the rule

$$\left(\begin{array}{c} \text{total} \\ \text{outage} \\ \text{time} \end{array} \right) = \left(\begin{array}{c} \text{uplink} \\ \text{outage} \\ \text{time} \end{array} \right) + \left(\begin{array}{c} \text{downlink} \\ \text{outage} \\ \text{time} \end{array} \right) \quad (7.3-2)$$

Using this outage time suballocation is particularly appropriate in digital systems where only a few dB separate nominal and barely acceptable performance. The nominal performance analyses (not syntheses) are performed in iterations subsequent to the initial design. These performance analyses must not be neglected, however, since a system design that meets a particular outage or availability criterion does not necessarily meet its other performance criteria (e.g., nominal performance). This is particularly important in analog systems where there can be a wide gap between what is considered an outage and what is required most of the time. Since it appears that most satellite systems being designed for above 10

GHz are digital, this difficulty is perhaps academic. In practice, the use of availability alone, or in conjunction with outage duration characteristics, is prevalent in the design of such systems.

In Table 7.3-1, we give the simplifying rules of thumb which may usually be employed for suballocation of outage time, T_{OUT} . In the duplex case, the exact value of T_{OUT} relative to its upper and lower bounds depends on the type of repeater and on the joint statistics of outage (i.e., the correlations between outages). The lower bound will apply if a perfect correlation of outages exists on the up- and downlink to a single terminal.

In general, the allocation of carrier-to-noise ratios among the several links is a more difficult problem. For the case of a bent-pipe repeater used for simplex service, the composite carrier-to-noise ratio $(C/N)_C$ for the circuit is given by

$$(C/N)_C = \left[(C/N)_U^{-1} + (C/N)_D^{-1} \right]^{-1} \quad (7.3-3)$$

where $(C/N)_U$ and $(C/N)_D$ are the individual carrier-to-noise ratios on the uplink and downlink, respectively. Figure 7.3-2 illustrates the trade-off between uplink and downlink C/N defined by the equation. The combination of C/N values for a digital circuit through a processing (demodulating-remodulating) satellite repeater is different. In that case, it is the errors on the uplink and downlink rather than the noise power that are added. The C/N trade-off curve for a regenerative repeater would be similar to that in Figure 7.3-2, but with a sharper "knee" because of the high sensitivity of error probability to C/N.

Curves such as Figure 7.3-2 allow convenient selection of uplink and downlink C/N values, but in the absence of propagation statistics, there are no other criteria for selection. At the first

Table 7.3-1. Outage Time Allocation

Allocation Relations:

Simplex Circuit Outage

$$T_{OUT} = T_{AS} + T_{SB}$$

Duplex Circuit Outage Bounds

$$T_{AS} + T_{SB} + T_{BS} + T_{SA} \geq T_{OUT} \geq \text{Larger of } \left\{ \begin{array}{l} (T_{AS} + T_{SB}) \\ \text{or} \\ (T_{BS} + T_{SA}) \end{array} \right\}$$

Definition of Terms:

Total Outage Time : T_{OUT}

Uplink outage, Terminal A to Satellite : T_{AS}

Downlink outage, Satellite to Terminal B : T_{SB}

Uplink outage, Terminal B to Satellite : T_{BS}

Downlink outage, Satellite to Terminal A : T_{SA}

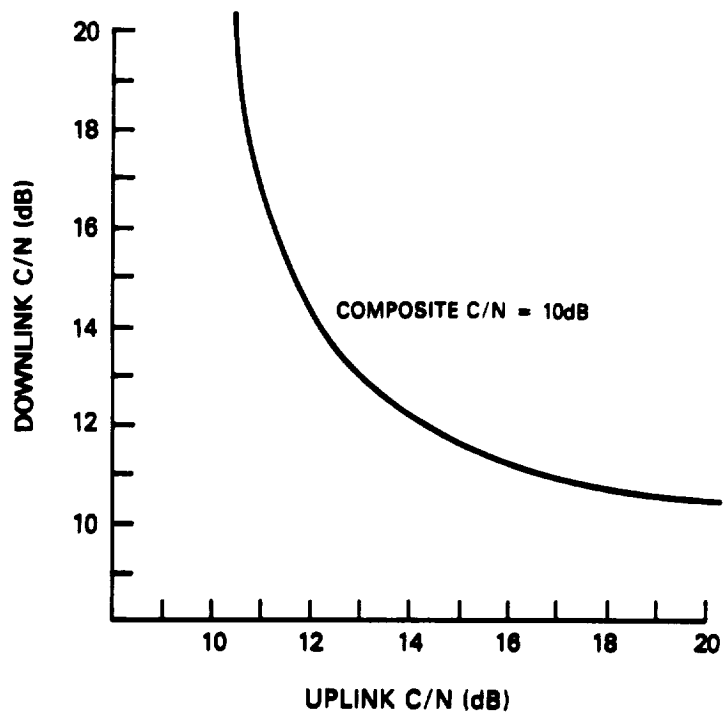


Figure 7.3-2. Uplink and Downlink Carrier-to-Noise Ratio (C/N) Trade-Off

iteration of the design synthesis phase, the selection is somewhat arbitrary. It will be refined in subsequent iterations. A good starting point may be equal C/N on both links. In this case, the link C/N must be 3 dB greater than the composite C/N. If allowed by system architecture, the uplink may be assigned a C/N value several dB more than that of the downlink because resources for achieving a high C/N (e.g., high-power amplifiers) are more readily available on the ground.

7.3.5.2 Power Budget Equation. The power budget equation relates the values of C/N or C/kT for individual uplinks or downlinks to physical system parameters. It defines the trade-offs possible between system components performance levels and is the basis of the

current phase of system design. In decibel form, the downlink power budget equation is:.

$$C/N = P_t + G_t + G_r - L_{fs} - L_1 - L_{rain} - 10 \log_{10} [kB (T_r + T_{sky})] \quad (7.3-4)$$

where:

- P_t = satellite transmitter power, dBW
- G_t = satellite antenna gain, dBi
- G_r = ground receiving terminal antenna gain, dBi
- L_{fs} = free space path loss, dB
- L_1 = attenuation losses which are constant, especially gaseous absorption, dB
- L_{rain} = attenuation from rain, dB
- k = Boltzmann's constant, 1.38×10^{-23} J/K
($10 \log_{10} k = -228.6$ dB-K⁻¹-Hz⁻¹)
- B = bandwidth, Hz
- T_r = receiving terminal noise temperature, K
- T_{sky} = sky noise temperature, K

To calculate C/kT, the bandwidth B is simply left out of the equation. The equation for the uplink is the same except the satellite and earth terminal parameters are interchanged and T_{sky} is replaced with T_{earth} , the satellite antenna noise temperature increase due to the earth (discussed in Section 6.8.5). In these first phase iterations, one assumes $L_{rain}=0$ dB, $L_1=0$ dB, $T_{sky}=0$ K or some small clear air value. Note that $(P_t + G_t)$ is the satellite EIRP, and that $(G_r - 10 \log T_r)$ is often given as a single parameter, the terminal's Figure of Merit or G/T.

7.3.5.3 Further Development of Design Examples. For the digital system example, the following assumptions are made:

- 1) The system will be assumed to operate in a simplex (one-way) mode for purpose of availability calculation (the necessary acknowledgments of data are assumed to occur at much lower data rates, therefore much higher availability).
- 2) TDMA is assumed. Therefore power sharing in the repeater is not a problem.
- 3) For initial system design, we will assign the same carrier-to-noise ratio to both the uplink and the downlink.
- 4) Nominal (long term) propagation characteristics will be assumed to apply, on the average, on both up and downlinks at the same times. Outage level fades in up and down directions will be assumed uncorrelated.
- 5) No terminal diversity will be employed.

We now apply the power budget equation to the downlink for the digital example. From the initial system parameters given in Section 7.3.4, we have

- Satellite EIRP = $P_t G_t = 40$ dBW
- Earth terminal antenna receive gain = G_r
 $= 18.2 + 20 \log (\text{freq.}-\text{GHz}) + 20 \log (\text{diam.}-\text{m})$
 $= 18.2 + 20 \log (12) + 20 \log (3) = 49.3$ dBi
- Bandwidth = symbol rate = 53.5×10^6
- Free space loss = L_{fs}
 $= 92.4 + 20 \log (\text{range}-\text{km}) + 20 \log (\text{freq.}-\text{GHz})$
 $= 92.4 + 20 \log (35,780) + 20 \log (12) = 205.1$

The value of composite C/N used for the nominal (clear sky) condition will be that which must be exceeded at least 80% of the time, or 10.7dB. From assumption 3) above and the C/N allocation formula of Section 7.3.5.1, we select downlink C/N = 13.7 dB.

Substituting into the power budget equation, we find the required ground terminal noise temperature:

$$13.7 = 40 + 49.3 - 205.1 + 228.6 - 10 \log_{10} (53.5 \times 10^6) - 10 \log_{10} T_r$$

$$T_r = 152 \text{ K}$$

We note that this violates the minimum value restriction of 300 K assumed at the outset. Suppose we determine from spacecraft design considerations that it is possible to double the output power of the satellite. Doing this, we have the compatible initial values,

- $T_r = 300 \text{ K}$
- $G_t + P_t = 43\text{dB}$

For the uplink in the digital example, we note from the initial parameter values assumed in Section 7.3.4 that everything is specified except ground terminal transmit power. We now use the power budget to find what value is required. First, we compute

- Free space loss for 14 GHz downlink = $L_{fs} = 206.4 \text{ dB}$
- Ground terminal transmit gain = 50.6 dBi

The power budget equation, again assuming a link C/N of 13.7dB is required, gives the following

$$13.7 = P_t + 50.6 + 33 - 206.4 + 228.6 - 77.3 - 30$$

$$P_t = 15.2 \text{ dBW (approx. 30W)}$$

For the analog system example, we will proceed on the following assumptions:

1) Initial system sizing will assume equal carrier-to-noise density on the uplink and downlink. A better allocation for the duplex link, which cannot be made at this time, would be such that both the uplink and downlink at a given terminal reach the outage

threshold simultaneously (since there is no need to be capable of transmitting when one cannot receive).

2) Outage time will be split evenly between uplink and downlink.

3) Dual site diversity will be used if necessary to enhance availability on the downlink. We assume uplink diversity will not be necessary.

For the downlink, at 20 GHz, we have

- Free space loss = $L_{fs} = 209.5$ dB
- Nominal (clear air) C/kT required is 3dB more than the composite C/kT that must be exceeded at least 80% of the time. Thus, downlink C/kT = 87.1 dB.
- From Section 7.3.4, ground terminal G/T = 40 dB/K and satellite transmit gain = 36 dB.

We use the power budget equation to find the missing parameter, the satellite transmitted power P_t .

$$C/kT = P_t + G_t + G_r - L_{fs} - 10 \log_{10}K$$

$$87.1 = P_t + 36 + 40 - 209.5 + 228.6$$

$$P_t = -8.0 \text{ dBW}$$

The 30 GHz uplink power budget requires the ground terminal transmit gain, which is $20 \log(30/20) = 3.5$ dB greater than the receive gain. The receive gain is found from the specified G/T (40dB) and noise temperature (200K) to be $40 + 23 = 63$ dBi so the transmit gain is 66.5 dBi. Other parameters are

- Satellite G/T = 3 dB
- Free space loss = $L_{fs} = 213$ dB

We again solve for the required ground terminal transmit power:

$$87.1 = P_t + 66.5 + 3 - 213 + 228.6$$

$$P_t = 2 \text{ dBW}$$

It should be evident by now that, even prior to explicitly incorporating the various propagation elements, the system design process involves an iterative and interactive series of choices of parameter values. Each choice must be tempered by pragmatic considerations. There are in the above examples numerous unstated assumptions. For example, for the 12/14 GHz digital system, the earth terminal antenna diameter of about 3 meters is appropriate for a direct user-to-user application. Subsequent tradeoffs might influence a change to, say, 5 meters at most. It is not feasible, nor appropriate, to set down all of these system engineering considerations in this Handbook.

7.3.6 Propagation Analysis and Iterations Phase

7.3.6.1 Compute Rain Margin (less diversity gain) and Adjust System Parameters Accordingly. The rain margin is the increase in system transmission parameters (such as power or gain) needed to offset the attenuation caused by rain and other precipitation. Note that since precipitation also increases the effective noise temperature on downlink paths, the margin should include this effect as well. If the system employs diversity (particularly, but not exclusively, space diversity), there is an effective "diversity gain" which can be obtained. This diversity gain can be subtracted from the rain margin. These calculations are described in detail in Chapter 6 for rain and section 7.4 for diversity. The (possibly adjusted) rain margins must be applied on the up and downlinks in accordance with the performance suballocation decisions made in the previous phase. Once again, this is best illustrated through the examples.

We address the digital system example first. We will assume no measured attenuation or rain rate statistics are available, and will use the analytic estimation technique of Figure 6.3-1 (the Global Model). The location of the ground terminal is in climate region D3 at 35° N latitude and sea level, and the path elevation angle is 20°.

We are interested in the attenuation at 12 and 14 GHz exceeded 0.5% of the time. For this case, we calculate the horizontal projection distance of the path to be 9.9 km. The point rain rate exceeded in region D3 for 0.5% of the time is 7.8 mm/hr. The attenuation values exceeded for this time are predicted at 2.9 dB for 12 GHz and 4 dB for 14 GHz. The composite C/N for the circuit can be less than 9 dB for 1% of the time or less. Using an equal allocation philosophy, the carrier-to-noise ratio not exceeded on either link for 0.5% of the time should be 12 dB. With the current initial parameter values, the downlink clear air C/N is 13.7 dB. The rain attenuation expected would drop this to 9.7 dB, so at least 2.3 dB of downlink rain margin is needed. In a similar manner the required uplink margin is found to be 1.2 dB. The uplink margin could easily be provided by increasing the ground terminal transmitter power. The downlink margin can be gained either through an increase in satellite EIRP or ground station G/T. Rather than attempting to again increase the satellite EIRP, we shall exercise our option for 5-meter ground station antennas, which provides 4.4 dB more gain. (Note that ground stations located in drier climates may meet the availability requirements with 3-meter antennas.) Since a given ground terminal will presumably be used for transmitting as well as receiving, the antenna size increase also increases the ground station EIRP by 4.4 dB, providing more than ample uplink margin without increasing the transmitter power.

For the analog example, assume the same ground station location and path elevation angle. The outage time percentage of interest in this case is 0.15% for each link. The attenuation exceedance curves given by the computation of Figure 6.3-1 are shown in Figure 7.3-3. On the downlink, the attenuation exceeded for 0.15% of the time is 17.2 dB. From Figure 7.4-4, we see that up to 12 dB of diversity gain may be obtained at large separations. Here, we will assume that 10 dB can be achieved, so the attenuation exceeded is effectively 7.2 dB. Accompanying 7.2 dB of attenuation, there is (by Section 6.7.4) a sky noise increase of 220K. The noise temperature of the ground station (200K in clear air) increases by this amount, so the

downlink C/N is reduced by a total of 10.4 dB. Recall that the composite C/N was allowed to be 10 dB worse than the nominal value for 0.3% of the time. Thus, provided we can limit the uplink degradation to less than 10 dB for at least 0.15% of the time, the downlink is nearly sufficient as is. We shall increase the satellite transmitted power by 2 dB to -6 dBW to guarantee its adequacy.

We can now determine how many 120 channel trunks may share the satellite repeater passband. Given that FDMA requires that the power amplifier be "backed off" from saturation for intermodulation noise reduction, and that solid state transmitter technology is limited to a few watts, we may decide that about 8 trunk-paths should be established per transponder channel. Following established practice for lower frequencies, these transponder channels will be 35 or 40 MHz wide.

For the 30 GHz uplink, Figure 7.3-3 shows that the attenuation value exceeded 0.15% of the time is 38.2 dB. Recall that under clear air conditions, a 2 dBW ground terminal transmitter yielded $C/kT = 87.1$ dB on the uplink. For $C/kT = 77.1$ dB with 38.2 dB of rain attenuation, the transmitter power would need to be increased to 30.2 dBW, or more than 1 kW. Considering the losses in transmitter output components and waveguide runs, this may require a power tube of several kilowatts, which is not now technologically feasible at 30 GHz. To provide the required uplink margin, then, either the satellite G/T must be drastically increased, or we must abandon our original assumption of no uplink diversity. We choose the diversity route as the more feasible. (Uplink diversity presents a technological problem of its own: the switchover of uplink transmissions between diversity sites is more difficult and potentially more disruptive to circuit integrity than diversity switching of downlink signals.) See Section 7.4 for a more detailed discussion of diversity problems.

Let us assume that 100W or 20 dBW of output power is readily achievable in the ground station. This means that the effective

attenuation exceeded for 0.15% of the time cannot exceed 28 dB. This would require a diversity gain of at least 10.2 dB. Alternately, we may specify a diversity advantage (see Section 7.4.1). Figure 7.3-3 indicates that an attenuation of 28 dB is exceeded for about 0.3% of the time on the 30 GHz link. The required diversity advantage is therefore 2, which most available data (Engelbrecht-1979 and Hogg and Chu-1975) indicates is easily obtained. With some foresight, we will stipulate that 13 dB of diversity gain is required for the uplink (or the diversity advantage must be 2.3). See Figure 7.4-1 for definitions of diversity gain and diversity advantage.

7.3.6.2 Apply Depolarization Analysis. The transmission of two orthogonally polarized signals from one satellite is employed to double the spectrum utilization by frequency reuse. Not every system, of course, will need to employ this technique, in view of the additional complexity and the added potential contribution to propagation caused outages.

The term "depolarization" is commonly employed to designate the reduction in cross-polarization discrimination seen at the receiving location under some propagation conditions. When this occurs, each of the two received channels (polarizations) contains an interference signal from the other polarization. Therefore, this signal is similar to interference which may occur from other satellites, terrestrial systems, or other beams of the same satellite.

Depolarization is caused by rain, as well as by ice layers, in the troposphere. The rain can cause strong depolarization events, in which the cross-polarization discrimination drops to 20 or 15 dB. Ice depolarization is quantitatively milder, but appears to occur more often. It is therefore convenient to treat two cases of depolarization effects, strong and weak.

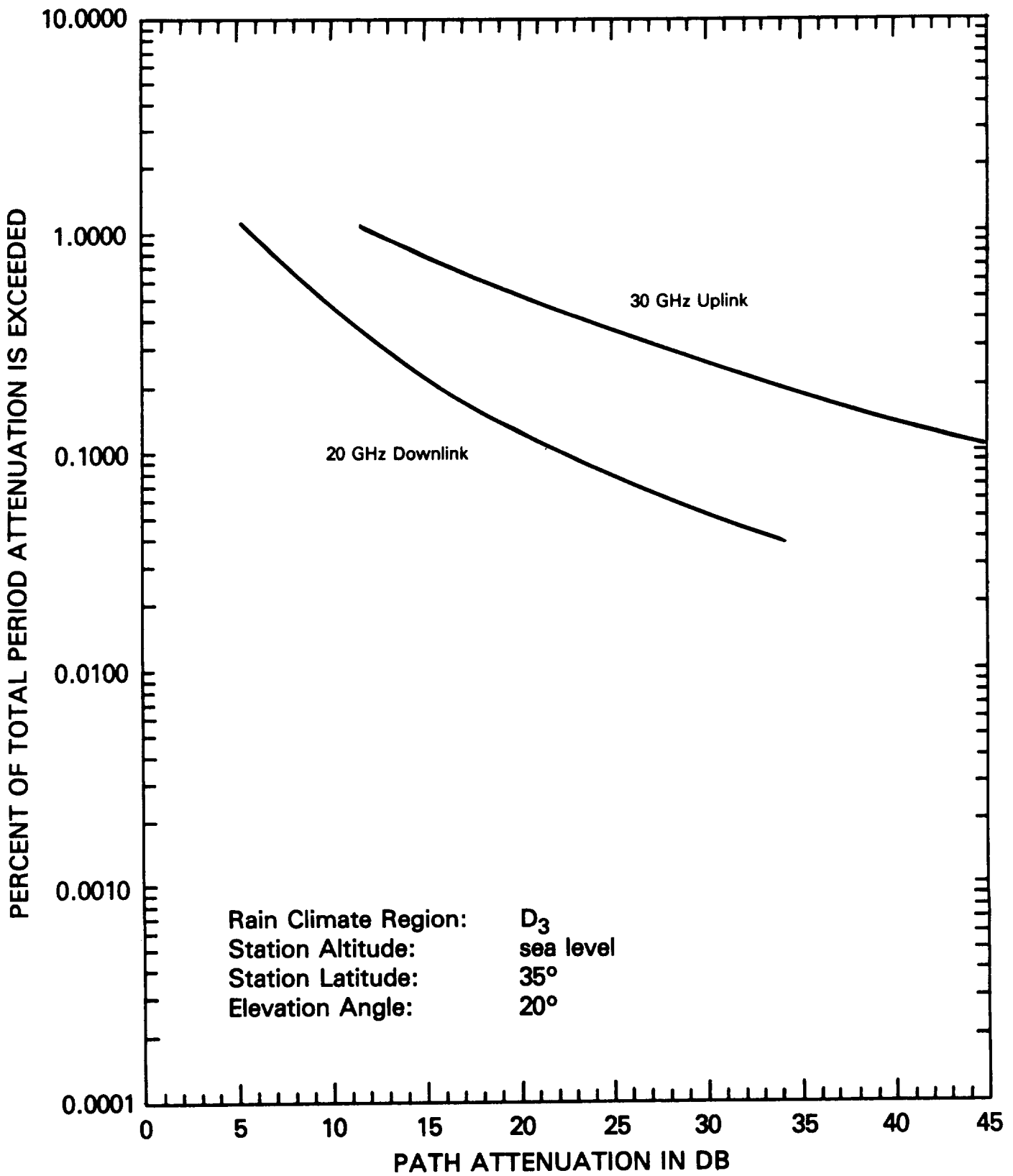


Figure 7.3-3. Analytic Estimate of Attenuation for 20 and 30 GHz Links of Example

Strong depolarization events should be correlated with deep attenuation events, since both stem from the same physical cause, namely rain. Both the deep attenuation fades and the strong depolarization intervals can cause outages. In order to perform a composite outage analysis, it is convenient to have joint statistical data, for example in the form introduced by Arnold, et. al. (1979). In Figure 7.3-4, we show a hypothetical version of such a joint outage plot. The parameter on the curves represents the threshold value of depolarization above* which the given system is inoperable, i.e., an outage exists. It can be seen that there may be many combinations of attenuation and depolarization that will result in any given probability of outage. Typically, the threshold depolarization is not an independent variable, but is fixed by the modulation parameters. Then, it can be immediately determined whether the previously computed rain margin is sufficient for the desired system availability.

In most cases, such joint statistics are not available. Section 6.6 presents methods for prediction of depolarization statistics, including functional relationships between attenuation and depolarization statistics. Using these prediction methods, it is possible to approximate curves like those in Figure 7.3-4, though the exact shape of each curve will not be mathematically precise. For example, the curve for "percent of time attenuation or depolarization exceeded" for the depolarization parameter equal to -10 dB is essentially the same as the attenuation versus percent exceeded curve alone (since depolarization is effectively "never" so large). For intermediate values of the depolarization parameter such as -25 dB, the appropriate curve is horizontally asymptotic to the percentage of time that depolarization alone exceeds the percentage. Each such horizontal asymptote then smoothly curves

*Here depolarization in dB is given a minus sign so that the term "exceeded" can correctly apply.

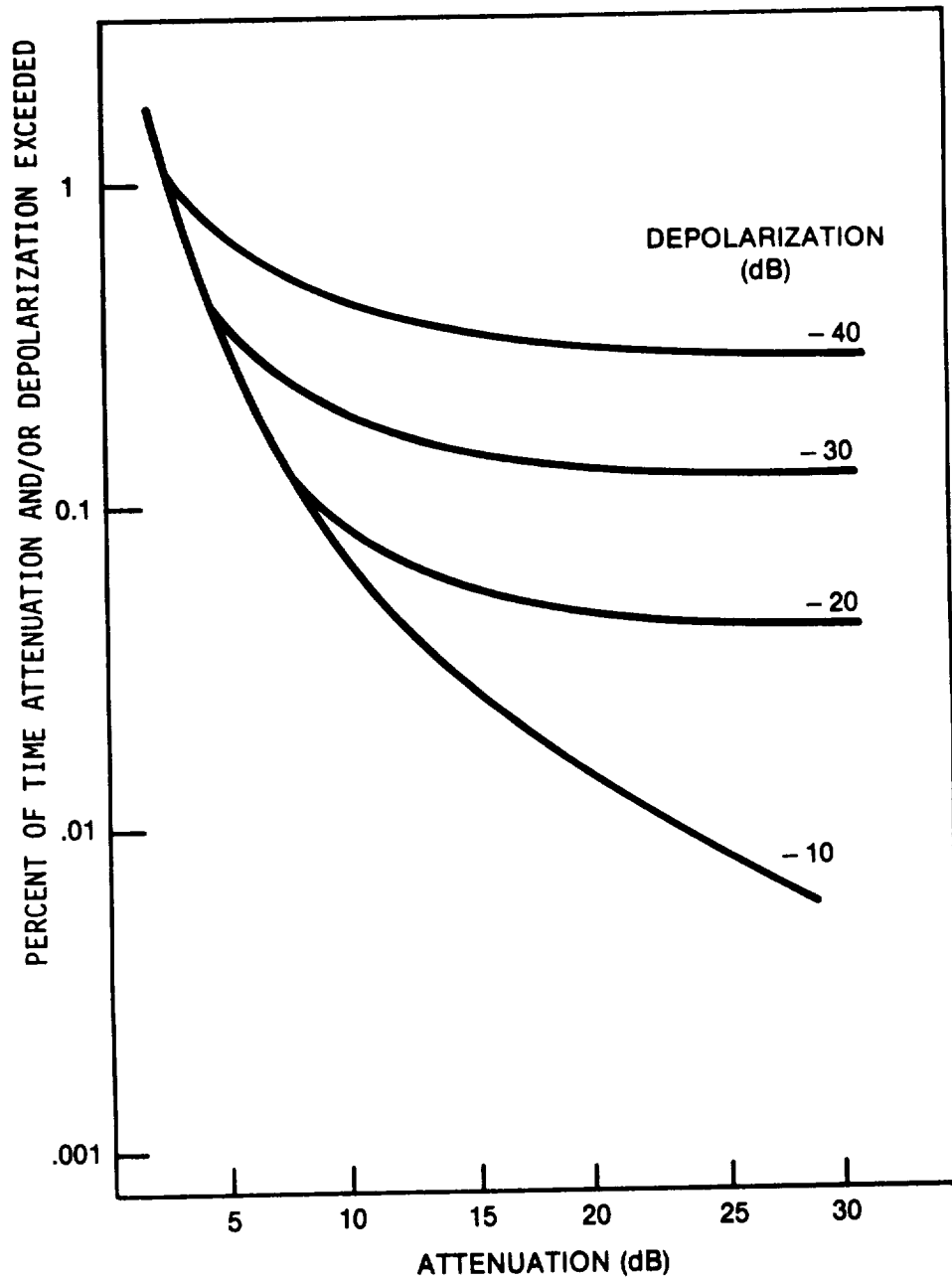


Figure 7.3-4. Composite Outage Versus Attenuation with Depolarization as a Parameter (Hypothetical Case)

into the attenuation only curve. Only this curved portion involves estimation by eye, and will introduce negligible error for initial design purposes.

The effect of diversity in reducing depolarization outage has received little attention to date (see Wallace-1981). The procedure outlined above applies to single-terminal attenuation and depolarization. When outages from attenuation and depolarization are each of the same order of magnitude, it is not clear that the concept of diversity gain (Section 7.4.1) is appropriate, since diversity should reduce depolarization outages as well.

In contrast to the "outage" values of depolarization, the smaller but more frequent values of depolarization can be accommodated in the system power margins. In almost all satellite communications systems, the thermal noise is the dominant portion of the total noise and interference. Small cross-polarized components may therefore be treated like any other interference. Castel and Bostian (1979) point out that depolarization on digital systems can be regarded as an equivalent C/N degradation. The equivalent degradation D due to depolarization for a n-ary PSK system is bounded by

$$D(\text{db}) < -20 \log [1 - (\log^{-1} x/20) / \sin (\pi/n)] \quad (7.3-5)$$

where x is minus the cross polarization discrimination (XPD), in decibels. The effect of crosspolarization (and interference in general) on digital systems is considered more precisely by Rosenbaum (1970) and Rosenbaum and Glave (1974). The determination of link availability considering the equivalent degradation in combination with rain attenuation is discussed by Wallace (1981).

Similar procedures apply in analog systems. In practice, the equivalent noise powers from all thermal noise and interference sources, including intermodulation and depolarization, are added together, in pWOp for example, to produce a total link noise power

which must meet the appropriate performance criterion (e.g., 10,000 pWOp). This adjustment to the system noise budget results in a further modification to the previously calculated system parameters. For example, the INTELSAT V system has been designed to meet a 10,000 pWOp criterion (Gray and Brown-1979). The composite received downlink must meet 7500 pWOp, with the remaining 2500 allocated to terrestrial and intersystem interference. This 7500 pWOp corresponds to a C/N of about 14 dB, yet the composite downlink thermal noise C/N is about 5 to 8 dB larger than this value, to allow for intermodulation products and for frequency reuse interference.

We do not consider here the employment of adaptive techniques to cancel cross-polarized components and to enable systems to operate at high levels of depolarization (e.g., 10 dB). By using such techniques, one pushes the outage threshold level of depolarization back to a value which effectively "never" occurs, so that the outages stem from attenuation alone.

7.3.6.3 Apply Lesser Propagation Effects. Attenuation effects from other than precipitation generally are of "second order" for system design purposes. Indeed, they may not need to be considered in the first iteration. They will be needed, however, for later, more accurate, estimates of performance.

"Clear air" attenuation, in excess of free space path loss, will typically be less than one or two dB except at the shortest millimeter wavelengths (greater than 50 GHz) or near absorption bands. These values may be calculated as shown in Figure 6.2-3. Adjustments are then made to the nominal performance power budgets (previously computed on a free-space-loss basis).

Cloud, fog, and dust attenuation factors may be very difficult to incorporate unless adequate statistics for their occurrence are available. These phenomena have significant effect only in unusual system designs, because the amount of attenuation is generally much less than that of rain. In general, a system with a fair amount of

rain margin will also have sufficient margin to operate through clouds. In addition, clouds and fog are not likely to occur so often as to influence the nominal performance value (50 or 80% of the time). Where appropriate, however, the system designer may incorporate an additional margin to allow for these attenuation effects. Similarly, signal fluctuations and antenna gain degradations, as treated in Paragraph 6.5, are relatively small and need be considered only in later iterations of performance analysis, at which time the effect can be accounted for through small margin adjustments to the nominal path loss.

7.3.6.4 Adjust System Parameters and Analyze System Performance.

In the foregoing, adjustment of system parameters has been carried out simultaneously with the development of the examples. The system designer may choose to use this approach, or to defer these adjustments until this point in the process. To do this in an organized manner, one should accumulate all propagation impairments which are (or can be equated to) attenuations or losses into a composite margin. Increases in sky noise, and the interference components, can be equated to losses in signal power, as previously discussed. This composite margin will be offset by power or gain adjustments. These margins and consequent system parameter adjustments are applied to the nominal system performance budget. In the analog example, this was the 10,000 pW0p criterion. Separately, the more severe effects which cannot be offset by (reasonable) margin are treated according to an outage criterion, i.e., by addition of outages contributed by each. Adjustments to system parameters resulting from a deficiency in meeting this criterion often involve fundamental changes in qualitative system design rather than simply margin changes. As an example, if the outage time is excessive because the system concept is very sensitive to mild depolarization, it may be necessary to use a different type of polarization, adaptive polarization techniques, or a different modulation technique.

In order to illustrate this step of the design process using the examples, a recapitulation of the constraints and parameters determined up to this point is in order. This is done in Table 7.3-2 for the digital system, and in Table 7.3-3 for the analog system.

The parameters for the digital system example from Table 7.3-2 are now used to carry out a detailed link power budget analysis, shown in Table 7.3-4. Here the power budget equation is applied to determine the C/N on the uplink and downlink separately. The individual C/N values are then combined to give the composite C/N. This is done for both the clear air or nominal case and the degraded case. The clear air budget includes an allowance of 0.5 dB for clear air attenuation (estimated using the data of Section 6.2.2), antenna pointing error, and other minor degradations. The degraded budget includes the rain attenuation exceeded for 0.5% of the time, as estimated earlier, and the increase in ground terminal noise temperature that is expected during the 0.5% downlink rain. This "sky noise" contribution was neglected earlier.

The nominal composite C/N for the digital system clearly exceeds the minimum required for at least 80% of the time (10.7 dB). When rain attenuation and sky noise have been included, however, the composite C/N is 0.4 dB less than the required value for 99% of the time (9.0 dB). We note that this deficiency can be easily made up by increasing the uplink transmitted power to 40W (16dBW), shown in parentheses in the Table 7.3-4 budget table.

The corresponding power budget calculations are carried out for the analog example in Table 7.3-5. In this case, the nominal composite C/N exceeds the minimum by nearly 4 dB, and the degraded value is 0.8 dB better than required. The 4 dB "overkill" under nominal conditions suggests that uplink power control would be advisable in this case to decrease the disparity in power level between the nominal and faded carriers in a transponder's passband.

Table 7.3-2. Digital System Summary

<p><u>Specified Performance Criteria</u></p>	<p>Bit Error Rate $\leq 10^{-6}$ $\geq 80\%$ of the time $\leq 10^{-4}$ $\geq 99\%$ of the time (outage time $\leq 1\%$)</p>
<p><u>Modulation and Performance</u></p>	<p>Data Rate: 40 Mb/s Modulation: QPSK Coding: Rate 1/2, Convolutional Required C/N (in symbol rate bandwidth) BER = 10^{-4} : 9.0 dB BER = 10^{-6} : 10.7 dB</p>
<p><u>System Parameters</u></p>	<p>14 GHz uplink, 12 GHz downlink TDMA (no power sharing or intermodulation in satellite repeater)</p>
<p><u>Satellite Parameters</u></p>	<p>EIRP = 43 dBW G/T = 3 dB</p>
<p><u>Ground Terminal Parameters</u></p>	<p>Receive noise temperature = 300K Receive antenna gain = 53.7 dBi Transmit antenna gain = 55 dBi Transmitted power = 15.2 dBW</p>

Table 7.3-3. Analog System Summary

<u>Specified Performance Criteria</u>	<p> $\leq 10,000$ pWOp $\geq 80\%$ of the time $\leq 100,000$ pWOp $\geq 99.7\%$ of the time "Outage" exists when 500,000 pWOp is reached </p>								
<u>Modulation and Performance</u>	<p>120 channel FDM-FM trunks</p> <table style="margin-left: auto; margin-right: auto;"> <thead> <tr> <th style="text-align: center;"><u>pWOp</u></th> <th style="text-align: center;"><u>C/kT</u></th> </tr> </thead> <tbody> <tr> <td style="text-align: center;">10,000</td> <td style="text-align: center;">84.1</td> </tr> <tr> <td style="text-align: center;">100,000</td> <td style="text-align: center;">74.1</td> </tr> <tr> <td style="text-align: center;">500,000</td> <td style="text-align: center;">67.1</td> </tr> </tbody> </table>	<u>pWOp</u>	<u>C/kT</u>	10,000	84.1	100,000	74.1	500,000	67.1
<u>pWOp</u>	<u>C/kT</u>								
10,000	84.1								
100,000	74.1								
500,000	67.1								
<u>System Parameters</u>	<p> 30 GHz uplinks, 20 GHz downlinks Dual (site) diversity, up- and downlinks Number of trunks per transponder: 8 Transponder channel bandwidth: 40 MHz </p>								
<u>Satellite Parameters</u>	<p> Antenna transmit gain: 36 dBi Receive G/T: 3 dB Transmit power total (with backoff): 3 dBW per carrier: -6 dBW </p>								
<u>Ground Terminal Parameters</u>	<p> Receive noise temperature: 200 K Receive antenna gain: 63 dBi Transmit antenna gain: 66.5 dBi Transmitted power (per carrier): 20 dBW </p>								

Table 7.3-4. Digital Example Power Budgets

	Uplink (14GHz)	Downlink (12GHz)
Transmit Power (dBW)	15.2 (16)*	
Antenna Gain (dBi)	55	
EIRP (dBW)	70.2	43
Free Space Loss (dB)	-206.4	-205.1
G/T (dBK ⁻¹)	3	28.9
Boltzmann's Constant (dB)	-(-228.6)	-(-228.6)
Clear Air and Other Propagation Losses (dB)	<u>-0.5</u>	<u>-0.5</u>
Nominal Link C/kT(dB-Hz)	94.9 (95.7)*	94.9
Reference Bandwidth, 80MHz (dBHz)	79	79
Nominal Link C/N (dB)	15.9 (16.7)*	15.9
Nominal Composite C/N (dB)		12.9 (13.3)*
Rain Attenuation, ≤0.5% of Time (dB)	-4	-2.9
Sky Noise Increase, 134K (dB)	<u> </u>	<u>-1.6</u>
Degraded Link C/N (dB)	11.9 (12.7)*	11.4
Degraded Composite C/N, ≤1% of Time (dB)		8.6 (9.0)*

* 40 Watt transmit power case

Table 7.3-5. Analog Example Power Budgets

	Uplink (30GHz)	Downlink (20GHz)
Transmit Power (dBW)	20	-6
Antenna Gain (dBi)	66.5	36
Free Space Loss (dB)	-213	-209.5
G/T (dBK ⁻¹)	3	40
Boltzmann's Constant (dB)	-(-228.6)	-(-228.6)
Clear Air and Other Propagation Losses (dB)	<u>-1.5</u>	<u>-1.2</u>
Nominal Link C/kT (dB-Hz)	103.6	87.9
Nominal Composite C/kT (dB-Hz)		87.8
Rain Attenuation, ≤0.15% of Time (dB)	-38.2	-17.2
Diversity Gain	+13	+10
Sky Noise Increase, 220K (dB)	<u> </u>	<u>-3.2</u>
Degraded Link C/kT (dB-Hz)	78.4	77.5
Degraded Composite C/kT, ≤0.3% of Time (dB-Hz)		74.9

The power budget shown for the analog system does not include some noise contributions that should be considered in the next iteration of the design. Those contributions include self-interference, interference from other satellite and terrestrial systems, and intermodulation in the satellite repeater. Self-interference may arise from crosstalk between frequency bands, orthogonal polarizations, antenna patterns, or combinations of the three, as determined by the system architecture.

7.3.6.5 Iterate System Design and Analysis. This phase needs little explanation. If the initial design does not, per analysis, deliver the level of performance required, the design must be changed in some way. Various trade-off techniques may be used to assist the design engineer in deciding what to change. The next section describes some of these techniques. In some cases, a critical look at the system requirements themselves must be taken. The examples that have been presented here were simplified in several respects, so that the several modifications to initial design assumptions could be made as the design proceeded. In an actual, real-world design, more refined analyses and iterations would be needed. Both of the examples used a particular terminal rain rate and elevation angle assumption. For a real system with a distribution of terminals in various locations, considerable refinement of the approaches would be possible, and could have significant impact in reduction of power requirements and/or outage times. Also, the examples did not illustrate the consideration of criteria other than long term (outage percentage) statistics.

7.3.7 Supplementary Design Tools

Techniques are available for assigning rain margins and allocating link performance parameters with more precision than has been used in the examples. We describe two of them here and provide references to others.

The first technique incorporates rain attenuation, sky noise temperature increase due to rain, and satellite repeater non-linearity into the carrier-to-noise trade-off relation given earlier. The composite carrier-to-noise ratio $(C/N)_C$ on a satellite circuit with rain effects is given by the formula

$$(C/N)_C = \left[(C/N)_U^{-1} L_U^{-1} + (C/N)_D^{-1} L_D^{-1} n(L_D) b^{-1}(L_U) \right]^{-1} \quad (7.3-6)$$

where

- $(C/N)_U$ = clear air value of uplink carrier-to-noise ratio
- L_U = uplink rain attenuation
- $(C/N)_D$ = clear air value of downlink carrier-to-noise ratio
- $n(L_D)$ = downlink noise power increase factor due to sky noise temperature
- $b(L_U)$ = satellite repeater output power reduction factor due to decrease in input power

All the parameters in the formula are expressed as numerical values, rather than decibels. The factor $n(L_D)$ is the fractional increase in noise temperature (and therefore downlink noise power) corresponding to the downlink rain attenuation L_D . For example, by the formulas in Section 6.7.4, the increase in antenna noise temperature accompanying a rain producing a 5 dB fade is about 188K (assuming surface temperature = 290K). If the ground terminal clear sky noise temperature was 300K, then the temperature increase factor $n(5dB)$ would be $488/300 = 1.6$ (2.1 dB). The factor $b(L_U)$ is a function of the nominal operating point and the characteristics of the satellite repeater (typically a TWT operating near saturation). If the fractional output power reduction corresponding to an input power reduction (uplink loss, L_U) of 5 dB were 3 dB, then $b(5dB) = 0.5$.

Figure 7.3-5 shows the trade-off curve defined by the equation for three conditions. (All parameters are shown in decibels for convenience.) Curve A corresponds to the clear-air condition and is the same as Figure 7.3-2. For curve B we assume uplink rain only. It is curve A shifted up by the factor $b(L_U)$ (in decibels) and to the right by the uplink attenuation L_U . Curve C assumes downlink rain only, and it is curve A shifted up by the downlink rain attenuation L_D plus the noise temperature increase factor $n(L_D)$ (in decibels). If L_U is the uplink attenuation exceeded for P_D % of the time, then curve B gives the corresponding values of $(C/N)_U$ and $(C/N)_D$ that will achieve at least the required $(C/N)_C$ except for P_U % of the time, assuming no downlink rain. Likewise if L_D is the downlink attenuation exceeded P_D % of the time, then curve C gives the corresponding C/N combinations assuming no uplink rain. The intersection of the two shifted curves B and C is the combination of C/N values that gives at least the required composite $(C/N)_C$ except for $P_U + P_D$ % of the time, assuming uplink and downlink rain do not occur simultaneously. Since the probability of jointly determined outages is much less than that of uplink or downlink outages (see Section 7.3.5.1), this technique gives a good approximation to the values of $(C/N)_U$ and $(C/N)_D$ needed to achieve the required outage time percentage $P_U + P_D$. The method requires an initial allocation of outage time to the uplink and downlink. To optimize system parameters, it could be carried out for a range of allocations.

This technique, since it does not consider carrier suppression, interference, or intermodulation noise, is most applicable to single carrier operation as in TDMA systems. The method is discussed by Calo, et. al. (1978) who carry out the computation of optimum uplink and downlink system parameters for a 12/14 GHz TDMA system. It is also used by McGregor (1981) in an example system design.

The second method of analysis to be described was used by Kittiver and Westwood (1976) in supporting the satellite-ground system design of the Satellite Business Systems network. This method, termed the Composite Margin Plane (CMP) analysis, permits a

precise calculation of link availability (or alternately, outage time percentage) given the rain attenuation statistics for the uplink and downlink and the system performance parameters. The CMP analysis is based on the equation for composite carrier-to-noise ratio given earlier, but takes the uplink and downlink rain attenuations as the independent variables. Satellite repeater non-linearity and downlink sky noise are not considered explicitly, but may be allowed for. The equation for $(C/N)_c$, disregarding these terms, can be plotted on the L -L coordinates as shown in Figure 7.3-6. The region contained within the curve represents the combination of uplink and downlink attenuation values that will result in a composite carrier-to-noise ratio less than $(C/N)_c$, taken as the outage value. The CMP plot is dependent on the clear-air values of $(C/N)_U$, $(C/N)_D$, and $(C/N)_c$ assigned, so requires an allocation of these parameters at the outset. Its utility lies in the fact that the independent variables coincide with those of the measured (or predicted) attenuation statistics. To determine circuit availability (1-outage probability) we must calculate the integral

$$P_{avail} = \int \int P_{xy} (x, y) dx dy \quad (7.3-7)$$

$$(C/N)_c > \min (C/N)_c \quad (7.3-8)$$

where

- P_{avail} = availability
- X = uplink attenuation
- Y = downlink attenuation
- p_{xy} = Joint probability density function of X, Y

The CMP defines the boundary of the region of the X-Y plane over which the integral is carried out. On the boundary the "composite" rain margin is zero. Outside the boundary the margin is negative

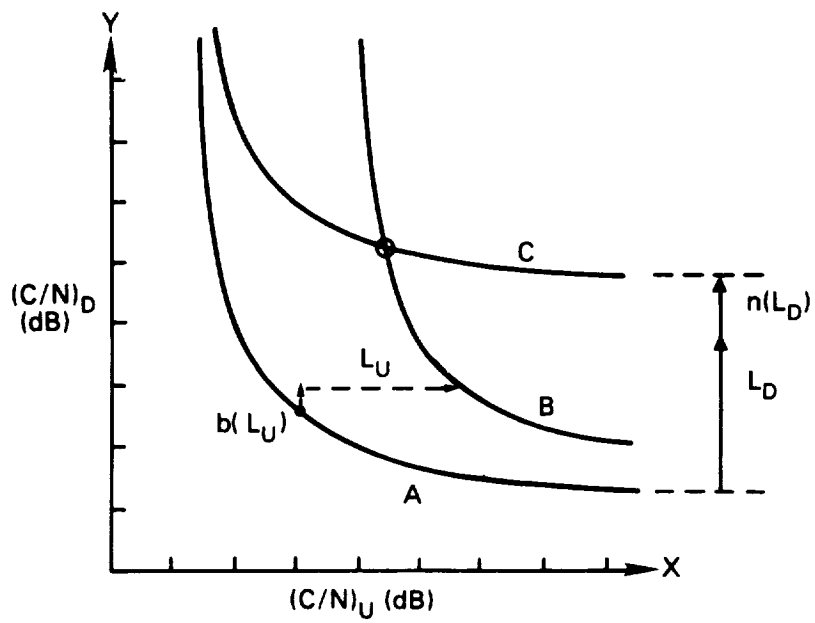


Figure 7.3-5. Uplink and Downlink Carrier to Noise Ratio Tradeoff

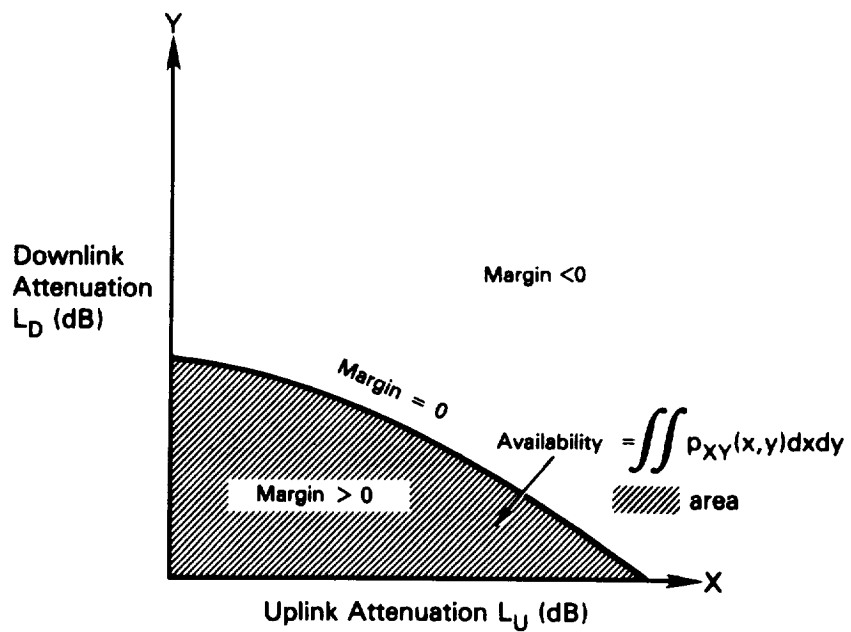


Figure 7.3-6. Composite Margin Plane

or the circuit is unavailable. The probability density function p_{xy} is given by the product of the uplink and downlink probability density functions (pdf's), which are in turn determined from the attenuation exceedance statistics plots for the uplink and downlink ground terminal locations. Since the joint pdf is taken as the product of the individual pdf's, we are implicitly assuming that the uplink and downlink attenuations are statistically independent, which is usually a reasonable assumption.

Kittiver and Westwood (1976) carried out the availability calculation by this method for 12/14 GHz circuit between Washington, D.C. and Atlanta, Georgia. The steps are illustrated in Figure 7.3-7, reproduced from the referenced paper. The CMP is shown in part (a) for the selected clear air values of $(C/N)_U$ and $(C/N)_D$. The dotted lines indicate that the C/N on each link is considered to be reduced by an implementation margin of 1.5 dB. The CMP, adjusted by this margin, is again modified by the downlink sky noise contribution. Part (b) shows the effect of downlink sky noise as an equivalent increase in downlink attenuation. Using part (b) to revise the ordinate of the CMP yields part (c). Part (d) shows the attenuation exceedance statistics measured for the up- and downlink locations at the respective frequencies. This is used to label the axes of the CMP with the exceedance percentages, as shown in part (e). Using the data in part (e), it is possible to graphically integrate the joint pdf and arrive at a value for the availability. Further details are given in the references.

A simplification of the CMP graphical integration is used by Calo, et. al. (1976) and McGregor (1981). The simplification consists of finding the sum of the integrals over two regions of the CMP, $L_U > L_{UMAX}$ and $L_D > L_{DMAX}$, as indicated in Figure 7.3-8. The approximate value of availability obtained in this way does not include the integral over the region bounded by the zero margin line and the L_{UMAX}, L_{DMAX} rectangle, but includes twice the integral over $L_U > L_{UMAX}, L_D > L_{DMAX}$. The unavailability (1-availability) given by this is equal to the probability that uplink rain reduces the margin

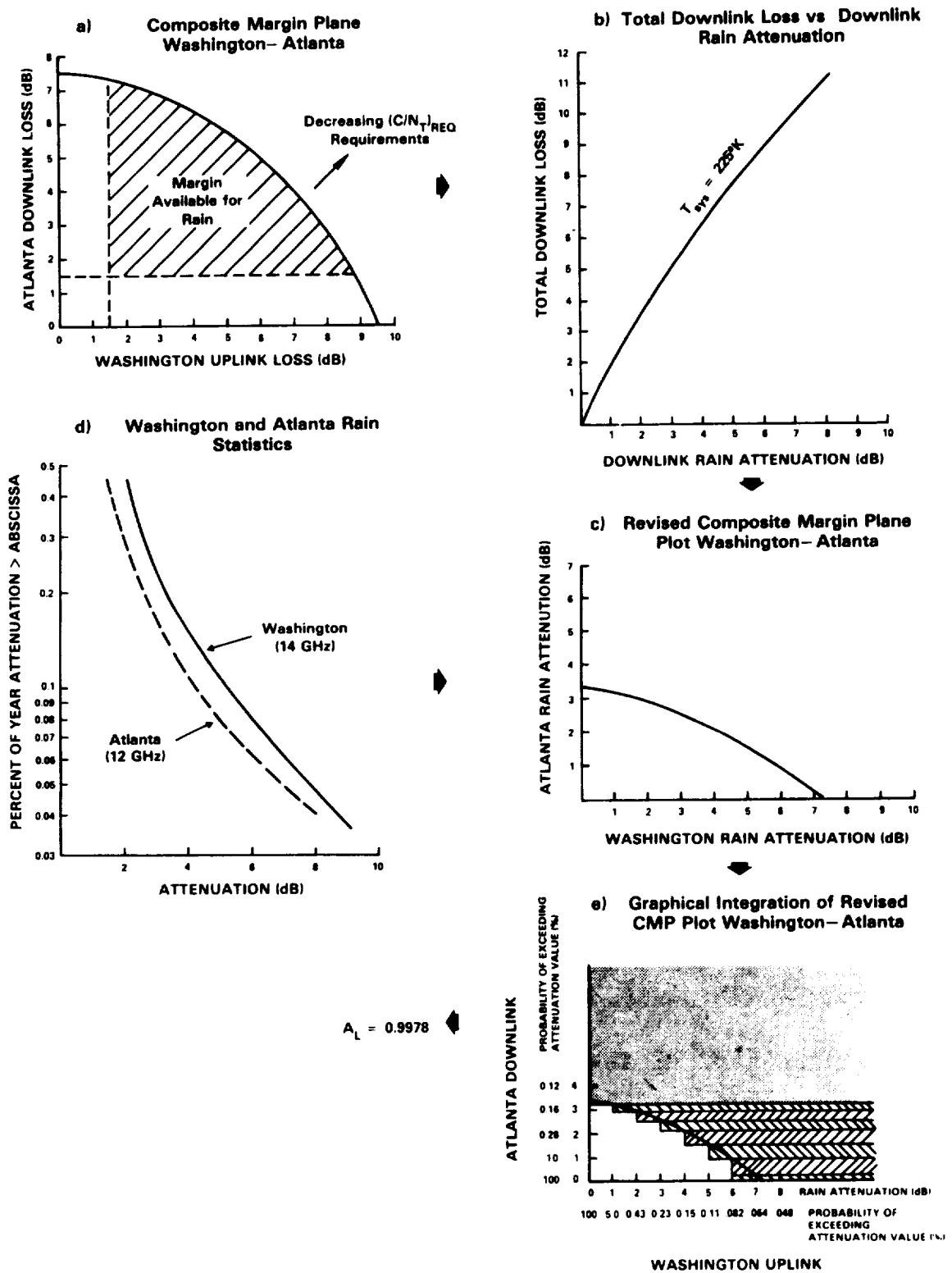


Figure 7.3-7. Composite Margin Plane Availability Analysis (from Kittiver - 1976)

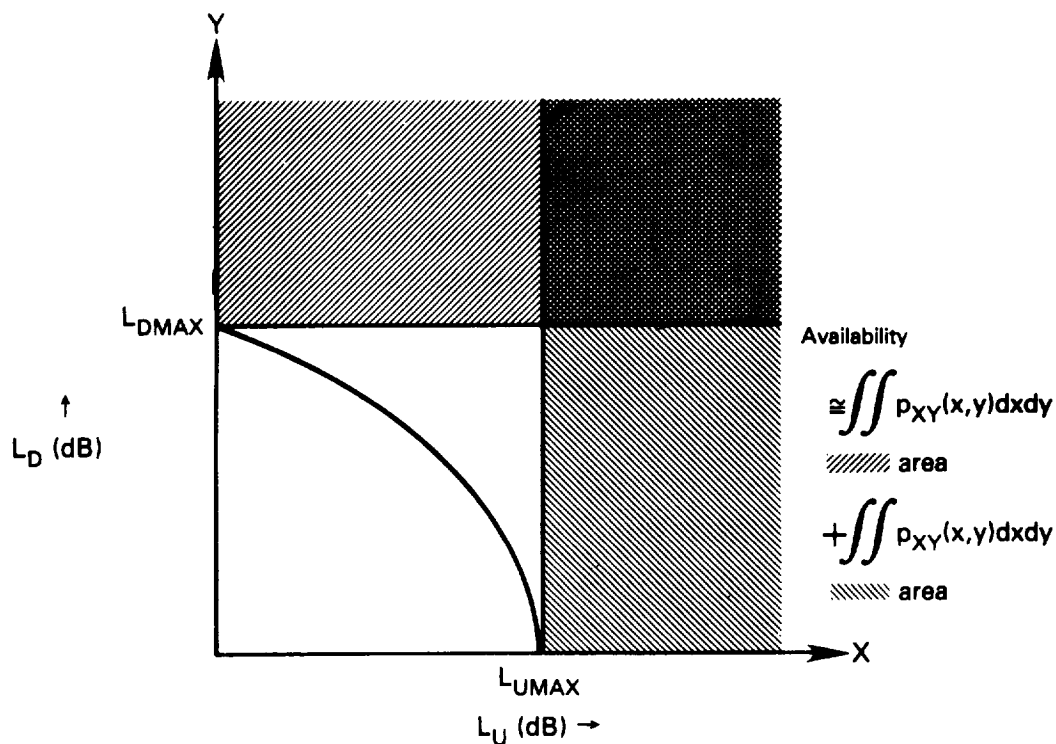


Figure 7.3-8. Approximate Composite Margin Plane Analysis

to zero with no downlink rain, or, that the downlink rain reduces the margin to zero with no uplink rain. Thus the approximation is the same as that used in the C/N trade-off analysis of Figure 7.3-4.

Other techniques for calculating system availability have been described in the literature. Lyons (1974, 1976) has performed statistical availability analyses including the effects of repeater non-linearity and limiting, intermodulation noise, and uplink power control in FDMA systems. Bantin and Lyons (1978) studied the effects of rain, scintillation, ground terminal antenna pointing error, and satellite station-keeping on system availability statistics. Because they require complex computer evaluation, the techniques described in these papers are not easily applied. Also,

their use is limited to one or two multiple access configurations. McGregor (1981) presents a method of finding system availability that is general in its approach and does not require computer evaluation. The method allows one to find the pdf of the composite carrier-to-noise ratio for a satellite circuit, considering the characteristics of the multiple access configuration, the propagation effects statistics, and the statistical characteristics of the body of users accessing the satellite. In the referenced report, the method is applied to the availability analysis of a code-division (spread-spectrum) multiple access system.

7.4 RAIN FADE MITIGATION

There are, of course, several brute-force methods that can be used to combat rain attenuation. One method is simply to operate at as low a carrier frequency as possible. However, for reasons already discussed, satellite communication is going to higher rather than lower frequencies. Another method of combatting rain attenuation is to increase either the transmitter EIRP or the receiver G/T, or both, in order to improve the performance margin. However, because of technological, regulatory, and radio interference considerations, one can go only so far in raising system EIRPs and G/Ts to improve performance margins. In fact, rain attenuation statistics presented in Chapter 3 of this Handbook indicate that highly reliable satellite communication systems operating in the millimeter-wave bands above 20 GHz would need excessive power margins to mitigate rain fades. So other, more clever, means for mitigating rain fades are clearly needed for good system performance.

With a view toward commercial utilization of the 20/30 GHz satellite bands, researchers are investigating techniques for dealing with the problem in elegant and cost-effective ways. Much of this work (Bronstein - 1982) is sponsored by NASA as part of the Advanced Communication Technology Satellite (ACTS) program, which

has the goal of making the 20/30 GHz bands technologically accessible to U.S. industry (NASA - 1987).

The amount of rain attenuation is, of course, extremely time and space sensitive. For example, in many densely populated areas on the eastern seaboard of the United States, propagation impairments due to rain are especially acute because of the timing of thunderstorm activity. Thunderstorms occur predominately during the peak in communication traffic between the east and west coasts. Nevertheless, one can overcome this extreme spatial sensitivity by using various space diversity techniques to combat rain fades. Space diversity involves the use of two or more spatially separated links for redundancy. If, at some instant, one of the redundant links experiences a fade, a spatially separated link may not experience a fade at the same instant. So we can switch to the link that provides the better performance. Careful timing of link switchovers can overcome the time sensitivity of rain fades. Examples of appropriate space diversity techniques for combatting rain fades are:

1. Site diversity (multiple transmitting and/or receiving terminals), and
2. Orbit diversity (multiple satellites).

In a similar vein, one can combat rain fades either by adaptively adjusting certain signal parameters to existing propagation conditions, or by using redundant signals. For example, a link experiencing a fade at one frequency may not experience fading at another (lower) frequency. So one can switch to a frequency that provides acceptable performance whenever a severe rain fade occurs. Examples of appropriate signalling techniques for combatting rain fades are:

1. Transmitter power control
2. Adaptive forward error correction

3. Frequency diversity

4. Data rate reduction.

In this Handbook these signalling techniques are considered as possible implementations of "signal diversity" schemes.

These and other approaches (Ippolito - 1986, Brandinger - 1978, and Engelbrecht - 1979) have been suggested as techniques for significantly improving communication reliability in the presence of rain attenuation. More experimental results have been obtained for site diversity than for any other form of rain fade mitigation. However, system designers will want to consider combinations of all diversity options. Complexity and cost will play major roles in the ultimate decision to use any diversity technique.

The following sections discuss each of these techniques for rain mitigation.

7.4.1 Measures of Diversity Performance

To characterize the performance of diversity systems, one must establish suitable performance parameters. One such parameter in common use is "diversity gain". Suppose the rain attenuation on a single diversity branch (a single propagation path or a single carrier frequency, for example) is A dB at some instant. The attenuation will vary with time, so let $A(T)$ be the value of A that is exceeded T percent of the time. To obtain good fade statistics (and therefore an accurate estimate of T), we must assume that the attenuation has been measured over a sufficiently long time period. Now suppose additional diversity branches (site diversity or frequency diversity, for example) are introduced to reduce the effective rain attenuation. Let $A_{div}(T)$ be the value of A that is exceeded T percent of the time after diversity has been introduced. As illustrated in Figure 7.4-1, we can define the diversity gain (Hodge - 1974a) to be the difference between $A(T)$ and $A_{div}(T)$ at the value of T that has been selected:

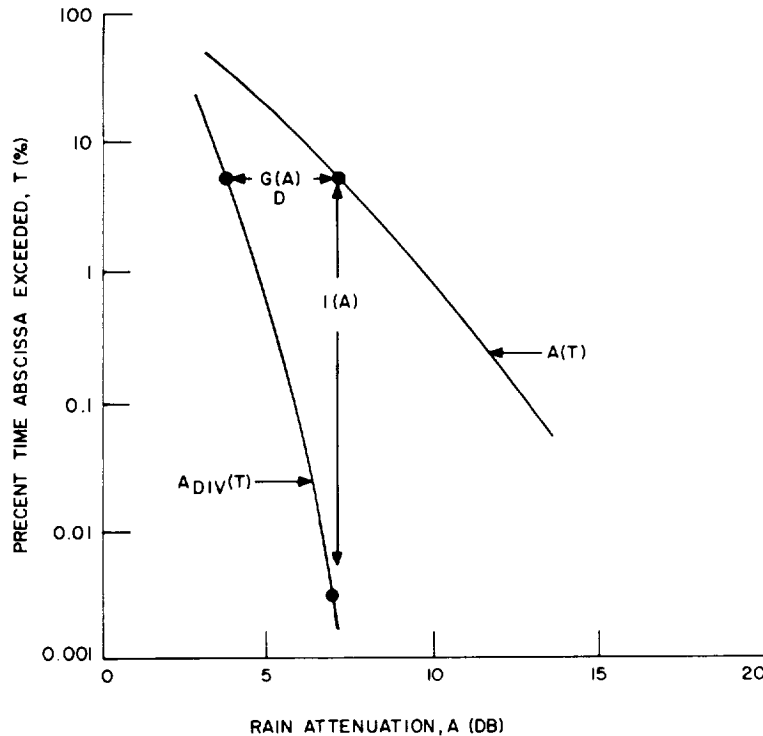


Figure 7.4-1. Definition of Diversity Gain and Advantage

$$G_D(A) = A(T) - A_{div}(T) \quad (7.4-1)$$

Another measure of diversity performance is "diversity advantage" (Wilson and Mammel - 1973). Let $T(A)$ be the percentage of time that some attenuation A (in dB) is exceeded when there is no diversity. Similarly, let $T_{div}(A)$ be the corresponding value of T when diversity is employed. As illustrated in Figure 7.4-1, we can define diversity advantage as the ratio of these two quantities at the selected value of A :

$$I(A) = \frac{T(A)}{T_{div}(A)} \quad (7.4-2)$$

If the system designer specifies that a given attenuation A (with or without diversity) may not be exceeded more than T percent of the time, then the diversity gain turns out to be the reduction in EIRP or G/T that the introduction of diversity permits, while maintaining the specified value of T . On the other hand, suppose instead that the system designer wants to specify the value of the

attenuation above which a rain-induced system outage is considered to occur. Then the diversity advantage is the factor by which the outage duration can be reduced by introducing diversity, while maintaining other system parameters such as EIRP and G/T constant. Clearly, these two parameters (diversity gain and diversity advantage) are not independent descriptors of diversity performance because Figure 7.4-1 shows that when one of the two parameters is known, the other is readily determined.

Up to now we have implicitly assumed that the fade statistics associated with each diversity branch are identical. In practice this is seldom the case. Attenuation statistics differ on the two branches either because of measurement uncertainty or because of real differences that exist among the diversity branches. A quantitative description of this effect would require more than one parameter to characterize diversity performance. But the use of only a single parameter is very convenient, and furthermore there is little reason a priori to assign more weight to one branch than to another. One way to get around this difficulty is to use average values for the single-branch attenuation and time percentage, and to define the diversity gain and diversity advantage as

$$G_D(A) = A_{ave}(T) - A_{div}(T) \quad (7.4-3)$$

$$I(A) = \frac{T_{ave}(A)}{T_{div}(A)} \quad , \quad (7.4-4)$$

which are simple generalizations of eqs. 7.4-1 and 7.4-2. The averages in eqs. 7.4-3 and 7.4-4 are over the possible diversity branches.

Allnutt (1978) used both diversity gain and diversity advantage to compare diversity data. He showed that the use of diversity gain allows trends and similarities to be readily observed, while the use of diversity advantage with the same data produces results with a large amount of scatter. In explaining these observations, Hodge (1982) pointed out that the use of diversity advantage requires

measurements over widely different time intervals. Uncertainties in the values of $T_{ave}(A)$ and $T_{div}(A)$ being compared are therefore very different, which apparently accounts for the widely fluctuating values. A second drawback to using diversity advantage as a performance parameter is that it often cannot be defined when deep fades occur because the estimate of $T_{div}(A)$ for large A requires excessively long measurement times. These arguments suggest that data analysis and comparison are better done on the basis of diversity gain than diversity advantage. If required, diversity advantage can then be determined later, when the analysis in terms of diversity gain is complete.

7.4.2 Space Diversity

At carrier frequencies exceeding 10 GHz, rain attenuation often degrades earth-space propagation paths so seriously that the requirements of economical design and reliable performance cannot be achieved simultaneously. To overcome this problem, Hogg(1968) proposed the use of site diversity on earth-space paths to achieve the desired level of system reliability at reasonable cost. This proposal was based on the hypothesis that the intense rain cells that cause the most severe fading are rather limited in spatial extent. Furthermore, these rain cells are usually separated from one another, which means that the probability of simultaneous fading on two paths to spatially separated earth terminals is less than that associated with either individual path. Wilson (1970) first tested this hypothesis, using radiometric noise emission measurements to determine the rain attenuation on separated paths. Hodge (1974a) later tested the hypothesis, using actual earth-space paths. These and other ensuing experiments have demonstrated that site diversity is an effective technique for improving system reliability in the presence of rain attenuation.

Figure 7.4-2 shows a typical configuration employing site diversity. Also indicated are definitions of the following parameters, which are needed in later discussions:

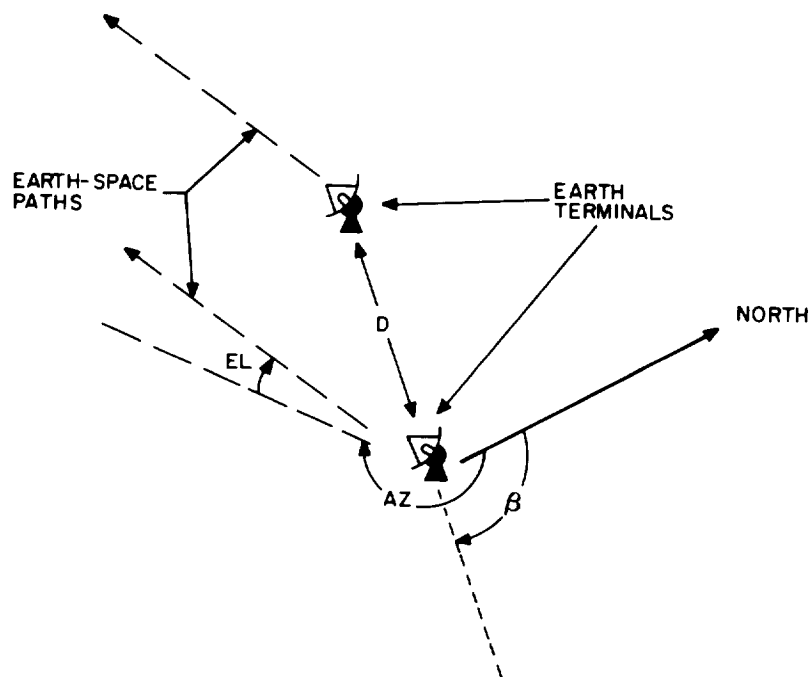


Figure 7.4-2. Site Diversity Configuration

AZ = azimuth of earth-space path (degrees)

EL = elevation of earth-space path (degrees)

d = distance between earth terminals (km)

β = orientation of earth terminal baseline (degrees)

Orbit diversity, on the other hand, uses only one ground site to communicate via two or more earth-space paths with satellites located in separated orbital positions, as illustrated in Figure 7.4-3. If a rain cell is far from the terminal, so that the cell is not likely to intercept more than one path to the terminal, the result will be similar to that for site diversity. However, if a rain cell is near the terminal, little improvement results because

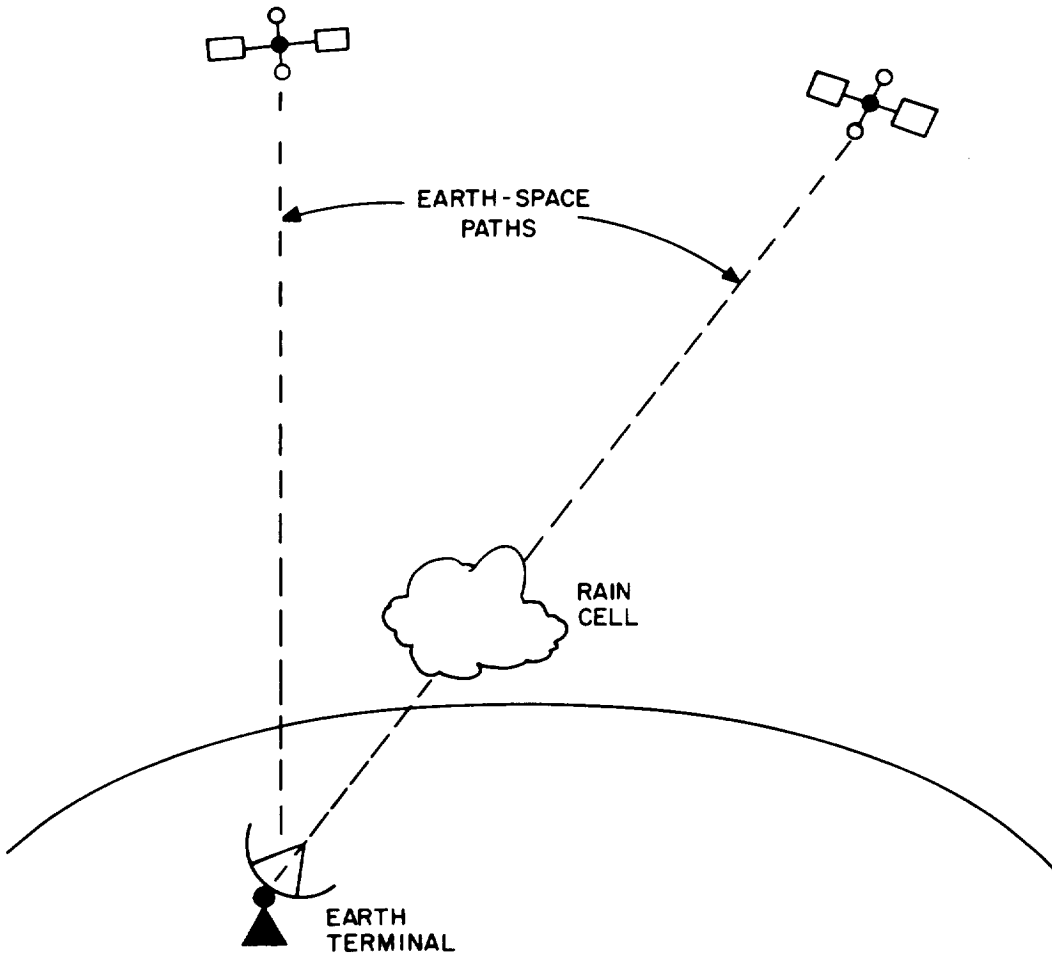


Figure 7.4-3. Orbit Diversity Configuration

all paths to the terminal pass through the same cell. Orbit diversity is therefore not as effective as site diversity in some cases. Nevertheless, in other situations orbit diversity can provide significant rain fade mitigation whenever multiple satellites are available.

7.4.2.1 Site Diversity

The following discussion of site diversity begins with a summary of numerous site diversity experiments that have been performed. Then, after discussing the various design factors that are required to quantitatively describe site diversity, some mathematical models for estimating the diversity gain that is achievable from site diversity are presented. The first model to be discussed is empirical in the sense that measured diversity data are fitted to simple equations in order to obtain formulas for the diversity gain. The second model is analytical in the sense that a definite statistical distribution for the rain attenuation is used to estimate the diversity gain.

7.4.2.1.1 Site Diversity Experiments

Table 7.4-1 presents a list of experimental diversity measurements available in the literature provided by Hodge (1982). [Additional information on diversity measurements can be found in Figures 4 and 5 of Annex I to Report 564-3 of CCIR (1986).] This table includes the results reported for each of the four methods -- direct measurement of satellite beacons, radiometric measurement of the sky temperature, radar measurements of rain structures and radiometric measurements of solar emission. In each case the reference is cited along with the location of the experiment, the frequency, station separation distance, baseline orientation, path azimuth, and path elevation. In cases where multiple measurements are reported, the range of the appropriate parameters is indicated. A fifth method, rapid response raingauges, has been attempted, but has not been accurate for predicting diversity gain. The two reasons cited (Allnutt-1978) are: 1) the rainfall rate on the

Table 7.4-1. Summary of Diversity Experiments

I. SATELLITE EXPERIMENTS

REFERENCE	LOCATION	FREQ.	SEPARATION(d)	BASELINE ORIENTATION (p')	AZ	EL
Hodge (1974)	Columbus, Ohio	15.3 GHz	4.0-8.3 km	159-164 ⁰	210 ⁰	38 ⁰
Westinghouse (1975)+	Washington, DC area	20, 30	27.9-75.8	Several	≈ 206 ⁰	≈ 40 ⁰
Hodge (1976b)	Columbus, Ohio	20, 30	13.2-14.0	33-151 ⁰	197 ⁰	40 ⁰
Vogel, et al (1976)	Austin, Texas	30	11.0	0 ⁰	172 ⁰	55 ⁰
Hyde (1976)	Boston, Mass.	18	6.7-35.2	74-93 ⁰	212 ⁰	36 ⁰
	Columbus, Ohio	18	5.1-38.9	91-95 ⁰	196 ⁰	42 ⁰
	Starkville, Miss.	18	8.3-40.0	105-113 ⁰	190 ⁰	51 ⁰
Hosoya, et al (1980)	Yokohama, Japan	20	19	164 ⁰	188 ⁰	48 ⁰
Suzuki, et al (1982)	Kashima, Japan	20	45	0 ⁰	190 ⁰	48 ⁰
Tang, et al (1982)	Tampa, Florida	19, 29	11, 16, 20	157, 244, 210	198-205 ⁰	31 ⁰ -57 ⁰
Towner, et al (1982)	Blacksburg, Va.	11.6	7.3	160 ⁰	106 ⁰	10.7 ⁰

II. RADIOMETER EXPERIMENTS

Wilson (1970)	Crawford Hill, N.J.	16	3.2-14.4	135 ⁰	226 ⁰	32 ⁰
Wilson & Mammel (1973)	Crawford Hill, N.J.	16	11.2-30.4	135 ⁰	226 ⁰	32 ⁰
Gray (1973)	Crawford Hill, N.J.	16	19.0-33.0	45-135 ⁰	226 ⁰	32 ⁰
Funakawa & Otsu (1974)	Kokubunji, Japan	35	15.0	---	180 ⁰	45 ⁰
Hall & Allnutt (1975)	Slough, England	11.6	1.7-23.6 ⁰	20-106 ⁰	198 ⁰	30 ⁰
Allnutt (1975)	Slough, England	11.6	1.7-23.6 ⁰	20-106 ⁰	198 ⁰	30 ⁰
Strickland (1977)	Quebec, Canada	13	18.0	11 ⁰	122 ⁰	19 ⁰
	Ontario, Canada	13	21.6	1 ⁰	116 ⁰	16 ⁰
Bergmann (1977)	Atlanta, Georgia	17.8	15.8-46.9	141-146 ⁰	228 ⁰	38 ⁰
	Denver, Colorado	17.8	33.1	86 ⁰	197 ⁰	43 ⁰
Rogers (1981)	Graz-Michelbachberg, Austria	11.4/12	10.9	---	154 ⁰	33 ⁰
	Etam-Lenox, WV	11.6	35	---	114 ⁰	18 ⁰
	Kurashiki City - Shimotsui, Japan	12	17	---	260 ⁰	6 ⁰

III. RADAR EXPERIMENTS

Goldhirsh & Robison (1975)	Wallops Island, Va.	13-18	2-20	0-180 ⁰	0-360 ⁰	45 ⁰
Goldhirsh (1975)	Wallops Island, Va.	13-100	2-20	0-180 ⁰	0-360 ⁰	45 ⁰
Goldhirsh (1976)	Wallops Island, Va.	18	2-20	0-180 ⁰	0-360 ⁰	45 ⁰
Hodge (1978)	Montreal, Quebec	13	4-42	0-180 ⁰	122-240 ⁰	19-40 ⁰

IV. SUNTRACKER EXPERIMENTS

Wulfsburg (1973)	Boston, Mass.	35	11.2	158 ⁰	---	---
Funakawa & Otsu (1974)	Kokubunji, Japan	35	15.0	---	---	---
Davies & Croom (1974)	Slough, England	37	10.3	67 ⁰	---	---
Davies (1976)	Slough, England	37	10.3-18.0	67-110 ⁰	---	---

+ Long-Baseline Site Diversity Experiment

ground cannot be accurately converted to a rainfall rate on the path, and 2) the rainfall-rate model giving the drop-size distribution is not accurate enough to calculate the attenuation on the path.

In the radar-based diversity experiments, an S-band radar was used to accumulate detailed reflectivity measurements of the space surrounding the radar during rain events. These data were then used to calculate the rain attenuation along hypothetical Earth-space paths through the rain volume by applying the observed relation between reflectivity and attenuation. Diversity results were obtained by hypothesizing parallel paths, with their endpoints separated by a given distance. Results from a large number of different path pairs and a number of rain events were used to derive attenuation statistics and diversity gain. Because this method does not actually require a pair of diversity terminals, it is simple to vary the terminal spacing and baseline orientation.

7.4.2.1.2 Site Diversity Design Factors

7.4.2.1.2.1 Separation Distance. Diversity gain depends strongly upon the earth terminal separation distance, d . The diversity gain increases rapidly as d is increased over a small separation distance, i.e., up to about 10 km; thereafter the gain increases more slowly until a maximum value is reached, usually between about 10 and 30 km. This maximum value is generally quite close to that value associated with uncorrelated fading at the individual earth terminals. Radar-based results, showing the variation of diversity gain with separation, are given in Figure 7.4-4.

In contrast to the uncorrelated case, one may argue that correlated fading may occur for paths separated by distances associated with typical rain cell separation distances. Such an effect may be inferred from the rainfall statistics of Freeny and Gabbe (1969); however, these statistics are associated with point rainfall rates rather than path average rainfall rates. No definitive report of this effect has been published to date.

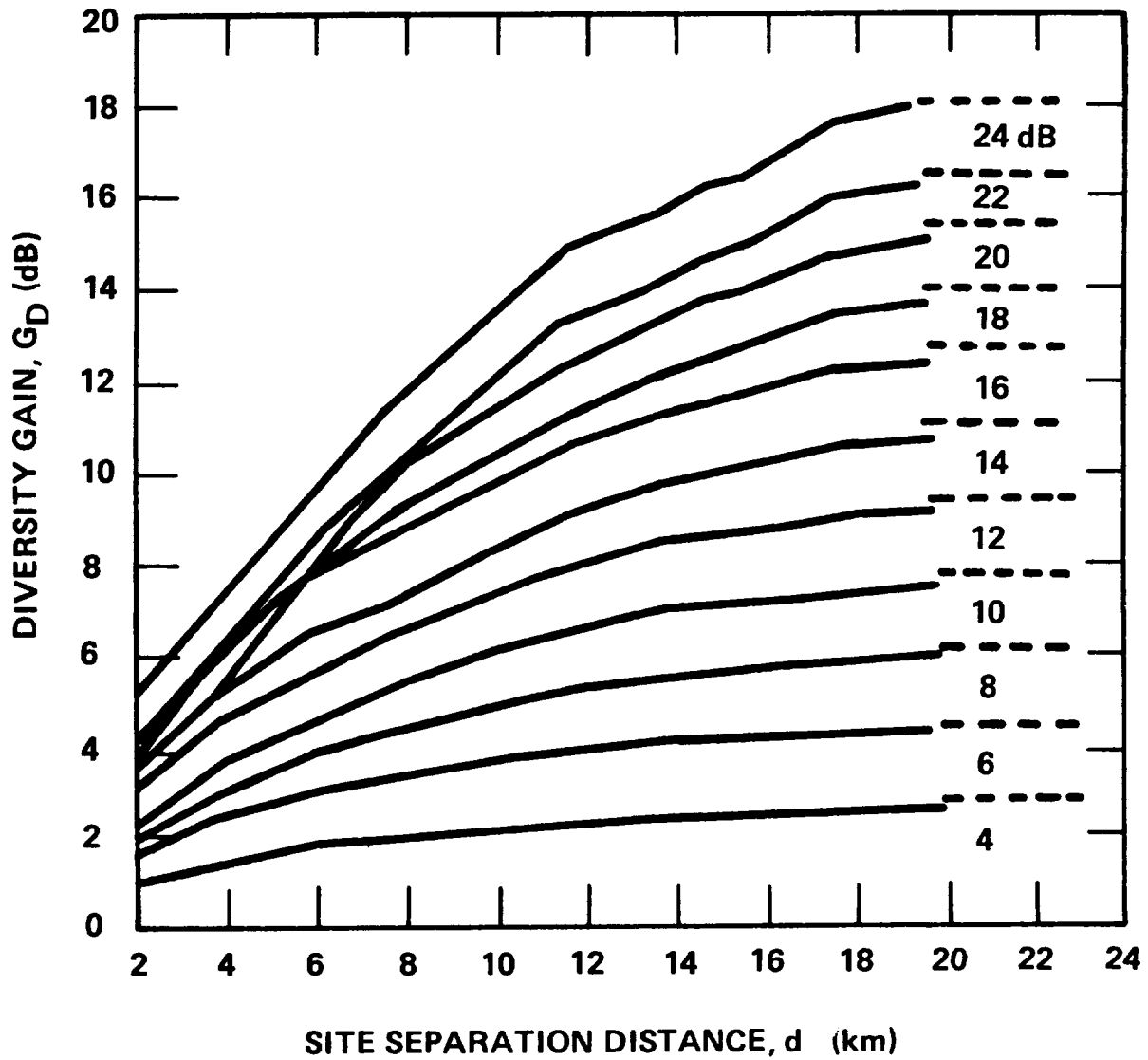


Figure 7.4-4. Diversity Gain, G_D , versus Separation Distance, d , for 18 GHz. (Horizontal Dashed Lines Represent Optimum Levels) (Goldhirsh and Robison-1975)

7.4.2.1.2.2 Baseline Orientation. The perpendicular separation between parallel paths is greatest when the earth terminals are located on a baseline perpendicular to the projections of the paths on the earth's surface. This arrangement minimizes the possibility of both paths passing through the same rain cell. Nevertheless, the dependence of diversity gain on baseline orientation is quite weak except, possibly, for very short separation distances.

Mass (1979) has shown analytically for circular rain cells over two ground station sites alternately positioned transverse and parallel to the earth-space path, that only a small (0.3 to 0.4 db) difference in diversity gain is to be expected. It is anticipated that the orographic effects will overshadow these orientation effects.

The baseline orientation problem is further complicated if spatial anisotropy of the rain cells, i.e., a preferred direction of rain cell elongation, is known to exist in the region of interest. In this case, a baseline orientation perpendicular to the preferred axis of rain cell orientation would be desirable if the direction of the propagation path were ignored.

Considering both factors together, it appears that the most desirable baseline orientation is that which bisects the larger of the two angles between the projection of the propagation path and the preferred axis of rain cell orientation.

7.4.2.1.2.3 Path Elevation Angle. The separation distance required to achieve a given level of diversity gain increases as the path elevation angle decreases (Hodge-1978). This is due to the increased likelihood of path intersections with rain cells at lower elevation angles. This effect is coupled to the problem of rain cell anisotropy and path azimuth as noted below. Stated differently, the diversity gain decreases with decreasing elevation angle (Allnutt-1978).

7.4.2.1.2.4 Path Azimuth Angle. For synchronous satellites the path azimuth and elevation angles are not independent, and, thus, the dependence of diversity performance on these variables cannot be fully separated. If all rain cells were isotropic, one would expect no variation in diversity performance with azimuth angle other than that associated with the elevation angles. However, when rain cell anisotropy is considered, there appears to be a weak improvement in diversity performance for path azimuths in the southerly compass quadrant (in the northern hemisphere) that do not contain the preferred axis of rain cell orientation.

7.4.2.1.2.5 Link Frequency. Experimental measurements to date have shown a slight inverse dependency of site diversity gain on the link frequency for a given single-site attenuation over the 10-35 GHz frequency range (Hodge-1982). For link frequencies above 30 GHz, attenuation on both paths simultaneously due to uniform rain systems can be significant. This results in an apparent frequency threshold to the diversity gain (Kaul-1980) and will be discussed later.

7.4.2.1.2.6 Anisotropy of Rain Cells Along a Front. There is a tendency for convective rain cells associated with frontal activity to occur in bands nearly perpendicular to the direction of movement of the front. The direction of motion of the cells within such a band tends to be along or slightly ahead of the direction of the front. Furthermore, the more intense cells tend to elongate in their direction of motion (Harrold and Austin-1974). Thus, two types of anisotropy are evident. The first is associated with the elongation of individual cells and is related to the probability of parallel paths passing through the same cells. The second is associated with the statistics of the vector separation between rain cells and is associated with the probability of parallel paths simultaneously intersecting two different rain cells. Fortunately, these two preferred orientations are nearly parallel, and thus the same corrective action is required in each case. Namely, the baseline orientation should be nearly perpendicular to these preferred directions.

7.4.2.1.2.7 Local Climatology. To a first order of approximation it is commonly assumed that the probabilities of rain cell occurrence are uniformly distributed over rather large regions of the earth's surface. This assumption may be invalidated by the presence of any one of the following features: mountains, large valleys, large bodies of water, or urban heat "islands". These features can give rise to nonuniform spatial distributions of rain cell probabilities.

Spatial distributions of rainfall accumulation are readily available in the meteorological literature; however, it is not currently known whether the use of these data is applicable to the question of earth terminal siting. For example, it may be argued that these rainfall accumulations are dominated by low rainfall rates and thus do not reflect the spatial distributions of intense rain cells that produce high attenuation levels on earth-space paths.

7.4.2.1.2.8 Switching Rates. The rate of change of attenuation on a single path is relatively slow. The highest rates reported are on the order of 0.6 dB/S at 11.8 GHz (Dintelmann, 1981) and 0.4 dB/S at 11.7 GHz (Nakoney, 1979), as reported in CCIR Report 564-3, Annex I (CCIR-1986). This implies that the decision and switching process for diversity paths may be quite slow and should pose no significant problem in the system design.

7.4.2.1.2.9 Connecting Link. The implementation of a path diversity system must incorporate a connecting link between the two earth terminals. If this link is closed, i.e., waveguide, coax, etc., its performance will be independent of meteorological variables and will not directly influence the reliability improvement provided by the use of path diversity. If, however, the connecting link operates above 10 GHz in the atmosphere, the joint fading statistics of the connecting link with the earth-space paths must be considered. This degrading effect appears to be small except for

cases of very long baselines or baseline orientations parallel to the earth-space propagation paths (Ferguson and Rogers-1978).

7.4.2.1.2.10 Multiple Earth Terminals. Substantial link reliability improvements result from the use of two earth-space propagation paths. Thus one may conjecture that further improvement might result from the addition of additional diversity paths. Determination of diversity gain for N diversity terminals shows that most of the gain is realized for two terminals with very little further increase in gain for additional terminals (Hodge-1974b).

7.4.2.1.3 Empirical Model for Site Diversity Gain

7.4.2.1.3.1 Description of the Model. The data available from early diversity experiments in New Jersey and Ohio (Hodge-1974a, Wilson-1970, Wilson and Mammel-1973, Gray-1973) were used to develop an empirical model for the dependence of diversity gain on separation distance, d, and single site attenuation, A (Hodge-1976a). The resulting model is of the form

$$G_D = a'(1-e^{-b'd}) \quad (7.4-5)$$

where the coefficients a' and b' depend upon the single site attenuation according to

$$a' = A - 3.6 (1-e^{-0.24A}) \quad (7.4-6)$$

$$b' = 0.46 (1-e^{-0.26A}) \quad (7.4-7)$$

The empirical diversity gain model has been improved (Hodge - 1982) to include other factors besides single-site attenuation and separation distance. Based on data from thirty-four diversity experiments, the improved model takes into account the following variables, listed in decreasing degree of dependence

- Separation distance d
- Single-site attenuation A
- Link frequency f

Elevation angle EL

Baseline-to-path angle Δ

The variable Δ is the angle between the intersite baseline and the ground projection of the Earth-space propagation path, measured in such a way that $\Delta \leq 90^\circ$. Using the definitions of Figure 7.4-2,

$$\Delta = |AZ - \beta| \quad (7.4-8)$$

The improved model also eliminates the implication of the earlier model that diversity gain approaches a constant (3.6 dB) for very deep fades. This has been found to be incorrect in more recent experiments.

The model gives the diversity gain as

$$G_D = G_d G_f G_E G_\Delta \quad (7.4-9)$$

where each factor contains the dependence of the variable denoted by its subscript. The first factor is the same as the gain of the earlier model:

$$G_d = a(1 - e^{-bd}) \quad (7.4-10)$$

The regression coefficients are given by

$$a = 0.64A - 1.6 (1 - e^{-0.11A}) \quad (7.4-11)$$

$$b = 0.585 (1 - e^{-0.98A}) \quad (7.4-12)$$

The remaining factors are

$$G_f = 1.64 e^{-0.025f} \quad (7.4-13)$$

$$G_E = 0.00492(EL) + 0.834 \quad (7.4-14)$$

$$G_\Delta = 0.00177 \Delta + 0.887 \quad (7.4-15)$$

In these formulas, d is in kilometers, A is in decibels, f is in gigahertz, and EL and Δ are in degrees. Figure 7.4-5 gives graphs of a , b , G_f , G_E and G_Δ to assist in application of the model.

The improved model predictions were compared with the original data set and produced an rms error of 0.73 dB. The data set used consisted of the results of thirty-four diversity experiments (including most of those listed in Table 7.4-1), covering a wide range of variable values.

Use of the empirical model is illustrated in Figure 7.4-6. It shows measured diversity gain as a function of average single-site attenuation for the VPI and SU SIRIO Diversity Experiment (Towner, et al - 1982). As indicated, the curve applies to one full year of data at 11.6 GHz. The figure also shows the predictions of the empirical model. The improved version of the model appears to give a better agreement with experimental measurements than the original version. However, the measured diversity gain falls well below that predicted for single site attenuation values above about 11 dB. The reason for this typical behavior is not known, but it could be attributed to the limited time period (one year), or to the especially low elevation angle (10.7°).

7.4.2.1.3.2 Extension of the Empirical Model. Kaul (1980) has introduced meteorological considerations to the original empirical model which establish practical limits on the diversity gain depending on A , f , EL and other system parameters.

The extended empirical model considers that diversity gain is only realized when spatially nonuniform rain rates occur near the ground station. (A ground system imbedded in a uniform rain experiences zero diversity gain.) Convective (thunderstorm) rains are assumed to represent these non-uniform rain systems. Rice and Holmberg (1973) described rain types analytically as Mode 1 (thunderstorm) and Mode 2 (stratiform) rains (see Section 3.2). Using the Rice and Holmberg model, the cumulative distributions of

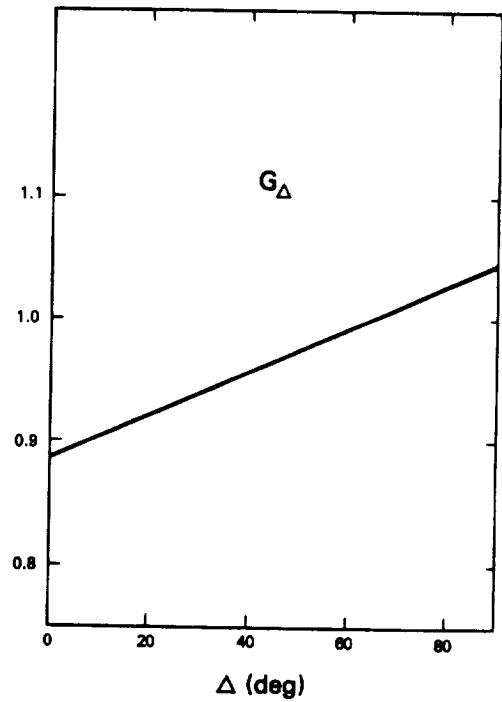
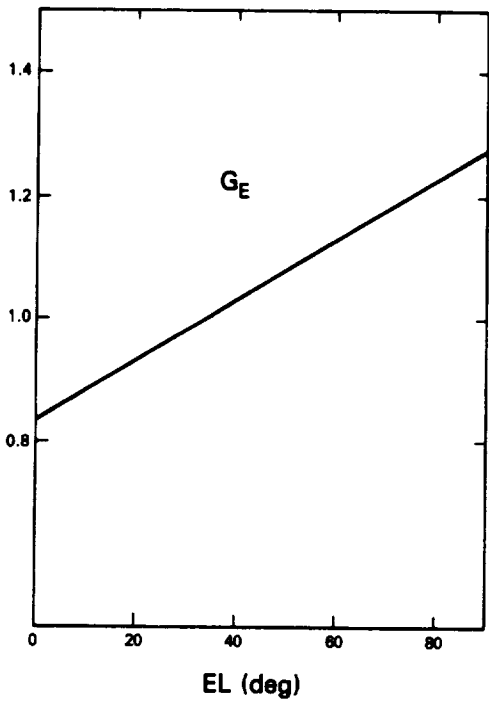
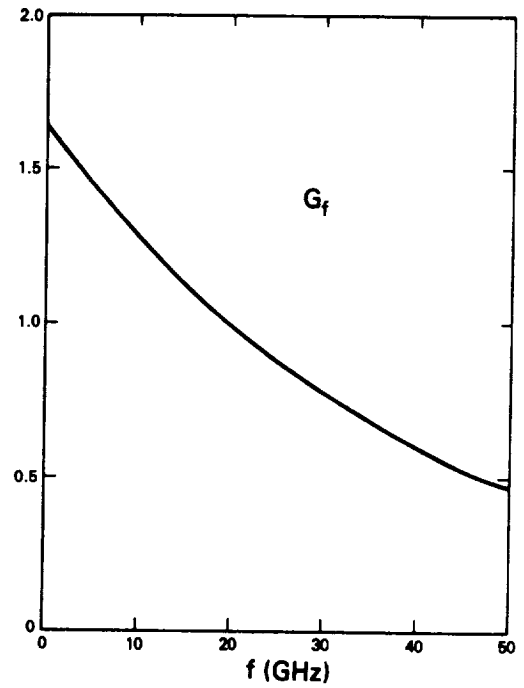
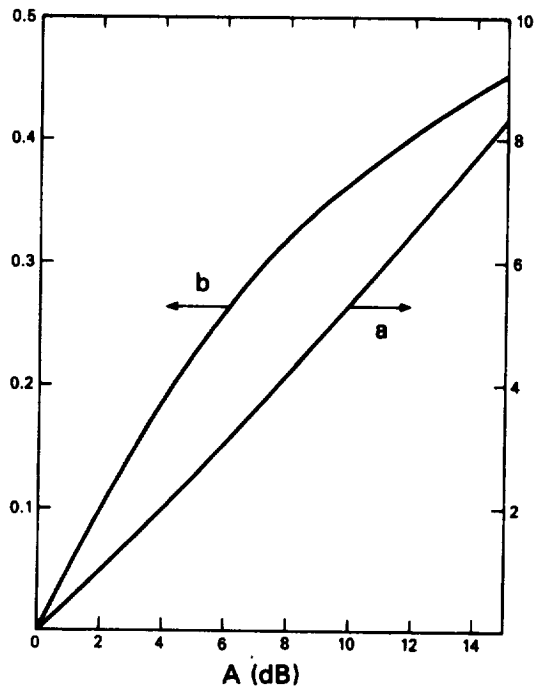


Figure 7.4-5. Parameters of Improved Diversity Model

5-6

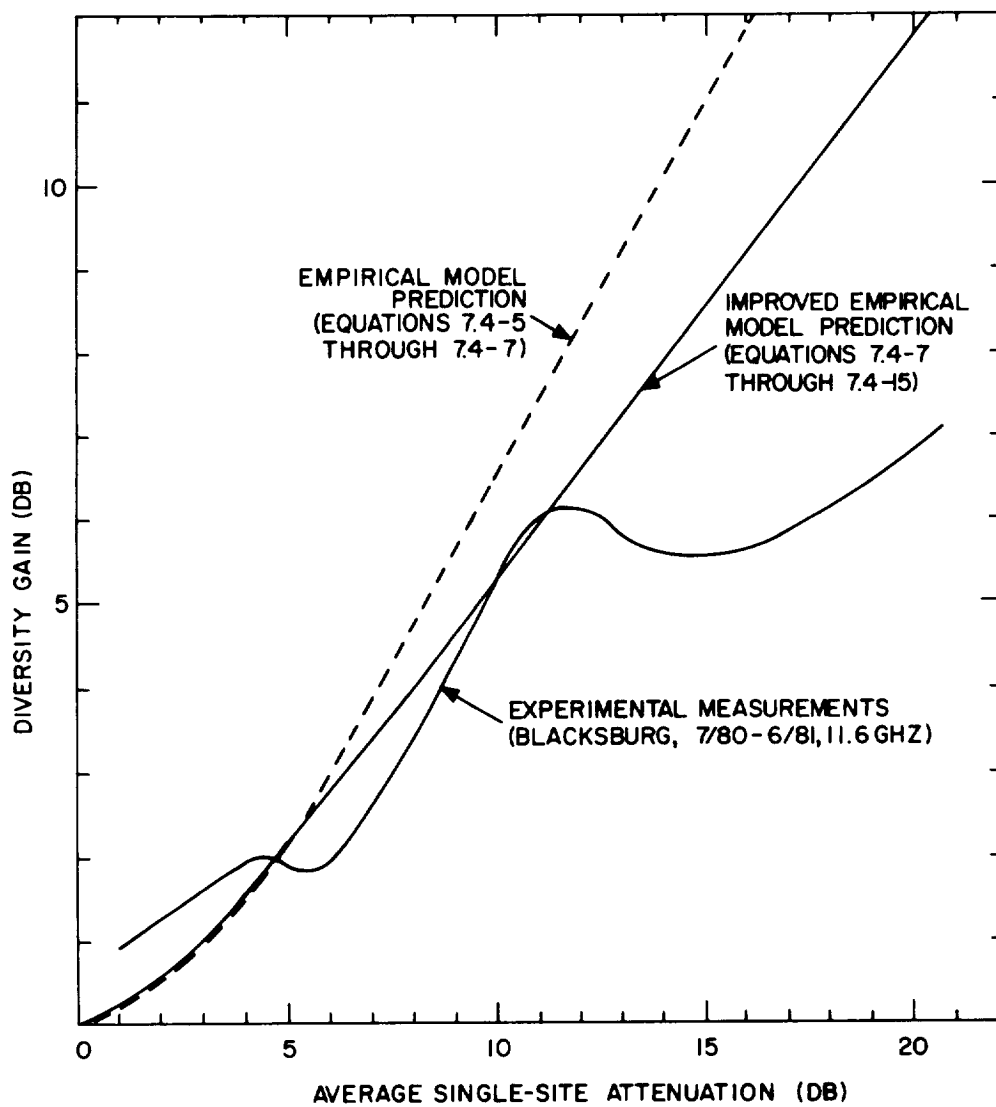


Figure 7.4-6. Comparison of Diversity Models and Experimental Results

total rain rate and uniform (Mode 2) rain rate may be developed as shown in Figure 7.4-7. Diversity gain will be obtained only for that portion of time between the stratiform and total rain curves. For $\beta = 0.3$ and $R < 10$ mm/h, this time is small (7.6 h/yr) and decreases (increases) as β and M decrease (increase). Therefore diversity gain will be large in Florida ($M \approx 1000$ mm and $\beta = 0.7$; $M\beta \approx 700$ mm) but will be small in Los Angeles ($M \approx 250$ mm and $\beta = 0.1$; $M\beta \approx 25$ for a given percentage of time). It appears that the $M\beta$ product is a good measure of the available diversity gain.

The amount of diversity gain available is also a function (to first order) of frequency, elevation angle and other meteorological parameters (height of the zero degree isotherm, etc.) as described in the attenuation model of Crane (1980). The results for a 30 GHz earth-space signal to a 40 degree elevation angle station located at sea level are shown in Figure 7.4-8. The difference between the attenuation arising from all rain events and uniform (stratiform) events is the maximum gain available for a diversity system. The time has been normalized to the amount of time the rain rate exceeds 0.25 mm/h (0.01 inch/h) in a year (350h). This same threshold value was selected by Lin (1973).

The total diversity gain available (see Figure 7.4-8) is the difference between the attenuation associated with all rain events and the attenuation attributed to stratiform (uniform) rain events. The maximum diversity gain available for one additional earth station (total of two identical earth stations) is G_1 and is computed from the cumulative distribution determined by the relation (Hodge-1978)

$$P_{cn}(A) = \left\{ P_c(A) \right\}^n \quad (7.4-16)$$

where:

n = the number of (identical) earth stations,

Figure 7.4-7. Cumulative Distribution of Rain Rate for Uniform and All Rain Events

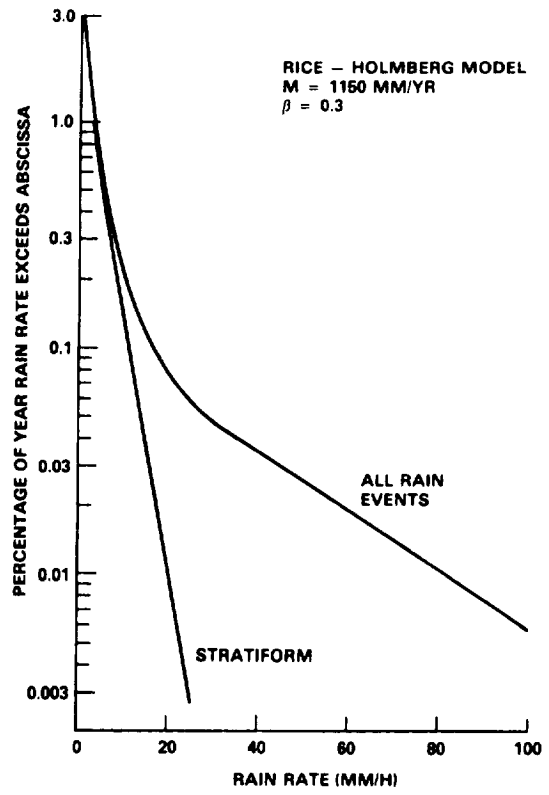
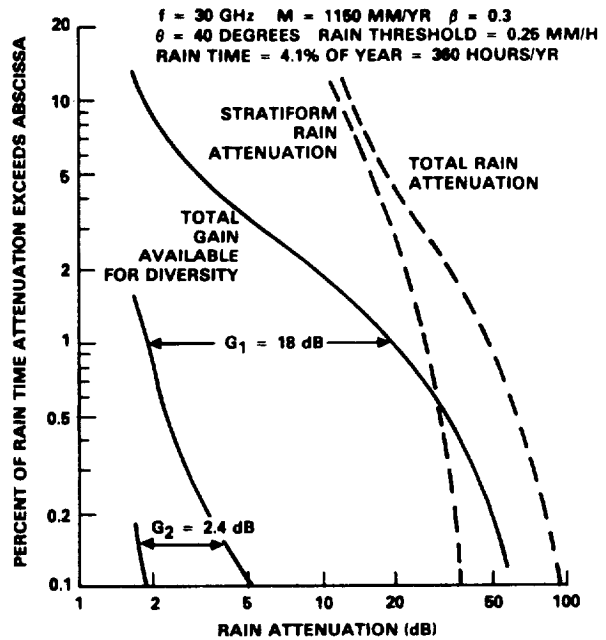


Figure 7.4-8. Cumulative Distribution of Total and Stratiform Rain Attenuation Plus Gain Available for Diversity Systems



$P_c(A)$ = the percent of time the attenuation A is exceeded for a single site, and

$P_{cn}(A)$ = the percent of time the attenuation A is exceeded for n identical sites.

G_1 and G_2 (the gain added by a third station) are shown in Figure 7.4-8. Plots of G_1 and G_2 versus the total attenuation on the worst path are given in Figure 7.4-9 for the region with $M = 1150$ and $\beta = 0.3$. The corresponding plots for a region with $\beta = 0.7$, such as Florida, are also given. Note the shift off zero which arises due to the effect of the uniform rains. For the case of $\beta = 0.7$ the gain G_1 saturates. This saturation prevents unrealistic system gains from being estimated as shown earlier. The saturation effect is believed to exist whenever the Mode 1 rain term dominates, but this has not been proven.

The maximum diversity gain G_1 for a two-station diversity system at selected frequencies is shown in Figure 7.4-10. Here the effects of stratiform rain at higher frequencies are clearly evident. For example at 45 GHz the zero diversity gain intercept occurs near 40 dB attenuation which will be observed about 0.4% (35 hours) of each year. Therefore for 45 GHz system links which can accommodate outages in excess of 35 hours per year, a diversity system will reduce the outage time or reduce the link margin required for 0.4% availability by only a small amount.

Based on the experimental results (Goldhirsh- 1979) and the analytic results (Morita and Higuti- 1978 and Wallace - 1981) the term G_1 may be related to the empirical a' multiplier by the approximate relation

$$a' \approx 0.9 G_{D1} \quad (7.4-17)$$

Also the station separation dependence may be retained as before so that

$$G = 0.9 G_1(1 - e^{-b \cdot d}) \quad (7.4-18)$$

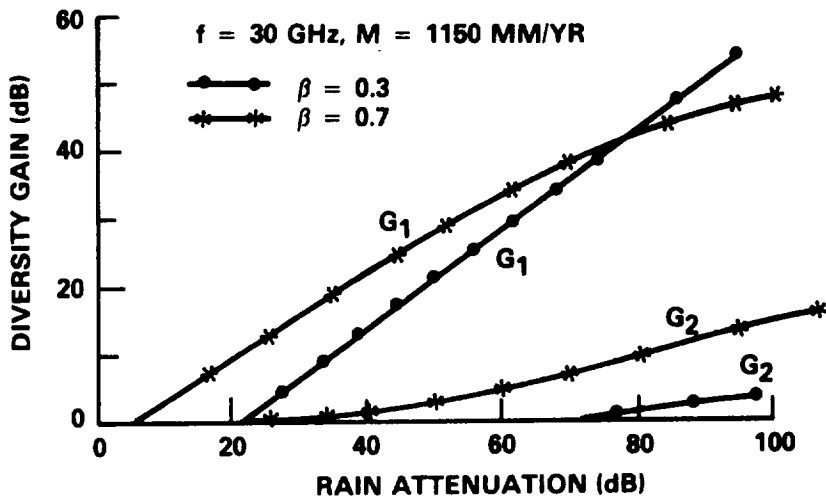


Figure 7.4-9. Maximum Diversity Gains G_1 (Two Stations) and G_2 (Three Stations) Versus Single-Site Attenuation

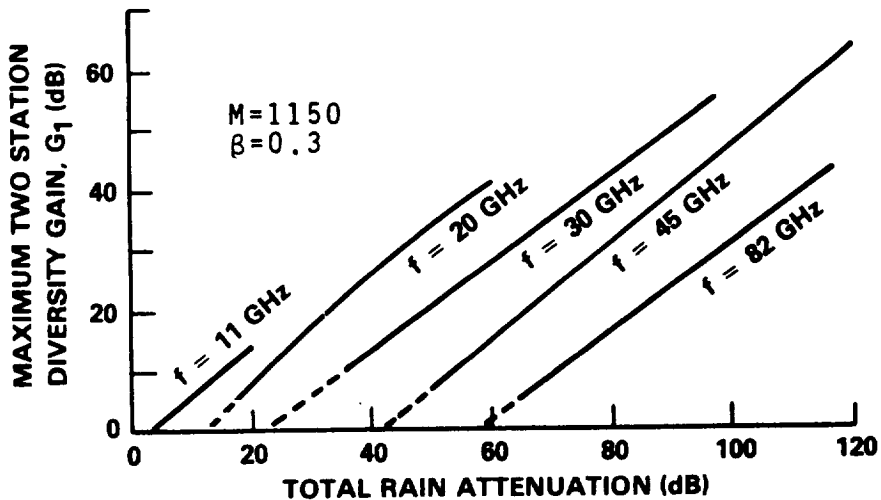


Figure 7.4-10. Maximum Diversity Gain, G_1 Versus Attenuation for Selected Frequencies

except that

$$b'' = 0.46 (1 - e^{-0.24(A-A_i)}), A > A_i \quad (7.4-19)$$

which accounts for the frequency dependent intercept attenuation A_i as shown in Figure 7.4-10.

The observation that diversity gain is obtained only for nonuniform rains has been used to devise a very simple approximation to diversity gain versus single-site attenuation (Allnutt & Rogers - 1982). As shown in Figure 7.4-11, the relation is assumed to be approximated by two straight line segments. One line is parallel to the "ideal diversity gain" curve (diversity gain = attenuation). The second line joins the origin and the first line at a point called the "knee." The single-site attenuations at the "knee" and the "offset" determines the relation for a particular location, frequency, and elevation angle. Site spacing and baseline orientation are assumed to be such that, to first order, site separation effects are removed. The value of the "offset" attenuation is the single-site attenuation exceeded for 0.3% of the time, which is assumed to correspond to uniform rainfall. The "knee" attenuation is the single-site attenuation corresponding to a 25 mm/hr rain rate, considered to be the breakpoint between stratiform and convective rain. This simple model provided a good fit to one year of radiometric measurements obtained in West Virginia, at 11.6 GHz. However, the fit to data from Austria and Florida was poor. A subsequent refinement to the model (Allnutt & Rogers-1983) utilized the CCIR rain attenuation model as modified by CCIR Interim Working Party 5/2 in May 1982. These predictions were much more consistent, and a clear trend of increasing diversity performance with elevation angle and rain convectivity was established.

7.4.2.1.4 An Analytical Diversity Model

An alternate model of site diversity has been proposed (Wallace-1981) that is derived from analytical representations of the joint

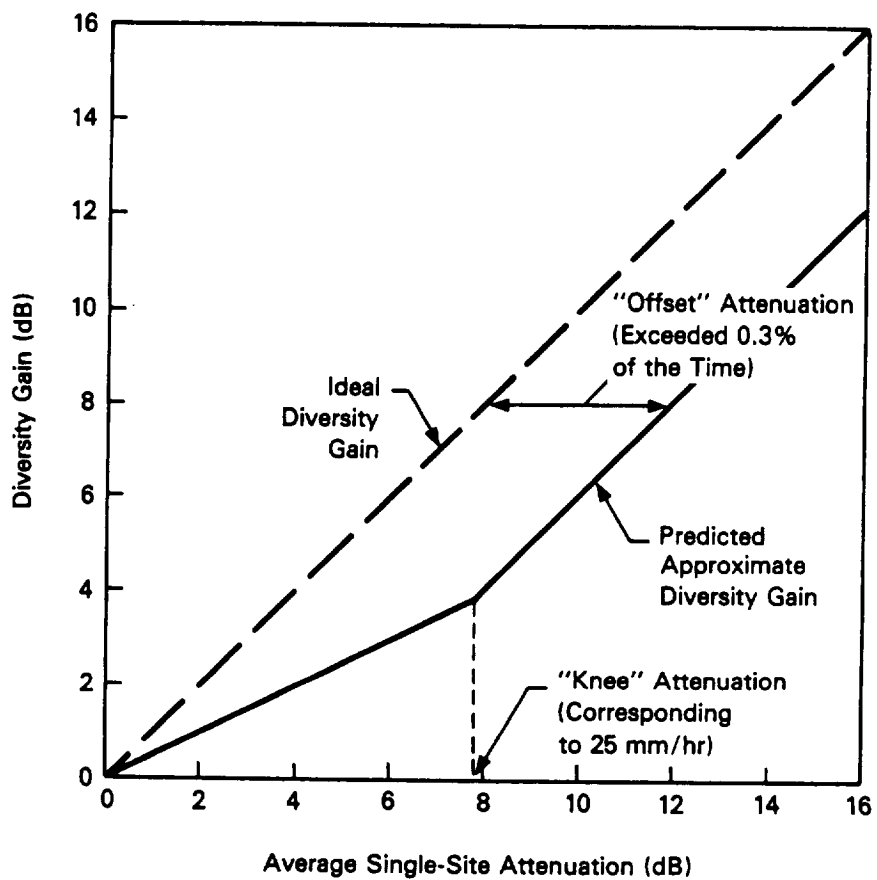


Figure 7.4-11. Construction of Approximation to Diversity Gain Prediction

site rain attenuation statistics. It is based on the well-known observation (Lin-1973) that rain attenuation in decibels, conditioned on the presence of rain, is approximately log-normally distributed. This is expressed analytically by the following:

$$\text{Prob} (A < a) = F_A(a) = P_0 K \Phi(Z, m, \sigma) \quad (7.4-20)$$

where

A = attenuation in decibels, a random variable

a = a particular value of A

$F_A(a)$ = cumulative distribution function (CDF) of A

P_0 = probability of rain

K = $\log_{10} e$, a scaling factor

$$\Phi(z, m, \sigma) = \frac{1}{\sqrt{2\pi} \sigma} \int_0^z \exp \left[-\frac{1}{2} \left(\frac{x-m}{\sigma} \right)^2 \right] dx \quad (7.4-21)$$

m = mean of $\log A$

σ = variance of $\log A$

The "exceedance probability" or "time percentage of exceedance" customarily used as the abscissa in presenting attenuation or rain rate statistics is the inverse, or one minus, the CDF (see Section 6.3.1.1). The factor P_0 expresses conditioning on the presence of rain mentioned above. This conditioning effectively reduces the time during which the log-normal distribution applies to the fraction of time that it is raining. The parameter m is the same as the logarithm of the median attenuation during the time it is raining, or the value that is exceeded for half the raining time. σ is a measure of variability of the attenuation. It is large if the attenuation is much greater or much less than the median value for significant periods of time. Typical values of median attenuation,

or 10^m , lie in the 0.3 to 0.5 dB range for 16 GHz links (Lin-1973), and understandably increase with frequency. σ is typically 0.5 to 0.8 and is highly dependent on the nature of the rain in a given location.

Given a log-normal estimate of the rain attenuation at a single ground station, it is a natural step to hypothesize that the attenuation experienced on links to two diversity sites is approximately jointly log-normal. This means that the logarithm of the attenuations at the two sites have a joint CDF that is bivariate Gaussian. The attenuation values are probabilistically related by a correlation coefficient, r , that varies with the site spacing. When the sites are distant from each other, we can say that their respective rain attenuations are uncorrelated, which corresponds to $r = 0$. The correlation coefficient increases to a maximum of one as the sites become closer together. One would intuitively expect the diversity gain achieved with two sites to be an inverse function of this correlation coefficient.

The effective amount of rain attenuation experienced by a diversity pair of earth stations is just the minimum of the values of attenuation seen at each site, since ideally one would always be using the site that has the least. Applying this fact, the CDF of the diversity pair rain attenuation can be determined from the joint CDF of the attenuation of the individual sites. This was done by Morita and Higuti (1978) using the joint log-normal hypothesis. The resulting CDF is also approximately log-normal, but with parameters m and σ both less than the corresponding parameters for either site. By comparing the single-site attenuation CDF with the diversity pair attenuation CDF, the diversity gain can be found. This has been done for a range of parameter values, and the results are shown in Figure 7.4-12. The axes in this figure are normalized by dividing the variables by the median single-site attenuation value, 10^m . A significant observation made from the figure is the insensitivity of diversity gain on the value of σ , except for very low values of r .

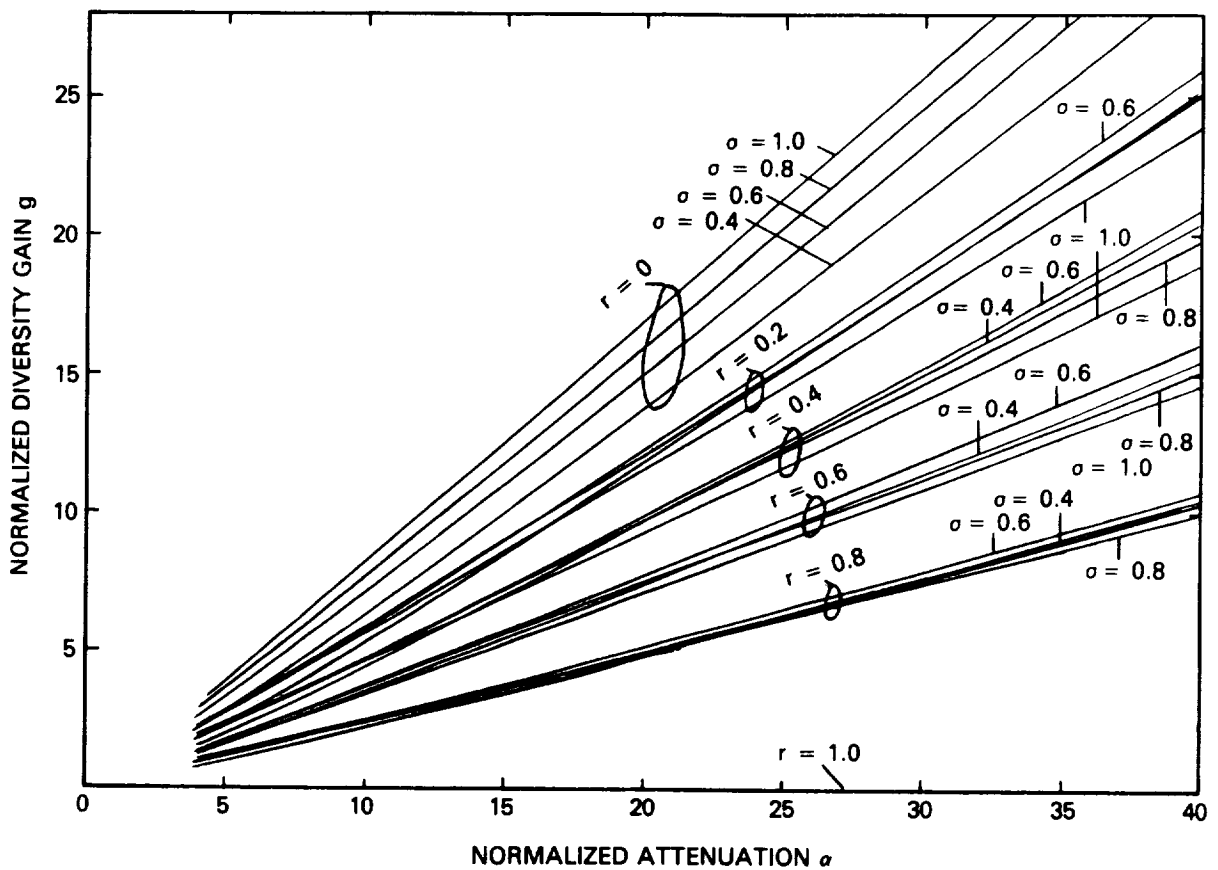


Figure 7.4-12. Diversity Gain Versus Attenuation for Varying Distribution Parameters (Normalization is with Respect to Median Attenuation)

A drawback of this analytical model is that it requires values of parameters that are not normally computed in current experiment data analysis. Specifically, the median value of attenuation, conditioned on the presence of rain, is usually unknown, as is the correlation coefficient. Morita and Higuti (1978) computed a theoretical correlation coefficient as a function of site separation that is consistent with Japanese experimental results. However, there is some evidence suggesting that the Japanese correlation model does not apply as well to U.S. data (Wallace-1981). It is likely that the correlation coefficient is highly dependent on other factors besides site separation, such as local "microclimate" variations and orographic effects (Allnutt-1978).

7.4.2.1.5 Relative Diversity Gain

Based on radar-derived diversity gain data, Goldhirsh (1975) observed that the frequency dependence of site diversity gain can be eliminated by introducing a new parameter: relative diversity gain. Relative diversity gain $G_r(d)$ for any particular site spacing d is equal to the measured diversity gain at spacing d and frequency f divided by the maximum diversity gain achievable at that frequency:

$$G_r(d) = G_d(d, f) / \text{Max}[G_d(d, f)] \quad (7.4-22)$$

The maximum achievable diversity gain, assumed to be that corresponding to statistically independent rain attenuation at the two diversity sites, is not precisely defined. For any particular single-site attenuation value, the diversity gain approaches an asymptotic value as separation distance is increased, but it is often difficult to say what that value is. Goldhirsh assumed that 35 or 40 km was the distance giving the maximum diversity gain for purposes of defining G_r .

An analytical best-fit to the relative diversity gain versus site separation curve was found by Goldhirsh (1982) to be as follows:

$$G_r(d) = 1 - 1.206 \exp(-0.53 \sqrt{d}) \quad (7.4-23)$$

The difference between radar-derived G_r values and this function was less than 5% over the $d = 1$ to 30 km range.

7.4.2.2 Orbit Diversity

As already discussed, orbit diversity refers to the use of two satellites at separate orbital positions, which provide two paths to a single ground terminal (Ippolito-1986). Orbit diversity is generally less effective than site diversity for rain fade mitigation because the diversity paths are more highly correlated. Nevertheless, orbit diversity has the advantage that the two satellites can be shared (as part of a resource-sharing scheme) with many ground sites. This is in contrast to the case of site

diversity, where the redundant ground site can generally be dedicated to only one primary ground site (Matricciani-1987). Therefore, site diversity is somewhat inefficient in the sense that the redundant ground site is not used most of the time. On the other hand, if an orbit diversity scheme does not take advantage of its capability for resource-sharing with several ground sites it, too, is inefficient and is likely to prove too expensive for the amount of diversity gain that it does provide.

Of course, operational considerations other than rain fades can also make the use of orbit diversity more attractive. Examples of such operational considerations include satellite equipment failures, and sun transit by the primary satellite, both of which require handover to a redundant satellite to maintain communication. So the use of a redundant satellite for other reasons in addition to rain fades can help to make orbit diversity economically practical.

If a ground terminal is to take full advantage of orbit diversity, it really should have two antenna systems, so that the switching time between propagation paths can be minimized. If the terminal has only one antenna system with a relatively narrow beamwidth, switching time can be excessive because of the finite time required to slew the ground antenna from one satellite to another, and because of the finite time needed for the receivers to re-acquire the uplink and downlink signals. Of course, the use of two spatially separated ground antennas provides an opportunity for site diversity in addition to orbit diversity.

Satellites in geostationary orbit are desirable for orbit diversity because they appear to the ground station to be fixed in space. Such orbits simplify satellite acquisition and tracking, and alleviate satellite handover problems. However, satellite coverage of high northern and southern latitudes is limited - requiring ground antennas at these latitudes to operate at low elevation angles. In addition, rain attenuation is greater at low elevation angles because of the longer path lengths through rain cells. To overcome this difficulty with high-latitude stations, elliptical

orbits whose apogees occur at high latitudes can be used, allowing satellite coverage for a relatively large fraction of the orbit period. However, not only are the advantages of geostationary orbits then lost, but in addition several satellites must be used in order to provide coverage at all times.

Although data concerning the improvement achievable with orbit diversity are currently rather sparse, recent predictions of the achievable improvement have been made (Matricciani-1987). One configuration that has been analyzed consists of:

1. A ground station at Spino d'Adda in Northern Italy
2. Satellite 1 (Italsat) at 13 deg. E longitude
3. Satellite 2 (Olympus) at 19 deg. W longitude.

For a 20 GHz downlink, the predicted single-path and double-path statistics are shown in Figure 7.4-13. The diversity (double path) predictions shown in this figure assume that Satellite 1 is normally used, and that Satellite 2 is switched in only when the rain attenuation for Satellite 1 exceeds some selected value. Because Satellite 2 would therefore be used only a small fraction of the time, it can be time shared with several ground stations for large-scale orbit diversity. The predictions are based on single-path measurements of the rain-rate probability distribution, and the joint distribution for the double-path attenuation is assumed to be log-normal.

Measurements of orbit diversity improvement have been made (Lin, et al-1980) for a configuration consisting of:

1. A ground station at Palmetto, GA
2. Path 1 - 18 GHz radiometer pointed in direction of COMSTAR D1 at 128 deg. W longitude
3. Path 2 - 19 GHz beacon of COMSTAR D2 at 95 deg. W longitude.

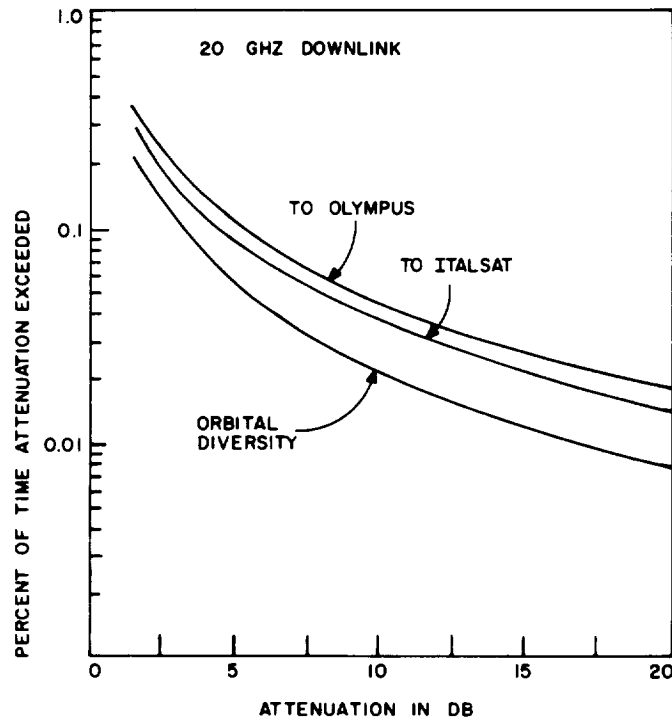


Figure 7.4-13. Predicted Orbit Diversity Performance at Spino d'Adda, Italy

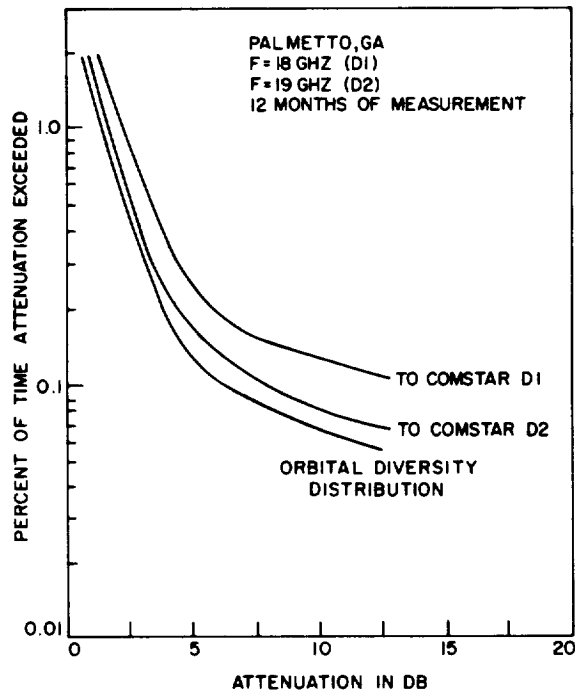


Figure 7.4-14. Orbital diversity measurements at Palmetto, GA

Figure 7.4-14 shows measurement results at 18 and 19 GHz. One might expect the diversity gain to improve markedly as the angle subtended increases. However, it turns out (Ippolito-1986) that except when the single-path attenuation is large to begin with, the diversity gain actually increases rather slowly with the subtended angle. This is because most of the rain attenuation is at low altitudes, so that even widely diverging propagation paths often pass through the same rain cell.

Of course, the measurements in Figure 7.4-14 cannot be directly compared with the predictions in Figure 7.4-13 because the rain statistics and geometrical configurations differ. Nevertheless, the limited measurements and calculations that have been made both indicate that a modest diversity gain is achievable from orbit diversity. In any case, orbit diversity gain is less than that achievable with site diversity. Figure 7.4-6, for example, shows that one can expect roughly five dB site diversity gain when the average single-site rain attenuation is 10 dB. Figures 7.4-13 and 7.4-14, on the other hand, show that one can expect only two or three dB gain from orbit diversity.

7.4.3 Signal Diversity

Rain attenuation is not only spatially sensitive, as discussed earlier, but also time and frequency sensitive. This property provides an opportunity to combat rain fades by adjusting certain signal parameters in accordance with existing propagation conditions.

Suppose, for example, that the ground terminal continually adjusts its uplink power to maintain a constant signal level at the satellite, regardless of propagation conditions. Then rain fade mitigation is achieved without a need for redundant signal paths. In a similar way, the satellite can use transmitter power control to mitigate downlink rain fades.

Alternatives to transmitter power control for combatting the time dependence of rain fades in digital communication systems are to use either forward error correction (FEC) or data rate control. Rather than raising the transmitter power when propagation conditions worsen, one can temporarily apply FEC to improve the power margin at the expense of a wider signalling bandwidth or longer transmission time. However in some situations, both power and bandwidth in the digital communication system may be limited. If this is the case, one can always temporarily lower the data rate to improve the power margin - the price being a slower communication rate.

The natural way to exploit the frequency dependence of rain attenuation is to use frequency diversity. When rain attenuation rises to some specified value, high priority traffic can be diverted to a lower frequency that is less susceptible to rain fades. The price paid in this case is a reduction in channel capacity during rain fades, and the requirement for additional frequency assignments.

All of these techniques for incorporating signal diversity in satellite communication are discussed in the following paragraphs.

7.4.3.1 Power Control

The objective of power control is to vary the transmitted power in direct proportion to the attenuation on the link, so that the received power stays constant through rain fades. This can be employed, in principle, on either the uplink or downlink. There are two reasons for using power control rather than a very high transmitted power level to mitigate rain fades. When used on the uplink, the reason is usually to prevent the transponder on the satellite from being overdriven, or to keep from upsetting the power balance among several uplink carriers using the same transponder. (When multiple carriers share a non-linear transponder near saturation, variations in the input level of one of them are enhanced at the output.) When used on the downlink, the reason is

that a temporary power boost can be provided to combat fades on selected links while requiring only a modest increase in satellite solar array power. The array power not needed during clear-sky operation is used to charge batteries, which supply the energy needed to transmit the added power during fades.

Through power control, the maximum amount of rain attenuation that can be compensated is equal to the difference between the maximum output of the Earth station or satellite power amplifier and the output required under clear-sky conditions. The effect of power control on availability, assuming that control is perfect, is the same as having this power margin at all times. A perfect power control system varies the power exactly in proportion to the rain attenuation. Errors in the power control result in added outages, effectively decreasing this margin. Maseng and Baaken (1981) have studied this effective margin reduction due to power control delay.

A drawback of power control is a potential increase in intersystem interference. A power boost intended to overcome rain attenuation along the direct Earth-space path will produce an increase in power on interfering paths as well. If the same rain fade does not exist on these paths, the interference power received by interferees, such as other terrestrial stations, will increase. Due to the inhomogeneity of heavy rain, attenuation on interfering paths at large angles from the direct earth-space path will often be much less than the attenuation on that path. Terrestrial system interference caused by the earth station, although tolerable under clear-sky conditions, may therefore become intolerable in the presence of rain when uplink power control is used. Downlink power control will likewise increase the potential for interference with earth stations using adjacent satellites. A downlink power boost for the benefit of a receiving station experiencing a rain fade will be seen as an increase in interference by vulnerable stations that are not experiencing fades.

7.4.3.1.1 Uplink Power Control

A frequency-division multiple-access (FDMA) satellite communication system trying to operate with large spatial and time variations in rain fades will experience significant nonlinear distortion when fades are mitigated by the use of large power margins alone. Nonlinear distortion, which occurs when the satellite transmitter is operated near saturation, includes AM-to-PM conversion and generation of intermodulation products.

By continually adjusting the uplink power from each ground station in accordance with uplink fade conditions, variations in the operating point of the satellite TWTA can be minimized, thereby minimizing nonlinear distortion. However, this does not completely solve the problem because downlink rain fades must also be considered. Lyons (1976) showed that if the uplink power control algorithm accounts not only for uplink fades but also for downlink fades, good performance can be achieved in the presence of fading on both links by using uplink power control alone. Although individual signal levels at the satellite receiver will vary widely in this situation, the TWTA operating point will still remain relatively fixed so long as there is a sufficiently large number of users, all having controlled access to the satellite. So if deep fades occur on only a few of the uplink and downlink paths, variations in the received downlink signal levels will be relatively small, thus requiring smaller fade margins.

However, uplink power control of such systems requires that each station accessing the satellite possess knowledge not only of its uplink fade characteristics, but also of the downlink fade characteristics for all stations to which it is transmitting. Power control of all transmitting stations can be achieved from a single location at the cost of control delays, which result in relatively slow fade mitigation. If instead, we have distributed control in the sense that each station controls its own transmitted power, delays are minimized. However, performance may suffer because the total received uplink power at the satellite can no longer be

maintained approximately constant under widely fluctuating propagation conditions. Furthermore, with distributed control, fade information must be exchanged continually among all participating stations to make the system work.

These arguments indicate that if the uplink power control algorithm does not take into account the downlink fade characteristics, then power control can likely be applied only to single-service, single-user links. For such links, there are two types of uplink power control that can be used (Ippolito-1986). The first is a closed-loop system that adjusts uplink power in accordance with the satellite received signal level returned to the transmitting station via telemetry. The second is an open-loop system that adjusts uplink power in accordance with either the downlink signal (or beacon) level, or the attenuation calculated from ground-based radiometer or radar measurements. Figures 7.4-15 and 7.4-16 illustrate closed-loop and open-loop uplink power control for single-carrier links.

7.4.3.1.2 Downlink Power Control

More and more satellite communication systems are going to on-board signal processing, not only to improve bit error rate performance (in the case of digital modulation), but also to improve terminal interconnectivity and to make downlink performance independent of the uplink. On-board processing simplifies power control for rain fade mitigation (especially in FDMA systems) because the uplink power control algorithm no longer needs to take into account downlink fade conditions. Therefore, uplink and downlink power control can be done independently, which alleviates many problems associated with the use of FDMA during rain fades. This assumes that on-board processing includes demodulation to baseband, followed by remodulation onto a downlink carrier. The following discussion assumes that downlink power control can be accomplished essentially independent of the uplink regardless of whether or not on-board processing is being used.

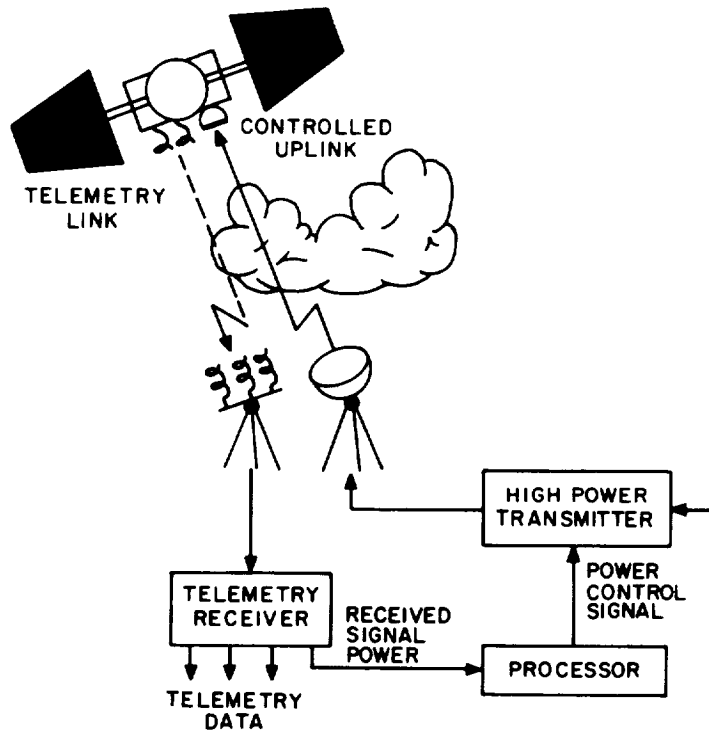


Figure 7.4-15. Closed loop uplink power control

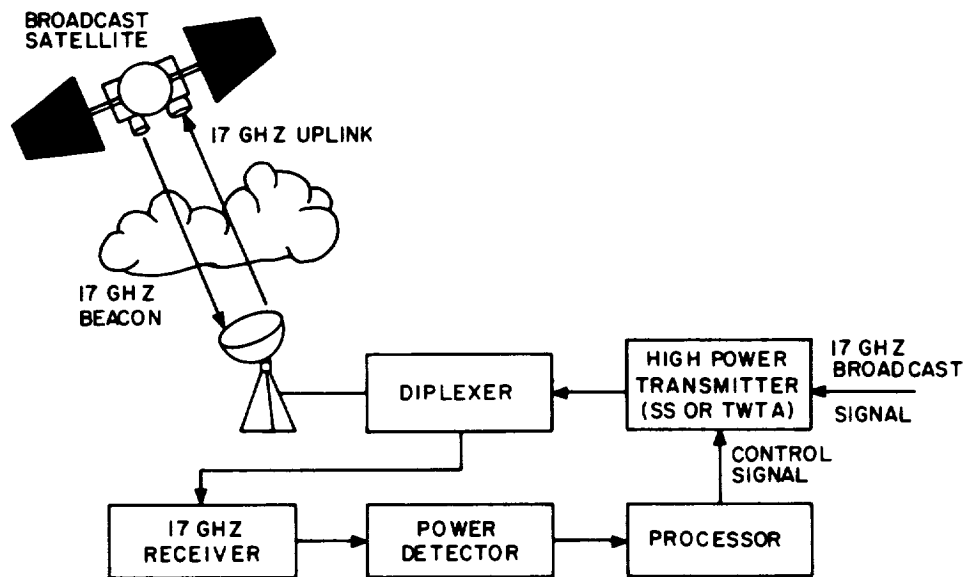


Figure 7.4-16. Open loop uplink power control

The satellite transmitter usually has only one or two switchable output power levels, so downlink power control for rain fade mitigation is less flexible than uplink power control. One example is ACTS (Holmes and Beck-1984), which operates at 30/20 MHz and has a transmitter output power of either 8 or 40 watts. The high-power mode therefore provides 7 dB additional margin against rain fades. Because the entire antenna footprint receives the added power in the high-power mode, those stations not experiencing rain attenuation will receive more power than they require. Downlink power control is therefore not efficient in directing the added power to the stations needing it.

This problem with downlink power control is somewhat alleviated by the use of switchable spot beams on the satellite. The reason for this is that the antenna footprints are relatively small, thereby allowing added downlink power to be directed only to those terminals that require it. In fact, switching to spot beams is, in itself, an effective technique for mitigating rain fades, even when satellite transmitter power is not controlled. The use of downlink power control together with switchable antenna beams might better be called EIRP control rather than power control.

7.4.3.2 Adaptive Forward Error Correction. In Time Division Multiple Access (TDMA) systems, each earth station is periodically assigned a time interval during which it alone may access the entire satellite bandwidth. The time between accesses by a given station is called the TDMA frame period, and each station is assigned a fixed fraction of the frame. This fraction is proportional to the traffic the station is carrying, or to its average bit rate. By leaving a portion of the frame period unassigned, those stations experiencing rain fades can be temporarily assigned a larger fraction of the frame for fade mitigation. One way to exploit this additional time resource is to apply forward error correction (FEC). The same number of information bits is transmitted each frame period as before. However FEC reduces the required received signal level, thereby at least partially offsetting the loss in received power

experienced during rain fades. Alternatively, the additional allotted time allows a reduction in data rate during rain fades. Data rate control will be discussed further in paragraph 7.4.3.4.

This scheme is adaptive in the sense that FEC is applied only when the rain attenuation has exceeded a selected threshold. When FEC is used, the symbol timing hardware still operates at the same fixed rate. In principle, FEC can be implemented in software, which may be advantageous in some systems.

There is a limit to the mitigation that coding can provide (Bronstein-1982). This is because a minimum symbol energy must be maintained to ensure proper recovery of symbol timing in the receiver. Therefore, because the symbol rate is fixed, a minimum received signal power level must be maintained. The fade margin achieved with FEC must be traded off against the reduction in total system capacity that occurs. As propagation conditions worsen, the fraction of the frame duration needed for fade mitigation must increase, thereby reducing the fraction available for use during clear weather.

FEC can be used to mitigate either uplink or downlink fades. A station affected by uplink fades would encode its entire burst - lengthening its burst period by its allotted reserve time. Each station receiving that station's burst must decode the data in that burst. In contrast, a receiving station affected by downlink fading will receive all its data in coded form. Transmitting stations must encode that portion of the data that is transmitted to the affected station. It is apparent that a central control station must dynamically assign the extra time to the stations that require it. Furthermore, all stations in the network must know which stations require coding.

A satellite using on-board signal processing essentially decouples the downlink from the uplink, which allows the reserve time to be used more efficiently. Only those transmitting stations experiencing uplink fades then need to encode their data. The

satellite would not only demodulate the uplink signal, but would also decode those uplinks affected by fading. The satellite would then encode for downlink transmission only those signals affected by downlink fades. The reserve time used by faded uplinks is, in effect, freed up to be used by faded downlinks.

Acampora (1979, 1981) has studied the performance of a system using FEC coding to mitigate downlink fades. The hypothetical TDMA system studied operated in the 12/14 GHz bands, using a bent-pipe transponder. The traffic model used assigned traffic between the 100 most populous U.S. cities in proportion to their population ranking. The Earth stations were given a built-in fade margin, and the reduction in this margin made possible by time resource sharing was found, using a convolutional FEC code that gave a 10 dB power saving. A typical result of this analysis showed that reserving six percent of the frame period as a shared resource provided an outage of 30 minutes per year (.0057% of the time) with 9 dB less rain margin than would otherwise be needed.

Gains of up to 8 dB have been reported (Mazur, et. al.-1983) for 14/11 GHz TDMA networks with 32 ground terminals. Five of the 8 dB comes from the coding gain provided by a rate 1/2 code. The other 3 dB comes from a QPSK/PBSK switch capability.

7.4.3.3 Frequency Diversity. A straightforward method of improving the reliability of a millimeter-wave satellite system is to provide the capability for Earth stations to switch to a lower frequency band (say C-band) when rain fades occur at the normal operating band. This would require a satellite with a dual-band payload and a dual-frequency Earth station capability, but the improvement in overall system reliability may be worth the added cost. The bandwidth required in the lower, high-reliability, frequency band need be only a fraction of the total bandwidth used, since it needs to accommodate only the traffic of those stations undergoing rain fades. The probability of rain outage on a particular link with such a frequency diversity system is equal to the sum of the probabilities of two mutually exclusive events: (1) that the

reserve band is fully occupied by other links when a rain fade occurs, and (2) that a link is assigned to the reserve band, but the rain rate is so great that the reserve band suffers an outage while the link is using it. If 4/6 GHz is used for the reserve band, the probability of the second event can be considered nil. If the reserve band is wide enough for N links, the probability of the first event is the probability of N+1 simultaneous fades. The bandwidth required in the reserve band is therefore established by the simultaneous fade probability over all the Earth stations in the system. The dependence of system performance on simultaneous fade probability is common to all resource-sharing schemes. Because of this, it will be discussed separately later (paragraph 7.4.4).

7.4.3.4 Data Rate Control. If the satellite receiver monitors the uplink received signal level and feeds this information back to the transmitter, then various properties of the transmitted signal can be varied to mitigate uplink rain fades. Transmitter power control (paragraph 7.4.3.1) provides an example. However, we can vary the data rate rather than the transmitted power to accomplish the same results. This is because in digital data transmission the measure of system performance is the bit error rate, which ideally depends only on the received bit energy-to-noise density ratio. The bit energy in turn is equal to the received signal power divided by the data rate. So in principle, lowering the data rate by a factor of two, for example, has the same effect on error rate performance as raising the transmitted power 3dB.

It has been shown (Cavers-1972) that data rate control can completely eliminate the effect of fading if the feedback from the receiver is assumed to be ideal (no control delay). Even when control delay is included, however, data rate control can often be more effective than diversity reception, at a cost of bandwidth expansion to accommodate transmission of control information.

As we have seen in paragraph 7.4.3.2, a possible fade mitigation technique for TDMA communication is to leave a portion of the frame period unassigned - making it temporarily available to those

stations experiencing rain fades. Data rate control of such systems involves transmitting or receiving the same number of information bits each frame during the fade, but reducing the data rate in order to fully occupy the additional allotted time. As discussed above, this increases the transmitted energy per bit, which offsets the loss in received power during the fade.

For data rate control to work, the ground stations must at least have the synchronization hardware required to switch from the normal symbol rate to a lower rate. However, to achieve performance approaching that obtained when there are no fades, the use of several selectable data rates is required, with little delay in the control loop.

As with adaptive FEC coding, data rate reduction can be used to mitigate both uplink and downlink fades. Again, on-board signal processing essentially makes uplink data rate control independent of downlink control, thereby making efficient use of the reserve time and simplifying the control procedure. However, the satellite receiver must be capable of synchronizing to several data rates, which complicates the on-board processing hardware.

7.4.4 Simultaneous Fade Probabilities

When a resource-sharing scheme is used to provide additional fade margin, the amount of the resource (time or frequency) that must be set aside to provide the required margin is highly dependent on the probability of simultaneous fades on two or more links. If sufficient resources are reserved to back up two links, for example, then the outage probability is the probability that the fade depth exceeds the added margin provided, or that three or more links are suffering fades at the same time.

The probability of simultaneous fades is also of interest in connection with site diversity systems (paragraph 7.4.2.1). In that case, the sites are generally assumed to be close enough to each other to be affected by the same storm system. In the case of

resource-sharing systems, we are concerned with fades simultaneously occurring on links to Earth stations separated by much larger distances as well. A naive approach would be to assume that the rain attenuation at a given Earth station is statistically independent of that at another station substantially removed from the first. Closer examination reveals, however, that this is not the case.

Acampora (1981), in the analysis cited earlier, observed that the deep rain fades that are of concern are normally caused by thunderstorm activity, and that there is a definite correlation in thunderstorm activity at widely separated locations. In particular, thunderstorm activity is typically restricted to the four-month period from June through September, and to the quarter of the day lasting from 1:00 PM to 7:00 PM local time. Because of this, the occurrence of a deep fade at one site makes the probability of a deep fade at the same time at a second site much higher than the yearly average. The observation of the fade at the first site makes it highly probable that we are in the June-September, 1:00 PM - 7:00 PM thunderstorm period, therefore the chances of a thunderstorm at the second site are higher than average by a factor of at least $(12/4)(24/6)$, or 12, using the broad ranges of time given. In addition to this yearly-to-thunderstorm-period factor, α , a second factor β , accounts for the additional correlation of deep fades between sites that are spaced closely enough that they are affected by the same storm systems. This factor was considered by Acampora to range from 1, which implies independence of fades during the thunderstorm period, to a maximum value of 6. The factors α and β are applied as follows: The yearly average joint probability of the attenuation (A_1 and A_2) two sites exceeding their respective thresholds (T_1 and T_2) is given by

$$P(A_1 > T_1, A_2 > T_2) = \alpha \beta P(A_1 > T_1) P(A_2 > T_2)$$

ORIGINAL PAGE IS
OF POOR QUALITY

where the last two quantities are the individual yearly exceedance probabilities for the two sites. For $T_1 = T_2$, the factor $\alpha\beta$ is seen to be the diversity improvement defined in Section 7.4.1.

7.5 REFERENCES

- Acampora, A.S. (1979), "A Shared Resource TDMA Approach to Increase the Rain Margin of 12/14-GHz Satellite Systems," BSTJ, Vol. 58, No. 9 (Nov.) pp. 2097-2111.
- Acampora, A.S. (1981), "Rain Margin Improvement Using Resource Sharing in 12-GHz Satellite Downlinks," BSTJ, Vol. 60, No. 2 (Feb), pp 167-192.
- Allnutt, J.E. (1978), "Nature of Space Diversity in Microwave Communications via Geostationary Satellites: A Review," Proc. IEE, Vol. 125, p. 369.
- Allnutt, J.E. and D.V. Rogers (1982), "Novel Method for Predicting Site Diversity Gain on Satellite-to-Ground Radio Paths," Electronics Letters, Vol. 18, No. 5, pp. 233-235, 4 March.
- Allnutt, J.E. and D.V. Rogers (1983), "A Site Diversity Model for Satellite Communications Systems," IEE Third International Conference on Antennas and Propagation, April 1983, Norwich, U.K.,
- Arnold, H.W., D.C. Cox, H.H. Hoffman, and R.P. Leck (1979), "Characteristics of Rain and Ice Depolarization for a 19 and 28 GHz Propagation Path from a COMSTAR Beacon," Record, Int'l Conf. on Comm. (IEEE CH 1435-7/79/0000-0220), June.
- Bonhomme, R., B.L. Herdan, and R. Steels, (1984), "Development and Application of New Technologies in the ESA OLYMPUS Programme," Proceedings of the AIAA Comm. Sat. Sys. Conf., March.
- Braham, H.S., (1982), "Fleetsatcom - Current and Future," Int'l. Conf. on Comm. IEEE, pp. 6H.3.1-6H.3.5, June.
- Brayer, K., (1978), "Time, not Throughput, for Net Designs. Part 1: Techniques," Data Communications, October.
- Bantin, C. and R. Lyons (1978), "The Evaluation of Satellite Link Availability," IEEE Trans. Comm. Vol. COM-26, No. 6 (June), pp. 847-853.
- Brandinger, P. (1978), "Propagation Requirements for 30/20 GHz System Design," 1978 Spring URSI Meeting, Washington, D.C.

- Bronstein, L. M. (1982), "The Enhancement of Propagation Reliability for Millimeter Wave Satellite Communication Systems," Record, International Conference on Communication, Philadelphia, June, pp 1B.4.1-5.
- Calo, S., L. Schiff, and H. Staras (1978), "Effects of Rain on Multiple Access Transmission of Data via Satellite," Record, Internat. Conf. on Commun., Toronto, pp. 30.1.1-6.
- Castel, R.E. and C.W. Bostian (1979), "Combining the Effects of Rain-Induced Attenuation and Depolarization in Digital Satellite Systems," IEEE Transactions Aerosp. Elect. Syst., Vol. 15, No. 2, p. 299-301, March.
- Cavers, J.K. (1972), "Variable-Rate Transmission for Rayleigh Fading Channels," IEEE Trans. Comm., Vol COM-20, No. 1 (Feb.), pp. 15-22.
- CCIR (1978) "Allowable Noise Power in the Hypothetical Reference Circuit for Frequency-Division Multiplex Telephony in the Fixed Satellite Service," Recommendation 353-3, XIVth Plenary Assembly, Kyoto.
- Crane, R.K. (1980), "Prediction of Attenuation by Rain," IEEE Trans. Comm., Vol. COM-28, No. 9, pp.1717-1733.
- CSC (Computer Sciences Corp.) (1971), "Automated Satellite Terminal Control," RADC-TR-70-229, Volume I, for U.S. Air Force, Rome Air Development Center, March.
- Dintelmann, F. (1981), "Analysis of 11 GHz slant-path fade duration and fade slope," Electron. Lett., Vol. 17, No. 7, pp. 267-268.
- Donovan, R., R. Kelley, and K. Swimm, (1983), "Evolution of the DSCS Phase III Satellite through the 1990's," Record, Int'l. Conf. on Comm. IEEE, pp. C1.6.1-C1.6.9, June.
- Engelbrecht, R.S. (1979), "The Effect of Rain on Satellite Communications Above 10 GHz," RCA Review, June.
- Evans, J.V., (1986), "Twenty Years of International Satellite Communication," Radio Science, Vol. 21, No. 4, July-August.
- Freeny, A.E. and J.D. Gabbe (1969), "A Statistical Description of Intense Rainfall," Bell System Technical Journal, Vol. 48, p. 1789.
- Friedenthal, M.J., and E.K. Heist, (1976), "Fleet Satellite Communications Spacecraft," WESCON, September.
- Ghais, A., J. Martin, D. Arnstein, and H. Lewis, (1982), Summary of INTELSAT VI Communications Performance Specifications," COMSAT Technical Review, Vol. 12, No. 2, Fall.

- Giannone, B., E. Matricciani, A. Paraboni, and E. Saggese, (1986), "Exploitation of the 20-40-50 GHz Bands: Propagation Experiments with ITALSAT," Proceedings of the AIAA Communication Satellite Systems Conference, March.
- Goldhirsh, J. (1975), "Prediction Methods for Rain Attenuation Statistics at Variable Path Angles and Carrier Frequencies Between 13 and 100 GHz," IEEE Trans. Ant. Prop., Vol. AP-23, pp. 786.
- Goldhirsh, J. (1979), "The Use of Radar at Non-Attenuating Wavelengths as a Tool for the Estimation of Rain Attenuation at Frequencies above 10 GHz," Record, EASCON '79, pp. 48-55.
- Goldhirsh, J. and F. Robison (1975), "Attenuation and Space Diversity Statistics Calculated from Radar Reflectivity Data of Rain," IEEE Trans. Ant. Prop., Vol. AP-23, pp. 221.
- Goldhirsh, J. (1982), "Space Diversity Performance Prediction for Earth-Satellite Paths Using Radar Modeling Techniques," Radio Science, Vol. 17, No. 6, pp. (Nov.-Dec.).
- Graebner, J.C., and W.F. Cashmen, (1986), "Advanced Communication Technology Satellite: System Description," IEEE Transactions Comm., Vol. COM-16, September.
- Gray, D.A. (1973), "Earth-Space Path Diversity: Dependence on Base Line Orientation," 1973 G-AP/URSI Meeting, Boulder, Colorado.
- Gray, L.F. and M.P. Brown (1979), "Transmission Planning for the First U.S. Standard C (14/11 GHz) INTELSAT Earth Station," COMSAT Technical Review, Volume 9, Number 1, Spring.
- GTE (General Telephone & Electronics, Lenkurt, Inc.) (1972), Engineering Considerations for Microwave Communications Systems.
- Harrold, T.W. and P.M. Austin (1974), "The Structure of Precipitation Systems - A Review," Journal de Recherches Atmospherique, Vol. 8, pp. 41.
- Hodge, D.B. (1974a), "Path Diversity for Reception of Satellite Signals," Journal de Recherches Atmospherique, Vol. 9, pp. 443.
- Hodge, D.B. (1974b), "A 15.3 GHz Satellite-to-ground Path Diversity Experiment Utilizing the ATS-5 Satellite," Radio Science, Vol. 9, pp. 1.
- Hodge D B (1976a), "An Empirical Relationship for Path Diversity Gain," IEEE Trans. Ant. Prop. Vol. AP-24, pp. 250.

- Hodge, D.B. (1978), "Path Diversity for Earth-Space Communication Links," Radio Science, Vol. 13, pp. 481.
- Hodge, D.B. (1982), "An Improved Model for Diversity Gain on Earth-Science Propagation Paths", Radio Science, Vol. 17, No. 6, pp. 1393-1399.
- Hogg, D.C. (1968), "Millimeter Wave Communications through the Atmosphere," Science, Vol. 159, p. 39.
- Hogg, D.C. and T.S. Chu (1975), "The Role of Rain in Satellite Communications," Proc. IEEE, September.
- Holmes, W.M. Jr., and G.A. Beck, (1984), "The ACTS Flight System: Cost-Effective Advanced Communications Technology," AIAA 10th Communications Satellite Systems Conference, AIAA CP842, Orlando, Fla., pp. 196-201, March 19-22.
- Ippolito, L.J., Jr., (1986), "Radiowave Propagation in Satellite Communications," Van Nostrand Reinhold, New York.
- Kaul, R. (1980), "Extension of an Empirical Site Diversity Relation to Varying Rain Regions and Frequencies," URSI Commission F Symposium, Lennoxville, Quebec.
- Kehchiro K., T. Muratani and A. Ogawa (1977), "On-Board Regenerative Repeaters Applied to Digital Satellite Communications," Proc. IEEE, March.
- Kirk, K.W. and J.L. Osterholz (1976), "DCS Digital Transmission System Performance," Defense Communications Engineering Center (DCEC) Technical Report No. 12-76, November.
- Kittiver, C., and D. Westwood (1976), "The Composite Margin Plane - A Tool To Compute Overall Satellite Communications Link Availability," Record, Nat. Telecommun. Conf., Dallas, pp. 49.4.1-7.
- Lin, S.H. (1973), "Statistical Behavior of Rain Attenuation," BSTJ, Vol. 52, No. 4, pp. 557-581.
- Lin, S.H., H.J. Bergmann, and M.V. Pursley, (1980), "Rain Attenuation on Earth-Satellite Paths-Summary of 10-Year Experiments and Studies," Bell System Technical Journal, Vol. 59, No. 2 (Feb.), pp. 183-228.
- Lovell, R.R., (1984), "Giant Step for Communication Satellite Technology," Aerospace America, March.
- Lyon, D.L. (1985), "Personal Computer Communications via Ku-Band Small-Earth Stations," IEEE Journal on Selected Areas in Communications, Vol. SAC-3, No. 3, May 1985.

- Lyons, R.G., (1974) "Combined Effects of Up- and Down-Link Fading Through a Power-Limiting Satellite Repeater," IEEE Trans. Comm., Vol. COM-22, No. 4 (March), pp. 350-352.
- Lyons, R.G. (1976), "A Statistical Analysis of Transmit Power Control to Compensate Up- and Down-Link Fading in an FDMA Satellite Communications Systems," IEEE Trans. Comm., Vol. COM-24, No. 6 (June), pp. 622-636.
- Maseng, T. and P.M. Bakken (1981), "A Stochastic Dynamic Model of Rain Attenuation," IEEE Transa. on Comm., Vol. COM-29, No. 5 (May).
- Mass, J. (1979), "Diversity and Baseline Orientation," IEEE Trans. Ant. Prop. Vol. AP-27, No. 1, pp. 27.
- Matricciani, E., (1987), "Orbital Diversity in Resource-Shared Satellite Communication Systems Above 10 GHz," IEEE J. on Selected Areas In Communications, Vol. SAC-5, No. 4, pp. 714-723.
- Mazur, B., Crozier, S., Lyons, R., and Matyas, R. (1983), "Adaptive Forward Error Correction Techniques in TDMA," Sixth Int. Conf. on Digital Satellite Comm. (Sept.), pp. 12-8 through 12-15.
- McGregor, D.N. (1981), "Communication Satellite System Availability Models," ORI Technical Report 1890, prepared under contract NASW-3436 for NASA Headquarters.
- Moat, R.L., (1986), "ACTS Baseband Processing," IEEE Transactions Comm., Vol. COM-16, No. 4 (September), pp. 578-583.
- Morelli, T., and T. Matitti (1988), "The ITALSAT Satellite Program," proceedings of the AIAA 12th International Communications Satellite Systems Conference, Arlington VA, Mar. 13-17, 1988, pp. 112-121.
- Morgan, W.L., (1985), "The Olympus Family," Satellite Communications Magazine, pp. 35-36, June.
- Morita, K. and I. Higuti (1978), "Statistical Studies on Rain Attenuation and Site Diversity Effect on Earth-to-Satellite Links in Microwave and Millimeter Wavebands," Trans. of the IECE of Japan, Vol. E61, No. 6, pp. 425-432.
- Moy, L.L., Carroll, D.R., and Kirberg, R.J., (1986), "On the effectiveness of Onboard Processing," Proceedings of the AIAA Communication Satellite Systems Conference, March.

- Naderi, F.M., and Campanella, S.J., (1988), "NASA's Advanced Communications Technology Satellite (ACTS): An Overview of the Satellite, the Network, and the Underlying Technologies," Proceedings of 12th International AIAA Communications Satellite Systems Conference, Crystal City, VA, March 1988.
- Nakony, O.G. (1979), "CTS 11.7 GHz Propagation Measurements - Third Year's Data and Final Report," Tech. Rep. TR 79-471.3, GTE Laboratories, Inc., Waltham, MA.
- NASA (1987), Advanced Communications Tectinology Satellite (ACTS) Notice of Intent for Experiments, NASA Headquarters, Mar. 3 [Revision 4, Dec. 1987].
- Northrop, G.M. (1966), "Aids for the Gross Design of Satellite Communication Systems," IEEE Transactions Comm., Vol. COM-14, February.
- Parker, D.E. (1977), "Design Objectives for DCS LOS Digital Radio Links," Defense Communications Engineering Center (DCEC) Engineering Publication No. 27-77, December (DDC AD Number A065354).
- Poley, W.A., G.H. Stevens, S.M. Stevenson, J. Lekan, C.H. Arth, J.E. Hollansworth, and E.F. Miller, (1986), "An Assessment of the Status and Trends in Satellite Communications 1986-2000," NSAS Technical Memorandum #88867, November.
- Rice, P.L. and N.R. Holmberg (1973), "Culumative Time Statistics of SurfacePoint Rainfall Rates," IEEE Trans. Comm., Vol. COM-21, No. 10, pp. 1131-1136.
- Richens, D.M., (1987), "Very Small Aperture Terminals: An Overview," Satellite Directory, pp. 131-135.
- Rosenbaum, A.S. (1970), "Binary PSK Error Probabilities with Multiple Cochannel Interferences," IEEE Transactions on Communications, June.
- Rosenbaum, A.S. and F.E. Glave (1974), "An Error-Probability Upper Bound for Coherent Phase-Shift Keying with Peak-Limited Interference," IEEE Transactions on Communications, January.
- Scarcella, T., and R.V. Abbott, (1983), "Orbital Efficiency Through Satellite Digital Switching," IEEE Communications Magazine, May 1983, pp. 38-46.
- Schwartz, J.J., and L. Schuchman (1982), "Satellite Relayed Tracking and Data Acquisition for the 1990's," ICC'82 Conference Record.

- Schwartz, M., W.R. Bennett, and S. Stein (1966), Communication Systems and Techniques, McGraw-Hill.
- Spilker, J.J., Jr. (1977), Digital Communications by Satellite, Prentice-Hall.
- Strickland, J.I. (1977), "Radiometric Measurements of Site Diversity Improvement at Two Canadian Locations," Proceedings, URSI Commission F Symposium, 28 April - 6 May, LaBaule, France.
- Towner, G.C., R.E. Marshall, W.L. Stutzmann, C.W. Bostian, T. Pratt, E.A. Manus, P.H. Wiley (1982), "Initial Results from the VPI and SU SIRIO Diversity Experiment," Radio Science, Vol. 17, No. 6, pp. 1489-1494.
- Wallace, R.G. (1981), "Site Diversity Effects on Communications Satellite System Availability," ORI Technical Report 1891, prepared under contract NASW-3436 for NASA Headquarters.
- Wilson, R.W. (1970), "A Three-Radiometer Path Diversity Experiment," Bell System Technical Journal, Vol. 49, p. 1239.
- Wilson, R.W. and W.L. Mammel (1973), "Results from a Three Radiometer Path Diversity Experiment," Proceedings of Conference on Propagation of Radio Waves at Frequencies above 10GHz, London, p. 23.
- Wolejsza, C.J., D. Taylor, M. Grossman, and W.P. Osborne, (1987), "Multiple Access Protocols for Data Communications via VSAT Networks," IEEE Communications Magazine, Vol. 25, No. 7, July.

7

1

11

12

13

SUBJECT INDEX

-A-

- Adaptive forward error correction, 7-79, 7-117
- Advanced Communications Technology Satellite (ACTS), 7-18, 7-24, 7-78, 7-117
- Amplitude dispersion data, 5-39
- Amplitude fluctuations, 6-76, 6-101, 6-126, 6-129
- Angle diversity (see: Orbit diversity)
- Angle-of-arrival
 - definitions, 6-94
 - fluctuations, 6-103
- Antenna
 - aperture effects, 6-75
 - axial ratio, 4-15
 - gain equation, 7-52
 - non-ideal performance, 4-15
 - wave interaction, 4-8
- ATDRSS, 7-35
- ATS-5 satellite, 5-21
- ATS-6 satellite, 4-40, 5-3, 5-4, 5-22
- Attenuation
 - clear-air, see gaseous
 - cloud, 1-4, 7-63
 - co-polarized (CPA), 4-33
 - differential, 4-29
 - dust, 6-73, 7-63
 - fog, 1-4, 6-71
 - gaseous, 6-7, 7-63
 - rain, 1-6, 3-1
 - sand, 6-73
 - specific rain, 2-7, 2-11, 4-25
- Attenuation, rate of change, 6-56
- Attenuation statistics
 - 11.5 - 11.7 GHz, 5-8
 - 15 - 16 GHz, 5-18
 - 19 - 20 GHz, 5-22
 - 28 - 35 GHz, 5-22
 - analytic estimates, 6-20
 - diurnal distribution, 5-29
 - elevation angle scaling, 5-15, 6-48
 - extension, 6-44
 - extension example, 6-48
 - fade duration distribution, 5-35
 - format, 5-5
 - frequency scaling, 5-25, 6-47
 - histograms, 5-27, 5-31, 5-34
 - joint attenuation - depolarization, 5-36, 7-60

- monthly distribution, 5-28
- prediction
 - from limited rain rate and attenuation statistics, 6-43
 - from rain rate statistics, 6-41
 - using CCIR model, 6-32
 - using Global model, 6-23
- procedures for calculating, 6-20
- worst month, 6-59
- Availability, 7-8, 7-73
- Axial ratio 4-7, 4-16

-B-

- Bandwidth coherence
 - ionospheric effects, 6-129
 - tropospheric effects, 6-126
- Beacons (see: Propagation beacons)
- Bit error rate, 7-9
- BS satellite, 5-3, 5-4

-C-

- Canting angle, 4-29, 4-37
- CCIR (International Radio Consultative Committee), 5-1, 7-9
 - rain attenuation model, 3-2, 3-44, 6-32, 6-37
 - sample calculation, 6-35
 - rain depolarization model, 4-36
- Clear-air attenuation, 6-7, 7-63
- Clear-air fluctuations, 6-75
- Climatological Data Reports, 2-16
- Clouds
 - attenuation statistics, 6-67
 - measured attenuation, 6-64
 - water content, 6-64
- Coherence bandwidth
 - amplitude variations, 6-126
 - experimental results, 6-127
 - ionospheric effects, 6-129
 - phase variations, 6-129
 - tropospheric effects, 6-126
- COMSTAR satellite, 4-40, 5-4, 5-22, 5-28, 5-29, 5-36, 5-39
- Copolarized attenuation (CPA), 4-33, 5-33
- Copolarized wave, 4-2, 4-15
- Crosspolarization, 1-6
 - discrimination (XPD), 4-2, 4-13, 4-32, 5-33
 - isolation (XPI), 4-2
 - signal phase, 4-43
- Crosspolarized wave, 4-2
- CS satellite, 5-3, 5-4, 5-24
- CTS satellite, 4-40, 5-4, 5-8
- Cumulative statistics, 5-8
 - definition, 6-19
 - format, 5-5
- Cyclonic storm, 2-2

-D-

Data rate reduction, 7-80, 7-120

Debris rainfall, 3-42

Defense Communications Agency (DCA), 7-9

Delay

ionospheric, 6-5

tropospheric, 6-5

Department of Commerce (DOC), 6-2

Depolarization

analysis, 7-58

data, 4-39, 5-33, 6-105

11.7 GHz

19 GHz, 5-36

28 GHz, 5-36

joint depolarization - attenuation, 5-36, 7-60

phase variations, 4-43

definition of terms, 4-1

hail and snow, 4-6, 6-120

hydrometeor, 4-4, 6-104

ice crystal, 4-5, 4-47

elevation angle and frequency dependence, 6-113

ice crystal parameters, 4-47, 6-115

measurements, 6-115

model, 4-49, 6-119

mathematical formulations, 4-7, 6-105

multipath, 4-4, 6-120

due to refractivity gradients

prediction, 6-104

rain, 1-6, 4-4, 4-5, 4-23, 6-106

CCIR approximation, 1-7, 4-36, 5-33, 6-106

elevation angle dependence, 4-45, 6-113

experimental results, 4-39, 5-33, 6-107

frequency dependence, scaling, 4-45, 6-111

phase variations, 4-43, 6-115

prediction of statistics, 6-19

rate of change, 4-44

statistical characteristics, 4-39

theory, 4-23

versus rain attenuation, 4-33

snow, 6-120

sources, 6-104

Design procedure

examples, 7-44, 7-51, 7-68

introduction, 7-36

path performance, 7-37

Distrometer, 2-10

Dispersion, phase and amplitude, 5-39

Diversity

frequency, 7-79, 7-119

measures of performance, 7-80

orbit, 7-79, 7-84, 7-107

- measurements, 7-109
- path, see site
- signal 7-111
- site, 7-79, 7-86
 - definition, 7-80
 - design factors, 7-88
 - empirical models, 7-93, 7-95, 7-102, 7-107
 - experiments, 7-86
- space, 7-83
- Diversity advantage, 7-81
- Diversity improvement, 7-80
- Diversity gain
 - analytic model, 7-102
 - definition, 7-80
 - empirical model, 7-93
 - empirical model extension, 7-95
 - relative, 7-107
- Drop size distribution, 2-7
- DSCS III satellite, 7-30
- Dust attenuation, 6-73
- Dutton-Dougherty rain attenuation model, 3-2, 3-12

-E-

- ECS satellite, 5-3, 5-4
- Effective path length
 - attenuation model comparisons, 3-70
 - definition, 3-63
 - frequency dependence, 3-64
- Elevation angle scaling
 - depolarization, 6-113
 - rain attenuation, 6-48
- Elliptical polarization, 4-11
- ETS-II satellite, 5-3, 5-4, 5-19, 5-24, 5-35
- European Broadcasting Union, 7-32

-F-

- Fade
 - distribution function, 6-95
 - mitigation, 7-78
 - simultaneous probabilities, 7-121
 - temporal distribution, 5-28
- Fade duration, 5-32, 6-50
 - annual distribution, 5-35, 6-56
 - daily distribution, 6-56
 - versus frequency of occurrence, 6-50
- Federal Communications Commission (FCC), 6-2
- FLTSATCOM satellite, 7-30
- Fluctuations
 - amplitude, 6-76, 6-101
 - antenna aperture effects, 6-75
 - computation of
 - amplitude, 6-101

- angle-of-arrival, 6-103
- gain reduction, 6-103
- RMS phase delay, 6-103
- distribution function, 6-95
- example, 6-101
- gain degradation, 6-98
- overview of amplitude, 6-76
- phase, 6-90
- phase delay, 6-90
- phase ripple, 6-92
- phase ripple gain degradation, 6-94
- power spectral density of amplitude, 6-82
- variance of signal amplitude, 6-76

Fog

- attenuation, 6-71
- attenuation prediction model, 6-72
- visibility
- water content, 6-71

Forward error correction (FEC), 7-28, 7-118

- adaptive, 7-79, 7-117

Free space path loss, 7-52

Frequency bands, 6-2

Frequency diversity, 7-79, 7-119

Frequency reuse, 4-1, 5-36

Frequency scaling

- for polarization, 6-111
- for rain attenuation, 5-25, 6-47

-G-

Gain degradation, 6-82

- design information, 6-95
- domains, 6-98
- sample computation, 6-101

Gaseous attenuation

- elevation angle dependence, 6-12
- estimation procedure, 6-12
- frequency dependence, 6-7
- ground station altitude dependence, 6-8
- prediction, 6-6
- sample calculation, 6-16
- sources, 6-6
- standard deviation, 6-9
- surface temperature dependence, 6-12
- water vapor dependence, 6-8

Global rain attenuation model, 1-7, 3-2, 3-17, 6-23

- sample calculation, 6-29

-H-

Hourly Precipitation Data Report, 2-16

Hydrometeors, 4-4

-I-

Ice, meteorological presence, 4-47
Ice depolarization (see: Depolarization, ice crystal)
INTELSAT VI satellite, 7-19, 7-29
Intense rain events
 annual and daily distributions, 6-56
Interference, 6-75
International Radio Consultative Committee: see CCIR
International Telecommunications Union (ITU), 6-2
Ionospheric effects, 6-5
Isolation, 4-4, 4-17
Isotherm, 0°C, 2-4, 3-26, 3-38
ITALSAT satellite, 7-33

-J-

Joss drop size distributions, 2-7

-K-

Laws and Parsons drop size distribution, 2-7
Lin rain attenuation model, 3-2, 3-54
Local Climatological Data Report, 2-17
Low-angle fading, 6-85
 selected experimental results, 6-85
Low-angle scintillation, 6-82

-M-

Marshall-Palmer drop size distribution, 2-7
Model,
 CCIR, rain attenuation, 3-2, 3-44, 6-32
 CCIR, depolarization, 4-36, 5-33
 Dutton-Dougherty, 3-2, 3-12
 Global, 1-7, 3-2, 3-17, 6-23
 ice depolarization, 4-49
 Lin, 3-2, 3-54
 piecewise uniform, 3-59
 rain rate, 3-1
 rain depolarization, 4-23
 Rice-Holmberg, 3-2, 3-5
 SAM (Simple Attenuation Model), 3-2, 3-58
 two-component, 3-2, 3-39
Multipath depolarization, 6-120

-N-

National Climatic Data Center, 2-16
Noise (see also: Sky noise)
 cloud, 6-64
 sky, 1-4, 6-130
 temperature, 1-4
 uplink, 6-143
Non-ideal antenna, 4-15

-O-

OLYMPUS-1 satellite, 7-31, 7-34

On-board processing, 7-20, 7-25, 7-34
 Orbit diversity, 7-79, 7-84, 7-107
 measurements, 7-109
 OTS satellite, 5-3, 5-4, 5-18, 5-20
 Outage
 duration, 7-8
 period, 3-4
 time 7-49
 Oxygen absorption, 1-3

 -P-
 Partial pressure, saturated, 6-16
 Path diversity (see: Site diversity)
 Performance criteria, 7-7, 7-15
 analog transmission, 7-12
 digital transmission, 7-9
 examples, 7-44, 7-53, 7-68
 Phase dispersion data, 5-39
 Phase fluctuations, 6-90, 6-103, 6-129, 6-131
 Piecewise uniform rain rate model, 3-59
 Polarization isolation, 4-2
 Polarization mismatch factor, 4-10
 Polarization states, 4-7
 Power budget equation, 7-53
 Power control, 7-79, 7-112
 downlink, 7-115
 uplink, 7-114
 Power spectral density, 6-82
 Prediction
 amplitude fluctuations, 6-76
 angle of arrival, 6-94
 depolarization, 6-104, 6-122
 CCIR approximation for rain, 6-106
 CCIR factor for ice, 6-119
 fog, 6-72
 gaseous attenuation, 6-6, 6-11
 gain degradation, 6-82, 6-103
 introduction, 6-1
 phase delay, 6-90
 power spectral density, 6-82
 rain attenuation, 6-20
 CCIR model, 6-32
 Global model, 6-23
 Propagation beacons
 ACTS, 7-26
 Italsat, 7-33
 Olympus, 7-32
 summary table, 5-3
 Propagation data, 5-1
 11.5 - 11.7 GHz, 5-8
 15 - 16 GHz, 5-18
 19 - 20 GHz, 5-22

- 28 - 35 GHz, 5-22
- format, 5-5
- phase and amplitude dispersion, 5-39
- satellites used, 5-4
- summaries, 5-1
- temporal fade distribution, 5-28

-R-

Rain

- convective, 2-2
- debris, 3-42
- depolarization (see: Depolarization, rain)
- gauges, 2-23
- gauge integration time, 2-31
- spatial distribution, 2-2
- specific attenuation
- stratiform, 2-2
- volume cell, 3-41
- Rain attenuation, 1-6, 3-1
 - measurements (see: Propagation data)
 - models summary, 3-2
 - model comparisons, 3-61
 - statistics: see Attenuation statistics
 - prediction: see Prediction, rain attenuation
- Rain fade mitigation, 7-78
- Rain rate
 - climate regions
 - CCIR, 3-45, 6-38
 - Global, 3-21, 6-24
 - cumulative distribution, 3-3, 6-26, 6-34
 - estimation from rain gauge records, 2-25, 2-28
 - long term distributions, 2-3
 - measurement, 2-23
 - models, 3-2
 - path averaged, 3-29, 3-53, 3-55, 3-59
 - point, 3-1, 3-15, 3-18
 - short term distributions, 2-4
 - statistics, 2-1, 3-3
 - time variation, 2-25, 3-4, 5-28, 5-32
- Rainfall data, sources and types
 - Canada, 2-26
 - U.S., 2-13
 - worldwide, 2-28
- Rate of change of attenuation, 6-56
- Rate reduction, 7-80, 7-112
- Rayleigh scattering, 2-7
- Reflectivity factor, 2-4, 6-122
- Relative humidity, 6-16
- Resource sharing, 7-78
- Rice-Holmberg rain rate model, 3-2, 3-5

-S-

SAM (Simple Attenuation Model), 3-2, 3-58
 Sand attenuation, 6-73
 Satellites
 ACTS, 7-18, 7-24, 7-78, 7-117
 ATDRSS, 7-35
 ATS-5, 5-21
 ATS-6, 4-40, 5-3, 5-4, 5-22
 BS, 5-3, 5-4
 COMSTAR, 4-40, 5-4, 5-22, 5-28, 5-29, 5-36, 5-39
 CS, 5-3, 5-4, 5-24
 CTS, 4-40, 5-4, 5-8
 DSCS III, 7-30
 ECS, 5-3, 5-4
 ETS-II, 5-3, 5-4, 5-19, 5-24, 5-35
 FLTSATCOM, 7-30
 INTELSAT-VI, 7-19, 7-29
 ITALSAT, 7-33
 OTS, 5-3, 5-4, 5-18, 5-20
 SIRIO, 4-40, 5-3, 5-4, 5-18, 5-19, 5-20
 Saturated partial pressure, 6-16
 Scintillation
 amplitude, 6-76, 6-101
 distribution function, 6-95
 phase, 6-90, 6-103
 Signal diversity, 7-111
 SIRIO satellite, 4-40, 5-3, 5-4, 5-18, 5-19, 5-20
 Site diversity
 analytical model, 7-102, 7-107
 baseline orientation, 7-90
 definition, 7-80
 design factors, 7-88
 elevation angle, 7-90
 empirical model, 7-93
 experiments summary, 7-86
 extended empirical model, 7-95
 frequency dependence, 7-91
 interstation link, 7-92
 local climatology, 7-92
 multiple earth terminals, 7-93
 path azimuth angle, 7-90
 rain cell anisotropy, 7-91
 separation distance, 7-88
 switching rates, 7-92
 Sky noise, 1-4, 6-130
 clear-air, 6-131
 clouds, 6-139
 computation of multiple contributors, 6-140
 dust, 6-139
 extraterrestrial sources, 6-140
 fog, 6-139
 lunar, 6-142

- radio stars, 6-142
- rain, 1-6, 6-136
- sample calculations, 6-136
- sand, 6-139
- solar, 6-140
- uplink, 6-143
- Sky noise temperature, 1-6
- Space diversity, 7-83
- Specific attenuation
 - dry air, 6-13
 - rain, 2-7, 2-11
 - frequency dependence, 2-11
 - rain rate dependence, 2-11, 2-14
 - regression values, 2-12, 2-14, 6-40
 - water droplets, 6-62
 - water vapor, 6-62
- Storm Data Report, 2-17
- SS/TDMA 7-17, 7-32
- System design
 - availability allocation, 7-37, 7-73
 - clear-air absorption, 7-63
 - composite carrier-to-noise ratio, 7-48, 7-71
 - depolarization analysis, 7-58
 - initial phase, 7-43
 - overview of procedure, 7-1
 - phases, 7-40
 - power budget, 7-50
 - sample calculation, 7-64
 - process, 7-3, 7-41
 - propagation analysis, 7-42, 7-55, 7-63
 - rain margin, 7-55
 - synthesis phase, 7-46
 - sample calculation, 7-52
- System performance criteria
 - analog, 7-12
 - bit error rate, 7-9
 - CCIR, 7-9
 - DCA, 7-9
 - digital, 7-9
 - examples, 7-43
 - overview summary, 7-7

-T-

- TDMA (time division multiple access), 6-5, 7-17, 7-21, 7-117
 - satellite switched (SS), 7-17, 7-32
- Telecommunications services, 6-4
- Throughput, 7-11
- Transmission coefficient, 4-25
- Tropospheric delays, 6-5
- Two-component rain attenuation model, 3-2, 3-39

-U-

- Uplink Noise, 6-143

-V-

Volume cell rainfall, 3-41

VSAT, 7-23

-W-

Wave antenna interaction, 4-8

Water vapor

and relative humidity, 6-16

definition, 6-16

density, 6-14

specific attenuation, 6-13

Worst month statistics, 6-59

-X-

XPD (see: Crosspolarization discrimination)

XPI (see: Crosspolarization isolation)

-Z-

Zero degree isotherm, 2-4, 3-26, 3-38, 6-23



Report Documentation Page

1. Report No. NASA RP-1082(04)		2. Government Accession No.		3. Recipient's Catalog No.	
4. Title and Subtitle Propagation Effects Handbook for Satellite Systems Design - A Summary of Propagation Impairments on 10 to 100 GHz Satellite Links With Techniques for System Design			5. Report Date February 1989		
			6. Performing Organization Code		
7. Author(s) Louis J. Ippolito			8. Performing Organization Report No.		
			10. Work Unit No.		
9. Performing Organization Name and Address Westinghouse Electric Corporation Friendship Site Box 1897 Baltimore, MD 21203			11. Contract or Grant No. NAS7-100;958178(JPL)		
			13. Type of Report and Period Covered Reference Publication (Fourth Edition)		
12. Sponsoring Agency Name and Address National Aeronautics and Space Administration Washington, DC 20546 Office of Space Science and Applications			14. Sponsoring Agency Code		
			15. Supplementary Notes		
16. Abstract The NASA Propagation Effects Handbook for Satellite Systems Design provides a systematic compilation of the major propagation effects experienced on space-Earth paths in the 10 to 100 GHz frequency band region. It provides both a detailed description of the propagation phenomena and a summary of the impact of the effect on communications system design and performance. Chapters II through V describe the propagation effects, prediction models, and available experimental data bases. In Chapter VI, design techniques and prediction methods available for evaluating propagation effects on space-Earth communications systems are presented. Chapter VII addresses the system design process and how the effects of propagation on system design and performance should be considered and how they can be mitigated. Examples of operational and planned K_u , K_a , and EHF satellite communications systems are given.					
17. Key Words (Suggested by Author(s)) Microwave Propagation, Rain Attenuation, Satellite Communications Systems, K_u , K_a , EHF Propagation, Radio Noise			18. Distribution Statement Unclassified - Unlimited Subject Category 32		
19. Security Classif. (of this report) Unclassified		20. Security Classif. (of this page) Unclassified		21. No. of pages 536	22. Price A23

